

OCEANOLOGIA

QUARTERLY JOURNAL
OF BASIC RESEARCH
IN MARINE SCIENCES
WITH EMPHASIS ON
EUROPEAN SEAS

66(2)
2024



Oceanologia

Official Journal of the Polish Academy of Sciences



EDITOR-IN-CHIEF

Jacek Piskozub
Institute of Oceanology, Polish Academy of Sciences, Sopot, Poland

MANAGING EDITOR

Agata Bielecka – abielecka@iopan.pl

Editorial Office Address

Institute of Oceanology, Polish Academy of Sciences (IO PAN)
Powstańców Warszawy 55
81–712 Sopot, Poland
e-mail address: editor@iopan.pl

THEMATIC EDITORS

Katarzyna Błachowiak-Samołyk – Institute of Oceanology, Polish Academy of Sciences, Sopot, Poland

Artur Burzyński – Institute of Oceanology, Polish Academy of Sciences, Sopot, Poland

Piotr Kowalczyk – Institute of Oceanology, Polish Academy of Sciences, Sopot, Poland

Krzysztof Opaliński – Institute of Ecology and Bioethics, Warsaw, Poland

Żaneta Polkowska – Gdańsk University of Technology, Gdańsk, Poland

Krzysztof Rychert – Pomeranian University in Stupsk, Poland

Marek Zajączkowski – Institute of Oceanology, Polish Academy of Sciences, Sopot, Poland

ADVISORY BOARD

Xosé Antón Álvarez Salgado
Marine Research Institute, Spanish Research Council (CSIC), Vigo, Spain

Mirosław Darecki
Institute of Oceanology, Polish Academy of Sciences, Sopot, Poland

Jerzy Dera
Institute of Oceanology, Polish Academy of Sciences, Sopot, Poland

Jan Harff
University of Szczecin, Poland; Leibniz-Institute for Baltic Sea Research, Warnemünde, Germany

Agnieszka Herman
Institute of Oceanography, University of Gdańsk, Gdynia, Poland

Alicja Kosakowska
Institute of Oceanology, Polish Academy of Sciences, Sopot, Poland

Matti Leppäranta
Institute of Atmospheric and Earth Sciences, University of Helsinki, Finland

Ewa Lupikasza
Faculty of Earth Sciences, University of Silesia, Sosnowiec, Poland

Hanna Mazur-Marzec
Institute of Oceanography, University of Gdańsk, Gdynia, Poland

David McKee
University of Strathclyde, Glasgow, Scotland, United Kingdom

Dag Myrhaug
Norwegian University of Science and Technology (NTNU), Trondheim, Norway

Tarmo Soomere
Tallinn University of Technology, Estonia

Hans von Storch
Institute of Coastal Research, Helmholtz Center Geesthacht, Germany

Piotr Szefer
Department of Food Sciences, Medical University of Gdańsk, Poland

Muhammet Türkoğlu
Çanakkale Onsekiz Mart University, Turkey

Jan Marcin Węśławski
Institute of Oceanology, Polish Academy of Sciences, Sopot, Poland

This journal is supported by the Ministry of Science and Higher Education, Warsaw, Poland

Indexed in: ISI Journal Master List, Science Citation Index Expanded, Scopus, Current Contents, Zoological Record, Thomson Scientific SSCI, Aquatic Sciences and Fisheries Abstracts, DOAJ

IMPACT FACTOR ANNOUNCED FOR 2022 IN THE 'JOURNAL CITATION REPORTS' IS 2.9; 5-year IF is 2.8. CITESCORE ANNOUNCED FOR 2022 IS 4.3

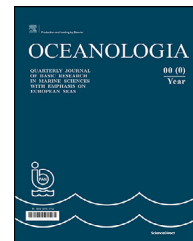
Publisher
Elsevier B.V.
Radarweg 29
1043 NX Amsterdam
The Netherlands

Senior Publisher
Tobias Wesselius
+31 6 5370 3539

ISSN 0078-3234

Available online at www.sciencedirect.com

ScienceDirect

journal homepage: www.journals.elsevier.com/oceanologia

ORIGINAL RESEARCH ARTICLE

Fluctuations of ice in a lake due to the impact of the North Atlantic Oscillation (1960/61–2009/10) – a case study of Łebsko Lake

Artur Młodzik, Roman Cieśliński*, Izabela Chlost

Department of Hydrology, Faculty of Oceanography and Geography, University of Gdańsk, Gdańsk, Poland

Received 13 July 2022; accepted 13 October 2023

Available online 13 November 2023

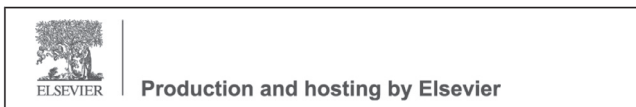
KEYWORDS

Ice conditions;
North Atlantic
Oscillation;
Air temperature;
Global warming;
Satellite imagery

Abstract The paper represents an attempt to understand the impacts produced by the North Atlantic Oscillation on the ice cover regime of the largest coastal lake in Poland situated in the northern part of the country. The purpose of the study was to estimate the impact of the North Atlantic Oscillation on selected ice cover parameters. The study also attempts to examine other factors that may affect its significant impact on observed changes in the climate. Water temperature data are used to assess temperature conditions in aqueous ecosystems as well as determine the heat absorption capacity of these systems. This allows one to then determine cooling rates in the event of ice cover formation. The data analysis provided in the paper focuses on selected characteristics of ice cover conditions (i.e. dependent variables) including the number of days with ice and maximum ice thickness in relation to NAO index changes (i.e. independent variables) for the reference period 1960/61–2009/10. In addition, the paper divides the studied period into 10-year subperiods in order to capture the weakest and strongest phases of NAO and assess the extent to which they affect the duration of ice cover. A large increase in the mean air temperature (1.8°C) occurred in the years 1960–2010. Trendline analysis indicates that the number of days with ice cover declined by about 60 days

* Corresponding author at: University of Gdańsk, Faculty of Oceanography and Geography, Department of Hydrology, Bażyńskiego 4, 80–309, Gdańsk, Poland.

E-mail addresses: arturro19@onet.pl (A. Młodzik), georc@univ.gda.pl (R. Cieśliński), izabela.chlost@ug.edu.pl (I. Chlost).
Peer review under the responsibility of the Institute of Oceanology of the Polish Academy of Sciences.



<https://doi.org/10.1016/j.oceano.2023.10.004>

0078-3234/© 2023 Institute of Oceanology of the Polish Academy of Sciences. Production and hosting by Elsevier B.V. This is an open access article under the CC BY-NC-ND license (<http://creativecommons.org/licenses/by-nc-nd/4.0/>).

and the maximum thickness of ice cover decreased by about 10 cm. Oceanographic research employs satellite image data in order to accurately assess human impact. Therefore, ice cover forecasts generated for consecutive winter seasons may become an important tool in this type of assessment.

© 2023 Institute of Oceanology of the Polish Academy of Sciences. Production and hosting by Elsevier B.V. This is an open access article under the CC BY-NC-ND license (<http://creativecommons.org/licenses/by-nc-nd/4.0/>).

1. Introduction

Research related to the North Atlantic Oscillation remains a mainstream trend given the multiple impacts it produces on the natural environment. Its effects are examined in terms of important hydrologic characteristics such as water level fluctuations (Neves et al., 2019; Sezen and Pertal, 2017; Wrzesiński et al., 2018), the magnitude of river water influx (Wrzesiński and Paluszkiwicz, 2011), and the occurrence of extreme events such as sea storms (West et al., 2018). Many studies also focus on relationships with key meteorologic characteristics such as atmospheric pressure, pluvial conditions, air temperature, as well as wind strength and direction (Dunstone et al., 2016; Smith et al., 2014). Finally, some studies examine the relationship with air mass circulation (Polvani et al., 2017).

Some studies also investigate the effects of NAO on living organisms (Weidberg and Bascadow, 2019). For example, Pärn et al. (2022) examined both temporal and spatial trends in hydrologic characteristics (i.e. water temperature and sea ice) and biochemical characteristics (i.e. concentration of alpha cholesterol) in marine environments. Many papers have been written in the last decade or so on the effects of the North Atlantic Oscillation on changes in ice cover conditions including accelerated ice cover melting (Sharma et al., 2016; Soja et al., 2014).

Ice formation marks a characteristic change in annual temperature conditions in water ecosystems in temperate climate zones. The close relationship between hydrologic processes, climate conditions, and present-day climate change is readily observable in the functioning of bodies of water, especially in the area of ice formation. Air temperature is a climate factor that affects the amount and duration of ice cover. These, in turn, are affected to varying degrees by teleconnection patterns. One of the best-known atmospheric teleconnections dominant over the European continent throughout the year is the North Atlantic Oscillation (NAO) (Delpeche-Ellmann et al., 2016; Haapala et al., 2015; Höglund et al., 2017; Jakimavičius et al., 2020; Vihma and Haapala, 2009).

Given the nontypical location of Lake Łebsko in very close proximity to the Baltic Sea it is reasonable to assert that its local conditions will be determined largely by marine factors. The response time of Lake Łebsko to changes in meteorologic conditions is shorter than usual and the proof for this lies in the lake's observed ice cover patterns. Similar ice cover durations are noted for sea ice in the waters of the southern Baltic Sea; for example, the Gulf of Gdańsk. Omstedt and Chen (2001) note that ice cover is an important indicator when examined together with water circulation patterns and changes in water temperature, which fluctu-

ate significantly from year to year. Research on the Baltic Sea covering the period of the last 100 years shows that the maximum extent of sea ice has ranged from 12% to 100%. In addition, the length of the Baltic Sea ice season has ranged from an average of four to seven months.

The first signs of ice formation are observed more or less in early November, mostly in the Gulf of Bothnia. Maximum ice cover in the Baltic Sea occurs sometime in late February or early March (Höglund et al., 2017; Lepparanta and Seina, 1985). The ice cover begins to break up in April and disappears completely in late May or early June, depending on air temperature patterns in the given season. Research by government agencies in Sweden and Finland shows certain patterns in the appearance of ice cover in the Baltic Sea. This information was then used to create an index that would help classify each ice cover season in the region.

A number of such analyses have confirmed the presence of strong relationships between the extent of ice cover and wintertime air temperature patterns noted for both Stockholm and Helsinki (Omstedt and Chen, 2001; Pärn et al., 2022; Rjazin and Parn, 2020; Vihma and Haapala, 2009). Long-term research on sea ice present near the coastline of Estonia (Jaagus, 2006), Lithuania (Dailidienė et al., 2012; Jakimavičius et al., 2020), Finland (Lepparanta and Seina, 1985; Wenta et al., 2021), and Sweden (Makynen et al., 2020) has made it possible to perform accurate climate trend analyses on the formation and break-up of ice cover. An additional key element of these studies was an analysis of sea and ice cover coupling models that aim to help explain the degree to which ice cover is sensitive to climate change.

Research has shown that sea ice is characterized by high sensitivity to climate factors such as air temperature, wind strength, and snow cover. Ice formation in the ocean occurs differently than that in coastal waters and semi-enclosed seas. Research on changes in ice cover in Hudson Bay and Baffin Bay – in relation to NAO patterns – provided valuable data on ice formation patterns affected by NAO. The general finding was that there exists a fairly strong relationship between ice formation in the sea and variable atmospheric circulation represented by the North Atlantic Oscillation (Omstedt and Axell, 1998; Omstedt and Chen, 2001).

In addition, Wolski and Wiśniewski (2022) were also able to determine the effects of changes in circulation (NAO and AO) on changes in sea levels. Their research has shown that the strongest correlations between sea level and NAO/AO indices occur in the winter months. Consequently, this produces a strong impact on hydrologic characteristics and ice conditions in lakes located very close to the coastline. Lake Łebsko in northern Poland is linked with the sea via a canal that allows for occasional seawater intrusions throughout

the year, which leads to changes in both water chemistry and select physical indicators due to the influx of brackish waters. According to Miller and Hutchins (2017) global climate change will lead to a warmer and wetter winter in temperate climate zones.

Ice cover parameters strongly reflect changes in the water temperature regime noted in the course of each studied year, which is particularly easy to observe for large bodies of water. The first appearance of ice limits the vertical exchange of energy between the water surface and the atmosphere. Ice cover is very sensitive to changes in climate conditions. The positive NAO trend observed over the last decade or so in the wintertime and its larger magnitude are linked with observed climate warming and an enhanced greenhouse effect. The impacts of ongoing climate change are also affecting hydrologic conditions that lead to a delay in the appearance of ice cover or its complete absence in aqueous ecosystems, especially those found in temperate climate zones (Hurrell et al., 2001; Karetnikov and Nauhenko, 2008; Livingstone, 2000).

The main purpose of the paper is to compare the degree to which ice formation patterns noted for Lake Łebsko resemble those noted for the Baltic Sea. Several research questions are posed herein in order to examine this subject. Do changes in air temperature at the moment of ice formation in the water produce the same effects in bays and coastal estuaries? How do local conditions in bays and coastal estuaries accelerate and retard ice cover formation and break-up? Existing studies indicate the existence of a relationship between ice formation parameters and atmospheric circulation parameters; however, the mechanism governing differences in the various areas of the marine environment has not yet been fully deduced.

Research on the relationship between ice cover formation and atmospheric circulation represented by the North Atlantic Oscillation is important, especially when the reference period is divided into shorter subperiods (i.e. decades). The use of shorter time series allows for a more accurate analysis of patterns in place in the course of changes in meteorologic conditions and to assess how local factors affect ice formation in water.

This is confirmed by Athanasiadis et al. (2020) who were able to determine that climate variances in the temperate zone are relatively predictable, although their level of predictability becomes limited over the long term. They were also able to determine that forecasts covering decades are exceptionally good at reflecting observed changes in ice cover formation over the long term and the North Atlantic Oscillation itself. This is partly due to the large size of the dataset, which makes it possible for the predictable component of atmospheric variation to emerge from a chaotic background component. Predictable atmospheric anomalies represent therefore a forced response to oceanic variation occurring with low frequency, which closely resembles the Atlantic Multidecadal Variability (AMV), properly reflected in reverse forecasts for decadelong periods of time thanks to realistic ocean initialization and dynamics.

2. Study area

The object of study in this paper is Lake Łebsko (Figure 1), located in Słowiński National Park in north-

ern Poland. The Park is part of the UNESCO Biosphere Reserve. Lake Łebsko and its catchment formed when a marine bay became separated from the sea by a sandy spit created by wind and wave action on the Baltic Sea. Favorable wind conditions triggered the transport of clastic material, which became deposited over time to form a long sand bar.

Another hypothesis of the formation of the Lake Łebsko catchment is an abrupt rise in groundwater levels across the Gardnieńsko-Łebski Lowland due to poor drainage conditions (Rosa, 1963). The Baltic Sea coastal area in northern Poland consists of a land belt several tens of kilometers wide. It is characterized by a coastal landscape featuring the mouth sections of a number of rivers including the Łeba River. The area also features flat wetlands as well as dune, delta, and marsh-lake-type landscapes. The diverse relief of the area surrounding the Łebsko drainage basin was formed over the course of the last 8,000 years and remains a dynamically changing place affected by wind and wave action coming from the Baltic Sea.

Landform characteristics of the Łebska Sandbar include dune complexes situated up to about 60 meters above sea level. The quaternary soil cover surrounding Lake Łebsko varies in thickness and originates in the Pleistocene and Holocene. The Pleistocene sediments found in the immediate vicinity of the lake's basin consist mainly of sand and gravel. The southeastern part of the lake's catchment area consists mostly of clay and silt. The Holocene soil cover in the study area consists of river-based, lake-based, marine, aeolian, as well as organic-based sediments; these are mostly aeolian sands, while the southern part of the catchment consists mostly of sand, gravel, alluvial material, peat, and silt (Marks et al., 2006). Of the lakes found along the Baltic Sea coastline in Poland, Lake Łebsko is characterized by the most favorable hydrologic conditions. It also features the largest general catchment area at 1,594 km². A beneficial hydrological feature of the lake is undoubtedly it is a drainage with the waters of the Baltic Sea. During stormy situations, the physical and chemical properties of lake waters are changed as a result of the inflow of salty sea water.

The main watercourse recharging the lake is the Łeba River, with average discharge of 13.6 m³ s⁻¹ in the years 1960–2010. Lake Łebsko is a hydraulically active body of water with water exchange occurring more than once per year. Periodic retention is yet another indicator of the storage of water originating in rivers and marine environments. The general vicinity of the studied lake is also characterized by a dense network of drainage ditches that continuously remove water from areas adjacent to the lake. Polders represent yet another landform in the area that occupies about 5,900 hectares of land in the studied catchment. The lake's surroundings also feature wetlands that represent a very unique environmental characteristic protected by the Ramsar Convention. Lake Łebsko is linked with the Baltic Sea via a permanent canal serving also as the mouth section of the Łeba River. The canal is quite deep and was partially rebuilt in early 2001 (Cieśliński and Olszewska, 2018). Lake Łebsko is the largest (71.4 km²) and deepest (6.3 m) coastal lake in Poland; it also stores the largest amount of water (117.5 m³ 10⁶). Its average depth is 1.6 m and the length of its shoreline is 55.4 km.

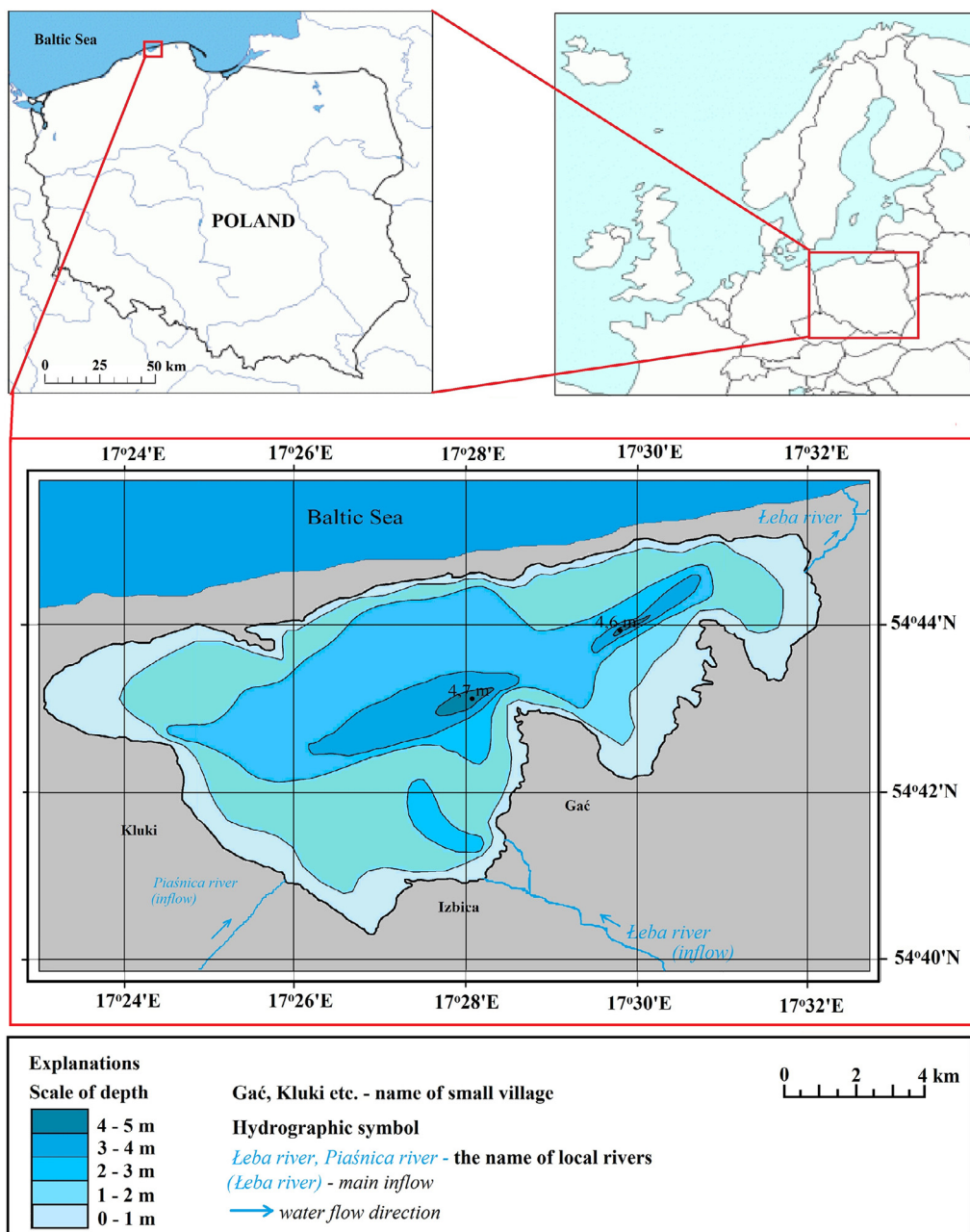


Figure 1 Location of Lake Łebsko along the Baltic Sea coastline.

3. Material and methods

The main source of data in the present study consists of observations of ice conditions in the studied lake. The observations were performed every year at two sites located near the villages of Rąbki and Izbica. The study aims to examine two characteristics of ice cover: (1) number of days with ice cover, (2) maximum thickness of ice cover. The reason why these two particular characteristics were selected in this study is the need to examine the most important ice cover characteristics that also yield the most easy-to-understand results. The study period consisted of the cooler half of the hydrologic year between November and April in the period 1960/61–2009/10. Each studied half-year was further divided into five subperiods.

This division helps to more easily capture key relationships with ice cover conditions. Selected ice cover data were obtained from the Polish Met Office IMGW PIB bureau in Gdynia. The observation of the number of days with ice consisted of average ice cover durations. The thickness of ice cover was measured using a traditional ice sampler. The sampling sites were situated 100 m from the lake's shoreline. Measurements were performed every 10 days during period of stable ice cover. In situations where the ice cover appeared to be too thin to walk across it, ice cover thickness was estimated visually. In order to better understand the reasons for changes in ice cover parameters the study also examines average monthly values of air temperature and water surface temperature (10 cm from the lake) in the Łeba River for the period 1960–2010.

NAO patterns for the study period are presented using normalized values of differences in deviations from average atmospheric pressure at sea level for pressure systems such as the Icelandic Low and Azores High (winter Hurrell index). The study is based on average monthly values collected for cold half-year from November to April in the period 1960/61–2009/10. The values were calculated by NCAR/UCAR and are available at the following web address: https://climatedataguide.ucar.edu/nao_monthly.txt.

The North Atlantic Oscillation Pattern is the dominant atmospheric teleconnection that is present throughout the year. It is referred to as the primary climatic factor that influences the climatic variations observed over the area around the Atlantic. As a result of its operation, precipitation anomalies and variability of air temperature are noted, most pronounced in winter. During the intensification of positive NAO phases, northern Europe experiences wet and warmer winters, and the southern part of the continent experiences a lack of rainfall. The negative NAO phase is the other way around, with cold winters in the north and milder winters in the south (Hurrell, 1995; Visbeck et al., 2001).

Satellite images were also employed to examine visible changes in ice cover in various phases of the Hurrell NAO. Satellite data provide the newest and most up-to-date views of the investigated patterns generated via teleconnections. Such data may be used to assess changes in a lake catchment area. The images were selected from the USGS Earth Explorer database and represent measurements using the synthetic aperture radar used on observational missions by Landsat-1A and Landsat 1-B. In this study, we examine im-

ages with a resolution of 250 m in the visible range obtained via moderate resolution imaging (MODIS).

The next step in the search for the highest legibility consisted of the rejection of images with errors in the form of clouds and areas of fog and the selection of images without the aforementioned errors. The last stage of the process consisted of the vectorization of selected satellite images using ArcGIS Pro in order to obtain the best possible outcomes of image analysis. Most of the graphical illustrations in the paper were created using Corel Draw 4 and Microsoft Excel and Word. The Pearson correlation coefficient was used to analyze data in the study. The statistical significance of these coefficients was examined using the Fisher-Snedecor test. Satellite images obtained from Earth Explorer were analyzed using ArcGIS Pro and subsequently superimposed upon a topographic map of Lake Łebsko (scale: 1:50,000). In addition, the RStudio software package was used to assess the relationship between the Hurrell NAO index and the examined parameters of ice.

4. Results

One effect of changes affecting the ice cover regime in lakes is the shorter duration of ice cover. In light of the variability of the number of days with ice (Figure 2) and maximum ice thickness values (Figure 3) it appears that the ice cover is gradually becoming thinner over time. The number of days with ice in the winter season declined by an average of – 1.2 days per year, while the maximum ice thickness declined at a rate of – 2 mm per year in the study period.

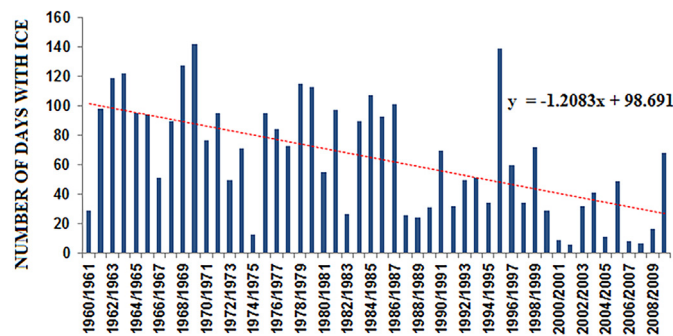


Figure 2 Variability of the number of days with ice observed for Lake Łebsko in the years 1960/61–2009/10.

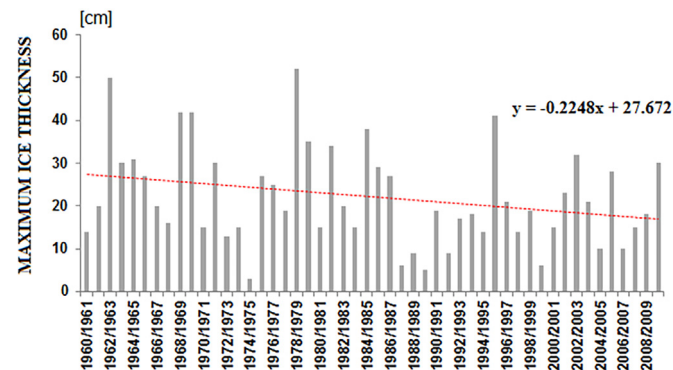


Figure 3 Variability in maximum thickness of ice observed for Lake Łebsko in the years 1960/61–2009/10.

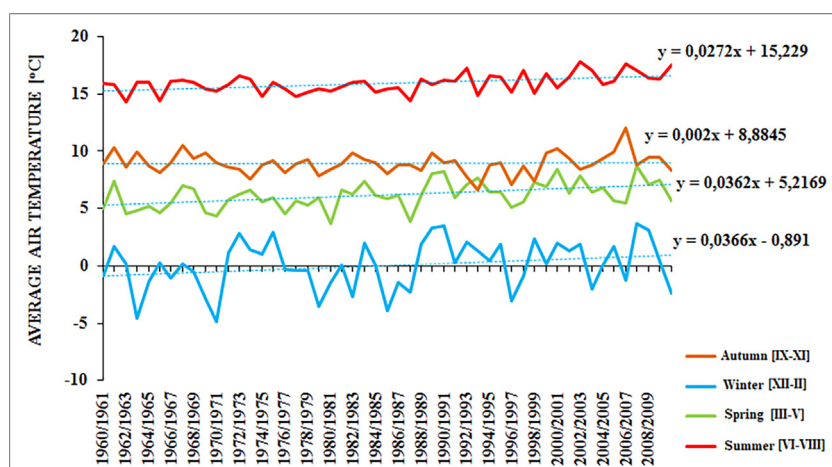


Figure 4 The average air temperature trend for Łeba in the period 1960/61–2009/10 by season.

Table 1 Ice cover characteristics, including three stages of formation and maximum thickness, divided into five-decade time intervals, for Lake Łebsko in the period 1960/61–2009/10.

Łebsko Lake	Freeze up (Date)			Break up (Date)			Duration of ice cover (Days)			Ice cover thickness (cm)		
	earl.	last	avr.	earl.	last	avr.	shrt.	long.	avr.	max.	min.	avr.
I	14.11	17.01	14.12	14.02	17.04	23.03	29	142	108	50	14	29
II	1.11	22.12	11.12	26.02	7.04	16.03	69	159	112	52	3	23
III	7.11	4.02	22.12	22.12	3.04	5.03	27	130	88	38	5	19
IV	18.11	24.12	28.12	29.01	13.04	27.02	34	144	78	41	6	17
V	7.12	9.02	16.01	16.01	18.04	2.03	24	98	53	32	3	15

The number of days with ice decreased by an average of 60 days, while the maximum ice thickness by an average of 10 cm in the study period 1960/61–2009/10. According to [Choiński et al. \(2015\)](#), the duration of ice cover decreased by 56 days, while the ice thickness declined by 6.1 cm in the case of 18 lakes in northern Poland in the period 1960/61–2009/10. These new results closely mirror data provided in earlier research studies. The small difference is likely to be the result of different local conditions present around the lakes studied by Choiński including air temperature, insolation conditions, and various morphometric parameters. Local conditions do play an important role in the formation and break-up of ice cover in each given winter season.

Analysis of ice cover conditions for Lake Łebsko indicates variability in the appearance, duration, and break-up of ice cover. The average date of the first appearance of ice indicates a significant shift from one decade to another. In the first measurement period, ice appeared in mid-December, while in later periods it appeared either in late December or mid-January (Table 1). On the other hand, the average break-up date for ice in the studied area followed a similar pattern in each examined decade. Ice cover duration followed a strong declining trend – in the first and second decades of the study period ice cover remained intact for an average of 108 to 112 days; however, by the years 2001–2010 ice cover duration declined to about 53 days. Yet another examined parameter was ice thickness. As in the case of the previous parameters, the thickness of the studied ice

cover was characterized by a declining rate of 2.5 cm per year, on average.

The description of the impacts of the North Atlantic Oscillation on selected ice cover parameters is based on an analysis of ice cover conditions for Lake Łebsko in the years 1960/61–2009/10. Average monthly air temperature values were compared for the time period from November to April along with changes in the number of days with ice cover and maximum ice thickness values for the study period. The average monthly air temperature in Łeba was found to increase significantly over time (Figure 4). Trend line analysis shows that the largest increase in average air temperature occurred in the winter and spring seasons at 0.03°C ($p < 0.05$). Data on the largest positive change in air temperature for Łeba for the winter and spring clearly show a decline in the duration of ice cover on Lake Łebsko. One effect of the observed changes will be a systematic shift in ice formation and ice break-up dates. The duration of the ice cover in the studied area was found to be significantly shorter over time.

An increasing trend in water temperature in Lake Łebsko was noted up to a maximum depth of 6.3 m. The trend line (Figure 5) indicates that the largest increase occurred in spring, for an average of 0.04°C, and in summer, for an average of 0.03°C ($p < 0.05$). The observed rise in water temperature in spring indicates a faster break-up of the ice cover, while high values in the summertime alter the temperature regime of the lake. In light of these patterns, the time it will take for water to freeze will be longer, leading

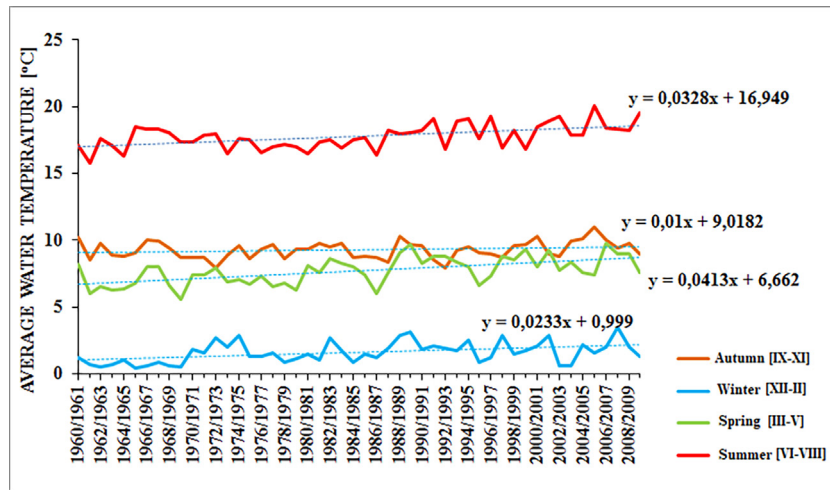


Figure 5 Average water temperature in Lake Łebsko in the years 1960/61–2009/10 by season.

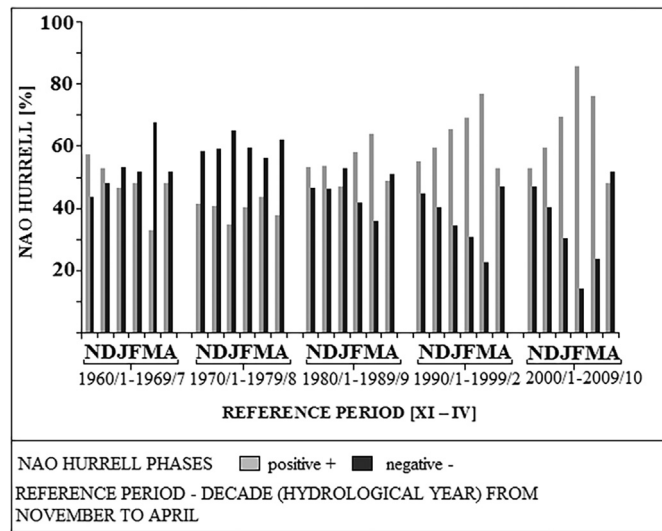


Figure 6 Percentage breakdown of the Hurrell NAO index for the colder half of the year, November to April, by decade for the period 1960/61–2009/10.

to a delay in ice cover formation. The currently observed global increase in air temperatures strongly affects the heat regime of both flowing and standing water. Global warming is producing irreversible changes in water ecosystems. The results obtained in this study confirm the presence of climate warming via changes in air circulation in the Earth’s atmosphere, which in turn either accelerates or retards the formation and break-up of ice cover. In effect, the ice cover duration in water is becoming shorter and the ice is also becoming thinner.

Large seasonal fluctuations in the value of the Hurrell NAO index were noted for the cooler months of the year, from November to April. The first decade (Figure 6) is characterized by a fairly balanced situation, although one dominated by negative values. In the second decade, negative values occur more often than positive values, which is reflected in ice cover duration values for Lake Łebsko. The share of positive Hurrell NAO index values for the winter-time significantly increases in the third, fourth, and fifth decades of the study period. The fluctuation in the Hurrell

NAO index with a predominance of positive values implies an increasing trend in air temperature, which is rather strongly correlated with the aforementioned index.

Correlation coefficients between the studied ice cover parameters and the NAO index range from -0.3 to -0.8 for each decade. A negative NAO phase is noted for the years 1961–1970, which extends the period with ice cover and maximum ice thickness, with a range of correlation values from -0.69 to -0.78 (Table 2). Correlation coefficients for the period 1971–1980 are much smaller and do not exceed 0.69. In the years 1981–1990, the strongest correlation is noted for maximum ice thickness in January and February at approximately -0.8 ($p < 0.001$). Positive correlation coefficients between ice cover parameters and the NAO index were noted for February and March – the likelihood of the occurrence of such coefficients was higher for the late winter season and early winter season.

The values obtained herein suggest significant warming that prevented the formation of ice on the water surface or ice formation across small surfaces subject to rapid melting.

Table 2 Pearson's coefficients of linear correlation between the Hurrell NAO index and the number of days with ice and maximum ice thickness on Lake Łebsko during the ice season in the years 1960/61–2009/10.

North Atlantic Oscillation (Hurrell) Monthly									
Ice season	XI-XII	XI-I	XII-I	XII-II	I-II	I-III	II-III	II-IV	XI-IV
I	-0.619	-0.778	-0.780	-0.725	-0.551	-0.751	-0.564	-0.453	-0.733
1961/1970	-0.303	-0.751	-0.767	-0.695	-0.735	-0.775	-0.354	-0.214	-0.602
II	-0.226	-0.548	-0.627	-0.503	-0.447	-0.295	0.129	0.252	-0.250
1971/1980	-0.082	-0.492	-0.685	-0.603	-0.599	-0.441	-0.014	0.091	-0.292
III	0.136	-0.349	-0.417	-0.599	-0.659	-0.674	-0.516	-0.376	-0.601
1981/1990	0.393	-0.100	-0.358	-0.654	-0.799	-0.652	-0.418	-0.334	-0.379
IV	-0.726	-0.622	-0.487	-0.606	-0.514	-0.728	-0.721	-0.695	-0.708
1991/2000	-0.746	-0.639	-0.528	-0.672	-0.572	-0.694	-0.670	-0.648	-0.704
V	-0.377	-0.498	-0.557	-0.724	-0.761	-0.666	-0.595	-0.601	-0.669
2001/2010									

Row #1: Number of days with ice. Row #2: Maximum ice thickness. Black numbers shown in bold indicate the strongest negative correlations. Statistical significance level – dark color < 0.001, lighter color < 0.02, lightest color < 0.05.

The next decade (1991–2000) (Table 2) was characterized by a stronger, negative NAO phase, and correlation coefficients ranged from -0.65 to -0.75 . The difference is related to ice duration in water. In the first studied decade correlation coefficients reflected a relatively stable ice season. Gaps were observed since the fourth studied decade in the form of coefficients as low as -0.62 . Correlation coefficients for the fifth decade (2011–2010) were highly variable – the strongest correlations were noted between December and February or in the middle of winter when ice cover appears most frequently. The remaining 3 seasons were characterized by much weaker correlations – in most cases, they were statistically significant.

On the graph illustrating the relationship between NAO values and selected data on ice cover (Figure 7a,b) most of the points are scattered. The distance to the regression curve is a reflection of each given winter season. In the period 1961–1970, the strongest relationship between the number of days with ice and Hurrell's NAO index was noted from late December to early January (-0.78), while for maximum ice thickness, the strongest relationship was noted between January and March (-0.77). In addition, NAO index values explain about 60% of the variance in selected characteristics of ice cover.

Most of the NAO values obtained in the study for the period 1991–2000 were positive. The scattered pattern of points observed in Figure 8a,b also indicates a different course of ice events during each studied winter season. The strongest relationship between the parameters used in the study occurred for days with ice cover in the period January–March (-0.72) and for maximum ice thickness in November and December (-0.74). Fluctuations in the NAO index explain about 53% of the variation in the number of days with ice and 56% of the variation in maximum ice thickness.

The last studied decade (2001–2010) was characterized by some of the lowest numbers of days with ice and the smallest ice thickness only slightly exceeding 30 cm. The largest changes were observed for days with ice cover, although in most cases this was no more than 60 days. The strongest relationship between the NAO index and num-

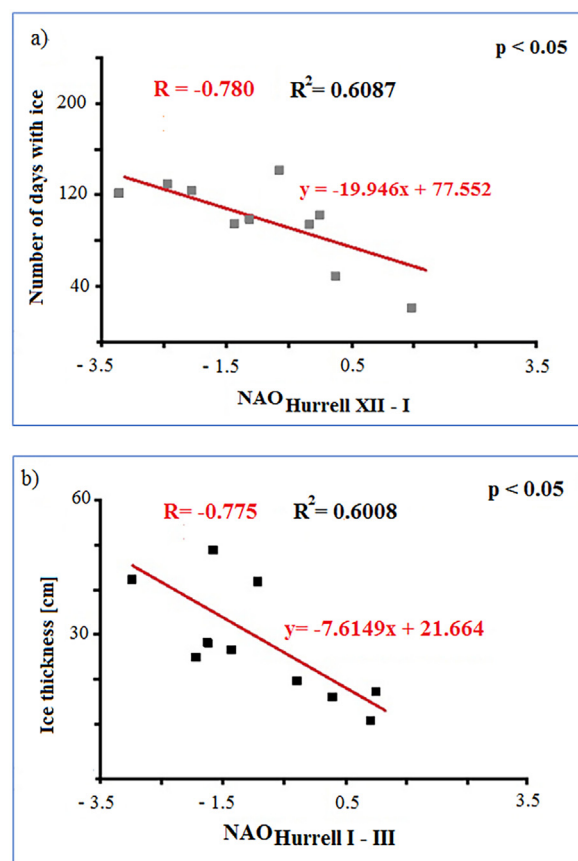


Figure 7 Relationship between the number of days with ice (a), maximum ice thickness (b), and the NAO index for ice cover present on Lake Łebsko in the years 1961–1970.

ber of days with ice (Figure 9a) was noted for January and February (-0.76), while for maximum ice thickness (Figure 9b) this was both December and January (-0.72). Fluctuations in the NAO index explain about 58% of the variance in the number of days with ice and 52% of the variance in maximum ice thickness.

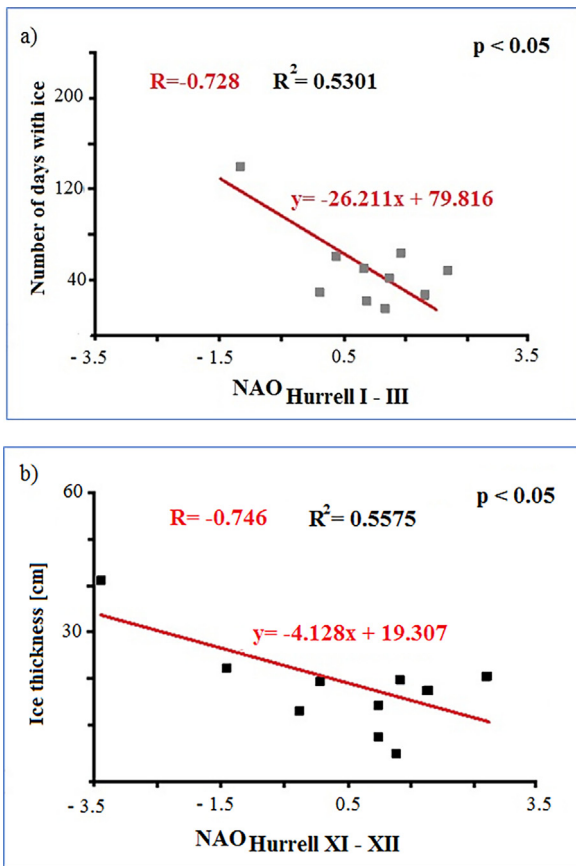


Figure 8 Relationship between the number of days with ice (a), maximum ice thickness (b), and the NAO index for ice cover present on Lake Łebsko in the years 1991–2000.

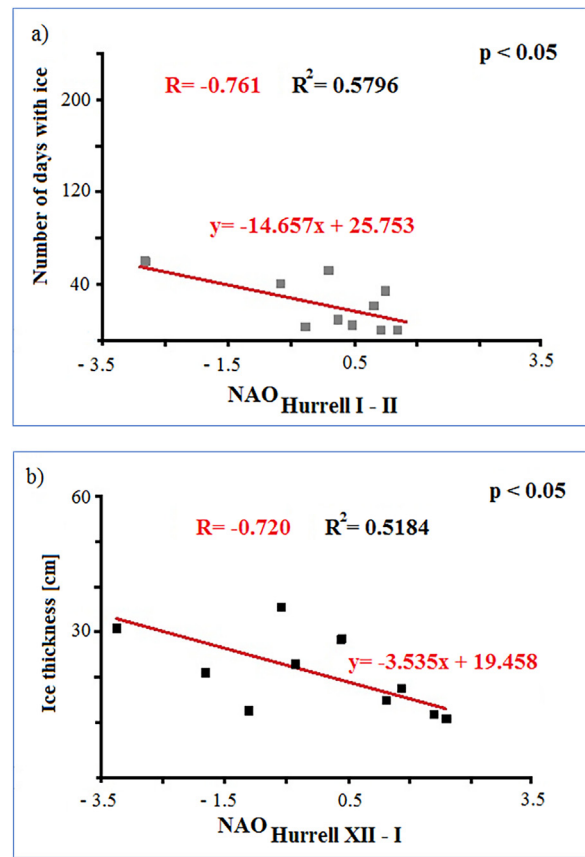


Figure 9 Relationship between the number of days with ice (a), maximum ice thickness (b), and the NAO index for ice cover present on Lake Łebsko in the years 2001–2010.

The interpretation of satellite images represents a simple way to determine the tendency to form ice cover in a given area. The choice of the right timeframe when the first signs of ice formation appear in the water helps explain the entire process of ice formation in a given area. Lake Łebsko is quite large and features a highly irregular shoreline. Large parts of the lake are characterized by shallow waters along its shoreline. It is in these shallow areas where water is most rapidly affected by fluctuations in air temperature. The water cools quickly and allows for freezing to occur. Figure 10 shows the situation in mid-November 2002 – only some ice cover across the shallower parts of the lake was observed.

In spite of the fact that the air temperature oscillates around -0.8°C , air masses arriving from the northwest do not permit significant ice formation on the surface of the studied lake. The situation changes after only a few days when the NAO phase shifts to negative, with air temperatures falling to about -8.9°C and the dominant wind direction is NE. Ice cover grows almost fourfold from a mere 7%. The NAO affected the situation somewhat differently between January 11 and January 15, 2005. At first, the air temperature approaches $+1.1^{\circ}\text{C}$, and ice cover encompasses about 25% of the surface area of the lake. The situation deteriorates over the next few days, with the dominant wind direction being N, air temperature oscillating around -5.6°C (Figure 10), and ice covering about 82% of the lake.

A water mass free of ice is found only at the deepest sites in the lake, where it cools much more slowly.

The third air circulation scenario affects the studied ice regime in a very different way compared with the previous two (Figure 10). On December 2, 2010, the lake was 94% covered in ice. The air temperature was about -12.6°C and remained at that level for the next few days. The main wind direction was ENE. The freezing continental air masses led to significant ice cover on the studied lake. The situation began to change on December 9, 2010. Air temperature increases to $+6.4^{\circ}\text{C}$, with the dominant wind direction being NW, and the NAO phase shifts to positive. The outcome of shifts in air masses is a reduction in ice cover from 94% to 58%. What is also noteworthy is the site where the Łeba River enters the lake, as this is the place where the ice breaks up faster.

The ice breaks up usually in the second half of March. This was the situation prior to the 1980s. While some winters were in fact harsh, it was possible to observe ice break-up during milder winters. Winters in the last 20 years or so have been characterized by medium ice cover duration and mostly low snowfall amounts. All of the above trends have gradually produced a global rise in air temperatures that continues to alter the heat regime of flowing bodies of water as well as of bodies of standing water. The description of the break-up of ice cover begins with the situation shown in Figure 11. The date is February 4, 2003. Lake Łebsko is fully

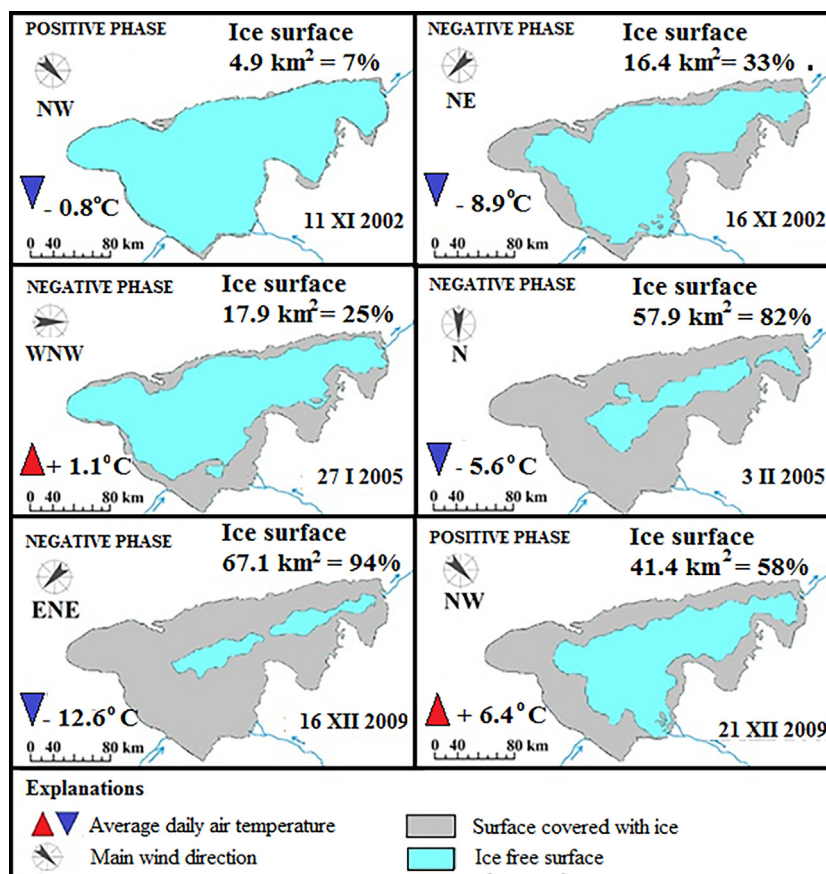


Figure 10 Characteristics of each Hurrell NAO phase (positive +) (negative -) for Lake Łebsko for ice cover events on the lake – based on satellite images.

covered with ice of variable thickness. The dominant wind direction is W, while the air temperature is around the -18.2°C mark. The low temperature remains in place for several days, strengthening the growing negative NAO phase.

After several days, by February 9, 2003, the situation in the area changed substantially. Lake Łebsko was no longer fully covered with ice, but 78% covered (Figure 11). The predominant wind direction was now NW. The positive NAO phase gained strength, leading to an increase in air temperature, although still below freezing (-0.4°C), which led to the breakup of about 22% of the ice cover. The March 28, 2005 situation illustrates another NAO pattern during the ice season on Lake Łebsko. The predominant wind direction is NE, and the wind is rather cool. The air temperature measures at $+2.3^{\circ}\text{C}$. Most of the lake's surface is free of ice – the remaining ice cover stands at about 36%.

By April 3, 2005 (Figure 11) the negative NAO phase becomes stronger. This does not lead to an increase in the amount of ice; in fact, it leads to a gradual reduction in ice cover – a threefold reduction. The air temperature rises substantially to $+9.4^{\circ}\text{C}$, and the dominant wind direction is WSW. This air mass fluctuation scenario yields similar results to the previous two, with only the date of ice break-up being different. This third ice break-up date occurs later than the two previous dates – on April 7–11, 2010.

In the first scenario (i.e. April 7) the air temperature oscillates near -1.1°C . The surface of the lake is 67% cov-

ered with ice, but of course, there are sites where ice is not present. These include the deepest parts of the lake and the site where the Leba River flows into the lake. After a few days, ice cover declined more than 32% and the air temperature stands at $+11.2^{\circ}\text{C}$. The positive NAO phase becomes stronger and the ice on the lake gradually breaks up.

The study also focused on correlations between selected ice cover parameters and the pattern of teleconnections associated with time delays. No meaningful effects on the ice cover were detected for the studied lakes for 1, 2, 3, and 6-month time delays.

5. Discussion

A comparison of results obtained for Lake Łebsko with results for large areas of marine waters, shows significant similarities. Just like Lake Łebsko, large surface areas of the marine environment are susceptible to major changes in ecosystem response time. Shorter ice cover durations for Lake Łebsko are matched by the decline in ice duration for the various parts of the nearby Baltic Sea, as shown in the research of Granskog et al. (2014), Vihma and Haapala (2009), Löptien et al. (2013), and Höglund et al. (2017). The area of research that deserves more attention is key

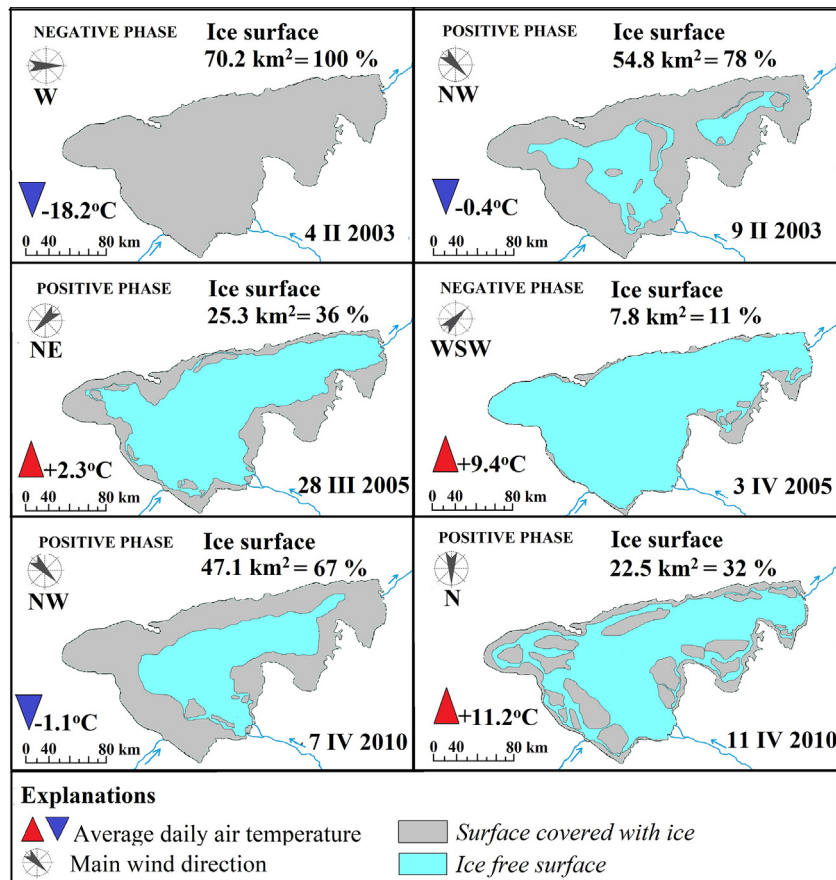


Figure 11 Characteristics of Hurrell NAO phases (positive +) (negative –) for Lake Łebsko in the course of ice cover break-up, based on satellite images.

differences in local conditions between the studied ecosystems.

Ice cover patterns for the Baltic Sea tend to be different for each part of the sea due to its irregular shape in the form of shielded bays and arms, variable depth, scattered sites of river inflow, and variable salinity levels. The Baltic Sea is also quite large. The study of the water temperature in Lake Łebsko clearly shows that the lake’s response time is short when the air temperature remains below freezing for an extended period of time. Existing studies on smaller bodies of water provide a basis for increased interest in research on larger bodies of water.

One current direction in oceanological research is the examination of mechanisms that drive changes in the time of ice formation and break-up in the various parts of the Baltic Sea. This is especially true of the interaction between the active surface of the sea and the ambient atmosphere. The analysis of air temperature changes prompting changes in the overall thermal conditions in seawater provided in this paper suggests an ever increasing tendency towards the occurrence of warmer winter seasons. Another aspect of this study which helps explain the ice cover pattern on Lake Łebsko is the inflow of water from the Łeba River, leading to delayed ice formation and faster ice break-up at selected sites. This observation also helps shed light on ice cover formation patterns for the various sections of the much larger Baltic Sea.

A possible research could focus on sites along the Baltic coastline in the various arms and bays characterized by special conditions including the inflow of the Neva River in the Gulf of Finland, inflow of the Daugava River in the Gulf of Riga, and the inflow of the Kemijoki River in the Gulf of Bothnia. Given the above, local proxies with high sensitivity should be used, such as lakes located in the vicinity of given sub-basins of the Baltic Sea, from which larger rivers flow.

Such research would help to understand whether every inflow of potamic water affects ice cover duration in a body of water and to what extent. It is easy to conclude that ice duration in the southern and western areas of the Baltic Sea would be characterized by delayed sea ice formation and early sea ice break-up relative to the eastern and northern parts of this particular sea. This is due to much milder winters in the western and southern reaches of the Baltic Sea. Data on a body of water located adjacent to the Baltic Sea clearly indicate that local factors produce an effect upon water bodies experiencing ice cover in the various seasons of the year. Hence, the use of data on Lake Łebsko in relation to the various parts of the Baltic Sea requires a consideration of various degrees of susceptibility to key local factors. One additional area of investigation that merits attention is the analysis of sites where river water enters lakes and seas. The very flow of water slows down the freezing process, and this is in itself an important area of inquiry. Research has shown that ice forms somewhat later and breaks

up much earlier at the site on Lake Łebsko where the Łeba River enters the lake. Salinity is yet another important factor. The northeastern part of Lake Łebsko freezes over later than other parts of the lake due to the presence of a canal leading to the Baltic Sea. A similar pattern of ice formation may be determined for the Baltic Sea itself, where some areas of the sea are more saline than others, and ice cover formation follows a different pattern in each type of area of the sea. What would also be very useful in this type of study would be the utilization of tools designed to assess the thickness of ice cover and possibly the direction of ice expansion in each given area of the Baltic Sea.

The nature of the North Atlantic Oscillation represents a highly relevant factor affecting variances in the European climate, as described in the works of [Hurrell et al. \(2001\)](#), [Hanna and Cropper \(2017\)](#) and [Dunstone et al. \(2016\)](#). The data obtained in the present study allow one to readily conclude that Lake Łebsko responds more rapidly to changes associated with elevated air temperatures in conjunction with local catchment factors and a strengthening, positive phase of the North Atlantic Oscillation. One effect of this trend is increasingly warm winter seasons featuring much shorter ice cover durations or only sporadic ice cover formation.

The strongest relationships between the examined ice cover parameters, taking the form of strong, negative correlations, were most frequently noted between the first and third of the herein studied time periods (i.e. decades). Subsequent study periods were characterized by the presence of more positive NAO values. The study was able to demonstrate that regional shifts in the climate are reflected by the North Atlantic Oscillation pattern. Research on changes in ice cover duration in relation to the NAO effect was conducted, for example, by [Karpechko et al. \(2015\)](#) and [Omstedt et al. \(2014\)](#).

Our study on selected NAO effects has produced results that mirror those obtained by [Dailidiene et al. \(2012\)](#) as well as [Hanna and Cropper \(2017\)](#). Research by [Kļaviņš et al. \(2016\)](#) concentrates on variances in ice cover in relation to the NAO and concludes that mechanisms driving atmospheric circulation in the North Atlantic affect ice conditions along the coastline of the Gulf of Riga. [Idzylete et al. \(2019\)](#) studied ice conditions on the Curonian Lagoon and found that sea ice durations are substantially extended in the presence of a stronger, negative NAO phase characterized by a long period of below-freezing air temperatures.

Both of the examples above may be connected with ice conditions observed on Lake Łebsko. The two bodies of water differ in terms of ice conditions first and foremost due to the different local factors that shape their climate. Analysis of correlations between the selected ice cover parameters (i.e. number of days with ice, maximum ice thickness) and the Hurrell NAO index for Lake Łebsko shows a correlation first and foremost for the first three decades of the study period. The last two of the studied decades are characterized by the impact of positive NAO coefficients and shorter durations of ice cover characteristics.

This confirms the studied lake's strongly reduced response time in relation to leading meteorologic factors. Earlier studies have shown the variable effects of the NAO on different regions of the Baltic Sea due to the presence of the different impacts of key local factors acting across

each given area of the sea, driven by various degrees of shielding.

The use of satellite images to assess ice cover duration for Lake Łebsko made it possible to identify key points in the investigated period of time. Research by [Lavrova et al. \(2019\)](#) and [Kozlov et al. \(2020\)](#) focused on the use of remote sensing (SAR) to assess the extent of the ice cover on the Caspian Sea and the Curonian Lagoon, but also to estimate the thickness of the ice in relation to key hydrometeorological changes. The use of satellite data and associated research methods continues to become refined, especially due to the availability of high-resolution data.

The analysis of ice conditions on Lake Łebsko and any discernible mechanisms that can delay ice cover formation may be useful in new oceanographic research studies. Yet another area of new research on ice cover formation patterns is the assessment of the susceptibility to freezing across different parts of the sea, i.e. its constituent parts in the form of bays and arms.

6. Conclusions

The present paper describes issues associated with the formation, maintenance, and then break-up of ice cover in relation to the currently observed warming of the lower layer of the Earth's atmosphere, which is linked with the impacts of the North Atlantic Oscillation. The one key pattern observed in the study of ice regimes of various aquatic ecosystems is the decline in ice cover duration in sea water due to a steady rise in air temperature on a global scale. A similar trend is shown in a number of other research works based on bodies of water located in many different parts of the northern hemisphere, although some exceptions do apply. The most often encountered exception consists of local hydrometeorological factors that affect local ice regimes present in aquatic ecosystems.

Our study of ice conditions on Lake Łebsko for the period 1960–2010 demonstrates a clear trend of increasing air temperatures that affects the temperature of water in lakes and the sea. One key outcome of the above process is a change in the degree of susceptibility of Lake Łebsko to the effects of meteorological factors. Another signal associated with global change in air temperature and intensity of atmospheric circulation is the delayed time of ice formation in bodies of water along with shorter ice cover duration times. The occurrence of positive values of the North Atlantic Oscillation index is related to the global increase in air temperature. The impact of global warming is a real possibility of changes taking place in the variability of NAO phases ([Blackport and Fyfe, 2022](#)).

The effect of the NAO on different areas of the Baltic Sea is different. Small bodies of water such as Lake Łebsko, which are more susceptible to forced effects, and their behavior may serve as a case study in the assessment of water body susceptibility to large changes occurring in different areas of the Baltic Sea.

A closer look at the results for Lake Łebsko suggests that much larger bodies of marine water and geographically unique areas of large bodies of marine water are also susceptible to major changes in the aquatic ecosystem response. The only difference consists of variances

in observed characteristics and is associated with rates of change determined by local conditions including meteorological conditions such as air temperature as well as morphologic conditions in the various areas of the Baltic Sea. These will also impact the water body's response time.

Declaration of competing interest

The authors declare that they have no known competing financial interests or personal relationships that could have appeared to influence the work reported in this paper.

References

- Athanasiadis, P.J., Yeager, S., Kwon, Y., Bellucci, A., Smith, D.W., Tibaldi, S., 2020. Decadal predictability of North Atlantic blocking and the NAO, npj Clim. Atmos. Sci. 3 (20). <https://doi.org/10.1038/s41612-020-0120-6>
- Blackport, R., Fyfe, J.C., 2022. Climate models fail to capture strengthening wintertime North Atlantic jet and impacts on Europe. *Sci. Adv.* 8 (45), eabn3112. <https://doi.org/10.1126/sciadv.abn3112>
- Choiński, A., Ptak, M., Skowron, R., Strzelczak, A., 2015. Changes in ice phenology on Polish lakes from 1961 to 2010 related to location and morphometry. *Limnologia* 53, 42–49. <https://doi.org/10.1016/j.limno.2015.05.005>
- Cieśliński, R., Olszewska, A., 2018. New insight into defining the lakes of the southern Baltic coastal zone. *Environ. Monitor. Assess.* 190 (102). <https://doi.org/10.1007/s10661-017-6447-8>
- Dailidienė, I., Davulienė, L., Kelpsaite, L., Razinkovas, A., 2012. Analysis of the climate change in Lithuanian coastal areas of the Baltic Sea. *J. Coast. Res.* 28 (3), 557–569. <https://doi.org/10.2112/JCOASTRES-D-10-00077.1>
- Delpeche-Ellmann, N., Torsvik, T., Soomere, T., 2016. A comparison of the motions of surface drifters with offshore wind properties in the Gulf of Finland, the Baltic Sea. *Estuar. Coastal Shelf Sci.* 172 (5), 154–164. <https://doi.org/10.1016/j.ecss.2016.02.009>
- Dunstone, N., Smith, D., Scaife, A., Hermanson, L., Eade, R., Robinson, N., Andrews, M., Knight, J., 2016. Skilful predictions of the winter North Atlantic Oscillation one year ahead. *Nature Geosci.* 9, 809–814.
- Granskog, M.A., Gerland, S., Perovich, D.K., 2014. Arctic sea ice in transformation: A review of recent observed changes and impacts on biology and human activity. *Rev. Geophys.* 9, 185–217.
- Hanna, E., Cropper, T.E., 2017. North Atlantic Oscillation. *Oxford Research Encyclopedia of Climate Sci.* <https://doi.org/10.1093/9780190228620.013.22>
- Haapala, J.J., Ronkainen, I., Schmelzer, N., Sztobryn, M., Bolle, H.J., Menenti, M., Ichtiague Rasool, S., 2015. Recent Change—Sea Ice. In: The BACC II Author Team (Eds.), *Second Assessment of Climate Change for the Baltic Sea Basin. Regional Climate Studies*. Springer, Cham. https://doi.org/10.1007/978-3-319-16006-1_8
- Höglund, A., Pemberton, P., Hordoir, R., Schimanke, S., 2017. Ice conditions for maritime traffic in the Baltic Sea in future climate. *Res. Boreal Environ.* 22, 245–265.
- Hurrell, J.W., 1995. Decadal trends in the North Atlantic Oscillation, Regional temperatures and precipitation. *Science* 269, 676–679.
- Hurrell, J.W., Kushnir, Y., Visbeck, M., 2001. The North Atlantic Oscillation. *Science* 291 (5504), 603–605. <https://doi.org/10.1126/science.1058761>
- Idzylete, R., Kozlov, I.E., Umgiesser, G., 2019. Remote sensing of ice phenology and dynamics of Europe's largest coastal lagoon (The Curonian Lagoon). *Remote Sens.* 11 (17), 2059. <https://doi.org/10.3390/rs11172059>
- Jaagus, J., 2006. Trends in sea ice conditions in the Baltic Sea near the Estonian coast during the period 1949/50–2003/2004 and their relationships to large scale atmospheric circulation. *Boreal Environ. Res.* 11, 169–183.
- Jakimavičius, D., Šarauskiene, D., Kriaučiūnienė, J., 2020. Influence of climate change on the ice conditions of the Curonian Lagoon. *Oceanologia* 62 (2), 164–172. <https://doi.org/10.1016/j.oceano.2019.10.003>
- Karetnikov, S.G., Naumenko, M.A., 2008. Recent trends in lake Ładoga ice cover. *Hydrobiologia* 599, 41–48. https://doi.org/10.1007/978-1-4020-8379-2_5
- Karpechko, A.Y., Peterson, K.A., Scaife, A.A., Vainio, J., Gregow, A., 2015. Skilful seasonal predictions of Baltic Sea ice cover. *Environ. Res. Lett.* 10 (4).
- Kļaviņš, M., Avotniece, Z., Rodinovs, V., 2016. Dynamics and impacting factors of ice regimes in Latvia inland and coastal waters. *Proc. Latv. Acad. Sci. Section B* 70 (6), 400–408. <https://doi.org/10.1515/prolas-2016-0059>
- Kozlov, I.E., Krek, E.V., Kostianoy, A.G., Dailidienė, I., 2020. Remote Sensing of Ice Conditions in the Southeastern Baltic Sea and in the Curonian Lagoon and Validation of SAR-Based Ice Thickness Products. *Remote Sens.* (12) 3754. <https://doi.org/10.3390/rs12223754>
- Lavrova, O.Y., Kostianoy, A.G., Mityagina, M.I., Strochkov, A.Y., Bocharova, T.Y., 2019. Remote sensing of sea ice in the Caspian Sea. *Proc. SPIE* 11150, Remote sensing of the Ocean, Sea Ice, Coastal Waters and Large Water Regions. <https://doi.org/10.1117/12.2532136>
- Lepparanta, M., Seina, A., 1985. Freezing maximum annual ice thickness and breakup of ice on the Finnish coast during 1830–1984. *Geophysica* 21 (2), 87–104.
- Livingstone, D.M., 2000. Large-scale climatic forcing detected in historical observations of lake ice break-up. *Verhandlungen der Internationalen Vereinigung für Limnologie* 27 (5), 205–220. <https://doi.org/10.1080/03680770.1998.11898171>
- Löptien, U., Mårtensson, S., Meier, H.E.M., Höglund, A., 2013. Long-term characteristics of simulated ice deformation in the Baltic Sea (1962–2007). *JGR Ocean* 118 (2), 801–815. <https://doi.org/10.1002/jgrc.20089>
- Makynen, M., Karvonen, J., Cheng, B., Hiltunen, M., Eriksson, P., 2020. Operational Service for mapping the Baltic Sea Landfast Ice Properties. *Remote Sens.* 12 (24). <https://doi.org/10.3390/rs12244032>
- Marks, L., Bera, A., Golek, W., 2006. Geological map of Poland on a scale of 1:50000, sheet: Łeba. *Geological Publ.*
- Miller, J.D., Hutchins, M., 2017. The impacts of urbanisation and climate change on urban flooding and urban water quality: A review of the evidence concerning the United Kingdom. *J. Hydrol.* 12, 345–362. <https://doi.org/10.1016/j.ejrh.2017.06.006>
- Neves, M.C., Jerez, S., Trigo, M.R., 2019. The response of piezometric levels in Portugal to NAO, EA, and SCAND climate patterns. *J. Hydrol.* 568, 1105–1117. <https://doi.org/10.1016/j.jhydrol.2018.11.054>
- Omstedt, A., Axell, L.B., 1998. Modeling the seasonal interannual and long term variations of salinity and temperatures in the Baltic proper. *Tellus A: Dynam. Meteorol. Oceanography* 50, 637–652. <https://doi.org/10.3402/tellusa.v50i5.14563>
- Omstedt, A., Chen, D., 2001. Influence of atmospheric circulation on the maximum ice extent in the Baltic Sea. *J. Geophys. Res. Oceans*. 106 (C3), 4493–4500. <https://doi.org/10.1029/1999jc000173>
- Omstedt, A., Elken, J., Lehmann, A., Lepparanta, M., Meier, H.E.M., Myrberg, K., Rutgersson, A., 2014. Progress in physical oceanography of the Baltic Sea during the 2003–2014 period. *Prog. Oceanogr.* 128, 139–171. <https://doi.org/10.1016/j.pocean.2014.08.010>

- Pärn, O., Friedland, R., Rjazin, R., Stips, A., 2022. Regime shift in sea-ice characteristics and impact on the spring bloom in the Baltic Sea. *Oceanologia* 64 (2), 312–326. <https://doi.org/10.1016/j.oceano.2021.12.004>
- Polvani, L.M., Lantao, S., Butler, A.H., Richter, J.H., Deser, C., 2017. Distinguishing Stratospheric Sudden Warmings from ENSO as Key Drivers of Wintertime Climate Variability over the North Atlantic and Eurasia. *J. Climate* 30, 1959–1969. <https://doi.org/10.1175/JCLI-D-16-0277.1>
- Rjazin, J., Parn, O., 2020. Determining the regime shift of the Baltic Sea Ice Seasons during 1982–2016. *Int. J. Marit. Sci. Technol.* 67 (1), 53–59. <https://doi.org/10.17818/NM/2020/1.8>
- Rosa, B., 1963. On the morphological development of the Polish coast in the light of old coastal forms. *Studia Societatis Scientiarum Torunensis sectio C.* 5.
- Sezen, C., Peral, T., 2017. The relation of North Atlantic Oscillation (NAO) and North Sea Caspian pattern (NCP) with climate variables in Mediterrean region of Turkey. *The Eurasia Proc. Sci., Technol. Engineer. Mathematics (EPSTEM)* 1, 366–371.
- Sharma, S., Magnuson, J.J., Batt, R.D., Winslow, R.A., Korhonen, J., Aono, Y., 2016. Direct observations of ice seasonality reveal changes in climate over the past 320–570 years. *Sci. Rep.* 6. <https://www.nature.com/articles/srep25061>.
- Smith, D.M., Scaife, A.A., Eade, R., Knight, J.R., 2014. Seasonal to decadal prediction of the winter North Atlantic Oscillation: emerging capability and future prospects. *Q. J. Roy. Meteor. Soc.* 142 (695), 611–617. <https://doi.org/10.1002/qj.2479>
- Soja, A.M., Kutics, K., Maracek, K., Molnár, G., Soja, G., 2014. Changes in ice phenology characteristics of two Central European steppe lakes from 1926 to 2012 - influences of local weather and large scale oscillation patterns. *Climatic Change* 126, 119–133. <https://doi.org/10.1007/s10584-014-1199-8>
- Vihma, T., Haapala, J., 2009. Geophysics of sea ice in the Baltic Sea: A review. *Prog. Oceanogr.* 80, 129–148.
- Visbeck, M.H., Hurrell, J.W., Polvani, L., Cullen, H.M., 2001. The North Atlantic Oscillation: Past, present and future. *PNAS (Proc. Nat. Acad. Sci.)* 98 (23), 12876–12877.
- Weidberg, N., Bascadow, S.L., 2019. Long-term variability in over-wintering copepod populations in the Lofoten Basin: The role of the North Atlantic oscillation and trophic effects. *Limnol. Oceanogr.* 64 (5), 2044–2058. <https://doi.org/10.1002/lno.11168>
- Wenta, M., Brus, D., Doulgeris, K., Vakkari, V., Herman, A., 2021. Winter atmospheric boundary layer observations over sea ice in the coastal zone of the Bay of Bothnia (Baltic Sea). *Earth Syst. Sci. Data* 13, 33–34. <https://doi.org/10.5194/essd-13-33-2021>
- West, H., Quinn, N., Horswell, M., 2018. Regionalising the influence of the North Atlantic Oscillation on seasonal hydrological extremes in Great Britain. *Geophys. Res. Abstracts* 20.
- Wolski, T., Wiśniewski, B., 2022. Characteristics of seasonal changes of the Baltic Sea extreme sea levels. *Oceanologia* 65 (1), 151–170. <https://doi.org/10.1016/j.oceano.2022.02.006>
- Wrzesiński, D., Paluszkiewicz, R., 2011. Spatial differences in the impact of the North Atlantic Oscillation on the flow of rivers in Europe. *Hydrol. Res.* 42 (1), 30–39. <https://doi.org/10.2166/nh.2010.077>
- Wrzesiński, D., Ptak, M., Plewa, K., 2018. Effect of the North Atlantic Oscillation on water level fluctuations in lakes of northern Poland. *Geographia Polonica* 91 (2), 243–259.

Available online at www.sciencedirect.com

ScienceDirect

journal homepage: www.journals.elsevier.com/oceanologia

ORIGINAL RESEARCH ARTICLE

Cooperation between the fishery sector and science: CTD probe measurements during fishing catches on the feeding grounds of herring (*Clupea harengus*) and sprat (*Sprattus sprattus*) in the south-eastern part of the Baltic Sea

Piotr Piecki^{a,*}, Diana Dziaduch^a, Lidia Dzierzbicka-Głowacka^b, Marcin Kalarus^a

^aGdynia Maritime University, Gdańsk, Poland

^bInstitute of Oceanology, Polish Academy of Sciences, Sopot, Poland

Received 23 February 2023; accepted 13 October 2023

Available online 21 October 2023

KEYWORDS

Temperature;
Salinity;
Hypolimnion layer;
Pelagic fishery;
Catch results

Abstract 282 CTD probe measurements were analysed for the parameters of temperature, salinity, depth and oxygen saturation of the water column. These measurements were taken during commercial pelagic fishing for herring (*Clupea harengus*) and sprat (*Sprattus sprattus*). These species are currently the main target of commercial fishing in the Baltic Sea. Research was carried out throughout the years 2018–2022 in the south-eastern Baltic Sea, mainly in the Gdańsk Deep, mostly during the daytime. The main factor that influenced both, fishing strategy and the increase in catch per unit effort throughout each year, was temperature. Regardless of the season, the most frequent temperature measured was around 5.8°C during fishing, and 5°C in the most abundant winter season. This is the value occurring within the boundaries of the formation of the thermocline and the hypolimnion layer in the Baltic Sea. The formed shoals of fish moved dynamically with this layer in the daytime and occurred throughout the year at various depths in a range of up to 65.7 m. A stronger reaction to temperature changes was also

* Corresponding author at: Gdynia Maritime University, Department of Ecology, Długi Targ 41/42, 80-830 Gdańsk, Poland.

E-mail address: ppiecki@im.umg.edu.pl (P. Piecki).

Peer review under the responsibility of the Institute of Oceanology of the Polish Academy of Sciences.



<https://doi.org/10.1016/j.oceano.2023.10.001>

0078-3234/© 2023 Institute of Oceanology of the Polish Academy of Sciences. Production and hosting by Elsevier B.V. This is an open access article under the CC BY-NC-ND license (<http://creativecommons.org/licenses/by-nc-nd/4.0/>).

observed for sprat, which is the most exploited fish in the Baltic Sea. This species was observed to be more numerous in the deeper layers of the water column and at lower temperatures than herring. In the winter, shoals of fish were observed at the level of the halocline, which may be strongly related to the presence of a preferred optimal food base in this season.

© 2023 Institute of Oceanology of the Polish Academy of Sciences. Production and hosting by Elsevier B.V. This is an open access article under the CC BY-NC-ND license (<http://creativecommons.org/licenses/by-nc-nd/4.0/>).

1. Introduction

Salinity and temperature are very important determinants of fish stock and recruitment for herring (*Clupea harengus*) and sprat (*Spratts sprattus*) (Akimova et al., 2016; Saraux et al., 2014), the most important commercial pelagic fish in the Baltic Sea. These waters are a special sea basin with the lowest salinity on a world scale, relatively small average depths, and high-water dynamics (ICES, 2018; Meier et al., 2022). Typical marine species found here, originating from the Atlantic area, such as herring and sprat, are forced to look for optimal and sensitive environmental conditions in the water column, often determining their survival, especially during the reproduction and maturation of fry (Parmanne et al., 1994).

One of the important factors related to the occurrence of both of these fish stocks at the given place and time in the water column is the presence of concentrations of zooplankton, as herring and sprat are the dominant zooplanktivorous species in the Baltic Sea. Their diel vertical migration (DVM) mirrors the zooplankton diel movements in the water column as well as its response to select optimal water temperature (bioenergetic optimisation) and minimal exposure to predators (Cardinale et al., 2003; Holland et al., 2021; Möllmann et al., 2004). Both of these species are similar to each other through shared locations of feeding grounds and similar food preferences (Arrhenius and Hansson, 1993; Cardinale et al., 2003; Casini et al., 2004; Lankov et al., 2010; Möllmann et al., 2004), but smaller sprat feed upon zooplankton, while larger herring prefer nektonbenthos such as Mysidacea and Amphipoda (Cardinale et al., 2003; Casini et al., 2004; Dziaduch, 2011).

Different species of fish, including sprat, change their locations in the water column at different temperatures during the day, affecting their metabolism. In sprat, these summer movements to warm surface layers at night speed up digestion and release of metabolic waste and feces, which is likely to increase fattening intensity (Andersen et al., 2017; Neverman and Wurtsbaugh, 1994). In winter, however, when the food resources are scarcer, the same direction of migration at night to the zone of shallower water with lower temperature slows metabolism down, which may contribute to reducing of energy losses (Andersen et al., 2017).

The main goal of this research was to determine the precise values for the most important basic physical and chemical factors of water parameters which determine the occurrence of herring and sprat shoals, such as temperature, salinity, oxygenation and depth and identifying the most important ones. The significant step was identifying the ability to determine the impact on the reaction that these species will have when affected by climatic changes, mainly related

to temperature changes, which are taking place very dynamically in the Baltic Sea basin (Meier et al., 2022). Currently, many studies are focused on the modeling of the impact of climate warming on major fish stocks such as herring and sprat in the Baltic Sea (Bauer et al., 2019; Harvey et al., 2003; Maravelias et al., 2000; Tamm et al., 2018; Voss et al., 2011). Such precise determination of the values in all seasons for the tested parameters as in this work has not been described so far in the Baltic Sea.

The cooperation of the two sectors, commercial fishery and science, interested in living marine resources may further enable their better protection, rational exploitation and enable the flow of knowledge about their condition and directions of changes. The collection of the data analysed here is the first research project of this type in Poland. Collaboration with the fishing industry is a good way to generate new environmental data, filling many gaps in the unexplored marine environment (Van Vranken et al., 2020).

2. Material and methods

2.1. Data acquisition method and measuring equipment

Catches were carried out in the southern Baltic Sea, mainly in the Gulf of Gdańsk (Figure 1). Catch data was reported for commercial Polish fishing rectangles: M, N, O, P, R, S, T, U and W, up to the height of 11 (Figure 1). However, most of the catch (83%) was reported in the S and T rectangles.

The CTD surveys were carried out during regular pelagic catches of herring and sprat. The data came from 282 fishing expeditions in the period between 2018–2022 (Figure 2).

Fishery catches were performed on several anonymous fishing vessels (total number = 8) with overall hull dimensions from 18 to 25 m, 113–133 GT (Gross Tonnage) and an engine power range between 375 and 386 kW. All fishing vessels were equipped with standard echo sounders to locate fish schools. The main tool utilized for locating fishing grounds in these surveys was the echo sounder.

Water parameters were measured by using the MIDAS CTD+ Valeport probe placed on the upper bridle of the pelagic trawl net. The probe was housed in a lightweight steel cage with a float, giving it neutral buoyancy. During the data collection period, the probes were calibrated by the manufacturer once every quarter to ensure the most accurate measurement of data. Data was collected from the probe for four parameters: pressure, conductivity, temperature, and dissolved oxygen DO (calibrated in open air for 0–100%) (Table 1). Salinity was calculated from conductivity, temperature and pressure in the range of 0 to

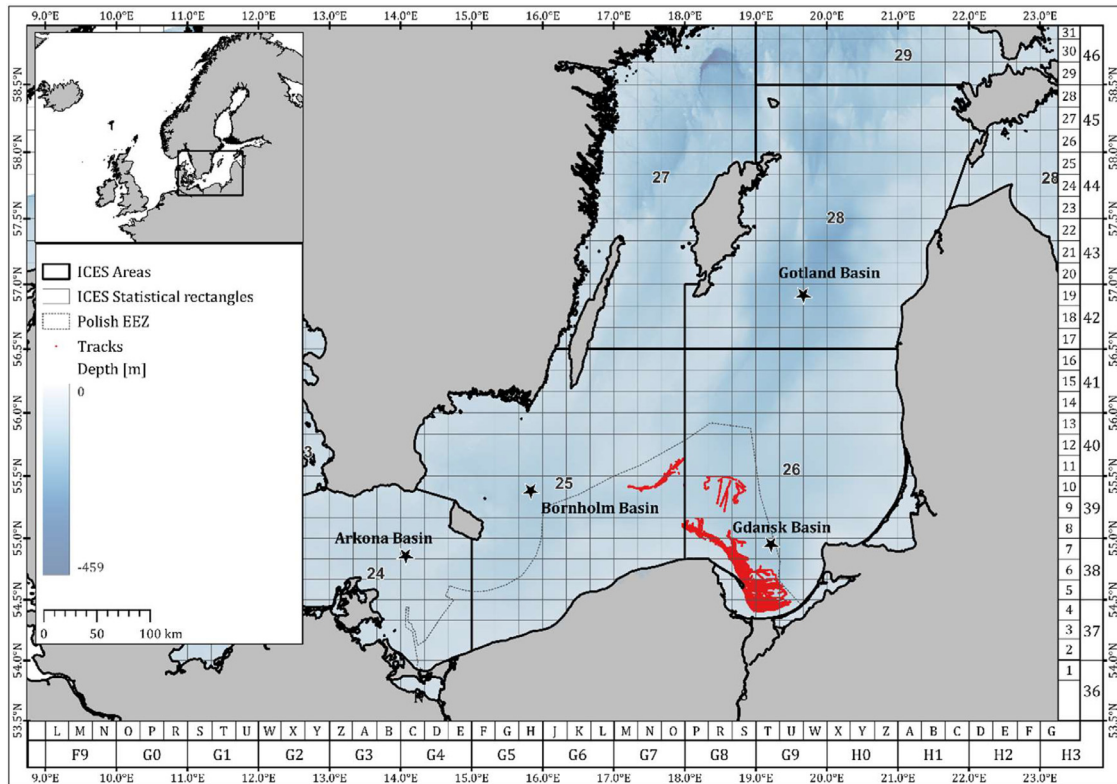


Figure 1 Location of fishing expeditions (red tracks) with CTD probe surveys. Polish fishing areas are layered on the map with marked rectangles, used to collect fishing data by the government administration.

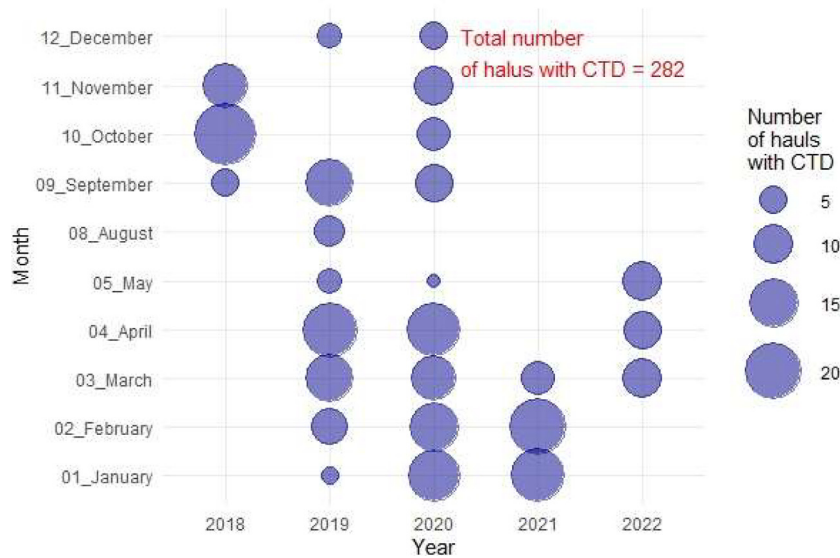


Figure 2 Number of fishing expeditions in given months with CTD probe, aggregated for years 2018–2022.

Table 1 Specification of the MIDAS CTD+ Valeport sensors.

Sensor	Type	Range	Accuracy	Resolution
[A] Conductivity	Inductive Cell	0–80 mS/cm	+/-0.01 mS/cm	0.002 mS/cm
[B] Temperature	PRT	-5 – +35°C	+/-0.005°C	0.002°C
[C] Pressure	Piezo-Resistive	Up to 600 Bar	+/-0.01%	0.001%
[D] DO	Clark Cell	0–16 ml/l	+/-0.07 ml/l	0.017 ml/l

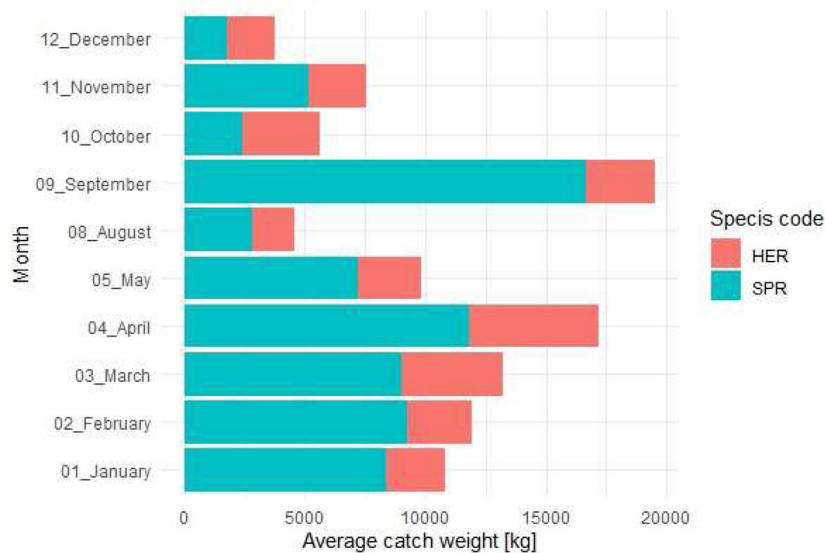


Figure 3 Comparison of average catch weight between herring [HER] and sprat [SPR] in months from the period between 2018–2022, for which the CTD probe measurement was performed.

40 in resolution 0.01 ppt. and accuracy ± 0.02 ppt using dedicated Valeport Software.

2.2. Statistical analysis

Data from the CTD probe was processed for the purpose of eliminating data originating outside of the actual fishing catch, such as open-air measurements on board when the probe is turned on, measurements taken during gear release and gear collection and data incorrectly recorded or incorrect data, such as commonly observed incorrect operation of the 'Clark Cell' oxygen sensor sensitive to mechanical damage.

The PCA (principal component analysis) test was performed on the set of all data for all analysed parameters: salinity [A], temperature [B], catch depth (pressure) [C], and dissolved oxygen (DO) [D] in order to select the most important parameters determining commercial fishing. Measurements at depths greater than 20 m were extracted from the entire pre-prepared database. This depth of 20 m was the catch limit value based on the entire series of data and logbook data from fishing boats. The data was then transformed using the Hellinger method (Simpson, 1989).

In order to select the characteristic values of the measured parameters: salinity [A], temperature [B], catch depth (pressure) [C], and dissolved oxygen (DO) [D] for individual months of the year, the boxplot method was used (Schwertman et al., 2004). Data was then converted to medians (Becker et al., 2018), which showed the most characteristic value present in single hauls. This allowed for the comparison of each series (282) of probe measurements characterized by a different length of the vector of the collected data. The median was calculated for the data sequentially filtered from the set. The entire data set was subjected to a one-way analysis of variance (ANOVA), (Chambers and Hastie, 2018; Kim, 2017; McHugh, 2011).

Subsequently, a comparative analysis was performed for all the examined parameters, depending on the size of the

catch and the composition of the catch, using the linear Pearson correlation and an analysis of the fishing effort calculated on the CTD probe clock was performed for all catches. Additionally, the fishing effort calculated on the clock of the CTD probe was also analysed for catch size. Finally, for trawl hauls, a 24-hour interval was calculated for both species. In this case, cumulative catch results were made in order to compare the most productive months for pelagic fisheries in the study area.

The analyses were performed in R, version 4.1.2 (2021-11-01) – "Bird Hippie" Copyright (C) 2021 The R Foundation for Statistical Computing. The following packages were used to filter and organize the data: 'dplyr' version 1.0.7, 'tidyverse' version 1.3.1, 'tidyr' version 1.1.4, 'purrr' version 0.3.4, 'car' version 3.0-12. 'Ggplot2' version 3.3.5 package was used for the graphical analysis. The 'vegan' package version 2.6-4 was used to perform the PCA test (principal component analysis).

3. Results

3.1. Characteristics of performed fishing catches results

The composition of the analysed catches was dominated by sprat (Figure 3). The best period with the best fishing results was in the winter and spring months: January, February, March, April and late summer (September).

3.2. Characteristics of the acquired data

About 4.5 million records from 282 commercial fishing cruises were collected. Commercial fishing was carried out in all seasons and in various weather conditions, in Beaufort scale state from 0 to 7. CTD probe measurements under such conditions produced unique values for the study area. All catches were performed at depths below 20 m. Preliminary

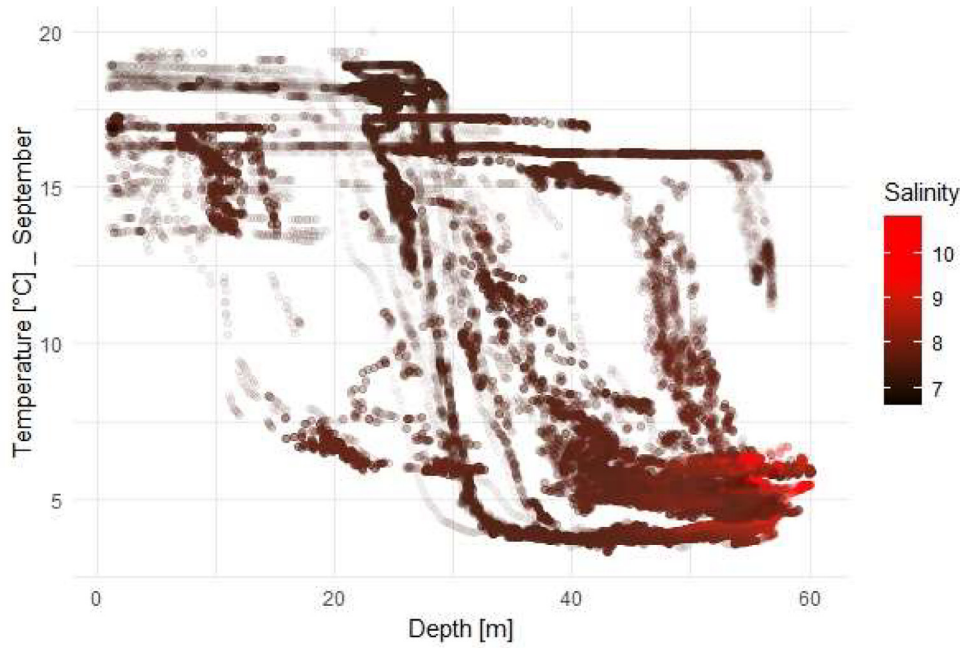


Figure 4 Measurement profiles of the CTD probe raw data for the temperature, salinity, and depth aggregated for September, characterizing a daily dynamically changing thermocline and halocline.

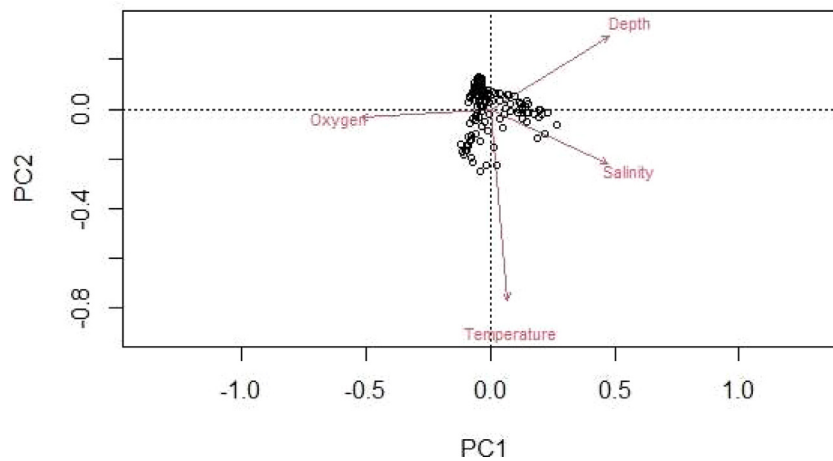


Figure 5 Biplot for principal component analysis (PCA) for salinity [A], temperature [B], catch depth (pressure) [C], and dissolved oxygen (DO) [D], dots for observations for multiple parameters which shows correlation only between pair: temperature and salinity, where temperature is the more important factor. The percentage of variance for the principal component analysis model (PCA) for the first axis was 65.99 for the second axis 29.29, the broken-stick percentage for the first axis was 52.08 and for the second axis 27.08 and the eigenvalue for the first axis was 2.64, and for second axis 1.17.

analyses have shown that fish shoals, localized by using the echo sounder only, occur at different depths where stable temperature conditions prevail. This occurrence is clearly visible in the example of September, which annually is characterized by high variability of the location of the thermocline (Figure 4).

Conducted PCA (principal component analysis test) showed that the pair: temperature and salinity were the main determinants of the use of fishing strategy among the examined parameters (Figure 5). The trawl hauls depths were characterized by high variability, mainly due to the dynamic changes in the occurrence of stable temperature conditions associated with the formation of the thermocline,

which was clearly visible even on the raw profiles of the CTD probe (Figure 4). In the southern Baltic Sea in depth areas such as the Gdańsk Basin, the salinity increases with depth (Kniebusch et al., 2019; Lehmann et al., 2022). In the examined fishing strategy it is also very common to reach depths below the halocline (Figure 4, Figure 6A).

3.3. Values of salinity, temperature, depth and oxygen dissolved in water during hauls

The locations of fish shoals were concentrated throughout the year mainly in the layer of the water column with

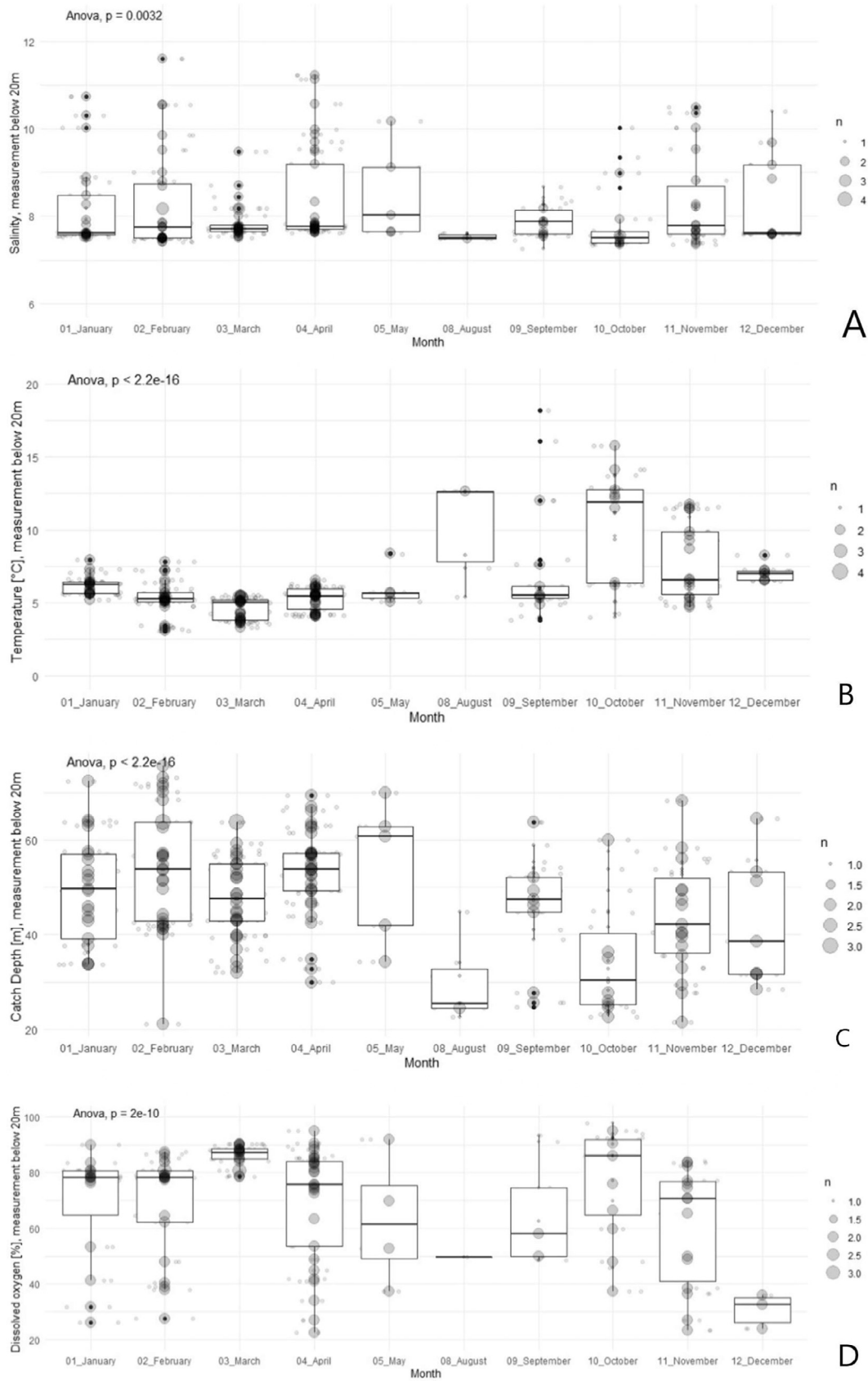


Figure 6 Boxplots for salinity [A], temperature [B], catch depth (pressure) [C], and dissolved oxygen (DO) [D], from particular measurement sets grouped in months. Data were converted to medians, which show the most common appearing value in a single haul. The entire data set was subjected to one-way ANOVA analysis.

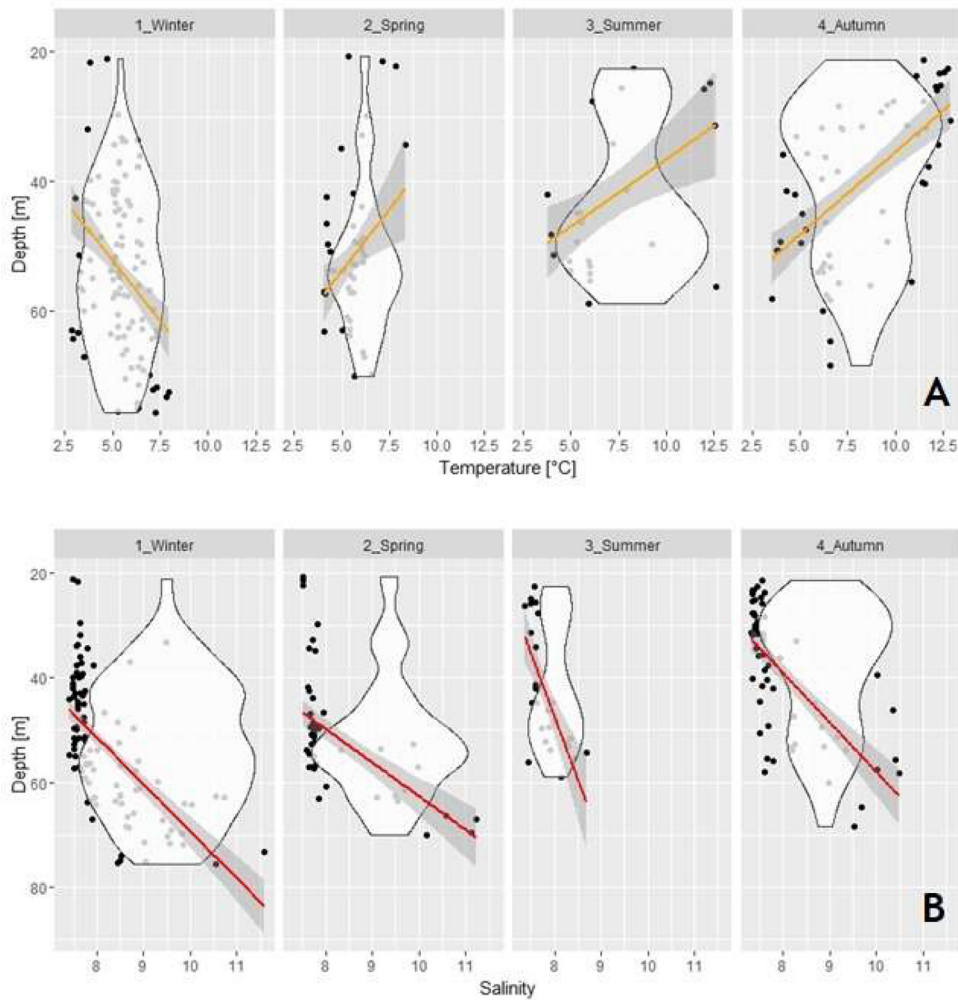


Figure 7 Seasonal changes in thermal conditions [A] and salinity [B] in relation to depth for the concentration of fish shoals during the daytime.

stabilized values for temperature, in hypolimnion layer. This dependency is mainly visible in December, January, February, March, April and May (Figure 6B), which are characterized by the lowest data dispersion among the other parameters. The temperature throughout the examined years oscillated around 5.8°C, which is the median of the data set. In addition, shoals of fish changed their location in the water column during the year, depending on the season. In winter, they were at the deepest, where the temperature was the highest in the water column, unlike during the summer when the opposite is true for the temperature (Figure 7A). Salinity constitutes the most stable parameter for trawl hauls (Figure 6A), with the median of the data set equal to 7.7, which is a value above the halocline formation in the Baltic Sea (Lehmann et al., 2022). However, for this parameter, significant changes occur in the winter season, when the location of fish shoals was often mainly in the halocline zone (Figure 7B). The halocline was crossed reaching maximum values for salinity above 11 in January, February, April and also in September and October (Figure 6A). The most common depth in fishing activity across the examined years was 48.1 m, however, here the depth significantly depended on the optimal temperature, and it fluctuated dynami-

cally with every catch, in the range of as much as 65.7 m (Figure 6C).

Additionally, the dissolved oxygen values varied greatly from full oxygenation of 100% down to the extreme of 1%, however, most of the catches were in the range of 78.1%. The range for 75 and 25 percentiles of dissolved oxygen ranged from 87.2% to 54.2%. The values of oxygenation fell significantly with the increase in depth (Figure 6D).

3.4. Dependence between salinity, temperature, depth, oxygen dissolved in water, time, and catch biomass

Most of the parameters did not show strong dependencies to the catch biomass, which was mainly dependent on temperature, with a statistically significant correlation between temperature decrease and catch weight increase for sprat (Figure 8B). Most of the catches performed around 5.8°C had common biomass results ranging around 5 tons. With the decrease in temperature, the share of sprat in the catch also increased, with its share in the catch further increasing

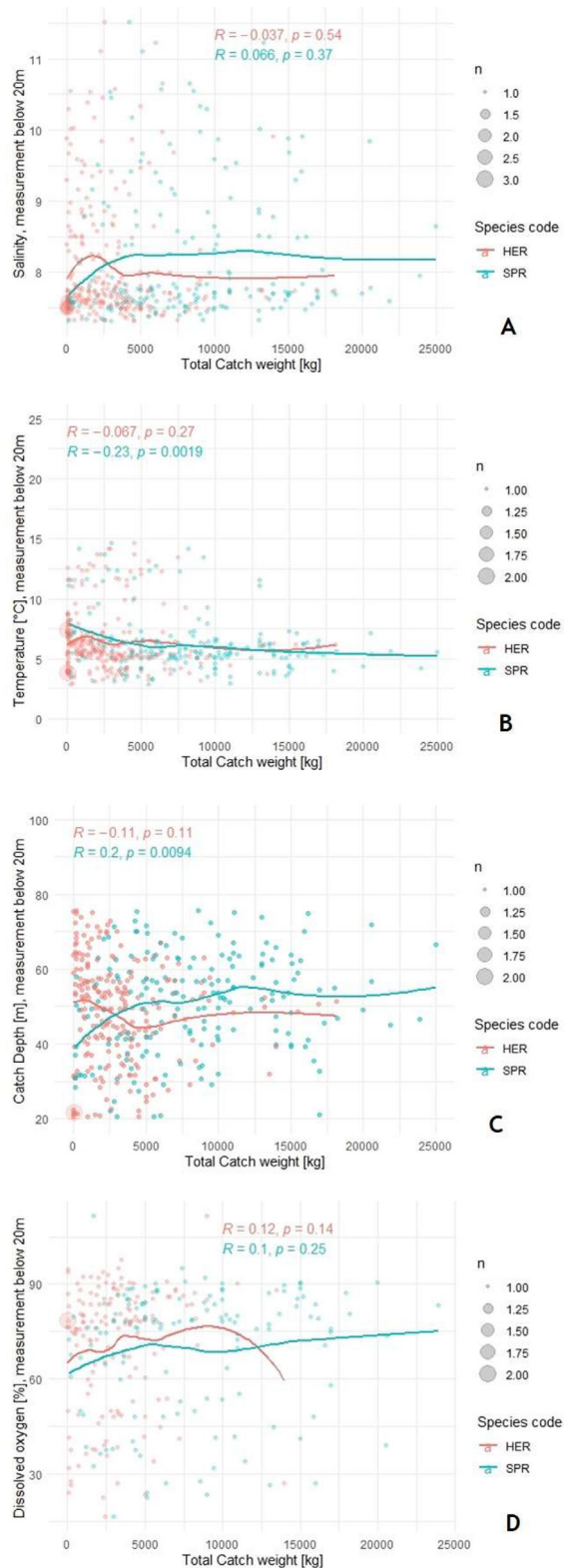


Figure 8 Dependency comparison for salinity [A], temperature [B], catch depth (pressure) [C], and dissolved oxygen (DO) [D], for catch size composition containing species: herring [HER] and sprat [SPR]. Data were converted to medians, which show the most common appearing value in a single haul. Pearson's r correlation coefficient was calculated with p -value statistical significance based on ANOVA by species composition.

with the increase in depth, where the maximum catch for this species was about 24 tonnes.

Catches were also dependent on fishing effort, but only for herring, where in the studied case, longer catches had a statistically significant higher fish tonnage ($p=0.08$). The most common catches were conducted for 3.8 h (Figure 9).

Fishing took place mainly from dawn to sunset, regardless of the season. Most often, fishing started between 5 and 6 AM and ended between 3 and 4 PM (Figure 10). The most productive months with the highest catch effort were January, February, March and April.

4. Discussion

Fishing was carried out on medium-sized vessels, in comparison to the conditions of fishing fleets on the Baltic Sea (ICES Advisory Committee, 2019). The catches that were analysed, which in most cases consisted of combined catches of two pelagic species of herring and sprat, were similar to the characteristics of forage fishery, which has been increasing in frequency in the Baltic Sea for years (Alder et al., 2008; ICES, 2022; Pihlajamäki et al., 2019). This frequency is increasing not only because of the availability of these resources but also due to the fishing bans for cod (*G. morhua*) which was the main catch for many local fishermen in the studied area (Figus et al., 2017). As a result, herring and sprat remain the only permitted catch for the most important commercial fishing in the Baltic Sea (ICES 2021; Receveur et al., 2022). Based on the fishing data across the Baltic Sea in the 1960s-70s, in the 1970s herring, exceeded sprat in the commercial fishery – even twice as much herring as sprat was caught (ICES Advisory Committee, 2019; Parmanne et al., 1994). However, this trend changed over time towards equalizing the tonnage of catches of both species until the current dominance in sprat catches, mainly due to the increasing share of forage catches over consumption catches (ICES, 2022). At the same time, changes in fish stocks between herring and sprat, beyond fishing pressure, arise for other reasons such as an important existing change in the food base. Since the 1980s the decline of herring was likely initiated by a change in the species composition of the zooplankton community and by an increased food competition between herring and sprat (ICES, 2010). The primary prey for sprat and herring are Calanoid copepods and cladocerans (Arrhenius and Hansson, 1993). Sprat feed exclusively upon zooplankton while herring change their diet with fish size and also feed upon nektobenthos. Until the late 1980s the main food of herring were *Pseudocalanus* spp. and Mysidacea (Hansson et al., 1990; Möllmann et al., 2000, 2004; Załachowski et al., 1975). Considerable changes in fish composition in both species have been suggested to be a result of changes in the deep-water salinity and decline in *Pseudocalanus* spp. The food spectrum of herring has significantly changed since the mid-1980s. The shares of *Pseudocalanus* spp. and Mysidacea have considerably diminished. Additionally, the food composition of herring has undergone certain changes as a shortage of Mysidacea was replaced with Amphipoda (Dziaduch, 2011; Kornilovs et al., 2001) and a large share of *Temora longicornis*, *Eurytemora affinis* and *Acartia* spp. in their food base (Möllmann et al.,

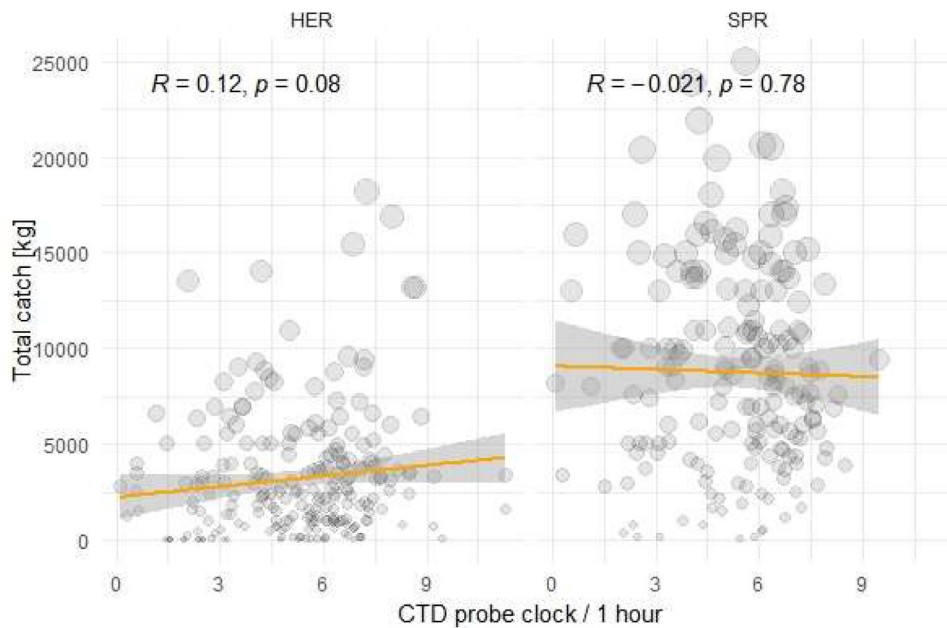


Figure 9 Correlation between fishing effort (measured by time) and catch tonnage for sprat [SPR] and herring [HER], with Pearson’s r and p -value and statistical significance based on ANOVA.

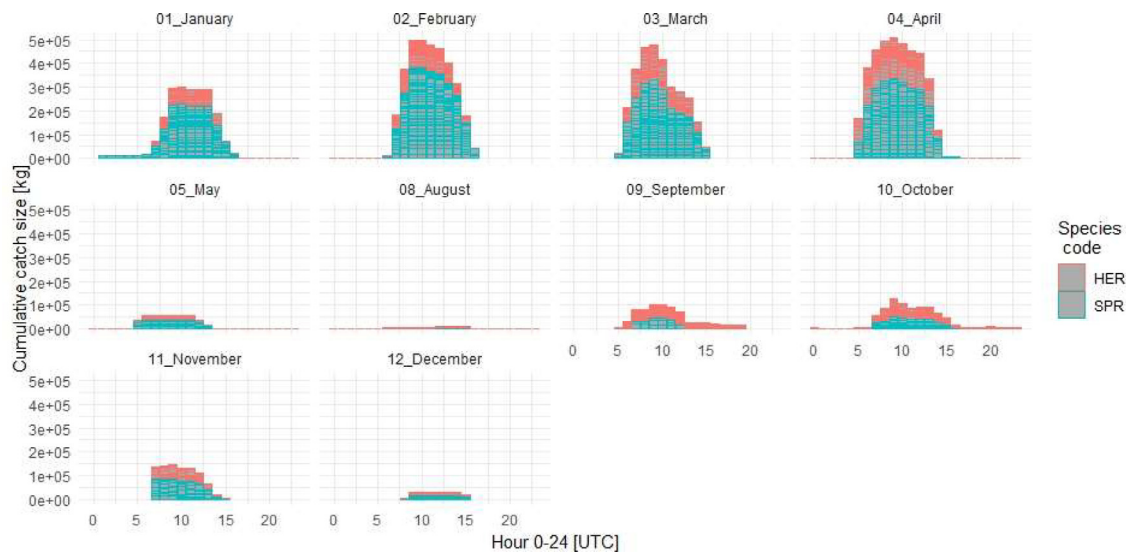


Figure 10 Cumulative catch effort and weight in a daily dimension, characterizing the best period preferred by the fishermen for herring [HER] and sprat [SPR] catches. Data were broken down into months.

2004; Ojaveer et al., 2018). The increase in the average water temperature in late 1980s caused the increase the biomass of *Acartia* spp. and, consequently, the sprat population increased. Sprat seems to be more successful than herring in finding and consuming prey when the zooplankton community is dominated by small-sized taxa. It feeds on a broad diversity of prey types and can feed during the entire day, while herring feeds mostly during dusk and dawn (Ojaveer et al., 2018). The cooperation with fishermen in the case analysed here is a very good step in the understanding of the problem of overfishing and in the protection of fish stocks, as these sensitive resources are still at the disposal of fisheries (Mills et al., 2021). Juvenile pelagic fish stocks, which are the main component of forage fishing, provide key

ecosystem services for both the natural environment and humans (Pikitch et al., 2014). They make up the key ingredient of food for predators and they are a key food base for the cod (*G. morhua*) overfished in the Baltic Sea (Eero et al., 2012).

Temperature may become a key parameter for many economically important fish species in the Baltic Sea, constituting the basis for maintaining the food chain. The same conclusions have already been drawn for the North Atlantic in Freitas et al. (2021), where research was performed for this parameter for the concentration of schools of cod, pollock and ballan wrasse fish based on fish telemetry. It was shown that the water temperature conditioned the preferences of these fish species, as it was in the case anal-

ysed here. In addition, it was shown that the body size of cod was also dependent on thermal conditions. This phenomenon was observed here, based on locating shoals of fish using echo sounders in 282 cases and taking precise temperature measurements throughout the years, which is a very large and unique data set. The temperature observed from these studies oscillated around 5.8°C throughout the years. In the months of February and March, it approached 5.0°C. This temperature is closely related to the formation of the thermocline in the Baltic Sea (Dargahi et al., 2017; Janecki et al., 2022) and the hypolimnion layer (Dargahi et al., 2017). Data from these cruises helped formulate new methods for determining the thermocline for shallow-water marine areas (Janecki et al., 2022). In the work of Janecki et al. (2022), high precision of fishing in the thermocline regions was demonstrated, and it is worth noting that the fishermen did it unknowingly. The thermocline appeared in almost every fishing catch, even in dynamically changing months such as September, where there was very high variability, with the thermocline appearing in the range from 30 m to 60 m (Figure 4). Fishing throughout the years depended on this fishing strategy of reaching depths where the thermocline and hypolimnion layer occurred, with slight deviations in autumn. It can therefore be concluded that the formation of clustered schools of herring and sprat feeding on various Copepoda species at a certain depth depends on its presence, and thus on the other components of the trophic chain that these fish form, such as food for salmonids or cod. Such food chain dependency has already been confirmed for tuna feeding on forage fish in the open ocean thermocline (Snyder et al., 2017). Dependency between the presence of zooplankton biomass and the thermocline has also been demonstrated (Ibáñez-Tejero et al., 2018; Madhupratap et al., 1981), however, these rules are changeable and ambiguous and depend on many factors, such as water dynamics and the nature of the study area. A study was also carried out by Holland et al. (2021), based on the study of the dependency between the presence of pelagic fish shoals, temperature and zooplankton density, where the dependency between the movement of fish shoals along the temperature gradient was confirmed, but no dependency was found between the presence of their potential zooplankton food (Holland et al., 2021). Such phenomenon, however, was observed in the shelf zone off the coast of Australia, but outside the zone of formation of the permanent thermocline. The hydrological conditions in the Baltic Sea are characterized by a completely different temperature distribution and cannot be directly compared. However, it is worth emphasizing that, regardless of geographical distribution, there are links between temperature variability and the occurrence of zooplankton and pelagic fish. In the era of dynamic climatic changes and changes in water thermals in the Baltic Sea (Serykh and Kostianoy, 2019), more research should be devoted to this. The problem that pelagic fish in the Baltic Sea might face may be related to the lowering of the thermocline to zones with low oxygenation and higher salinity, where at higher temperatures there is already a greater need for oxygen in the fish by increasing the metabolic rate, which puts the organisms under increasing oxidative stress (Wang and Overgaard, 2007). These studies have observed frequent drops in oxygenation under the thermocline below 50% oxygen satu-

ration in water. However, it was also noted that the oxygen saturation in most of the catches was 78.1%. In addition, good fishing performance was also dependent on high concentrations of dissolved oxygen in the water. Here again it was proved that oxygenation and temperature conditions are crucial for the development and functioning of pelagic fish (Almatar, 1984; Cardinale et al., 2002; Coombs et al., 1985; Holliday et al., 1964; Karaseva and Ivanovich, 2010; Kiørboe and Møhlenberg, 1987; Margonski et al., 2010; Petereit et al., 2008, 2009; Voss et al., 2008, 2011).

The diurnal migration of planktivorous fish found in the Baltic Sea is well known and is characterized by the formation of fish shoals during the daytime feeding phase in the lower water layers and dispersal at night in the upper water layers (Kulke et al., 2018; Nilsson et al., 2003) and fits perfectly with the fishing results obtained here (Figure 10). Research conducted in August in the summer season based on 26 hauls by Kulke et al. (2018) for sprat in the Arkona Basin, Bornholm Basin and Gotland Basin confirms this relationship and provide comparative material with the analyzes performed here. During the feeding phase, this species was present in the Bornholm Basin and Gotland Basin in deeper layers at a temperature consistent with the results obtained here. In addition, the data obtained here also confirms the presence of shoals of these fish feeding deepest throughout the year during the day in starving winter. According to Anderson et al. (2017), sprat follows the same direction of migration into the upper layers in winter as in summer at nighttime. Thanks to this summer migration, the fish speed up their metabolism to increase food intake, and in winter they can slow it down, thus reducing mortality caused by starvation. At the same time, shoals were observed here in winter at temperatures of up to 6–7°C, which may also be the subject of further research on changes in metabolism for sprat during all seasons. The daily migration of these fish may be strongly related to the search for optimal thermal conditions in order to regulate the level of metabolism throughout the whole year, depending on the availability of food and not necessarily its specific composition. This may be the reason for the concentration of fish shoals at different depths so dynamically. As it is the case in the results of the work of Holland et al. (2021), where the presence of shoals of forage fish was correlated with temperature, not with food, this principle can also be followed here. However, not only optimal temperature and salinity are responsible for the migration of clupeids, but also it depends on the season and prey abundance as well as composition during the year. Clupeids show DVM and migration during the year similar to the zooplankton species that they eat. Migrations of zooplankton and their distribution in the water column are limited by physical barriers, such as thermocline or halocline. The settlement of zooplankton along with these barriers depends on the ecophysiological tolerance of the species. Changes in the structure and abundance of plankton, especially in winter, have a decisive impact on the decrease in the growth rate of clupeids, e.g. the decrease in Mysidacea biomass contributed to a decrease in the growth rate of herring in the 1908s (Horbowy, 1997). During the winter small herring and sprat principally select *Pseudocalanus* spp., but larger herring prefer amphipods and polychaetes. Interannual variability of zooplankton abundance might be affected by clupeid predation pressure (Casini et al., 2004).

5. Conclusion

Based on 282 hauls in pelagic fisheries, the method of fishing and the increase in catch biomass of the catch statistically depended on the key parameter which turned out to be the temperature. The remaining accompanying parameters varied but, typically for the Baltic Sea, were dependent on depth – the oxygenation decreased with the depth, while the salinity increased. During the shoaling, the range of optimal thermal conditions throughout the year oscillating at 5.8°C, that pelagic fish sought was associated with the forming of thermocline and hypolimnion layers at varying depths. In the winter season, shoals of sprat were observed in the deepest zones, where the highest temperatures prevailed in the entire water column, and in the warmer seasons, they were observed higher, which is probably related to the regulation of the species' metabolism and, at the same time, adaptation to the presence of food and predators. This confirms the assumptions of many authors regarding the diurnal migration of sprat in the spring and summer seasons during the fattening period when warm surface waters at night accelerate the digestion of food obtained during the day in zones with a low temperature of about 5–6°C. During the winter starvation season, the sprat does not change direction and continues to migrate during the night to shallower zones where this time there are lower temperatures than in the feeding zone, which allows it to conserve energy by slowing down its metabolism. Furthermore, fishermen, using only the echo sounder to locate schools of fish and perform hauls, find the thermocline and the hypolimnion layer directly and with high precision. Below the thermocline, unfavourable conditions were often observed for pelagic fish with dissolved oxygen contents in water falling below 50% saturation, this phenomenon, in the face of climate change and the lowering of the thermocline, may intensify and drastically threaten the stocks of pelagic fish that tolerate high concentrations of dissolved oxygen in water.

6. Lessons learned

During measurements with the CTD probe on fishing vessels, the weakest sensor turned out to be the “Clark cell” which measures the oxygen content in water, which was subject to mechanical failures and required frequent calibration at an authorized service. Due to this, about 39% of the data for this parameter was lost. For further research in this capacity, more robust sensors are recommended, such as those based on the optical method (Fulford et al., 2005). Other sensors did not fail and did not require servicing, which made it easier for the crew of the fishing vessel to work with the probe after a short training, and the main errors that were observed resulted only from user errors: about 96% of valuable data was obtained here.

Declaration of competing interest

The authors declare that they have no known competing financial interests or personal relationships that could have appeared to influence the work reported in this paper.

Acknowledgment

The data was obtained in the project: Knowledge transfer platform FindFISH, Numerical Forecasting System for the Marine Environment of the Gulf of Gdańsk for Fisheries. The leader of the project was the Institute of the Oceanology of the Polish Academy of Sciences, and the partners were Maritime Institute – Gdynia Maritime University and the Association of Fishermen's of Sea – PO. The project was financed under the Pomorskie Voivodeship Regional Operational Program for 2014–2020.

References

- Akimova, A., Núñez-Riboni, I., Kempf, A., Taylor, M.H., 2016. Spatially-Resolved Influence of Temperature and Salinity on Stock and Recruitment Variability of Commercially Important Fishes in the North Sea. *PLoS ONE* 11 (9), e0161917. <https://doi.org/10.1371/journal.pone.0161917>
- Alder, J., Campbell, B., Karpouzi, V., Kaschner, K., Pauly, D., 2008. Forage fish: From ecosystems to markets. *Annu. Rev. Environ. Resour.* 33, 153–166. <https://doi.org/10.1146/annurev.enviro.33.020807.143204>
- Almatar, S.M., 1984. Effects of acute changes in temperature and salinity on the oxygen uptake of larvae of herring (*Clupea harengus*) and plaice (*Pleuronectes platessa*). *Mar. Biol.* 80 (2). <https://doi.org/10.1007/BF02180178>
- Andersen, N.G., Lundgren, B., Neuenfeldt, S., Beyer, J.E., 2017. Diel vertical interactions between Atlantic cod *Gadus morhua* and sprat *Sprattus sprattus* in a stratified water column. *Mar. Ecol. Prog. Ser.* 583, 195–209. <https://doi.org/10.3354/meps12319>
- Arrhenius, F., Hansson, S., 1993. Food consumption of larval, young and adult herring and sprat in the Baltic Sea. *Mar. Ecol. Prog. Ser.* 96 (2), 125–137. <https://doi.org/10.3354/meps096125>
- Bauer, B., Horbowy, J., Rahikainen, M., Kulatska, N., Müller-Karulis, B., Tomczak, M.T., Bartolino, V., 2019. Model uncertainty and simulated multispecies fisheries management advice in the Baltic Sea. *PLoS ONE* 14 (1), e0211320. <https://doi.org/10.1371/journal.pone.0211320>
- Becker, R.A., Chambers, J.M., Wilks, A.R., 2018. *The New S Language*. The New S Language. Chapman and Hall/CRC. <https://doi.org/10.1201/9781351074988>
- Cardinale, M., Casini, M., Arrhenius, F., 2002. The influence of biotic and abiotic factors on the growth of sprat (*Sprattus sprattus*) in the Baltic Sea. *Aquat. Living Resour.* 15 (5), 273–281. [https://doi.org/10.1016/S0990-7440\(02\)01188-9](https://doi.org/10.1016/S0990-7440(02)01188-9)
- Cardinale, M., Casini, M., Arrhenius, F., Håkansson, N., 2003. Diel spatial distribution and feeding activity of herring (*Clupea harengus*) and sprat (*Sprattus sprattus*) in the Baltic Sea. *Aquat. Living Resour.* 16 (3), 283–292. [https://doi.org/10.1016/S0990-7440\(03\)00007-X](https://doi.org/10.1016/S0990-7440(03)00007-X)
- Casini, M., Cardinale, M., Arrhenius, F., 2004. Feeding preferences of herring (*Clupea harengus*) and sprat (*Sprattus sprattus*) in the southern Baltic Sea. *ICES J. Mar. Sci.* 61 (8), 1267–1277. <https://doi.org/10.1016/j.icesjms.2003.12.011>
- Chambers, J.M., Hastie, T.J., 2018. *Statistical Models*. In: *Statistical Models in S*. Routledge, 13–44. <https://doi.org/10.1201/9780203738535-2>
- Coombs, S.H., Fosh, C.A., Keen, M.A., 1985. The buoyancy and vertical distribution of eggs of sprat (*Sprattus sprattus*) and pilchard (*Sardina pilchardus*). *J. Mar. Biol. Assoc. UK* 65 (2). <https://doi.org/10.1017/S0025315400050542>
- Dargahi, B., Kolluru, V., Cvetkovic, V., 2017. Multi-Layered Stratification in the Baltic Sea: Insight from a Modeling Study with

- Reference to Environmental Conditions. J. Mar. Sci. Eng. 5 (1), 2. <https://doi.org/10.3390/JMSE5010002>
- Dziaduch, D., 2011. Diet composition of herring (*Clupea harengus* L.) and cod (*Gadus morhua* L.) in the southern Baltic sea in 2007 and 2008. Oceanol. Hydrobiol. St. 40 (4), 96–109. <https://doi.org/10.2478/s13545-011-0046-z>
- Eero, M., Vinther, M., Haslob, H., Huwer, B., Casini, M., Storr-Paulsen, M., Köster, F.W., 2012. Spatial management of marine resources can enhance the recovery of predators and avoid local depletion of forage fish. Conserv. Lett. 5 (6), 486–492. <https://doi.org/10.1111/j.1755-263X.2012.00266.x>
- Figus, E., Carothers, C., Beaudreau, A.H., 2017. Using local ecological knowledge to inform fisheries assessment: Measuring agreement among Polish fishermen about the abundance and condition of Baltic cod (*Gadus morhua*). ICES J. Mar. Sci. 74 (8). <https://doi.org/10.1093/icesjms/fsx061>
- Freitas, C., Villegas-Ríos, D., Moland, E., Olsen, E.M., 2021. Sea temperature effects on depth use and habitat selection in a marine fish community. J. Anim. Ecol. 90 (7), 1787–1800. <https://doi.org/10.1111/1365-2656.13497>
- Fulford, J.M., Davies, W.J., Garcia, L., 2005. Field comparison of optical and Clark cell dissolved-oxygen sensors. World Water Congress 2005: Impacts of Global Climate Change – Proc. 2005 World Water Environ. Res. Congress. [https://doi.org/10.1061/40792\(173\)312](https://doi.org/10.1061/40792(173)312)
- Hansson, S., Larsson, U., Johansson, S., 1990. Selective predation by herring and mysids, and zooplankton community structure in a Baltic sea coastal area. J. Plankton Res. 12 (5), 1099–1116. <https://doi.org/10.1093/plankt/12.5.1099>
- Harvey, C.J., Cox, S.P., Essington, T.E., Hansson, S., Kitchell, J.F., 2003. An ecosystem model of food web and fisheries interactions in the Baltic Sea. ICES J. Mar. Sci. 60 (5). [https://doi.org/10.1016/S1054-3139\(03\)00098-5](https://doi.org/10.1016/S1054-3139(03)00098-5)
- Holland, M.M., Everett, J.D., Cox, M.J., Doblin, M.A., Suthers, I.M., 2021. Pelagic forage fish distribution in a dynamic shelf ecosystem – Thermal demands and zooplankton prey distribution. Estuar. Coast. Shelf. S. 249. <https://doi.org/10.1016/j.ecss.2020.107074>
- Holliday, F.G.T., Blaxter, J.H.S., Lasker, R., 1964. Oxygen Uptake of Developing Eggs and Larvae of the Herring (*Clupea Harengus*). J. Mar. Biol. Assoc. UK 44 (3). <https://doi.org/10.1017/S0025315400027880>
- Horbowy, J., 1997. Growth of the Baltic herring as a function of stock density and food resources. Acta Ichthyol. Piscat. 1, 27–39. <https://doi.org/10.3750/AIP1997.27.1.02>
- Ibáñez-Tejero, L., Ladah, L.B., Sánchez-Velasco, L., Barton, E.D., Filonov, A., 2018. Vertical distribution of zooplankton biomass during internal tidal forcing under mesoscale conditions of upwelling and relaxation. Cont. Shelf Res. 171. <https://doi.org/10.1016/j.csr.2018.10.003>
- ICES, 2010. Advice 2010. Book, 8 8.4.4.
- ICES, 2018. Baltic Sea Ecoregion – Ecosystem overview. ICES Ecosystem Overviews 2.
- ICES, 2021. Cod (*Gadus morhua*) in subdivisions 24–32, eastern Baltic stock (eastern Baltic Sea). In: Report ICES Advisory Committee, 2023. ICES Advice 2023, cod.27.24-32. <https://doi.org/10.17895/ices.advice.21820497>
- ICES, 2022. Baltic Fisheries Assessment Working Group (WGBFAS). ICES Scientific Rep. 4(44). <https://doi.org/10.17895/ICES.PUB.19793014.V2>
- ICES Advisory Committee, 2019. ICES Fisheries overviews Baltic Sea Ecoregion 4.2 Baltic Sea Ecoregion – Fisheries overview. ICES Fish. Rep.
- Janecki, M., Dybowski, D., Rak, D., Dzierzbicka-Głowacka, L., 2022. A New Method for Thermocline and Halocline Depth Determination at Shallow Seas. J. Phys. Oceanogr. 1. <https://doi.org/10.1175/jpo-d-22-0008.1>
- Karaseva, E.M., Ivanovich, V.M., 2010. Vertical distribution of eggs and larvae of the Baltic Sprat *Sprattus sprattus balticus* (Clupeidae) in relation to seasonal and diurnal variation. J. Ichthyol. 50 (3). <https://doi.org/10.1134/S0032945210030069>
- Kim, T.K., 2017. Understanding one-way anova using conceptual figures. Korean J. Anesthesiology 70 (1). <https://doi.org/10.4097/kjae.2017.70.1.22>
- Kjørboe, T., Møhlenberg, F., 1987. Partitioning of oxygen consumption between “maintenance” and “growth” in developing herring *Clupea harengus* (L.) embryos. J. Exp. Mar. Biol. Ecol. 111 (2). [https://doi.org/10.1016/0022-0981\(87\)90048-7](https://doi.org/10.1016/0022-0981(87)90048-7)
- Kniebusch, M., Meier, H.E.M., Radtke, H., 2019. Changing Salinity Gradients in the Baltic Sea As a Consequence of Altered Freshwater Budgets. Geophys. Res. Lett. 46 (16). <https://doi.org/10.1029/2019GL083902>
- Kornilovs, G., Sidrevics, L., Dippner, J.W., 2001. Fish and zooplankton interaction in the Central Baltic Sea. ICES J. Marine. Sci. 58, 579–588. <https://doi.org/10.1006/jmsc.2001.1062>
- Kulke, R., Bödeewadt, V., Hänselmann, K., Herrmann, J.P., Temming, A., 2018. Ignoring the vertical dimension: biased view on feeding dynamics of vertically migrating sprat (*Sprattus sprattus*). ICES J. Mar. Sci. 75 (7), 2450–2462. <https://doi.org/10.1093/ICESJMS/FSY136>
- Lankov, A., Ojaveer, H., Simm, M., Pöllupüü, M., Möllmann, C., 2010. Feeding ecology of pelagic fish species in the Gulf of Riga (Baltic Sea): The importance of changes in the zooplankton community. J. Fish. Biol. 77 (10), 2268–2284. <https://doi.org/10.1111/j.1095-8649.2010.02805.x>
- Lehmann, A., Myrberg, K., Post, P., Chubarenko, I., Dailidienė, I., Hinrichsen, H.H., Hüsey, K., Liblik, T., Meier, H.E.M., Lips, U., Bukanova, T., 2022. Salinity dynamics of the Baltic Sea. Earth Syst. Dynam. 13 (1). <https://doi.org/10.5194/esd-13-373-2022>
- Madhupratap, M., Nair, V., Nair, S., Achuthankutty, C., 1981. Thermocline and zooplankton distribution. Indian J. Geo-Mar. Sci. (IJMS) 10 (3).
- Maravelias, C.D., Reid, D.G., Swartzman, G., 2000. Modelling spatio-temporal effects of environment on Atlantic herring, *Clupea harengus*. Environ. Biol. Fish. 58 (2). <https://doi.org/10.1023/A:1007693732571>
- Margonski, P., Hansson, S., Tomczak, M.T., Grzebielec, R., 2010. Climate influence on Baltic cod, sprat, and herring stock-recruitment relationships. Prog. Oceanogr. 87 (1–4), 277–288. <https://doi.org/10.1016/j.pocean.2010.08.003>
- Markus Meier, H.E., Kniebusch, M., Dieterich, C., Gröger, M., Zorita, E., Elmgren, R., Myrberg, K., Ahola, M.P., Bartosova, A., Bonsdorff, E., Börgel, F., Capell, R., Carlén, I., Carlund, T., Carstensen, J., Christensen, O.B., Dierschke, V., Frauen, C., Frederiksen, M., Zhang, W., 2022. Climate change in the Baltic Sea region: A summary. Earth Syst. Dynam. 13 (1), 457–593. <https://doi.org/10.5194/esd-13-457-2022>
- McHugh, M.L., 2011. Multiple comparison analysis testing in ANOVA. Biochem. Medica 21 (3). <https://doi.org/10.11613/bm.2011.029>
- Mills, K.E., Kerr, L., Reidmiller, D., Tokunaga, K., 2021. Future fisheries in a changing ocean. MAR Technol. Soc. J. 55 (3). <https://doi.org/10.4031/MTSJ.55.3.32>
- Möllmann, C., Kornilovs, G., Fetter, M., Köster, F.W., 2004. Feeding ecology of central Baltic Sea herring and sprat. J. Fish. Biol. 65 (6), 1563–1581. <https://doi.org/10.1111/j.0022-1112.2004.00566.x>
- Möllmann, C., Kornilovs, G., Sidrevics, L., 2000. Long-term dynamics of the main mesozooplankton species in the central Baltic Sea. J. Plankton Res. 22, 2015–2038. <https://doi.org/10.1093/plankt/22.11.2015>
- Neverman, D., Wurtsbaugh, W.A., 1994. The thermoregulatory function of diel vertical migration for a juvenile fish, *Cottus extensus*. Oecologia 98 (3–4), 247–256. <https://doi.org/10.1007/BF00324211>

- Nilsson, L.A.F., Thygesen, U.H., Lundgren, B., Nielsen, B.F., Nielsen, J.R., Beyer, J.E., 2003. Vertical migration and dispersion of sprat (*Sprattus sprattus*) and herring (*Clupea harengus*) schools at dusk in the Baltic Sea. *Aquat. Living Resour.* 16 (3), 317–324. [https://doi.org/10.1016/S0990-7440\(03\)00039-1](https://doi.org/10.1016/S0990-7440(03)00039-1)
- Ojaveer, H., Lankov, A., Raid, T., Pollumae, A., Klais, R., 2018. Selecting for three copepods – feeding of sprat and herring in the Baltic Sea. *ICES J. Marine Sci.* 75 (7), 2439–2449. <https://doi.org/10.1093/icesjms/fsx249>
- Parmanne, R., Rechlin, O., Sjöstrand, B., 1994. *Status and future of herring and sprat stocks in the Baltic Sea* (Vol. 10).
- Petereit, C., Haslob, H., Kraus, G., Clemmesen, C., 2008. The influence of temperature on the development of Baltic Sea sprat (*Sprattus sprattus*) eggs and yolk sac larvae. *Mar. Biol.* 154 (2), 295–306. <https://doi.org/10.1007/s00227-008-0923-1>
- Petereit, C., Hinrichsen, H.H., Voss, R., Kraus, G., Freese, M., Clemmesen, C., 2009. The influence of different salinity conditions on egg buoyancy and development and yolk sac larval survival and morphometric traits of Baltic Sea sprat (*Sprattus sprattus* Schneider). *Sci. Mar.* 73 (S1). <https://doi.org/10.3989/scimar.2009.73s1059>
- Pihlajamäki, M., Asikainen, A., Ignatius, S., Haapasaari, P., Tuomisto, J.T., 2019. Forage fish as food: Consumer perceptions on Baltic herring. *Sustainability* 11 (16), 4298. <https://doi.org/10.3390/su11164298>
- Pikitch, E.K., Rountos, K.J., Essington, T.E., Santora, C., Pauly, D., Watson, R., Sumaila, U.R., Boersma, P.D., Boyd, I.L., Conover, D.O., Cury, P., Heppell, S.S., Houde, E.D., Mangel, M., Plagányi, É., Sainsbury, K., Steneck, R.S., Geers, T.M., Gownaris, N., Munch, S.B., 2014. The global contribution of forage fish to marine fisheries and ecosystems. *Fish. Fish.* 15 (1), 43–64. <https://doi.org/10.1111/faf.12004>
- Receveur, A., Bleil, M., Funk, S., Stötera, S., Gräwe, U., Naumann, M., Dutheil, C., Krumme, U., 2022. Western Baltic cod in distress: decline in energy reserves since 1977. *ICES J. Mar. Sci.* 79 (4). <https://doi.org/10.1093/icesjms/fsac042>
- Saroux, C., Fromentin, J.M., Bigot, J.L., Bourdeix, J.H., Morfin, M., Roos, D., van Beveren, E., Bez, N., 2014. Spatial structure and distribution of small pelagic fish in the northwestern mediterranean sea. *PLoS ONE* 9 (11). <https://doi.org/10.1371/journal.pone.0111211>
- Schwertman, N.C., Owens, M.A., Adnan, R., 2004. A simple more general boxplot method for identifying outliers. *Computation. Statistics Data Anal.* 47 (1). <https://doi.org/10.1016/j.csda.2003.10.012>
- Serykh, I.v., Kostianoy, A.G., 2019. About the climatic changes in the temperature of the Baltic Sea. *Fund. Appl. Hydro.* 12 (3). <https://doi.org/10.7868/S207366731903002X>
- Simpson, D.G., 1989. Hellinger deviance tests: Efficiency, breakdown points, and examples. *J. Am. Stat. Assoc.* 84 (405), 107–113. <https://doi.org/10.1080/01621459.1989.10478744>
- Snyder, S., Franks, P.J.S., Talley, L.D., Xu, Y., Kohin, S., 2017. Crossing the line: Tunas actively exploit submesoscale fronts to enhance foraging success. *Limnol. Oceanogr. Lett.* 2 (5). <https://doi.org/10.1002/lo2.10049>
- Tamm, O., Maasikamäe, S., Padari, A., Tamm, T., 2018. Modelling the effects of land use and climate change on the water resources in the eastern Baltic Sea region using the SWAT model. *CATENA* 167. <https://doi.org/10.1016/j.catena.2018.04.029>
- Van Vranken, C., Vastenhou, B.M.J., Manning, J.P., Plet-Hansen, K.S., Jakoboski, J., Gorrige, P., Martinelli, M., 2020. Fishing Gear as a Data Collection Platform: Opportunities to Fill Spatial and Temporal Gaps in Operational Sub-Surface Observation Networks. *Front. Mar. Sci.* 7, 864. <https://doi.org/10.3389/fmars.2020.485512>
- Voss, R., Dickmann, M., Hinrichsen, H.H., Floeter, J., 2008. Environmental factors influencing larval sprat *Sprattus sprattus* feeding during spawning time in the Baltic Sea. *Fish. Oceanogr.* 17 (3). <https://doi.org/10.1111/j.1365-2419.2008.00474.x>
- Voss, R., Hinrichsen, H.H., Quaas, M.F., Schmidt, J.O., Tahvonen, O., 2011. Temperature change and Baltic sprat: From observations to ecologicaleconomic modelling. *ICES J. Mar. Sci.* 68 (6). <https://doi.org/10.1093/icesjms/fsr063>
- Wang, T., Overgaard, J., 2007. The heartbreak of adapting to global warming. *Science* 315 (5808). <https://doi.org/10.1126/science.1137359>
- Załachowski, W., Szypuła, J., Krzykowski, S., Krzykawska, I., 1975. Feeding of some commercial fishes in the southern region of the Baltic Sea – in 1971 and 1972. *Pol. Arch. Hydrobiol.* 22 (3), 429–448 (in Polish with Engl. summ).

Available online at www.sciencedirect.com

ScienceDirect

journal homepage: www.journals.elsevier.com/oceanologia

ORIGINAL RESEARCH ARTICLE

Long-term statistics of atmospheric conditions over the Baltic Sea and meteorological features related to wind wave extremes in the Gulf of Gdańsk

Witold Cieślíkiewicz^{a,*}, Aleksandra Cupiał^b

^a*Institute of Hydro-Engineering, Polish Academy of Sciences, Gdańsk, Poland*

^b*Department of Physical Oceanography and Climate Research, University of Gdańsk, Gdynia, Poland*

Received 5 October 2021; accepted 13 October 2023

Available online 7 November 2023

KEYWORDS

Atmospheric pressure;
Wave climate;
Extreme waves;
EOF analysis

Abstract The goal of this study is to describe wind wave climate and wave extremes of the Gulf of Gdańsk in the southern Baltic Sea and associated meteorological conditions over the Baltic Sea. We obtain the characteristic features of 34 severe historical storms in the Gulf of Gdańsk during the period 1958–2001 and link them with extreme significant wave heights hindcast for five grid points in this gulf. The long-term statistics of atmospheric pressure systems over central and northern Europe, and the north-eastern Atlantic Ocean are derived from a 44-year REMO reanalysis database. A link between the mean, minimum and variability range of atmospheric pressure has been quantified. In general, the higher the mean pressure the smaller its variability and vice versa. Long-term characteristic features of winds over the Baltic Sea have been estimated from the REMO database. Strong winds directions vary from W, WSW to SW in the southern Baltic to more southerly SSW directions in the northern part of the Baltic Sea. The Empirical Orthogonal Functions (EOF) analysis shows that more than 50% of the variability in the atmospheric pressure in the Baltic Sea can be explained by the first EOF mode. The first four EOF modes can reproduce above 90% variability of the hindcast pressure time series. Statistical properties of the hindcast significant wave height over the Gulf of Gdańsk are computed based on the 44-year HIPOCAS database. All the computed statistics of wave heights reveal a very strong sheltering effect caused by the Hel Peninsula.

© 2023 Institute of Oceanology of the Polish Academy of Sciences. Production and hosting by Elsevier B.V. This is an open access article under the CC BY-NC-ND license (<http://creativecommons.org/licenses/by-nc-nd/4.0/>).

* Corresponding author at: Institute of Hydro-Engineering, Polish Academy of Sciences, Kościarska 7, 80–328 Gdańsk, Poland.

E-mail address: ciesl@ibwpan.gda.pl (W. Cieślíkiewicz).

Peer review under the responsibility of the Institute of Oceanology of the Polish Academy of Sciences.



Production and hosting by Elsevier

<https://doi.org/10.1016/j.oceano.2023.10.002>

0078-3234/© 2023 Institute of Oceanology of the Polish Academy of Sciences. Production and hosting by Elsevier B.V. This is an open access article under the CC BY-NC-ND license (<http://creativecommons.org/licenses/by-nc-nd/4.0/>).

1. Introduction

Nowadays, with possible changes in wind patterns (e.g. Suursaar and Kullas, 2009), particularly during the winter period (Bierstedt et al., 2015), as well as growing interests in the development of wind farms and other forms of renewable energy on the Baltic Sea (Bernhoff et al., 2006; Cieřlikiewicz et al., 2015) statistical characteristics of prevailing wind wave conditions and changes in their spatial patterns are essential. In what follows we speak about waves and wave climate, having in mind wind waves.

The knowledge of wave climate understood as a set of spatial distributions of long-term properties of waves is vital for populations living near the coast and for many marine activities. For example, in offshore and coastal engineering, one can estimate probabilistic characteristics of waves and wave loads on marine structures (see amongst others Chakrabarti, 1994; Cieřlikiewicz, 1990; Cieřlikiewicz and Massel, 1988; Dean and Dalrymple, 1991; Jose et al., 2017, 2018) or wave-induced transport on the sea surface (Cieřlikiewicz and Gudmestad, 1994), which can be directly linked with a wind-driven surface current. Those and similar estimations can be done using the concept of extreme design wave (see e.g. Tucker and Pitt, 2001) or by application of wave spectra inferred from the wave climate information (see e.g. Massel, 2017).

Numerous researchers have explored the wave climate in the Baltic Sea, both on a broad scale encompassing the entire Sea (Björkqvist et al., 2018; Soomere and Räämet, 2011) and on a local scale focusing on selected Baltic areas. For example, Soomere (2005) concentrated on the Gulf of Tallinn, demonstrating that even in sheltered regions, winds conducive to generating substantial wave heights can create devastating wave conditions. A comprehensive review of wave climate studies was recently provided by Soomere (2023).

The Gulf of Gdańsk, located in the southeastern part of the Baltic Sea (Figure 1) is an important sea basin for Poland. The Tricity metropolitan area containing Gdynia, Gdynia and Sopot is located on the south-western coast of the gulf. Together with minor towns in its vicinity, it

has a population of over one million people. Two of the three largest ports in Poland are located in this gulf: the Port of Gdańsk and the Port of Gdynia. The north-western part of the Gulf of Gdańsk is separated from the Baltic Proper by a long sandspit, the Hel Peninsula, which defines the Bay of Puck and strongly affects wave propagation into the gulf from the open Baltic Sea. The Hel Peninsula has a significant impact on wave energy distribution in the western part of the gulf, in particular in the vicinity of the Tricity's ports. The strategic role of the Gulf of Gdańsk together with significant investments in the port's infrastructure and other maritime engineering activities, that are planned, make crucial the knowledge of long-term statistical characteristics of predominant and extreme wave conditions, various return periods and design wave parameters.

The principal goal of this work is to develop a comprehensive description of wave climate and wave extremes in the Gulf of Gdańsk and associated meteorological conditions over the Baltic Sea. This is reached using modelled data spanning over almost half a century. We also obtain the characteristic features of storms that had created extreme risks and hazards in the Gulf of Gdańsk during the period 1958–2001. Though our study's timeframe (1958–2001) may not reflect the current wave climate, it offers valuable retrospective data, enriching the understanding of long-term wave patterns.

The long-term statistical characteristics of significant wave heights H_s in the Gulf of Gdańsk were also analysed by Badur and Cieřlikiewicz (2018) based on the output of wave model WAM (WAVE Model) over a relatively short period. They used System Identification (SI) techniques to extend the time span of the H_s data. Namely, in Badur and Cieřlikiewicz (2018) the SI techniques were applied to wind and wave data, corresponding to 29 extreme storms selected from a 4-year long period, to build a parametric model. That model was then used to reconstruct the Gulf of Gdańsk's 138-year wave height time series. In our study, the statistical properties of significant wave heights over the Gulf of Gdańsk are inferred directly from the data modelled with WAM over the 1958–2001 period.



Figure 1 Location of the Gulf of Gdańsk in the Baltic Sea.

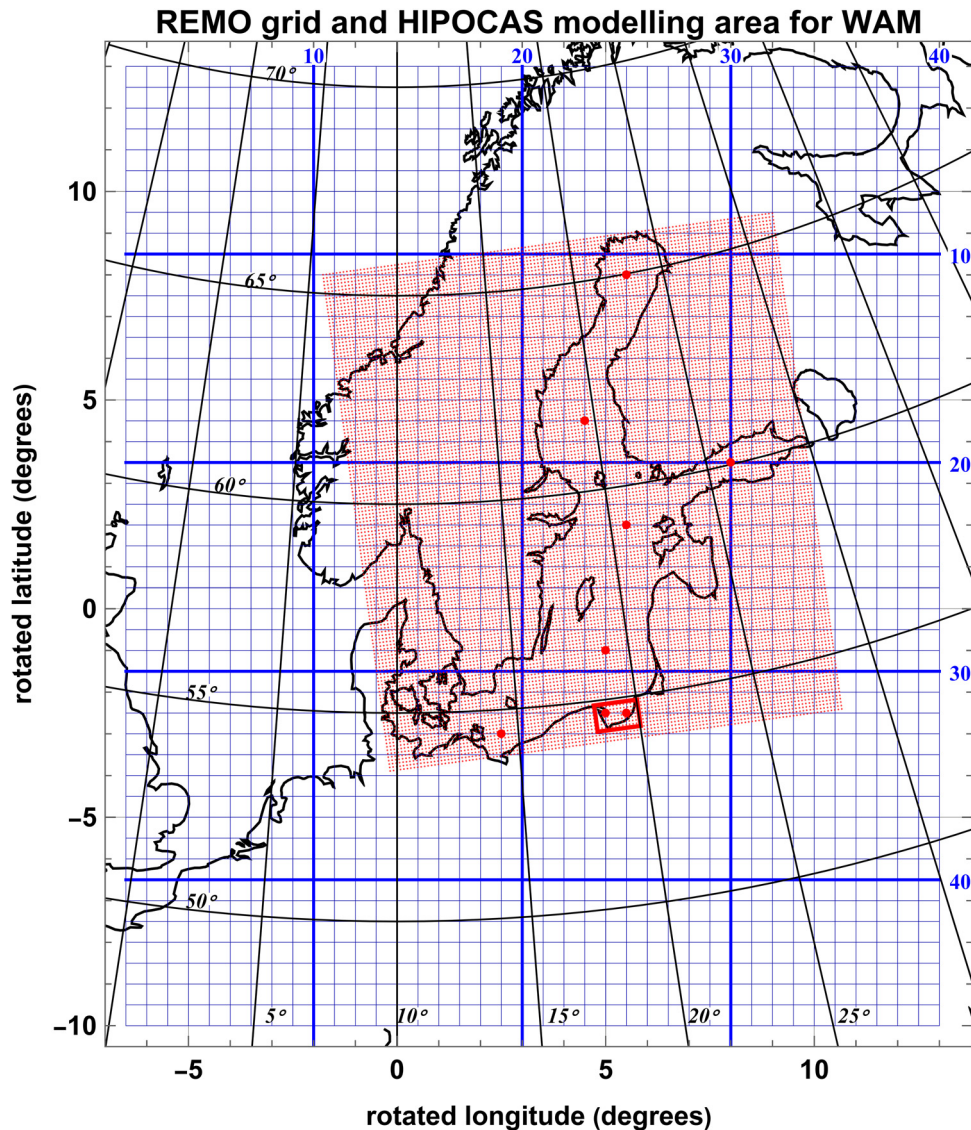


Figure 2 Sub-grid of REMO meteorological data extracted for the wave modelling over the Baltic Sea. The computational grid for wave modelling with WAM is marked with red. The Gulf of Gdańsk area is shown in the red frame. Red dots indicate the points selected for the presentation of long-term characteristics of wind properties.

2. Data and methods

We analyse two hindcast datasets: the 44-year-long reanalysis of meteorological data produced with the atmospheric model REMO (REgional MOdel; Feser et al., 2001; Jacob and Podzun, 1997; von Storch et al., 2000) and the time series of wave properties produced with the wave model WAM. Both these datasets are the result of an EU-funded project HIPOCAS (Cieřlikiewicz et al., 2005; Cieřlikiewicz and Paplińska-Swerpel, 2008). Its objective was to obtain a high-resolution homogeneous multi-decadal hindcast of wind, wave, sea-level, and current parameters for European waters and coastal areas.

The meteorological forcing data, used within the HIPOCAS project, were 1-hourly gridded wind velocity fields provided by Forschungszentrum Geesthacht GmbH (GKSS,

also Helmholtz-Zentrum Geesthacht–HZG; now Hereon). The wind hindcast covering the period 1958–2001 was performed with the atmospheric REMO model. The REMO modelling area covers Europe and NE Atlantic with a $0.5^\circ \times 0.5^\circ$ resolution. For the modelling of currents and waves over the Baltic Sea, a subset of gridded REMO data was extracted (Figure 2). Wave data were produced on a rectangular grid in spherical rotated coordinates with the resolution of $5' \times 5'$ and validated against observed records in Cieřlikiewicz and Paplińska-Swerpel (2008).

The objective of this work is dual. First, we want to estimate long-term stochastic characteristics of the basic meteorological parameters, such as atmospheric pressure at sea level and the wind velocity at 10 m height, on the one hand, and wave field, on the other hand, over the entire Baltic Sea.

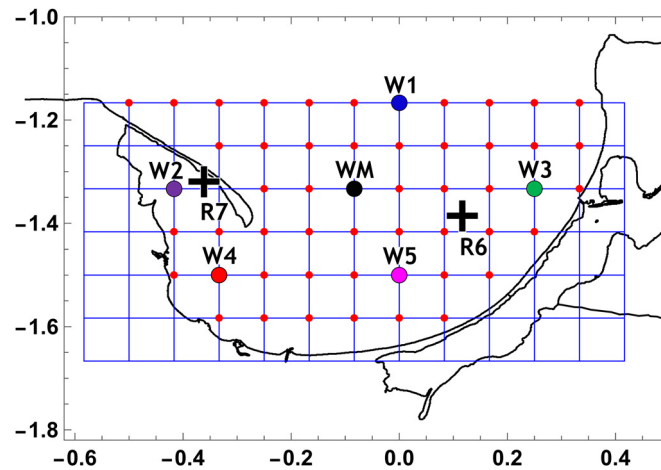


Figure 3 Gulf of Gdańsk part of computational grid for wave modelling in rotated WAM coordinates labelled in degrees. Small red circles indicate sea nodes used in modelling. Larger circles indicate points selected in the Gulf of Gdańsk for the analysis (W1–W5 and WM). REMO grid points R6 and R7 are marked with black crosses.

To characterise long-term statistical features of wind properties over the Baltic Sea, eight locations R1, R2, ..., R8 representing various Baltic Sea basins were selected (Figure 2) to evaluate various statistics in these locations. We focus on significant wave height, mean wave period and the mean direction of wave propagation. We also look for the essential characteristics of the meteorological conditions using the Empirical Orthogonal Functions (EOF) method, applied to the mean sea level atmospheric pressure fields over the whole REMO area.

To determine the characteristic features of meteorological conditions causing extreme sea states in different areas of the Gulf of Gdańsk, a number of extreme storms, that are critical for five different Gulf of Gdańsk regions, are selected based on significant wave height time series for the computational grid points in these regions. For those storms, the depressions’ tracks and the overall evolution of atmospheric pressure and wind velocity fields were examined.

The relevant locations of five WAM grid nodes W1, W2, ..., W5 are shown in Figure 3. The points R6 and R7 in the Gulf of Gdańsk are shown together with location WM representing the central part of the gulf (Table 1).

For each location W1–W5, an associated threshold value of H_5 was established. Each threshold is defined in such a way that there are exactly 15 events, in which the modelled H_5 time series exceeds this threshold. The final list of selected storms was created by merging all storms that were among these top 15 at least in one of the locations W1–W5. The resulting number of storms may vary between 15 and $5 \times 15 = 75$. The number of selected storms in the range [15, 75] is a kind of variability measure of the analysed sea basin in terms of significant wave height. The greater this number, the greater the differences between the extreme meteorological conditions that drive extreme wave conditions at different locations. Conversely, the smaller the number of selected storms, the less the variety of extreme storm events over the area of interest. In the case of the HIPOCAS significant wave height data and the selected locations in the Gulf of Gdańsk (Figure 3), the number of extreme storm events was 34 (Table 2). Those

storm events will be referred to as storms S1, S2, ..., S34. The resulting number of extreme wave events obtained for the Gulf of Gdańsk based on this algorithm, showed that this area is surprisingly diverse in terms of strong storm events.

It is worth mentioning that 18 extreme storm events from that list (S1, S3–S6, S8, S13, S15, S18–S21, S23–S25, S28, S30 and S32) correspond to the extreme storms discussed in Cieřlikiewicz et al. (2018, 2017).

3. Results

We start from the presentation of the principal results of this work in terms of long-term basic statistics like spatial distributions of mean, standard deviation, maximum and minimum values of atmospheric pressures in Section 3.1. This is followed by a description of long-term basic statistics for wind velocity in terms of frequency histograms of the velocity for the eight selected locations R1–R8 in Section 3.2. Because points R6 and R7 are located close to each other in the Gulf of Gdańsk, we will show a frequency histogram of the time series of their averaged velocity.

The EOF method (Cieřlikiewicz and Graff, 1996, 1997; Obukhov, 1960; Lorenz, 1956; Prandtl and Matthews, 1990) was applied to atmospheric pressure fields (Section 3.3). The analysis of temporal variations of the most significant principal components as well as associated spatial patterns, being the corresponding EOF modes, provided a deeper insight into the meteorological conditions prevailing over the study area and a better knowledge of their relation to wind wave characteristics in the Gulf of Gdańsk. Finally, we characterize the wave climate of the Gulf of Gdańsk with three integral wave parameters, namely: significant wave height H_5 , mean wave period T_z and the mean direction of wave propagation θ (Section 3.4).

3.1. Atmospheric pressure

The spatial distributions of long-term basic statistical properties for the mean sea level atmospheric pressure were

Table 1 Coordinates of REMO and WAM nodes selected for the analysis.

Data set	ID	Location		
		Geographical coordinates	Rotated coordinates [°]	Grid coordinates
Meteorological (REMO)	R1	64.9740° N, 22.9656° E	5.5, 8.0	25, 11
	R2	61.6853° N, 19.4918° E	4.5, 4.5	23, 18
	R3	60.0461° N, 26.1537° E	8.0, 3.5	30, 20
	R4	59.0647° N, 20.7388° E	5.5, 2.0	25, 23
	R5	56.1683° N, 19.0049° E	5.0, -1.0	24, 29
	R6	54.6144° N, 19.5180° E	5.5, -2.5	25, 32
	R7	54.6810° N, 18.6623° E	5.0, -2.5	24, 32
	R8	54.4210° N, 14.2936° E	2.5, -3.0	19, 33
Wind wave (WAM)	W1	54.8333° N, 19.3000° E	0.0000, -1.166(6)	69, 135
	W2	54.6645° N, 18.5798° E	-0.416(6), -1.333(3)	64, 137
	W3	54.6666° N, 19.7322° E	0.2500, -1.333(3)	72, 137
	W4	54.4986° N, 18.7262° E	-0.333(3), -1.5000	65, 139
	W5	54.5000° N, 19.3000° E	0.0000, -1.5000	69, 139
	WM	54.6666° N, 19.1559° E	-0.083(3), -1.333(3)	68, 137

computed for each REMO computational grid node for the period of interest 1958–2001. The distributions of mean and standard deviation and maximum and minimum values of atmospheric pressure will be given in the form of contour plots resulting from 2D cubic spline interpolation.

The mean value of atmospheric pressure at the sea level (Figure 4a) varies over the area of interest from 1007 hPa over the Norwegian Sea to about 1015 hPa over land in the southern part of the area. The mean pressure over the Baltic Sea changes from about 1009 hPa in its northern part to about 1013 hPa over the southern Baltic. The orientation of the average isobars over the Baltic represents WSW winds in the southern Baltic and SW winds in the eastern Baltic Proper and the Gulf of Finland.

The dispersion of atmospheric pressure time series, relative to their means, is characterised in terms of the standard deviation (Figure 4b). It spans between 8 hPa over the southern land part of the study area and about 14 hPa over the Norwegian Sea. Interestingly, the spatial distribution of standard deviation is, to a certain extent, an inverse of the distribution of the mean atmospheric pressure. The greater the mean value, the smaller the standard deviation of the atmospheric pressure time series. Indeed, the Pearson correlation coefficient equal to -0.93 confirms that there is a high and negative correlation between these variables. This correlation is statistically significant (p -value $< .001$).

The overall range of sea level atmospheric pressure (Figure 5 a,b) spans between the minimum value of 924 hPa over the Norwegian Sea and the maximum value of 1061 hPa Northeast of the White Sea. The minimum value of atmospheric pressure (Figure 5a) is the largest in the SE part of the analysed area, where it is about 977 hPa. While the deepest minimum atmospheric pressure reaches 924 hPa

over the North Sea, another region of low minimum values (about 936 hPa) exists over the southern part of the Bothnian Sea in the vicinity of the Fasta Island (Åland Islands). The maximum atmospheric pressure varies between 1044 hPa over the Norwegian Sea adjacent to Northern Scandinavia and 1061 hPa north-west of the White Sea. The maximum values over the Baltic Sea span between about 1047 hPa in the east Pomeranian coast and about 1057 hPa in the north-eastern Bothnian Bay (Figure 5b).

The range between the maximum and minimum atmospheric pressure spans between 75 hPa and 125 hPa (Figure 6). The distribution of this range matches the distribution of the standard deviation (Figure 4b) that indicates the areas with the lowest (in the SE part of the studied area) and highest (over the Norwegian Sea) variability. A region of greater range reaching 115 hPa is located in the southern Bothnian Sea, with a centre in the vicinity of the Fasta Island. A comparison of distributions presented in Figure 5a and Figure 6 reveals a notable finding: the spatial distribution of atmospheric pressure range reflects almost exactly the opposite of minimum atmospheric pressure. This observation shows that the greater the average atmospheric pressure the smaller its variability. In essence, this feature reflects the difference between the range of variations of the maxima (about 17 hPa) and minima (about 53 hPa). Of course, in the hypothetical case of constant maximum pressure, the range of pressure values will exactly correspond to the opposite values of minimum pressures, with accuracy up to an additive constant, that is, this constant maximum pressure. In our study, however, the variability range of maximum pressure is noticeable, being equal to about one-third of the range of minimum pressure variability. To quantify the relationship between the minimum pressure and its range, the Pearson correlation coefficient between

Table 2 Selected extreme storms, maximum wave height and wind speed over the Gulf of Gdańsk.

No. of storm	Start date	End date	Max H_5 [m]	Max wind speed U averaged for R6 and R7 [m/s]
1	1961-Dec-20 06:00	1961-Dec-22 08:00	6.09	19.4
2	1962-Feb-11 19:00	1962-Feb-13 23:00	3.81	19.2
3	1962-Feb-16 20:00	1962-Feb-19 08:00	6.91	20.6
4	1962-Feb-20 00:00	1962-Feb-22 07:00	7.22	19.5
5	1967-Nov-18 04:00	1967-Nov-20 05:00	5.82	19.2
6	1975-Nov-20 06:00	1975-Nov-22 13:00	6.65	19.4
7	1976-Jan-04 21:00	1976-Jan-07 09:00	6.57	22.0
8	1976-Dec-25 08:00	1976-Dec-27 20:00	6.42	21.2
9	1977-Dec-23 19:00	1977-Dec-26 04:00	4.87	19.2
10	1981-Nov-20 06:00	1981-Nov-22 11:00	4.03	20.4
11	1981-Nov-23 10:00	1981-Nov-26 11:00	4.37	21.7
12	1982-Dec-15 13:00	1982-Dec-17 19:00	4.24	21.5
13	1983-Jan-18 04:00	1983-Jan-21 05:00	6.78	20.9
14	1984-Jan-12 15:00	1984-Jan-14 19:00	2.14	17.8
15	1986-Apr-09 16:00	1986-Apr-12 01:00	5.40	18.2
16	1986-Oct-20 15:00	1986-Oct-22 18:00	4.04	20.8
17	1986-Dec-01 06:00	1986-Dec-03 10:00	4.56	20.2
18	1988-Nov-28 15:00	1988-Dec-01 06:00	8.00	21.6
19	1988-Dec-13 16:00	1988-Dec-16 00:00	6.36	18.1
20	1989-Sep-29 23:00	1989-Oct-02 01:00	5.78	17.8
21	1989-Dec-06 08:00	1989-Dec-08 16:00	6.50	19.4
22	1990-Jan-25 05:00	1990-Jan-27 14:00	3.47	19.6
23	1992-Jan-16 05:00	1992-Jan-18 16:00	7.34	22.1
24	1992-Oct-11 01:00	1992-Oct-13 04:00	6.18	17.6
25	1992-Nov-07 11:00	1992-Nov-09 18:00	6.21	19.1
26	1993-Jan-13 06:00	1993-Jan-15 14:00	4.69	22.3
27	1993-Jan-21 08:00	1993-Jan-25 23:00	4.25	20.9
28	1997-Apr-10 15:00	1997-Apr-13 11:00	7.46	20.8
29	1997-Oct-23 02:00	1997-Oct-25 11:00	7.33	24.7
30	1998-Jan-30 02:00	1998-Feb-01 18:00	6.74	19.5
31	1999-Dec-02 23:00	1999-Dec-05 12:00	5.21	23.0
32	2000-Jan-17 14:00	2000-Jan-22 09:00	7.06	21.8
33	2001-Oct-31 01:00	2001-Nov-02 03:00	4.77	21.2
34	2001-Dec-20 03:00	2001-Dec-22 09:00	5.36	21.8

these two variables was calculated. It appeared to be statistically significant (p -value $< .001$) and equal to -0.94 , which confirms a strong negative correlation. In Figure 7 the scatter plots of the pressure range Δp against the minimum p_{\min} and the maximum p_{\max} are presented. The linear regression line, fitted by the least squares method, $\Delta p = -0.98 p_{\min} + 1030$ hPa is also shown in Figure 7. The regression slope, which is very close to -1 , demonstrates the fact that indeed the pressure range, over the analysed area, is close to the opposite of minimum pressure.

3.2. Wind velocity

In this section, we focus on wind velocity at 10 m above the sea level. The cumulative distributions of wind speed and direction frequency in locations across the entire sea (Figure 2) over the period 1958–2001 are presented as polar plots of frequency histograms in a wind rose-like form in Figure 8.

Each plot is an elaborated presentation of the 2D frequency histogram over the wind speed and direction. The direction angle of the wind velocity vector is counted anticlockwise from the east. Thus, the diagrams in Figure 8 show the directions towards which the wind blows in polar coordinates. The direction bins (direction sectors) cover sectors of 10° width counted from -180° to $+180^\circ$ with centres at directions from -170° to $+180^\circ$. Thus, western winds are shown as the winds with the direction 0° (that represents the direction to the East).

Figure 8 highlights a strong anisotropy of wind directions, that is clearly stronger for stronger winds. For higher wind speeds, W, WSW to SW winds dominate in the southern part of the Baltic Sea and more southerly (SSW) in the northern Baltic areas. More to the north, the predominant wind direction, especially for stronger winds, is either from almost south or from almost north. Measurements at coastal stations in the Bay of Bothnia (1977–1982) show that while south-westerly winds are most frequent in the

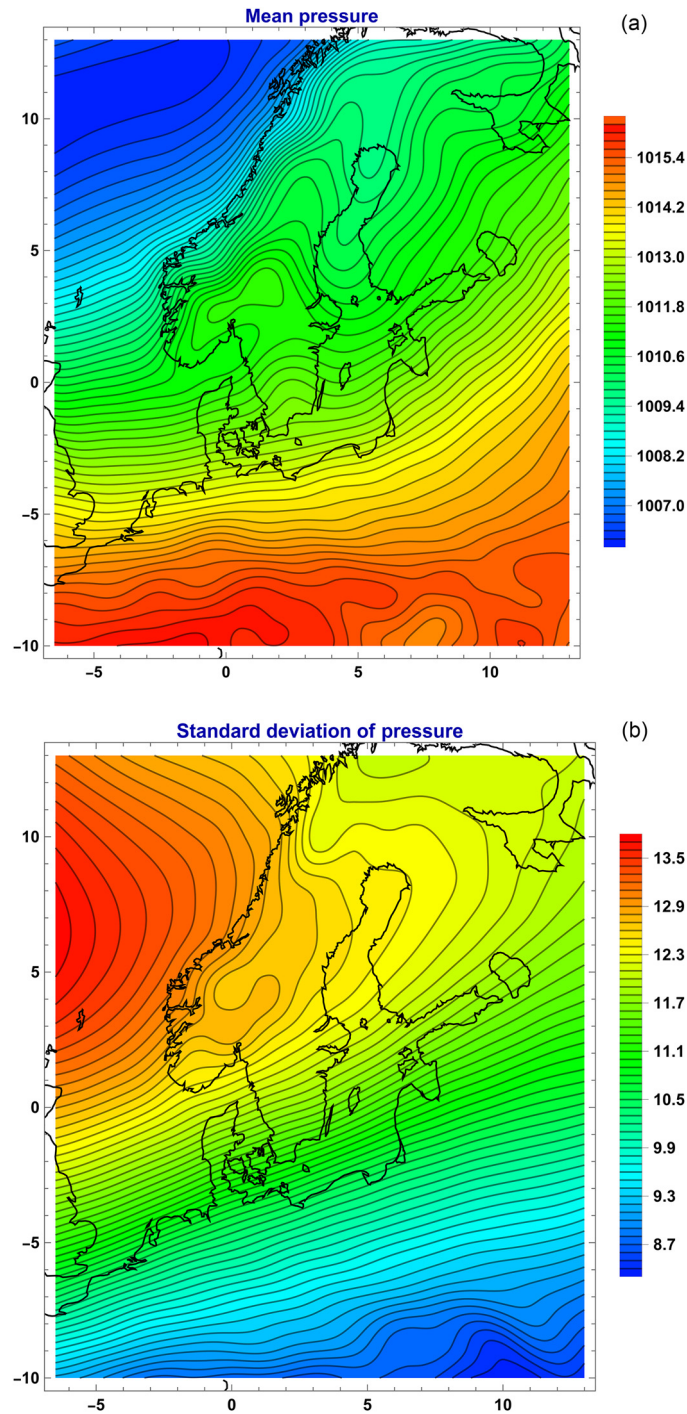


Figure 4 Mean (a) and standard deviation (b) of pressure in 1958–2001 (in hPa).

area, north and north-easterly winds are also quite common (Launiainen and Laurila, 1984). In all the Baltic Sea sub-basins wind speed of 5–10 m/s occurs most often. The highest wind speeds are in the south-western Baltic Sea (point R8) and in the centre of the Baltic Proper (point R5). Note that the distribution of the most frequent wind directions reflects, to a certain degree, the directions of maximum fetches in most areas. This characteristic of the Baltic Sea wind regime shows that dominant wind direc-

tions depend either on large-scale circulation (westerlies from the North Atlantic) or local conditions. This determines considerable anisotropy of wind fields which was also presented in measured data from meteorological stations in Baltic Proper (Soomere, 2003). Stronger winds have more pronounced anisotropy than weaker winds (Bierstedt et al., 2015). The described pattern of prevailing strong wind directions is in good agreement with isobar directions of the mean atmospheric pressure (Figure 4a).

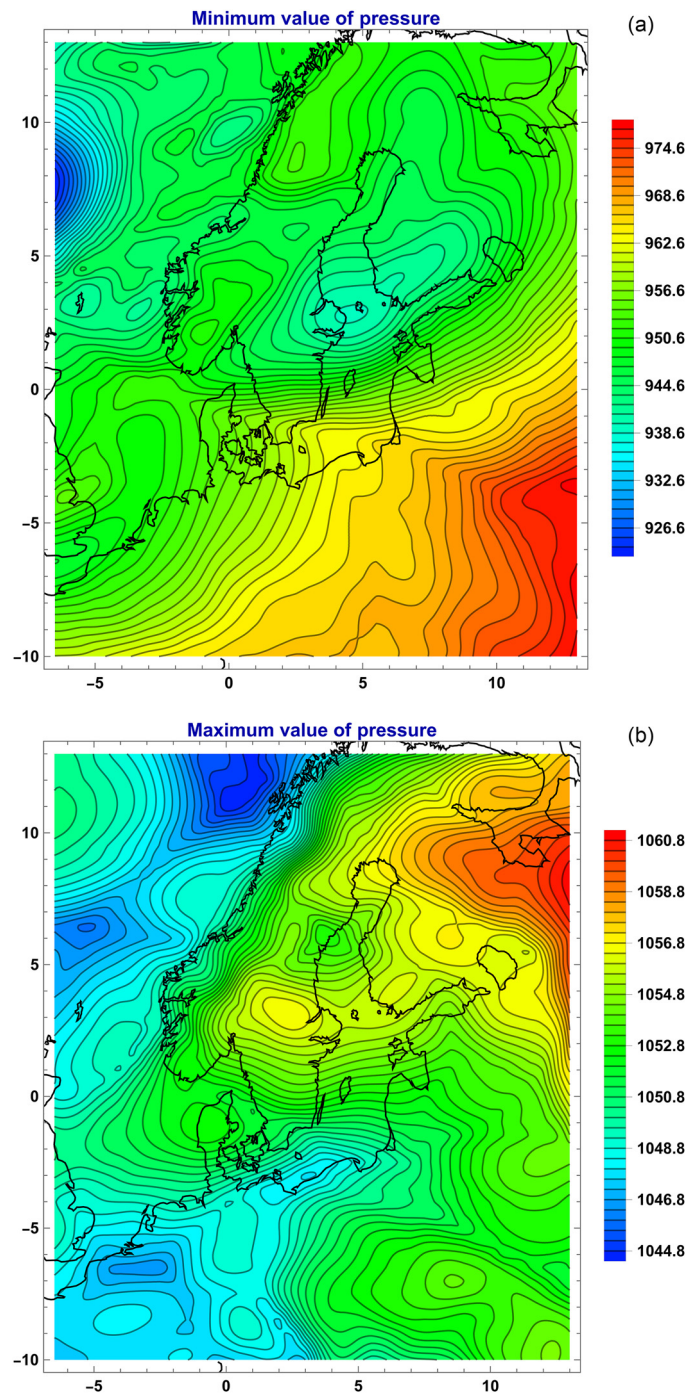


Figure 5 Minimum (a) and maximum (b) value of pressure in 1958–2001 (in hPa).

3.3. EOF analysis for atmospheric pressure

The EOF analysis in the time domain has been widely used in meteorological, environmental, and oceanographic studies for a few decades (see e.g. Cieřlikiewicz and Graff, 1996; Prandtle and Matthews, 1990). This method is utilised herein to decompose the REMO mean sea level atmospheric pressure time series, effectively illustrating the variability inherent in the spatial patterns of 1-hourly atmospheric pressure fields. To perform the EOF analysis, the gridded

pressure data $q_{mt} = q_m(t)$ were collected in the $M \times N$ matrix $Q = [q_{mt}]$ with its columns being the snapshots of pressure distribution over the REMO grid for a given time instant. Here, $M = 47 \times 40 = 1880$ is the number of REMO grid points and $N = 385\,698$ is the number of 1-hourly intervals in the 1958–2001 period. Each row of matrix Q represents the mean sea level atmospheric pressure time series for a given REMO grid point.

Let p_t , with $t = 1, 2, \dots, N$, denotes the pointwise demeaned matrix of pressure snapshots at each grid point. We

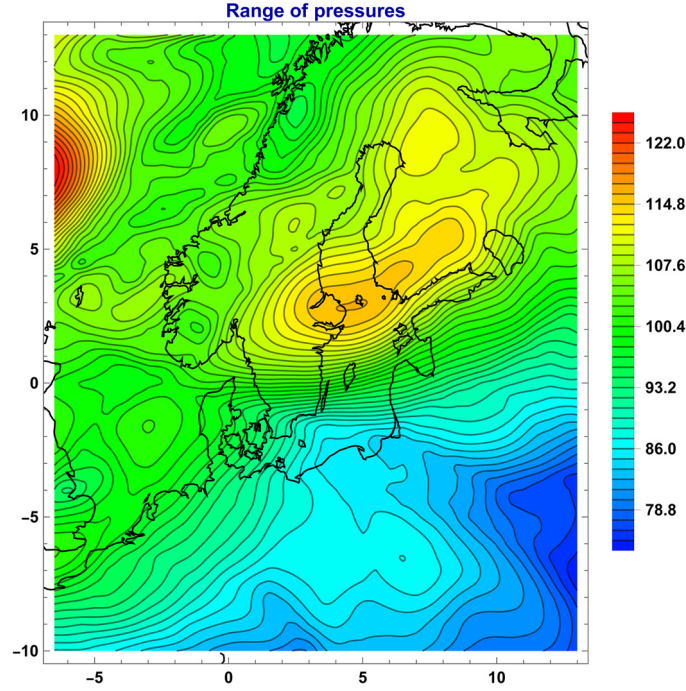


Figure 6 Range of pressures in 1958–2001 (in hPa).

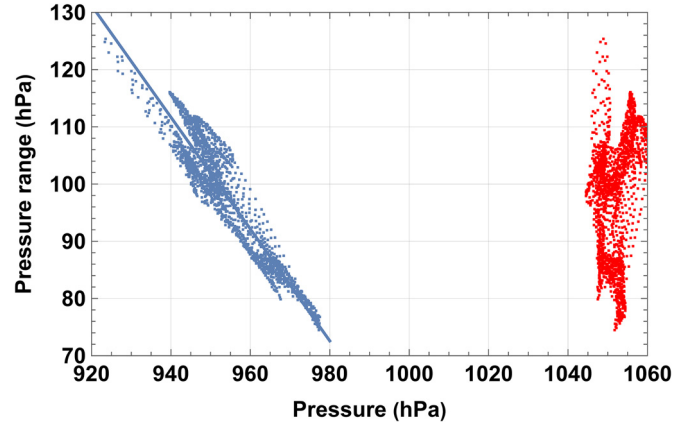


Figure 7 Scatter plots for pressure range against minimum (blue) and maximum (red) pressures. The fitted regression line representing the relationship between the pressure range and minimum pressure is shown in the left plot.

will refer to \mathbf{p}_t as state vector formed by the M functions of time $p_m(t)$, where $m = 1, 2, \dots, M$

$$p_m(t) = q_m(t) - \langle q_m \rangle \quad (1)$$

where $q_m(t)$ is the atmospheric pressure in m th of M locations and $\langle \cdot \rangle$ is the expected value of a quantity. As the covariance matrix \mathbf{H}

$$\mathbf{H} = \langle \mathbf{p}_t \mathbf{p}_t^T \rangle \quad (2)$$

is real and symmetric (T denotes transposition) it has M real eigenvalues λ_m and real unitary eigenvectors \mathbf{e}_m (which are called EOF modes) and may be normalised

$$\mathbf{e}_m^T \mathbf{e}_n = \delta_{mn}, \quad (3)$$

where δ_{mn} is the Kronecker delta.

The EOF modes \mathbf{e}_m , as eigenvectors, form a complete and orthonormal basis for \mathbf{p}_t . Thus, the original pressure state

vector \mathbf{p}_t may be expanded in terms of the EOF modes

$$\mathbf{p}_t = \sum_n P_n(t) \mathbf{e}_n \quad (4)$$

The so-called *principal components* $P_n(t)$ are obtained as

$$P_n(t) = \mathbf{e}_n^T \mathbf{p}_t \quad (5)$$

It can be shown that the principal components compose a set of orthogonal vectors satisfying the relation $\sum_{v=1}^N P_{nv} P_{mv} = N \lambda_n \delta_{nm}$. In other words, the principal components corresponding to different EOF modes are uncorrelated in time and $\lambda_m = (\sum_{v=1}^N |P_{mv}|^2) / N$ is the mean energy contained in the EOF mode \mathbf{e}_m . The fraction χ_m of the total variance (total in the sense that this is the local variance of atmospheric pressure summed over all locations, i.e., $\text{Tr}(\mathbf{H})$), corresponding to the EOF mode \mathbf{e}_m , with the

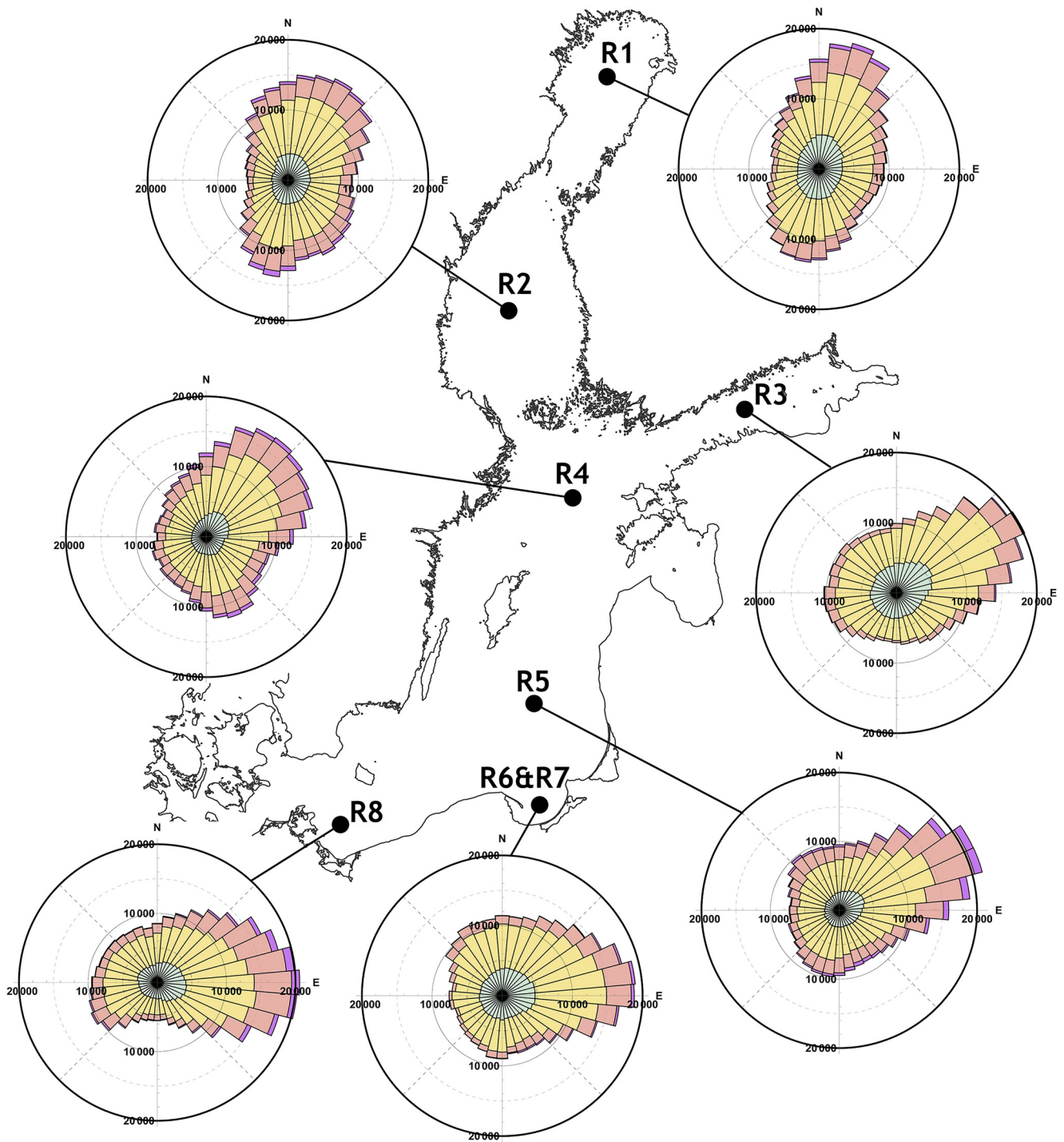


Figure 8 Cumulative distributions of wind speed and direction frequency over the period 1958–2001 at selected points; wind speed ranges marked with different colours are: 0–5, 5–10, 10–15, 15–20 m/s. The numbers labelling radii indicate the numbers of data points that fall into the given wind speed-direction angle bin.

eigenvalue λ_m , is given by

$$\chi_m = \lambda_m / \text{Tr}(\mathbf{H}). \quad (6)$$

We shall assume henceforth that EOF modes are ranked in descending order according to that fraction.

The determination of EOF modes and corresponding principal components within the EOF analysis is not unique. Various approaches can be used to produce a covari-

ance/correlation matrix based on analysed data series. Computing eigenvectors and eigenvalues is not unique, and they can be ordered and normalised in different ways. EOF modes and principal components may be rotated using linear transformations to improve the possibility of physically interpreting the results of EOF analysis, which is not always straightforward. This situation underscores the importance of presenting the mathematical formalism used.

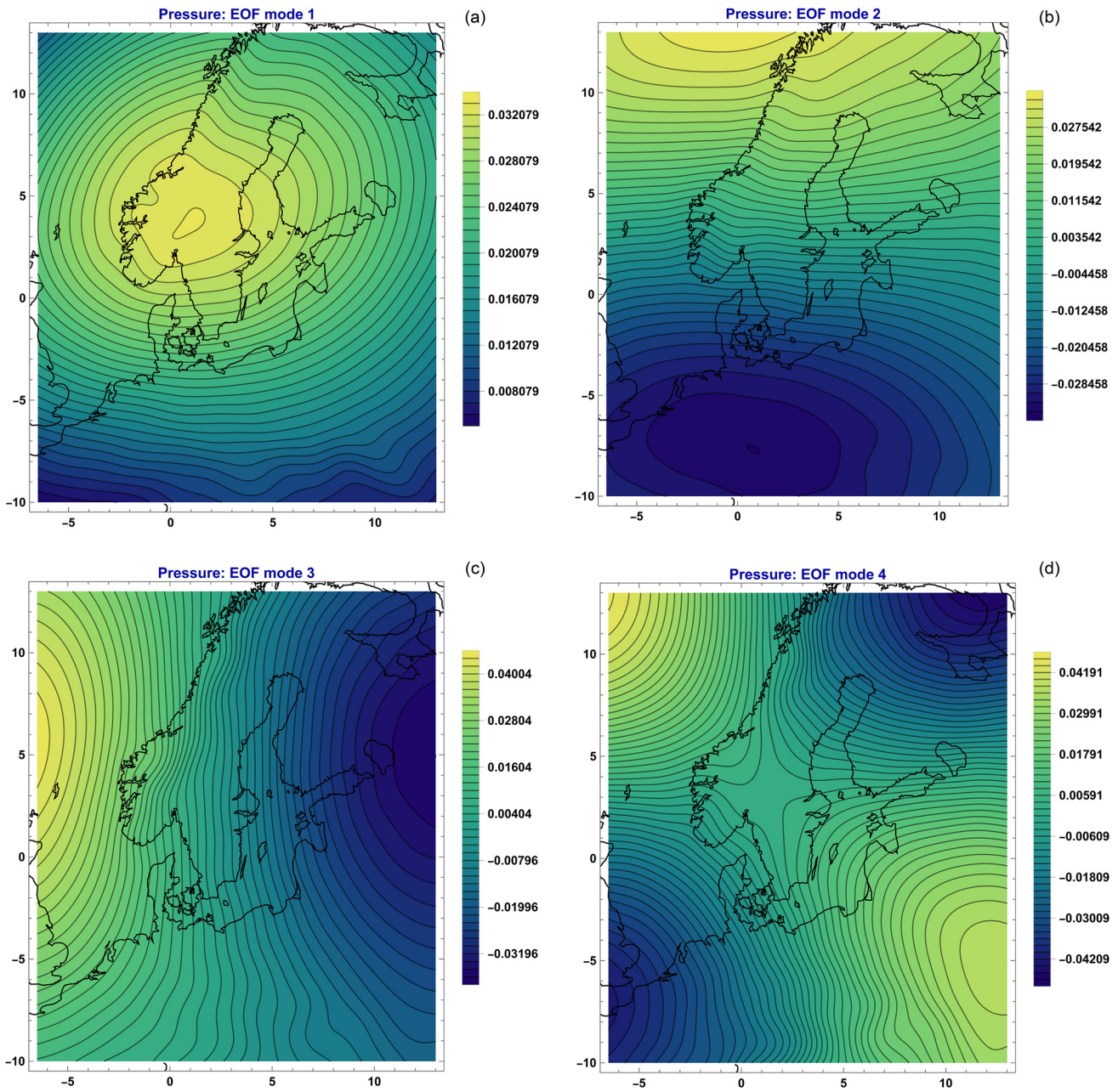


Figure 9 First 4 EOF modes for atmospheric pressure (a–d), explaining together 91.32% of the total variability.

However, it may also create difficulties in directly comparing the results of EOF analysis obtained by different researchers. Different studies using EOF analysis, including those on atmospheric pressure fields, encompass different areas at varying scales and spatial resolutions and are conducted for different time periods of varying lengths. It has been observed in numerous studies that the results of EOF analysis reflect this variability (Chen and Wang, 2014; Lehmann 2011, 2017). This further complicates comparisons of results obtained by different researchers.

In the Baltic Sea area, Miętus and von Storch (1997) investigated the relationship between large-scale air pressure variability over Europe and the spatial distribution of modelled wave data for the years 1988–1993. Using EOFs, they discerned patterns in the distribution of

these parameters. Miętus (1999) later extended the analysis of pressure patterns for a more extensive time series. Lehmann et al. (2017) and Schimanke et al. (2014) demonstrated how the spatial distribution of atmospheric pressure relates to the development of Major Baltic Inflows (MBIs). The spatial patterns derived from their EOF analyses were ordered differently, a discrepancy they attribute to variations in spatial and temporal scales. More recently, Najafzadeh et al. (2021) used this technique to identify spatial patterns in the Baltic Sea’s wind waves using altimetry data. These patterns were consistent with those observed by Miętus and von Storch (1997), differing from previously mentioned studies.

The EOF modes presented in this study are dimensionless. The values of the contour lines in Figure 9 are nor-

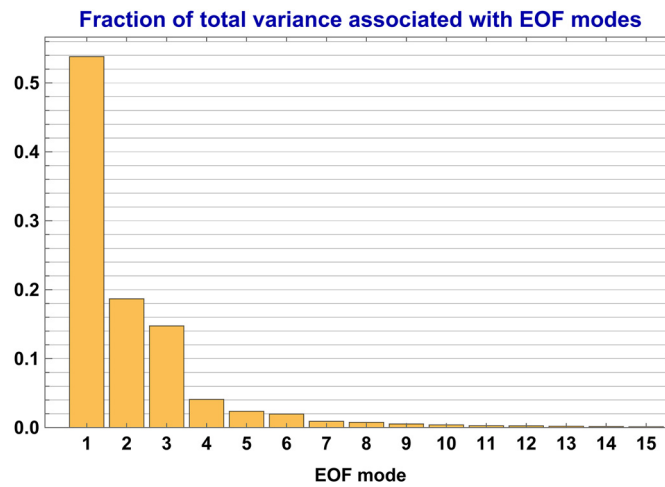


Figure 10 The fraction of total variance “explained” by the first 15 EOF modes of atmospheric pressure over the REMO area.

malised to the range [0,1] by Eq. (3). The dominant wind directions, inferred from the pressure anomalies presented, are contingent upon the state of their corresponding principal components. It should be noted that per (4), multiplying each EOF mode e_m and corresponding principal component $P_m(t)$ by -1 neither affects the capacity to reconstruct the original pressure time series nor contravenes the normalization constraint (3). This operation can be viewed as altering the polarity of the EOF modes. For conciseness, wind directions will be discussed with reference to the sign (or polarity) of each EOF mode, with parenthetical descriptions provided for wind directions associated with the inverse polarity of the EOF patterns.

Figure 9 displays the first four EOF mode patterns, accounting for 53.81%, 18.67%, 14.74%, and 4.10% of the total atmospheric pressure variance, respectively. Values for higher modes, up to mode No. 15, are exhibited in Figure 10. More than 90% variability of atmospheric pressure is included in the first four EOF modes.

The spatial pattern of EOF 1 exhibits a single wide maximum situated over southern Scandinavia, with the entire area displaying same-sign anomalies. This pattern reveals a pressure gradient linked to N to NE winds within the Baltic Sea. The inverse sign of this pattern aligns with southwesterly and westerly winds in the southern Baltic Sea and southern winds in the north, consistent with the prevailing W-SW-S wind directions along the main Baltic Sea axis (Figure 8).

Distinct spatial distributions are manifested in the second and third EOFs, characterised by meridional (EOF 2) and zonal (EOF 3) pressure gradients. EOF 2 presents a gradient corresponding to easterly (or westerly for inverse polarity) winds. The frequency distribution in Figure 8 suggests a higher likelihood for spatial patterns inducing westerly winds. The meridional pressure gradient in EOF 3 would result in N (or S) winds over the Baltic Sea.

The behaviours of the first three patterns align with observations by Horel (1981 as cited by Chen and Wang, 2014), namely, if the first pattern presents a uniform sign anomaly across the entire area of interest, the subsequent pattern will feature opposite-sign anomalies, with the zero isoline

intersecting the area of EOF 1’s absolute maximum anomaly (Chen and Wang, 2014).

The fourth EOF pattern is characterised by four relatively minor anomalies situated at the corners of the analysed region. This pattern bears a resemblance to the pressure pattern known as ‘col’ (saddle), characterised by two adjacent highs and two lows. Such a pressure system configuration is relatively uncommon over the analysed area, which corresponds to the fact that this pattern explains only about 4% of the total variance. On the other hand, the low variance may suggest that this pattern does not represent naturally occurring phenomena but rather maintains the required condition of orthogonality.

3.4. Wind wave field over the Gulf of Gdańsk

We characterise the wave climate of the Gulf of Gdańsk in terms of long-term basic statistics of modelled significant wave height (the mean, standard deviation, and maximum of H_s) in the form of contour plots. The plots in Figure 11 are constructed using the 2D cubic spline interpolation method.

All three statistical properties clearly reflect a strong sheltering effect of the Hel Peninsula located in the northwestern part of the gulf (Figure 1). Mean values of H_s range from 0.19–0.93 m, with minimum values observed in the inner Puck Bay sheltered with Hel Peninsula, and maximum in the open part of the gulf, at the open boundary between the gulf and the southern Baltic Sea.

These values are comparable to mean values of H_s in the open part of the Baltic Sea, that are in the range of 0.5–1.5 m (Björkqvist et al., 2018, Soomere and Räämet, 2011), and 0.6–0.8 m in semi-closed areas, like the Gulf of Finland (Giudici et al., 2023). Wave heights in the sheltered Puck Bay are similar to those in Tallinn Bay (0.29–0.32 m; Soomere, 2005). The standard deviation of H_s varies between 0.15 and 0.9 m, demonstrating the highest variability of the H_s field in the open part of the gulf where both the mean and maximum wave heights are the largest. The maximum modelled H_s is 8.90 m (Figure 11c) in the open part of the gulf. That high value of significant wave height in the open part of the gulf may be seen as unrealistic – es-

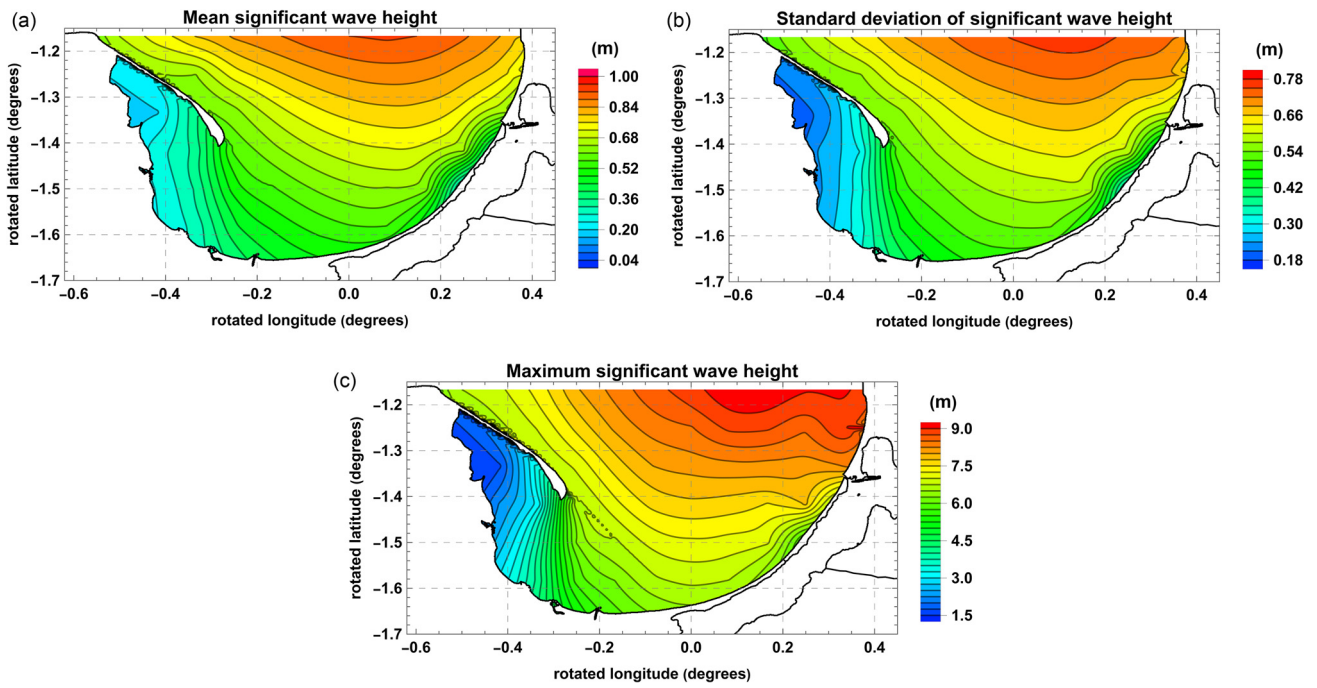


Figure 11 Spatial distribution of mean significant wave height (a), standard deviation (b) and maximum significant wave height (c) for 1958–2001 in the Gulf of Gdańsk.

Table 3 Significant wave height statistics in the central part of the Gulf of Gdańsk (point WM).

	Mean [m]	Standard Deviation [m]	Maximum [m]	99 th Percentile [m]
Entire period of study	0.74	0.65	8.00	3.19
Extreme wave events	2.93	1.61	8.00	6.91

pecially when one realises the individual wave heights during the storm may be even greater by a factor of almost 2. That value exceeds the highest recorded value of significant wave height in the Baltic (8.2 m, recorded in Baltic Proper on 22.12.2004, Björkqvist et al., 2017) but is lower than H_s of 9.0 m modelled for storm conditions in Bothnian Sea for January 2019 (Björkqvist et al., 2020) and 9.5 m estimated in the Baltic Proper for extreme windstorm Gudrun in 2005 (Soomere et al., 2008). For the years 1965–2005 the maximum modelled H_s in the southern Baltic was determined to be 10.1 m, based on the BaltAn65+ winds and modelling with the SWAN model (Björkqvist et al., 2018). Although it is challenging to assess the realism of these modelling estimates for the open part of the Gulf of Gdańsk, given the absence of long-term observational records in this Baltic Sea region, significant wave heights of around 8–9 m could indeed occur under very strong NNW, N to NNE winds.

The mean and maximum properties of waves for the central point in the Gulf of Gdańsk (WM in Figure 3) in Table 3 are estimated for the entire period of study 1958–2001 and the selected 34 storm events S1, S2, ..., S34. The mean value of H_s for the entire period is almost four times lower than that estimated for the most extreme events only.

4. Discussion and conclusions

In this study two extensive databases were utilised: the REMO meteorological database and the HIPOCAS ocean hydrodynamic database, both covering the 1958–2001 period. These numerically modelled data obviously do not possess the advantages of observed data. However, those data compare well with measured data (Cieřlikiewicz and Paplińska-Swerpel, 2008). The long-term hindcast data collections, such as those applied in the present study, allow for a comprehensive examination of long-term statistical characteristics of and changes in wind-wave climate due to their consistency, continuity, and high resolution over both time and space domains. Potential for research based on such databases is advantageous over possibilities inherent in recorded data that are usually local and spanned over shorter time intervals.

While our analysis focuses on the Gulf of Gdańsk’s wave climate from 1958 to 2001, and may not directly represent the current situation, it provides valuable retrospective insights. The authors believe the insights gleaned remain relevant and provide valuable retrospective context for current and future wave climate studies in the Baltic Sea.

We first address atmospheric pressure fields. Then, some basic statistical characteristics of wind velocity were com-

puted. Finally, the analysis of significant wave height over the Gulf of Gdańsk was carried out.

The key result of the present study is efficient estimation and comprehensive graphical presentation of the basic statistical properties of the atmospheric pressure data over almost half a century (1958–2001). The spatial distributions of the mean, standard deviation, maximum and minimum values together with their range were computed for 1880 REMO grid nodes based on 385 698 data points in time. We found the following particular and interesting features of the atmospheric pressure fields over the study area: (i) the greater the mean value the smaller the variability of the atmospheric pressure field presented by both the standard deviation and the min-max range; (ii) the range of variations of pressure maxima is about three times smaller than the variability range of pressure minima; therefore, the spatial distribution of the range of hindcast atmospheric pressure pattern, defined as the difference between maximum and minimum values found in time series, almost exactly mimics the inverted distribution of minimal pressure found in the hindcast pressure data.

The efficiency of the EOF method applied to atmospheric pressure data appeared to be quite good. The first EOF mode accounts for more than half of the total variance, specifically 53.81%. The first four EOF modes can reproduce >90% variability of the pressure time series over the study area. The disparity in explained variability between the first and second EOF patterns exceeds 35 percentage points, a difference also observed in the analysis of pressure patterns over the North Atlantic and Europe (Lehman et al., 2011). Interestingly, Surkova et al. (2015) reported a pressure pattern with an anomaly centre over Scandinavia and the Baltic Sea, which was derived from an analysis of pressure during storm conditions. Similarly, Schimanke et al. (2014), who focused on MBIs, presented a corresponding pattern. Both types of events are closely associated with zonal winds. The negative anomaly in the first EOF mode, as obtained in this study, would result in westerly-south-westerly winds, which are frequently reported as the dominant winds in the southern Baltic (Leppäranta and Myrberg, 2009). This pattern is also evident in the frequency distribution of wind speeds.

The established properties of wind velocity fields over the Baltic Sea demonstrate directional characteristics consistent with the spatial distribution of the mean atmospheric pressure and its isobars. The information presented by the cumulative frequency histograms of wind velocity is consistent with generally known climatic characteristics of prevailing winds over the Baltic Sea that are determined by the general climate of central and northern Europe, and the north-eastern Atlantic Ocean. The directional properties of the strongest winds over the Baltic are, to a certain extent, consistent with directions of maximum fetches in local sea basins.

The long-term statistical properties of the significant wave height over the Gulf of Gdańsk are characterised using its spatial distributions of mean and standard deviation. All properties of significant wave height reveal a strong sheltering effect due to the Hel Peninsula. The maximum of hindcast significant wave height ranges from a fraction of a meter, in the inner Puck Bay sheltered from the open sea, to above 8 m in the open part of the Gulf of Gdańsk. That rel-

atively large value of the modelled significant wave height should be treated with caution; however, it is difficult to speculate how realistic such estimates are due to the lack of long-term observational data collected in this region of the Baltic Sea.

The most extreme wave events in the Baltic Sea are created by cyclones (low-pressure systems) travelling over it or nearby. The Baltic Sea is located under the North Atlantic storm track (Lehmann et al., 2017; Mailier et al., 2006) and remains under its strong influence (Rogers, 1990; Sepp, 2009; Sepp et al., 2018; Ulbrich and Christoph, 1999). Visual assessment of REMO atmospheric pressure distributions during extreme wave events in the Gulf of Gdańsk confirmed that most of the storms here are driven by a low-pressure system approaching the Baltic Sea from the North Atlantic. In 11 cases of 34 analysed in this study, a low-pressure system travelled from the North Atlantic either across northern Scandinavia, often crossing Norway just above Trondheim, or from over southern England, across the North Sea and Denmark and further travelling across the Baltic Sea.

As the presence of cyclones is strongly connected to various atmospheric indices, like the North Atlantic Oscillation (NOA) index (Gulev et al., 2001; Lehmann et al., 2017), any change in them will influence storm conditions in the Baltic Sea and in the Gulf of Gdańsk.

Declaration of competing interest

The authors declare that they have no known competing financial interests or personal relationships that could have appeared to influence the work reported in this paper.

Acknowledgements

Computations performed within this study were conducted in the TASK Computer Centre, Gdańsk with partial funding from eCUDO.pl project No. POPC.02.03.01-00-0062/18-00 and the University of Gdańsk Project for Young Scientist No. 539-O190-B412-19. The authors sincerely thank an anonymous reviewer for critically reading the manuscript and suggesting substantial improvements to the presentation of this study.

References

- Badur, J., Cieřlikiewicz, W., 2018. Spatial variability of long-term trends in significant wave height over the Gulf of Gdańsk using System Identification techniques. *Oceanol. Hydrobiol. Stud.* 47, 190–201. <https://doi.org/10.1515/ohs-2018-0018>
- Bernhoff, H., Sjöstedt, E., Leijon, M., 2006. Wave energy resources in sheltered sea areas: A case study of the Baltic Sea. *Renew. Energy* 31, 2164–2170. <https://doi.org/10.1016/j.renene.2005.10.016>
- Bierstedt, S.E., Hünicke, B., Zorita, E., 2015. Variability of wind direction statistics of mean and extreme wind events over the Baltic Sea region. *Tellus A* 67, 29073. <https://doi.org/10.3402/tellusa.v67.29073>
- Björkqvist, J.-V., Tuomi, L., Tollman, N., Kangas, A., Pettersson, H., Marjamaa, R., Jokinen, H., Fortelius, C., 2017. Brief communi-

- cation: Characteristic properties of extreme wave events observed in the northern Baltic Proper, Baltic Sea. *Nat. Hazards Earth Syst. Sci.* 17, 1653–1658. <https://doi.org/10.5194/nhess-17-1653-2017>
- Björkqvist, J.-V., Lukas, I., Alari, V., van Vledder, G.Ph., Hulst, S., Petterson, H., Behrens, A., Männik, A., 2018. Comparing a 41-year model hindcast with decades of wave measurements from the Baltic Sea. *Ocean Eng.* 152, 57–71.
- Björkqvist, J.-V., Rikka, S., Alari, V., Männik, A., Tuomi, L., Petterson, H., 2020. Wave height return periods from combined measurement–model data: a Baltic Sea case study. *Nat. Hazards Earth Syst. Sci.* 20, 3593–3609. <https://doi.org/10.5194/nhess-20-3593-2020>
- Chakrabarti, S.K., 1994. *Hydrodynamics of offshore structures*. WIT Press, 464 pp.
- Chen, G., Wang, X., 2014. Impact of domain geometry on the results of empirical orthogonal function analysis. *Annals of GIS* 20 (3), 205–216.
- Cieślíkiewicz, W., 1990. Determination of the surface elevation probability distribution of wind waves using maximum entropy principle. In: Tørum, A., Gudmestad, O.T. (Eds.), *Proc. NATO-ARW Water Wave Kinematics*. Presented at the NATO Advanced Research Workshop on Water Wave Kinematics, Molde. Kluwer Academic, 345–348.
- Cieślíkiewicz, W., Dudkowska, A., Gic-Grusza, G., Jędrasik, J., 2017. Extreme bottom velocities induced by wind wave and currents in the Gulf of Gdańsk. *Ocean Dynam.* 67, 1461–1480. <https://doi.org/10.1007/s10236-017-1098-4>
- Cieślíkiewicz, W., Dudkowska, A., Gic-Grusza, G., Jędrasik, J., 2018. Assessment of the potential for dredged material dispersal from dumping sites in the Gulf of Gdańsk. *J. Soils Sediments* 18, 3437–3447. <https://doi.org/10.1007/s11368-018-2066-4>
- Cieślíkiewicz, W., Graff, J., 1996. Sea state parameterisation using empirical orthogonal functions. In: *25th Coastal Eng. Conf.*, Orlando, Florida. ASCE, 703–716.
- Cieślíkiewicz, W., Graff, J., 1997. Parametric modelling of storm wave fields over the Irish Sea, 1955–1993. In: *Third International Symposium on Ocean Wave Measurement and Analysis, WAVES'97*, Virginia Beach, 896–910.
- Cieślíkiewicz, W., Gudmestad, O.T., 1994. Mass transport within the free surface zone of water waves. *Wave Motion* 19, 145–158. [https://doi.org/10.1016/0165-2125\(94\)90063-9](https://doi.org/10.1016/0165-2125(94)90063-9)
- Cieślíkiewicz, W., Massel, S.R., 1988. Interaction of wind waves with a vertical wall. *J. Waterw. Port Coast. Ocean Eng.* ASCE 114, 653–672. [https://doi.org/10.1061/\(ASCE\)0733-950X\(1988\)114:5\(653\)](https://doi.org/10.1061/(ASCE)0733-950X(1988)114:5(653))
- Cieślíkiewicz, W., Papińska-Swerpel, B., 2008. A 44-year hindcast of wind wave fields over the Baltic Sea. *Coast. Eng.* 55, 894–905. <https://doi.org/10.1016/j.coastaleng.2008.02.017>
- Cieślíkiewicz, W., Papińska-Swerpel, B., Soares, C.G., 2005. Multi-decadal wind wave modelling over the Baltic Sea. In: *Coastal Engineering 2004*, Vol. 4. World Scientific Publishing Company, Lisbon, Portugal, 778–790. https://doi.org/10.1142/9789812701916_0062
- Cieślíkiewicz, W., Podrażka, O., Gudmestad, O.T., 2015. Breaking wave loads on truss support structures for offshore wind turbines. In: *Presented at the MARTECH 2014–2nd International Conference on Maritime Technology and Engineering*, Lisbon, Portugal, 1205–1211.
- Dean, R.G., Dalrymple, R.A., 1991. *Water wave mechanics for engineers and scientists*. World Scientific Publ. Co., 368 pp.
- Feser, F., Weisse, R., von Storch, H., 2001. Multi-decadal atmospheric modelling for Europe yields multi-purpose data. *Eos* 82. <https://doi.org/10.1029/01EO00176>
- Giudici, A., Jankowski, M.Z., Männikus, R., Najafzadeh, F., Suur Saar, Ü., Soomere, T., 2023. A comparison of Baltic Sea wave properties simulated using two modelled wind data sets. *Estuar. Coast. Shelf Sci.* 290, 108401.
- Gulev, S.K., Zolina, O., Grigoriev, S., 2001. Extratropical cyclone variability in the Northern Hemisphere winter from the NCEP/NCAR reanalysis data. *Clim. Dynam.* 17, 795–809. <https://doi.org/10.1007/s003820000145>
- Jacob, D., Podzun, R., 1997. Sensitivity studies with the regional climate model REMO. *Meteorol. Atmos. Phys.* 63, 119–129. <https://doi.org/10.1007/BF01025368>
- Jose, J., Podrażka, O., Gudmestad, O.T., Cieślíkiewicz, W., 2017. Characteristics of the wave slamming forces on jacket structures under plunging breaking waves based on experimental data. *ASME 2017 36th International Conference on Ocean, Offshore & Arctic Engineering OMAE2017*, Trondheim, Norway, V07BT06A036. <https://doi.org/10.1115/OMA2017-61789>
- Jose, J., Podrażka, O., Gudmestad, O.T., Cieślíkiewicz, W., 2018. Detailed study on breaking wave interactions with a jacket structure based on experimental investigations. *J. Offshore Mech. Arct. Eng.-Trans. ASME* 140 (2), 021301. <https://doi.org/10.1115/1.4037829>
- Launiainen, J., Laurila, T., 1984. Marine wind characteristics in the northern Baltic Sea. *Finn. Mar. Res.* 250, 52–86.
- Lehmann, A., Getzlaff, K., Harlaß, J., 2011. Detailed assessment of climate variability in the Baltic Sea area for The period 1958 to 2009. *Clim. Res.* 46 (2), 185–196.
- Lehmann, A., Höflich, K., Post, P., Myrberg, K., 2017. Pathways of deep cyclones associated with large volume changes (LVCs) and major Baltic inflows (MBIs). *J. Marine Syst.* 167, 11–18. <https://doi.org/10.1016/j.jmarsys.2016.10.014>
- Leppäranta, M., Myrberg, K., 2009. *Physical oceanography of the Baltic Sea*. Springer Praxis, Chichester, 401 pp.
- Lorenz, E.N., 1956. *Technical Rep., Statistical Forecast Project Rep. 1*. Department of Meteorology, MIT, 49 pp.
- Mailier, P.J., Stephenson, D.B., Ferro, C.A.T., Hodges, K.I., 2006. Serial Clustering of Extratropical Cyclones. *Mon. Weather Rev.* 134, 2224–2240. <https://doi.org/10.1175/MWR3160.1>
- Massel, S.R., 2017. *Ocean surface waves: their physics and prediction*, 3rd edn. World Scientific Publication Company, 800 pp.
- Mietus M., von Storch H., 1997. Reconstruction of the wave climate in the proper Baltic basin, April 1947–March 1988. *GKSS Report 97/E/28*, Geesthacht.
- Miętus, M., 1999. Rola regionalnej cyrkulacji atmosferycznej kształtowaniu warunków klimatycznych i oceanograficznych w polskiej strefie brzegowej Morza Bałtyckiego. *Materiały Badawcze IMGW, Meteorologia* 29.
- Najafzadeh, F., Kudryavtseva, N., Soomere, T., 2021. Effects of large-scale atmospheric circulation on the Baltic Sea wave climate: application of the EOF method on multi-mission satellite altimetry data. *Clim. Dynam.* 57, 3465–3478.
- Obukhov, A.M., 1960. The statistically orthogonal expansion of empirical functions. *Bull. Acad. Sci. U.S.S.R., Geophys. Ser.* 3, 288–291.
- Prandle, D., Matthews, J., 1990. The dynamics of nearshore surface currents generated by tides, wind and horizontal density gradients. *Cont. Shelf Res.* 665–681. [https://doi.org/10.1016/0278-4343\(90\)90044-M](https://doi.org/10.1016/0278-4343(90)90044-M)
- Rogers, J.C., 1990. Patterns of low frequency monthly sea level pressure variability (1899–1986) and associated wave cyclone frequencies. *J. Climate* 3, 1364–1379.
- Schimanke, S., Dieterich, C., Meier, H.E.M., 2014. An algorithm based on sea-level pressure fluctuations to identify major Baltic inflow events. *Tellus A* 66, 23452.
- Sepp, M., 2009. Changes in frequency of Baltic Sea cyclones and their relationships with NAO and climate in Estonia. *Boreal Environ. Res.* 14, 143–151.
- Sepp, M., Post, P., Mändla, K., Aunap, R., 2018. On cyclones entering the Baltic Sea region. *Boreal Environ. Res.* 23, 1–14.
- Soomere, T., 2003. Anisotropy of wind and wave regimes in the Baltic Proper. *J. Sea Res.* 49, 305–316. [https://doi.org/10.1016/S1385-1101\(03\)00034-0](https://doi.org/10.1016/S1385-1101(03)00034-0)

- Soomere, T., 2005. Wind wave statistics in Tallinn Bay. *Boreal Environ. Res.* 10, 103–118.
- Soomere, T., Behrens, A., Tuomi, L., Nielsen, J.W., 2008. Wave conditions in the Baltic Proper and in the Gulf of Finland during windstorm Gudrun. *Nat. Hazards Earth Syst. Sci.* 8, 37–46. <https://doi.org/10.5194/nhess-8-37-2008>
- Soomere, T., Räämet, A., 2011. Long-term spatial variations in the Baltic Sea wave fields. *Ocean Sci.* 7 (1), 141–150.
- Soomere, T., 2023. Numerical simulations of wave climate in the Baltic Sea: a review. *Oceanologia* 65 (1), 117–140. <https://doi.org/10.1016/j.oceano.2022.01.004>
- Surkova, G.V., Arkhipkin, V.S., Kislov, A.V., 2015. Atmospheric circulation and storm events in the Baltic Sea. *Open Geosci.* 7 (1), 332–341.
- Suursaar, Ü., Kullas, T., 2009. Decadal variations in wave heights off Cape Kelba, Saaremaa Island, and their relationships with changes in wind climate. *Oceanologia* 51 (1), 39–61. <https://doi.org/10.5697/oc.51-1.039>
- Tucker, M.J., Pitt, E.G., 2001. *Waves in ocean engineering*. Elsevier Science, 521 pp.
- Ulbrich, U., Christoph, M., 1999. A shift of the NAO and increasing storm track activity over Europe due to anthropogenic greenhouse gas forcing. *Clim. Dynam.* 15, 551–559. <https://doi.org/10.1007/s003820050299>
- von Storch, H., Langenberg, H., Feser, F., 2000. A spectral nudging technique for dynamical downscaling purposes. *Mon. Weather Rev.* 128, 3664–3673. [https://doi.org/10.1175/1520-0493\(2000\)128%3C3664:ASNTFD%3E2.0.CO;2](https://doi.org/10.1175/1520-0493(2000)128%3C3664:ASNTFD%3E2.0.CO;2)

Available online at www.sciencedirect.com

ScienceDirect

journal homepage: www.journals.elsevier.com/oceanologia

ORIGINAL RESEARCH ARTICLE

Seasonal enhancement of phytoplankton biomass in the southern tropical Indian Ocean: Significance of meteorological and oceanography parameters

Chinnadurai Karnan*, Sreedharan Gautham

CSIR – National Institute of Oceanography, Dona Paula, Goa, India

Received 19 October 2022; accepted 13 October 2023

Available online 31 October 2023

KEYWORDS

Southern Tropical Indian Ocean;
Chlorophyll *a*;
Primary production;
Seasonality;
Oligotrophy

Abstract The present study focused on understanding the seasonality of the phytoplankton biomass (chlorophyll *a*) distribution in the oligotrophic, Equatorial, and Southern Tropical Indian Ocean (ESTIO; 0–30°S and 60–90°E). The long-term satellite data analyses (2003–2020) showed a strong seasonality in sea surface temperature (SST), wind, currents, mean sea level anomaly (MSLA), photosynthetically available radiation (PAR), euphotic depth (ZEU) and mixed layer depth (MLD). As a response to the hydrographical changes, the phytoplankton biomass showed noticeable seasonal variation with the highest biomass during the Austral Winter (AW; June–September; avg. 0.11 ± 0.03 mg/m³) and lowest during the Austral Summer (AS; November–February; avg. 0.07 ± 0.03 mg/m³). High chlorophyll patches (>0.1 mg/m³) were found between 0°–8°S during the AS and expanded over 0°–18°S during the AW. As multi-year mean chlorophyll *a* was higher (>0.1 mg/m³) in the northern part of the ESTIO (north of ~13°S; HCD: high chlorophyll *a* domain) than the southern side (LCD: low chlorophyll *a* domain), the study area was divided into two domains and all the variables were analysed. In the HCD, enhancement of chlorophyll *a* was positively correlated with variables such as wind speed, wind stress, Ekman pumping, stronger northward and westward winds, as well as the presence of cyclonic eddies. These features are likely to stimulate primary production by uplifting the thermocline and enhancing nutrient supply. In the LCD, mixed layer depth also showed a strong positive correlation with elevated chlorophyll *a*, apparently because it is deep throughout the year (thereby keeping lower biomass) and deepens more strongly in winter than in the HCD. Another contrast with the

* Corresponding author at: CSIR – National Institute of Oceanography, Dona Paula, Goa, India.

E-mail address: karnanc@nio.org (C. Karnan).

Peer review under the responsibility of the Institute of Oceanology of the Polish Academy of Sciences.



HCD is that the cyclonic eddies appear to be insufficiently abundant to influence its chlorophyll *a*. Pearson's multivariable correlation analysis and principle component analysis confirmed the statistical significance of the above parameters on the enhancement of chlorophyll *a* in the ESTIO.

© 2023 Institute of Oceanology of the Polish Academy of Sciences. Production and hosting by Elsevier B.V. This is an open access article under the CC BY-NC-ND license (<http://creativecommons.org/licenses/by-nc-nd/4.0/>).

1. Introduction

The equatorial and southern tropical waters of the Indian Ocean sector have a vast area of open ocean (avg. depth ~4200 m) which is highly oligotrophic and less studied as compared to the Pacific and Atlantic oceans (Hood et al., 2009). The oligotrophy is further enhanced by anti-cyclonic subtropical gyre, advection of low saline water through Indonesian through-flow and high precipitation that strengthen stratification (George et al., 2018; Huang et al., 2020; Morel et al., 2010; Stramma and Lutjeharms, 1997). The equatorial upwelling is absent in the Indian Ocean due to the weaker and north-south directions of the trade winds (Schott et al., 2009; Tomczak and Godfrey, 2003). In the southern tropical Indian Ocean, the Seychelles – Chagos thermocline ridge (SCTR; 5°S–10°S; 50°E–80°E) region is relatively productive, where the upwelling is reported throughout the year due to negative wind stress curl (Dilmahamod et al., 2016; George et al., 2018; Hermes and Reason, 2008; McCreary et al., 1993; Nagura and McPhaden, 2018; Resplandy et al., 2009; Woodberry et al., 1989). The Wyrtki jet is a strong surface current, which flows eastward along the equatorial Indian Ocean (4°S–4°N) during the inter-monsoon months (May and October; Wyrtki, 1973) and supports phytoplankton production in the western region by shallowing the thermocline and decreases it by deepening the thermocline in the eastern region (George et al., 2013; Wiggert et al., 2006; Wyrtki, 1973). The other major water currents that flow in the Equatorial and Southern Tropical Indian Ocean (ESTIO) are the south equatorial current, which flows westward between 10°S–20°S during both seasons (AS and AW), and the south equatorial counter-current, which flows eastward between 0–5°S during the AS and between 0–5°N during the AW (Schott and McCreary Jr, 2001; Stramma and Lutjeharms, 1997). The south equatorial current is stronger during the AW than during the AS (Schott and McCreary Jr, 2001).

The presence of continents/landmasses around the northern Indian Ocean is the reason for high biological productivity in the northern Indian Ocean (the Arabian Sea and Bay of Bengal). It is well known that the biological productivity of these regions is triggered by the Asian monsoon system, which is activated by the differential heating between the land and the ocean (Banse, 1987; Bhattathiri et al., 1996; Madhupratap et al., 1996; Naqvi et al., 2010; Qasim, 1982; Wiggert et al., 2005). The seasonal reversal of winds has a potential role in transporting nutrients to the euphotic ocean water column directly (vertical mixing, upwelling, currents, eddies, advection, and eolian input, etc.) as well as indirectly (e.g., terrestrial runoff through rain-

fall), that enhances the primary productivity. However, the southern Indian Ocean has a large area of open ocean which has limited impacts (north of 10°S) from the Asian monsoon system (Gao and Wang, 2012; Shankar et al., 2002), and the nutrient sources are also meagre in this region (Harms et al., 2019; Twining et al., 2019; Wiggert et al., 2006). The southern Indian Ocean lacks continental interferences as well and it is freely open to the global oceans, i.e., the Southern Ocean in the south, the Atlantic in the west and the Pacific in the east (Michel and Sticklor, 2012). Due to the above reasons, the southern Indian Ocean can be considered a desert (highly oligotrophic) as compared to the northern Indian Ocean. Though it is oligotrophic, in a very large area the seasonal changes in the atmospheric and oceanographic parameters impact the primary production (Dilmahamod et al., 2016; George et al., 2018, 2013; Resplandy et al., 2009). The Indian Ocean is considered a single large ocean basin. However, the meteorological, oceanographical processes and biological productions demarcate it into two regions: the oligotrophic southern and productive northern Indian Ocean.

Focused ocean surveys started in the Indian Ocean in the 1960s, the International Indian Ocean Expedition (Banse, 1968; Desai, 1965; Krey and Babenerd, 1976) and Joint Global Ocean Flux Studies in the 1990s (JGOFS) (Madhupratap et al., 1996; Smith et al., 1998; Wishner et al., 1998), put benchmarks, and after that abundant in situ scientific studies were carried out in the northern Indian Ocean than the south. The southern Indian Ocean gets its significance in maintaining the global climate by efficiently transferring the heat energy from the tropics to the surrounding Atlantic and Southern Oceans. Hence, the warming tendency is weaker than in the northern Indian Ocean (Gopika et al., 2020; Gordon, 1985; Lee et al., 2015; van Ballegooyen et al., 1994). Due to long distances from the continents and rough weather conditions, the in situ scientific research observations are less in the ESTIO. The remotely sensed ocean colour data sets, ARGO floats and modelling outputs along with limited on-site studies provide a basic understanding of this region (Brewin et al., 2012; George et al., 2018, 2013; Hermes and Reason, 2009, 2008; Huot et al., 2019; Kawamiya and Oschlies, 2001; McCreary Jr et al., 2009; Wiggert et al., 2006). Studies show that the surface phytoplankton production in this region is driven by vertical mixing of the water column, mesoscale eddies, Ekman pumping and propagation of upwelling Rossby waves (Agawin et al., 2000; Gaube et al., 2013; George et al., 2013; Kawamiya and Oschlies, 2001; Liao et al., 2020; Ma et al., 2014; Wiggert et al., 2006). Levy et al. (2007) hypothesized that high chlorophyll *a* (bloom) in the southern Indian Ocean, north of 17°S is due to Ekman upwelling of

nutrients and on the southern side is due to deeper vertical mixing, where sub-tropical gyre persists. The Indian Ocean Dipole (IOD) is an uneven fluctuation in the sea surface temperatures of the western (50°E–70°E, 10°S–10°N) and the eastern equatorial Indian Ocean (90°E–110°E, 10°S–equator). The Dipole Mode Index (DMI) is a measure of IOD by calculating the difference between those regions. The warmer western region (colder east) is known as positive IOD and the colder western part (warmer east) is known as negative IOD (Saji et al., 1999; Vinayachandran et al., 2007). The IOD events have specific roles in shaping phytoplankton biomass and size structure in the southern tropical Indian Ocean (Brewin et al., 2012; Currie et al., 2013; Siswanto et al., 2020).

Many studies focused on the SCTR region of the southern Indian Ocean reported an occurrence of year-round upwelling in this region due to negative wind curl, which shallows thermocline (George et al., 2018; Hermes and Reason, 2008; McCreary Jr et al., 2009; Resplandy et al., 2009). However, high phytoplankton production/blooms were reported mainly in June–September and February months (Gaube et al., 2013; Levy et al., 2007; Liao et al., 2014; Resplandy et al., 2009). In this study, we attempt to understand the variability of the ESTIO and the seasonality of phytoplankton production in this region. The major objectives of the present study are (a) to understand the seasonal variability of selected meteorological and physical oceanographic parameters in the equatorial and southern tropical Indian Ocean, (b) to define the specific roles of individual parameters in structuring phytoplankton biomass (chlorophyll *a*) in the northern and southern domains of the ESTIO, and (c) to demarcate key variables which control biological productivity in both domains of the study area.

2. Methods

2.1. Satellite and Argo data products

The present study utilized various satellite-measured and ARGO derived, and calculated long-term data sets (18-years; 2003–2020; monthly scale – temporal resolution) to understand the seasonal variability that occurred in the ESTIO (0–30°S and 60–90°E; Figure 1a). The satellite-measured monthly data sets of SST (sea surface temperature; MODIS-Aqua; 4 km spatial resolution; coastwatch.pfeg.noaa.gov), MSLA (mean sea level anomaly; AVISO; 0.25° spatial resolution; marine.copernicus.eu), PAR (photosynthetically available radiation; MODIS-Aqua; 4 km spatial resolution; giovanni.gsfc.nasa.gov), ZEU (euphotic depth; Morel et al. (2007); $\log_{10}Z_{eu}=1.524 - 0.436 X - 0.0145 X^2 + 0.0186 X^3$, whereas, $X=\log_{10}$ of surface chlorophyll; MODIS-Aqua; 4 km spatial resolution; giovanni.gsfc.nasa.gov; data distribution discontinued), MLD (mixed layer depth; either change in temperature by 0.2°C or density by 0.03 kg/m³ from that at 10 m depth; argo.ucsd.edu/data/argo-data-products/; Mixed Layer data set of Argo, Grid Point Value [MILA GPV] of JAMSTEC, 2003, Hosoda et al. (2010); BOA-Argo dataset generated by following Barnes Method; CSIO, MNR; 2004–2020; Li et al. (2017); 1° resolution), zonal (west to east or east to west) and meridional (north to south or south to north

flow) components of geostrophic currents (AVISO; 0.25° spatial resolution; marine.copernicus.eu), zonal and meridional components of wind (QuikSCAT and ASCAT; 0.125° and 0.25° spatial resolution; coastwatch.pfeg.noaa.gov), chlorophyll *a* (MODIS-Aqua; 4 km spatial resolution; giovanni.gsfc.nasa.gov) and primary productivity (MODIS-Aqua; 4 km spatial resolution; chlorophyll *a* based experimental product; coastwatch.pfeg.noaa.gov) retrieved from the respective web servers. The daily data sets of ASCAT wind and MODIS chlorophyll *a* for 2016 were also retrieved to correlate with each other. The calculated monthly dipole mode index (DMI) data of the Indian Ocean Dipole (IOD) was retrieved (2003–2020) from the NOAA ESRL Physical Sciences Laboratory website (https://psl.noaa.gov/gcos_wgsp/Timeseries/DMI/). The QuikSCAT (January 2003–March 2007) and ASCAT (April 2007–December 2020) wind products were combined to get a continuous time series of 18 years. Other than MODIS products, all the above time series data sets were resampled/re-gridded at 4 km resolution (PyFerret v7.4) to maintain uniform spatial resolution for further analysis. The MODIS chlorophyll *a* data was derived by applying the colour index (CI) algorithm (Hu et al., 2012, 2019) for the concentration <0.25 mg/m³ and along with an updated OCx algorithm (O'Reilly and Werdell, 2019) for higher concentrations (https://oceancolor.gsfc.nasa.gov/atbd/chlor_a/). The above algorithms made MODIS Aqua or any other ocean colour sensor-based data sets more accurately represent the oligotrophy, such as the present study area (Table 1).

2.2. Discrimination of seasons

After retrieval of the data sets, the monthly means and monthly climatology (mean of 18 individual months) were calculated (using PyFerret v7.4) to define the regional seasonality of the ESTIO. We have used the recent five-year monthly data sets (2013–2018) for statistical analysis purposes. The monthly means of the selected meteorological and oceanic variables (SST, PAR, ZEU, wind parameters and MSLA) were used to construct the similarity/hierarchical clusters using R-studio (Euclidean distance method; *dist* and *hclust* commands). It formed three clusters with substantial distance (c1 – November–February; c2 – March–May; c3 – June–October), similar to the JGOFS classification of seasons (meteorological data based; Morrison et al., 1998). As most past studies have classified October as inter-monsoon and relatively high Euclidean distance is found in October, we have classified two major seasons as austral summer (November–February; AS) and austral winter (June–September; AW), which shows major variation in an annual distribution. As the variance in hydrographical characters of spring (March–May) and the fall inter-monsoon (October) were comparatively weaker than the AS and AW, those were limitedly emphasized in the present study. The derived seasonality of variables also clearly evidenced the above classification (methods given in the following section).

2.3. Data process, derivation and analysis

The monthly and seasonal climatology (AS and AW) of each variable were constructed by averaging the retrieved data

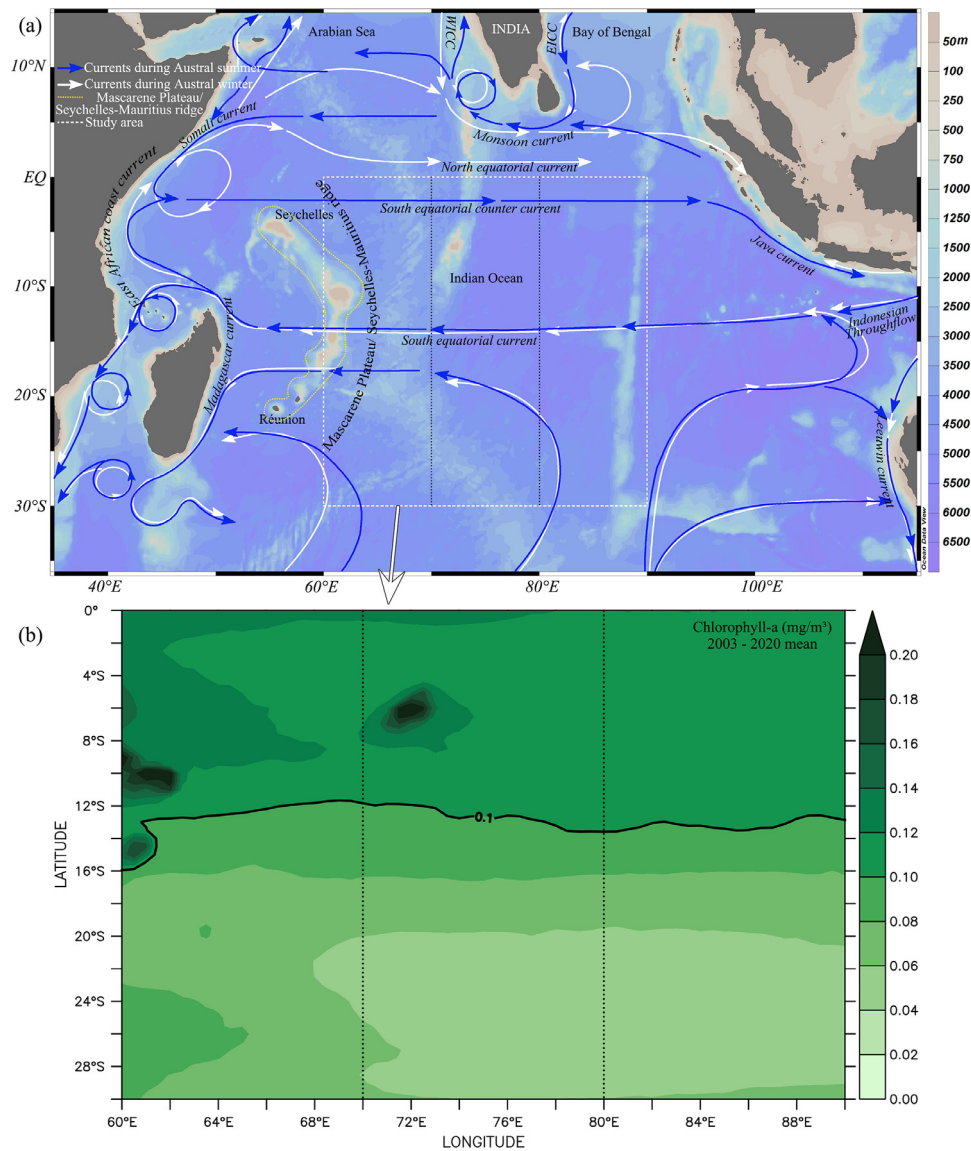


Figure 1 a) The study area in the equatorial and southern tropical Indian Ocean (ESTIO; 0°–30°S and 60°E–90°E) is marked by a dashed square box (white). The patterns of major near-surface currents during the austral summer (blue arrows) and austral winter (white arrows) overlaid (Schott et al., 2001; Shenoi et al., 1999). The dotted lines in black split the study area into three sub-regions (60°E–70°E, 70°E–80°E and 80°E–90°E) for detailed study. b) MODIS-AQUA mean (2003–2020) chlorophyll *a* concentration in the study area. A 0.1 mg/m³ chlorophyll *a* contour line divides the study area into high (northern; HCD) and low (southern; LCD) chlorophyll *a* domains. Abbreviations: – WICC: West India Coastal Current; EICC: East India Coastal Current.

sets (2003–2020) using the software PyFerret v7.4. The seasonal and monthly anomalies were calculated for chlorophyll *a* and other parameters by subtracting the 18-year mean from the seasonal and monthly means. The meridional/latitudinal variations from 0 to 30°S were calculated by averaging the longitudinal values (60°E–90°E) of each unit of the latitude for each parameter. In addition, we have split the ESTIO into three sub-regions (60°E–70°E, 70°E–80°E and 80°E–90°E) and analysed the distributional patterns in each region to distinguish any sub-regional variations that occur in the SCTR (60°E–70°E) and eastern regions (Wiggert et al., 2009) (Table 2). As the 18-year mean chlorophyll *a* showed higher concentration in the northern and lower in the southern domain (at ~13°S; Figure 1b),

we divided the entire study area into two domains as high chlorophyll *a* domain (HCD; Chl-*a* > 0.1 mg/m³) and low chlorophyll *a* domain (LCD; Chl-*a* < 0.1 mg/m³). The speed (*S*) of winds and geostrophic currents were calculated from the zonal (*u*) and meridional (*v*) components of each parameter ($S = \sqrt{u^2 + v^2}$). The surface wind stress was estimated using the bulk formula ($\tau = \rho \times C_d \times S^2$), where τ is the momentum flux of surface wind stress, ρ is the air density (1.225 kg/m³), C_d is the drag coefficient that varies with respect to the wind speed (Large and Pond, 1981), and *S* is the average wind speed at 10 m height. The wind stress curl was computed as, ($\tau \text{ curl} = \frac{\partial \tau_y}{\partial x} - \frac{\partial \tau_x}{\partial y}$), where τ_x and τ_y are the zonal and meridional components of surface wind stress. The Ekman pumping velocity (EPV) was calculated

Table 1 Range of chlorophyll *a* concentration reported in the oligotrophic southern Indian Ocean (0–30°S and 60°E–90°E) measured by in situ (Laboratory fluorometer and CTD/ARGO fluorescence sensor) and remote sensing satellite (SeaWiFS and MODIS). Abbreviations: AS – Austral Summer and AW – Austral Winter.

Sl. No	Author	Year	In-situ/Sat.	AS: Chl- <i>a</i> (mg/m ³)	AW: Chl- <i>a</i> (mg/m ³)
1	Fernandes et al.	2008	In-situ	<0.2	<0.2
2	Jena et al.	2012	In-situ	<0.1	-
3	George et al.	2013	In-situ	0.04–0.3	0.13–0.4
4	Strutton et al.	2015	In-situ & Sat.	<0.5	<0.2
5	Estrada et al.	2016	In-situ	<0.2	-
6	Anand et al.	2018	In-situ	<0.3 (Mar.)	-
7	Anand et al.	2017	In-situ	<0.5 (Apr.)	-
8	Levy et al.	2007	Sat.	<0.3	<0.3
9	Resplandy et al.	2009	Sat.	<0.15	<0.25
10	Morel et al.	2010	Sat.	0.05	0.05
11	Liao et al.	2014	Sat.	<0.2	<0.4
12	Dilmahamod et al.	2016	Sat.	<0.15	<0.25
13	Kumar et al.	2016	Sat.	<0.25	<0.25
14	George et al.	2018	Sat.	0.12–0.14	0.16–0.26
15	Liao et al.	2020	Sat.	<0.07	-

Table 2 Range of coordinates defining different regions and domains in this study.

Sl. No	Region/Domain	Geographic boundary
1	Low chl- <i>a</i> domain (LCD)	30°S–~13°S; 60°E–90°E
2	High chl- <i>a</i> domain (HCD)	~13°S–0°; 60°E–90°E
3	Western region	30°S–0°; 80°E–90°E
4	Central region	30°S–0°; 70°E–80°E
5	Eastern region	30°S–0°; 60°E–70°E
6	Seychelles – Chagos thermocline ridge (SCTR)	5°S–10°S; 50°E–80°E

by following the equation used by Gaube et al. (2013) as, $(EPV = \frac{\nabla \times \tau}{\rho_0 f})$, where τ is the wind stress, $\rho_0=1025 \text{ kg/m}^3$ is the average surface density of sea water and f is the Coriolis coefficient. The inter-annual signals/variabilities of chlorophyll *a* were extracted by applying a low pass filter with a high cut-off frequency of 1.5 years using climate data operator software (CDO; version 1.9.9rc1). All other high-frequency signals such as monthly and seasonal phenomenon/variabilities were eliminated to relate with the dipole mode index. The monthly DMI data (216 months) was assigned to a 4° resolution spatial grid to correlate with spatial chlorophyll *a* data (pixel-by-pixel relationship; Brewin et al., 2012). The 18-years of monthly anomalies of wind speed and chlorophyll *a* in the LCD and HCD were zonally averaged to represent time vs meridional shift in those features (Hovmöller plots). Similarly, the zonal and meridional means of 2016-daily data sets of wind components and chlorophyll *a* were presented to understand their origin and shifts with respect to time. The eddy features were identified, as done by Chinnadurai et al. (2021), using the contour generation method followed by manual verification. A $\pm 0.1 \text{ m}$ of MSLA along with ≥ 3 closed contours considered to detect cyclonic (MSLA $\leq -0.1 \text{ m}$; clockwise circulation) and anticyclonic (MSLA $\geq 0.1 \text{ m}$; anti-clockwise circulation) features. Areas of these features were calculated from the monthly MSLA data sets, as the percentage of pixels that fol-

lowed the above criteria in a total number of pixels covered the entire study area. The average chlorophyll *a* concentration was calculated from both groups of pixels (cyclonic and anti-cyclonic), separately in HCD and LCD using PyFerret software (v7.4).

2.4. Statistical analyses

Suitable statistical analyses were conducted to delineate the principal variables that have a significant role in governing the enhancement of chlorophyll *a* and to understand the relationship among the variables in the HCD and LCD of the ESTIO. The monthly means of each parameter at both domains (HCD and LCD) were calculated in PyFerret for 216 months (January 2003–December 2020) and the same data was used for the following statistical analyses. We have selected the principal component analysis (PCA), which reduced numerous variables as few principal dimensions (RStudio; *factoextra* and *FactoMineR* packages; code: *PCA*). The PCA was performed on 17 variables containing 216 individual samples, to provide various results such as eigenvalues, contributions, correlations dimensions, \cos^2 , summary statistics, etc. The percentage contribution (code: *var\$contrib*) of each variable to the top two dimensions in HCD and LCD can explain the significant amount of variance, calculated and plotted. The PCA results are plotted as a bi-

plot (code: *fviz_pca_var*) with the top two dimensions in x- and y-axes respectively to pictorially show the significant contributions to the variance, homogeneity and relationships among the variables (\cos^2). Pearson's multivariable correlation analysis was carried out (RStudio; *corrgram* and *corrplot* packages) and plotted with both ellipses and coefficients to straightforwardly and accurately understand the relationship among the variables. The darker shades in the output figure indicate a statistically significant relationship ($p < 0.05$) and the insignificant ($p > 0.05$) correlations are indicated with a cross mark (\times). A t-test was conducted to check the variability between paired samples such as parameters in HCD and LCD. The study area map made with Ocean Data View, the spatial data analysis and distribution maps were made with CDO (1.9.9rc1) and PyFerret v7.4, respectively and the graphs were plotted in R-Studio and Grapher, v7.2. (Golden Software, USA).

3. Results

3.1. Chlorophyll *a* and primary production (MODIS Aqua)

The phytoplankton biomass (chlorophyll *a*) was higher during the AW season (avg. 0.11 ± 0.03 mg/m³) than the AS season (avg. 0.07 ± 0.03 mg/m³) (Figure 2). Especially in the HCD (north of $\sim 13^\circ\text{S}$), the concentration was higher during both seasons (AW: 0.13 ± 0.02 mg/m³; AS: 0.1 ± 0.02 mg/m³) as compared to LCD (south of 12°S ; AW: 0.09 ± 0.01 mg/m³; AS: 0.05 ± 0.01 mg/m³). The seasonal variation was statistically significant in both HCD and LCD ($df=69$; t-test $p < 0.0001$). During the AS, the high chlorophyll *a* patches (>0.1 mg) were found in the equatorial and near-equatorial regions (up to 7.5°S) and it was well expanded over a large area (up to 17.5°S) during the AW. An ultra-oligotrophic condition was represented by an extremely low chlorophyll *a* concentration during both seasons in the south-eastern Indian Ocean ($\sim 21^\circ\text{S}$ to 30°S and $\sim 70^\circ\text{E}$ to 90°E). The seasonal anomaly of chlorophyll *a* clearly evidenced a noticeable decrease during the AS and an increase during the AW over a large area of the study domain (Figure 2c–d). The latitudinal profile showed a moderate concentration from the equator to $\sim 6^\circ\text{S}$ (avg. 0.12 ± 0.01 mg; during both seasons), and thereafter increased during the AW (till 10°S , then declined) and decreased during the AS (Figure 2e). The highest concentration of chlorophyll *a* was found between 8°S and 12°S (>0.15 mg) during the AW. During both seasons, the western sub-region contained the highest concentration of chlorophyll *a*. The meridional trend of net primary productivity was similar to the chlorophyll *a* distribution (Figure 2f). The mean productivity was highest during the AW (avg. 293.3 ± 32.8 mg C/m²/day; HCD: 295.3 ± 30.5 mg C/m²/day; LCD: 289.7 ± 29.9 mg C/m²/day) than the AS (avg. 212.2 ± 33.1 mg C/m²/day; HCD: 245.6 ± 30.2 mg C/m²/day; LCD: 190.6 ± 23 mg C/m²/day). The productivity in the equatorial region was lesser (255 ± 6.5 mg C) than the rest of the region during the AW (302 ± 30 mg C). Contrastingly, during the AS it was higher in the equatorial waters than in the southern region.

3.2. SST and PAR

In the ESTIO, the mean SST varied from 22.8°C (in the south) to 29.3°C (near the equator) during the AS and 18.9°C (in the south) to 29.7°C (near the equator) during the AW (Figure 3). During the AS, the warmer water mass (28°C surface isoline) was found north of 13°S in the western region, whereas north of 11°S in the eastern region of the study region (Figure 3a). During the AW, the 28°C isoline shifted northward by $\sim 9^\circ$ distance in the western sub-region and $\sim 3^\circ$ distance in the eastern sub-region (Figure 3b). From the equator to $\sim 5^\circ\text{S}$, the seasonal SST difference was minimum ($<0.5^\circ\text{C}$) and the difference increased pointedly till 10.5°S ($\sim 2^\circ\text{C}$) (Figure 3c). The SST difference almost flattened from there to $\sim 21^\circ\text{S}$ with a maximum difference of 2.4°C . Beyond 21°S , the difference increased up to 30°S with 3.9°C between the two seasons. The seasonal difference in SST in the HCD is narrow 28.1°C – 29°C and wider in LCD 23.1°C – 25.8°C . The difference was statistically significant ($df=69$; t-test $p < 0.0001$). The photosynthetically available solar radiation was highest in the study region during the AS (avg. 52.7 ± 4.4 E/m²/d) and lowest during the AW (avg. 37.8 ± 3.6 E/m²/d) (Figure 3d–f). During the AS, the highest PAR was received over the southern domain, especially the south of 15°S (avg. 56.7 ± 1.1 E/m²/d) than the northern domain (avg. 48.7 ± 2.3 E/m²/d). PAR in the sub-regions during each season was comparable. Similar to SST, the PAR showed a huge seasonal difference in LCD region than HCD.

3.3. Surface wind parameters and Ekman pumping velocity

The regional mean wind speed was remarkably more robust during the AW (6.8 ± 2.2 m/s) and higher (8.3 ± 1 m/s) between 6°S and 24°S . The wind speed was relatively weak during the AS (5.1 ± 1.3 m/s) than the AW ($n = 30$; t-test $p < 0.001$) and high speed (6.6 ± 0.3 m/s) winds were found between 14°S and 24°S , mainly in the eastern sub-region (Figure 4). The seasonal difference was minimum (<1 m/s) between 0 – 3.5°S ($n=14$, t-test $p > 0.5$), and 22.5°S – 27°S ($n=19$, t-test $p > 0.5$), and maximum ($n = 77$; t-test $p < 0.001$) between the rest of the study domain (Figure 4c). The most extensive seasonal variation, about 4 m/s, was found between 8°S and 12°S . The zonal wind was negative in most of the regions during the AW and weaker-positive between 0 and 8°S during the AS (Figure 4d). The meridional wind was more potent and positive during the AW, and weaker negative from 0 to 7°S and weaker positive beyond 7°S during the AS (Figure 4e). The wind stress during the AW was stronger than during the AS between 2°S and 24°S , and the highest values recorded (AW) were between 11°S and 18°S (Figure 4f). The wind stress curl was negative from 3°S to 18°S during the AS and from 0 to 15°S during the AW and positive in the rest of the area (Figure 4g). Though the mean wind speed was higher in LCD during AW (8.64 ± 0.55 m/s), the curl was positive ($5.88 \pm 1.32 \times 10^{-8}$ N/m³). In the HCD region, the curl was strongly negative ($-8.74 \pm 1.26 \times 10^{-8}$ N/m³), which causes divergence in the southern hemisphere and shoals the thermocline. The 18-year mean Ekman pumping velocity (EPV) was upward (positive) in the

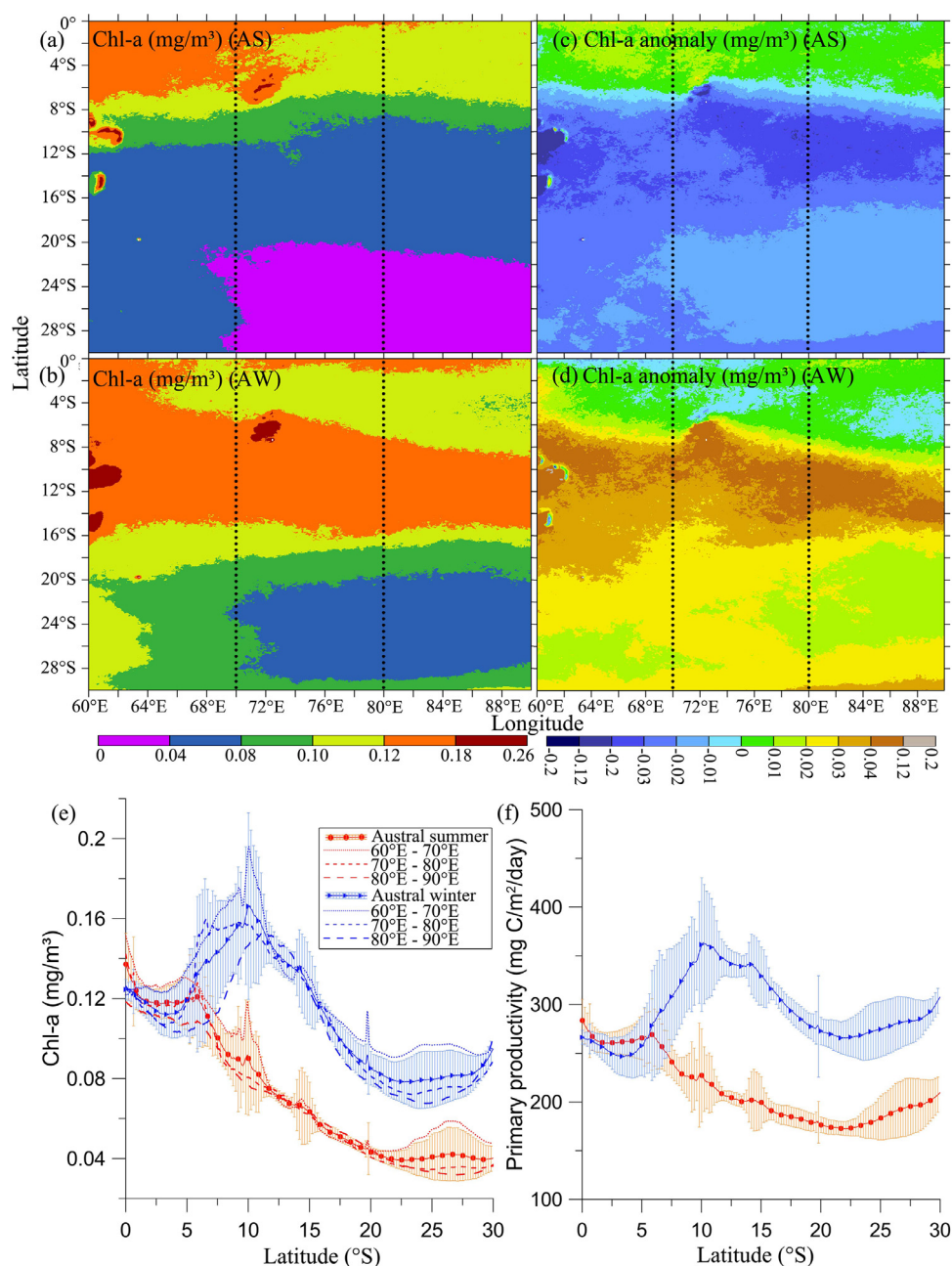


Figure 2 Spatial and seasonal mean distribution of chlorophyll *a* (chl-*a*) during a) the austral summer (AS), b) the austral winter (AW), and (c and d) seasonal anomaly during both seasons. The meridional means (dashed and dotted lines) along with the standard deviation (vertical bars) of e) chlorophyll *a* and f) primary productivity (chl-*a* based) during AS (orange lines) and AW (blue lines) in three sub-regions (60°E–70°E, 70°E–80°E and 80°E–90°E) and the ESTIO (60°E–90°E). The sub-regions are shown in the top and middle panels by dotted black lines.

northern half of the study area ($\sim 16^{\circ}\text{S}$ –equator), covering the entire HCD (Figure 5a). The EPV was negative in the southern region (south of $\sim 16^{\circ}\text{S}$). During the AW, the EPV was highly positive in the HCD ($0.94 \pm 0.2 \times 10^5 \text{ m/s}$) and negative in LCD ($-0.1 \pm 0.03 \times 10^5 \text{ m/s}$). During AS, the mean EPV was negative in entire regions, but the deviation was more in HCD. The long-term mean chlorophyll *a* shows high values north of $\sim 13^{\circ}\text{S}$ ($>0.1 \text{ mg/m}^3$) and lesser in the south (Figure 5b).

3.4. Two-dimensional time series analysis (Hovmöller) of wind and chlorophyll *a* anomaly

The Hovmöller plots of wind speed anomalies presented against chlorophyll *a* anomaly show concurrent positive and negative features in both (Figure 6a–d). During 2003–2006, the high frequency of occurrence of positive wind speed and high chlorophyll *a* was distinctively evident in HCD (Figure 6a–b). In HCD, anomalies of wind and chlorophyll

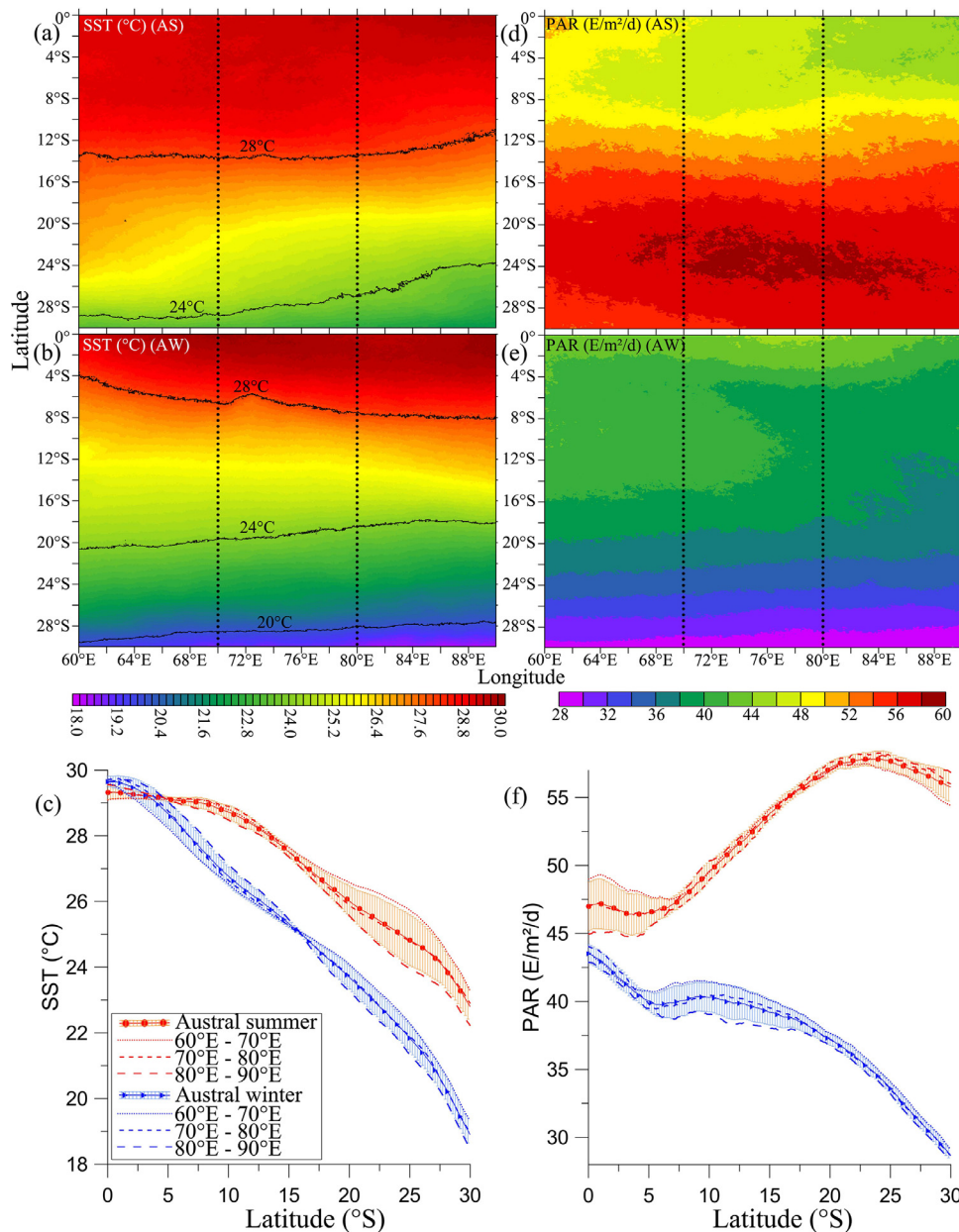


Figure 3 The seasonal and spatial mean sea surface temperature (SST) during a) the austral summer (AS), b) the austral winter (AW) and c) the SST’s meridional means (dashed and dotted lines) along with standard deviation (vertical bars) during AS (orange lines) and AW (blue lines) in the study region, in the left side panels, and (d, e and f) similar figures for photosynthetically available radiation (PAR) in the right side panels. The dotted black lines in the top and middle panels show three sub-regions (60°E–70°E, 70°E–80°E and 80°E–90°E), accordingly, the means presented in the bottom panels.

a were positive ($p < 0.01$; $df = 214$), and in LCD it shows no significant impact ($p > 0.05$; $df = 214$). The pixel-by-pixel correlation of wind speed and chlorophyll *a* also showed a significant positive relationship in almost the entire ESTIO (Figure 6e). The zonal flow of wind displayed a larger area of negative relationship (Figure 6f) and the meridional flow speed of wind opposite trend with a positive relationship (Figure 6g). The Hovmöller plots of daily data of chlorophyll *a*, zonal and meridional winds show an annual as well as spatial distribution (Figure 7a–f). The zonally averaged chlorophyll *a* shows comparatively high concentration throughout the year within the ~12°S–equator band (HCD; Figure 7a).

From May to September, the concentration increased in the entire study area (Figure 7a and d) and during the same period, the zonal wind was strongly negative (westward; Figure 6b and e) and meridional wind speed was strongly positive (northward; Figure 7c and f).

3.5. Euphotic depth (ZEU), mean sea level anomaly (MSLA) and mixed layer depth (MLD)

The seasonal euphotic depth was deeper during the AS (avg. 126.5 ± 18.8 m) than the AW (avg. 107 ± 8.3 m) (Figure 8a; Figure 9a–b). As usual, the ZEU during the AS was shall-

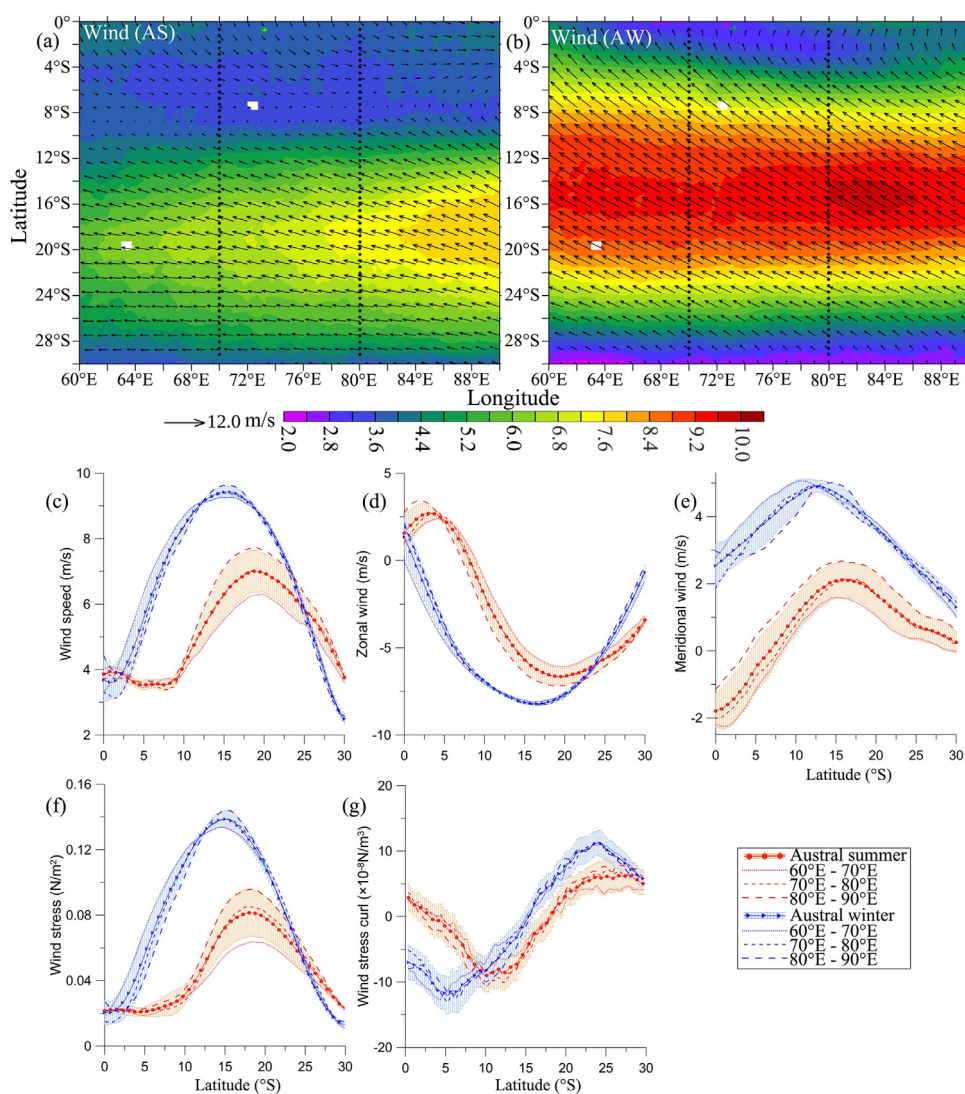


Figure 4 The seasonal and spatial mean wind velocity during a) the austral summer (AS), and b) the austral winter (AW). The meridional means (dashed and dotted lines) along with standard deviations (vertical bars) of c) wind speed, d) zonal wind, e) meridional wind, f) wind stress and (g) wind stress curl during AS (orange lines) and AW (blue lines) in the sub-regions and the entire study area. The dotted black lines in the top panels show sub-regions (60°E–70°E, 70°E–80°E and 80°E–90°E), accordingly, the means presented in the middle and bottom panels.

lower near-equator (0–6°S; avg. 101.7 ± 1.2 m) and gradually deepened towards the south (22.5°S–30°S; avg. 148.8 ± 0.7 m). During the AW, the latitudinal/meridional profile of ZEU was irregular with a deeper ZEU in the near-equator (0–4°S) and south of 16°S (avg. 112.8 ± 2.7 m), shallowed between 5°S–16°S (avg. 97.2 ± 4.8 m), and the shallowest at 10°S (89.6 m). From the west to east, the ZEU was mostly uniform. HCD has a relatively shallow ZEU (108.2 ± 6.5 m) and LCD has a deeper ZEU (131.2 ± 9.9 m). The MSLA was positive (zonally averaged) during both seasons in the study domain (Figure 8b; Figure 9c–d), and ranged from 0.03 to 0.15 m during the AS and from 0.04 to 0.1 m during the AW. A strong positive mean sea level (>0.1 m) was found during the AS between 8°S–22°S, and a weaker positive MSLA (<0.06 m) was found during the AW between 7°S–15°S. Mi-

nor disparities were noticed from west to east. HCD has relatively less MSLA than LCD. The MLD followed an almost similar trend during both seasons (except the southern domain), with relatively deep during the AW (avg. 63.6 ± 16.4 m) and shallow during the AS (avg. 30 ± 6.1 m) (Figure 8c; Figure 9e–f). The deepest mixing (>40 m) was found at the equator and between 11.5°S–19.5°S during the AS and almost the entire area (except 5.5°S–7.5°S) had mixed deeper during the AW. There were no significant variations found among the sub-regions, the MLD varied from 31.8 to 40 m during the AS ($n=30$; $p<0.05$) and 63.2–64.2 during the AW ($n=30$; $p>0.5$). The MLD was shallower in the HCD (34.7 ± 9.2 m) and deeper in LCD (50.1 ± 8.4 m). In both regions, MLD was ~ 35 m during the AS. During the AW, ~ 30 m difference was found between these two regions.

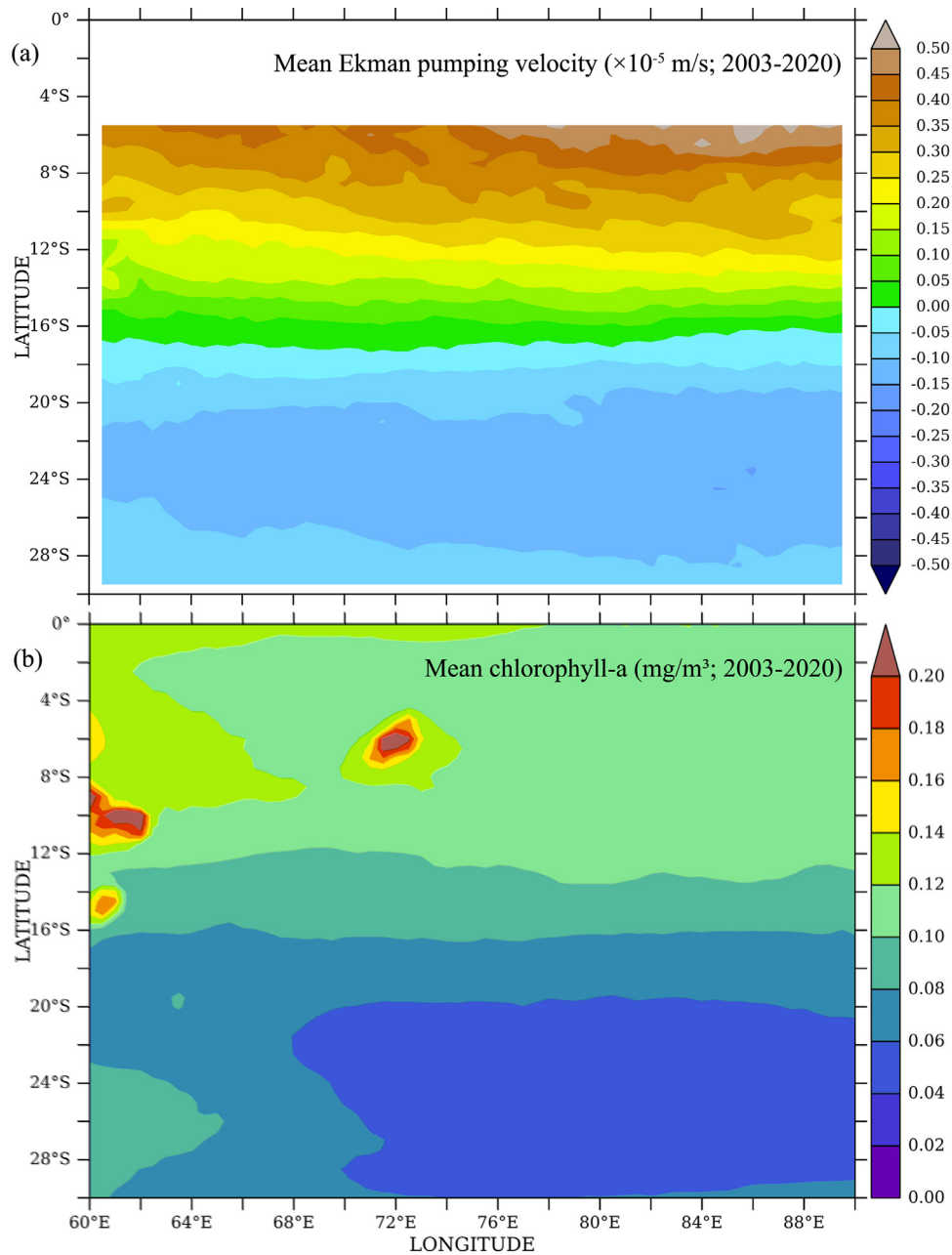


Figure 5 a) The multi-year mean Ekman pumping velocity in the ESTIO. Data masked over an equatorial region (0–5°S). b) average chlorophyll *a* concentration during the study period in the ESTIO.

3.6. MSLA, geostrophic currents and eddy features

The positive MSLA was found to be a predominant feature in the ESTIO. An average of ~37% of the area in the selected study area (ESTIO) was occupied by eddy features. Especially, anti-cyclonic features covered ~33% and cyclonic features covered ~4%. Statistically, the area of anti-cyclonic eddies (warm core) does not affect the chlorophyll *a* concentration observed in the same area ($r=-0.05$; $n=216$), but there was a significant positive relationship found between the area of cyclonic eddies (cold core) and chlorophyll *a* ($r=0.43$; $n=216$). The region-wise anal-

ysis shows that anti-cyclonic features occupied ~17.5% in the LCD (with avg. 0.07 mg/m³ chlorophyll *a* and ~15.6% in HCD (avg. 0.09 mg/m³ chlorophyll *a*). Similarly, the cyclonic eddy features occupied ~1.6% in the LCD (avg. 0.07 mg/m³) and ~2.4% in HCD (avg. 0.14 mg/m³) (Figure 10). The surface geostrophic currents were relatively strong during the AS (avg. 0.15 ± 0.14 m/s), especially in the equatorial region (0–3°S; 0.5 ± 0.18 m/s), that too in the western sub-region, and comparatively weak during the AW (0.12 ± 0.09 m/s and 0.35 ± 0.07 m/s) (Figure 11a–c). The zonal currents were positive (easterly) in the equatorial region (up to ~5.5°S) during both seasons (Figure 11d). It was

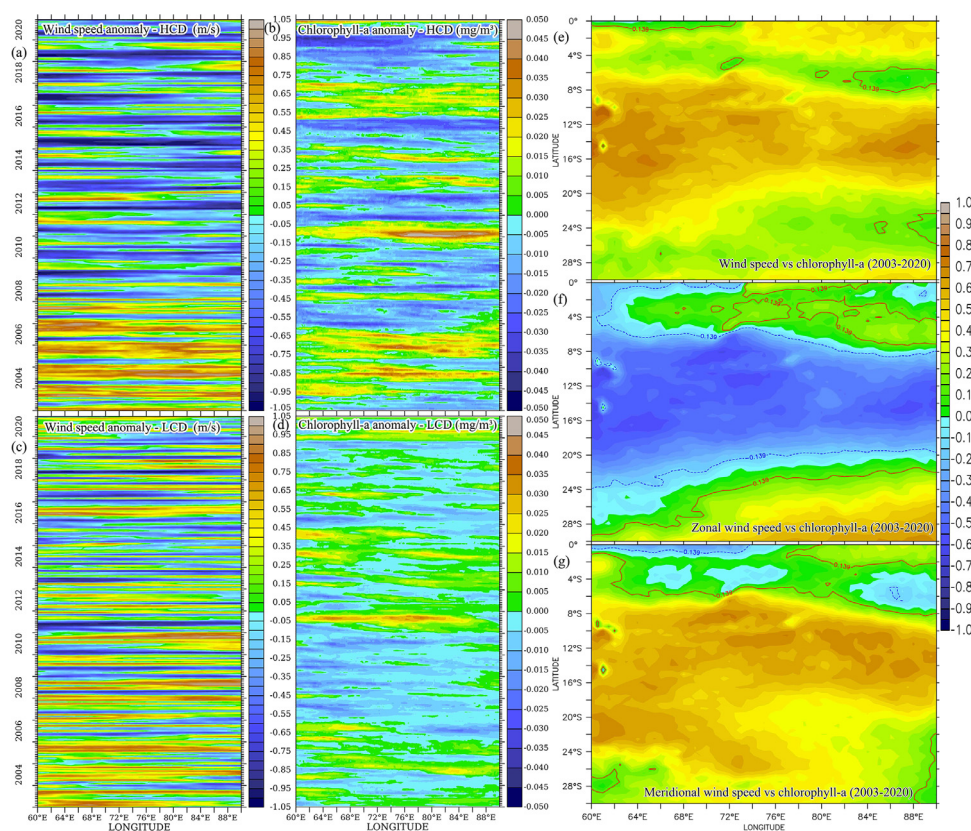


Figure 6 The Hovmöller plots of monthly wind speed and chlorophyll *a* anomalies over 18 years in (a–b) HCD and (c–d) LCD. Pixel-by-pixel correlation between chlorophyll *a* with e) wind speed, f) zonal wind and g) meridional wind.

well oriented, negative (westerly) and stronger between 8°S and 17°S during the AW (>0.1 m/s), and there was a sudden drop in zonal speed between ~10°S and 12°S during the AS. The meridional currents were mostly and significantly negative (southerly) during both seasons and it was stronger (>0.1 m/s) between 4°S and 8°S during the AW (Figure 11e). Throughout the year, HCD has stronger geostrophic currents (0.16 ± 0.03 m/s) than in the LCD (0.14 ± 0.01 m/s).

3.7. Inter-annual variability of chlorophyll *a* and its relation with IOD

The 1.5-year low-pass filtered chlorophyll *a* signals in HCD and LCD followed a comparable trend in the distribution with a higher magnitude in HCD and lower magnitude in LCD ($df=214$; t -test p -value <0.001; Figure 12a). The chlorophyll *a* signals showed a non-linear trend with four noticeable crests (>0.13 mg/m³) and three troughs (<0.09 mg/m³) during the study period in the HCD. In the LCD, the chlorophyll *a* signals showed one crest (>0.076 mg/m³) and two troughs (<0.06 mg/m³). The DMI displayed more number of positive events (>0.4; 26 months) than the negative (<-0.4; 14 months) in the study area. The crests of chlorophyll *a* anomaly and filtered signals of chlorophyll *a* aligned against the troughs of DMI which show a negative relationship with them. In particular, both filtered and unfiltered signals of chlorophyll *a* in HCD marked a highly significant

negative relation with DMI ($df=215$; $p<0.01$) as compared with the LCD ($df=214$; $p>0.05$). The spatial correlation between the filtered chlorophyll *a* and DMI evidences the significant negative impact of IOD on chlorophyll *a* distribution over a larger area of the ESTIO, especially the northern side (Figure 12b).

3.8. Climatology of parameters

A clear seasonality was noticed in the seasonal components of selected parameters (SST, PAR, ZEU and zonal winds) with low values during the AW and high values during the AS (Figure 13). Unlike the above variables, the wind speed, meridional wind, MLD, chlorophyll *a* and primary productivity showed distinctive seasonality with lower values during the AS and higher during the AW. The MSLA was negative during the March–May and positive during the November–January period. The chlorophyll *a* decreased from October to May, which indicates prolonged oligotrophy in this region.

3.9. Results of statistical analyses

The variance in the surface water properties of the ESTIO was summarily explained by a few principal dimensions/axes of the PCA (Figure 14). The eigenfactors revealed that the top two dimensions contributed a cumulative variance of 68% and 71.6% in the HCD and LCD respectively (Figure 14) and most of the variables significantly correlated

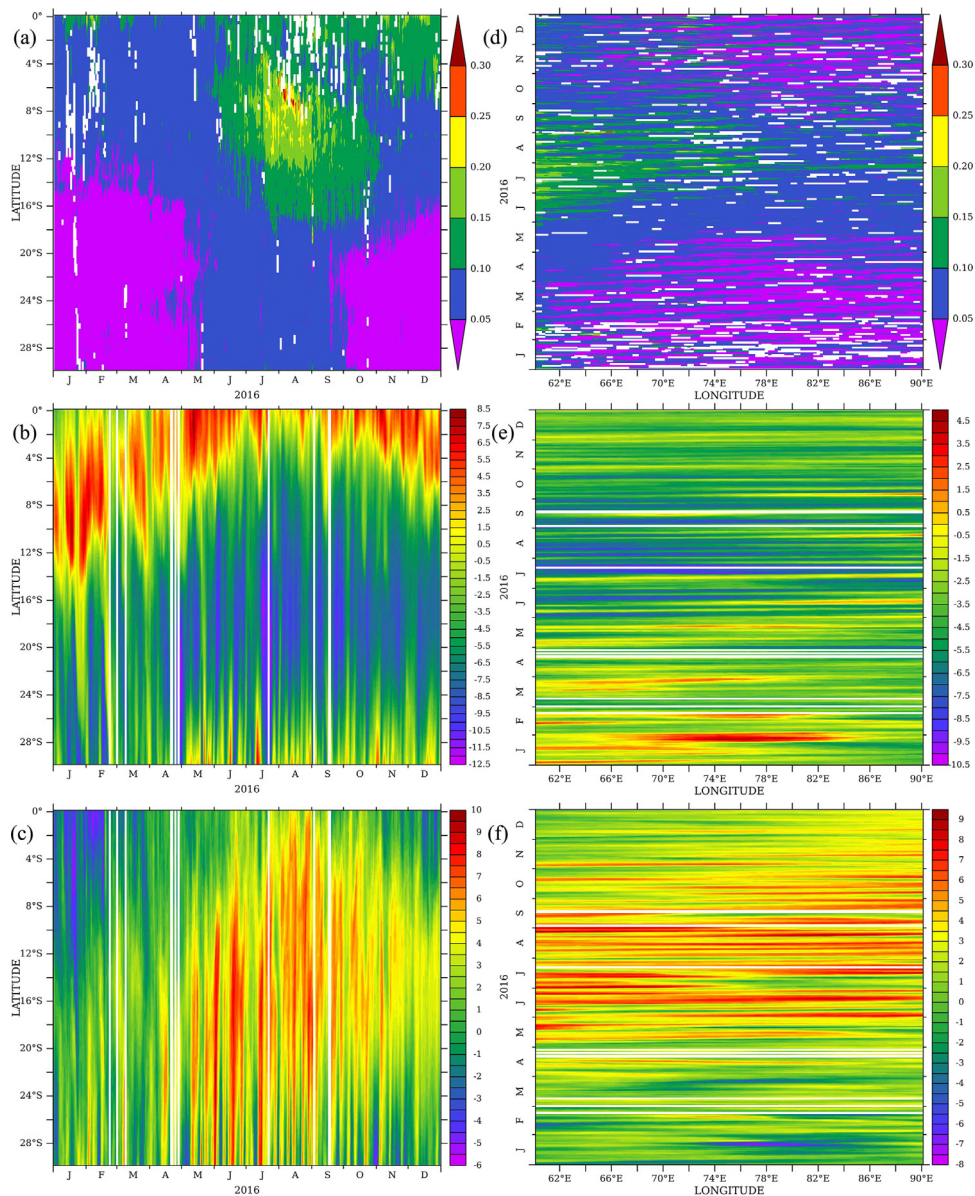


Figure 7 The Hovmöller plots of daily (reference year 2016) longitudinal means of a) chlorophyll *a*, b) zonal wind and c) meridional wind, and (d–f) their latitudinal means.

to those top principle dimensions. The variables such as wind stress, meridional wind, Ekman pumping velocity, wind speed, wind curl, SST, zonal wind, chlorophyll *a*, primary productivity, MLD and PAR are orderly contributing (> average) to the 1st dimension, and MSLA, DMI, zonal currents and ZEU to the 2nd dimension in the HCD (Figure 14a). In the LCD, MLD, chlorophyll *a*, meridional wind, primary productivity, SST, ZEU, wind curl, wind speed, Ekman pumping velocity, PAR, current speed and wind stress are orderly contributing to the 1st dimension, and zonal wind, wind stress, wind speed, Ekman pumping velocity, DMI and zonal current to the 2nd dimension (Figure 14b). The top two dimensions for HCD and LCD were used to plot the PCA biplot (Figure 14c–d), which illustrates the relationship among variables and clearly represents the significance/strength of the contribution of each parameter to the temporal variance. The multivariable correlation is sufficiently represented by a correl-

ogram (HCD: Figure 14e and LCD: Figure 14f). Chlorophyll *a* showed a positive response to wind stress, wind speed, meridional wind, Ekman pumping velocity, MLD and zonal currents, and negative to the ZEU, SST, wind curl, zonal wind, PAR, MSLA, meridional currents, DMI and geostrophic current speed in HCD (Figure 14e). In LCD, chlorophyll *a* showed positive relationship to MLD, meridional wind, wind speed, wind curl and wind stress, and negative to ZEU, PAR, SST, Ekman pumping velocity and geostrophic current speed (Figure 14f).

4. Discussion

Optimum light and nutrients are two essential parameters required for the growth and biomass build-up of phytoplankton (Dickman et al., 2006). As the study area is lo-

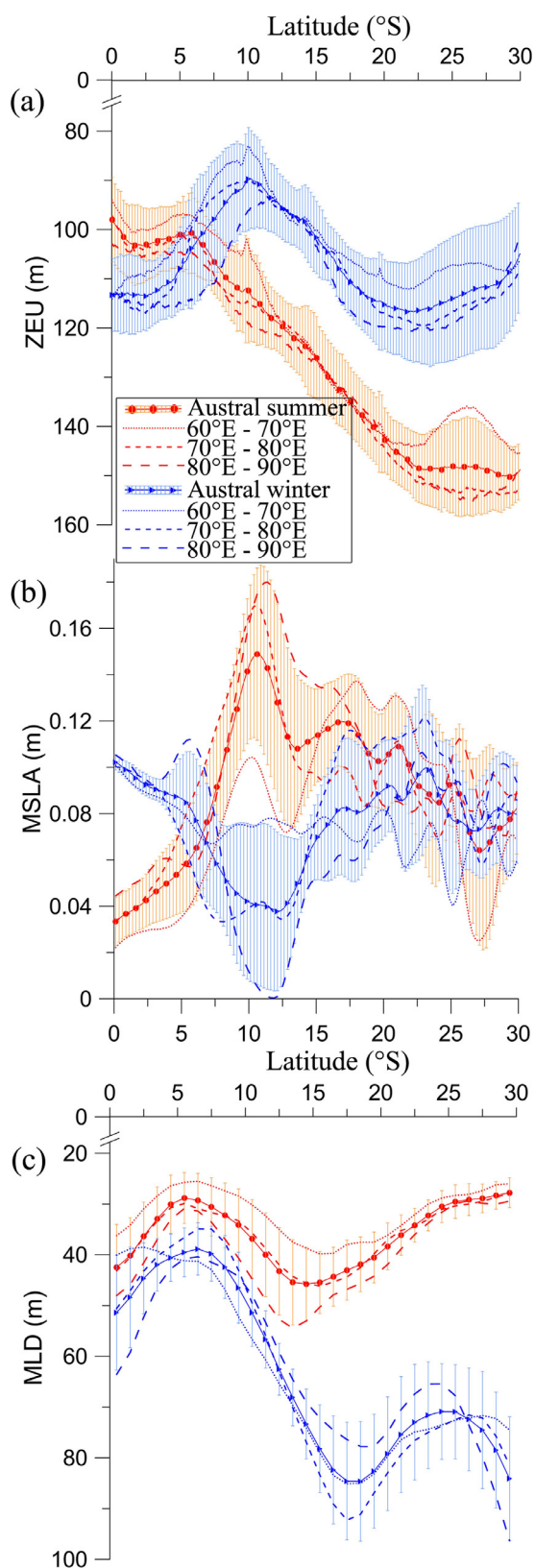


Figure 8 Latitudinal/meridional and seasonal means (dashed and dotted lines) along with standard deviations (vertical bars) of a) ZEU, b) MSLA and c) MLD during the austral summer (AS; orange lines) and the austral winter (AW; blue lines) presented for the sub-regions (60°E–70°E, 70°E–80°E and 80°E–90°E) and for the entire study area (60°E–90°E).

cated in the tropics (0–30°S), enough light could be available throughout the year. Typically, nutrients are supplied through two modes, such as from the above water column (aeolian and riverine) and from below the thermocline (upwelling and vertical mixing) (Maranon and Holligan, 1999). As the selected study domain is located much away from the continents, the first mode of nutrient addition is feeble (Fan et al., 2006), and possibly, the later mode could be the dominant route of nutrient supply to the ESTIO (George et al., 2018; Nagura and McPhaden, 2018; Resplandy et al., 2009; Song et al., 2004). The vertical mixing could be the least during the AS due to the weaker winds that could not break the thermal stratification created by increased SST. The warmer water piled up over a larger area during the AS could lead to either stronger stratification or deepened thermocline by pushing down, ultimately lack of nutrients to the surface water column and lower chlorophyll *a*. This condition primarily leads the southern tropical Indian Ocean water to be extremely oligotrophic as meagre nutrients are available in the surface water column. The high SST during the AS was due to the position of the sun above the head, which was directly heating, providing the highest PAR that ultimately increased the ZEU in the southern tropic. The lack of nutrients and high PAR could not support the phytoplankton production in the top portion of the photic zone, where the phytoplankton follow a photo-protective mechanism for survival (Giannini et al., 2021; Jyothibabu et al., 2018). Hence there was a clear sub-surface chlorophyll maxima (SCM) layer reported during the AS season around 50 m depth near-equator, deepened toward the south by 150 m near 16°S (high PAR and deeper ZEU) (Estrada et al., 2016; George et al., 2013) and shallowed at 40°S, where the light level was relatively less (Naik et al., 2015).

Unlike the northern Indian Ocean currents, there are no seasonally reversing patterns in the south, but the velocity is relatively strong during the first phase of AS (November–December) and there is a shift in the course of equatorial currents (Shenoi et al., 1999). The equatorward east African coastal current from the south and Somali current from the north bring continental shelf-derived nutrient-rich water mass to feed the stronger equatorial jet currents (Schott and McCreary Jr, 2001; Shenoi et al., 1999; Wyrki, 1973), which flow eastward could be one of the reasons for high chlorophyll *a* biomass in the western equatorial Indian Ocean during the AS (HCD). Also, the equatorial jet transports the warm water from the surface layer towards the east (Schott and McCreary Jr, 2001) and generates a surface water column turbulence that could bring nutrients and enhance phytoplankton biomass (Strutton et al., 2015). In the southern domain (LCD), the zonal current does not influence chlorophyll *a*, which could be due to the nutrient-poor water recirculation from the warm gyre of the south Indian Ocean. As per Liao et al. (2017), the wind blows across the equator (southward) during this period, possibly shallowing the thermocline by upwelling and mixing the water column with deep water nutrients which could jointly enhance the phytoplankton production. One-year daily data of wind and chlorophyll *a* also evidenced a positive response of chlorophyll *a* during strong positive meridional wind and strong negative zonal wind speeds. The seasonal MSLA over the southern tropical Indian Ocean (8°S–22°S) was positive

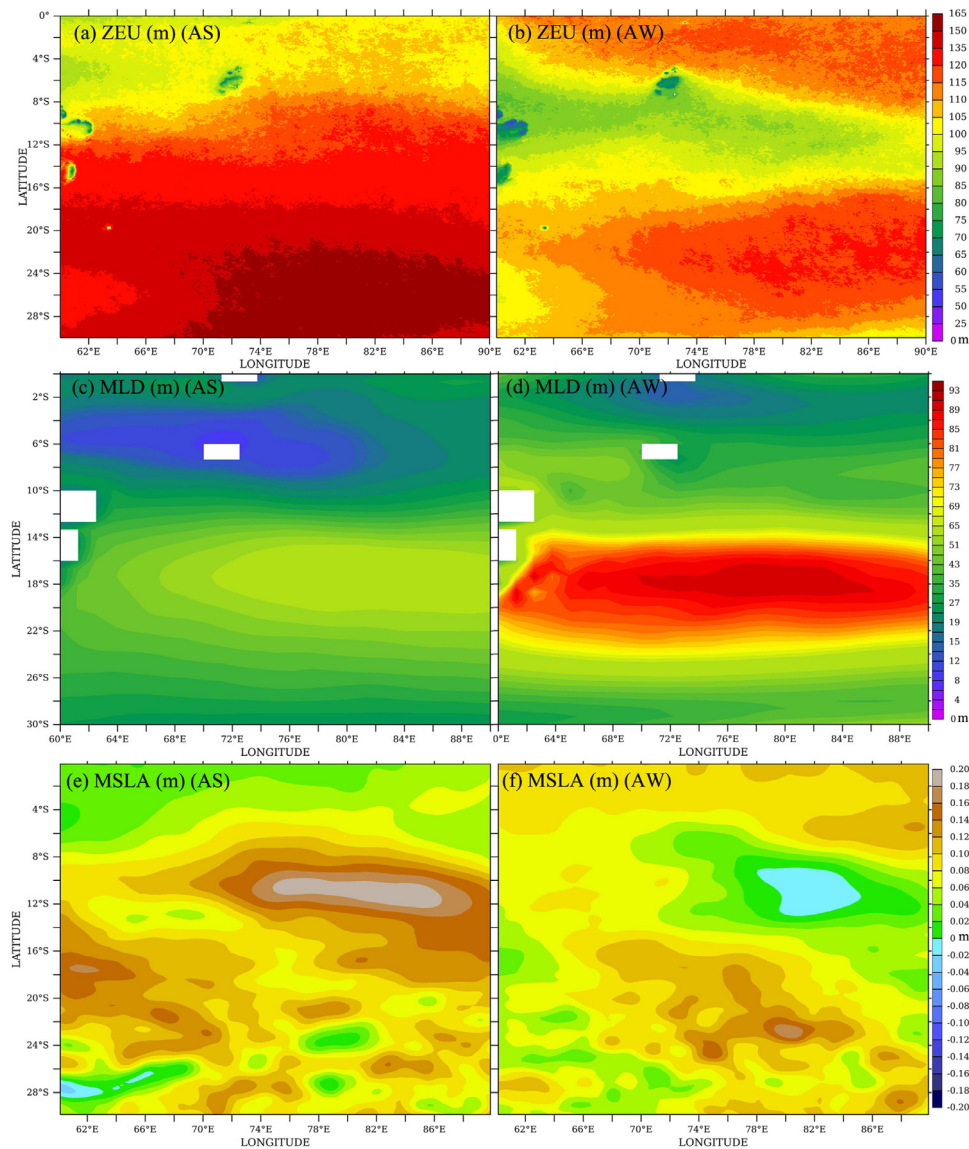


Figure 9 The spatial distribution of (a and b) euphotic depth, (c and d) MLD and (e and f) MSLA during the AS (left) and the AW (right), respectively.

and higher during the AS, which indicates a deeper thermocline that could not be lifted or mixed efficiently to bring nutrients to the surface layer by the weaker wind force applied over that region possibly an additional reason for the low chlorophyll *a* biomass (Mandal et al., 2021). This study presented zonal means of seasonal MSLA to generalize the meridional distribution that exhibited a strong negative relationship with chlorophyll *a* and phytoplankton production. Comparatively high chlorophyll in the anti-cyclonic eddies (warm core) reported in the south-eastern sub-tropical Indian Ocean (Feng et al., 2007; Thompson et al., 2007; Waite et al., 2007), explained as they have the source water from western Australian Shelf, which supplies nutrients to the anti-cyclonic eddies. Later studies by Gaube et al. (2013 and 2014) and Dufois et al. (2014 and 2016) found that those anti-cyclonic eddies generated over the western shelf of Australia could not propagate to a long distance into the interior south Indian Ocean. They reported a weaker strat-

ification in the anticyclone eddies than in the cyclone eddies, and the anticyclone eddy induces a deeper convective mixing during the AW, which introduces nutrients into the thick mixed layer and possibly increases phytoplankton production. The positive Ekman pumping velocity was termed to be a reason for high chlorophyll *a* in the cores of anticyclone eddies when they have opposite polarity between wind stress curl and vorticity of eddy (Gaube et al., 2014). Unlike northern Indian Ocean anti-cyclonic eddies, which negatively impact chlorophyll *a* (e.g., Jyothibabu et al., 2021), anti-cyclonic eddies in the present study area do not significantly reduce chlorophyll *a* ($r=-0.05$), which could be due to weaker stratification and convective mixing happening in the anti-cyclonic eddies of southern Indian Ocean (Dufois et al., 2014, 2016; Gaube et al., 2013, 2014). Cyclonic eddy-induced upwelling has a significant impact on bringing up nutrients and enhancement of phytoplankton in the HCD. Due to persistent warm gyre in the southern region

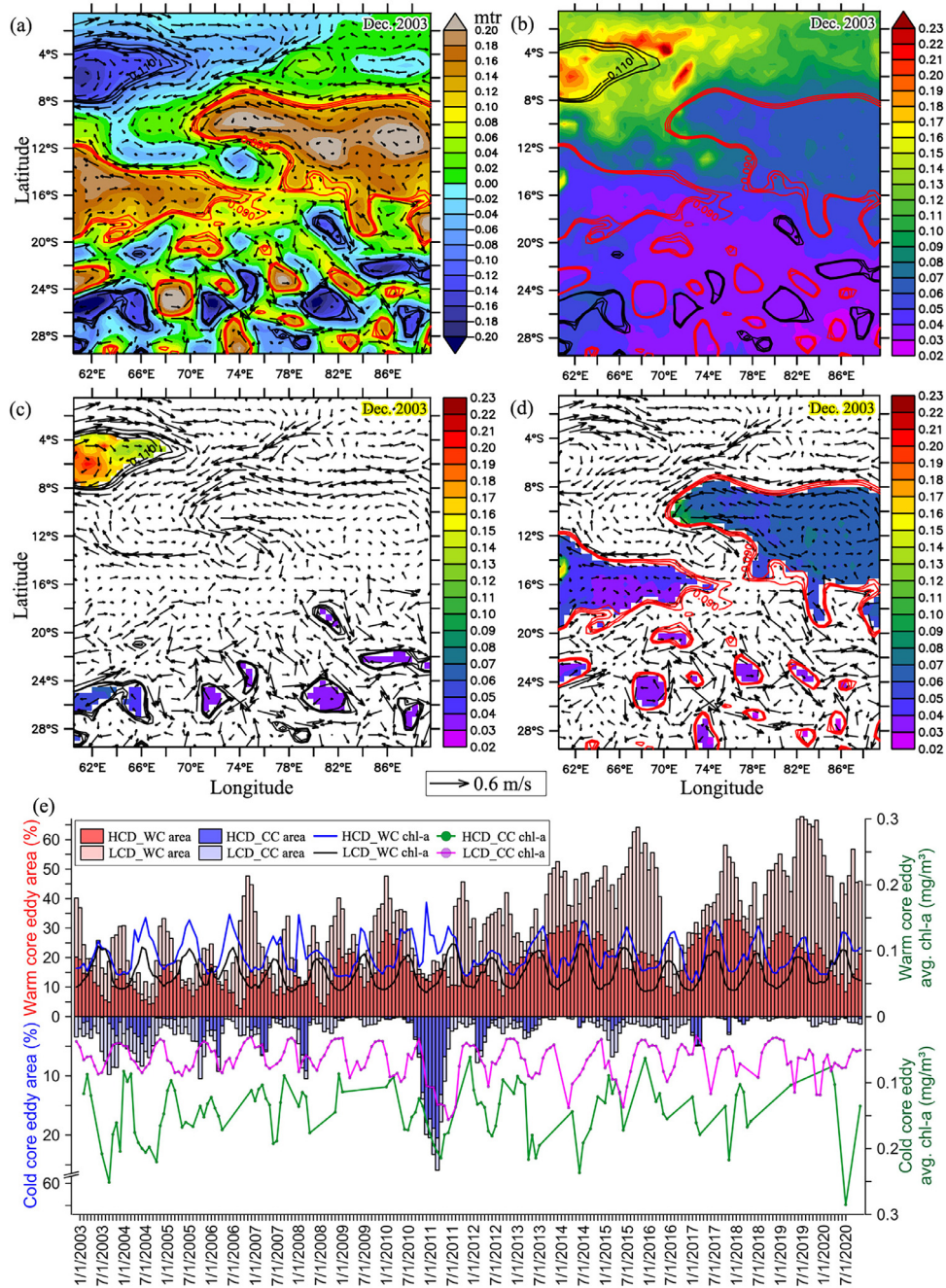


Figure 10 Representative maps of December 2003 presented to show the identification of the areas of cyclonic (clockwise circulation) and anti-cyclonic (anti-clockwise circulation) features by applying contours of $\text{MSLA} \leq -0.1$ m and $\text{MSLA} \geq 0.1$ m, respectively over a) MSLA, (b–d) extraction of chlorophyll *a* in respective features. (e) Stacked bars representing the percentage area of anti-cyclonic features (WC area; upper bars; HCD: dark orange; LCD: light orange) and cyclonic features (CC area; lower bars; HCD: dark blue; LCD: light blue) during the study period. The mean chlorophyll *a* in the anti-cyclonic features (WC chl-*a*; upper lines; HCD: blue; LCD: black) and in the cyclonic features (CC chl-*a*; lower lines; HCD: green; LCD: magenta).

(Jena et al., 2013; Stramma and Lutjeharms, 1997), which deepens the thermocline, the cyclonic eddies have a lesser impact in the pumping up of nutrient-rich water ($r=0.12$; $p>0.05$; $df=201$).

Usually, the western region of the equatorial Indian Ocean is cooler than the eastern region, which is accompanied by shallow thermocline and mixing that supports predominant upwelling in the western region (Saji et al.,

1999; Shi and Wang, 2021). During the positive IOD events, the thermal variation shifts between both regions with relatively warm water in the west and cooler water mass in the east that lifts up the thermocline and shallows mixed layer. The shallow thermocline in the east enhances the upwelling which brings nutrient-rich water mass towards the euphotic zone and increases the phytoplankton biomass (Iskandar et al., 2009). During our study period, more num-

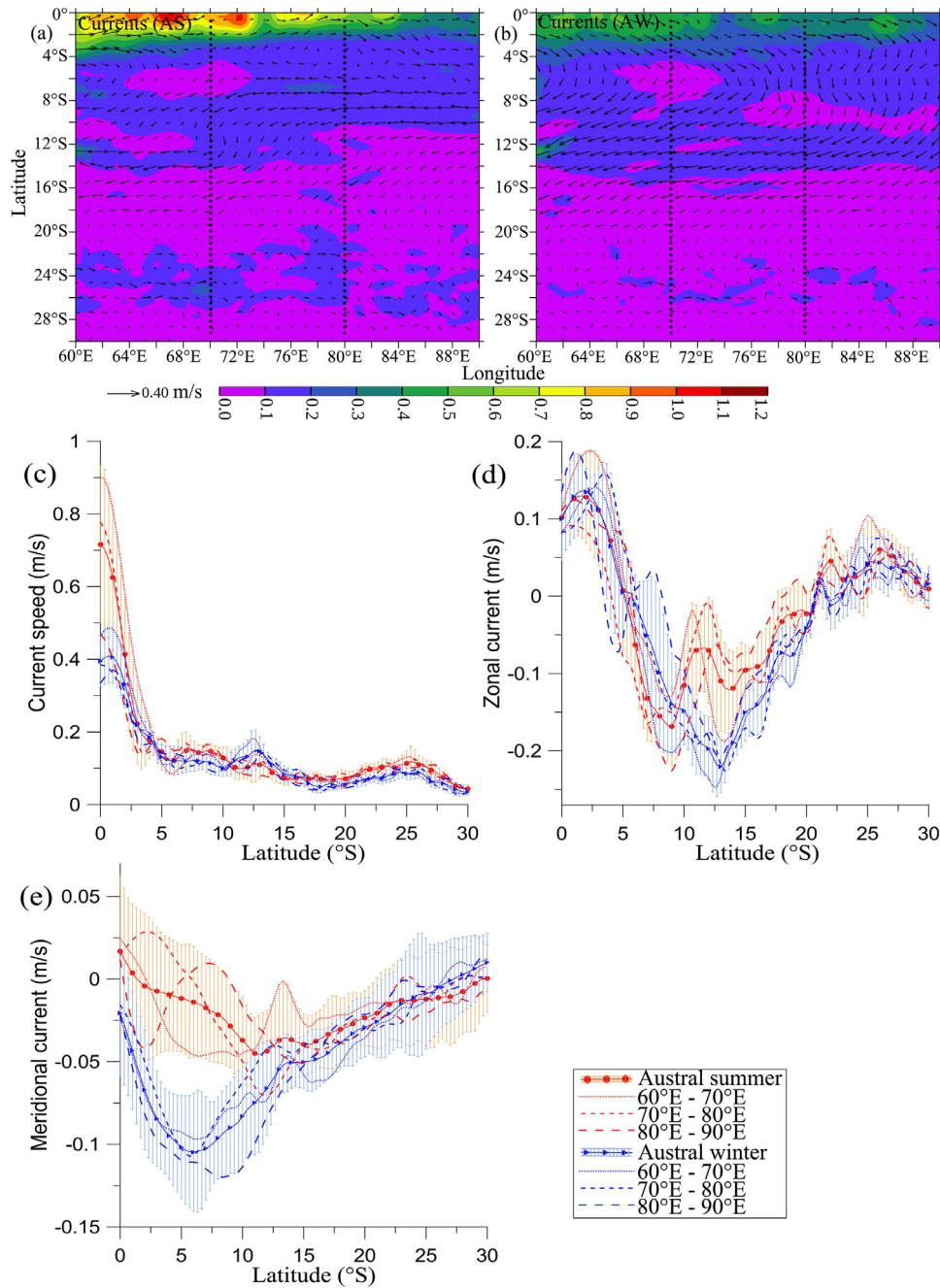


Figure 11 The seasonal mean geostrophic current velocity during a) the austral summer (AS), and b) the austral winter (AW). The meridional means (dashed and dotted lines) along with standard deviations (vertical bars) of c) current speed, d) zonal current and e) meridional current during AS (orange lines) and AW (blue lines) in the sub-regions (60°E–70°E, 70°E–80°E and 80°E–90°E) and entire ESTIO (60°E–90°E). The sub-regions are shown in the top panels by dotted black lines.

ber (26 months) of positive dipole mode index were found (positive IOD) and they significantly reduced the chlorophyll *a* content in the HCD (north of ~13°S), but much lesser in the LCD (south of ~13°S). This and the pixel-by-pixel relationship evidenced that a larger area of the ESTIO is responding negatively to the positive IODs. A comprehensive data analysis showed that during the positive IODs, most part of the ESTIO is occupied by warm water mass which deepens the thermocline and mixed layer depth along with increased MSLA altogether reduces the possibility of up-

welling and nutrient enhancement in the photic water column. The lack of nutrients in the surface water column significantly controls the phytoplankton growth and biomass during the positive IODs.

The wind force is an important reason for ocean mixing processes which bring nutrients to the euphotic zone from the subsurface water column. During the monsoon period, wind speed is higher in the northern Indian Ocean (during the AW), where coastal upwelling and vertical mixing of the water columns are experienced (Banse, 1959). In the south-

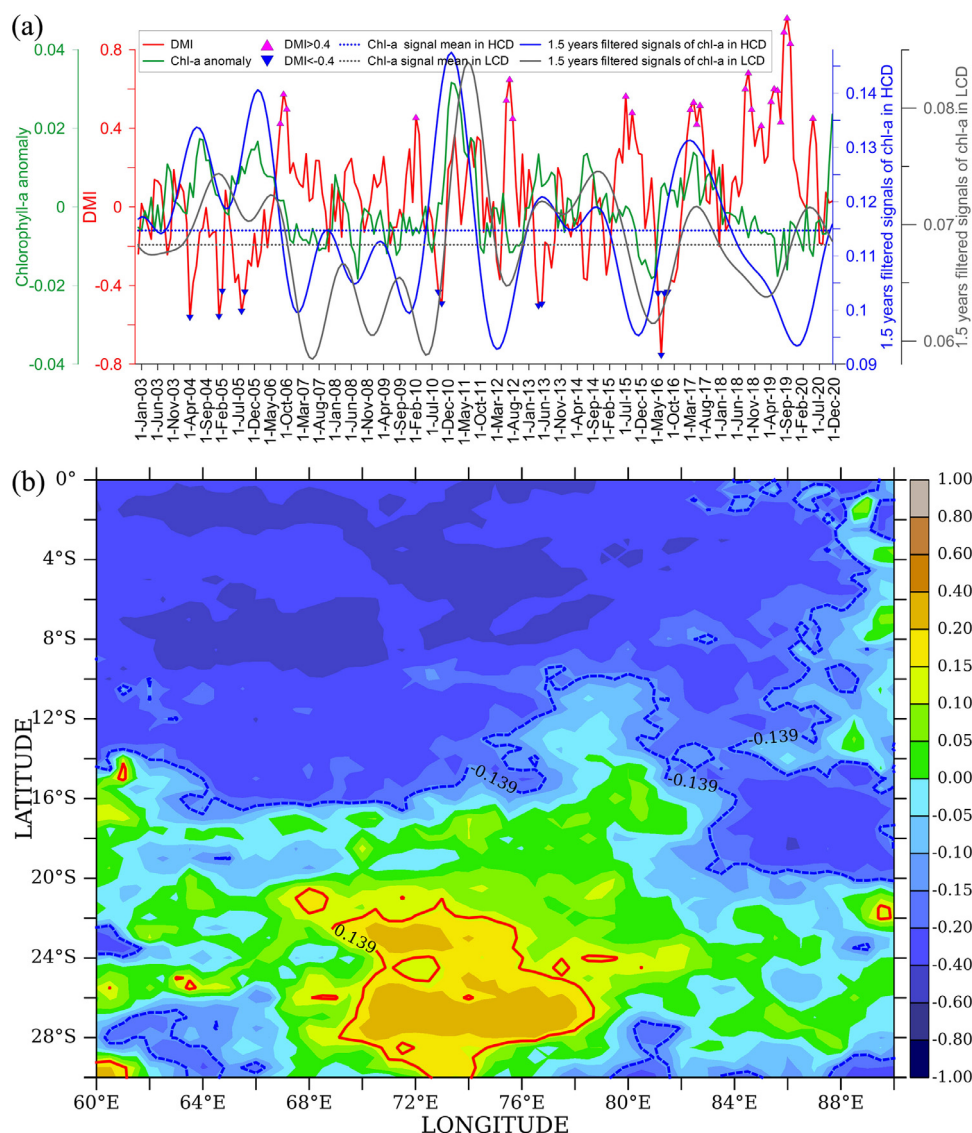


Figure 12 The monthly time series of a) dipole mode index (DMI;°C), chlorophyll *a* anomaly, 1.5 years filtered signals of chlorophyll *a* and its mean in HCD and LCD. b) Pixel-by-pixel correlation between DMI and chlorophyll *a*. The areas have significant positive and negative correlations demarcated in red and dashed blue contour lines.

ern tropical Indian Ocean, the south-easterly trade wind speed was highest during the AW, which applied maximum stress over a large sea surface. As reported by [Hermes and Reason \(2008\)](#) and [McCreary Jr et al. \(2009\)](#) in the SCTR region, we could see in the present study that the meridional component of the wind was positive (northward force) and zonal wind was strongly negative (westward force), which could cause a net movement of surface water in the left directions of respective winds due to Ekman drift and result in surface divergence induced positive Ekman pumping during the AW. The Ekman pumping velocity in HCD is highly positive which could lift up the thermocline significantly which leads to the cooling of the upper water column along with the pumping of nutrients altogether enhancing the phytoplankton biomass ([Trenary and Han, 2008](#)). This was evidenced in the correlation plot with a strong positive relation of Ekman pumping velocity with chlorophyll *a* and a strong negative relation with sea surface temperature. The

positive Ekman pumping is due to the negative wind curl, which diverges the surface water and causes upwelling. In the LCD, the Ekman pumping velocity was negative which represents downwelling and reflected as low chlorophyll *a*. The Hovmöller plots of daily data sets also evidenced the strengthening of westward flowing zonal wind (easterlies; strong negative values) and enhancement of meridional wind (southerly; strong positive) which could induce the surface water divergence as the water moves leftward during the AW. The surface water divergence causes the pumping of nutrient-rich sub-surface water towards the surface and wind-induced mixing enhances chlorophyll *a* during the AW. The positive relationship between wind and chlorophyll *a* was reported when the MLD is shallower, and negative when MLD is deeper ([Kahru et al., 2010](#)). In the ESTIO, the MLD depends on the water temperature which is usually lesser as it lifts up the thermocline ([Shi and Wang, 2021](#)). We could suggest two possible reasons for the deepening of MLD and

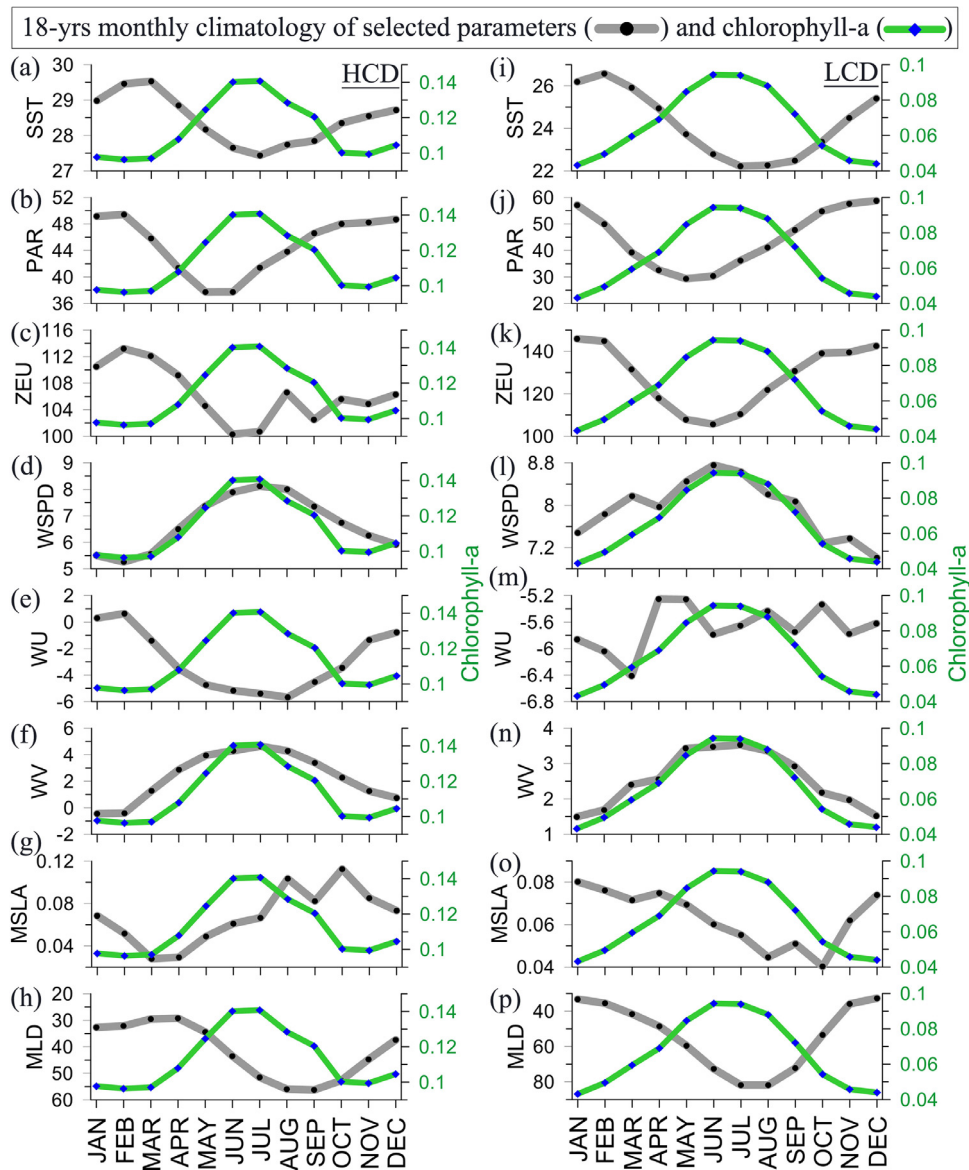


Figure 13 Monthly climatology (18 years) of chlorophyll *a* plotted against selected parameters, such as a) sea surface temperature (SST; °C), b) photosynthetically available radiation (PAR; E/m²/d), c) euphotic depth (ZEU; m), (d) wind speed (WSPD; m/s), e) zonal wind (WU; m/s), f) meridional wind (WW; m/s), g) mean sea level anomaly (MSLA; m) and h) mixed layer depth (MLD; m) of HCD and (i–p) same parameters of LCD.

thermocline, (i) due to overlaying or piling up of warmer water mass which can push down the thermocline as reported during the positive IOD events and (ii) due to erosion of thermocline by strong wind induced mixing which gradually deepens mixed layer/thermocline. During the first situation, MLD becomes deeper but no nutrients mix with the above water. During the later situation, nutrients mix with the above water column and enhance phytoplankton production. The zonal and meridional wind-induced open-ocean upwelling and mixing could have enhanced the phytoplankton biomass by entraining nutrients from the deeper waters (Levy et al., 2007; Mandal et al., 2021). Along with nutrient supply, a relatively shallow ZEU may support the phytoplankton with suitable light conditions (Giannini et al., 2021; Jyothibabu et al., 2018), which could have enhanced

the photosynthetic production. The shallow ZEU centred at 10°S could result from high absorption/scatter of the light by phytoplankton and other particulate matter, and could not be due to cloud cover (Roy et al., 2020). The high wind speed was centred at 16°S, and the major surface current flow and the high chlorophyll *a* were found north of it. This follows the hypothesis of Levy et al. (2007), that the upwelling-induced nutrient supply in the north of the south equatorial current (high chlorophyll *a*) and mixing-induced nutrient supply in the south (deep MLD and low chlorophyll *a*) (Gallienne and Smythe-Wright, 2005). The multivariate correlation analysis clearly evidences that the negative wind curl (divergence) and positive Ekman pumping velocity (indicates upwelling induced nutrient supply) in the high chlorophyll *a* domain (HCD), and significant posi-

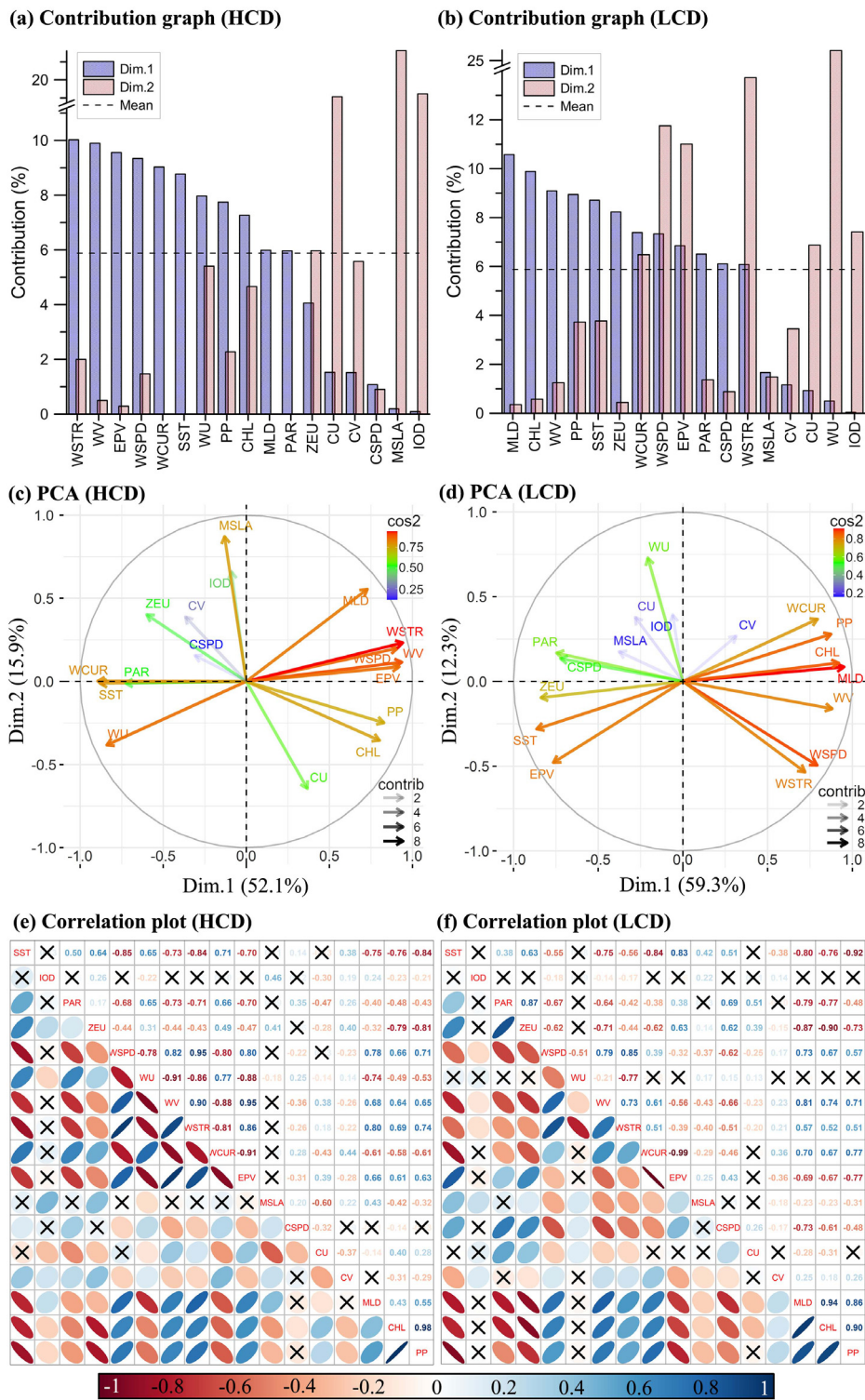


Figure 14 The results of statistical analysis present (a–b) the percentage contribution of variables to the top two dimensions, (c–d) the PCA plotted with the top two dimensions show key parameters behind the variations (colour, transparency, length and orientation of vector) and (e–f) multivariable correlation plots show the relationship among variables represented by ellipses in the lower left diagonal and correlation coefficients in the upper right diagonal. The darker shades of brown and blue indicate a highly significant relationship ($p < 0.05$) and cross marks indicate insignificant ($p > 0.05$) correlations. The plots on the left represent HCD and the right represent LCD. Abbreviations: SST: sea surface temperature, IOD: dipole mode index, PAR: photosynthetically available radiation, ZEU: euphotic depth, WSPD: wind speed, WU: zonal wind, WV: meridional wind, WSTR: wind stress, WCUR: wind curl, EPV: Ekman pumping velocity, MSLA: mean sea level anomaly, CSPD: current speed, CU: zonal currents, CV: meridional currents, MLD: mixed layer depth, CHL: chlorophyll a and PP: primary productivity.

tive relationship of MLD (deepening of MLD, eroded thermocline and nutrient injection) in the low chlorophyll *a* domain (LCD), as possible reasons for enhancement of chlorophyll *a*.

The Mascarene Plateau (Seychelles-Mauritius ridge) in the south-western Indian Ocean forms a crescent-shaped shallow shelf structure and the shadow zone (western side) of the plateau was well productive during the AW due to the upwelling caused by the divergence of the south equatorial current (Ragoonaden et al., 1987; Sarma et al., 1990). The results of the study carried out later by Gallienne and Smythe-Wright (2005) and New et al. (2005) showed that both sides (west and east) of the plateau have an almost similar trend in physicochemical characteristics with comparable biological productivity and presented noticeable meridional variations. During El-Niño years, the negative Ekman pumping generates westward propagating downwelling Rossby waves in the southern tropical Indian Ocean, which deepens the thermocline and increases the warming in the western region (George et al., 2018; Liao et al., 2020). The deep thermocline, suck nutrient deficient surface water and leads to low chlorophyll *a*. Similarly, during the La Niño years, the positive Ekman pumping generates westward propagating upwelling Rossby waves in the southern tropical Indian Ocean, which shoals the thermocline and decreases the warming in the western region. The shallow thermocline pumps nutrient-rich deep water and leads to high chlorophyll *a*. The upwelling Rossby waves may feel the bottom of the shallow Mascarene Plateau and that could be an inducer of efficient upwelling in the eastern side of the plateau (Schouten et al., 2002), where we noticed a large area of high chlorophyll *a*. The high primary production found in the entire zonal stretch was centred at 10°S. Part of the plankton food material may have been transported along with the prevailing strong west-south-westerly currents, which could be the possible reason, along with the plateau-upwelling-induced organic production for the model-reported high organic material fluxes in the western tropical Indian Ocean (Wiggert et al., 2006).

Exceptional to the isolated anti-cyclonic eddy features that meander from the western shelf of Australia, which are nutrient-rich with high chlorophyll *a* production (Gaube et al., 2013; Moore et al., 2007), the rest of the southeastern tropical Indian Ocean can be considered as ultra-Oligotrophic region due to extremely low chlorophyll *a* production (Jena et al., 2012; Visser et al., 2015). The large anti-cyclonic gyre circulation favours the downwelling by the convergence of nutrient-poor surface water (Jena et al., 2012) and the weaker winds in this region that could not support vertical mixing are probably the reason for ultra-oligotrophic conditions (stated as ‘biological desert’ by Jena et al., 2012). The seasonal features of the physical variables correlate with chlorophyll *a* and primary production in the entire study domain.

However, there was an increasing trend in chlorophyll *a* concentration (centred at 10°S) towards the west, primarily due to the slope of the thermocline, which was relatively deep in the east and shallow in the west (Murtugudde et al., 2000). Additionally, the westward increase of the area of high chlorophyll *a* is probably due to the wide Mascarene Plateau, which shoals the thermocline due to the shallow bathymetry. During the negative IOD events (colder in the western Indian Ocean and warmer in the east), the slope

of the thermocline increases further which brings up the nutrient-rich deeper water mass towards the surface of the western equatorial Indian Ocean. The negative IOD-induced upwelling significantly enhances the phytoplankton biomass over the western region of the Indian Ocean by entraining the nutrients from a shallow thermocline (Currie et al., 2013; Shi and Wang, 2021; Vinayachandran et al., 2007).

Our results showed significant negative DMI (<-0.4) in 14 out of 216 months of observation in the study area which is much less as compared with the positive IODs (26 months of positive DMI; >0.4). Even in the eastern region of the study area (86°E–90°E), the chlorophyll *a* responded negatively to the DMI but was insignificant. Overall the inter-annual anomalies in chlorophyll *a* in HCD of ESTIO can be explained well by the significant variations in the zonal temperature (IOD; correlation $p<0.01$; $df=214$) and the larger area of LCD showed no significant impact by IOD as it is restricted to the north of 15°S (Rao et al., 2002).

Though the ESTIO is considered a biologically less productive ocean, this region holds an essential role in maintaining the climate system by containing and transferring heat energy. The southwest monsoon system transports latent heat energy from the high-pressure southern tropical Indian Ocean to the low-pressure Asian continent (Clemens et al., 1991). The strong meridional trade wind flow over the present study area during the AW evidences the continuity and prominent energy supply to the southwest monsoon by which a large area of the Arabian Sea gets coastal upwelling and vertical mixing leading to noticeable biological productivity (Banse, 1959; Wiggert et al., 2005). The southwest monsoon sucks the air mass from the southern tropical Indian Ocean and indirectly induces the vertical mixing by which the thermocline layer can be eroded and nutrients pumped towards the surface ocean (Dilmahamod et al., 2016; George et al., 2018; Resplandy et al., 2009). As the shallow ZEU prevails during the AW, the wind mixing process brings nutrients from deep that support relatively high primary production in the mixed water column of the extensive open ocean system.

The results from a combination of satellite observations, ARGO float measurements and the biogeochemical model of Dufois et al. (2016) demonstrated higher chlorophyll *a* in the anticyclone eddies (warm-core) than in the cyclone eddies in the sub-tropical gyre (south Indian Ocean) during the AW. As the stratification is relatively weak in anticyclone eddies than in the cyclone eddies, the anticyclone eddy induces a deeper convective mixing during the AW, which introduces nutrients (modelled nitrate) into the thick mixed layer and possibly increases phytoplankton production. They recognised that the light limitation is not significant as compared with the nutrient limitation in the southern tropical Indian Ocean. According to the model study carried out by Resplandy et al. (2009), the wind-induced mixing during the AW and the Madden–Julian Oscillation, the surface phytoplankton production enhanced. Still, there is a compensative reduction in the sub-surface waters which was explained to be due to light limitation. Strutton et al. (2023) reported vertical (downward) redistribution of chlorophyll *a* due to anticyclone eddies in the southeast Indian Ocean.

According to the above studies, both upward as well as downward redistribution of phytoplankton along with

the water mass is apparent. The high chlorophyll *a* in the deep chlorophyll maxima was reported to be due to photo-acclimation in response to low light (Strutton et al., 2023). Monthly (Figure 13) and seasonal (Figures 8 and 9) climatology results from the present study showed a deeper euphotic depth (>75 m) throughout the year and noticeably shallow MLD (30–90 m) than the ZEU at any point of time (Figures 8 and 13). This suggests that light could not be limiting the phytoplankton production in the mixed layer and even it could support a dense deep chlorophyll *a* maxima (Estrada et al., 2016; George et al., 2013). There are lesser chances to be due to the photo-acclimated high chlorophyll *a* showed in satellite observation during the AW.

5. Conclusion

The satellite and ARGO measured and derived variables from the least studied oligotrophic ESTIO (2003–2020). They revealed a distinct seasonality of meteorological and oceanographic factors, which modulated the phytoplankton biomass. During the AW, the northern section of ESTIO (HCD) experienced positive Ekman pumping (upwelling) as a result of strong zonal (westward) and meridional (northward) wind that imposed additional stress and negative wind curl on the surface, diverging the surface water. The upward Ekman pumping and cyclonic eddy generated nutrient entrainment to the surface water column and increased chlorophyll *a* concentrations in the HCD. A deep mixed layer noticed in the southern section of the ESTIO (LCD) due to the continuous presence of warm gyre and dominance of anti-cyclonic features, along with the deep euphotic depth, resulted in lower chlorophyll *a* biomass at the surface water column. The high wind speed (during AW) was centred at 16°S, and the major surface current flow, as well as the high chlorophyll *a*, were found north of it, supporting Levy et al. (2007)'s hypothesis that upwelling-induced nutrient supply in the north of the south equatorial current (high chlorophyll *a*) and mixing induced nutrient supply in the south (deep MLD and low chlorophyll *a*). Inter-annual changes in chlorophyll *a*, generated by the Indian Ocean Dipole mode, have a greater influence on the HCD and a lower impact on the LCD. Pearson's multivariable correlation analysis and principal component analysis statistically validated the significance of chosen factors on chlorophyll *a* enhancement in the ESTIO. Additional work is needed to estimate the Ekman pumping efficiency of nutrients from below the thermocline to the MLD of the study area. To validate the seasonal shift in the vertical distribution of chlorophyll *a* and comprehend the food web structure, detailed in situ measurements/quantifications of plankton components over those domains (HCD and LCD) are required.

Declaration of competing interest

We wish to confirm that there are no known conflicts of interest associated with this publication and there has been no significant financial support for this work that could have influenced its outcome.

CRedit authorship contribution statement

Chinnadurai Karnan: Conceptualization, Methodology, Investigation, Visualization, Writing – original draft, Writing – review & editing. **Sreedharan Gautham:** Methodology, Visualization, Writing – review & editing.

Availability of data and materials

The data sets used in this study are available in online databases as mentioned in the methods section.

Acknowledgements

The authors thank the Director (Prof. Sunil Kumar Singh) of CSIR – National Institute of Oceanography, India for his thoughtful discussion, inspiration, and facility provided. We are thankful to three anonymous reviewers for their constructive comments to improve the quality of this article. We thank Dr. Sandhya and Dr. Subhashree of CSIR-NIO for their assistance in language/grammatical corrections. This research was funded by CSIR-NIO (OLP2005/MLP2018) and the contribution number is 7142.

References

- Agawin, N.S.R., Duarte, C.M., Agusti, S., 2000. Nutrient and temperature control of the contribution of picoplankton to phytoplankton biomass and production. *Limnol. Oceanogr.* 45, 591–600.
- Banse, K., 1959. On upwelling and bottom-trawling off the south-west coast of India. *J. Mar. Biol. Assoc. India* 1, 33–49.
- Banse, K., 1968. Hydrography of the Arabian Sea Shelf of India and Pakistan and effects on demersal fishes. *Deep Sea Res.* 15, 45–79. [https://doi.org/10.1016/0011-7471\(68\)90028-4](https://doi.org/10.1016/0011-7471(68)90028-4)
- Banse, K., 1987. Seasonality of phytoplankton chlorophyll in the central and northern Arabian Sea. *Deep Sea Res.* 34, 713–723. [https://doi.org/10.1016/0198-0149\(87\)90032-X](https://doi.org/10.1016/0198-0149(87)90032-X)
- Bhattathiri, P.M.A., Pant, A., Sawant, S.S., Gauns, M., Matondkar, S.G.P., Mahanraju, R., 1996. Phytoplankton production and chlorophyll distribution in the eastern and central Arabian Sea in 1994–1995. *Curr. Sci.* 71, 857–862.
- Brewin, R.J.W., Hirata, T., Hardman-Mountford, N.J., Laverder, S.J., Sathyendranath, S., Barlow, R., 2012. The influence of the Indian Ocean Dipole on interannual variations in phytoplankton size structure as revealed by Earth Observation. *Deep Sea Res. Pt. II Top. Stud. Oceanogr.* 77, 117–127. <https://doi.org/10.1016/j.dsr2.2012.04.009>
- Chinnadurai, K., Retnamma, J., Nagarathinam, A., Subramanian, P.R., Singaram, P., Shoba, S., 2021. Microplankton size structure induced by a warm-core eddy in the western Bay of Bengal: Role of *Trichodesmium* abundance. *Oceanologia* 63 (3), 283–300. <https://doi.org/10.1016/j.oceano.2021.02.003>
- Clemens, S., Prell, W., Murray, D., Shimmield, G., Weedon, G., 1991. Forcing mechanisms of the Indian Ocean monsoon. *Nature* 353, 720–725. <https://doi.org/10.1038/353720a0>
- Currie, J.C., Lengaigne, M., Vialard, J., Kaplan, D.M., Aumont, O., Naqvi, S.W.A., Maury, O., 2013. Indian Ocean Dipole and El Niño/southern oscillation impact on regional chlorophyll anomalies in the Indian Ocean. *Biogeosciences* 10, 6677–6698. <https://doi.org/10.5194/bg-10-6677-2013>

- Desai, B.N., 1965. A brief review of the existing theories of the southwest monsoon and of the proceedings of the symposium on meteorological results of IIOE, 22nd–26th July 1965, Bombay. *Curr. Sci.* 34, 657–659.
- Dickman, E.M., Vanni, M.J., Horgan, M.J., 2006. Interactive effects of light and nutrients on phytoplankton stoichiometry. *Oecologia* 149, 676–689. <https://doi.org/10.1007/s00442-006-0473-5>
- Dilmahamad, A.F., Hermes, J.C., Reason, C.J.C., 2016. Chlorophyll-*a* variability in the Seychelles-Chagos Thermocline Ridge: Analysis of a coupled biophysical model. *J. Marine Syst.* 154, 220–232. <https://doi.org/10.1016/j.jmarsys.2015.10.011>
- Dufois, F., Hardman-Mountford, N.J., Greenwood, J., Richardson, A.J., Feng, M., Herbert, S., Matear, R., 2014. Impact of eddies on surface chlorophyll in the South Indian Ocean. *J. Geophys. Res. Oceans* 119, 8061–8077. <https://doi.org/10.1002/2014JC010164>
- Dufois, F., Hardman-Mountford, N.J., Greenwood, J., Richardson, A.J., Feng, M., Matear, R.J., 2016. Anticyclonic eddies are more productive than cyclonic eddies in subtropical gyres because of winter mixing. *Sci. Adv.* 2, e1600282. <https://doi.org/10.1126/sciadv.1600282>
- Estrada, M., Delgado, M., Blasco, D., Latasa, M., Cabello, A.M., Benitez-Barrios, V., Fraile-Nuez, E., Mozetic, P., Vidal, M., 2016. Phytoplankton across tropical and subtropical regions of the Atlantic, Indian and Pacific oceans. *PLoS One* 11, e0151699. <https://doi.org/10.1371/journal.pone.0151699>
- Fan, S., Moxim, W.J., Levy, H., 2006. Aeolian input of bioavailable iron to the ocean. *Geophys. Res. Lett.* 33. <https://doi.org/10.1029/2005GL024852>
- Feng, M., Majewski, L.J., Fandry, C.B., Waite, A.M., 2007. Characteristics of two counter-rotating eddies in the Leeuwin Current system off the Western Australian coast. *Deep Sea Res. Pt II Top. Stud. Oceanogr., The Leeuwin Current and its Eddies* 54, 961–980. <https://doi.org/10.1016/j.dsr2.2006.11.022>
- Gallienne, C.P., Smythe-Wright, D., 2005. Epipelagic mesozooplankton dynamics around the Mascarene plateau and basin, south-western Indian Ocean. *Philos. Trans. R. Soc. Math. Phys. Eng. Sci.* 363, 191–202. <https://doi.org/10.1098/rsta.2004.1487>
- Gao, Y., Wang, H., 2012. Pan-Asian monsoon and its definition, principal modes of precipitation, and variability features. *Sci. China Earth Sci.* 55, 787–795. <https://doi.org/10.1007/s11430-012-4382-7>
- Gaube, P., Chelton, D.B., Strutton, P.G., Behrenfeld, M.J., 2013. Satellite observations of chlorophyll, phytoplankton biomass, and Ekman pumping in nonlinear mesoscale eddies. *J. Geophys. Res. Oceans* 118, 6349–6370.
- Gaube, P., McGillicuddy Jr., D.J., Chelton, D.B., Behrenfeld, M.J., Strutton, P.G., 2014. Regional variations in the influence of mesoscale eddies on near-surface chlorophyll. *J. Geophys. Res. Oceans* 119, 8195–8220. <https://doi.org/10.1002/2014JC010111>
- George, J.V., Nuncio, M., Chacko, R., Anilkumar, N., Noronha, S.B., Patil, S.M., Pavithran, S., Alappattu, D.P., Krishnan, K.P., Achuthankutty, C.T., 2013. Role of physical processes in chlorophyll distribution in the western tropical Indian Ocean. *J. Marine Syst.* 113, 1–12.
- George, J.V., Nuncio, M., Anilkumar, N., Chacko, R., Rajashekhar, D., 2018. Seasonal surface chlorophyll *a* variability in the Seychelles-Chagos Thermocline Ridge. *Curr. Sci.* 114, 868. <https://doi.org/10.18520/cs/v114/i04/868-878>
- Giannini, F., Mendes, C.R.B., Garcia, C.A.E., Carvalho, A.C.O., Ciotti, A.M., 2021. Phytoplankton community and the fluorescence-derived photo-physiological parameters in the South Atlantic Ocean. *J. Marine Syst.* 218, 103538. <https://doi.org/10.1016/j.jmarsys.2021.103538>
- Gopika, S., Izumo, T., Vialard, J., Lengaigne, M., Suresh, I., Kumar, M.R.R., 2020. Aliasing of the Indian Ocean externally forced warming spatial pattern by internal climate variability. *Clim. Dynam.* 54, 1093–1111. <https://doi.org/10.1007/s00382-019-05049-9>
- Gordon, A.L., 1985. Indian-Atlantic transfer of thermocline water at the Agulhas retroflexion. *Science* 227, 1030–1033. <https://doi.org/10.1126/science.227.4690.1030>
- Harms, N.C., Lahajnar, N., Gaye, B., Rixen, T., Dahnke, K., Ankele, M., Schwarz-Schampera, U., Emeis, K.-C., 2019. Nutrient distribution and nitrogen and oxygen isotopic composition of nitrate in water masses of the subtropical southern Indian Ocean. *Biogeosciences* 16, 2715–2732. <https://doi.org/10.5194/bg-16-2715-2019>
- Hermes, J.C., Reason, C.J.C., 2008. Annual cycle of the South Indian Ocean (Seychelles-Chagos) thermocline ridge in a regional ocean model. *J. Geophys. Res. Oceans* 113. <https://doi.org/10.1029/2007JC004363>
- Hermes, J.C., Reason, C.J.C., 2009. The sensitivity of the Seychelles-Chagos thermocline ridge to large-scale wind anomalies. *ICES J. Mar. Sci.* 66, 1455–1466. <https://doi.org/10.1093/icesjms/fsp074>
- Hood, R.R., Wiggert, J.D., Naqvi, S.W.A., 2009. Indian Ocean research: Opportunities and challenges. *Geophys. Monogr. Ser.* 185, 409–428. <https://doi.org/10.1029/2008GM000714>
- Hosoda, S., Ohira, T., Sato, K., Suga, T., 2010. Improved description of global mixed-layer depth using Argo profiling floats. *J. Oceanogr.* 66, 773–787. <https://doi.org/10.1007/s10872-010-0063-3>
- Hu, C., Lee, Z., Franz, B., 2012. Chlorophyll *a* algorithms for oligotrophic oceans: A novel approach based on three-band reflectance difference. *J. Geophys. Res. Oceans* 117. <https://doi.org/10.1029/2011JC007395>
- Hu, C., Feng, L., Lee, Z., Franz, B.A., Bailey, S.W., Werdell, P.J., Proctor, C.W., 2019. Improving Satellite Global Chlorophyll *a* Data Products Through Algorithm Refinement and Data Recovery. *J. Geophys. Res. Oceans* 124, 1524–1543. <https://doi.org/10.1029/2019JC014941>
- Huang, J., Zhuang, W., Yan, X.-H., Wu, Z., 2020. Impacts of the upper-ocean salinity variations on the decadal sea level change in the southeast Indian Ocean during the Argo era. *Acta Oceanol. Sin.* 39, 1–10. <https://doi.org/10.1007/s13131-020-1574-4>
- Huot, Y., Antoine, D., Daudon, C., 2019. Partitioning the Indian Ocean based on surface fields of physical and biological properties. *Deep Sea Res. Pt. II* 166, 75–89. <https://doi.org/10.1016/j.dsr2.2019.04.002>
- Iskandar, I., Rao, S.A., Tozuka, T., 2009. Chlorophyll-*a* bloom along the southern coasts of Java and Sumatra during 2006. *Int. J. Remote Sens.* 30, 663–671. <https://doi.org/10.1080/01431160802372309>
- Jena, B., Swain, D., Avinash, K., 2012. Investigation of the biophysical processes over the oligotrophic waters of South Indian Ocean subtropical gyre, triggered by cyclone Edzani. *Int. J. Appl. Earth Obs. Geoinformation* 18, 49–56. <https://doi.org/10.1016/j.jag.2012.01.006>
- Jena, B., Sahu, S., Avinash, K., Swain, D., 2013. Observation of oligotrophic gyre variability in the south Indian Ocean: Environmental forcing and biological response. *Deep Sea Res.* 80, 1–10. <https://doi.org/10.1016/j.dsr.2013.06.002>
- Jyothibabu, R., Arunpandi, N., Jagadeesan, L., Karnan, C., Lallu, K.R., Vinayachandran, P.N., 2018. Response of phytoplankton to heavy cloud cover and turbidity in the northern Bay of Bengal. *Sci. Rep.* 8, 1–15. <https://doi.org/10.1038/s41598-018-29586-1>
- Jyothibabu, R., Karnan, C., Arunpandi, N., Santhi Krishnan, S., Balachandran, K.K., Sahu, K.C., 2021. Significantly dominant warm-core eddies: An ecological indicator of the basin-scale low biological production in the Bay of Bengal. *Ecol. Indic.* 121, 107016. <https://doi.org/10.1016/j.ecolind.2020.107016>
- Kahru, M., Gille, S.T., Murtugudde, R., Strutton, P.G., Manzano-Sarabia, M., Wang, H., Mitchell, B.G., 2010. Global correlations

- between winds and ocean chlorophyll. *J. Geophys. Res. Oceans* 115. <https://doi.org/10.1029/2010JC006500>
- Kawamiya, M., Oschlies, A., 2001. Formation of a basin-scale surface chlorophyll pattern by Rossby waves. *Geophys. Res. Lett.* 28, 4139–4142. <https://doi.org/10.1029/2001GL013347>
- Krey, J., Babenerd, B., 1976. *Phytoplankton production: atlas of the international Indian Ocean expedition*. UNESCO, Intergovernmental Oceanographic Commission, Paris.
- Large, W.G., Pond, S., 1981. Open Ocean Momentum Flux Measurements in Moderate to Strong Winds. *J. Phys. Oceanogr.* 11, 324–336. [https://doi.org/10.1175/1520-0485\(1981\)011<0324:OOMFM>2.0.CO;2](https://doi.org/10.1175/1520-0485(1981)011<0324:OOMFM>2.0.CO;2)
- Lee, S.K., Park, W., Baringer, M.O., Gordon, A.L., Huber, B., Liu, Y., 2015. Pacific origin of the abrupt increase in Indian Ocean heat content during the warming hiatus. *Nat. Geosci.* 8, 445–449. <https://doi.org/10.1038/ngeo2438>
- Levy, M., Shankar, D., Andre, J.M., Shenoi, S.S.C., Durand, F., de Boyer Montegut, C., 2007. Basin-wide seasonal evolution of the Indian Ocean's phytoplankton blooms. *J. Geophys. Res. Oceans* 112.
- Li, H., Xu, F., Zhou, W., Wang, D., Wright, J.S., Liu, Z., Lin, Y., 2017. Development of a global gridded Argo data set with Barnes successive corrections. *J. Geophys. Res. Oceans* 122, 866–889. <https://doi.org/10.1002/2016JC012285>
- Liao, X., Du, Y., Zhan, H., Shi, P., Wang, J., 2014. Summertime phytoplankton blooms and surface cooling in the western south equatorial Indian Ocean. *J. Geophys. Res. Oceans* 119, 7687–7704. <https://doi.org/10.1002/2014JC010195>
- Liao, X., Du, Y., Zhan, H., Wang, T., Feng, M., 2017. Winter-time phytoplankton blooms in the western equatorial Indian Ocean associated with the Madden-Julian Oscillation. *J. Geophys. Res. Oceans* 122, 9855–9869. <https://doi.org/10.1002/2017JC013203>
- Liao, X., Du, Y., Wang, T., He, Q., Zhan, H., Hu, S., Wu, G., 2020. Extreme phytoplankton blooms in the southern tropical Indian Ocean in 2011. *J. Geophys. Res. Oceans* 125, e2019JC015649.
- Ma, J., Du, Y., Zhan, H., Liu, H., Wang, J., 2014. Influence of oceanic Rossby waves on phytoplankton production in the southern tropical Indian Ocean. *J. Marine Syst.* 134, 12–19. <https://doi.org/10.1016/j.jmarsys.2014.02.003>
- Madhupratap, M., Kumar, S.P., Bhattachiri, P.M.A., Kumar, M.D., Raghukumar, S., Nair, K.K.C., Ramaiah, N., 1996. Mechanism of the biological response to winter cooling in the northeastern Arabian Sea. *Nature* 384, 549–552.
- Mandal, S., Behera, N., Gangopadhyay, A., Susanto, R.D., Pandey, P.C., 2021. Evidence of a chlorophyll “tongue” in the Malacca Strait from satellite observations. *J. Marine Syst.* 223, 103610. <https://doi.org/10.1016/j.jmarsys.2021.103610>
- Maranon, E., Holligan, P.M., 1999. Photosynthetic parameters of phytoplankton from 50 N to 50 S in the Atlantic Ocean. *Mar. Ecol. Prog. Ser.* 176, 191–203. <https://www.jstor.org/stable/24831883>
- McCreary, J.P., Kundu, P.K., Molinari, R.L., 1993. A numerical investigation of dynamics, thermodynamics and mixed-layer processes in the Indian Ocean. *Prog. Oceanogr.* 31, 181–244.
- McCreary Jr, J.P., Murtugudde, R., Vialard, J., Vinayachandran, P.N., Wiggert, J.D., Hood, R.R., Shankar, D., Shetye, S., 2009. Biophysical processes in the Indian Ocean. *Indian Ocean Biogeochem. Process. Ecol. Var.* 185, 9–32. <https://doi.org/10.1029/2008GM000768>
- Michel, D., Sticklor, R., 2012. *Indian Ocean rising: maritime security and policy challenges*. Stimson, Washington.
- Moore, T.S., Matear, R.J., Marra, J., Clementson, L., 2007. Phytoplankton variability off the Western Australian Coast: Mesoscale eddies and their role in cross-shelf exchange. *Deep Sea Res. Pt. II* 54, 943–960. <https://doi.org/10.1016/j.dsr2.2007.02.006>
- Morel, A., Huot, Y., Gentili, B., Werdell, P.J., Hooker, S.B., Franz, B.A., 2007. Examining the consistency of products derived from various ocean color sensors in the open ocean (Case 1) waters from the perspective of a multi-sensor approach. *Remote Sens. Environ.* 111, 69–88. <https://doi.org/10.1016/j.rse.2007.03.012>
- Morel, A., Claustre, H., Gentili, B., 2010. The most oligotrophic subtropical zones of the global ocean: similarities and differences in terms of chlorophyll and yellow substance. *Biogeosciences* 7, 3139–3151. <https://doi.org/10.5194/bg-7-3139-2010>
- Morrison, J.M., Codispoti, L.A., Gaurin, S., Jones, B., Manghiani, V., Zheng, Z., 1998. Seasonal variation of hydrographic and nutrient fields during the US JGOFS Arabian Sea Process Study. *Deep Sea Res. Part II* 45, 2053–2101. [https://doi.org/10.1016/S0967-0645\(98\)00063-0](https://doi.org/10.1016/S0967-0645(98)00063-0)
- Murtugudde, R., McCreary Jr, J.P., Busalacchi, A.J., 2000. Oceanic processes associated with anomalous events in the Indian Ocean with relevance to 1997-1998. *J. Geophys. Res. Oceans* 105, 3295–3306. <https://doi.org/10.1029/1999JC900294>
- Nagura, M., McPhaden, M.J., 2018. The Shallow Overturning Circulation in the Indian Ocean. *J. Phys. Oceanogr.* 48, 413–434. <https://doi.org/10.1175/JPO-D-17-0127.1>
- Naik, R.K., George, J.V., Soares, M.A., Devi, A., Anilkumar, N., Roy, R., Bhaskar, P.V., Murukesh, N., Achuthankutty, C.T., 2015. Phytoplankton community structure at the juncture of the Agulhas Return Front and Subtropical Front in the Indian Ocean sector of Southern Ocean: Bottom-up and top-down control. *Deep Sea Res. Pt. II* 118, 233–239. <https://doi.org/10.1016/j.dsr2.2015.01.002>
- Naqvi, S.W.A., Moffett, J.W., Gauns, M.U., Narvekar, P.V., Pratihary, A.K., Naik, H., Shenoy, D.M., Jayakumar, D.A., Goepfert, T.J., Patra, P.K., 2010. The Arabian Sea as a high-nutrient, low-chlorophyll region during the late Southwest Monsoon. *Biogeosciences* 7, 2091–2100. <https://doi.org/10.5194/bg-7-2091-2010>
- New, A.L., Stansfield, K., Smythe-Wright, D., Smeed, D.A., Evans, A.J., Alderson, S.G., 2005. Physical and biochemical aspects of the flow across the Mascarene Plateau in the Indian Ocean. *Philos. Trans. R. Soc. Math. Phys. Eng. Sci.* 363, 151–168. <https://doi.org/10.1098/rsta.2004.1484>
- O'Reilly, J.E., Werdell, P.J., 2019. Chlorophyll algorithms for ocean color sensors – OC4, OC5 & OC6. *Remote Sens. Environ.* 229, 32–47. <https://doi.org/10.1016/j.rse.2019.04.021>
- Qasim, S.Z., 1982. Oceanography of the northern Arabian Sea. *Deep Sea Res. Part Oceanogr. Res. Pap.* 29, 1041–1068.
- Ragoonaden, S., Babu, V.R., Sastry, J.S., 1987. Physico-chemical characteristics and circulation of waters in the Mauritius-Seychelles Ridge zone, Southwest Indian Ocean. *Indian J. Geo-Mar. Sci.* 16, 184–191.
- Rao, S.A., Behera, S.K., Masumoto, Y., Yamagata, T., 2002. Inter-annual subsurface variability in the tropical Indian Ocean with a special emphasis on the Indian Ocean Dipole. *Deep Sea Res. Pt. II Top. Stud. Oceanogr., World Ocean Circulation Experiment* 49, 1549–1572. [https://doi.org/10.1016/S0967-0645\(01\)00158-8](https://doi.org/10.1016/S0967-0645(01)00158-8)
- Resplandy, L., Vialard, J., Levy, M., Aumont, O., Dandonneau, Y., 2009. Seasonal and intraseasonal biogeochemical variability in the thermocline ridge of the southern tropical Indian Ocean. *J. Geophys. Res. Oceans* 114.
- Roy, K., Mukhopadhyay, P., Krishna, R.P.M., Ganai, M., Mahakur, M., Rao, T.N., Nair, A.K.M., Ramakrishna, S., 2020. Assessment of climate models in relation to the low-level clouds over the southern Indian Ocean. *Q. J. R. Meteorol. Soc.* 146, 3306–3325. <https://doi.org/10.1002/qj.3847>
- Saji, N.H., Goswami, B.N., Vinayachandran, P.N., Yamagata, T., 1999. A dipole mode in the tropical Indian Ocean. *Nature* 401, 360–363. <https://doi.org/10.1038/43854>
- Sarma, Y.V.B., Krishna, V.V., Rao, D.P., Sastry, J.S., 1990. Thermohaline circulation and water characteristics around Mauritius group of islands. *Indian J. Geo-Mar. Sci.* 19, 196–200.

- Schott, F.A., McCreary Jr, J.P., 2001. The monsoon circulation of the Indian Ocean. *Prog. Oceanogr.* 51, 1–123. [https://doi.org/10.1016/S0079-6611\(01\)00083-0](https://doi.org/10.1016/S0079-6611(01)00083-0)
- Schott, F.A., Xie, S.P., McCreary Jr, J.P., 2009. Indian Ocean circulation and climate variability. *Rev. Geophys.* 47, RG1002. <https://doi.org/10.1029/2007RG000245>
- Schouten, M.W., de Ruijter, W.P.M., van Leeuwen, P.J., Dijkstra, H.A., 2002. An oceanic teleconnection between the equatorial and southern Indian Ocean. *Geophys. Res. Lett.* 29, 59–1–5–94. <https://doi.org/10.1029/2001GL014542>
- Shankar, D., Vinayachandran, P.N., Unnikrishnan, A.S., 2002. The monsoon currents in the north Indian Ocean. *Prog. Oceanogr.* 52, 63–120.
- Shenoi, S.S.C., Shankar, D., Shetye, S.R., 1999. On the sea surface temperature high in the Lakshadweep Sea before the onset of the southwest monsoon. *J. Geophys. Res. Oceans* 104, 15703–15712.
- Shi, W., Wang, M., 2021. A biological Indian Ocean Dipole event in 2019. *Sci. Rep.* 11, 2452. <https://doi.org/10.1038/s41598-021-81410-5>
- Siswanto, E., Horii, T., Iskandar, I., Gaol, J.L., Setiawan, R.Y., Susanto, R.D., 2020. Impacts of climate changes on the phytoplankton biomass of the Indonesian Maritime Continent. *J. Marine Syst.* 212, 103451. <https://doi.org/10.1016/j.jmarsys.2020.103451>
- Smith, S.L., Codispoti, L.A., Morrison, J.M., Barber, R.T., 1998. The 1994–1996 Arabian Sea Expedition: An integrated, interdisciplinary investigation of the response of the northwestern Indian Ocean to monsoonal forcing. *Deep-Sea Res. Pt. II* 45, 1905–1915. [https://doi.org/10.1016/S0967-0645\(98\)00058-7](https://doi.org/10.1016/S0967-0645(98)00058-7)
- Song, Q., Gordon, A.L., Visbeck, M., 2004. Spreading of the Indonesian throughflow in the Indian Ocean. *J. Phys. Oceanogr.* 34, 772–792. [https://doi.org/10.1175/1520-0485\(2004\)034<0772:SOTIT1>2.0.CO;2](https://doi.org/10.1175/1520-0485(2004)034<0772:SOTIT1>2.0.CO;2)
- Stramma, L., Lutjeharms, J.R.E., 1997. The flow field of the subtropical gyre of the South Indian Ocean. *J. Geophys. Res. Oceans* 102, 5513–5530.
- Strutton, P.G., Coles, V.J., Hood, R.R., Matear, R.J., McPhaden, M.J., Phillips, H.E., 2015. Biogeochemical variability in the central equatorial Indian Ocean during the monsoon transition. *Biogeosciences* 12, 2367–2382. <https://doi.org/10.5194/bg-12-2367-2015>
- Strutton, P.G., Trull, T.W., Phillips, H.E., Duran, E.R., Pump, S., 2023. Biogeochemical Argo Floats Reveal the Evolution of Subsurface Chlorophyll and Particulate Organic Carbon in Southeast Indian Ocean Eddies. *J. Geophys. Res. Oceans* 128, e2022JC018984. <https://doi.org/10.1029/2022JC018984>
- Thompson, P.A., Pesant, S., Waite, A.M., 2007. Contrasting the vertical differences in the phytoplankton biology of a dipole pair of eddies in the south-eastern Indian Ocean. *Deep Sea Res. Pt. II* 54, 1003–1028.
- Tomczak, M., Godfrey, J.S., 2003. *Regional oceanography: an introduction*. Daya Books, Delhi.
- Trenary, L.L., Han, W., 2008. Causes of decadal subsurface cooling in the tropical Indian Ocean during 1961–2000. *Geophys. Res. Lett.* 35. <https://doi.org/10.1029/2008GL034687>
- Twining, B.S., Rauschenberg, S., Baer, S.E., Lomas, M.W., Martiny, A.C., Antipova, O., 2019. A nutrient limitation mosaic in the eastern tropical Indian Ocean. *Deep Sea Res. Pt. II* 166, 125–140. <https://doi.org/10.1016/j.dsr2.2019.05.001>
- van Ballegooyen, R.C., Grundlingh, M.L., Lutjeharms, J.R.E., 1994. Eddy fluxes of heat and salt from the southwest Indian Ocean into the southeast Atlantic Ocean: A case study. *J. Geophys. Res. Oceans* 99, 14053–14070. <https://doi.org/10.1029/94JC00383>
- Vinayachandran, P.N., Kurian, J., Neema, C.P., 2007. Indian Ocean response to anomalous conditions in 2006. *Geophys. Res. Lett.* 34. <https://doi.org/10.1029/2007GL030194>
- Visser, A.W., Nielsen, T.G., Middelboe, M., Hoyer, J.L., Markager, S., 2015. Oceanography and the base of the pelagic food web in the southern Indian Ocean. *J. Plankton Res.* 37, 571–583. <https://doi.org/10.1093/plankt/fbv019>
- Waite, A.M., Pesant, S., Griffin, D.A., Thompson, P.A., Holl, C.M., 2007. Oceanography, primary production and dissolved inorganic nitrogen uptake in two Leeuwin Current eddies. *Deep Sea Res. Pt. II Top. Stud. Oceanogr., The Leeuwin Current and its Eddies* 54, 981–1002. <https://doi.org/10.1016/j.dsr2.2007.03.001>
- Wiggert, J.D., Hood, R.R., Banse, K., Kindle, J.C., 2005. Monsoon-driven biogeochemical processes in the Arabian Sea. *Prog. Oceanogr.* 65, 176–213. <https://doi.org/10.1016/j.pocean.2005.03.008>
- Wiggert, J.D., Murtugudde, R.G., Christian, J.R., 2006. Annual ecosystem variability in the tropical Indian Ocean: Results of a coupled bio-physical ocean general circulation model. *Deep Sea Res. Pt. II* 53, 644–676. <https://doi.org/10.1016/j.dsr2.2006.01.027>
- Wiggert, J., Vialard, J., Behrenfeld, M., 2009. Basin-Wide Modification of Dynamical and Biogeochemical Processes by the Positive Phase of the Indian Ocean Dipole During the SeaWiFS Era. *Am. Geophys. Union Geophys. Monogr. Ser.*, Washington DC 185, 385–407. <https://doi.org/10.1029/2008GM000776>
- Wishner, K.F., Gowing, M.M., Gelfman, C., 1998. Mesozooplankton biomass in the upper 1000 m in the Arabian Sea: overall seasonal and geographic patterns, and relationship to oxygen gradients. *Deep Sea Res. Pt. II* 45, 2405–2432. [https://doi.org/10.1016/S0967-0645\(98\)00078-2](https://doi.org/10.1016/S0967-0645(98)00078-2)
- Woodberry, K.E., Luther, M.E., O'Brien, J.J., 1989. The wind-driven seasonal circulation in the southern tropical Indian Ocean. *J. Geophys. Res. Oceans* 94, 17985–18002. <https://doi.org/10.1029/JC094iC12p17985>
- Wyrtki, K., 1973. An equatorial jet in the Indian Ocean. *Science* 181, 262–264. <https://doi.org/10.1126/science.181.4096.262>

Available online at www.sciencedirect.com

ScienceDirect

journal homepage: www.journals.elsevier.com/oceanologia

ORIGINAL RESEARCH ARTICLE

Low abundance and high patchiness of decapod fauna sampled with van Veen grab on the West African continental margin (Gulf of Guinea, Ghana)

Krzysztof Podwysocki^{a,*}, Krzysztof Pabis^a, Ferran Palero^b,
Magdalena Błażewicz^a, Bjørn Serigstad^c

^a Faculty of Biology and Environmental Protection, University of Lodz, Łódź, Poland

^b Cavanilles Institute of Biodiversity and Evolutionary Biology, Valencia, Paterna, Spain

^c Institute of Marine Research, Bergen, Norway

Received 15 December 2022; accepted 16 November 2023

Available online 4 December 2023

KEYWORDS

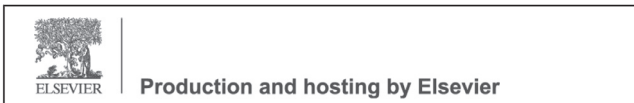
Benthos;
Deep sea;
Depth gradient;
Distribution patterns;
Diversity

Abstract Sixty morphospecies of Decapoda (Malacostraca: Crustacea) representing 34 families were recorded in the material collected in 2012 from 265 van Veen grab (0.1 m²) samples, from the nine transects distributed along the coast of Ghana in the 25–1000 m depth range. The examined material was dominated by the Diogenidae, Panopeidae, Leucosiidae, Pilumnidae and Xanthidae families. Species accumulation curves showed undersampling of the studied area and a large number of the morphospecies comprised singletons and doubletons. *Panopeus africanus* was the most frequent morphospecies in the analysed material (9.1% of all samples). We observed a substantial decrease of diversity (Shannon Index) and abundance along a depth gradient. Species richness also decreased with depth, starting from the highest number of morphospecies – 38 at 25 m depth, then 33 at 50 m, 17 at 100 m, 11 at 250 m, 8 at 500 m and ending with 1 morphospecies at 1000 m bottom depth. Higher diversity was observed on the continental shelf (25–250 m – 57 morphospecies), while on the slope (500–1000 m) only eight morphospecies were recorded. Numerous factors of natural and anthropogenic origin may

* Corresponding author at: Department of Invertebrate Zoology and Hydrobiology, Faculty of Biology and Environmental Protection, University of Łódź, Łódź, Poland.

E-mail address: krzysztof.podwysocki@biol.uni.lodz.pl (K. Podwysocki).

Peer review under the responsibility of the Institute of Oceanology of the Polish Academy of Sciences.



<https://doi.org/10.1016/j.oceano.2023.11.003>

0078-3234/© 2023 Institute of Oceanology of the Polish Academy of Sciences. Production and hosting by Elsevier B.V. This is an open access article under the CC BY-NC-ND license (<http://creativecommons.org/licenses/by-nc-nd/4.0/>).

affect decapod communities on the coast of Ghana. Since our material was collected using a sampler collecting material at a very small scale, the observed patterns might be affected by the sampling method.

© 2023 Institute of Oceanology of the Polish Academy of Sciences. Production and hosting by Elsevier B.V. This is an open access article under the CC BY-NC-ND license (<http://creativecommons.org/licenses/by-nc-nd/4.0/>).

1. Introduction

Decapods belong to the most important macro and mega epibenthic marine invertebrates (Boudreau and Worm, 2012; Wolfe et al., 2019). They are a significant element of marine trophic webs and represent a wide range of feeding modes, including predators, detritivores and scavengers (Boudreau and Worm, 2012). Moreover, decapods are characterized by high species richness (Appeltans et al., 2012; Ateş et al., 2006; Coelho et al., 2008; Muñoz et al., 2012; Rosa et al., 2012), represent high functional and morphological diversity (Boudreau and Worm, 2012; Carvalho et al., 2017; Sahlmann et al., 2011) and are a significant component of benthic biomass (Cartes and Sardà, 1992; Thurston et al., 1994). These crustaceans are also associated with a great variety of microhabitats and can be found from the intertidal zone, down to the hadal depths (Cartes et al., 2014; Fanelli et al., 2007; Jamieson et al., 2009; Pajuelo et al., 2015; Rosa et al., 2012). All those features make them important for the functioning of marine ecosystems, including processes such as the decomposition of organic matter, nutrient cycling and benthic-pelagic coupling (Agnetta et al., 2019; Boudreau and Worm, 2012).

Studies analysing depth-related changes in the abundance and diversity of decapod crustaceans demonstrated substantial differences between the investigated regions (Company et al., 2004 and references therein). Some analyses from the Mediterranean Sea showed an increase in biodiversity from shelf to bathyal (Fanelli et al., 2007), and a similar pattern was observed in the waters of Guinea-Bissau (Muñoz et al., 2012). In the central-eastern Atlantic, the highest diversity was recorded on a lower shelf and upper slope, and the lowest diversity on a lower slope (Pajuelo et al., 2015). Those discrepancies emphasize the importance of local conditions on the distribution of decapods along a depth gradient, and the need for further studies since similar questions occur also in the analysis of more general distribution patterns of the benthic macrofauna. For example, one of the common assumptions in marine biology states that the diversity of the benthos increases along a depth gradient, reaching its maximum at the bathyal zone (Levin and Dayton, 2009; Rex and Etter, 2010). Therefore, the continental slope is often considered to be the major diversity hotspot of benthic marine diversity (Danovaro et al., 2009). This opinion is rationalized by high habitat heterogeneity resulting from geomorphological variability (e.g. steep bottoms, presence of canyons) and high dynamics of environmental conditions, e.g. differences in sediment structure, changes of the hydrostatic pressure and decrease in food availability (Levin and Dayton, 2009). Nevertheless, it was already suggested by Gray (2001) and fur-

ther supported in later studies by Levin and Sibuet (2012), that this pattern is not universal. Results may differ depending on the taxonomic groups studied or between regions, for example in areas characterized by the presence of oxygen minimum zone or as a result of differences in food availability between shelf and slope (Brandt et al., 2009; Levin, 2003; McCallum et al., 2015).

One such area is the Gulf of Guinea. It is a large marine ecosystem (LME) characterized by the presence of natural oxygen minimum zones between 200 and 500 m, the high dynamic of water masses, and differences in productivity (Djagoua et al., 2011; Guiavarc'h et al., 2009; Levin, 2003). At the same time, knowledge about the diversity and distribution patterns of benthic communities of this basin is still very scarce and mostly restricted to shallow shelf areas. The marine waters of Ghana are among the most scarcely sampled areas of the East Atlantic, and most of the studies there were performed over 40 years ago (Bassindale, 1961; Buchanan, 1958), except for some recent studies on *Lophelia* reefs (Buhl-Mortensen et al., 2017), and coastal shallows (Olomukoro and Dirisu, 2019), as well as studies on Tanaidacea (Józwiak et al., 2022), Cumacea (Stępień et al., 2021), Polychaeta (Sobczyk et al., 2021, 2023) and higher taxa (Pabis et al., 2020) along a depth gradient. There is almost no data about the distribution patterns and ecology of the decapod fauna of the Ghanaian shelf and slope. Previous studies mainly focused on taxonomy or provided only species lists (Bassindale, 1961; Bayer, 1966; Forest, 1956; Forest and Guinot, 1966; Gauld, 1960; Guinot, 1966; Monod, 1956) and generally, our knowledge about the decapod fauna associated with the whole western continental margin of Africa is scanty. The majority of studies concern taxonomy (e.g. Emmerson, 2016; Kensley, 1980; Macpherson, 1988), although there are also some studies analysing the zoogeography (Matos-Pita et al., 2016) and diversity of crustaceans from various parts of African continental margin, like South Africa (Kensley, 2006), Côte-d'Ivoire (Le Loeuff and Intès, 1999), Namibia (Macpherson, 1991) or Canary Current LME (García-Isarch and Muñoz, 2015). Decapods were also analysed as part of the demersal communities in Angola (Bianchi, 1992a), as well as in Congo and Gabon (Bianchi, 1992b). Only the studies from Guinea-Bissau (Muñoz et al., 2012) and Mauretania (García-Isarch et al., 2017; Moctar et al., 2020) included analysis of decapod communities at a wider depth range, down to the slope depths.

In this study, we aimed to analyse distribution patterns, diversity and abundance of the decapod fauna of the Ghanaian marine waters from six different bottom depths ranging from 25 up to 1000 m. This will fill a substantial knowledge gap, as there have been no decapod studies conducted in Ghana for over half a century.

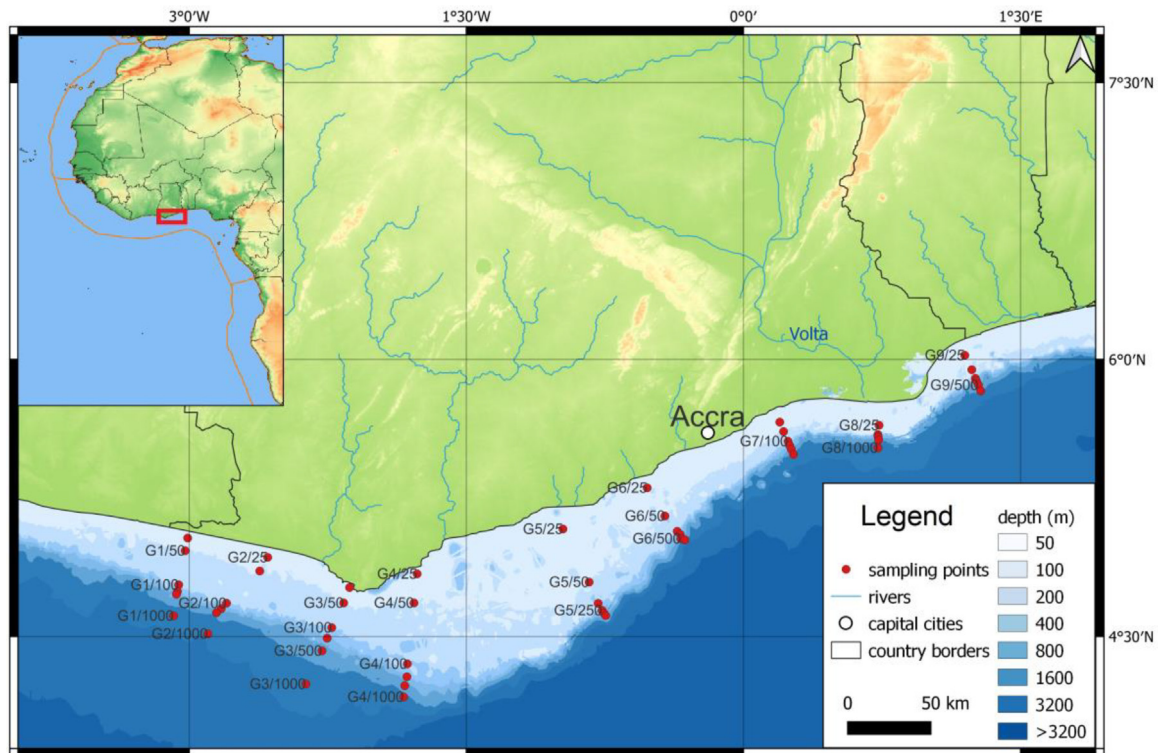


Figure 1 Distribution of transects (G1–G9) and sampling points along the coast of Ghana. The auxiliary map in the top left corner presents Western Africa with the area of LMEs delineated by an orange line and the study area outlined by a red rectangle.

2. Material and methods

2.1. Study area

The Gulf of Guinea is a large embayment on the Atlantic coast of Africa (Ukwe et al., 2003). Marine ecosystems of the tropical and subtropical part of the East Atlantic African coast are shaped by a very dynamic and diverse set of factors. The Gulf of Guinea is influenced by the Guinea, the Benguela, and the South Equatorial Counter Currents (Ukwe et al., 2006), oxygen minimum zones (Levin, 2003), coastal erosion (Ukwe et al., 2003) and upwellings (Djagoua et al., 2011). The total length of the coast of Ghana is 565 km. The River Volta is the only large river system on the Ghanaian coast (Humphries et al., 2014). The marine ecosystem of the Gulf of Guinea is also affected by numerous threats of anthropogenic origin, including urban pollution, the dyeing industry in the coastal areas and the oil industry (Scheren et al., 2002). Growing industrialization as well as gas and oil extraction results in increasing risk of disturbance, not only in the coastal zone but also in the deep sea (Acquah, 1995; Boadi and Kuitunen, 2002).

2.2. Sampling

The material was collected from onboard the *r/v Dr Fridtjof Nansen* in October and November 2012 along the nine transects located along the whole coast of Ghana. Altogether 265 van Veen grab (0.1 m²) samples were collected. The

use of Video Assisted Monitoring System (VAMS) allowed us to monitor the sampling process. When sediment penetration by the grab was inappropriate (e.g. partially opened grab), the samples were discarded from further analysis. Sampling points were distributed from shallow shelf areas down to bathyal depths. Six points were sampled along each transect: 25 m, 50 m, 100 m, 250 m, 500 m and 1000 m (Figure 1). Five samples were collected at each sampling point. The material was sieved using 0.3 mm mesh sieves and fixed in formalin (40% solution of formaldehyde). The methodology was consistent with the recommendations of the Oil Spill Prevention, Administration and Response Fund (OSPAR) (Coit and Ball, 2012).

2.3. Environmental data

Temperature, conductivity, and oxygen concentration were measured using Seabird 911 CTD Plus and SBE 21 Seacat thermosalinograph from each sampling point. The sediment was mixed with water (solubilized) and sieved through 0.063 mm mesh size sieve and Endecott sieves to analyse sediment grain size. The formulae of Blott and Pye (2001); Buchanan (1984) and Folk and Ward (1957) (GradiStat 4.01) were used. Total organic matter was determined as the weight loss in a 2–3 gram dried sample (dried at 105°C for 20 hours) after two hours of combustion at 480°C. Petroleum hydrocarbon content (GC/FID) analysis of the extracts was obtained as described in the Report of the Intergovernmental Oceanographic Commission on its activities during 1980–1982 (Intergovernmental Oceanographic Commission, 1983). Metal concentrations (Ba, Cd, Cr, Cu, Pb,

Zn, Hg) were determined by Inductively Coupled Plasma – Atomic Emission Spectrometry (ICP – AES), apart from mercury, which was determined by Cold Vapour Atomic Emission Spectrometry (CVAAS). Full details of the analysis of environmental factors can be found in [Pabis et al. \(2020\)](#); here we only summarize the most important data that are of relevance to this study ([Table 1](#)).

2.4. Data analysis

The material was identified to the morphospecies level ([Horton et al., 2021](#); [Sigovini et al., 2016](#); [Wägele, 2005](#)) using a stereoscope Opta-tech, based on morphological traits, among others carapace shape, proportions and shape of particular sections of appendages, using appropriate taxonomic literature (e.g. [Fransen, 2014a,b](#); [Ingle, 1996](#); [Manning and Holthuis, 1981](#); [Mavidis et al., 2009](#); [McLaughlin, 1980](#); [Poore, 2004](#); [Tan, 2007](#)). If necessary for identification purposes, certain specimens were dissected. After identification, the specimens were kept separately in vials and preserved in 96% ethanol. However, the previous preservation in formalin excludes the possibility of molecular analyses.

If identification was possible to the genus or family level, we used the open nomenclature abbreviations: “sp.” for morphospecies from a particular genus (e.g. *Dardanus* sp.) and gen. sp. for morphospecies representing higher taxonomic units (e.g. Porcellanidae gen. sp.), according to the latest taxonomical recommendations ([Horton et al., 2021](#); [Sigovini et al., 2016](#)). If there were more morphospecies representing a given family or genus, these were numbered continuously (e.g. Callianassidae gen sp. 1, Callianassidae gen. sp. 2). If we were able to assign the given morphospecies to an already described species, we used the full taxonomic name (e.g. *Panopeus africanus* A. Milne-Edwards, 1867). Part of the material was identified only to a higher taxonomic level due to the poor condition of the material, and such specimens were excluded from the diversity and morphospecies richness analyses to avoid potential errors in the calculation of diversity indices and cluster analysis.

Mean density, richness (S – number of morphospecies per sample) and Shannon index (\log_e) ([Magurran, 2004](#)) were calculated with standard deviation for each depth: 25 m, 50 m, 100 m, 250 m, 500 m and 1000 m (for each depth samples from all sampling points were used). Differences between the depths were tested using the Kruskal-Wallis test. Post hoc testing was performed using Dunn’s test in the Statistica 13 package. Chao 1 and Chao 2, as well as Jackknife 1 and Jackknife 2 estimators of species richness ([Canning-Clode et al., 2008](#)), were calculated using Primer package ([Clarke and Gorley, 2015](#)). Frequency of occurrence (F – percentage (%) of samples where a morphospecies was found out of the total number of samples) was calculated for each morphospecies, in each depth zone and also for the whole material ([Table 2](#)).

Rare morphospecies, defined as singletons, doubletons and tripletons (morphospecies represented by only one, two or three individuals in the whole material, respectively), as well as uniques, duplicates and triplicates (morphospecies found in one, two or three samples, respectively), were also counted ([Table 3](#)).

Hierarchical agglomerative clustering was performed using the Bray-Curtis formula (non-transformed data, group

average method) to assess faunistic similarity between the samples. Since there were no strong disproportions in the abundance of particular morphospecies, and generally the abundance per sample was low, the data were not transformed. The SIMPROF test with a 1% significance level was performed ([Clarke and Gorley, 2015](#)). The SIMPROF routine confirms statistically significant evidence of genuine clusters, and therefore the determination of groupings. It provides objective stopping rules for the dissection of the dendrogram into groups ([Clarke and Warwick, 2001](#); [Clarke et al., 2008](#)). Such clusters are indicated on the dendrogram using dotted lines.

3. Results

Environmental factors changed along the depth gradient ([Table 1](#)). The highest oxygen concentrations were recorded on the shelf and decreased in the 250–500 m depth range. Shelf sediments were characterized by higher heterogeneity (from silt clay to coarse sand) compared to slope sampling points, which were homogenous and characterized by silt clay fractions. Total organic matter content was highest on the slope. At the same time, 500–1000 m bottom deposits were characterized by the highest concentrations of barium and other metals, as well as the highest hydrocarbon concentrations.

Altogether 60 morphospecies of Decapoda, representing 34 families (613 individuals), were recorded ([Table 2](#)). The most speciose families were Hexapodidae and Inachidae, with four morphospecies recorded, followed by the Diogenidae, Epiplatidae, Majidae, Parthenopidae, Portunidae and Xanthidae families (each represented by three morphospecies). The majority of morphospecies were rare and patchily distributed. Thirty-two morphospecies (53.3% of all morphospecies) were recorded from less than four samples (20 uniques, 5 duplicates, 7 triplicates). Twenty-eight morphospecies (46.7% of all morphospecies) were represented by one to three individuals (18 singletons, 6 doubletons, 4 tripletons) ([Table 3](#)). The most abundant morphospecies, with 63 individuals, was *Dardanus* sp. (Diogenidae), although 25 of these were found from a single sample. The highest frequency of occurrence (9.1% of samples, only 24 out of 265 samples) in the whole material was recorded for *Panopeus africanus* (Panopeidae) and *Dardanus* sp. (Diogenidae) ([Table 2](#)). The general frequency of occurrence of Decapoda in the whole material was low, as they were recorded from 132 samples (49.8% of all collected samples).

Diversity, morphospecies richness and abundance of decapods decreased along a depth gradient ([Figure 2](#)). The mean number of morphospecies (S) per sample and mean values of the Shannon index were low. The highest values (mean \pm SD, max) were recorded at 25 m (S : 2.9 ± 2.8 , max=10.0; Shannon Index: 0.7 ± 0.7 , max=2.1), while the lowest values were found at 1000 m (S : 0.0 ± 0.2 , max=1; Shannon Index: 0.0 ± 0.0 , max=0.0). A similar pattern was found for mean densities. The highest abundance was found at 25 m (6.8 ± 9.3 ind./0.1 m², max=44) and the lowest at 1000 m (0.1 ± 0.5 ind./0.1 m², max=3). Differences in diversity, morphospecies richness and density were statistically significant between shelf and slope depths ([Figure 2](#))

Table 1 Mean values of environmental parameters at individual depth samples (standard deviations omitted for clarity). FLU – fluorescence concentration as a measure of the level of chlorophyll *a*. Percentages of Silt, Sand and Gravel show the percentage of individual sediment fractions in the samples.

Depth (m)		Temperature	Salinity	Oxygen	FLU	As	Ba	Cd	Cr	Cu	Ni	Pb	Zn	Hg	THC	PAH	NPD	TOM	Silt	Sand	Gravel	Pressure
		(°C)	(PSU)	(ml/l)	(µg/l)	(µg/g)								(ppm)	(µg/g)	(µg/g)	(%)	(%)			(at)	
25	mean	28.0	35.1	4.2	0.2	44.8	11.5	0.1	38.8	3.2	10.7	7.5	35.1	0.01	5.3	40.7	21.3	4.5	32.8	57.5	9.7	22.7
25	min	26.2	34.7	3.7	0.1	4.6	3.4	0.0	12.2	0.5	2.4	1.4	6.2	0.01	1.1	4.6	4.1	0.9	1.1	18.8	0.0	18.0
25	max	28.9	35.3	4.6	0.4	109.5	23.1	0.1	90.9	10.5	23.1	24.0	84.2	0.03	10.3	204.0	64.1	8.4	81.3	94.0	30.2	24.0
50	mean	26.9	35.5	4.1	0.2	31.4	21.0	0.1	46.7	5.3	15.9	6.3	46.7	0.01	6.2	142.2	48.5	5.1	44.9	51.5	3.6	46.3
50	min	24.1	35.4	3.2	0.1	6.8	11.4	0.0	27.8	2.4	7.9	2.8	29.2	0.01	3.1	6.7	12.5	0.9	19.8	14.4	0.0	43.0
50	max	28.9	35.5	4.5	0.3	185.8	32.6	0.4	62.9	9.7	29.5	19.8	99.5	0.04	11.7	1117.1	229.6	9.1	85.0	72.5	12.6	48.0
100	mean	25.2	35.8	2.5	0.1	11.0	29.1	0.1	41.6	7.4	17.5	4.3	42.9	0.01	6.6	23.6	25.5	7.2	52.9	45.4	1.6	96.4
100	min	17.1	35.7	2.1	0.1	4.7	14.7	0.1	31.1	4.1	11.0	2.5	30.7	0.01	4.0	9.9	12.3	5.1	29.5	2.7	0.0	93.0
100	max	28.9	35.9	2.8	0.1	34.8	51.0	0.3	59.9	17.7	30.3	8.9	54.5	0.02	10.4	66.9	52.7	10.8	97.3	68.8	4.3	99.0
250	mean	23.6	35.4	1.5	0.0	21.5	28.5	0.2	63.9	7.5	19.7	5.3	68.9	0.01	7.1	23.3	28.9	7.5	48.8	50.4	0.8	248.3
250	min	13.3	35.3	1.2	0.0	6.9	15.0	0.1	42.6	4.4	13.3	2.8	47.2	0.01	3.7	8.4	14.4	5.4	18.5	2.2	0.0	240.0
250	max	28.9	35.5	1.7	0.1	66.9	51.5	0.2	89.2	14.6	26.7	9.1	102.0	0.02	14.5	72.7	69.6	9.5	97.9	79.2	2.3	267.0
500	mean	22.1	34.6	1.9	0.0	10.6	87.8	0.2	64.5	12.4	27.2	4.8	59.9	0.02	17.4	47.8	48.8	9.8	80.8	19.2	0.1	500.9
500	min	6.2	34.1	1.7	0.0	5.8	27.5	0.1	46.4	4.5	16.0	2.5	47.9	0.01	3.5	12.0	13.4	6.7	42.2	1.1	0.0	492.0
500	max	28.7	34.8	2.2	0.1	18.8	185.6	0.3	94.6	20.1	38.8	8.9	74.5	0.02	59.2	109.9	94.5	12.2	98.9	57.8	0.5	528.0
1000	mean	15.9	34.7	3.6	0.0	10.4	188.8	0.2	60.2	18.1	34.7	6.2	64.9	0.02	13.0	53.4	44.2	12.0	95.1	4.9	0.0	1060.8
1000	min	4.2	34.6	3.2	0.0	5.9	100.9	0.2	54.2	12.5	26.6	3.9	57.5	0.02	5.1	26.9	20.7	9.8	87.4	0.5	0.0	970.0
1000	max	28.2	34.8	4.0	0.0	21.6	363.3	0.3	64.3	22.6	43.2	9.2	76.6	0.04	19.4	86.7	67.1	17.6	99.5	12.6	0.1	1226.0

Table 2 List of Decapoda morphospecies recorded at the six depths along the nine transects in the Gulf of Guinea. N – total number of individuals; F – frequency of occurrence, i.e. percentage (%) of samples where the morphospecies was present.

Morphospecies	25 m		50 m		100 m		250 m		500 m		1000 m		Total	
	N	F	N	F	N	F	N	F	N	F	N	F	N	F
Anomura														
Family: Diogenidae														
<i>Dardanus</i> sp.	39	15.6	20	28.3	4	8.9	-	-	-	-	-	-	63	9.1
<i>Clibanarius</i> sp.	4	4.4	2	4.4	3	4.4	-	-	1	2.3	-	-	10	2.6
Diogenidae gen. sp.	5	6.7	8	10.9	-	-	-	-	-	-	-	-	13	3.0
Family: Galatheidae														
Galatheidae gen. sp.	-	-	1	2.2	-	-	-	-	-	-	-	-	1	0.4
<i>Galathea</i> sp.	26	17.8	8	8.7	1	2.2	-	-	-	-	-	-	35	4.9
Family: Munididae														
Munididae gen. sp.	-	-	-	-	-	-	-	-	3	4.7	-	-	3	0.8
Family: Paguridae														
Paguridae gen. sp.	-	-	2	2.2	-	-	-	-	-	-	-	-	2	0.4
Family: Porcellanidae														
Porcellanidae gen. sp.	1	2.2	-	-	-	-	-	-	-	-	-	-	1	0.4
<i>Petrolisthes</i> sp.	7	6.7	1	2.2	-	-	-	-	-	-	-	-	8	1.5
Axiidea														
Family: Callianassidae														
Callianassidae gen. sp. 1	4	4.4	22	19.6	-	-	-	-	-	-	-	-	26	4.2
Callianassidae gen. sp. 2	-	-	-	-	-	-	3	6.8	2	4.7	-	-	5	1.9
Brachyura														
Family: Atelecyclidae														
<i>Atelecyclus rotundatus</i> (Olivi, 1792)	-	-	1	2.2	-	-	-	-	-	-	-	-	1	0.4
Family: Calappidae														
<i>Acanthocarpus brevispinis</i> Monod, 1946	-	-	-	-	-	-	2	4.6	-	-	-	-	2	0.8
<i>Calappa pelii</i> Herklots, 1851	-	-	1	2.2	-	-	-	-	-	-	-	-	1	0.4
Family: Dorippidae														
<i>Phyllodorippe armata</i> (Miers, 1881)	1	2.2	-	-	-	-	-	-	-	-	-	-	1	0.4
Family: Epiplatidae														
<i>Herbstia rubra</i> A. Milne-Edwards, 1869	12	11.1	-	-	-	-	-	-	-	-	-	-	12	1.9

(continued on next page)

Table 2 (continued)

Morphospecies	25 m		50 m		100 m		250 m		500 m		1000 m		Total	
	N	F	N	F	N	F	N	F	N	F	N	F	N	F
<i>Pisa carinimana</i> Miers, 1879	12	11.1	3	6.5	3	6.7	1	2.3	-	-	-	-	19	4.5
<i>Pisa</i> sp.	-	-	1	2.2	-	-	-	-	-	-	-	-	1	0.4
Family: Ethusidae														
<i>Ethusa mascarone</i> (Herbst, 1785)	1	2.2	-	-	-	-	-	-	-	-	-	-	1	0.4
<i>Ethusa rosacea</i> A. Milne-Edwards & Bouvier, 1897	1	2.2	-	-	1	2.2	-	-	2	4.7	-	-	4	1.5
Family: Geryonidae														
<i>Chaceon affinis</i> (A. Milne-Edwards & Bouvier, 1894)	-	-	-	-	-	-	1	2.3	2	4.7	-	-	3	1.1
Family: Goneplacidae														
<i>Goneplax barnardi</i> (Capart, 1951)	-	-	-	-	-	-	1	2.3	-	-	-	-	1	0.4
Family: Grapsidae														
<i>Geograpsus lividus</i> (H. Milne Edwards, 1837)	-	-	-	-	1	2.2	-	-	-	-	-	-	1	0.4
Family: Hexapodidae														
Hexapodidae gen sp.	-	-	1	2.2	-	-	-	-	-	-	-	-	1	0.4
<i>Parahexapus africanus</i> Baiss, 1922	1	2.2	-	-	-	-	-	-	-	-	-	-	1	0.4
<i>Pseudohexapus platydactylus</i> Monod, 1956	21	15.6	3	6.5	-	-	-	-	-	-	-	-	24	3.8
<i>Theoxapus buchanani</i> (Monod, 1956)	1	2.2	1	2.2	-	-	-	-	-	-	-	-	2	0.8
Family: Inachidae														
<i>Achaeus cranchii</i> Leach, 1817	2	2.2	-	-	4	6.7	-	-	-	-	-	-	6	1.5
<i>Achaeus</i> sp.	1	2.2	-	-	-	-	-	-	-	-	-	-	1	0.4
<i>Calypsachaeus calypso</i> (Forest & Guinot, 1966) ()	2	2.2	2	4.4	-	-	-	-	-	-	-	-	4	1.1
<i>Macropodia macrocheles</i> (A. Milne-Edwards & Bouvier, 1898)	1	2.2	-	-	2	4.4	-	-	-	-	-	-	3	1.1
Family: Leucosiidae														
<i>Ebalia</i> sp.	2	4.4	7	15.2	8	15.6	-	-	-	-	-	-	17	6.0
<i>Ilia</i> sp.	2	4.4	1	2.2	5	8.9	23	22.7	-	-	-	-	31	6.4

(continued on next page)

Table 2 (continued)

Morphospecies	25 m		50 m		100 m		250 m		500 m		1000 m		Total	
	N	F	N	F	N	F	N	F	N	F	N	F	N	F
Family: Majidae														
<i>Eurynome aspera</i> (Pennant, 1777)	-	-	3	6.5	2	4.4	-	-	-	-	-	-	5	1.9
<i>Eurynome</i> sp.	-	-	1	2.2	-	-	-	-	-	-	-	-	1	0.4
<i>Micippa</i> sp.	3	6.7	1	2.2	-	-	-	-	-	-	-	-	4	1.5
Family: Panopeidae														
<i>Panopeus africanus</i> A. Milne-Edwards, 1867	26	26.7	1	2.2	22	22.2	1	2.3	-	-	-	-	50	9.1
Family: Parthenopidae														
<i>Distolambrus maltzami</i> (Miers, 1881)	2	4.4	5	8.7	1	2.2	-	-	-	-	-	-	8	2.6
<i>Parthenopoides massena</i> (Roux, 1830)	2	4.4	2	4.4	-	-	-	-	-	-	-	-	4	1.5
<i>Spinolambrus notialis</i> (Manning & Holthuis, 1981)	-	-	4	8.7	-	-	-	-	-	-	-	-	4	1.5
Family: Pilumnidae														
<i>Pilumnus</i> sp.	20	15.6	5	6.5	21	22.2	1	2.3	-	-	-	-	47	7.9
Family: Pinnotheridae														
<i>Nepinnotheres pinnotheres</i> (Linnaeus, 1758)	-	-	-	-	-	-	1	2.3	-	-	-	-	1	0.4
<i>Pinnotheres</i> sp.	-	-	1	2.2	-	-	-	-	-	-	-	-	1	0.4
Family: Plagusiidae														
<i>Plagusia depressa</i> (Fabricius, 1775)	1	2.2	-	-	-	-	1	2.3	-	-	-	-	2	0.8
Family: Portunidae														
<i>Achelous inaequalis</i> (Miers, 1881)	2	4.4	-	-	-	-	-	-	-	-	-	-	2	0.8
<i>Callinectes amnicola</i> (de Rochebrune, 1883)	5	8.9	-	-	-	-	-	-	-	-	-	-	5	1.5

(continued on next page)

Table 2 (continued)

Morphospecies	25 m		50 m		100 m		250 m		500 m		1000 m		Total	
	N	F	N	F	N	F	N	F	N	F	N	F	N	F
<i>Cronius ruber</i> (Lamarck, 1818)	3	6.7	-	-	-	-	-	-	-	-	-	-	3	1.1
Family: Raninidae														
<i>Ranilia constricta</i> (A. Milne-Edwards, 1880)	-	-	1	2.2	-	-	-	-	-	-	-	-	1	0.4
Family: Xanthidae														
<i>Monodaeus rouxi</i> (Capart, 1951)	27	8.9	3	4.4	-	-	-	-	-	-	-	-	30	2.3
<i>Paractaea</i> sp.	4	6.7	-	-	-	-	-	-	-	-	-	-	4	1.1
<i>Paraxanthias eriphioides</i> (A. Milne-Edwards, 1867)	5	6.7	-	-	-	-	-	-	-	-	-	-	5	1.1
Caridea														
Family: Alpheidae														
<i>Alpheus</i> sp.	25	11.1	-	-	-	-	-	-	-	-	-	-	25	1.9
Family: Crangonidae														
Crangonidae gen. sp.	-	-	-	-	-	-	-	-	1	2.3	-	-	1	0.8
Family: Ogyrididae														
<i>Ogyrides</i> sp.	3	4.4	-	-	1	2.2	-	-	-	-	-	-	4	1.1
Dendrobranchiata														
Family: Luciferidae														
<i>Belzebub faxoni</i> (Borradaile, 1915)	11	17.8	9	13.0	-	-	-	-	-	-	-	-	20	5.3
Luciferidae gen. sp.	-	-	-	-	-	-	-	-	1	2.3	-	-	1	0.4
Family: Penaeidae														
<i>Parapenaeopsis</i> sp.	9	13.3	16	8.7	-	-	-	-	-	-	-	-	25	3.8
Family: Processidae														
Processidae gen. sp.	-	-	2	2.2	-	-	-	-	-	-	-	-	2	0.4
Family: Sergestidae														
<i>Sergia</i> sp.	-	-	-	-	-	-	5	11.4	11	18.6	3	2.4	19	5.3
Gebiidea														
Family: Upogebiidae														
Upogebiidae gen. sp.	11	13.3	17	26.1	7	8.9	-	-	-	-	-	-	35	8.3

Table 3 The number of rare morphospecies: singletons, doubletons and tripletons (morphospecies represented by only one, two or three individuals in the whole material, respectively), uniques, duplicates and triplicates (morphospecies present in one, two or three samples, respectively) recorded at the six depths (25–1000 m) along the nine transects in the Gulf of Guinea.

Morphospecies	Depth (m)						All depths
	25	50	100	250	500	1000	
singletons	9	13	5	7	3	0	18
doubletons	7	5	2	1	3	0	6
tripletons	3	4	2	1	1	1	4
represented by more than three individuals	19	11	7	2	1	0	32
uniques	11	15	5	7	3	1	20
duplicates	8	4	3	1	4	0	5
triplicates	6	4	2	1	0	0	7
present in more than three samples	13	10	6	2	1	0	28
Total	38	33	16	11	8	1	60

(Kruskal-Wallis test, Dunn’s test, $p < 0.05$). The species accumulation curves did not reach the asymptote (Figure 3).

Total number of morphospecies also decreased with depth (25 m – 38 morphospecies, 50 m – 33 morphospecies, 100 m – 16 morphospecies, 250 m – 11 morphospecies, 500 m – 8 morphospecies, 1000 m – 1 morphospecies). Some morphospecies were common to different depth zones (Figure 4). However, there were substantial differences in morphospecies number between the shelf (25–250 m – 57 morphospecies) and the slope (500–1000 m – 8 morphospecies). Only two morphospecies (i.e. *Clibanarius* sp. and *Ethusa rosacea*) were found in the shallows (25–100 m) and on the upper slope (500 m). Three other morphospecies (i.e. Callianassidae gen. sp. 2, *Chaceon affinis* and *Sergia* sp.) were recorded on the lower shelf (250 m) and upper slope (500 m).

The highest number of species unique to a given depth zone was found at 25 m (12 morphospecies) and 50 m (11 morphospecies), while the number of unique morphospecies recorded deeper was lower, e.g. one (*Geograpsus lividus*) at 100 m, three (*Acanthocarpus brevinispinis*, *Geograpsus barnardi*, *Nepinnotheres pinnotheres*) at 250 m, and three morphospecies (Muninidae gen. sp., Crangonidae gen. sp. and Luciferidae gen. sp.) at 500 m. No unique decapod morphospecies were identified from a depth of 1000 m. The frequency of occurrence of the majority of morphospecies in particular depth zones was very low. Only *Panopeus africanus* was relatively frequent (26.7%) in samples collected at 25 m. At 50 m, *Dardanus* sp. and Upogebiidae gen. sp. were the most frequent morphospecies, with frequencies of 28.3% and 26.1%, respectively (Table 2).

Cluster analysis yielded seven groups, although the majority of these were on a low or very low level of similarity (Figure 5). The clearest pattern is the separation of the more diverse shallow water shelf communities from shelf break and slope samples, which were species-poor. There was no pattern associated with the distribution of transects. All the groups were characterized by the constant presence of only one to three morphospecies (Figure 5) and all of those morphospecies had low abundances (mostly one or two individuals per sample).

4. Discussion

4.1. Overall species richness

Virtually all of our current knowledge of the decapod fauna of the Ghanaian coast is the result of a single survey (Bassindale, 1961), although information about the species number of decapods from the intertidal zone and shallow sublittoral of the Gold coast has been reported by Bassindale (1961); Forest (1956); Gauld (1960); Monod (1956). The list of 109 species (54 from the intertidal zone) presented in those studies were the result of 90 dredging samples and Agassiz Beam trawl exploring a narrow depth range from 7 to 64 m, while in our studies there were 50 morphospecies found in 67 samples from 25 to 50 m. A short species list was also provided in the study of Buchanan (1958).

Those restricted studies which used only trawling samples to assess decapod diversity along the coast of Ghana hamper reliable comparison with our quantitative results. Nevertheless, the total number of species collected during other Atlantic surveys was very variable. For example, Muñoz et al. (2012) collected 122 (including at least 21 pelagic and nectobenthic) decapod species from a 20 to 1000 m depth range in 98 trawls in the waters of Guinea-Bissau, while in the waters of Angola, Bianchi (1992a) collected only nine decapod species in 163 samples at depths ranging from 20 to about 500 m. Fariña et al. (1997) found 40 species in 293 samples collected on shelf and upper slope (100–500 m) along the Galician coast of Spain, while Moctar et al. (2020) collected 100 species (including 37 swimming) from 95 sampling points distributed along the coast of Mauritania. Similar results were recorded in an earlier study of Mauritanian waters at an 81–1825 m depth range (García-Isarch et al., 2017). Even in the Mediterranean Sea – one of the diversity hot spots for the decapod fauna – total species number in various surveys based on trawling samples was variable, e.g. 97 species in 113 trawls at 1–200 m depth range (Ateş et al., 2007), 53 species in 46 samples at 10–700 m depth range (Fanelli et al., 2007), 42 species in 109 samples at 140–730 m depth range

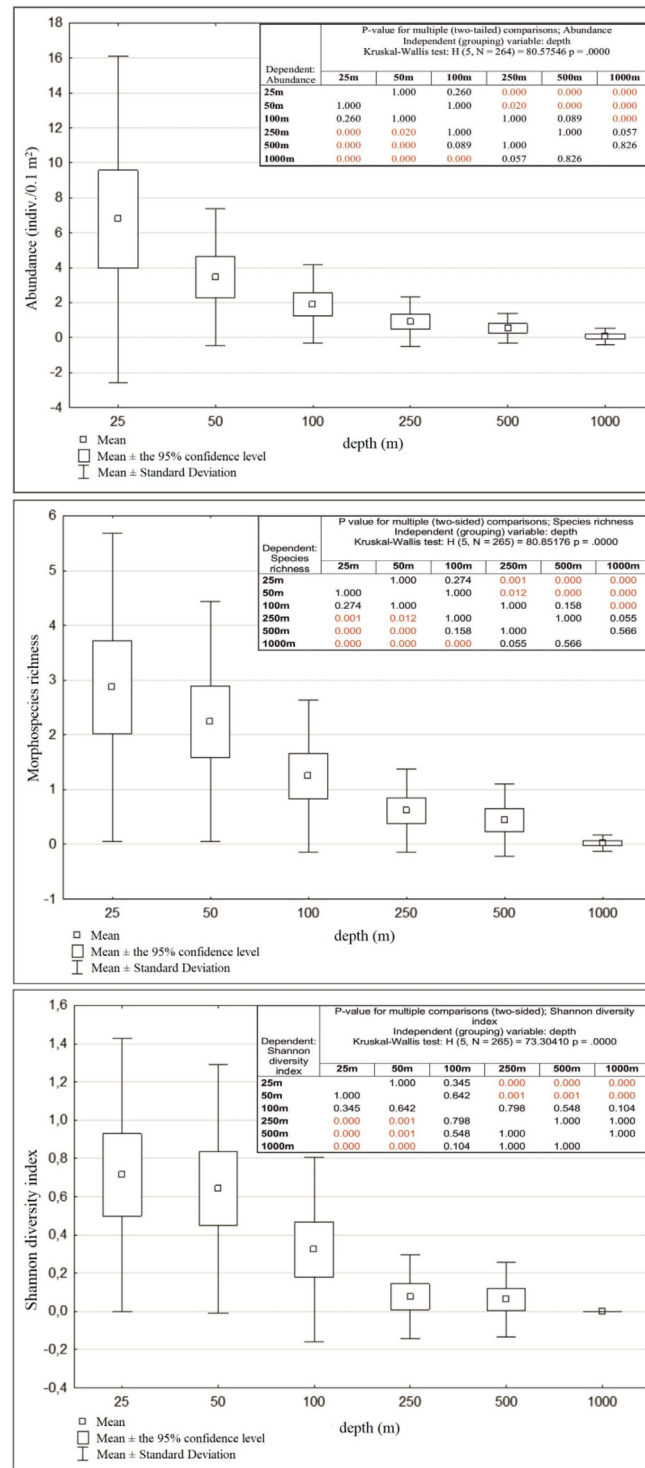


Figure 2 Abundance, species richness and Shannon diversity index calculated for each depth.

(Cartes et al., 1994), 23 species in 32 samples at 800–1500 m depth range (Follesa et al., 2009) and 40 species in 67 samples at 550–2200 m depth range (Cartes and Sarda, 1992). Despite the very high efficiency of trawling in terms of abundance –even up to 200 000 individuals in one survey– the number of recorded species was not much higher than in the present study (García-Isarch et al., 2017;

Muñoz et al., 2012). Moreover, morphospecies accumulation curves (Figure 3) indicated undersampling of the studied area. It is probably partially related to a type of sampling gear used in combination with a highly patchy distribution of decapods. Based on our morphospecies list, we suggest the undersampling, especially regarding highly mobile taxa, such as Dendrobranchiata and Caridea (Poore et al., 2015).

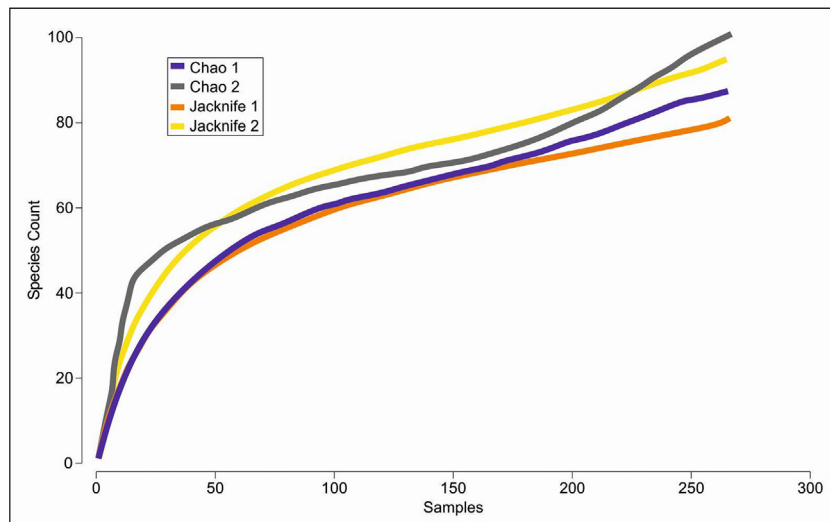


Figure 3 Species accumulation curves (Chao and Jackknife) for the material examined in the study area (excluding non-identifiable individuals).

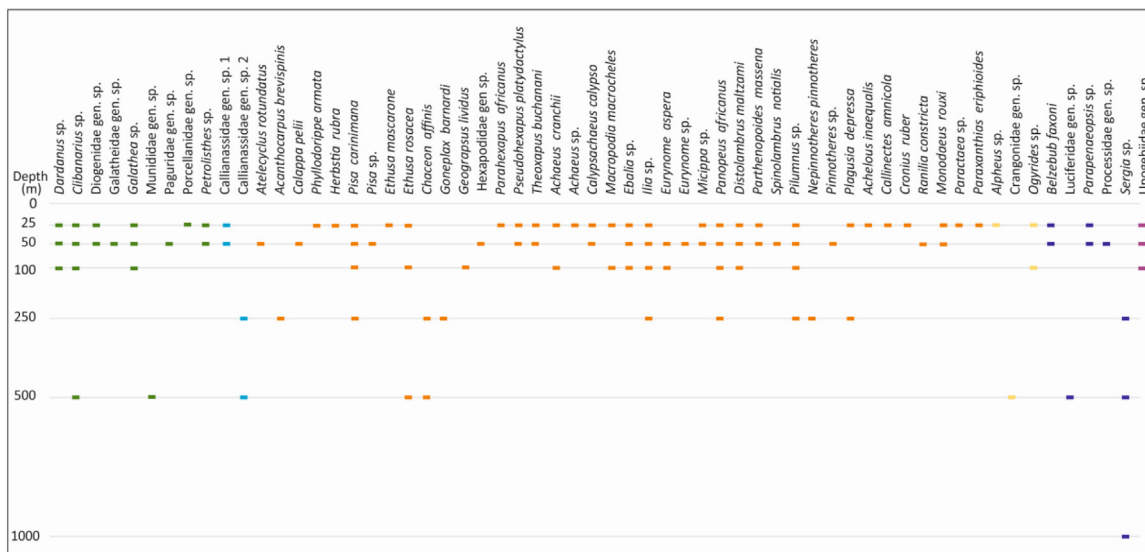


Figure 4 Bathymetric distribution of decapod morphospecies collected at six depths along the nine transects in the Gulf of Guinea. Groups of Decapoda can be distinguished by colours of plots: green – Anomura; blue – Axiidea; orange – Brachyura; yellow – Caridea; dark blue – Dendrobranchiata; purple – Gebiidea.

Thus, we can expect significantly higher diversity and morphospecies richness of those taxa than we report in our study.

The lack of other more comprehensive decapod studies from the West African continental margin makes comparisons of species composition difficult. Only a few species recorded in the Guinea-Bissau were also found in our study, including typical benthic species, such as *Atelecyclus rotundatus*, *Acanthocarpus brevispinis*, *Goneplax barnardi* or genera like *Pisa*, *Ilia* and *Chaceon* (Muñoz et al., 2012). *Calappa pelii* was an important element of communities in the water of Mauritania (Moctar et al., 2020). In the case of the brachyuran fauna, our results confirm available zoogeographic data (Gauld, 1960; Matos-Pita et al., 2016). One of the more frequent morphospecies in samples collected in shallow waters of Ghana was *Panopeus*

africanus, a common crab with wide geographic distribution in the African waters that was found mainly in shallow shelf sites (estuaries and lagoons) up to 140 m depth (Manning and Holthuis, 1981; Rodriguez et al., 1997). In our material, it was also the most abundant morphospecies in shallow waters, although the species was also recorded at a depth of 250 m. However, this species was not recorded in the study of Muñoz et al. (2012). Contrastingly, some taxa, such as *Acanthocarpus brevispinis* or highly mobile brachyurans (such as Portunidae), were very abundant in the Guinea-Bissau survey (Muñoz et al., 2012) but extremely rare in our material. Those differences might also reflect the advantages and disadvantages of different sampling methods (grabs and corers vs. trawls, dredges and sledge), which we discuss at the end of this study.

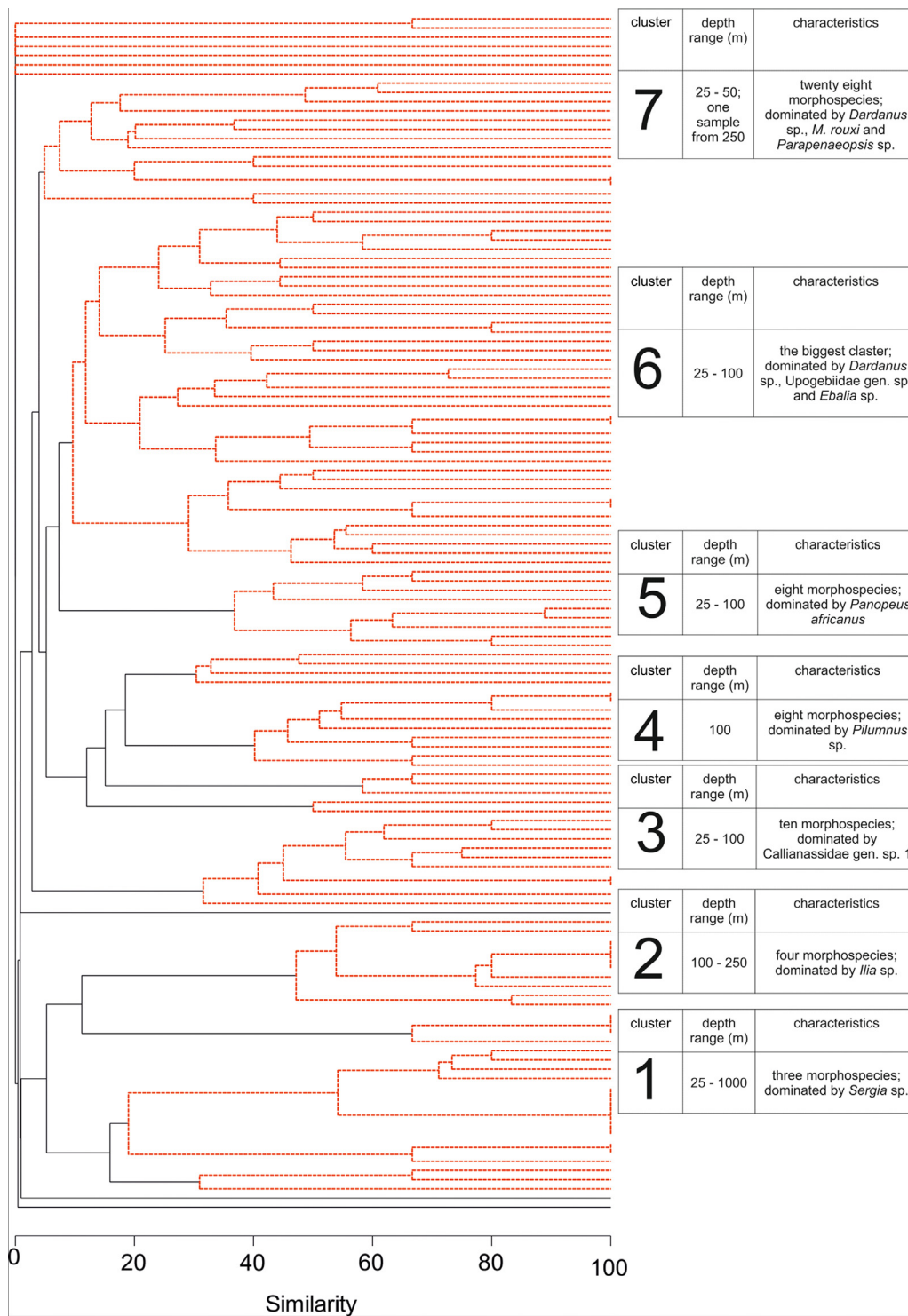


Figure 5 Dendrogram of decapod samples collected in the study area (Bray-Curston similarity, group average method, non-transformed abundance per 0.1 m²). Dashed red lines indicate the samples that cannot be significantly differentiated by SIMPROF.

4.2. Diversity and distribution along a depth gradient

Our study demonstrated a substantial decrease in abundance, species richness and diversity along a depth gradient. There were almost no species associated only with deeper bottom areas. Clear differences between the shelf

and slope were observed also in Guinea-Bissau (Muñoz et al., 2012) and in other surveys (Abelló et al., 1988; Cartes et al., 1994; Fanelli et al., 2007; García-Isarch et al., 2017; Macpherson, 1991; Moctar et al., 2020; Pajuelo et al., 2015). Although, decapod abundance increased along a depth gradient in Guinea-Bissau, reaching the highest values on the upper slope, a clear zonation of fauna was

observed. Diversity on the Ghanaian slope sampled with the van Veen grab was low. Earlier observation has also shown that the distribution of decapods along a depth gradient can be very variable depending on the region being studied (Company et al., 2004). Some studies suggest that bathyal communities are often diversity hotspots for the decapod fauna (Company et al., 2004; Follesa et al., 2009; Maynou and Cartes, 2000) because of higher habitat heterogeneity and stability of environmental variables (especially temperature and oxygen concentration), resulting in co-occurrence of nectobenthic and benthic species (e.g. Abelló et al., 1988; Fanelli et al., 2007; Muñoz et al., 2012). Those earlier observations were also in agreement with a commonly held hypothesis that bathyal is a major diversity hotspot of benthic fauna (Danovaro et al., 2009; Levin and Dayton, 2009). However, Cartes and Sardà (1993) reported decapod fauna impoverishment on deep slopes, below 1200 m, and linked this pattern with lower food availability and degradation of organic matter. Moreover, McCallum et al. (2015) reported that a general pattern of higher slope diversity is not universal and may vary depending on the region. Food availability is also important for the distribution of decapods and might influence diversity and abundance, both on the slope and in the shallow shelf waters (Cartes and Sardà, 1993; Woolley et al., 2016). Values of total organic matter (TOM) increased along a depth gradient on the coast of Ghana but the highest levels of hydrocarbons and some toxic metals were found at the 500 and 1000 m sampling points (Table 1). Those factors affect polychaete and peracarid communities (Jóźwiak et al., 2022; Sobczyk et al., 2021, 2023; Stępień et al., 2021) and probably also affect decapod distribution. A recent study of depth-related changes in total macrozoobenthic abundance based on the same set of samples also showed a decrease in mean densities along a depth gradient, while cluster analysis separated disturbed sampling sites from unaffected bottom areas (Pabis et al., 2020). Contrary to our results, Jóźwiak et al. (2022) showed the highest Tanaidacea species richness on the slope. In the case of Cumacea, the highest number of species was recorded in the 25–50 m depth range and on the slope (Stępień et al., 2021), while polychaetes followed the pattern observed for decapod fauna, both in terms of species richness and abundance (Sobczyk et al., 2021, 2023).

Cluster analysis did not reveal any clear patterns besides the difference between shelf (morphospecies rich) and slope (morphospecies poor) (Figure 5). The results demonstrated seven, most probably incidental groupings. It seems that mobile decapods do not form stable, evenly distributed faunal assemblages, but only temporary patches, most probably associated with food availability, which was already observed for Decapoda (Boada et al., 2018). Mobility is an important feature of decapods (Florko et al., 2021), which allows them not only to actively search for food (Gomes et al., 2019), but also, at least to some point, avoid various types of disturbances or unpreferred environmental conditions (Attrill and Thomas, 1996; Felder et al., 2014).

It is difficult to study the ecological diversity of decapod fauna in Ghanaian waters since there is only scanty knowledge about the biology or habitat preferences of particular species. Nevertheless, the shelf fauna was ecologi-

cally diverse. We have recorded a group of species associated with sandy or muddy bottoms, including *A. rotundatus*, *E. rosacea*, *G. barnardi*, and *M. macrocheles*, species associated with shell debris or gravel, including *C. pelii* and *A. brevispinis*, and species with wide habitat preferences, recorded from mud and sand, shell debris and solid rock, such as *D. maltzami*, *E. aspera* and *S. notialis* (De Matos-Pita et al., 2016). These results confirm high microhabitat diversity, which has also been reported from polychaete studies (Sobczyk et al., 2021, 2023) and are congruent with sediment characteristics of the studied area (Pabis et al., 2020). Moreover, the majority of these species have a wide bathymetric range from the shallow shelf down to the slope depths (De Matos-Pita et al., 2016), which was also confirmed in our results. Part of our results is also confirmed by historical data from the Gulf of Guinea. This includes the presence of the genus *Dardanus* on the shelf (Bayer et al., 1966). Such taxa as *Dardanus* and *Goneplax* were also found on the shelf in Mauritanian waters, while such genera as *Sergia* occurred in the deep sea, though many species had a wide bathymetric distribution (García-Isarch et al., 2017).

The availability of organic matter was high on shallow shelf stations (Pabis et al., 2020) which is important for such taxa as Galatheididae or Porcellanidae (Nicol, 1932). Moreover, many decapods, e.g. crabs are generalists which may feed on algae or prey on small crustaceans and molluscs (Sant'Anna et al., 2015). The 25–50 m depth range was also characterized by high diversity and abundance of polychaetes (Sobczyk et al., 2023) and peracarid crustaceans (Jóźwiak et al., 2022; Stępień et al., 2021), and generally high macrofaunal abundance (Pabis et al., 2020), and therefore, variety of potential prey for omnivorous or predatory decapods like *Ebalia* (Schembri, 1981). Decapods sampled on the Ghanaian shallow shelf represent high ecological and functional diversity, similarly to polychaetes (Sobczyk et al., 2021) and suggest that the Ghanaian shelf is a diverse system characterized by a high variety of ecological interactions associated with high habitat heterogeneity compared to deeper bottom areas (Pabis et al., 2020; Sobczyk et al., 2023). Heterogeneity was evident in the character of the bottom deposits, which were diversified on the shelf, and homogenous on the slope (dominated by silt clay fractions) (Table 1).

4.3. van Veen grab in decapod sampling

Quantitative samplers (van Veen grabs or box corers) are not perfect for collecting large and motile decapods (Frutos et al., 2022). Underestimation of mobile epifauna might be associated with the bow wave effect and closing mechanism of the grab (Eleftheriou and McIntyre, 2005; Lozach et al., 2011). On the other hand, broadly used trawling or dredging devices are excellent for assessing diversity or benthic zonation, though they preclude detailed quantitative analysis and/or reliable estimation of rarity, patchiness and small-scale distribution patterns (Frutos et al., 2022; García-Isarch et al., 2017). Trawling or dredging also facilitates the collection of pelagic and nectobenthic decapods (Fanelli et al., 2007; Furlan et al., 2013; Moctar et al., 2020; Muñoz et al., 2012), which are only sporadically recorded in van Veen grabs. Large sampling efforts, such as that of the present study, might to some

point minimise the underestimations associated with the use of quantitative samplers which collect the fauna at a very fine spatial scale, although it is worth mentioning that decapods were found only in 49.8% out of 265 collected samples. Nevertheless, the van Veen grab has already been used in studies of benthic decapods (e.g. Ateş and Katağan, 2008; Fanelli et al., 2007) and some decapod taxa have been mostly (or exclusively) sampled via grabs or corers (Dworschak, 2015). Generally, each of those two sampling protocols may sample different, unique fauna (Jóźwiak et al., 2020). Grab samples permit quantitative analysis, assuming that the level of underestimation is similar for all of the samples (Eleftheriou and McIntyre, 2005), especially when we use monitoring like VAMS which allows us to discard poor samples. Moreover, in the case of trawling, it is almost impossible to link the data on abundance and diversity with environmental variables that are collected using samplers like grabs and corers (if collected at all) and do not describe the microhabitat diversity sampled during trawling (Eleftheriou and McIntyre, 2005; Frutos et al., 2022; Pabis et al., 2015; Sobczyk et al., 2023). For example, our results demonstrated that decapods in Ghana form small temporary patches. Those conclusions are supported by our analysis of video recordings from ROV (Remote Operated Vehicle), performed at the same sampling sites (Jóźwiak P., Podwysocki K., Pabis K. unpublished data). Such evidence of patchiness is only collected when using samplers like van Veen grab, and is usually lost in the case of trawling samples, which tend to mix materials from large bottom areas, and various microhabitats (Eleftheriou and McIntyre, 2005; Frutos et al., 2022). In the case of slope fauna results from Remote Operated Vehicle (ROV) movies (Jóźwiak P., Podwysocki K., Pabis K. unpublished results) partially confirmed results based on analysis of van Veen grab samples. Only at 500 m depth from three transects, i.e. G2, G3 and G6, we have recorded large aggregations of Caridea (up to 400 individuals on several square meters).

The very low frequency of decapods occurrence in van Veen grab samples, together with the almost complete absence of those crustaceans in the 250–1000 m depth range, precludes meaningful cluster analysis or detailed analysis of depth-related changes in diversity and abundance against a background of environmental conditions, e.g. modelling or Canonical Correspondence Analysis (Reiss et al., 2015). It is a general problem of many deep-sea studies of benthic macrofauna (Jóźwiak et al., 2022 and references therein). An attempt to perform such analysis resulted in lack of clear patterns, low eigenvalues and a low percentage of explained variability, therefore, it was impossible to interpret such not informative results, and they were not included in the manuscript according to Occam's razor principle. Comparisons of our results with the above-mentioned studies show the importance of using combined approaches in decapod sampling. Trawling allows for describing more general spatial patterns, while grabs or corers allow for studying small-scale variability. It is also worth mentioning that earlier studies of quantitative sampling efficiency suggest that box corers are more useful in the deep-sea studies than in shelf sampling (Eleftheriou and McIntyre, 2005). On the African coast, such an approach was used by Eisenbarth and Zettler (2016) and van Veen grab was used only down to

300 m depth, while deep-sea sampling was conducted using a box corer. The use of VAMS is also important because the problems are associated mostly with the closing mechanisms and appropriate sediment penetration of the grabs in the deep-seabed. Results may also differ depending on the region studied, especially the type of sediment sampled, which may affect the functioning of the grab-closing mechanism (Eleftheriou and McIntyre, 2005).

4.4. Concluding remarks

Earlier studies on other taxonomic groups (Jóźwiak et al., 2022; Sobczyk et al., 2021, 2023; Stępień et al., 2021) demonstrated that the coast of Ghana is under the influence of numerous interacting environmental factors, of both natural (e.g. oxygen minimum zones, productivity, upwellings) and anthropogenic (heavy metals and THC) origin, and those factors might affect decapods, especially in the larval stage (Felder et al., 2014; Katz, 1973), resulting in changes in abundance of adults. Further studies using different sampling protocols are needed to fill the knowledge gaps of decapod biodiversity in the area studied. Although, it is worth mentioning that previous studies on decapods sampled with more efficient equipment, such as trawls in most cases, were not supplemented with detailed knowledge about relevant environmental factors (e.g. Cartes and Sardà, 1993; Fariña et al., 1997; Follesa et al., 2009; Muñoz et al., 2012), therefore, documented mostly depth-related trends. Therefore, despite some limitations of van Veen grab, our study conducted on a wide depth range in the tropical Eastern Atlantic still stands out from earlier similar decapod research. It also showed the great need for applying different types of sampling methods in studies on decapods.

Declaration of competing interest

The authors declare that they have no known competing financial interests or personal relationships that could have appeared to influence the work reported in this paper.

Acknowledgements

Krzysztof Podwysocki's trip to the Centre d'Estudis Avançats de Blanes in Spain to perform taxonomic identification of decapods with Ferran Palero was financed by University of Lodz (Studenckie Granty Badawcze program). We would like to thank Stephen Venn (University of Lodz) for language corrections and for providing valuable insights and suggestions that significantly enhanced the overall quality of this paper. We are grateful to Aleksandra Jabłońska (University of Lodz) for help in taxonomic identification of the part of the material, Robert Sobczyk (University of Lodz) for help in statistical analysis and Andrea Desiderato (University of Lodz) for help in preparing the map of the study area. Thanks are also due to anonymous reviewers of the manuscript for their invaluable contributions to the improvement of this manuscript. Their valuable comments played a pivotal role in shaping the final version of this manuscript.

Funding

The sampling cruise and the environmental data analysis within this program were funded by the Norwegian Agency for Development Cooperation (NORAD) (Oil for Development Program – OfD) and by the Food and Agriculture Organization of the United Nations (FAO). K. Pabis and K. Podwysoccki were also supported by the University of Lodz.

References

- Abelló, P., Valladares, F.J., Castellón, A., 1988. Analysis of the structure of decapod crustacean assemblages off the Catalan coast (North-West Mediterranean). *Mar. Biol.* 98, 39–49. <https://doi.org/10.1007/BF00392657>
- Acquah, D., 1995. Prospects for Photovoltaics Applications at Dromankese.
- Agnetta, D., Badalamenti, F., Colloca, F., D'Anna, G., Di Lorenzo, M., Fiorentino, F., Garofalo, G., Gristina, M., Labanchi, L., Patti, B., Pipitone, C., Solidoro, C., Libralato, S., 2019. Benthic-pelagic coupling mediates interactions in Mediterranean mixed fisheries: An ecosystem modeling approach. *PLoS One* 14, 1–24. <https://doi.org/10.1371/journal.pone.0210659>
- Appeltans, W., Ah Yong, S.T., Anderson, G., Angel, M.V., Artois, T., Bailly, N., Bamber, R., Barber, A., Bartsch, I., Berta, A., Błażewicz-Paszkowycz, M., Bock, P., Boxshall, G., Boyko, C.B., Brandão, S.N., Bray, R.A., Bruce, N.L., Cairns, S.D., Chan, T.Y., Cheng, L., Collins, A.G., Cribb, T., Curini-Galletti, M., Dahdouh-Guebas, F., Davie, P.J., Dawson, M.N., De Clerck, O., Decock, W., De Grave, S., de Voogd, N.J., Domning, D.P., Emig, C.C., Erséus, C., Eschmeyer, W., Fauchald, K., Fautin, D.G., Feist, S.W., Franssen, C.H., Furuya, H., Garcia-Alvarez, O., Gerken, S., Gibson, D., Gittenberger, A., Gofas, S., Gómez-Daglio, L., Gordon, D.P., Guiry, M.D., Hernandez, F., Hoeksema, B.W., Hopcroft, R.R., Jaume, D., Kirk, P., Koedam, N., Koenemann, S., Kolb, J.B., Kristensen, R.M., Kroh, A., Lambert, G., Lazarus, D.B., Lemaitre, R., Longshaw, M., Lowry, J., Macpherson, E., Madin, L.P., Mah, C., Mapstone, G., McLaughlin, P.A., Mees, J., Meland, K., Messing, C.G., Mills, C.E., Molodtsova, T.N., Mooi, R., Neuhaus, B., Ng, P.K., Nielsen, C., Norenburg, J., Opresko, D.M., Osawa, M., Paulay, G., Perrin, W., Pilger, J.F., Poore, G.C., Pugh, P., Read, G.B., Reimer, J.D., Rius, M., Rocha, R.M., Saiz-Salinas, J.I., Scarabino, V., Schierwater, B., Schmidt-Rhaesa, A., Schnabel, K.E., Schotte, M., Schuchert, P., Schwabe, E., Segers, H., Self-Sullivan, C., Shenkar, N., Siegel, V., Sterrer, W., Stöhr, S., Swalla, B., Tasker, M.L., Thuesen, E.V., Timm, T., Todaro, M.A., Turon, X., Tyler, S., Uetz, P., van der Land, J., Vanhoorne, B., van Ofwegen, L.P., van Soest, R.W., Vanaverbeke, J., Walker-Smith, G., Walter, T.C., Warren, A., Williams, G.C., Wilson, S.P., Costello, M.J., 2012. The magnitude of global marine species diversity. *Curr. Biol.* 422 (23), 2189–2202. <https://doi.org/10.1016/j.cub.2012.09.036>
- Ateş, A.S., Katağan, T., Kocataş, A., 2006. Bathymetric distribution of decapod crustaceans on the continental shelf along the Aegean coasts of Turkey. *Crustaceana* 79 (2), 129–141. <https://doi.org/10.1163/156854006776952928>
- Ateş, A.S., Katağan, T., Kocataş, A., 2007. Decapod Crustaceans on the Coast of Gökova Bay (the southeastern Aegean Sea). *Ege J. Fisheries Aquat. Sci.* 24 (1), 159–164.
- Ateş, A., Katağan, T., 2008. Decapod crustaceans of soft-sediments on the Aegean Sea coast of Turkey (the eastern Aegean Sea). *Oceanol. Hydrobiol. Stud.* 37 (1), 17–30. <https://doi.org/10.2478/v10009-007-0040-3>
- Attrill, M.J., Thomas, R.M., 1996. Long-term distribution patterns of mobile estuarine invertebrates (Ctenophora, Cnidaria, Crustacea: Decapoda) in relation to hydrological parameters. *Mar. Ecol. Prog. Ser.* 143 (1/3), 25–36. <http://www.jstor.org/stable/24857280>
- Bassindale, R., 1961. On the marine fauna of Ghana. *P. Zool. Soc. Lond.* 137, 481–510. <https://doi.org/10.1111/j.1469-7998.1961.tb06086.x>
- Bayer, F.M., 1966. Dredging and Trawling Records of R/V John Eliot Pillsbury for 1964 and 1965: The R/V Pillsbury Deep-Sea Biological Expedition to the Gulf of Guinea, 1964-65, 3. *Studies in Tropical Oceanography (Miami)* 4 (1), 82–105.
- Bianchi, G., 1992a. Demersal assemblages of the continental shelf and upper slope of Angola. *Mar. Ecol. Prog. Ser.* 81, 101–120. <https://doi.org/10.3354/meps081101>
- Bianchi, G., 1992b. Study of the demersal assemblages of the continental shelf and upper slope off Congo and Gabon, based on the trawl surveys of the RV 'Dr Fridtjof Nansen'. *Mar. Ecol. Prog. Ser.* 85, 9–23. <https://doi.org/10.3354/meps085009>
- Blott, S.J., Pye, K., 2001. GRADISTAT: a grain size distribution and statistics package for the analysis of unconsolidated sediments. *Earth Surf. Process. Landforms* 26, 1237–1248. <https://doi.org/10.1002/esp.261>
- Boada, J., Pagès, J.F., Gera, A., Macpherson, E., Santana, Y., Romero, J., Alcoverro, T., 2018. The richness of small pockets: Decapod species peak in small seagrass patches where fish predators are absent. *Mar. Environ. Res.* 142, 1–6. <https://doi.org/10.1016/j.marenvres.2018.09.012>
- Boadi, K.O., Kuitunen, M., 2002. Urban Waste Pollution in the Korle Lagoon, Accra, Ghana. *The Environmentalist* 22, 301–309. <https://doi.org/10.1023/A:1020706728569>
- Boudreau, S.A., Worm, B., 2012. Ecological role of large benthic decapods in marine ecosystems: a review. *Mar. Ecol. Prog. Ser.* 469, 195–213. <https://doi.org/10.3354/meps09862>
- Brandt, A., Linse, K., Schüller, M., 2009. Bathymetric distribution patterns of Southern Ocean macrofaunal taxa: Bivalvia, Gastropoda, Isopoda and Polychaeta. *Deep-Sea Res. Pt. I* 56, 2013–2025. <https://doi.org/10.1016/j.dsr.2009.06.007>
- Buchanan, J.B., 1958. The bottom fauna communities across the continental shelf off Accra, Ghana (Gold Coast). *P. Zool. Soc. London* 130, 1–56. <https://doi.org/10.1111/j.1096-3642.1958.tb00562.x>
- Buchanan, J.B., 1984. Sediment analysis. In: Holme, N.A., McIntyre, A.D. (Eds.), *Methods for the study of marine benthos*. Blackwell Sci. Publ., Oxford, 41–65.
- Buhl-Mortensen, L., Serigstad, B., Buhl-Mortensen, P., Olsen, M.N., Ostrowski, M., Błażewicz-Paszkowycz, M., Appoh, E., 2017. First observations of the structure and megafaunal community of a large Lophelia reef on the Ghanaian shelf (the Gulf of Guinea). *Deep-Sea Res. Pt. II* 137, 148–156. <https://doi.org/10.1016/J.DSR2.2016.06.007>
- Canning-Clode, J., Valdivia, N., Molis, M., Thomason, J.C., Wahl, M., 2008. Estimation of regional richness in marine benthic communities: quantifying the error. *Limnol. Oceanogr.* 6, 580–590. <https://doi.org/10.4319/lom.2008.6.580>
- Cartes, J.E., Sardà, F., 1992. Abundance and diversity of decapod crustaceans in the deep-Catalan Sea (Western Mediterranean). *J. Nat. Hist.* 26, 1305–1323. <https://doi.org/10.1080/00222939200770741>
- Cartes, J.E., Sardà, F., 1993. Zonation of deep-sea decapod fauna in the Catalan Sea (Western Mediterranean). *Mar. Ecol. Prog. Ser.* 94, 27–34. <https://doi.org/10.3354/meps094027>
- Cartes, J.E., Company, J.B., Maynou, F., 1994. Deep-water decapod crustacean communities in the Northwestern Mediterranean: influence of submarine canyons and season. *Mar. Biol.* 120, 221–229. <https://doi.org/10.1007/BF00349682>
- Cartes, J.E., Papiol, V., Frutos, I., Macpherson, E., González-Pola, C., Punzón, A., Valeiras, X., Serrano, A., 2014. Distribution

- and biogeographic trends of decapod assemblages from Galicia Bank (NE Atlantic) at depths between 700 and 1800 m, with connections to regional water masses. *Deep-Sea Res. Pt. II* 106, 165–178. <https://doi.org/10.1016/j.dsr2.2013.09.034>
- Carvalho, D.A., Viozzi, M.F., Collins, P.A., Williner, V., 2017. Functional morphology of comminuting feeding structures of *Trichodactylus borellianus* (Brachyura, Decapoda, Trichodactylidae), an omnivorous freshwater crab. *Arthropod Struct. Dev.* 46 (4), 472–482. <https://doi.org/10.1016/j.asd.2017.05.001>
- Clarke, K.R., Warwick, R.M., 2001. *Change in marine communities. An approach to statistical analysis and interpretation 2*, 1–168.
- Clarke, K.R., Somerfield, P.J., Gorley, R.N., 2008. Testing of null hypotheses in exploratory community analyses: similarity profiles and biota-environment linkage. *J. Exp. Mar. Biol. Ecol.* 366 (1–2), 56–69. <https://doi.org/10.1016/j.jembe.2008.07.009>
- Clarke, K.R., Gorley, R.N., 2015. *Getting started with PRIMER v7. PRIMER-E Ltd, United Kingdom*, 18 pp.
- Coelho, P.A., De Almeida, A.O., Bezerra, L., 2008. Checklist of the marine and estuarine Brachyura (Crustacea: Decapoda) of northern and northeastern Brazil. *Zootaxa* 1956, 1–58. <https://doi.org/10.11646/zootaxa.1956.1.1>
- Coit, J., Ball, J., 2012. Oil Spill Prevention, Administration and Response (OSPAR) Fund. Annual Report FY 2012. Ospar Commission.
- Company, J.B., Maiorano, P., Tselepides, A., Plaiti, W., 2004. Deep-sea decapod crustaceans in the Western and Central Mediterranean Sea: preliminary aspects of species distribution, biomass and population structure. *Sci. Mar.* 68, 73–86. <https://doi.org/10.3989/scimar.2004.68s373>
- Danovaro, R., Canals, M., Gambi, C., Heussner, S., Lampadariou, N., Vanreusel, A., 2009. Exploring benthic biodiversity patterns and hotspots on European margin slopes. *Oceanography* 22, 16–25. <https://www.jstor.org/stable/24860919>
- De Matos-Pita, S.S., Ramil, F., 2016. New species of Neopilumnoplax Serène in Guinot, 1969 (Decapoda, Brachyura, Mathildellidae) from Northwest Africa with a key to the genus. *Mar. Biodivers.* 46, 253–260. <https://doi.org/10.1007/s12526-015-0361-5>
- Djagoua, E.V., Kassi, J.B., Mobio, B., Kouadio, J.M., Dro, C., Afian, K., Saley, B., 2011. Ivorian and Ghanaian upwelling comparison: intensity and impact on phytoplankton biomass. *Am. J. Sci. Ind. Res.* 2, 740–747. <https://doi.org/10.5251/ajsir.2011.2.5.740.747>
- Dworschak, P.C., 2015. *Methods collecting Axiidea and Gebiidea (Decapoda): a review. Annalen des Naturhistorischen Museums in Wien. Serie B für Botanik und Zoologie* 117, 5–21.
- Eisenbarth, S., Zettler, M., 2016. Diversity of the benthic macrofauna off northern Namibia from the shelf to the deep sea. *J. Marine Syst.* 155, 1–10. <https://doi.org/10.1016/j.jmarsys.2015.10.017>
- Eleftheriou, A., McIntyre, A.D., 2005. *Methods for the study of marine benthos*. Blackwell Publishing Company, Oxford, 493 pp.
- Emmerson, W.D., 2016. *A Guide to, and Checklist for, the Decapoda of Namibia, South Africa and Mozambique (Volume 3)*. Cambridge Scholars Publishing, Newcastle upon Tyne, 711 pp.
- Fanelli, E., Colloca, F., Ardizzone, G., 2007. Decapod crustacean assemblages off the West coast of central Italy (western Mediterranean). *Sci. Mar.* 71, 19–28. <https://doi.org/10.3989/scimar.2007.71n119>
- Fariña, A.C., Freire, J., Gonzáles-Gurriarán, E., 1997. Megabenthic decapod crustacean assemblages on the Galician continental shelf and upper slope (north-west Spain). *Mar. Biol.* 127, 419–434. <https://doi.org/10.1007/s002270050029>
- Felder, D.L., Thoma, B.P., Schmidt, W.E., Sauvage, Self-Krayesky, S.L., Chistoserdov, A., Bracken-Grissom, H.D., Fredericq, S., 2014. Seaweeds and decapod crustaceans on Gulf deep banks after the Macondo Oil Spill. *Bioscience* 64 (9), 808–819. <https://doi.org/10.1093/biosci/biu119>
- Florko, K.R.N., Davidson, E.R., Lees, K.J., Hammer, L.J., Lavoie, M.F., Lennox, R.J., Simard, E., Archambault, P., Auger-Methe, M., McKindsey, C.W., Whoriskey, F.G., Furey, N.B., 2021. Tracking movements of decapod crustaceans: a review of a half-century of telemetry-based studies. *Mar. Ecol. Prog. Ser.* 679, 219–239. <https://doi.org/10.3354/meps13904>
- Folk, R.L., Ward, W.C., 1957. Brazos River bar [Texas]; a study in the significance of grain size parameters. *J. Sediment. Res.* 27, 3–26. <https://doi.org/10.1306/74D70646-2B21-11D7-8648000102C1865D>
- Follesa, M.C., Porcu, C., Gastoni, A., Mulas, A., Sabatini, A., Cau, A., 2009. Community structure of bathyal decapod crustaceans off South-Eastern Sardinian deep-waters (Central-Western Mediterranean). *Mar. Ecol.* 30, 188–199. <https://doi.org/10.1111/j.1439-0485.2009.00323.x>
- Forest, J., 1956. Sur une collection de Paguridae de la Côte de l'Or. *Proc. zool. Sac. Lond.* 126 (3), 335–367.
- Forest, J., Guinot, D., 1966. Crustacés Décapodes: Brachyours. In: *Campagne de la Calypso dans le Golfe de Guinée et aux îles Principe, São Tomé, et Annobon (1956). Résultats scientifiques des Campagnes de la 'Calypso'. Fascicule VII. 16. Annales de l'Institut Océanographique* 44 (1), 23–124.
- Fransen, C.H.J.M., 2014a. Anomurans. In: *Carpenter, K.E., De Angelis, N. (Eds.), The living marine resources of the Eastern Central Atlantic. Volume 1, Introduction, crustaceans, chitons, and cephalopods. Food and Agriculture Organization of the United Nations, Rome*, 235–248.
- Fransen, C.H.J.M., 2014b. True Crabs. In: *Carpenter, K.E., De Angelis, N. (Eds.), The living marine resources of the Eastern Central Atlantic. Volume 1, Introduction, crustaceans, chitons, and cephalopods. Food and Agriculture Organization of the United Nations, Rome*, 249–358.
- Frutos, I., Kaiser, S., Pułaski, Ł., Błażewicz, M., 2022. Challenges and advances in the taxonomy of deep-sea Peracarida: from traditional to modern methods. *Front. Mar. Sci.* 9, 799191. <https://doi.org/10.3389/fmars.2022.799191>
- Furlan, M., Castilho, A.L., Fernandes-Goes, L.C., Fransozo, V., Bertini, G., Costa, R.C., 2013. Effect of environmental factors on the abundance of decapod crustaceans from soft bottoms off southeastern Brazil. *An. Acad. Bras. Ciênc.* 85 (04), 1345–1356. <https://doi.org/10.1590/0001-3765201394812>
- García-Isarch, E., Muñoz, I., 2015. Biodiversity and biogeography of decapod crustaceans in the Canary Current Large Marine ecosystem. In: *Valdés, L., Déniz-González, I. (Eds.), Oceanographic and biological features in the Canary Current Large-sea Marine Ecosystem. IOC Tech. Ser. 115, IOC-UNESCO, Paris*, 257–271.
- García-Isarch, E., de Matos-Pita, S.S., Muñoz, I., Moctar, S.M.M., Ramil, F., 2017. Chapter 9 Decapod Assemblages in Mauritanian Waters. In: *Ramos, A., Ramil, F., Sanz, J.L. (Eds.), Deep-Sea Ecosystems Off Mauritania. Springer, Dordrecht*, 355–391. https://doi.org/10.1007/978-94-024-1023-5_1
- Gauld, D.T., 1960. Brachyura: An Annotated Check-List of the Crustacea of Ghana. IV. *J. West African Sci. Assoc.* 6 (1), 68–72.
- Gomes, T.T., Gheler-Costa, C., Rinaldi, C.A., Santana, W., 2019. Natural diet of *Ocypode quadrata* (Fabricius, 1787) (Crustacea, Decapoda, Brachyura) from the Northern Coast of São Paulo, Brazil. *Pap. Avulsos Zool.* 59, e20195957. <https://doi.org/10.11606/1807-0205/2019.59.57>
- Gray, J.S., 2001. Marine diversity: the paradigms in patterns of species richness examined. *Sci. Mar.* 65, 41–56. <https://doi.org/10.3989/scimar.2001.65s241>
- Guiavarc'h, C., Treguier, A.M., Vangriesheim, A., 2009. Deep currents in the Gulf of Guinea: Along slope propagation of intraseasonal waves. *Ocean Sci.* 5 (2), 141–153. <https://doi.org/10.5194/os-5-141-2009>
- Guinot, D., 1966. *Recherches préliminaires sur les groupements naturels chez les Crustacés Décapodes Brachyours. I. Les affinités des genres Aethra, Osachila, Hepatus, Hepatella et Actaeomorpha. Bull. Muséum National d'Histoire Naturelle* 38 (5), 744–762.

- Horton, T., Marsh, L., Bett, B.J., Gates, A.R., Jones, D.O.B., Benoist, N.M.A., Pfeifer, S., Simon-Lledó, E., Durden, J.M., Vandepitte, L., Appeltans, W., 2021. Recommendations for the Standardisation of Open Taxonomic Nomenclature for Image-Based Identifications. *Front. Mar. Sci.* 8, 620702. <https://doi.org/10.3389/fmars.2021.620702>
- Humphries, P., Keckeis, H., Finlayson, B., 2014. The River Wave Concept: Integrating River Ecosystem Models. *Bioscience* 64 (10), 870–882. <https://doi.org/10.1093/biosci/biu130>
- Ingle, R.W., 1996. *Shallow water crabs*. Field Studies Council, Cambridge, 224 pp.
- Intergovernmental Oceanographic Commission, 1983. Report of the Intergovernmental Oceanographic Commission on its activities during 1980–1982. In: *General Conference, 22nd session, 1983*. UNESCO, 62 Document code: 22 C/81, IOC/INF.536.
- Jamieson, A.J., Fujii, T., Solan, M., Matsumoto, A.K., 2009. First findings of decapod crustacea in the hadal zone. *Deep Sea Res. Pt. I.* 56, 641–647. <https://doi.org/10.1016/j.dsr.2008.11.003>
- Jóźwiak, P., Pabis, K., Brandt, A., Błażewicz, M., 2020. Epibenthic sled versus giant box corer—Comparison of sampling gears for tanaidacean species richness assessment in the abyssal benthic ecosystem. *Prog. Oceanogr.* 181, 102255. <https://doi.org/10.1016/j.pocean.2019.102255>
- Jóźwiak, P., Pabis, K., Sobczyk, R., Serigstad, B., 2022. A paradise for rare species: tanaidacean fauna of the West African continental margin. *Front. Mar. Sci.* 9, 779134. <https://doi.org/10.3389/fmars.2022.779134>
- Katz, L.M., 1973. The effects of water soluble fraction of crude oil on larvae of the decapod crustacean *Neopanope texana* (Sayi). *Environ. Pollut.* 5 (3), 199–204. [https://doi.org/10.1016/0013-9327\(73\)90088-8](https://doi.org/10.1016/0013-9327(73)90088-8)
- Kensley, B., 1980. Decapod and isopod crustaceans from the west coast of Southern Africa, including seamounts Vema and Tripp. *Ann. S. Afr. Mus.* 83 (2), 13–32.
- Kensley, B., 2006. Pelagic shrimp (Crustacea: Decapoda) from the shelf and oceanic waters in the southeastern Atlantic Ocean off South Africa. *Proc. Biol. Soc.* 119, 384–394. [https://doi.org/10.2988/0006-324X\(2006\)119\[384:PSCDFS\]2.0.CO;2](https://doi.org/10.2988/0006-324X(2006)119[384:PSCDFS]2.0.CO;2)
- Le Loeuff, P., Intès, A., 1999. Macrobenthic communities on the continental shelf of Cote-d'Ivoire. Seasonal and diel cycles in relation to hydroclimate. *Oceanol. Acta* 22, 529–550. [https://doi.org/10.1016/S0399-1784\(00\)87685-9](https://doi.org/10.1016/S0399-1784(00)87685-9)
- Levin, L.A., 2003. Oxygen minimum zone benthos: Adaptation and community response to hypoxia. *Oceanogr. Mar. Biol.* 41, 1–45. <https://api.semanticscholar.org/CorpusID:85701346>
- Levin, L.A., Dayton, P.K., 2009. Ecological theory and continental margins: where shallow meets deep. *Trends Ecol. Evol.* 24 (11), 606–617. <https://doi.org/10.1016/j.tree.2009.04.012>
- Levin, L.A., Sibuet, M., 2012. Understanding Continental Margin Biodiversity: A New Imperative. *Annu. Rev. Mar. Sci.* 4, 79–112. <https://doi.org/10.1146/annurev-marine-120709-142714>
- Lozach, S., Dauvin, J.C., Méar, Y., Murat, A., Davoult, D., Migné, A., 2011. Sampling epifauna, a necessity for a better assessment of benthic ecosystem functioning: An example of the epibenthic aggregated species *Ophiothrix fragilis* from the Bay of Seine. *Mar. Pollut. Bull.* 62, 2753–2760. <https://doi.org/10.1016/j.marpolbul.2011.09.012>
- Macpherson, E., 1988. New records of Decapods Crustaceans from the coast off Namibia/South West Africa, with the descriptions of two new species. *Inv. Pesq.* 52 (1), 51–66.
- Macpherson, E., 1991. Biogeography and community structure of the decapod crustacean fauna off Namibia (Sothest Atlantic). *J. Crustac. Biol.* 11 (3), 401–415. <https://doi.org/10.2307/1548466>
- Manning, R.B., Holthuis, L.B., 1981. West african brachyuran crabs (Crustacea: Decapoda), Smithsonian Contributions to Zoology 306, City of Washington, 379 pp. <https://doi.org/10.5479/si.00810282.306>
- Magurran, A.E., 2004. *Measuring Biological Diversity*. Blackwell Publishing, Oxford, 256 pp.
- Mavidis, M., Kitsos, M.S., Turkey, M., Koukouras, A., 2009. The taxonomical status of the genus *Pilumnus* Leach, 1815 (Pilumnidae, Decapoda, Crustacea) in the Mediterranean Sea, focusing on three species in the Aegean Sea. *J. Biol. Res. (Thessalon)* 11, 13–20.
- Maynou, F., Cartes, J.E., 2000. Community structure of bathyal decapod crustaceans off south-west Balearic Islands (western Mediterranean): seasonality and regional patterns in zonation. *J. Mar. Biol. Assoc.* 80, 789–798. <https://doi.org/10.1017/S0025315400002769>
- McCallum, A.W., Woolley, S., Błażewicz-Paszkwycz, M., Browne, J., Gerken, S., Kloser, R., Poore, G.C.B., Staples, D., Syme, A., Taylor, J., Walker-Smith, G., Williams, A., Wilson, R.S., 2015. Productivity predicts benthic species richness. *Glob. Ecol. Biogeogr.* 24, 462–471. <https://doi.org/10.1111/geb.12255>
- McLaughlin, P.A., 1980. Order Decapoda. In: *McLaughlin, P.A. (Ed.), Comparative morphology of Recent Crustacea*. W. H. Freeman and Company, San Francisco, 126–137.
- Moctar, S.M.M., Ramos, A., de Matos-Pita, S.S., Ramil, F., Krakstad, J.O., 2020. Seasonal variations in the diversity and structure of decapod communities in the changing hydrological scenario of the northwest African upwelling. *Mar. Biodivers.* 50 (37), 1–12. <https://doi.org/10.1007/s12526-020-01058-8>
- Monod, T., 1956. Hippidea et Brachyura ouest-africains. *Dakar, IFAN* 45, 574 pp.
- Muñoz, I., García-Isarch, E., Sobrino, I., Burgos, C., Funny, R., González-Porto, M., 2012. Distribution, abundance and assemblages of decapod crustaceans in waters off Guinea-Bissau (north-west Africa). *J. Mar. Biol. Assoc. UK* 92 (3), 475–494. <https://doi.org/10.1017/S0025315411001895>
- Nicol, E.A.T., 1932. The feeding habits of the Galatheidea. *J. Mar. Biol. Assoc.* 18 (1), 87–106. <https://doi.org/10.1017/S0025315400051316>
- Olomukoro, J.O., Dirisu, A.R., 2019. Ecological survey of soft-sediment marine benthos of the Gulf of Guinea, Nigeria. *NISEB J.* 11 (3).
- Pabis, K., Kędra, M., Gromisz, S., 2015. Distinct or similar? Soft bottom polychaete diversity in Arctic and Antarctic glacial fjords. *Hydrobiologia* 742, 279–294. <https://doi.org/10.1007/s10750-014-1991-5>
- Pabis, K., Sobczyk, R., Siciński, K., Ensrud, T., Serigstad, B., 2020. Natural and anthropogenic factors influencing abundance of the benthic macrofauna along the shelf and slope of the Gulf of Guinea, a large marine ecosystem off West Africa. *Oceanologia* 62 (1), 83–100. <https://doi.org/10.1016/j.oceano.2019.08.003>
- Pajuelo, J.G., Triay-Portella, R., Santana, J.I., González, J.A., 2015. The community of deep-sea decapod crustaceans between 175 and 2600 m in submarine canyons of a volcanic oceanic island (central-eastern Atlantic). *Deep Sea Res. Pt. I.* 105, 83–95. <https://doi.org/10.1016/j.dsr.2015.08.013>
- Poore, G.C.B., 2004. Systematics. In: *Poore, G.C.B. (Ed.), Marine Decapod Crustacea: a guide to identification*. Museum Victoria, Melbourne, 281–304.
- Poore, G.C.B., Avery, L., Błażewicz-Paszkwycz, M., Browne, J., Bruce, N.L., Gerken, S., Glasby, C., Greaves, E., McCallum, A.W., Staples, D., Syme, A., Taylor, J., Walker-Smith, G., Warne, M., Watson, C., Williams, A., Wilson, R.S., Woolley, S., 2015. Invertebrate diversity of the unexplored marine western margin of Australia: taxonomy and implications for global biodiversity. *Mar. Biodivers.* 45, 271–286. <https://doi.org/10.1007/s12526-014-0255-y>
- Reiss, H., Birchenough, S., Borja, A., Buhl-Mortensen, L., Craeymeersch, J., Dannheim, J., Darr, A., Galparsoro, I., Gogina, M., Neumann, H., Populus, J., Rengstorf, A.M., Valle, M., van Hoey, G., Zettler, M.L., Degraer, S., 2015. Ben-

- thos distribution modelling and its relevance for marine ecosystem management. ICES J. Mar. Sci. 72 (2), 297–315. <https://doi.org/10.1093/icesjms/fsu107>
- Rex, M.A., Etter, R.J., 2010. Deep-sea biodiversity: patterns and scale. Harvard Univ. Press, Cambridge, Massachusetts, 354 pp.
- Rodriguez, A., Drake, P., Arias, A.M., 1997. Reproductive periods and larval abundance patterns of the crabs *Panopeus africanus* and *Uca tangeri* in a shallow inlet (SW Spain). Mar. Ecol. Prog. Ser. 149 (1/3), 133–142. <https://www.jstor.org/stable/24857513>.
- Rosa, R., Boavida, J., Trübenbach, K., Baptista, M., 2012. Descending into the abyss: Bathymetric patterns of diversity in decapod crustaceans shift with taxonomic level and life strategies. Deep Sea Res. Part I. 64, 9–21. <https://doi.org/10.1016/j.dsr.2012.01.002>
- Sahlmann, C., Chan, T.Y., Benny, C.K.K., 2011. Feeding modes of deep-sea lobsters (Crustacea: Decapoda: Nephropidae and Palinuridae) in Northwest Pacific waters: Functional morphology of mouthparts, feeding behaviour and gut content analysis. Zoologischer Anzeiger – J. Comparative Zool. 250 (1), 55–66. <https://doi.org/10.1016/j.jcz.2010.11.003>
- Sant'Anna, B.S., Branco, J.O., de Oliveira, M.M., Boos, H., Turra, A., 2015. Diet and population biology of the invasive crab *Charybdis hellerii* in southwestern Atlantic waters. Mar. Biol. Res. 11 (8), 814–823. <https://doi.org/10.1080/17451000.2015.1024134>
- Schembri, P.J., 1981. Feeding in *Ebalia tuberosa* (Pennant) (Crustacea: Decapoda: Leucoshaedae). J. Exp. Mar. Biol. Ecol. 55 (1), 1–10. [https://doi.org/10.1016/0022-0981\(81\)90088-5](https://doi.org/10.1016/0022-0981(81)90088-5)
- Scheren, P.A., Ibe, A.C., Janssen, F.J., Lemmens, A.M., 2002. Environmental pollution in the Gulf of Guinea – a regional approach. Mar Pollut Bull 44 (7), 633–641. [https://doi.org/10.1016/S0025-326X\(01\)00305-8](https://doi.org/10.1016/S0025-326X(01)00305-8)
- Sigovini, M., Keppel, E., Tagliapietra, D., 2016. Open Nomenclature in the biodiversity era. Methods in Ecology and Evolution 7 (10), 1217–1225.
- Sobczyk, R., Czortek, P., Serigstad, B., Pabis, K., 2021. Modelling of polychaete functional diversity: Large marine ecosystem response to multiple natural factors and human impacts on the West African continental margin. Sci. Total Environ. 792, 148075. <https://doi.org/10.1016/j.scitotenv.2021.148075>
- Sobczyk, R., Serigstad, B., Pabis, K., 2023. High polychaete diversity in the Gulf of Guinea (West African continental margin): The influence of local and intermediate scale ecological factors on a background of regional patterns. Sci. Total Environ. 859 (1), 160046. <https://doi.org/10.1016/j.scitotenv.2022.160046>
- Stępień, A., Pabis, K., Sobczyk, R., Serigstad, B., 2021. High Species Richness and Extremely Low Abundance of Cumacean Communities Along the Shelf and Slope of the Gulf of Guinea (West Africa). Front. Mar. Sci. 8, 703547. <https://doi.org/10.3389/fmars.2021.703547>
- Tan, S.H., Ng, P.K.L., 2007. Descriptions of new genera from the subfamily Parthenopinae (Crustacea: Decapoda: Brachyura: Parthenopidae). RBZ Suppl. No. 16, 95–119.
- Thurston, M.H., Bett, B.J., Rice, A.L., Jackson, P.A.B., 1994. Variations in the invertebrate abyssal megafauna in the North Atlantic Ocean. Deep Sea Res. Pt. I 41 (9), 1321–1348. [https://doi.org/10.1016/0967-0637\(94\)90100-7](https://doi.org/10.1016/0967-0637(94)90100-7)
- Ukwe, C.N., Ibe, C.A., Alo, B.I., Yumkella, K.K., 2003. Achieving a paradigm shift in environmental and living resources management in the Gulf of Guinea: the large marine ecosystem approach. Mar. Pollut. Bull. 47 (1–6), 219–225. [https://doi.org/10.1016/S0025-326X\(02\)00473-3](https://doi.org/10.1016/S0025-326X(02)00473-3)
- Ukwe, C.N., Ibe, C.A., Nwilo, P.C., Huidobro, P.A., 2006. Contributing to the WSSD targets on oceans and coasts in west and central Africa: The Guinea current large marine ecosystem project. Int. J. Oceans Oceanogr. 1 (1), 21–44.
- Wägele, J.W., 2005. Foundations of Phylogenetic Systematic. Verlag Dr Friedrich Pfeil, München, 365 pp.
- Wolfe, J.M., Breinholt, J.W., Crandall, K.A., Lemmon, A.R., Lemmon, E.M., Timm, L.E., Siddall, M.E., Bracken-Grissom, H.D., 2019. A phylogenomic framework, evolutionary timeline and genomic resources for comparative studies of decapod crustaceans. Proc. R. Soc. B. 286, 1–10. <https://doi.org/10.1098/rspb.2019.0079>
- Woolley, S.N.C., Tittensor, D.P., Dunstan, P.K., Guillera-Arroita, G., Lahoz-Monfort, J.J., Wintle, B.A., O'Hara, T.D., 2016. Deep-sea diversity patterns are shaped by energy availability. Nature 533, 393–396. <https://doi.org/10.1038/nature17937>

Available online at www.sciencedirect.com

ScienceDirect

journal homepage: www.journals.elsevier.com/oceanologia

ORIGINAL RESEARCH ARTICLE

Characterization of suspended particles at different glacial bays at Spitsbergen

Katarzyna Dragańska-Deja*

Institute of Oceanology, Polish Academy of Sciences, Sopot, Poland

Received 11 May 2023; accepted 6 December 2023

Available online 14 December 2023

KEYWORDS

Glacial meltwater;
Svalbard;
Geology;
Particular Size
Distribution;
Mineralogy

Abstract Particle size distribution (PSD) and concentration of mineral-suspended sediment released from melting glaciers are important factors affecting the local marine ecosystem, e.g. affecting the light availability in water columns, thus changing underwater light climate for photosynthetic organisms. We examined the characteristics of various samples of natural mineral assemblages suspended in different glacial bays in Hornsund and Kongsfjord at Spitsbergen. The concentrations of the total mass of particles (TSM) in suspended sediment as well as particular organic matter (POM) and particular inorganic matter mass (PIM) together with mineralogical composition and particular size distribution (PSD) were determined.

In this study, we investigated the PSD properties and variability in the front of different tidewater glaciers based, laser diffractometer measurements (LISST-100x), and XRD – techniques to obtain the mineralogical composition of the particles. The sampled sites are under the strong influence of freshwater discharge from the glacier. At each station, inorganic particulate matter contributed up to 98% to total suspended matter with the particle concentration of the particle reaches up to 111 mg/l with mean surface PSD slopes ranging from 3.24 to 3.85. The result provides valuable baseline information on the observed range of variability of the size of suspended particles due to glacial runoff and the presence of particles of different mineral origin in the glacial bays.

© 2023 Institute of Oceanology of the Polish Academy of Sciences. Production and hosting by Elsevier B.V. This is an open access article under the CC BY-NC-ND license (<http://creativecommons.org/licenses/by-nc-nd/4.0/>).

* Corresponding author at: Institute of Oceanology Polish Academy of Sciences, Powstańców Warszawy 55, 81-712 Sopot, Poland.
E-mail address: katarzyna@iopan.pl

Peer review under the responsibility of the Institute of Oceanology of the Polish Academy of Sciences.



<https://doi.org/10.1016/j.oceano.2023.12.001>

0078-3234/© 2023 Institute of Oceanology of the Polish Academy of Sciences. Production and hosting by Elsevier B.V. This is an open access article under the CC BY-NC-ND license (<http://creativecommons.org/licenses/by-nc-nd/4.0/>).

1. Introduction

Intense recession and glaciers melting in polar regions are some of the most spectacular effects of climate change (Overland et al., 2019). These processes are accompanied by intensification of meltwater discharge occurring as sediment plums with mineral particles (Urbanski et al., 2017; Zajączkowski, 2008). The trend and intensity of these changes are therefore a good, sensitive indicator of climate change, and are an important factor affecting light availability in the water column and thus local marine ecosystems (Deja et al., 2019). Quantifying meltwater discharge is a valuable tool for understanding the hydrology of tidewater glaciers and other environmental processes. Suspended particles are a very important component of natural water and play a significant role in its optical properties. High concentrations of minerals are also common in coastal waters, where large amounts of suspended particles are discharged from rivers or other sources, such as bottom resuspension, shore erosion by wave action and glacial melting (Babin and Stramski, 2004; Moskalik et al., 2018; Woźniak et al., 2010). In such waters, mineral particles can dominate the optical properties of waters, by influencing on spectral light distribution due to the absorption and scattering process (Woźniak and Stramski, 2004). The amount and distribution of the suspension affect the underwater light field and, thus, photosynthetic organisms and organisms living at the bottom (Deja et al., 2019; Urbanski et al., 2017; Węstawski et al., 1995). Mineral concentrations in water typically decrease with distance from land. The particle size of suspended particles determined the differential sinking rates of various types of particles and thus determines horizontal and vertical fluxes in the water column affect the distribution and composition of glacial sediments in the bays (Moskalik et al., 2018; Szczuciński et al., 2009; Zajączkowski, 2008).

Lithogenic particle meltwater run-off into glacial fjord in one of the most important drivers of benthic community change (Braeckman et al., 2021; Clark et al., 2017; Deja et al., 2016) and plankton distribution (Deja et al., 2019; Szeligowska et al., 2022, 2021). It was found that phytoplankton biomass near glacier front depending on

the glacier bedrock composition based on geological map (Halbach et al., 2019) but still lack information about mineral composition in water columns measured in situ.

Light scattering by particles depends on their composition, refraction index, size and shape. The study aims to describe and characterize particulate suspension in fjords waters concerning the difference in the mineral composition in different parts of the fjords (XRD method) by describing in situ parameters (suspended particular matter concentration) and particular size distribution (LISST 100X). The characteristics of the predominant mineral particles will provide a completely new quality for describing the contribution of calcium carbonate and other minerals by melting glaciers and establish a baseline of optical properties that may be useful in remote sensing interpretation or modelling of effects of climate change.

2. Material and methods

2.1. Study area

Hornsund is a fjord on the southwest side of Spitsbergen island. Is an open, medium size Arctic glacial fjord (30 km length, 12–15 km wide). Into the water of Hornsund flow cliffs of twelve tidewater glaciers (Błaszczuk et al., 2009). Is Bedrock in that area covers different geological formations, from metamorphic rocks of the Precambrian Hecla Hoek complex in northwestern part, through the lower Paleozoic carbonate rocks in the central part, to the west to the upper Mesozoic to the east (Gorlich, 1987). The sedimentary cover rocks start on the eastern side of Burgerbukta and Samarinvagen. On the northern side, it starts with Devonian conglomerates and sand stones ('Old Red'), followed by the Kapp Starostin Formation with its hard, fossil rich limestones (Dallmann, 2015).

In situ data were collected also in Kongsfjorden (79°N, 12°E, Figure 1) which is located in the northwest coast of Spitsbergen. Is medium-sized, open fjord, 27 km long and varying in width from 4 km at its head to 10 km at its mouth (Svendsen et al., 2002). Kongsfjorden is surrounded by five polythermal tidewater glacier: Blomstrandbreen,

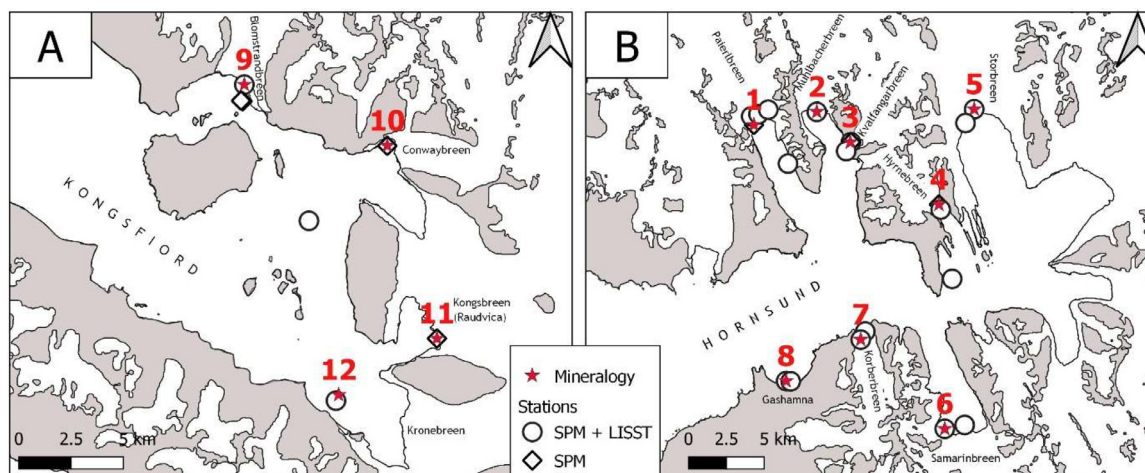


Figure 1 Map of the study area in Kongsfjorden (A) and Hornsund fjord (B).

Kongsvegen, Kronebreen, Kongsbreen and Conwaybreen. (Błaszczuk et al., 2009; Husum et al., 2019). Bedrock composition vary from carbonate bedrock with Devonana Old Red Sandstone deposit in the southern basin to domination of phyllite and quartzite minerals build bedrock in the northern basin (Dallmann, 2015).

2.2. Sampling design

The Supplementary Table 1 provides a detailed description of the surrounding rocks at the sampling site. The presented material was collected in the West Spitsbergen fjords using a Zodiac boat during the summer season (27th of July to 8th of August) in 2016–2018 at sampling station located in Hornsund and Kongsfjord fjords in the vicinity of tidewater glaciers. This study uses in situ measurements: LISST profiles (12 stations), discrete water sampling at the surface (0 m) for SPM (29 stations) and for mineralogical composition (12 stations).

At the time of sampling, the mean air temperature in Hornsund was approximately 5.7°C, and in Kongsfjord it was around 4.2°C. No precipitation was recorded in Hornsund (Wawrzyniak and Osuch, 2019), and the average rainfall in Kongsfjord was 3.4 mm (Supplementary Table 2).

2.2.1. Particle size distribution

The particle size distribution (PSD) was measured in situ during field measurements with an Laser In Situ Scattering and Transmissometry – LISST-100X type B instrument (Sequoia Scientific, Inc.), which estimates the PSD based on optical diffraction. LISST-100X provides the distribution of particle volume concentration in 32 size classes logarithmically spaced within the range 1.25–250 µm and the beam attenuation coefficient *c* at 670 nm. The LISST-100X measurement principle is based on Mie's theory and PSD is obtained from laser diffraction technology. The signal from instrument was corrected for imperfections in the optics and pure water scattering by background measurements using deionised water.

On order to assess the volumetric PSD, data were normalized by the width of each class to obtain instrument independent particle size distribution, following:

$$C_{vol}(size(i)) = \frac{C_{vol,i}}{\max(range(i)) - \min(range(i))}$$

were, *size(i)* is median diameter of particle size class *i* and *range(i)* is a the width of *i*-th class.

The surface PSDs were obtained by averaging PSDs from 1 to 5 m depth.

To describe shape of the aggregate size distribution and relationship between particle abundance and size PSD slope was calculated (Stemann and Boss, 2012).

2.2.2. Mass concentration determined by filtration

Surface – water samples at measured volume were filtered through specially prepared and 3-times pre-weighed fiber glass filters (Whatman GF/F, 25 mm diameter, 0.7 µm pore size). To determined concentration of total suspended matter (SPM) standard laboratory method was applied (Woźniak et al., 2016). To remove sea salt, at the end of the filtration of the samples, the filters were rinsed with 120 ml of deionized water. The filters were weighted

to determined total mass of suspended material (SPM) and combusted at 450 for 4 h and reweighted to obtain particulate inorganic matter concentration (PIM). The particulate organic matter concentration (POM) was obtained by subtracting PIM from SPM. Three replicates were measured at each station.

2.2.3. Mineralogical composition determined by X-Ray Refractive Diffraction (XRD)

Selected water samples with natural composition of particles were dried and analyzed with X-ray diffraction (XRD) method to identify major mineral species present in the samples. Mineral identification was based on matching the peaks of a given mineral species in the sample with a standard pattern of that mineral species from Inorganic Crystal Structure Database and Crystallography Open Database. A small amount of powder of each sample was ground in an agate mortar to a fraction of about 10 µm. The obtained powders were applied to zero-background holder silicon pads, which were then mounted in metal company rings. Co K α ($\lambda=1,789010 \text{ \AA}$) radiation was used, at 40 kV and 40 mA. The rings were scanned from 5 to 75° 2 θ with 0.02° 2 θ step with pulse counting time 7 seconds. All measurements were made using a PANalytical X-ray diffractometer, model X'Pert Pro MPD PW3040 /60.

The obtained diffractograms were processed in the High-Score + computer program of the Panalytical company (version 4.8) using the ICDD pattern database, PDF 4+ (version 2018). For quantitative calculations, ICSD (version 3.5 from 2015) and COD (Crystallography Open Database), version 07.2016 for PANalytical were used, containing structural data of all matched patterns.

2.3. Data analysis

In situ vertical profiles of the PSD were obtained by deployed LISST instrument through the water column. LISST data of angular scattering intensity and transmission were median filtered, then averaged into one-meter depth signals bins, which were then processed using the manufacturer's script for Matlab software to calculate vertical profiles of PSD and the particle beam attenuation coefficient at 670 nm.

All the plots were generated in Python 3.9.7 using Matplotlib 3.1.1 Seaborn and Pandas 1.0.5 (McKinney, 2010).

3. Results

3.1. Mineral composition

XRD analyses of the suspended sediment samples from the northern bays of Hornsund, from Burgerbukta to Brepolen, have revealed distinct mineralogical differences when compared to the stations located on the southern shore. Notably, significant amounts of carbonate minerals were observed at three stations situated on the southern part of Hornsund, namely Gashamna (8), near Korberbreen (7), and in Samarinavgen (6) (refer to Figure 2). These samples exhibited a marked decrease in the proportion of feldspars, as compared to other regions. In Gashamna, Calcite is the

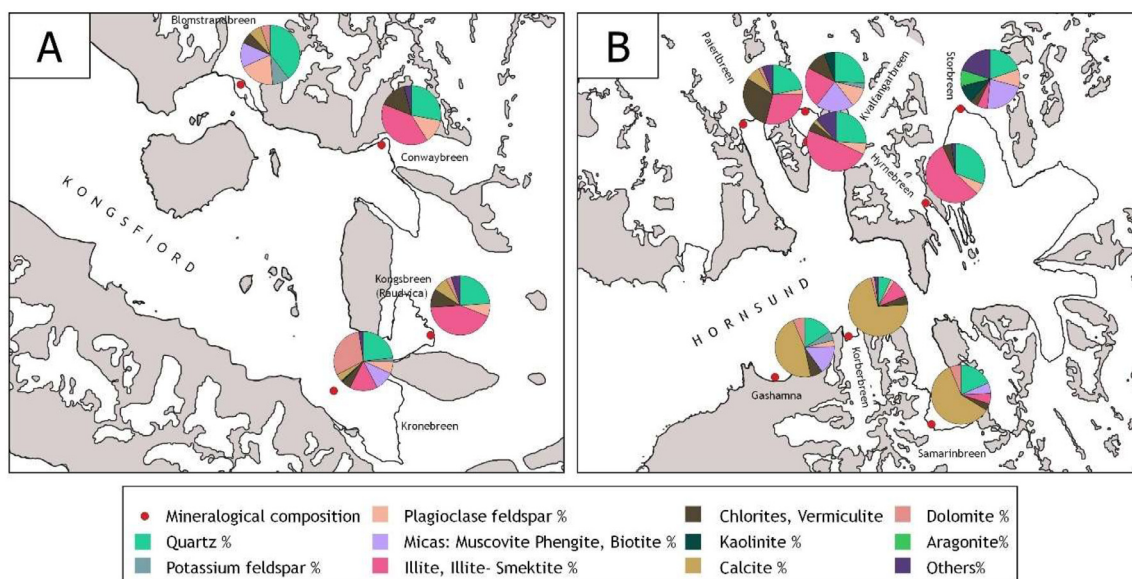


Figure 2 Map of the spatial distribution of mineral composition of suspended sediment in the studied area in Kongsfjorden (A) and Hornsund fjord (B).

principal phase, constituting approximately 47% by weight, while Quartz is present in smaller amounts, approximately 16% by weight. Calcite is accompanied by calcium and magnesium carbonate, known as Dolomite, and its share does not exceed 7% by weight. The low-angle range of the diffractogram reveals the presence of Chlorites from the Shamosite-Clinochlore series and light micas, with the share of Chlorite calculated to be 6 to 7% and the share of mica to be 15 to 16% by weight. The phase composition is further complemented by Feldspars, with the potassium varieties predominating at approximately 5%, in comparison to the sodium variety at approximately 3%. Near the front of the Korberbreen glacier, the sample comprised primarily calcite (approximately 72% by weight), which was accompanied by illite (10%) and quartz (7%). While the share of dolomite was relatively low, at approximately 2% by weight, the mineral composition was further complemented by feldspars, primarily the sodium variety (albite) at approximately 2% by weight, and Clinochlore below 5%. The primary mineral phase present in Samarinvagen is calcite. Its concentration in the sample was 60% by weight. The second carbonate identified in the sample, dolomite, was present in a minimal amount, approximately 6% by weight. The phase composition was further comprised of silicate and aluminosilicate phases, as well as clay minerals. The quantity of quartz in the sample exceeded 18% by weight. The mineral composition of Paierlbreen sample number 1 is well-balanced and comprises of minerals from the chlorite group (30%), illite–smectite (29%), quartz (22%), and an insignificant amount of feldspar (3%). In contrast, sample number 2, located in front of the Muhlbacherbreen glacier, has a lower content of clay minerals with 11.5% Chlorites, 22.1% Illite, and 5.9% kaolinite. Nevertheless, it still contains significant amounts of quartz (25.6%) and feldspars (13.9%), as well as micas (20.9%).

In other areas of the Hornsund fjord, such as the Kvalfangbreen glacier (3) and Hyrnebreen (4), the composition of the samples was found to be quite similar (Table 1). The

samples consist of approximately half illite, with a quarter of the weight being quartz, plagioclase at 6%, and chlorite at around 5%. In contrast, the XRD analysis of sample 5 from Storebreen (5) revealed a different mineral composition, with the majority of clay minerals consisting of kaolinite (9.4%), illite (5.6%), and chlorites (4.3%), along with quartz (19.7%), micas (22.4%), and a small percentage of feldspar (9.5%) (Table 1, Figure 2).

In Kongsfjorden, a sample from the most northerly location has significantly less clay minerals than the other samples (10, 11, and 12), with chlorite accounting for only 6.2%. The principal components of the sample were quartz (39.5%), plagioclase (19.6%), potassium feldspar (9.3%), micas (13.4%), and carbonates (calcite 6.8% and dolomite 5.3%). The eastern stations (9 and 10) showed high similarities, with the principal components being clays consisting of illite and smectite (approximately 40%), approximately 25% quartz, around 10% plagioclase (13 and 7), and 10% and 15% chlorite. The 11th sample had the highest content of carbonates, consisting of calcite and dolomite (8% and 3%, respectively). The sample from the front of the Kronebreen glacier had a varied composition, with the highest content of dolomite in both fjords (30.1%), quartz (23.2%), feldspars (8.5%), micas (10.6%), illite and smectite (15.2%) chlorites (5.1%), and calcite (4.0%) (Table 1, Figure 2).

Given the nature of the samples and the XRD method employed (as detailed in the methods section), certain assumptions were necessary to be made in the results description. Specifically, halite and calcium sulfates (Gypsum, Bassanite) were deemed to be products of the evaporated seawater. This is also reflected in the Table 1, where a low content of iron oxides and hydroxides is deemed uncertain.

3.2. Concentration and Particle size distribution of suspended particular matter

At all the stations examined, the percentage of Particulate Inorganic Matter (PIM) significantly exceeded that of

Table 1 Mineralogical composition of the sampling site in Hornsund and Kongsfjord by XRD analysis.

No.	Quartz %	Potassium feldspar [%]	Plagioclase feldspar [%]	Micas: Muscovite Phengite, Biotite [%]	Illite, Illite-Smectite [%]	Chlorites, Vermiculite	Kaolinite [%]	Calcite [%]	Dolomite [%]	Aragonite [%]	Others [%]
1	22.0		3.0		29.0	30.0		8.0	2.0		6.0
2	25.6	3.1	10.8	20.9	22.1	11.5	5.9				
3	26.0		6.0		49.0	5.0		2.0	0.0		12.0
4	31.0		6.0		56.0	5.0		0.0	0.0		2.0
5	19.7		9.5	22.4	5.6	4.3	9.4	0.5		8.7	20.0
6	18.5			5.8	5.8	3.7		60.0	6.2		
7	7.0		2.0		10.0	5.0		72.0	2.0		2.0
7	24.3		5.9	17.3		11.5		33.4	4.9		2.6
8	15.9		3.4	15.5		6.7		46.8	6.4		
9	39.5		19.6	13.4		6.2		6.8	5.3		
10	28.0		13.0		40.0	15.0		0.0	0.0		4.0
11	24.0		7.0		43.0	10.0		8.0	3.0		5.0
12	23.3	1.9	6.6	10.6	15.2	5.1	0.8	4.0	30.1		2.5

Particulate Organic Matter (POM) and averaged 89.9%. Maximum values of inorganic matter were recorded at stations located near the meltwater plume, with percentages ranging from 82.5% to 97.9%. While the share of organic matter slightly increased with distance from the outflow site, the range of inorganic matter share remained high, ranging from 67.9% to 92.7% (Figure 3).

Figure 4 illustrates the spatial distribution of suspended sediment matter concentration in the surface layer. The maximum concentrations of SPM occur in the vicinity of Paierlbreen (1), Hyrnebreen (4), Kvalfangerbreen (3), Gashamna (8) in Hornsund, and Conwaybreen (10) in Kongsfjord. In Hornsund, the total suspended matter concentration (TSM) near the meltwater source within three glacial bays where carbonate minerals are prevalent (6, 7, and 8) varies from 16.7 mg/dm³ to 71.71 mg/dm³, with a mean value of 36.72 mg/dm³. The mean particle inorganic concentration (PIM) is 33.83 mg/dm³ (14.38–68.22 mg/dm³). The organic component of the suspended matter, on average, does not exceed 14% of TSM (Figure 3). At slightly distant stations, the average TSM value is only 12.89 mg/dm³ (SD 2.54). SPM concentrations in Kongsfjord follow the same horizontal gradient as in Hornsund, with the highest levels of inorganic material also recorded near the source of the meltwater plume (up to 111.66 mg/dm³) (Figure 3). The total suspended particulate matter (TSM) concentrations in both fjords decrease with distance from the meltwater plume source in the surface layer.

3.3. Particle Size distribution

We observed median particle sizes in Hornsund ranging from 82.90 μm to 103.75 μm, while in Kongsfjord, we observed contrasting values. Notably, very small particles were found near Blomstradbreen (9) at a size of 37.86 μm, while large particles were found near Kronebreen at a size of 123.38 μm. In Hornsund, the biggest particles were observed near Hyrnebreen (4) at a size of 117.37 μm and Korberbreen (7) at a size of 103.75 μm (Figure 5, Table 2).

The PSD slopes ranged on surface layer (1–5 m) from 3.24 to 3.67 in Hornsund. In Kongsfjord near Blomstrandbreen PSD slope is the highest – 3.85, near Kronebreen is 3.26. Steeper slopes indicated that the relative abundance of smaller particles was higher, which is clearly visible for station 9 near Blomstrandbreen. On all depths o at 9 station median value of PSD Slope was higher than 3.5, and median size of particles was less than 80 μm. PSD slope near Gashamna has a very wide range of value 3.24 +/- 0.46 (Figure 6, Table 2).

The results of the ANOVA test indicate that there is a statistically significant difference between the means of the stations for median particle size (F=13.63, p=2.09e-14) and PSD slope (F=8.26, p=2.86e-9). The F-statistic values provide strong evidence against the null hypothesis of equal means and the extremely small p-values further confirm this. In order to determine which specific station differ from each other, a post hoc test Tukey was conducted. The Tukey test revealed significant differences between Station 9 on Blomstrandbreen and all other stations (Supplementary Table 3).

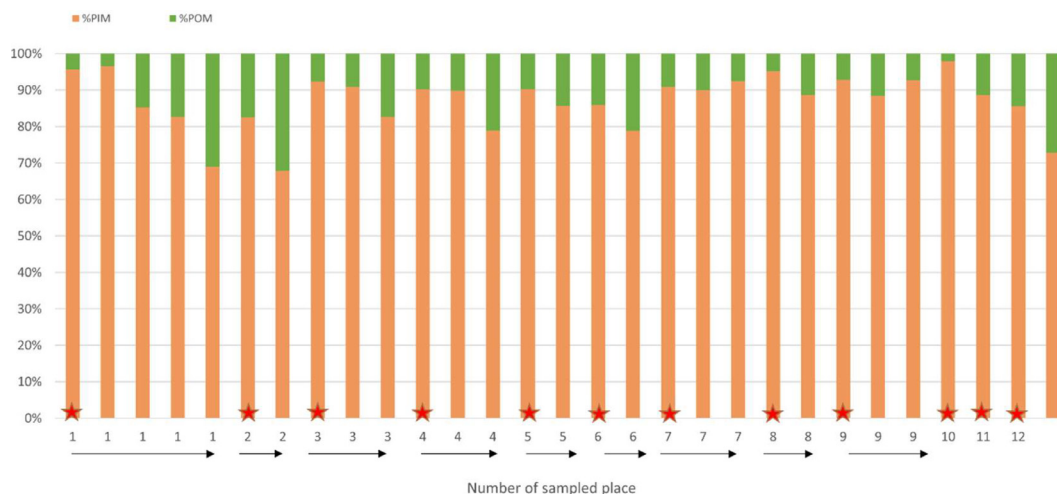


Figure 3 The bar chart exhibited the distribution of Particular Inorganic Matter (PIM) and Particular Organic Matter (POM) in percentage shares, with each examined glacial bay assigned a numerical designation consistent with Figure 1. The symbols employed in the graph, namely stars and arrows, denoted the collection sites for XRD analysis and the increasing distance from the site of water sampling for mineralogical composition, respectively.

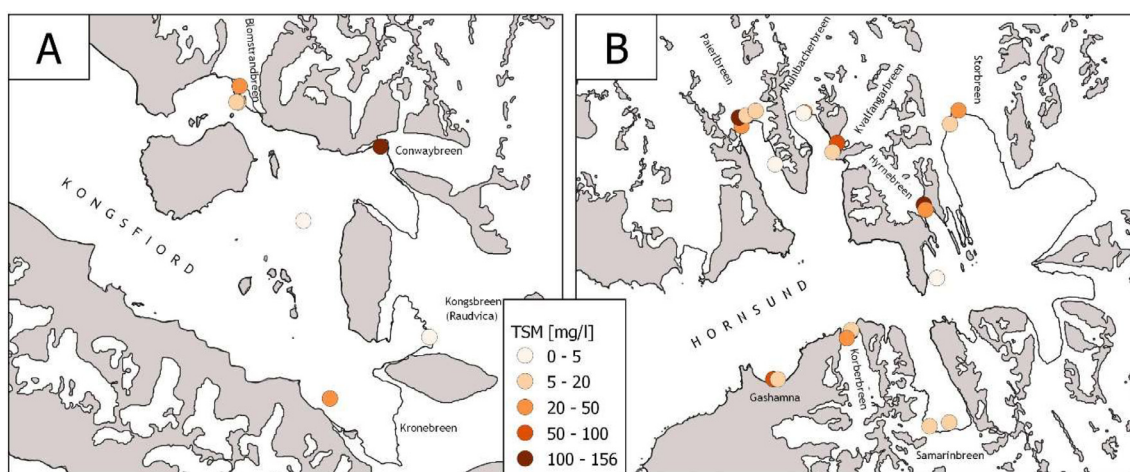


Figure 4 Map of the spatial distribution of Total Suspended Matter Concentration in Kongsfjord (A) and Hornsund (B).

Table 2 Basic statistic of Median size of Particle, Particular Size Distribution slope (PSD slope) and Total Particuar volume concentration (TotVC).

Sampling site	Median size [μm]	std	PSD slope mean	std	TotVC mean	std
1	81.06	3.49	3.29	0.23	111.21	58.27
2	91.07	8.18	3.39	0.08	33.05	4.39
3	87.34	6.40	3.32	0.02	31.80	16.37
4	117.37	12.08	3.37	0.07	39.62	22.63
5	82.90	4.98	3.42	0.09	122.11	26.23
6	95.38	1.80	3.67	0.12	23.75	1.51
7	103.75	16.31	3.61	0.16	79.51	27.83
8	99.80	22.86	3.24	0.46	60.01	78.91
9	37.86	26.15	3.85	0.09	49.32	13.02
12	123.38	13.08	3.26	0.02	95.94	31.26

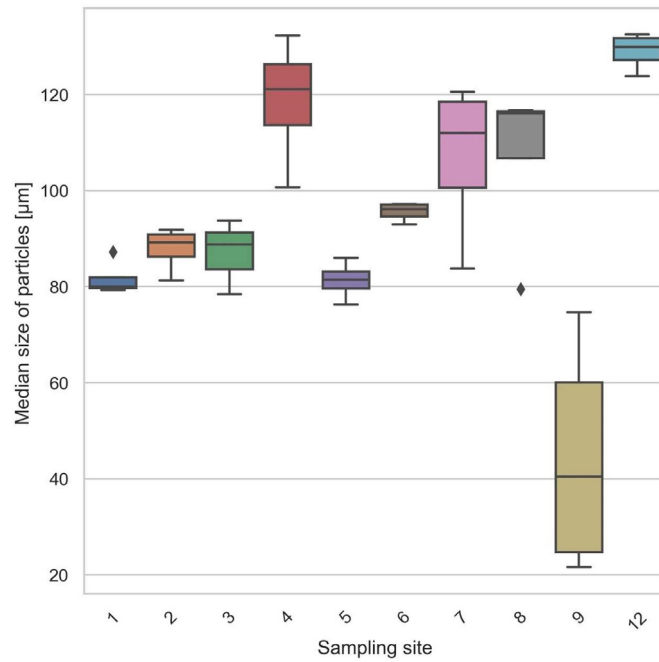


Figure 5 Boxplots of median size of particles over sampling site; box 25–75% quartiles, whiskers – non-outlier range, diamonds – outliers.

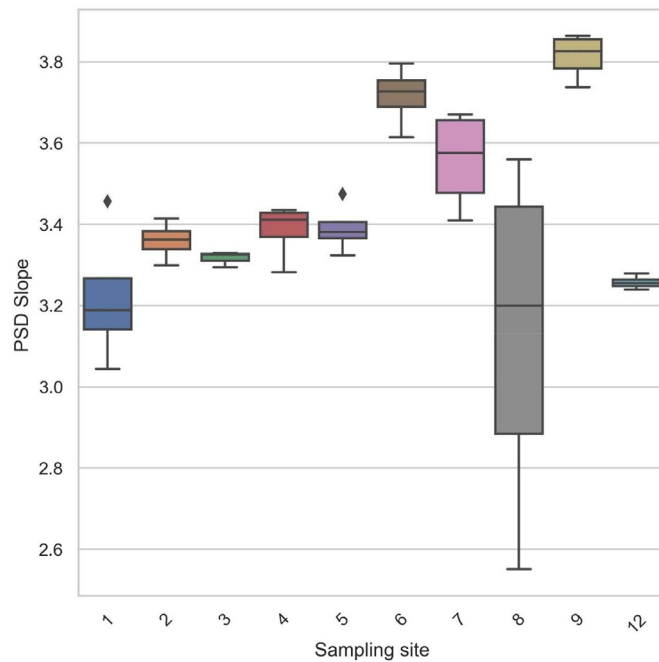


Figure 6 Boxplots of PSD slope over sampling site; box 25–75% quartiles, whiskers – non-outlier range, diamonds – outliers.

4. Discussion

The mineralogical composition of suspended sediments in glacial environments is a crucial element that influences polar ecosystems. Our research has advanced our understanding of the spatial variability of particle size distribution and suspended particle concentration in the region, as well as the influence of marine and land-terminating glaciers on

the mineral composition of particles suspended in the waters. In this study, we examined eight glacial bays in Hornsund and four in Kongsfjord, which allowed us to provide a comprehensive comparison of the conditions provided by melting glaciers. While the study of the characteristics and distribution of particles in the bays of glacial fjords is of a local nature, it is likely that the process is similar in other fjords. The melting of glaciers and the drainage of

meltwater through glacial outflows are recognized as the main sources not only of freshwater supply into the fjord but also of accumulated mineral and organic matter (Anesio and Laybourn-Parry, 2012; Hood et al., 2015, 2009). The elevated levels of particulate matter in the water column lead to significant absorption of light, resulting in a decrease in the vertical extent of the euphotic zone, as reported by Weslawski et al. (1995) and Konik et al. (2021). This decrease was also observed in the Secchi depth measurements taken in all of the studied glacial bays. The properties of particles and marine snow aggregates, such as size, structure, and transparency, also change drastically across gradients caused by the various glacier types (Trudnowska et al., 2021). Therefore, knowledge about the amount, nature, and fate of the material released to the water column through increasing glacial melting is critical to understanding the biogeochemical mechanisms that sustain and/or threaten life in the surrounding ecosystems.

Our findings demonstrate that the concentration of organic matter (POM) is significantly lower in proximity to glacier cliffs, in comparison to the concentration of inorganic matter (PIM) which ranges from 82.5% to 97.9% (Figure 3). The surface turbid plume exhibited a noticeable decline in SPM concentration, from the meltwater source, during the export process. This reduction could be attributed to several mechanisms. For instance, a significant sedimentation of the coarser sediment fraction had already been documented in the region (Svendsen et al., 2002). Researchers estimated that approximately 90% of the sediment originating from the Kronebreen-Kongsvegen complex was deposited in the first 400m from the ice front due to gravitational forces. However, this high concentration of inorganic matter, observed in close proximity to glaciers, is crucial in the biogeochemical cycle, as supported by previous studies (Bhatia et al., 2013; Hawkings et al., 2014). With respect of climate change, the special attention should be given to the carbonate minerals of the suspended material. Moving glacier ripping minerals form solid rocks found in its bedrock and transported with meltwater to marine environment. CaCO_3 is one of the more mobile chemical compounds and could play important role in circulation of greenhouse gas CO_2 (Bukowska-Jania, 2007; Fairchild et al., 1994; Martini et al., 2001). In the immediate vicinity of three bays, including Gashamna (8), near Korberbreen (7), and in Samarinvagen (6), as depicted in Figure 2, XRD analysis revealed a high content of carbonate minerals. Carbonate rocks of early Ordovician age, which may have been eroded by glaciers, are present in the area. Additionally, Supplementary Table 1 provides further details on the rocks found in the region. While carbonate rocks also occur in the vicinity of Paierlbreen (1), mineralogical analysis of these rocks revealed only 8% calcite by weight and less than 2% dolomite. The Cambrian and Early Ordovician age of the rocks was ascertained through geological studies, and these rocks are abundant on both sides of Burgerbukta Bay. However, it is likely that these rocks represent only a small portion of the Paierlbreen glacier bedrock. In light of the findings reported by Ericson et al. (2019, 2018), it is noteworthy that the freshwater input resulting from glacier retreat can enhance the uptake of CO_2 and exacerbate ocean acidification. However, the impact of such freshwater input can be diminished or even entirely mitigated if it contains a higher

alkalinity due to its passage through carbonate or silicate-rich bedrock. The nutrient delivery from melting glaciers affects the primary productivity in the ocean, as stated by Arrigo et al. (2017) and Bhatia et al. (2013). Historically, it was believed that nitrogen (N) and phosphorus (P) were the primary nutrients essential for maintaining primary productivity. However, recent evidence suggests that silicon (Si), iron (Fe), and other micronutrients are also crucial for maintaining primary productivity and shaping the phytoplankton community structure (Gerringa et al., 2012; Moore et al., 2013; Sunda, 2012). For instance, Si is vital for diatoms, which are the main component of marine phytoplankton blooms and play a significant role in ocean ecology and the global carbon cycle, as it is the key component of their cell walls. Additionally, the supply of Fe is critical for building the intercellular photosynthetic apparatus and nitrogen acquisition enzymes.

The mineral composition of the studied glacial bays varies significantly (as depicted in Figure 2) due to differences in glacial bedrock geology, age, and glacier erosion rate (as presented in Supplementary Table 1). The mechanical denudation of bedrock in glaciated catchments and elevated specific discharge (Hallet et al., 1996) are key factors that increase the supply of nutrients in polar regions. Bedrock crushing due to glacial erosion exposes trace reactive components in the rock to chemical weathering and generates highly reactive particles with large surface areas. The transport of glacially-derived nutrients from land to sea occurs either as dissolved or adsorbed on the suspended matter or reactive minerals. In glacierised basins, the flux of labile nutrients associated with suspended matter is significantly higher than the dissolved load (Anderson et al., 2000). The suspended matter with a very high specific surface area $>4 \text{ m}^2\text{g}^{-1}$ (Telling et al., 2015) is formed from physical weathering through the comminution of bedrock. These properties facilitate the adsorption of dissolved nutrients on the surface of suspended particles and create highly reactive amorphous mineral surfaces (Hawkings et al., 2018, 2014).

It has been observed through in situ measurements in this study that the particle median size characteristics in different glacial bays vary depending on the dominance of distinct mineralogical compositions (Figure 5). This may indicate differences between meltwater plums regarding particle sinking, aggregation and particle composition. The study conducted by Sagan and Darecki (2018) reported that the median particle size in the Kongsfjorden glacier area was $110.4 \mu\text{m}$ and $79.4 \mu\text{m}$ in the Hornsund area. In our study, measurements were conducted in the close vicinity of tidewater glaciers or river plumes in Hornsund, and the median size ranged from $82.9 \mu\text{m}$ to $103.7 \mu\text{m}$. It can be concluded that at the outflow, the particles are larger, but they can sediment quite quickly, and the finest particles remain on the surface until they form larger clusters. This trend of increasing particle size with distance from the shore was also observed in two northern Svalbard fjords, Wijdefjorden and Rijpfjorden (Trudnowska et al., 2020).

In conclusion, the multifaceted interactions between glacial processes and marine ecosystems underscore the profound implications of glacial meltwater on polar marine environments, highlighting the urgency for continued research and monitoring in these rapidly changing landscapes.

5. Conclusion

The glacial meltwater runoff in both Spitsbergen fjords significantly increases the concentration of silicate, carbonate, and other minerals in the surface water. Tidewater glaciers also contribute to a turbid water plume during the summer months, which alters the optical properties of the glacial bay. A comprehensive set of XRD, LISST, and SPM measurements were conducted, revealing several key findings: (1) The mineralogical composition of the suspended sediment exhibits a high degree of spatial variability; (2) SPM concentrations are very high near the source of the meltwater plume and contain a high content of mineral particles, particularly inorganic matter, with concentrations ranging from 82.5% to 97.9% of TSM; (3) The particle size distribution (PSD) reflects the mineral composition of the suspended sediment. These findings provide valuable insights into the mineralogical composition of suspended sediments in glacial environments and its broader implications for polar ecosystems. The findings have potential applications in understanding biogeochemical mechanisms, light absorption patterns, and nutrient delivery mechanisms in glacial regions.

Declaration of competing interest

The authors declare that they have no known competing financial interests or personal relationships that could have appeared to influence the work reported in this paper.

Acknowledgements

I extend my sincerest thanks to T. Krzykawski of the Silesia University for the XRD analysis, to A. Sztuczynska of the Polish Geological Institute National Research Institute for the XRD analysis, and to Mateusz Damrat for his invaluable geological knowledge and fieldwork support, as well as to Kajetan Deja for his support during fieldwork.

This study was the result of the implementation of the research project No. 2015/19/N/ST10/01659 financed by the National Science Center, Poland and financially supported the Norwegian Financial Mechanism 2014–2021 (85%) National Science Centre (15%) within GRIEG Programme (2019/34/H/ST10/00504).

Supplementary materials

Supplementary material associated with this article can be found, in the online version, at <https://doi.org/10.1016/j.oceano.2023.12.001>.

References

Anderson, S. P., Drever, J. I., Frost, C. D., Holden, P., 2000. Chemical weathering in the foreland of a retreating glacier. *Geochim-*

- ica at *Cosmochimica Acta* 64 (7), 1173–1189. [https://doi.org/10.1016/S0016-7037\(99\)00358-0](https://doi.org/10.1016/S0016-7037(99)00358-0)
- Anesio, A.M., Laybourn-Parry, J., 2012. Glaciers and ice sheets as a biome. *Trends Ecol. Evol.* 27, 219–225. <https://doi.org/10.1016/j.tree.2011.09.012>
- Arrigo, K.R., van Dijken, G.L., Castelain, R.M., Luo, H., Rennermalm, Å.K., Tedesco, M., Mote, T.L., Oliver, H., Yager, P.L., 2017. Melting glaciers stimulate large summer phytoplankton blooms in southwest Greenland waters. *Geophys. Res. Lett.* 44. <https://doi.org/10.1002/2017GL073583>
- Babin, M., Stramski, D., 2004. Variations in the mass-specific absorption coefficient of mineral particles suspended in water. *Limnol. Oceanogr.* 49, 756–767. <https://doi.org/10.4319/lo.2004.49.3.0756>
- Bhatia, M.P., Kujawinski, E.B., Das, S.B., Breier, C.F., Hender-son, P.B., Charette, M.A., 2013. Greenland meltwater as a significant and potentially bioavailable source of iron to the ocean. *Nat. Geosci.* 6, 274–278. <https://doi.org/10.1038/ngeo1746>
- Błaszczak, M., Jania, J.A., Hagen, J.O., 2009. Tidewater glaciers of Svalbard: Recent changes and estimates of calving fluxes. *Pol. Polar Res.* 30, 85–142.
- Braeckman, U., Pasotti, F., Hoffmann, R., Vázquez, S., Wulff, A., Schloss, I.R., Falk, U., Deregibus, D., Lefaible, N., Torstenson, A., Al-handal, A., Wenzhöfer, F., Vanreusel, A., 2021. Glacial melt disturbance shifts community metabolism of an Antarctic seafloor ecosystem from net autotrophy to heterotrophy. *Commun. Biol.* 4, 1–11. <https://doi.org/10.1038/s42003-021-01673-6>
- Bukowska-Jania, E., 2007. The role of glacier system in migration of calcium carbonate on Svalbard. *Pol. Polar Res.* 28, 137–155.
- Clark, G.F., Stark, J.S., Palmer, A.S., Riddle, M.J., Johnston, E.L., 2017. The roles of sea-ice, light and sedimentation in structuring shallow antarctic benthic communities. *PLoS One* 12, 1–20. <https://doi.org/10.1371/journal.pone.0168391>
- Dallmann, W.K., 2015. *Geoscience Atlas of Svalbard*. Norwegian Polar Institute, Tromsø Report 148.
- Deja, K., Ormańczyk, M., Dragańska-Deja, K., 2019. Plankton or benthos: where krill belongs in Spitsbergen fjords? (Svalbard Archipelago, Arctic). *Polar Biol* 42, 1415–1430. <https://doi.org/10.1007/s00300-019-02524-1>
- Deja, K., Węstawski, J.M., Borszcz, T., Włodarska-Kowalczyk, M., Kukliński, P., Bałazy, P., Kwiatkowska, P., 2016. Recent distribution of Echinodermata species in Spitsbergen coastal waters. *Pol. Polar Res.* 37, 511–526. <https://doi.org/10.1515/popore-2016-0027>
- Ericson, Y., Falck, E., Chierici, M., Fransson, A., Kristiansen, S., 2019. Marine CO₂ system variability in a high arctic tidewater-glacier fjord system, Tempelfjorden, Svalbard. *Cont. Shelf Res.* 181, 1–13. <https://doi.org/10.1016/j.csr.2019.04.013>
- Ericson, Y., Falck, E., Chierici, M., Fransson, A., Kristiansen, S., Platt, S.M., Hermansen, O., Myhre, C.L., 2018. Temporal Variability in Surface Water pCO₂ in Adventfjorden (West Spitsbergen) With Emphasis on Physical and Biogeochemical Drivers. *J. Geophys. Res. Ocean.* 123, 4888–4905. <https://doi.org/10.1029/2018JC014073>
- Fairchild, I.J., Bradby, L., Spiro, B., 1994. Reactive carbonate in glacial systems: a preliminary synthesis of its creation, dissolution and reincarnation. In: Domack, E.W., Young, G.M., Fairchild, I., Miller, J.M.G., Deynoux, M., Eyles, N. (Eds.), *Earth's Glacial Record, World and Regional Geology*. Cambridge University Press, Cambridge, 176–192. <https://doi.org/10.1017/CBO9780511628900.014>
- Gerringa, L.J.A., Alderkamp, A.C., Laan, P., Thuróczy, C.E., De Baar, H.J.W., Mills, M.M., van Dijken, G.L., Haren, H.van, Arrigo, K.R., 2012. Iron from melting glaciers fuels the phytoplankton blooms in Amundsen Sea (Southern Ocean): Iron biogeochemistry. *Deep. Res. Part II Top. Stud. Oceanogr.* 71–76, 16–31. <https://doi.org/10.1016/j.dsr2.2012.03.007>

- Gorlich, K., 1987. Glacimarine sedimentation of muds in Hornsund Fjord, Spitsbergen. *Deep Sea Res. Part B. Oceanogr. Lit. Rev.* 34, 1046. [https://doi.org/10.1016/0198-0254\(87\)95941-3](https://doi.org/10.1016/0198-0254(87)95941-3)
- Halbach, L., Vihtakari, M., Duarte, P., Everett, A., Granskog, M.A., Hop, H., Kauko, H.M., Kristiansen, S., Myhre, P.I., Pavlov, A.K., Pramanik, A., Tatarek, A., Torsvik, T., Wiktor, J.M., Wold, A., Wulff, A., Steen, H., Assmy, P., 2019. Tidewater Glaciers and Bedrock Characteristics Control the Phytoplankton Growth Environment in a Fjord in the Arctic. *Front. Mar. Sci.* 6. <https://doi.org/10.3389/fmars.2019.00254>
- Hallet, B., Hunter, L., Bogen, J., 1996. Rates of erosion and sediment evacuation by glaciers: A review of field data and their implications. *Glob. Planet. Change* 12, 213–235. <https://doi.org/10.1029/2004JF000189>
- Hawkings, J.R., Benning, L.G., Raiswell, R., Kaulich, B., Araki, T., Abyaneh, M., Stockdale, A., Koch-Müller, M., Wadham, J.L., Tranter, M., 2018. Biolabile ferrous iron bearing nanoparticles in glacial sediments. *Earth Planet. Sci. Lett.* 493, 92–101. <https://doi.org/10.1016/j.epsl.2018.04.022>
- Hawkings, J.R., Wadham, J.L., Tranter, M., Raiswell, R., Benning, L.G., Statham, P.J., Tedstone, A., Nienow, P., Lee, K., Telling, J., 2014. Ice sheets as a significant source of highly reactive nanoparticulate iron to the oceans. *Nat. Commun.* 5. <https://doi.org/10.1038/ncomms4929>
- Hood, E., Battin, T.J., Fellman, J., O'Neel, S., Spencer, R.G.M., 2015. Storage and release of organic carbon from glaciers and ice sheets. *Nat. Geosci.* 8, 91–96. <https://doi.org/10.1038/ngeo2331>
- Hood, E., Fellman, J., Spencer, R.G.M., Hernes, P.J., Edwards, R., Amore, D.D., Scott, D., D'Amore, D., Scott, D., 2009. Glaciers as a source of ancient and labile organic matter to the marine environment. *Nature* 462, 1044–1047. <https://doi.org/10.1038/nature08580>
- Husum, K., Howe, J.A., Baltzer, A., Forwick, M., Jensen, M., Jernas, P., Korsun, S., Miettinen, A., Mohan, R., Morigi, C., Myhre, P.I., Prins, M.A., Skirbekk, K., Sternal, B., Boos, M., Dijkstra, N., Troelstra, S., 2019. The marine sedimentary environments of Kongsfjorden, Svalbard: an archive of polar environmental change. *Polar Res.* 38, 1–16. <https://doi.org/10.33265/polar.v38.3380>
- Konik, M., Darecki, M., Pavlov, A. K., Sagan, S., Kowalczyk, P., 2021. Darkening of the Svalbard Fjords Water Observed With Satellite Ocean Color Imagery in 1997-2019. *Front. Mar. Sci.* 8, 699318. <https://doi.org/10.3389/fmars.2021.699318>
- Martini, I.P., Brookfield, M.E., Sadura, S., 2001. *Principles of glacial geomorphology and geology*. Prentice Hall, Upper Saddle River, New Jersey.
- McKinney, W., van der Walt, S., Millman, J. (Eds.), 2010. Data structures for statistical computing in Python TX(2010), 56–61. <https://doi.org/10.25080/Majora-92bf1922-00a>
- Moore, C.M., Mills, M.M., Arrigo, K.R., Berman-Frank, I., Bopp, L., Boyd, P.W., Galbraith, E.D., Geider, R.J., Guieu, C., Jaccard, S.L., Jickells, T.D., La Roche, J., Lenton, T.M., Mahowald, N.M., Marañón, E., Marinov, I., Moore, J.K., Nakatsuka, T., Oschlies, A., Saito, M.A., Thingstad, T.F., Tsuda, A., Ulloa, O., 2013. Processes and patterns of oceanic nutrient limitation. *Nat. Geosci.* 6, 701–710. <https://doi.org/10.1038/ngeo1765>
- Moskalik, M., Cwiąkała, J., Szczuciński, W., Dominiczak, A., Głowacki, O., Wojtyński, K., Zagórski, P., 2018. Spatiotemporal changes in the concentration and composition of suspended particulate matter in front of Hansbreen, a tidewater glacier in Svalbard. *Oceanologia* 60, 446–463. <https://doi.org/10.1016/j.oceano.2018.03.001>
- Overland, J., Dunlea, E., Box, J.E., Corell, R., Forsius, M., Kattsov, V., Olsen, M.S., Pawlak, J., Reiersen, L.O., Wang, M., 2019. The urgency of Arctic change. *Polar Sci* 21, 6–13. <https://doi.org/10.1016/j.polar.2018.11.008>
- Sagan, S., Darecki, M., 2018. Inherent optical properties and particulate matter distribution in summer season in waters of Hornsund and Kongsfjordened, Spitsbergen. *Oceanologia* 60 (1), 65–75. <https://doi.org/10.1016/j.oceano.2017.07.006>
- Stemann, L., Boss, E., 2012. Plankton and particle size and packaging: From determining optical properties to driving the biological pump. *Ann. Rev. Mar. Sci.* 4, 263–290. <https://doi.org/10.1146/annurev-marine-120710-100853>
- Sunda, W.G., 2012. Feedback interactions between trace metal nutrients and phytoplankton in the ocean. *Front. Microbiol.* 3, 1–22. <https://doi.org/10.3389/fmicb.2012.00204>
- Svendsen, H., Beszczynska-møller, A., Hagen, J.O., Lefauconnier, B., Tverberg, V., Gerland, S., Ørbæk, J.B., Bischof, K., Papucci, C., Zajaczkowski, M., Azzolini, R., Bruland, O., Wiencke, C., Winther, J., Dallmann, W., 2002. The physical environment of Kongsfjorden-Krossfjorden, an Arctic fjord system in Svalbard. *Polar Res.* 21, 133–166. <https://doi.org/10.3402/polar.v21i1.6479>
- Szczuciński, W., Zajaczkowski, M., Scholten, J., 2009. Sediment accumulation rates in subpolar fjords – Impact of post-Little Ice Age glaciers retreat, Billefjorden, Svalbard. *Estuar. Coast. Shelf Sci.* 85, 345–356. <https://doi.org/10.1016/j.ecss.2009.08.021>
- Szeligowska, M., Trudnowska, E., Boehnke, R., Błachowiak-Samotyka, K., 2022. Dark plumes of glacial meltwater affect vertical distribution of zooplankton in the Arctic. *Sci. Rep.* 12, 1–16. <https://doi.org/10.1038/s41598-022-22475-8>
- Szeligowska, M., Trudnowska, E., Boehnke, R., Dąbrowska, A.M., Dragańska-Deja, K., Deja, K., Darecki, M., Błachowiak-Samotyka, K., 2021. The interplay between plankton and particles in the Isfjorden waters influenced by marine- and land-terminating glaciers. *Sci. Total Environ.* 780. <https://doi.org/10.1016/j.scitotenv.2021.146491>
- Telling, J., Boyd, E.S., Bone, N., Jones, E.L., Tranter, M., Macfarlane, J.W., Martin, P.G., Wadham, J.L., Lamarche-Gagnon, G., Skidmore, M.L., Hamilton, T.L., Hill, E., Jackson, M., Hodgson, D.A., 2015. Rock comminution as a source of hydrogen for subglacial ecosystems. *Nat. Geosci.* 8, 851–855. <https://doi.org/10.1038/ngeo2533>
- Trudnowska, E., Dąbrowska, A.M., Boehnke, R., Zajaczkowski, M., Błachowiak-Samotyka, K., 2020. Particles, protists, and zooplankton in glacier-influenced coastal Svalbard waters. *Estuar. Coast. Shelf Sci.* 242 (2020), 106842. <https://doi.org/10.1016/j.ecss.2020.106842>
- Trudnowska, E., Lacour, L., Ardyna, M., Rogge, A., Irisson, J.O., Waite, A.M., Babin, M., Stemann, L., 2021. Marine snow morphology illuminates the evolution of phytoplankton blooms and determines their subsequent vertical export. *Nat. Commun.* 12, 1–13. <https://doi.org/10.1038/s41467-021-22994-4>
- Urbanski, J.A., Stempniewicz, L., Węśławski, J.M., Dragańska-Deja, K., Wochna, A., Goc, M., Iliszko, L., 2017. Subglacial discharges create fluctuating foraging hotspots for sea birds in tidewater glacier bays. *Sci. Rep.* 7, 43999.
- Wawrzyniak, T., Osuch, M., 2019. Daily precipitation (1979–2018) at the Arctic meteorological station Hornsund, Spitsbergen. <https://doi.org/10.1594/PANGAEA.909070>, [in:] Wawrzyniak, T., Osuch, M., A consistent High Arctic climatological dataset (1979–2018) of the Polish Polar Station Hornsund (SW Spitsbergen, Svalbard). PANGAEA. <https://doi.org/10.1594/PANGAEA.909042>
- Węśławski, J.M., Koszteyn, J., Zajaczkowski, M., Wiktor, J., Kwaśniewski, S., 1995. Fresh water in Svalbard fjord ecosystems. In: *Ecology of Fjords and Coastal Waters*. Elsevier, 229–241.
- Woźniak, S.B., Darecki, M., Zabłocka, M., Burska, D., Dera, J., 2016. New simple statistical formulas for estimating surface concentrations of suspended particulate matter (SPM) and particulate organic carbon (POC) from remote-sensing reflectance

- in the southern Baltic Sea. *Oceanologia* 58 (3), 161–175. <https://doi.org/10.1016/j.oceano.2016.03.002>
- Woźniak, S.B., Stramski, D., 2004. Modeling the optical properties of mineral particles suspended in seawater and their influence on ocean reflectance and chlorophyll estimation from remote sensing algorithms. *Appl. Opt.* 43, 3489–3503. <https://doi.org/10.1364/AO.43.003489>
- Woźniak, S.B., Stramski, D., Stramska, M., Reynolds, R.A., Wright, V.M., Miksic, E.Y., Cichocka, M., Cieplak, A.M., 2010. Optical variability of seawater in relation to particle concentration, composition, and size distribution in the nearshore marine environment at Imperial Beach, California. *J. Geophys. Res. Ocean.* 115, 1–19. <https://doi.org/10.1029/2009JC005554>
- Zajączkowski, M., 2008. Sediment supply and fluxes in glacial and outwash fjords, Kongsfjorden and Adventfjorden, Svalbard. *Pol. Polar Res.* 29, 59–72.

Available online at www.sciencedirect.com

ScienceDirect

journal homepage: www.journals.elsevier.com/oceanologia

ORIGINAL RESEARCH ARTICLE

Rapid coastal erosion, its dynamics and cause – an erosional hot spot on the southern Baltic Sea coast

Grzegorz Uścińowicz^{a,*}, Szymon Uścińowicz^b, Tomasz Szarafin^a,
Elżbieta Maszloch^a, Kamila Wirkus^a

^aPolish Geological Institute – National Research Institute, Marine Geology Branch, Gdańsk, Poland

^bInstitute of Hydro-Engineering, Polish Academy of Sciences, Gdańsk, Poland

Received 30 January 2023; accepted 14 December 2023

Available online 26 December 2023

KEYWORDS

Nontidal;
Sea ice;
Barrier coast;
Storminess

Abstract Coastal erosion is one of the major problems in coastal management. To adapt to it, and prevent it where possible and needed, it is important to recognize the temporal and spatial scale of the phenomenon as well as its causes. This paper describes the rapid erosion rate along an approximately 2.25 km stretch of the southern Baltic coast. The erosion occurs within a nature reserve, which is not subject to direct anthropogenic impact. Historical maps and modern remote sensing were used to trace changes in the shoreline position from 1875 to the present, and detailed DTMs derived from airborne LiDAR were used to trace elevation changes of the beach and dunes over the past years. The weighted maximum annual erosion rate since 1875 averages 2.3 m. An increase in this annual erosion rate has been observed since the turn of the millennium. The maximum average erosion rate from 2001 to 2005 was 15 m/year. The erosion has caused serious changes in elevation within the inland part of the coastal zone, manifested by a reduction in the width of the beach and a decrease in the height of the beach and dunes.

© 2023 Institute of Oceanology of the Polish Academy of Sciences. Production and hosting by Elsevier B.V. This is an open access article under the CC BY-NC-ND license (<http://creativecommons.org/licenses/by-nc-nd/4.0/>).

* Corresponding author at: Polish Geological Institute – National Research Institute, Marine Geology Branch, 5, Kościarska Street, 80-328 Gdańsk, Poland.

E-mail address: grzegorz.uscinowicz@pgi.gov.pl (G. Uścińowicz).

Peer review under the responsibility of the Institute of Oceanology of the Polish Academy of Sciences.



<https://doi.org/10.1016/j.oceano.2023.12.002>

0078-3234/© 2023 Institute of Oceanology of the Polish Academy of Sciences. Production and hosting by Elsevier B.V. This is an open access article under the CC BY-NC-ND license (<http://creativecommons.org/licenses/by-nc-nd/4.0/>).

1. Introduction

Coastal erosion is a worldwide phenomenon and one of the major problems in coastal management. To adapt to it, and sometimes prevent it, it is important to recognise the temporal and spatial scale of the phenomenon and its causes. Of special interest and importance are the shoreline segments where recession rates are significantly higher than for neighbouring shoreline segments. These areas of erosion anomalies (sensu Galgano, 2007) or so-called “erosional hot spots – EHSs” (sensu Kraus and Galgano, 2001) are a serious problem causing significant losses to coastal areas of high value, including natural habitats, and areas of economic importance such as forests, agricultural land, tourist resorts and residential areas. In general, EHSs are classified according to the duration of existence, lateral extent, processes responsible for the erosion, and predominant erosion mechanism as longshore or cross-shore transport (Kraus and Galgano, 2001). There are a number of natural and anthropogenic factors that cause beaches to erode at anomalous rates (e.g. Benedet et al., 2007; Bridges, 1995; Esteves and Finkl, 1998). Possible natural reasons that cause EHSs are evaluated, i.a. in terms of wave transformation over bathymetric irregularities located both offshore and shoreface, alongshore grain-size distribution, and shoreline orientation. EHSs are also frequently observed in response to human interventions such as the construction of jetties in river mouths or entrances to harbours, as well as to coastal protection structures like groins and seawalls. (Dean et al., 1999; Kraus and Galgano, 2001). The identification and assessment of EHS is crucial for coastal zone management.

Erosion is also a pervasive problem in the Polish coastal zone of the southern Baltic Sea. Studies of Polish coasts have a long tradition (Furmańczyk, 1994; Furmańczyk and Musielak, 1999, 2002; Musielak et al., 2017; Zawadzka, 1999, 2012; Zawadzka-Kahlau, 1999), however, they have mostly been limited to tracking changes in the position of the coastline. More valuable explanatory research focused on identifying coastal sections particularly affected by erosion, and attempting to determine the causes of erosion, were mainly limited to cliff coasts and were mainly published in Polish journals (Subotowicz, 1991; Uścińowicz et al., 2004). Studies focused on the identification of EHSs in relation to barriers along the Polish coast and cause-effect analyses of temporal changes in the rate of erosion are extremely rare.

This paper describes the spatial and temporal characteristics of a recently identified EHS that has modified an uninterrupted sandy coast completely free of human intervention. We present a case study of one of the most severely eroded sections of the Polish coast, tracking the range of coastal erosion and specifically changes in the erosion rates to define and understand EHS. In particular, we seek to answer the following questions:

- 1) How fast annually the coastal retreat can be,
- 2) How and why the rate of coastal erosion has changed,
- 3) If the location of the EHS is stable or changes over time and space,
- 4) What causes anomalously rapid local coastal erosion.

2. Regional setting

The Polish coast of the Baltic Sea has a total length of 498 km (without internal lagoonal coasts). The coastal zone, as central and northern Poland, is dominated by Pleistocene glacial and glaciofluvial deposits. In terms of morphology and geological structure, three types of coasts are distinguished: cliffs (ca. 101 km), barriers (ca. 380 km) and coasts similar to wetlands (ca. 17 km). The entire southern Baltic coast has been subject to erosion processes for centuries. Most of the cliffs have been affected by significant levels of erosion (Subotowicz, 1995; Terefenko et al., 2019; Uścińowicz et al., 2017). Behavioural changes taking place along the barrier coast are more complex. Most barriers are eroded to varying degrees and rates (Deng et al., 2017; Zawadzka, 2012), but unlike cliffs, they can recover and build seaward. A minor part of the Polish barrier coast is relatively stable or aggrading. While analysing changes in the location of the coastline on a decadal time scale, erosion-accumulation systems of different spatial scales were identified, with the predominance of erosion processes (Zawadzka, 1999). The average rate of shoreline retreat within the erosive sections was about 0.5–2 m/year, depending on the location and period of measurements (Meier et al., 2022; Michałowska and Głowienka, 2022; Zawadzka, 1999).

The study area extends from east to west along an approximately 5.5 km stretch of barrier coastline between 17°49'16" and 18°23'12"E, between the villages of Dębki and Karwia. According to the state coastline division system for the Polish coast, it stretches between km 142.5 and km 148 (Figure 1). The area has been affected by rapid coastal erosion during the past decades. The marine part of the site is entirely within a Natura 2000 Special Area of Conservation (PLB990002 – Przybrzeżne Wody Baltyku). The land part of the area is partly within the Coastal Landscape Park and, at the same time, within the Widowo Nature Reserve (Habitat Site PLH220054). The study area can be considered as an area where coastal processes are not directly disturbed by anthropogenic factors. Beach nourishment and the nearest breakwaters disturbing the longshore sand transport are located in Łeba, ca. 40 km west of the study area. To the east of the study area, an embankment has been constructed along a stretch of approximately 2 km to protect the fore-dune and coastal lowland against storm surge flooding.

The Baltic Sea is an intracontinental, semi-enclosed, brackish and non-tidal sea. The climate of the Baltic Sea region is influenced by the large-scale atmospheric circulation and shows a strong seasonal cycle, but also large inter-annual to multidecadal variability. There are no significant long-term trends in wind speed and direction, but there is considerable decadal variability. Correspondingly, there are no clear indications of long-term trends in the frequency of storm surges and wave height (Bärring and Fortuniak, 2009; Climate Change in the Baltic Sea, 2021; HELCOM, 2007, 2013; Rutgersson et al., 2014).

In general, westerly winds dominate over the southern Baltic Sea region. Typically, the highest wind speeds are associated with the passage of strong extratropical cyclones. These systems, and thus wind extremes, are most frequent and intense in the winter season. The wave climate in the

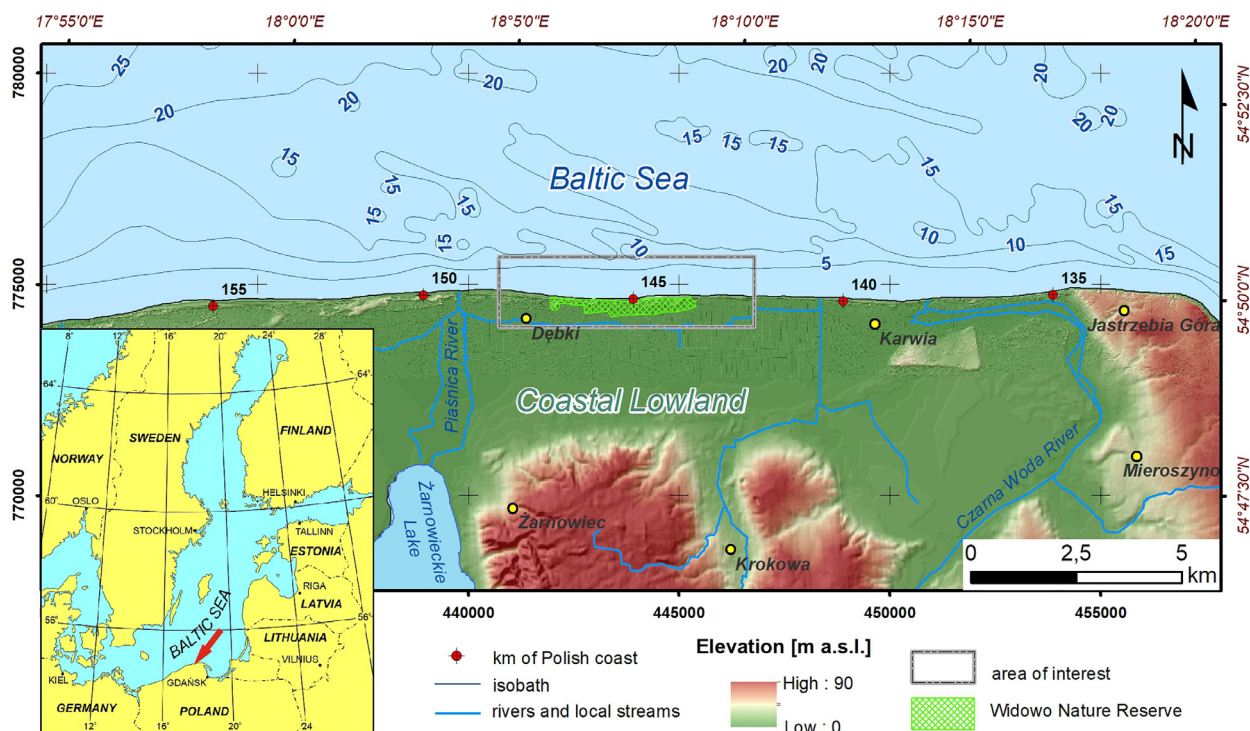


Figure 1 Location of the study area. Source of bathymetry – Polish Geological Institute – National Research Institute; source of DTMs – Maritime Office in Gdynia and Military Centre of Geodesy and Remote Sensing, and IT system for the Country's Protection Against Extreme Hazards (ISOK).

Baltic Sea strongly depends on the wind field, and consequently, waves from the western sector (SW, W, NW) dominate. Representative wave data for the study area are derived from the Coastal Research Station of the Institute of Hydro-Engineering of the Polish Academy of Sciences in Lubiatowo, located ca. 18 km to the west (Ostrowski et al., 2016). Waves from the western sector occur for ca. 50% of the year, more than from the eastern sector (NE, E, SE – 32%) and the northern sector (13.5% of the year). Storm winds (> 15 m/s) and waves also mostly come from SW, W and NW. During heavy storms, the parameters of deep-water waves may exceed: $H_{\max} > 7$ m, $H_s > 4$ m, $H_{\text{mean}} > 3$ m, $T_s > 9$ s, $T_{\text{mean}} > 8$ s. Owing to the existence of sandbars, most of the wave energy is dissipated when approaching the shore (Pruszek et al., 2011). In storm conditions, however, return currents in the surf zone reach velocities of up to 0.5 m/s, while the greatest velocities of longshore currents reach 1.2–1.5 m/s. Driven by longshore currents, the annual resultant (net) longshore sediment transport on the shoreface (in the zone up to 650 m from the shore) is ca. 111,000–145,000 m³/year, directed from west to east (Szmytkiewicz et al., 2021).

In general, the sea level is rising along the entire southern Baltic coast. According to the nearest mareographic station located in Władysławowo, ca. 20 km east of the study area, the average rate of water-level rise in the period 1951–2015 was 2.04 mm/year (Kowalczyk, 2019). In addition to long-term water-level rise, there are also sudden events when extremely high water level reaches of about 1.5 m above m.s.l. (mean sea level) within a few hours, during the migration of low-pressure storm systems. The max-

imum recorded water level in Władysławowo was 1.38 m above m.s.l. (Wiśniewski et al., 2009).

Morphologically, the coast in the area of interest is dissipative, with multiple nearshore bars and a lowland in the hinterland. The surface of this lowland is at 0.7–1.5 m a.s.l. and is cut by a network of drainage ditches. The barrier separating the lowland from the sea is relatively narrow and low. The width of the beach is 40–50 m in summer and is reduced to 10–20 m during autumn and winter storms. A strip of morphologically variable dunes extends landward beyond the beach. A 3–5 m high foredune occurs only in the western and eastern parts of the study area. The middle section, ca. 2 km long, is heavily eroded, so there is no foredune. Directly adjacent to the beach are dunes up to about 20 m high, which are erosional remnant of parabolic dunes (Figure 2).

The shoreface (underwater coastal slope) reaches a width of 1.0–1.3 km and has an average inclination of ca. 1:100. In the upper part of the shoreface, up to a depth of 5–6 m b.s.l. (below sea level), there are two to three low sandbars with a crest-to-trough amplitude of 0.5–2.5 m. The first sandbar, closest to shore, is usually a highly eroded form, i.e. faintly defined and merging with the beach. The second sandbar is more clearly defined along the length of the shore. Located at a distance of ca. 150–200 m from shore, it is semi-permanent and mostly continuous. The third sandbar, approximately 400–500 m from shore, is fragmented in places and transitions into a slightly inclined to the north sandy flat. This plain forms the lower shoreface and extends to an approximate depth of 10–12 m b.s.l. The shoreface at a depth of ca. 10–12 m b.s.l. is marked by

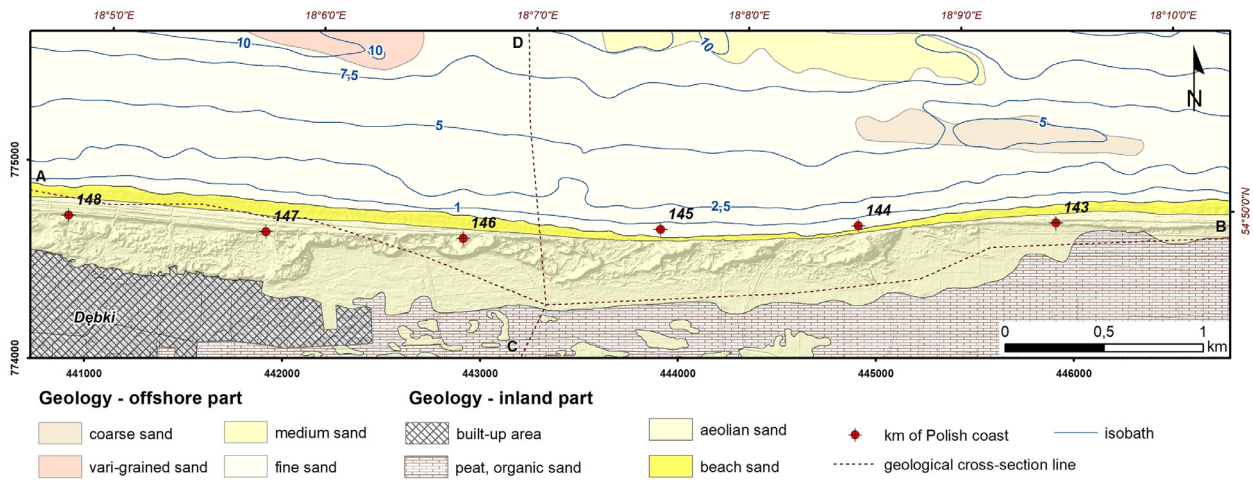


Figure 2 Geological map of the study area (Polish Geological Institute – National Research Institute materials).

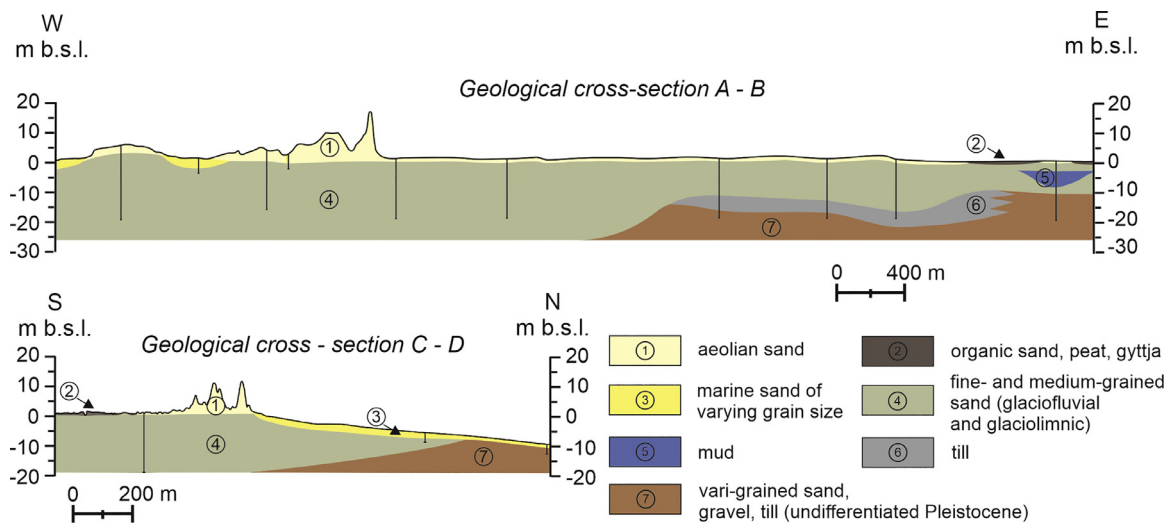


Figure 3 Geological cross-sections through the study area. The cross-section lines are shown in Figure 2 (Polish Geological Institute – National Research Institute materials).

a gradient change. In the northern part of the study area, seaward of the sandy plain at a depth of 12–20 m, there are shoreface-connected ridges with a depression between them. The axis of this swale is NW-SE oriented, i.e. obliquely towards the shore.

The onshore subsurface of the study area is composed of Quaternary formations with a thickness of ca. 40–50 m and consists mainly of a Pleistocene sequence of sand of glaciofluvial and glaciolimnic origin and till. Holocene peat with a thickness of up to 1.5 m forms the surface of the lowland (Figures 2 and 3). Thin layers of storm surge deposits (Moskalewicz D., 2016) and/or aeolian sands interfinger with the peat at the barrier-lowland transition zone (Uściniowicz et al., 2021).

As for the marine subsurface of the study area, the top-most part of the Pleistocene deposits was partly eroded during the Holocene marine transgression. Despite this truncation, the geological structure of the Pleistocene deposits is similar to its terrestrial equivalent. The overlying Holocene deposits are dominated by marine sand and, locally, gravel.

The thickness of marine sediments ranges from a few cm to 3–4 m (Uściniowicz et al., 2018). The largest thickness occurs within the sandbars and sand ridges. These landforms are composed of medium and fine sand with *Macoma* sp. shells and fragments of shells. In the depressions of the seabed between the sandbars and between the sand ridges, coarse-grained sand, locally with gravel admixture, occurs. Here, the thickness of marine sediments is locally reduced to a few centimetres.

3. Material and methods

An extensive remote sensing analysis was carried out for the study area, comparing multi-temporal digital elevation models and tracking changes in the position of the shoreline in relation to the oldest available and processed cartographic materials. The unquestionable advantage of this method is the possibility of quantifying changes over different periods. The following materials were used for this

analysis: (1) LiDAR data acquired by airborne laser scanning performed as part of coastal monitoring by the Maritime Office in Gdynia; (2) geoprocessed maps, aerial photos, DEMs and shorelines established/generated from these products that each represent the situation for a specific time.

According to the Maritime Office report, the airborne LiDAR mapping was designed to have at least one flight profile over water, so that the LiDAR beam could scan the northern side of dune slopes. The survey was carried out with the water level not exceeding 10 cm above m.s.l. The average scanning density was 8 points/m² and the overlap between areas covered with LiDAR beam was at least 20%. The total width of the mapped coastal zone was about 0.5 km.

Multi-temporal digital elevation model was developed to show changes in the topography of the coastal zone between 2016 and 2020. Individual digital elevation models have an average z (vertical) value inaccuracy of about 0.15 m. A series of control points were selected to check height differences between the individual DEMs to minimize the error in z-values on the final multi-temporal model. The maximum inaccuracy of two DEMs varied and ranged from 0.05 to 0.35 m.

The uniformity of the DEMs output allowed the comparison of models created based on different measurement series at different times. This methodological approach allowed vertical changes to be quantified. For the purpose of the analysis, the vertical changes between -0.5 and 0.5 m were classified as the “stable” state (gray), with positive values (two classes 0.5–2 m and 2–5 m) corresponding to an increase in the height of the measured areas (green) and negative values (two classes -0.5– -2 m and -2– -5 m) corresponding to a decrease in height (red). The obtained multi-temporal model provides information about the vertical changes that occur in individual coastal sections and facilitates the general parameterisation of these changes.

A second indicator of coastal change, shoreline migration, can be analysed for a longer time horizon. The 1875 shoreline generated from a geoprocessed, German archival topographic map (Topographische Karte, Messtischblatt 1:25,000, 136-Dembek) was compared with those from 1958, 1980, 2001, 2005, 2010, 2016 and 2020 (Table 1). The Messtischblatt maps are characterised by a high level of accuracy, reaching up to 4–6 m compared to modern cartographic materials (Deng et al., 2017). The shoreline on modern topographic maps (1980, 2001 – a year of the cartographic survey) is a linear feature with a width of approximately 0.5 mm. The position of the shoreline was GIS-digitized directly from the official cartographic materials. This methodological approach permits an accuracy of a few metres and ultimately up to 10 m, which depends on the accuracy of the original map. A similar procedure was applied to orthophotomaps (1958, 2005) and ultimately the fitting accuracy can be estimated at a level of 5 m, which in this case depended on the resolution and pixel size of the original photo. With regard to the DEMs, the shoreline was 0 m above sea level. The validity of this procedure was verified by comparing the shoreline derived from an orthophotomap taken at the same time. The shoreline position derived from the DEMs has an accuracy of 5 m, resulting from the original DEMs resolution. For technical reasons (the shoreline merges to the map frame), it was not possible to determine

Table 1 List of materials used in the study.

Type of source data	Year	Typ of analysis	Data source	Estimated lateral error or pixel size
DTM	2016	Multi-temporal DTM	Maritime Office in Gdynia	0.5 m – pixel size
DTM	2020	Multi-temporal DTM	Maritime Office in Gdynia	0.5 m – pixel size
Topographic map – Messtischblatte 1: 25 000	1875	shoreline position	PGI-NRI (derived from topographic map)	25 meters (Deng et al., 2017)
Aerial photo (orthophotomap)	1958	shoreline position	PGI-NRI (derived from aerial photo)	<5 m
Topographic map 1: 10 000	1980	shoreline position	PGI-NRI (derived from topographic map)	<10 m – map accuracy
Topographic map 1: 10 000	2001	shoreline position	PGI-NRI (derived from topographic map)	<10 m – map accuracy
Aerial photo (orthophotomap)	2005	shoreline position	PGI-NRI (derived from aerial photo)	2.0 m – pixel size
DTM	2010	shoreline position	PGI-NRI (derived from DTM)	0.5 m – pixel size
DTM	2016	shoreline position	PGI-NRI (derived from DTM)	0.5 m – pixel size
DTM	2020	shoreline position	PGI-NRI (derived from DTM)	0.5 m – pixel size

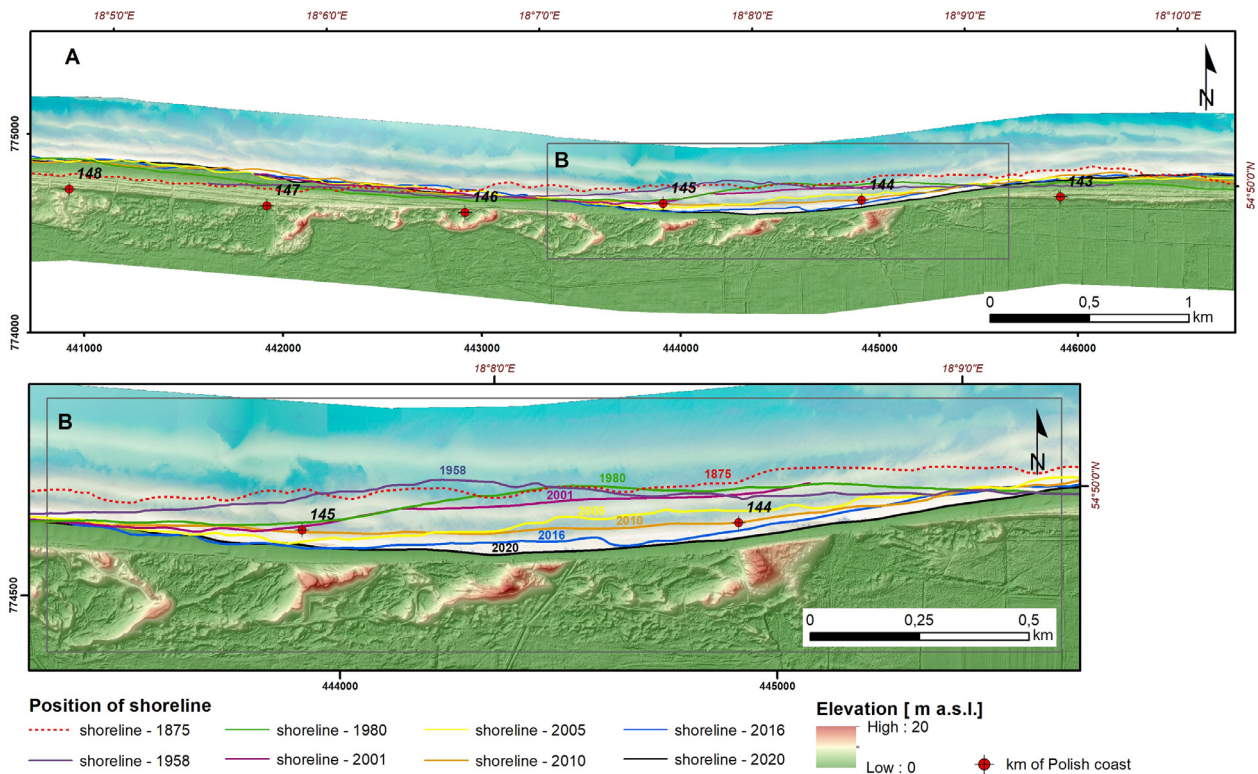


Figure 4 Shoreline position changes.

the position of the shoreline in 2001 in the vicinity of km 142–144 (the eastern part of the study area).

Additionally, to compare peak values of shoreline changes over time, the areas of erosion and accretion were calculated. For this purpose, the study area was divided into three sections bordered by “nodal points” corresponding to the EHS and adjacent areas. In these sections, the area bounded by the two respective shorelines was measured. Each created polygon was classified as either an area of erosion or accumulation depending on the layout of the boundary lines. The total area of erosion and accumulation in each section was then counted. In cases where the full course of shoreline was not available (due to lack of data) in a given section, polygons were created only based on the part covered by the common range. In this case, the results obtained should be regarded as minimum values. The data prepared in this way were used to calculate the average longshore erosion/accretion. This was achieved by dividing the respective area of erosion/accretion by the corresponding length of the shoreline.

4. Results

The general trend in changes of the coastal zone was analysed by comparing the changes in the erosion/accretion areas and position of the shoreline in 1875, 1958, 1980, 2001, 2005, 2010, 2016 and 2020 (Figure 4). The oldest analysed shoreline in the study area, i.e. the shoreline from 1875, is located mainly in the present sea area and encroaches on land at km 142.6 and 146.0 of the Polish coast. Only in a small, 0.5-km-long section (between km 144.45 and

144.95), is the 1958 shoreline located slightly (at most about 36 m) seaward of the 1875 shoreline. Even younger shorelines are located landward, but still in the sea area. They cross the present-day shoreline between km 143.4–143.7 to the east and km 145.3–145.6 to the west of the EHS. The strongest erosion occurred within a 2.2-km-long section between km 143.4 and 145.6 (Figure 4). The maximum shoreline retreat within this section was about 150 m between 1875 and 2020 and about 170 m between 1958 and 2020. As a result, a concave erosional section of ca. 3.4 km has been forming since at least 1875 (Figure 4). Owing to its large scale and high rate of erosion, it can be classified as an EHS (*sensu* Kraus and Galgano, 2001). When analysing in more detail the changes in the location of the shorelines within the hot spot over different periods, a large variability in the areas of erosion/accretion, range and rate of shoreline displacement was found, with erosion by far the dominant factor (Tables 2–4 and Figure 4). Between 1875 and 1958, the shoreline mostly shifted landward by an average of 25 m at an average rate of up to 0.3 m/year; only locally, in a 0.5-km section, it shifted seaward by a maximum of 36 m. The peak values and average peak rate were respectively 64 m and 0.8 m/yr. Next, in the period 1958–1980, the shoreline retreated by an average of 14 m (peak value of 64 m) with a corresponding average rate of 0.6 m/yr (peak rate increasing to 2.9 m/yr), but there were also short sections where the shoreline shifted seaward by up to 25 m.

Since 1980, no local accumulation has been recorded within the hot spot, while erosion clearly accelerated at the turn of the millennium. Between 1980 and 2001, the shoreline shifted at an average 14 m (peak value up to 33

Table 2 Shoreline position changes within the erosional hot spot and boundary areas.

Period	Shoreline position changes within the western boundary area (west of km 145.600)	Shoreline position changes within the “erosional hot spot” (km 143.4–145.6 km)	Shoreline position changes within the eastern boundary area (east of km 143.4)
1875–1958	local state of equilibrium erosion up to ca. 70 m accretion up to ca. 30 m	local state of equilibrium mostly erosion up to ca. 64 m local accretion up to ca. 36 m	erosion up to ca. 95 m
1958–1980	erosion up to ca. 22 m	local state of equilibrium mostly erosion up to ca. 64 m local accretion up to ca. 25 m	accretion up to ca. 21 m
1980–2001	accretion up to ca. 50 m	erosion up to ca. 33 m local state of equilibrium	lack of data
2001–2005	local state of equilibrium local erosion up to ca. 20 m local accretion up to ca. 25 m	erosion up to ca. 61 m	lack of data
2005–2010	local state of equilibrium local erosion up to ca. 29 m local accretion up to ca. 43 m	local state of equilibrium mostly erosion up to ca. 33 m local accretion up to ca. 26 m	local state of equilibrium local erosion up to ca. 20 m local accretion up to ca. 40 m
2010–2016	local state of equilibrium local erosion up to ca. 28 m local accretion up to ca. 37 m	erosion up to ca. 42 local state of equilibrium	local state of equilibrium local erosion up to ca. 15 m local accretion up to ca. 37 m
2016–2020	local state of equilibrium local erosion up to ca. 33 m local accretion up to ca. 26 m	erosion up to ca. 31 m local state of equilibrium	local state of equilibrium local erosion up to ca. 13 m local accretion up to ca. 10 m

m landward), but the average rate was still relatively slow at about 0.7 m/yr (peak rate 1.6 m/yr), whereas between 2001 and 2005 the average retreat reached 31 m (up to 61 m), at a rate of 7.7 m/yr (peak average of 15.3 m/yr!). In the period 2005–2010, the position of the shoreline generally retreated by an average of 6 m (peak value up to 33 m), corresponding to an average rate of 1.1 m/yr and maximum rate of 6.6 m/yr, and locally shifted seaward by a maximum of 26 m. After this period of a relatively slower rate of shoreline retreat, the process of erosion accelerated again. This manifested itself in average shoreline retreat across the erosional hot spot by approximately 21 m (peak value up to 42 m) in the period 2010–2016 and a further average of 13 m (maximum 31 m) in the period 2016–2020 at average rates 3.5 and 3.2 m/yr, respectively (maximum rates of 7.0 and 7.8 m/yr) (Tables 2 and 3, Figure 4).

Transformation within the EHS can also be reflected by changes in the area undergoing erosion or accumulation (Tables 3 and 4). These changes correlate very well with the phenomena described above and are based on the analysis of the position of the shorelines. Based on an analysis of the area subject to net erosion, it can be assumed that 54 591 m² were lost between 1875 and 1958. This results in an average loss of 658 m²/year. Between 1958 and 1980, a further 30 942 m² (1 406 m²/year) was eroded within the EHS. In the next analysed period (1980–2001), these values decreased and amounted to 24 574 m² (1 170 m²/year), only

to increase again at the turn of the century, i.e. between 2001 and 2005, amounting to 55 744 m² (13 936 m²/year). The period from 2005 to 2010 saw a repeated decrease in erosion (12 441 m²; 2 488 m²/year). Conversely, the following years 2010–2016 and 2016–2020 show a renewed increase in land loss, 45 818 m² and 28 467 m² (7 636 m²/year and 7 117 m²/year, respectively).

The range of changes on both sides of the erosional hot spot was much smaller, but more variable in terms of behaviour. East of the erosional hot spot, i.e. east of km 143.4, the shoreline moved landward by an average of 29 m and a maximum of about 95 m between 1875 and 1958. During the next measurement period 1958–1980, erosion slowed down and even reversed to accretion in some places, with the shoreline shifting seaward by an average of 4 m (up to 21 m). Unfortunately, it was not possible to describe the changes between 1980 and 2001 for this coastline section. Between 2005 and 2010, the position of the shoreline moved generally landward by an average value of 5 m and a maximum of approximately 20 m and locally shifted seaward by an average of 13 m (up to 40 m). Between 2010 and 2016, the changes were similar, varying between a local retreat (average of 7 m and up to approximately 15 m) and a local seaward shift (average of 10 m and maximum measured 37 m). Between 2016 and 2020, the position of the shoreline changed only slightly and oscillated between a local seaward or landward shift. Therefore, the period from 2005

Table 3 Area of erosion/accretion changes within the erosional hot spot and boundary areas.

Period	Area of erosion/accretion changes within the western boundary area (west of km 145.6)			Area of erosion/accretion changes within the “erosional hot spot” (143.4–145.6 km)			Area of erosion/accretion changes within the eastern boundary area (east of km 143.4)		
	Dominant process	Total area [m ²]	Longshore average erosion (total area/length of shoreline) [m]	Dominant process	Total area [m ²]	Longshore average erosion (total area/length of shoreline) [m]	Dominant process	Total area [m ²]	Longshore average erosion (total area/length of shoreline) [m]
1875–1958	erosion*	30163	20	erosion	63643	29	erosion*	43823	29
	accretion*	8768	6	accretion	9052	4	accretion*	0	0
1958–1980	erosion*	19642	13	erosion	44729	20	erosion*	118	0
	accretion*	6706	4	accretion	13787	6	accretion*	5370	4
1980–2001	erosion*	0	0	erosion**	24867	14	lack of data	lack of data	lack of data
	accretion*	48547	32	accretion**	293	0			
2001–2005	erosion*	1585	1	erosion**	57043	32	lack of data	lack of data	lack of data
	accretion*	10638	7	accretion**	1299	1			
2005–2010	erosion	21444	9	erosion	22964	10	erosion	4606	5
	accretion	17180	7	accretion	10523	5	accretion	11920	13
2010–2016	erosion	10782	4	erosion	46637	21	erosion	6723	7
	accretion	25627	11	accretion	819	0	accretion	9183	10
2016–2020	erosion	23234	10	erosion	30867	14	erosion	6264	7
	accretion	7161	3	accretion	2400	1	accretion	1784	2

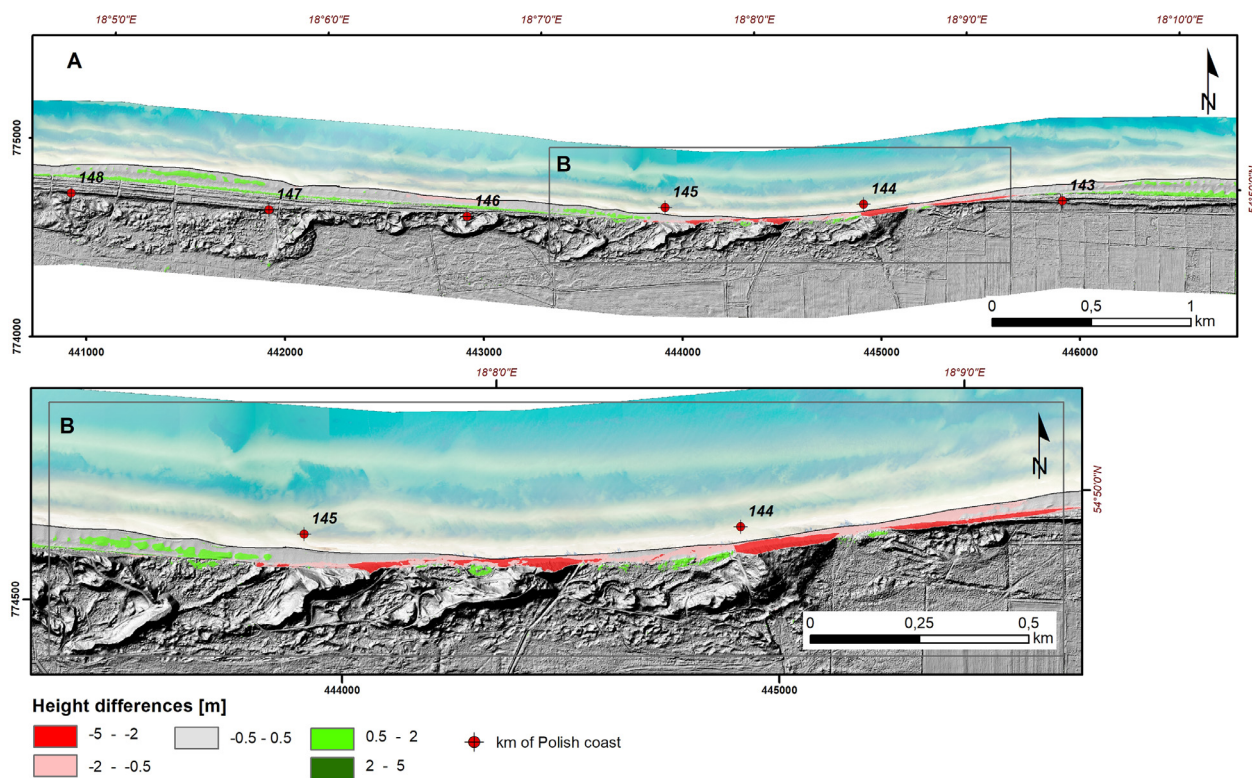


Figure 5 Multi-temporal DTM presenting the vertical change in beach and dune profiles between 2016 and 2020.

can be referred to as a “state of equilibrium” (Figure 4, Tables 2 and 3).

West of the erosional hot spot, i.e. west of km 145.6, the coast is characterised by the presence of a few local transition zones, i.e. points along the coast where local changes in erosion/accretion trends are observed. This is manifested by the oscillatory nature of changes. For instance, in the period 1875–1958, the average shoreline retreat was 20 m while the maximum shoreline retreat was up to 70 m, but in the same period, nearby areas experienced seaward shoreline migration (average value of 6 m and up to 30 m). While average and peak values of coastal erosion were lower between 1958 and 1980, with a shoreline retreat of 13 m (up to 22 m), average values of seaward accretion were 4 m with peak values up to 50 m. The period between 1980 and 2001 was characterised by seaward migration of the shoreline with an average of 32 m and maximum value of 50 m. The subsequent periods can be described as a state of equilibrium with a minor dominance of seaward shifts of the shoreline: 2001–2005 average 7 m, up to 25 m, 2005–2010 average 7 m, up to 43 m, 2010–2016 average 11 m, up to 37 m, 2016–2020 average 3 m, up to 26 m, while the erosion rate was as follows: 2001–2005 average 1 m, up to 20 m, 2005–2010 average 9 m, up to 29 m, 2010–2016 average 4 m, up to 28 m, 2016–2020 average 10 m, up to 33 m.

Although changes in the shoreline position within the eastern and western boundary zones of the erosional hot spot were relatively small and varied in time and space, it can be observed that accretion prevailed in the west and erosion prevailed in the east, with the erosional centre moving eastwards (Tables 2 and 3, Figure 4).

The above identification of the EHS and the two adjacent areas is clearly reflected in mapped vertical changes in the relief, i.e. changes in the volume of sediments in the inland part of the coastal zone. However, the western part of the EHS shows the opposite, vertical accretion. The central and eastern parts of the EHS are marked by decreased dune and beach height as well as reduced beach width (Figure 5). The beach was lowered by 0.5 to 1.5 m, but the most significant changes are observed within the remnant of parabolic dunes, up to 19 m above sea level (Figure 6). The reduction in height of the seaward slope of these dunes as well as on adjacent foredunes amounts to more than 2 m (Figure 5). In general, the beach and dunes in the western part of the EHS are in a state of equilibrium, with a local small increase in beach height (Figure 5). Importantly, these vertical changes indicate an eastward shift of the EHS.

The elevation changes outside the erosional hot spot, i.e. east of km 143.4 and west of km 145.6, show that they are much more stable. In between small, sparse, isolated patches of fields with a negative trend of change from -0.5 to -2 m, positive trends in elevation between 0.5 to 2 m were also recorded and can be considered dominant. They are mainly located at the base of and within the dunes, but also on some parts of the beach.

5. Discussion

The average rate of coastal retreat during 145 years between 1875 and 2020 was not steady over time. During the first 83 years (1875–1958), the average shoreline retreat was only 0.3 m/yr (average rate measured from peak

Table 4 Shoreline retreat rates (pick and average) and area loss calculated for the “erosional hot spot”.

Measured period	Maximum shoreline erosion [m]	Average peak shoreline erosion rate [m/yr]	Net longshore average erosion [m]	Average shoreline erosion rate (calculated from longshore average erosion) [m/yr]	Area of net erosion [m ²]	Average rate of area loss [m ² /yr]
1875–1958	64	0.8	25	0.3	54591	658
1958–1980	64	2.9	14	0.6	30942	1406
1980–2001	33	1.6	14	0.7	24574	1170
2001–2005	61	15.3	31	7.7	55744	13936
2005–2010	33	6.6	6	1.1	12441	2488
2010–2016	42	7.0	21	3.5	45818	7636
2016–2020	31	7.8	13	3.2	28467	7117



Figure 6 Aerial view (towards the ESE) of the study area (photo by: M. Olkowicz, 2018). No foredune within the “hot spot”; visible: very narrow beach in front of the erosional undercut in the remains of the parabolic dune.

values was 0.8 m/yr) and was close to or even slightly lower than the average erosion rate of the Polish coast (e.g. Zawadzka, 1999). The shoreline retreat significantly accelerated in the second half of the 21st century, especially at the beginning of the 21st century. The rate of the shoreline retreat in the analysed six periods between 1958 and 2020 varied greatly from 0.6 to 7.7 m/yr (1.6 to 15.3 m/yr according to peak values) (Table 4). The most rapid coastal retreat, 7.7 m/yr (peak value up to 15.3 m/yr), occurred in a relatively short period between 2001 and 2005, which then slowed down to 3.5–3.2 m/yr (peak rates 6.6–7.8 m/yr), i.e. for the next 15 years remained clearly higher than before 2000. The sandy barrier coastal long-term retreat rate exceeding 5–10 m/yr is rarely reported worldwide (e.g. Eberhards and Saltupe, 1995; Eberhards et al., 2006; List et al., 1997; Nanson et al., 2022; Stachurska, 2012), thus the average value of 7.7 m/yr and average peak erosion rate 15.3 m/yr is unique.

The average erosion parameters are in very good correlation with the average rate of area loss (Figure 7). This demonstrates the validity of the described shoreline behaviour trends.

To answer the question about the cause of changes in the coastal retreat rate, we analysed trends in the variability of the rate of relative water level changes, changes in storminess as well as changes of sea-ice extent. Climatic oscillations on the scale of decades and centuries are potentially of high geomorphological importance. A range of geomorphological effects of such climatic oscillations have been recognised, i.e. coastal erosion (e.g. Viles and Goudie, 2003). The climate variability over the North Atlantic is known to be dominated by decadal-to-multidecadal fluctuations that have profound global and regional climate impacts (e.g. Börgel et al., 2020; Chafik et al., 2019; Knight et al., 2006; Peings and Magnusdottir, 2014), including the Baltic Sea and the surrounding areas (e.g.

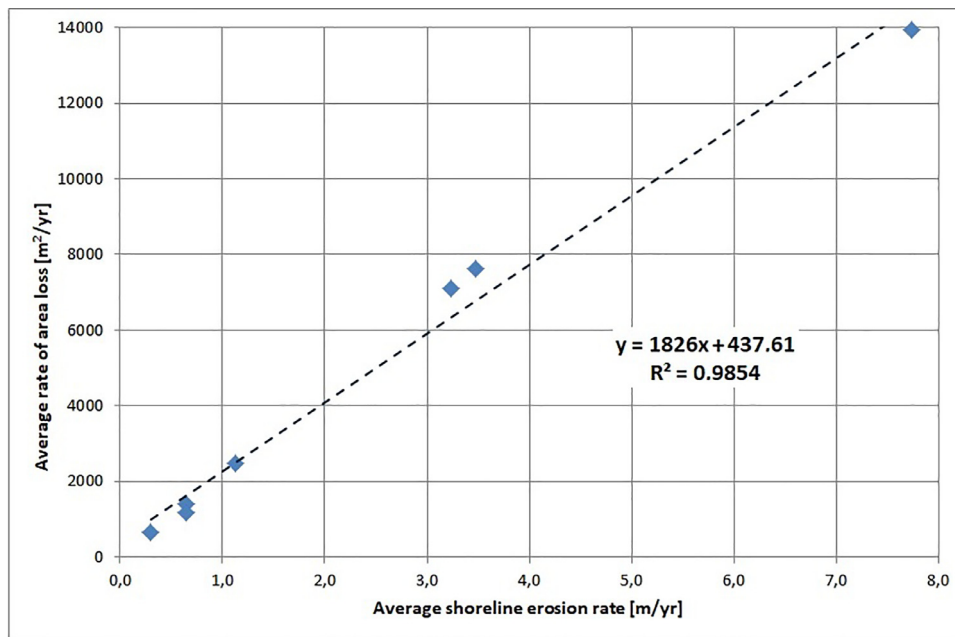


Figure 7 Correlations between average shoreline erosion rate (calculated from longshore average erosion) and average rate of area loss. The dashed blue line represents linear trend, the blue “diamonds” represents measured series.

Rutgersson et al., 2022; Slonosky et al., 2000). The North Atlantic Oscillation (NAO) and the Atlantic Multidecadal Oscillation (AMO), in particular, are two of the most prominent modes impacting the climate variability. The NAO index varies from days to decades. The long-term behaviour of the NAO is essentially irregular, and there is a large inter-annual to inter-decadal variability. The Atlantic Multidecadal Oscillation (AMO) has been identified as a coherent mode of natural variability occurring in the North Atlantic Ocean with an estimated period of 60–80 years (Rutgersson et al., 2022). NAO and AMO have a major impact on, among other features, sea level variability (e.g. Calafat et al., 2012, 2013; Chafik et al., 2019; Dangendorf et al., 2014) and changes in the frequency of storminess (e.g. Feser et al., 2015; Krueger et al., 2019). A positive high correlation coefficient of ≥ 0.5 for the NAO index, the maximum significant wave height H_s and the number of storms for Baltic Proper were identified for the period 1980–2015. A variability period of about 10–12 years was identified (Myslenkov et al., 2018). In summary, there has been considerable decadal and multidecadal variability in wind speed and direction for the last 200 years and correspondingly no clear indication of long-term trends in the frequency of storm surges and wave height (Bärring and Fortuniak, 2009; Feser et al., 2015; Rutgersson et al., 2014). Published trends in storm activity depend critically on the time analysed, data or the model used. Despite large decadal variations, a positive trend in the number of deep cyclones has been observed over the last six decades (Rutgersson et al., 2022). This is also recognised on the Polish coast, where an increasing trend in storm surge indicator values was observed in 1997–2008 (Stanisławczyk, 2012).

Storm surges have always been of interest to chroniclers and scientists (e.g. Dziadziuszko and Jednorat, 1996; Majewski, 1986, 1998; Rojecki, 1965; Sztobryn et al., 2005; Wiśniewski and Wolski, 2009; Wolski et al., 2014;

Extreme Wind Storms Catalogue, 2022; List of European Windstorms, 2022). A review of literature and internet databases also indicates an increased number of storm surges on the Polish coast since 1980. The literature also contains information about frequent and severe storms occurring in the southern Baltic at the end of the 19th century and in the first decade of the 20th century (e.g. Majewski, 1998), although quantitative data from that period are scarce and not very accurate. The same is true for almost the entire 20th century, which was probably due to little interest in climate change at that time and only exceptionally catastrophic storms were recorded.

The average rate of water level rise according to the mareograph in Władysławowo, the nearest to the study area, in the period 1951–2015 was 2.04 mm/year. For the same period, the average rate in Gdańsk was 2.43 mm/yr (Kowalczyk, 2019). This slight discrepancy may be caused by differences in vertical ground movements. A much longer record of water level changes, starting from 1886, comes from Gdańsk (Figure 8). Trends in mean annual water level changes for corresponding periods are the same along the Polish coast, therefore we use the record from Gdańsk to analyse potential relationships between changes in the shoreline position, water level and storminess. The average rate of water level rise in Gdańsk in the period 1886–2021 according to a linear trend was 1.54 mm/yr, however, it varied strongly on multidecadal and decadal time scales (Figure 8).

These facts clearly indicate the underlying cause of the increased rate of coastal retreat starting in the second half of the 20th century in the coastal retreat rate (Table 3) correlate well with an increasing multidecadal trend in storm activity starting in the mid-1960s and continuing into the 1990s (Krueger et al., 2019), as well as the increasing storminess occurring over the decades 2000–2020 (Rutgersson et al., 2022; Stanisławczyk, 2012). During the

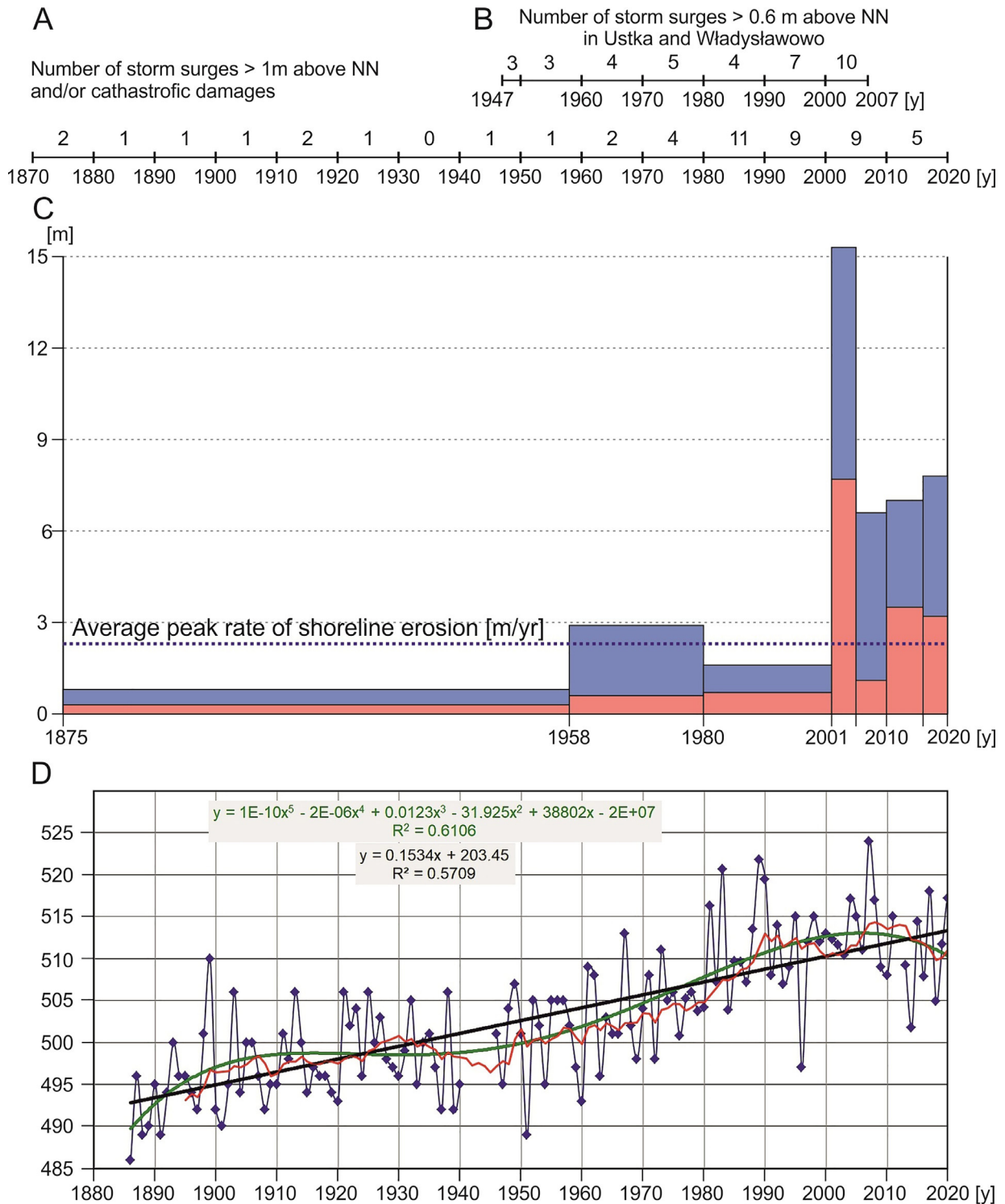


Figure 8 Erosion rate in relation to number of storms and sea level rise;
 A – Number of storm surges > 1 m above NN and/or catastrophic damages (according to Majewski (1986, 1998), Dziadziuszko and Jednorat (1996), Sztobryn et al. (2005), Extreme Wind Storms Catalogue (2022), List of European Windstorms (2022));
 B – Number of storm surges > 0.6 m above NN in Ustka and Władysławowo (according to Wiśniewski and Wolski (2009));
 C – Rate of average shoreline retreat (pink bars) and average peak shoreline retreat (blue bars);
 D – Annual average sea level changes according to the Gdańsk mareograph;
 The black line represents the linear trend, the red line is the 10-year running average and the green line is the trend approximated by a 5-degree polynomial.

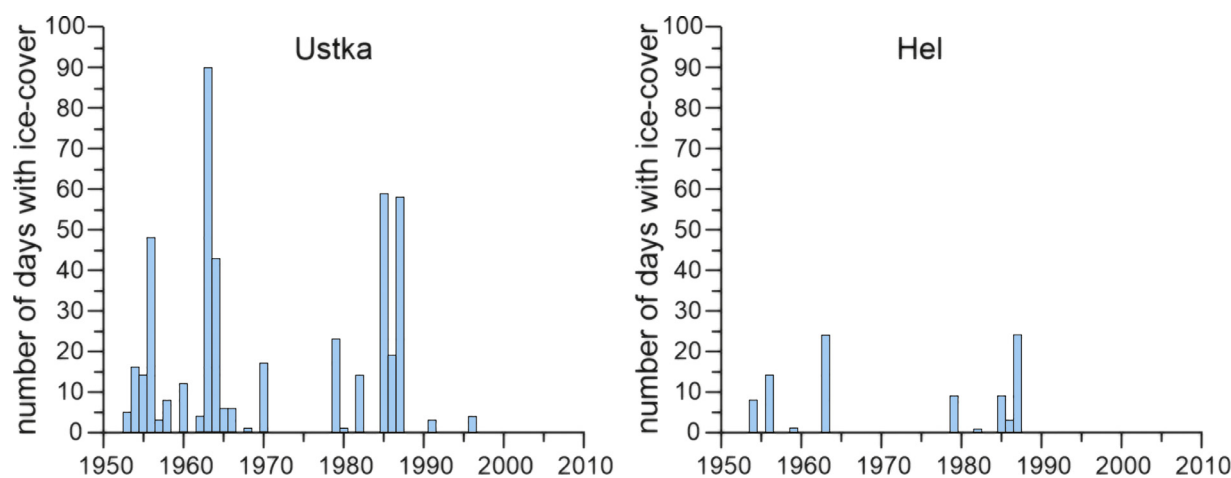


Figure 9 Ice-cover in Ustka and Hel, ports located west and east from discussed erosional hot spot (according to Sztobryn et al. (2012) – with changes).

same time, there were changes in decadal trends in water level changes (Figure 8). The highest rate of coastal retreat occurred between 2000 and 2005, when the NOA index was low (e.g. Krueger et al., 2019; Rutgersson et al., 2022) and the decadal trend of average sea level decreased (Figure 8), but there were several extremely severe storm surges, including in particular on 23 November 2004 (Elisabeth), 22 December 2004 (Rafael), and 9 January 2005 (Erwin-Gudrun), which caused catastrophic damage to the southern Baltic coast. For example, on December 22, 2004, during Storm Rafael, the height of the significant wave at the time was about 8.2 m, and the highest wave was estimated at a record 14 meters (<https://obserwator.imgw.pl/wielkie-fale-na-baltyku/>).

This means that NAO and AMO increased trends are of crucial importance for the rate of coastal retreat on the decadal and multidecadal time scales, while random extreme phenomena play an important role on a shorter time scale.

The increased rate of coastal retreat can also be explained by changes in sea ice cover, which is also one of the important factors suppressing surface waves and protecting shores against erosion by storm surges (Climate Change in the Baltic Sea, 2021). Maximum sea-ice extent of the Baltic Sea, duration of ice season and maximum thickness of level ice have been monitored regularly in the Baltic Sea since the late 19th century. All sea-ice observations demonstrated large inter-annual variations, but with a long-term, statistically significant trend to milder. Over the past 100 years, winters have become milder, the ice season shorter and the maximum ice extent has decreased and the period 1991–2020 was by far the mildest since ice conditions of 1720 (Meier et al., 2022). (e.g. Haapala et al., 2015, Meier et al., 2022). The interannual variability of the maximum ice extent of the Baltic Sea is owing to large-scale atmospheric circulation associated with the NAO. Greater ice extent occurs during negative phases of the NAO, while less ice extent occurs when the NAO is in a positive phase.

There has been a statistically significant decrease in the number of days with ice on the Polish coast in the period 1950–2010. Slightly less significant changes occur only in

Ustka, while the smallest changes occur in Hel (Figure 9), i.e. in ports located west and east from discussed erosional hot spot. In the case of the southern Baltic, the correlation between the NAO index (averaged over 4 winter months) and sea-ice is relatively weak (-0.23). (Sztobryn et al., 2012). The number of days with sea ice in Ustka in the period 1950–2010 ranged from 0 to 90. Despite the aforementioned relatively weak correlation (Figure 9), the highest number of days (>20) with sea ice in Ustka occurred in 1956, 1963–1964, 1979 and 1985–1987, i.e. during the negative winter NAO index (<https://commons.wikimedia.org/wiki/File:Winter-NAO-Index.svg>). However, there was no sea-ice in Ustka (and on the beaches between Ustka and Hel) after 1996 despite occurrence of negative winter NAO index in 2000, 2003–2005, 2008–2010 and 2020, so declining and lack of ice cover increases the risk and severity of coastal erosion.

At the end of the 19th century and during the first decade of the 20th century, the level of storminess was high, compared to the multidecadal upward trend in storm activity starting in the mid-1960s and continuing into the 1990s (Krueger et al., 2019). At the same time, the rate of annual average sea level rise increased up to about 10 mm/year (Figure 8). Due to the high storminess and high rate of sea level rise, the range and rate of coastal retreat must have been high at that time. However, there are no data on the range of coastal retreats for that period. The calculated rate of shoreline retreat for the period 1875–1958 is only 0.8 m/year, which is even lower than the average rate for the entire analysed period (Table 3). This is most likely because storm activity has decreased since 1914. Although severe storms occurred after 1914, the storm surges did not exceed 1.5 m. Until 1995, only one storm (1941) was recorded, when the water level exceeded the average sea level by 1.5 m (Majewski, 1998). There was also the increase of extent of sea-ice around 1916–1929 and 1940–1943 (Meier et al., 2022; <https://www.eea.europa.eu/data-and-maps/daviz/maximum-extent-of-ice-cover-3#tab-4186>). During the 30 years between 1910 and 1940, the annual average sea level decreased and then increased very slowly until ca. 1980

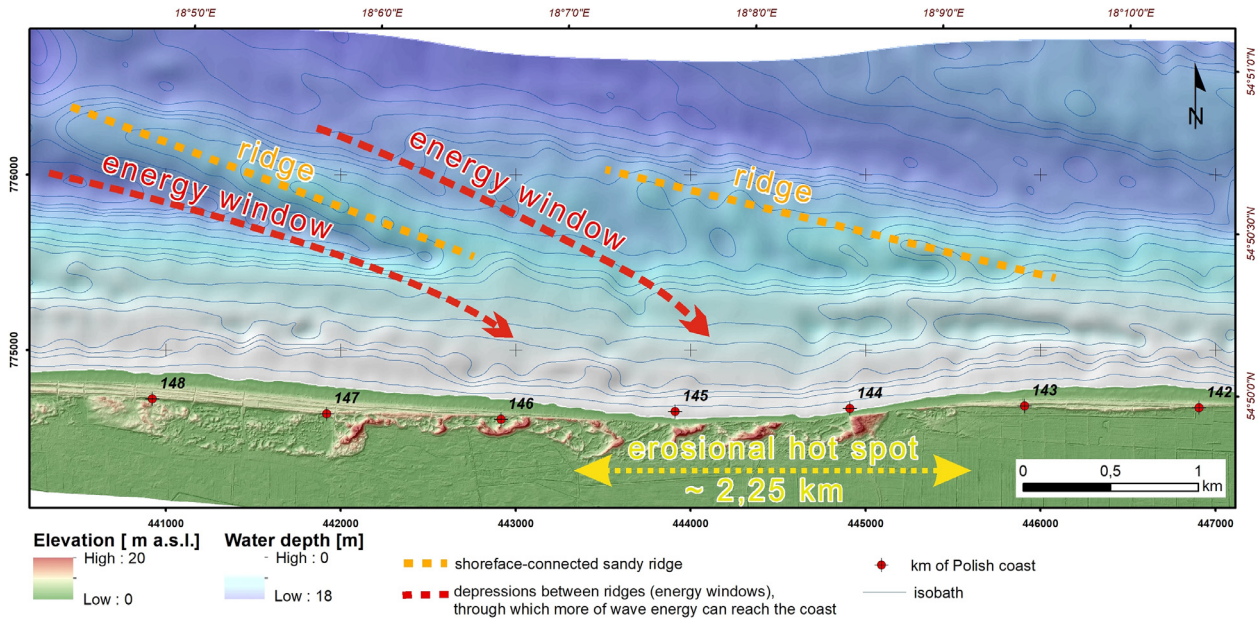


Figure 10 System of ridges and seabed depressions (energy windows) in the forefield of the erosional hot spot.

(Figure 8). As a result, the low coastal retreat rate calculated for the period 1875–1958 is most likely due to an averaging of changes from the periods of rapid coastal erosion (1875–1910) and the period of relative stabilisation (1910–1960). The discussed case of the erosion hot spot shows that the published data on the extent and rate of coastal retreat critically depend on the analysed period, and it is not always possible to clearly correlate the identified coastal erosion trends with the natural variability of the sea level and the frequency of storms.

According to the classification of erosional hot spots (Kraus and Galgano, 2001), the discussed hot spot can be classified as a type of translatable longshore sand wave (most probably) or a standing longshore sand wave with longshore dominant transport direction. The Translatable Longshore Sand Wave is indicated by the dominant (net) sediment transport direction from west to east (Szmytkiewicz et al., 2021), as well as greater accretion at the western boundaries and greater erosion at the eastern boundaries of the discussed hot spot (Table 2, Figures 4 and 5). If this is a Translatable Longshore Sand Wave, it cannot be classified as short/medium based on its duration (acc. to Kraus and Galgano, 2001; short = about a year; medium = about several years), as it has existed since the end of 19th century or at least since middle of 20th century. This discrepancy can be explained by the low offshore seabed dynamics of the tideless Baltic Sea, which is much lower than that known from tidal shelf seas and oceanic coasts. In such a case, the duration of the discussed hot spot is long-lasting, i.e. longer than the duration of a typical (e.g. investment) project, property ownership, or even longer, i.e. geologic time scale (Kraus and Galgano, 2001). The duration of the discussed EHS is longer than a century. Its lateral extent indicates that it is a local but most likely migratory phenomenon.

Consistent with the cause of erosion, the hot spot is associated with seasonal changes in wave climate over irregular offshore/nearshore topography and local wave focusing

(Figure 10) (Bender and Dean, 2003). Seaward, behind the shoreface, in the vicinity of the discussed erosional hot spot there are seabed depressions between shoreface-connected sand ridges oriented obliquely to the shore which are a kind of “energy windows”, through which more wave energy can reach the coast.

With regard to the issue as to whether the discussed hot spot could have been predicted, we can state that the existing bathymetric and topographic data allow this, but these data were not available a few years ago, whereas the discussed erosional hot spot has existed for more than a century.

Since most of the published data on erosive hot spots comes from the coasts of high-energy tidal seas or ocean coasts, it can be assumed, based on the data presented above, that the idea of erosional hot spots can also be successfully applied to the coasts of nontidal and semi-enclosed intercontinental seas. However, the guidelines and some rules for classifying hot spots, especially in terms of its duration of existence should be modified due to lower energy levels.

6. Conclusions

The shoreline follows a sinusoidal course, with a positive amplitude corresponding to accretion and a negative amplitude to erosion. An extremely erosive trend (hot spot) is distinguished between 143 and 146 km of the coastline, with an increased rate of erosion observed from 2001. Since then, it has increased several times and has led to the erosion of dunes, the maximum height of which reaches 19 m above sea level. This is attributed to geological, geomorphological and hydrodynamical factors. The depressions between shoreface-connected sand ridges are “energy windows”, through which more wave energy can reach the coast. As a result, erosional embayments are formed onshore.

The main reason for accelerated coastal erosion during the recent decades are increased number of storms and decrease extent of sea ice and decrease number of days with sea-ice. In addition to multidecadal and decadal climatic forcing, extraordinary events like storms in 2004–2005 played an important role in contributing to catastrophic changes on the coast in shorter periods.

According to the classification of erosional hot spots (Kraus and Galgano, 2001), the discussed hot spot can be classified as a type of translatory longshore sand waves, most likely with the dominant longshore direction of transport, and as indicated by the lateral extent, it is local but most likely advancing. Further research is required to fully address this question.

As for the cause of the erosional hot spot, it is related to seasonal changes in wave climate over irregular offshore/nearshore topography and local wave focusing.

In terms of duration, the hot spot in question is long lasting, i.e. lasted longer than the duration of i.a. a typical investment project, property ownership, or even longer (geologic time scale). The lifespan of the EHS is over one hundred years.

As for the question of whether the hot spot in question could have been predicted, we can argue that the existing bathymetric and topographic data allow this, but these data were not available a few years ago, whereas the hot spot has existed for more than a century.

Thus, multidecadal to decadal climate variability can trigger a pulse of hydrodynamic activity resulting in a complex coastal response. However, we have to remember that climate is not the only factor controlling the coastal processes, coastal geomorphology and geology is in many cases the determining factor.

The presented research allows us to conclude that the presented approach (EHS analyses) is also applicable to any barrier coast, including non-tidal basins.

Declaration of competing interest

The authors declare that they have no known competing financial interests or personal relationships that could have appeared to influence the work reported in this paper.

Acknowledgements

The authors express their gratitude to the Editor and Reviewers for their comments which helped to improve the article. The study presented may be considered as a contribution to EMODnet Geology project.

Funding

The authors disclose the receipt of the following financial support for research and the publication of this article: The data was collected under the project “4D cartography in the coastal zone of the southern Baltic Sea” financed by The National Fund for Environmental Protection and Water Management.

Data availability

LiDAR data (Digital Terrain Models), orthophotomaps are available via <https://sipam.gov.pl/> and <https://www.mediafire.com/folder/u95l9197wjsiv/Monitoring> (property of Maritime Office). The topographic maps were obtained from the state geodetic resource under license conditions. The restrictions do not allow open sharing of the proprietary data used in this research, but data are available upon request made to the General Office of Geodesy and Cartography or partially via www.geoportal.gov.pl.

Authors contribution

Grzegorz Uścińowicz: conceptualization, methodology, writing – original draft preparation. Szymon Uścińowicz: conceptualization, text review. Tomasz Szarafin: methodology, software, visualization. Elżbieta Maszloch: writing – regional settings. Kamila Wirkus: writing – regional settings, editing.

References

- Bärring, L., Fortuniak, K., 2009. Multi-indices analysis of southern Scandinavian storminess 1780–2005 and links to interdecadal variations in the NW Europe–North Sea region. *Int. J. Climatol.* 29, 373–384.
- Börgel, F., Frauen, C., Neumann, T., Meier, H.E.M., 2020. The Atlantic Multidecadal Oscillation controls the impact of the North Atlantic Oscillation on North European climate. *Environ. Res. Lett.* 15 (10), 104025. <https://doi.org/10.1088/1748-9326/aba925>
- Bender, C.J., Dean, R.G., 2003. Wave field modification by bathymetric anomalies and resulting shoreline changes: a review with recent results. *Coast. Eng.* 49 (1–2), 125–153.
- Benedet, L., Finkl, C.W., Hartog, W.M., 2007. Processes Controlling Development of Erosional Hot Spots on a Beach Nourishment Project. *J. Coast. Res.* 231, 33–48. <https://doi.org/10.2112/06-0706.1>
- Bridges, M.H., 1995. Analysis of the processes creating erosional hot spots in beach nourishment projects. Coastal & Oceanographic Engineering Program. University of Florida, Gainesville, FL, 135.
- Calafat, F., Chambers, D., Tsimplis, M., 2012. Mechanisms of decadal sea level variability in the eastern North Atlantic and the Mediterranean Sea. *J. Geophys. Res. Ocean.* 117, C09022. <https://doi.org/10.1029/2012JC008285>
- Calafat, F., Chambers, D., Tsimplis, M., 2013. Inter-annual to decadal sea-level variability in the coastal zones of the Norwegian and Siberian Seas: The role of atmospheric forcing. *J. Geophys. Res. Ocean.* 118 (3), 1287–1301. <https://doi.org/10.1002/jgrc.20106>
- Chafik, L., Nilsen, J.E.Ø., Dangendorf, S., Reverdin, G., Frederikse, T., 2019. North Atlantic Ocean circulation and decadal sea level change during the altimetry era. *Sci. Rep.* 9, 1041. <https://doi.org/10.1038/s41598-018-37603-69>
- Climate Change in the Baltic Sea, 2021. Fact Sheet. [in:] *Baltic Sea Environment Proceedings n°180*. HELCOM/Baltic Earth, 2021.
- Dangendorf, S., Calafat, F.M., Arns, A., Wahl, T., Haigh, I.D., Jensen, J., 2014. Mean sea level variability in the North Sea: Processes and implications. *J. Geophys. Res. Ocean.* 119, 6820–6841. <https://doi.org/10.1002/2014JC009901>

- Dean, R.G., Liotta, R., Simon, G., 1999. Erosional hot spots. Coastal and Oceanographic Engineering Program, Technical Report UFL/COEL-99/021, University of Florida, Gainesville, 60 pp.
- Deng, J., Harff, J., Zhang, W., Schneider, R., Dudzińska-Nowak, J., Terefenko, P., Giza, A., Furmańczyk, K., 2017. The dynamic equilibrium shore model for the reconstruction and future projection of coastal morphodynamics. [in:] Harff, J., Furmańczyk, K., von Storch, H. (Eds.), *Coastline Changes of the Baltic Sea From South to East, Past and Future Projection*. Coastal Research Library 19, Springer, 87–106.
- Dziadziuszko, Z., Jednorat, T., 1996. Zagrożenia powodziowe powodowane spiętrzeniami sztormowymi u brzegów Bałtyku i Zalewu Wiślanego, [Flood hazard caused storm surges off the coast of the Baltic Sea and the Vistula Lagoon]. *Wiad. IMGW*. 19 (3), 123–133.
- Eberhards, G., Saltupe, B., 1995. Accelerated coastal erosion – Implications for Latvia. *Baltica*. 9, 16–28.
- Eberhards, G., Lapinskis, J., Saltupe, B., 2006. Hurricane Erwin 2005 coastal erosion in Latvia. *Baltica* 19, 16–28.
- Esteves, L.S., Finkl, C.W., 1998. The Problem of Critically Eroded Areas (CEA): An Evaluation of Florida Beaches. *J. Coast. Res.* 11–18. <http://www.jstor.org/stable/25736114>
- Extreme Wind Storms Catalogue. <http://www.europeanwindstorms.org/cgi-bin/storms/storms.cgi>T (accessed May 2022).
- Feser, F., Barcikowski, M., Krueger, O., Schenk, F., Weisseaand, R., Xiae, L., 2015. Storminess over the North Atlantic and north-western Europe – A review. *Q. J. R. Meteorol. Soc.* 141, 350–382. <https://doi.org/10.1002/qj.2364>
- Furmańczyk, K., Musielak, S., 1999. Circulation systems of the coastal zone and their role in south Baltic morphodynamic of the coast. *Circulation systems of the coastal zone and their role in the South Baltic morphodynamics of the coast*. *Quart. Stud. Pol. Spec. Issue*, 91–94.
- Furmańczyk, K., Musielak, S., 2002. Important features of coastal dynamics in Poland: „Nodal Points” and „Gates. [in:] Schernewski, G., Schiwer, U. (Eds.), *Baltic coastal ecosystems. Structure, Function and Coastal Zone Management*. Springer-Verlag, Berlin, Heidelberg, New York, 141–147. <https://doi.org/10.1007/978-3-662-04769-9>
- Furmańczyk, K., 1994. Współczesny rozwój strefy brzegowej morza bezplywowego w świetle badań teledetekcyjnych [Present coastal zone development of the tide less sea in light of the South Baltic Sea coast remote sensing investigating], 161. Uniwersytet Szczeciński Rozprawy I Studia T, 179 CCXXXV, (in Polish with English summary).
- Galgano, F.A., 2007. Types and causes of beach erosion anomaly areas in the U.S. east coast barrier island system: stabilized tidal inlets. *Middle States Geogr.* 40, 158–170.
- Haapala, J.J., Ronkainen, I., Schmelzer, N., Sztobryn, M. The BACC II Author Team, 2015. Recent Change—Sea Ice. Second Assessment of Climate Change for the Baltic Sea Basin. *Regional Climate Studies*. Springer, Cham. https://doi.org/10.1007/978-3-319-16006-1_8
- HELCOM, 2007. Climate change in the Baltic Sea area – HELCOM thematic assessment in 2007. *Baltic Sea Environ. Proc.* 111, 49.
- HELCOM, 2013. Climate change in the Baltic Sea area – HELCOM thematic assessment in 2013. *Baltic Sea Environ. Proc.* 137, 66.
- Knight, J.R., Folland, C.K., Scaife, A.A., 2006. Climate impacts of the Atlantic Multidecadal Oscillation. *Geophys. Res. Lett.* 33, L17706. <https://doi.org/10.1029/2006GL026242>
- Kowalczyk, K., 2019. Changes in mean sea level on the Polish coast of the Baltic Sea based on tide gauge data from the years 1811–2015. *Acta Geodyn. Geomater.* 16 (2), 195–209.
- Kraus, N.C., Galgano, F.A., 2001. Beach erosional hot spots: types, causes, and solutions. *Coastal and Hydraulics Engineering Technical Note CHETN-II-44*. U.S. Army Engineer Research and Development Center, Vicksburg, MS, 1–17.
- Krueger, O., Feser, F., Weisse, R., 2019. Northeast Atlantic Storm Activity and Its Uncertainty from the Late Nineteenth to the Twenty-First Century. *J. Climate* 32, 1919–1931. <https://doi.org/10.1175/JCLI-D-18-0505.1>
- List, J.H., Sallenger, A.H., Hansen, M.E., Jaffe, B.E., 1997. Accelerated relative sea-level rise and rapid coastal erosion: testing a causal relationship for the Louisiana barrier islands. *Mar. Geol.* 140 (1997), 347–365. [https://doi.org/10.1016/S0025-3227\(97\)00035-2](https://doi.org/10.1016/S0025-3227(97)00035-2)
- List of European windstorms. https://www.wikiwand.com/en/List_of_European_windstorms# (accessed May 2022).
- Majewski, A., 1986. Skrajne wahania poziomu wody u polskich wybrzeży Bałtyku, [Extreme fluctuations of the water level on the Polish Baltic coast]. *Inżynieria Morska* 2, 46–50.
- Majewski, A., 1998. Największe wezbrania wód u południowych brzegów Morza Bałtyckiego, [The highest storm surges along the southern coast of the Baltic Sea]. *Wiad. IMGW*. 21 (2), 81–98.
- Meier, H.E.M., Kniebusch, M., Dieterich, C., Gröger, M., Zorita, E., Elmgren, R., Myrberg, K., Ahola, M.P., Bartosova, A., Bondorff, E., Börgel, F., Capell, R., Carlén, I., Carlund, T., Carstensen, J., Christensen, O.B., Dierschke, V., Frauen, C., Frederiksen, M., Galet, E., Galatius, A., Haapala, J.J., Halkka, A., Hugelius, G., Hünicke, B., Jaagus, J., Jüssi, M., Käyhkö, J., Kirchner, N., Kjellström, E., Kulinski, K., Lehmann, A., Lindström, G., May, W., Miller, P.A., Mohrholz, V., Müller-Karulis, B., Pavón-Jordán, D., Quante, M., Reckermann, M., Rutgersson, A., Savchuk, O.P., Stendel, M., Tuomi, L., Viitasalo, M., Weisse, R., Zhang, W., 2022. Climate change in the Baltic Sea region: a summary. *Earth Syst. Dynam.* 13, 457–593. <https://doi.org/10.5194/esd-13-457-2022>
- Michałowska, K., Głowienka, E., 2022. Multi-temporal analysis of changes of the southern part of the Baltic Sea coast using aerial remote sensing data. *Remote Sens.* 14, 1212. <https://doi.org/10.3390/rs14051212>
- Moskalewicz, D., 2016. Torfowiska Mierzei i Niziny Karwieńskiej potencjalnym archiwum ekstremalnych zalewów sztormowych (The peatlands of the Karwia Barrier and Karwia Lowland as a potential archive of extreme storm floods). *Acta Geogr. Lodz.*, 105, 141–148.
- Musielak, S., Furmańczyk, K., Bugajny, N., 2017. Factors and processes forming the Polish southern Baltic sea coast on various temporal and spatial scale. [in:] Harff, J., Furmańczyk, K., von Storch, H. (Eds.), *Coastline Changes of the Baltic Sea From South to East, Past and Future Projection*. Coastal Research Library 19, Springer, 69–85.
- Myslenkov, S., Medvedeva, A., Arkhipkin, V., Markina, M., Surkova, G., Krylov, A., Dobrolyubov, S., Zilitinkevich, S., Koltermann, P., 2018. Long-term statistics of storms in the Baltic, Barents and White Seas and their future climate projections. *Geogr. Environ. Sustain.* 11 (1), 93–112. <https://doi.org/10.24057/2071-9388-2018-11-1-93-112>
- Nanson, R., Bishop-Taylor, R., Sagar, S., Lymburner, L., 2022. Geomorphic insights into Australia’s coastal change using a national dataset derived from the multi-decadal Landsat archive. *Estuar. Coast. Shelf Sci.* 265, 107712. <https://doi.org/10.1016/j.ecss.2021.107712>
- Ostrowski, R., Schönhofer, J., Szymkiewicz, P., 2016. South Baltic representative coastal field surveys, including monitoring at the Coastal Research Station in Lubiato. *Poland. J. Marine Syst.* 162, 89–97. <https://doi.org/10.1016/j.jmarsys.2015.10.006>
- Peings, Y., Magnúsdóttir, G., 2014. Forcing of the wintertime atmospheric circulation by the multidecadal fluctuations of the North Atlantic ocean. *Environ. Res. Lett.* 9, 034018.
- Pruszek, Z., Ostrowski, R., Schönhofer, J., 2011. Variability and correlations of shoreline and dunes on the southern Baltic coast (CRS Lubiato, Poland). *Oceanologia* 53 (1), 97–120. <https://doi.org/10.5697/oc.53-1.097>

- Rojecki, A. (Ed.), 1965. Wyjątki ze źródeł historycznych o nadzwyczajnych zjawiskach hydrologiczno-meteorologicznych na ziemiach polskich w wiekach od X do XVI. Wydawnictwa Komunikacji i Łączności, Warszawa.
- Rutgersson, A., Jaagus, J., Schenk, F., Stendel, M., 2014. Observed changes and variability of atmospheric parameters in the Baltic Sea region during the last 200 years. *Clim. Res.* 61, 177–190. <https://doi.org/10.3354/cr01244>
- Rutgersson, A., Kjellström, E., Haapala, J., Stendel, M., Danilovich, I., Drews, M., Jylhä, K., Kujala, P., Larsén, X.G., Hal-snæs, K., Lehtonen, I., Luomaranta, A., Nilsson, E., Olsson, T., Särkkä, J., Tuomi, L., Wasmund, N., 2022. Natural hazards and extreme events in the Baltic Sea region. *Earth Syst. Dynam.* 13, 251–301. <https://doi.org/10.5194/esd-13-251-2022>
- Slonosky, V.C., Jones, P.D., Davies, T.D., 2000. Variability of the surface atmospheric circulation over Europe, 1774–1995. *Int. J. Climatol.* 20, 1875–1897.
- Stachurska, B., 2012. Analiza zmian położenia brzegu odmorskiej strony Półwyspu Helskiego na podstawie zdjęć lotniczych z lat 1947–1991. *Inżynieria Morska i Geotechnika* 4, 542–553.
- Stanisławczyk, I., 2012. Storm-surges Indicator for the Polish Baltic Coast. *TransNav – Int. J. Nav. Archit. Ocean Eng.* 6 (1), 123–129.
- Subotowicz, W., 1991. Ochrona brzegu klifowego na odcinku Jastrzębia Góra – Rozewie. *Inżynieria morska i geotechnika* 4, 143–145, (in Polish).
- Subotowicz, W., 1995. Transformation of the cliff coast in Poland. *J. Coast. Res.* 22, 5–62.
- Szmytkiewicz, P., Szmytkiewicz, M., Uściłowicz, G., 2021. Lithodynamic processes along the seashore in the area of planned nuclear power plant construction: A case study on Lubiatowo at Poland. *Energies* 14 (6), 1636. <https://doi.org/10.3390/en14061636>
- Sztobryn, M., Stigge, H.J., Wielbińska, D., Weidig, B., Stanisławczyk, I., Kańska, A., Krzysztofik, K., Kowalska, B., Letkiewicz, B., Mykita, M., 2005. Storm surges in the southern Baltic (western and central parts), Rep. No. 39, Ber. Bundesamt für Seeschiffahrt und Hydrographie (BSH), Hamburg, Rostock, 74 pp.
- Sztobryn, M., Wójcik, R., Miętus, M., 2012. Występowanie zlodzenia na Bałtyku – stan obecny i spodziewane zmiany w przyszłości. [in:] Jakusik, E., Wibig, J. (Eds.), *Warunki klimatyczne i oceanograficzne w Polsce i na Bałtyku Południowym. Spodziewane zmiany i wytyczne do opracowania strategii adaptacyjnych w gospodarce krajowej: Występowanie zlodzenia na Bałtyku – stan obecny i spodziewane zmiany w przyszłości*. Instytut Meteorologii i Gospodarki Wodnej, Warszawa, 189–215.
- Terefenko, P., Paprotny, D., Giza, A., Morales-Nápoles, O., Kubicz, A., Walczakiewicz, Sz., 2019. Monitoring Cliff Erosion with LiDAR Surveys and Bayesian Network-based Data Analysis. *Remote Sens.* 11 (7), 843. <https://doi.org/10.3390/rs11070843>
- Uściłowicz, G., Szarafin, T., 2018. Short-term prognosis of development of barrier-type coasts (Southern Baltic Sea). *Ocean Coast. Manage.* 165, 258–267. <https://doi.org/10.1016/j.ocecoaman.2018.08.033>
- Uściłowicz, S.Z., Zachowicz, J., Graniczny, M., Dobracki, R., 2004. Geological structure of the southern Baltic coast and related hazards. *Polish Geological Institute Special Papers* 15, 61–68.
- Uściłowicz, G., Jurys, L., Szarafin, T., 2017. The development of unconsolidated sedimentary coastal cliffs (Pobrzeże Kaszubskie, Northern Poland). *Geol. Q.* 61 (2), 491–501. <https://doi.org/10.7306/gq.1351>
- Uściłowicz, G., Szarafin, T., Pączek, U., Lidzbarski, M., Tarnawska, E., 2021. Geohazard assessment of the coastal zone – the case of the southern Baltic Sea. *Geol. Q.* 65 (5). <https://doi.org/10.7306/gq.1576>
- Viles, H.A., Goudie, A.S., 2003. Interannual, decadal and multi-decadal scale climatic variability and geomorphology. *Earth Sci. Rev.* 61, 105–131.
- Wiśniewski, B., Wolski, T., 2009. Katalogi wzbrań i obniżeń sztormowych poziomów morza oraz ekstremalne poziomy wód na polskim wybrzeżu, [Catalogues of storm-generated sea level surges and falls and extreme water levels on the Polish coast]. *Wyd. AM, Szczecin*.
- Wolski, T., Wiśniewski, B., Giza, A., Kowalewska-Kalkowska, H., Boman, H., Grabbi-Kaiv, S., Hammarklint, T., Holfort, J., Lydeikaite, Ž., 2014. Extreme sea levels at selected stations on the Baltic Sea coast. *Oceanologia* 56 (2), 259–290. <https://doi.org/10.5697/oc.56-2.259>
- Zawadzka, E., 1999. Tendencje rozwojowe polskich brzegów Bałtyku południowego [Development tendencies of the Polish shores of the southern Baltic Sea]. *Gdańskie Towarzystwo Naukowe, Gdańsk*, (in Polish with English summary).
- Zawadzka, E., 2012. Morfodynamika brzegów wydmych południowego Bałtyku. [Morphodynamics of the southern Baltic dune coasts]. *Wydawnictwo Uniwersytetu Gdańskiego, Gdańsk*, (in Polish with English summary).
- Zawadzka-Kahlau, E., 1999. Trends in southern Baltic coast development during the last hundred years. *Peribalticum* 7, 115–136.

Available online at www.sciencedirect.com

ScienceDirect

journal homepage: www.journals.elsevier.com/oceanologia

ORIGINAL RESEARCH ARTICLE

Evaluating and enhancing the performance of the K-Means clustering algorithm for annual coastal bed evolution applications

Andreas Papadimitriou*, Vasiliki Tsoukala

Laboratory of Harbour Works, School of Civil Engineering, National Technical University of Athens, Zografou, Greece

Received 28 December 2022; accepted 17 December 2023

Available online 6 January 2024

KEYWORDSWave input reduction;
Cluster analysis;
Morphological bed evolution;
K-Means algorithm;
Numerical modelling

Abstract The prediction of the coastal bed evolution at an annual scale utilizing process-based models is usually a complex task requiring significant computational resources. To compensate for this, accelerating techniques aiming at reducing the amount of input parameters are often employed. In the framework of this research, a comprehensive evaluation of the capacity of the widely-used K-Means clustering algorithm as a method to obtain representative wave conditions was undertaken. Various enhancements to the algorithm were examined in order to improve model results. The examined tests were implemented in the sandy coastline adjacent to the port of Rethymno, Greece, utilizing an annual dataset of wave characteristics using the model MIKE21 Coupled Model FM. Model performance evaluation was carried out for each test simulation by comparing results to a “brute force” one, containing the bed level changes induced from the annual time series of hourly changing offshore sea state wave characteristics, deeming the results very satisfactory. The best-performing configurations were found to be related to the implementation of a filtering methodology to eliminate low-energy sea states from the dataset. Employment of clustering algorithms utilizing “smart” configurations to improve their performance could become a valuable tool for engineers desiring to obtain

* Corresponding author at: Laboratory of Harbour Works, School of Civil Engineering, National Technical University of Athens, 5, Heroon Polytechniou Str. 15780, Zografou, Greece. Tel.: +30 210 7722351.

E-mail address: andrewtnt@mail.ntua.gr (A. Papadimitriou).

Peer review under the responsibility of the Institute of Oceanology of the Polish Academy of Sciences.



<https://doi.org/10.1016/j.oceano.2023.12.005>

0078-3234/© 2024 Institute of Oceanology of the Polish Academy of Sciences. Production and hosting by Elsevier B.V. This is an open access article under the CC BY-NC-ND license (<http://creativecommons.org/licenses/by-nc-nd/4.0/>).

an accurate representation of annual bed level evolution, while simultaneously reducing the required computational effort.

© 2024 Institute of Oceanology of the Polish Academy of Sciences. Production and hosting by Elsevier B.V. This is an open access article under the CC BY-NC-ND license (<http://creativecommons.org/licenses/by-nc-nd/4.0/>).

1. Introduction

The prediction of coastal bed morphological evolution along with the resulting shift in shoreline position at time scales ranging from a few days to decades has been at the forefront of coastal engineering research for several years, since coastal zones concentrate a multitude of human activities with implications to the economy, environment and community safety. Traditionally, process-based morphological models (Afentoulis et al., 2022; de Vriend et al., 1993; Roelvink and Renniers, 2012) are employed to predict the coastal bed evolution, able to resolve the complex processes that are inter-combined in the nearshore, such as wave transformation (refraction, shoaling, diffraction), hydrodynamics and circulation (e.g. shaping of rip currents) and sediment transport (e.g. sandbar movement and dune formation). The staggering drawback of said models is the high amount of computational resources they require (which can reach up to several days for a morphological simulation in a desktop computer with a CPU) in part due to their complexity as well as the different time scales in which the abovementioned processes have to be resolved, rendering a medium-term (inter-annual) prediction of coastal bed evolution a tedious task. In order to alleviate some computational burden, two distinct approaches have been employed in most applications, namely:

- Input reduction (or wave schematization), which is based on the principle that the long-term effects of smaller-scale processes can be obtained by forcing the morphodynamic models with “representative” inputs able to reproduce these effects accurately (Roelvink and Renniers, 2012). More specifically, the representative inputs comprise a set of sea state wave characteristics (significant wave height, peak wave period and mean wave direction) which when used to force the morphological process-based model are expected to create similar patterns of bed level change as an annual time series of wave characteristics (typically containing thousands of records).
- Model reduction, in which details of the smaller scale processes are omitted while the model simulation is performed at the scale of interest. The most commonly used acceleration technique of this type in 2-D area models is the morphological acceleration factor (Morfac), (Lesser, 2009), which essentially multiplies the bed level changes at each time step by a non-unity quantity.

In most coast configurations, waves are the driving factor that dictates the coastal bed evolution. When considering that a variety of wave characteristics are readily available nowadays as satellite observations or model pre-

dictions stemming from various operational oceanographic databases (e.g. Copernicus Marine Service, n.d.; ERA5-INTERIM, 1959–present), input reduction is a valuable tool commonly used in engineering practice to facilitate the prediction of annual morphological evolution (Benedet et al., 2016; Brown and Davies, 2009; Tsiaras et al., 2020; van Duijn et al., 2004; Walstra et al., 2013). Typically, annual time series of sea state wave characteristics (significant wave height, peak wave period and mean wave direction), varying at hourly intervals and reaching up to 8761 records (e.g. Papadimitriou et al., 2020) are reduced through the process of input reduction to a significantly lower number of representative wave characteristics, ranging from 6 to 30 (Benedet et al., 2016). It should be noted that the reduced input set of representative wave conditions inherently introduces numerical errors in model predictions and should include both mild and extreme wave conditions in order to retain some natural variability present in the full wave climate (i.e. the annual time series of offshore sea state wave records, typically varying at 1 hour or 3-hour intervals) (Walstra et al., 2013).

The general principle of input reduction is the division of a dataset of offshore sea state wave characteristics in wave height and directional bins, with each bin containing an equal portion of a quantity that influences longshore sediment transport, with energy flux and bulk longshore sediment transport rates being the most commonly selected ones. This category of wave schematization techniques is usually referred to as the binning methods. For more details on the binning input reduction methods the reader is referred to the paper of Benedet et al. (2016). Due to the common absence of simultaneous detailed bed elevation and offshore wave data measurements, to assess the performance of input reduction methods, model results are compared with those obtained through a simulation containing the full set of wave records of offshore sea state characteristics, which is commonly referred to as a brute force simulation (Benedet et al., 2016; de Queiroz et al., 2019). Model performance is in turn affected by a variety of parameters such as the number of representatives, duration of the wave climate and sequencing of wave conditions. Benedet et al. (2016), performed a comprehensive evaluation of five wave schematization techniques, concluding that an annual wave climate can be adequately reproduced by selecting 12 representatives and the best performing method was the one using wave energy flux as a proxy. Recently, a thorough investigation of a large number of input reduction methods and configurations utilizing a cross-shore model for the prediction of sandbar migration has been conducted (de Queiroz et al., 2019). Interestingly, the authors introduced the utilization of clustering algorithms as an alternative to the traditional binning methods of input reduc-

tion. They concluded that binning methods generally perform better than their clustering counterparts, while ordering the representatives randomly seems to give the most accurate results.

Clustering methods have been extensively utilized in the sector of data mining to efficiently deal with particularly large amounts of information. Thereafter, they have been employed in various studies in ocean and coastal engineering such as storm classification (Martzikos et al., 2018; Tsoukala et al., 2016), wave energy resources (Fairley et al., 2020), longshore transport rates (Splinter et al., 2011), cross-shore profile morphological evolution (Kelpšaitė-Rimkienė et al., 2021) and multivariate wave climate classification (Camus et al., 2011). Most clustering algorithms are based on the general principle of computing a distance metric as a similarity measure for a usually large number of variables to ultimately assign data to different clusters. Centroid-based clustering algorithms are based on the principle of segregating data points in clusters based on their squared distance from a predefined number of centroids, randomly selected at the start of the iterative procedure. Various centroid-based clustering algorithms have been developed to efficiently handle large quantities of data such as K-Means (MacQueen, 1967), Fuzzy C-Means (Bezdek, 1981) and CURE (Guha et al., 2001) among others. Particularly, K-Means is one of the most commonly used and notorious algorithms for multivariate clustering analysis that has been proven efficient in handling wave climate datasets (Camus et al., 2011) and sediment transport gradients (Splinter et al., 2011).

Recently, research efforts have been realized in investigating the possibility of utilizing clustering algorithms as an alternative to the traditional input reduction binning methods (de Queiroz et al., 2019) for a 1-D profile evolution case. However, a more detailed investigation on this topic for an extended coastal area, where longshore sediment transport dominates the coastal regime has yet to be undertaken due to the complexity of this task and the high computational effort it requires. The scope of this research is to evaluate the extensively used K-Means clustering algorithm while also examining a variety of alternative scenarios and configurations, aiming to ultimately enhance its performance in selecting the appropriate representative wave conditions to reduce the forcing input.

Essentially, the present paper explores whether the K-Means algorithm can be a viable method to select morphological representative wave heights while also evaluating if the examined alternative configurations of the default algorithm's instance can improve the annual coastal bed evolution predictions. The obtained findings have strong implications for the accurate prediction of the morphological bed evolution using process-based models, rendering the utilization of the K-Means algorithm a valuable tool for coastal engineers and scientists desiring to reduce the computational effort associated with these models.

2. Material and methods

In this section, the methodology to implement the K-Means algorithm for the purpose of reducing a dataset of annual time series of offshore sea state wave characteristics will

first be laid out, along with the configuration settings and examined enhancements to improve its performance. Subsequently, we will present a brief overview of the process-based model we utilized in this study, along with a robust wave model that we consider to be an integral part of the methodology.

2.1. Alternative examined configurations of the K-Means algorithm

The K-Means (KM) clustering algorithm divides a multi-dimensional data space into a number of clusters, each one defined by an arbitrary centroid and formed by the data for which the centroid is located the nearest (Camus et al., 2011). Essentially, given a dataset of d -dimensional vectors $X = \{x_1, x_2, \dots, x_d\}$, KM allocates each observation to the closest cluster, using the Euclidean distance between an observation and a cluster centroid as a metric to minimize the sum of squares obtained by the following objective function:

$$E = \sum \|x_i - \bar{m}_j\|^2 \quad (1)$$

where E is the sum of square error for all objects in the dataset, x_i is a point in a cluster, and \bar{m}_j the mean of each cluster (Kelpšaitė-Rimkienė et al., 2021). The assignment of centroids and corresponding clusters is an iterative procedure which is initiated by selecting k -initial centroids, usually obtained through the fast-converging K-Means++ initialization algorithm (Arthur and Vassilvitskii, 2007). Then each point is assigned iteratively to the cluster it is located closest to, in order to effectively minimize the objective function E until a user-defined convergence criterion is satisfied. It is noted that the number of initial centroids is chosen based on the user's discretion and most research efforts (Benedet et al., 2016; de Queiroz et al., 2019; Papadimitriou et al., 2020) have utilized a number ranging from 6–30 for wave input reduction applications. Within the framework of this research, the machine learning Python library "Scikit" (Pedregosa et al., 2011) was utilized for the cluster analysis. Particularly, six alternative configurations of the KM algorithm were investigated, with the following characteristics used separately or in combination, i.e. by introducing binning input reduction methods in cluster analysis, swapping of clustering variables, application of weights in the analysis and filtering of wave records. These alternative configurations are described in detail directly below.

2.1.1. 1st test KM-01

The first examined configuration KM-01 aims to evaluate the validity of utilizing the unsupervised K-means algorithm as a sound input reduction method for annual wave climate datasets. For this reason, the user interference in this case is minimal. The algorithm takes as input a dataset of wave characteristics, consisting of significant (H_s) or spectral (H_{mo}) wave height, peak wave period (T_p) and mean wave direction (MWD) which is thereafter transformed into wave incidence angle relative to the shore normal (a_0). Subsequently, the input parameters are normalized (following a minmax normalization principle) in order to perform the cluster analysis, and the algorithm outputs the centroids taken to be the representative wave conditions which will

be used afterwards as forcing input in the process-based numerical model. Care should be taken in prescribing a large number of iterations (1000 in our case) in order to avoid large differences in the obtained centroids due to non-convergence of the algorithm. In this particular case, this number was ultimately chosen by running a few instances of the algorithm and ensuring that this number of iterations gave a good compromise between execution time and achieving convergence. While increasing the number of iterations increases the computational intensity, for typical datasets of multivariate wave climates, this increase is inconsequential for practical applications (order of seconds to a few minutes). Lastly, the initial centroids have been selected by utilizing the K-means++ algorithm.

2.1.2. 2nd test KM-02

Test KM-01 can safely be applied for a variety of input time series of offshore sea state wave characteristics without expending many resources. However, when considering the nature of wave-induced hydrodynamics and sediment transport through a process-based modelling approach, the unsupervised nature of the algorithm (e.g. the quasi-random initial selection of the centroids) does not ensure accurate results in bed-level prediction. The next test case (hereafter denoted as KM-02) aims at counterbalancing this issue, by concerting the classic binning input reduction methods with clustering techniques. For this purpose, the widely-used Energy Flux method of wave schematization (Benedet et al., 2016; de Queiroz et al., 2019) was implemented at first. The main principle of the Energy Flux method is the division of the wave climate into wave height and wave direction bins, with each bin characterized by an equal fraction of the cumulative wave energy flux, which in turn is calculated by the following relationship:

$$E_f = \frac{1}{8} \rho g H_{mo}^2 C_g \quad (2)$$

where ρ is the water density, g is the gravity acceleration, H_{mo} is the spectral wave height and C_g is the wave group celerity.

The representatives of the Energy Flux method are then taken as the mean values of each bin ultimately obtaining a reduced set of wave characteristics. These values are then normalized and used as initial centers for the KM algorithm replacing those obtained by the default K-means++ initialization. Effectively, KM-02 test aims at forcing the algorithm to start iterations from “smartly” selected initial centroids that have been proven capable of reproducing the medium to long-term morphological evolution of coastal areas (Benedet et al., 2016).

2.1.3. 3rd test KM-03

For the next configuration denoted as KM-03, a slight modification was examined to the default KM-01 case, by calculating the wave energy flux of each individual sea state and using this quantity, after normalization, as weight for the cluster analysis. It can be deduced that the more energetic sea states, often associated with larger values of peak wave period and significant wave height, have the highest energy flux and therefore the KM algorithm is compelled into selecting more “energetic” wave representatives. Therefore, a significant difference in the contribution between mild

and energetic sea states is established, which significantly affects the selection of the wave-representative conditions. All other parameters (such as the initialization method and number of iterations) were taken identically to the KM-01 case.

2.1.4. 4th test KM-04

Assigning different input variables for the cluster analysis (instead of H_{mo} , T_p , a_0) has been established to lead to performance increase for the clustering algorithms for the prediction of sandbar migration (de Queiroz et al., 2019). The authors replaced the wave height values of the dataset with ones based on the premise that longshore sediment transport is the main driving factor for the medium-term morphological evolution of a coastal area.

Various bulk longshore sediment transport formulations exist in the literature (Bailard, 1985; Kamphuis, 1991; Komar and Inman, 1970) and most of them can be written in a general form as a function of the yx -component of the radiation stress gradients and wave celerity at breaking point as follows:

$$S = \frac{K}{\rho g (s-1)(1-n)} \cdot S_{yx,b} \cdot c_b \quad (3)$$

where K is a proportionality scaling factor, ρ is the water density, g is the acceleration of gravity, n is the sediment porosity, $S_{yx,b}$ is the shear component of the radiation stress tensor at breaking point and c_b is the wave celerity at breaking point.

Assuming the validity of linear wave theory, and a straight coastline with parallel depth contours, the well-known CERC formulation of bulk longshore sediment transport in deep water can be obtained from Eq. (3):

$$S = \frac{K}{32(s-1)(1-n)} \cdot \sin(2a_0) \cdot c_b \cdot H_o^2 \quad (4)$$

where a_0 is the deep-water wave incidence angle with respect to the shore-normal and H_o the deep-water wave height.

It can be deduced from both Eqs. (3) and (4) that for a bed where sediment characteristics can be considered homogenous and constant, then the bulk longshore transport rate for each sea state is essentially dependent on the product of the shear component of the radiation stress tensor and the wave celerity at breaker line.

An additional test case was set up (KM-04) based on the above, by swapping the cluster analysis input data from H_{mo} , T_p , a_0 to S , E_{fl} , a_0 , incorporating both bulk longshore sediment transport rates and energy flux which are associated with the morphological coastal evolution. For the purpose of our research, we calculate S as the product of $S_{yx,b} \cdot c_b$ by utilizing a spectral form of a Parabolic Mild Slope wave model with non-linear dispersion characteristics (Chondros et al., 2021) which will be presented in more detail in section 2.2.2. While S can be calculated through the use of Eq. (4), the limitations associated with the consideration of depth-parallel contours and the need to calculate at least one quantity at the breaker line, we consider the utilization of a robust wave propagation model superior, especially for mildly-sloping complex bathymetries where the processes of refraction-diffraction contribute significantly in the nearshore wave transformation. By executing sepa-

rate simulations for each wave record, the dataset is normalized and transformed to the desirable variables and then the KM algorithm is applied to obtain the clusters. Finally, bearing in mind that each wave record belongs uniquely in a single cluster and taking advantage of the “1-1” correspondence of H_{m0} , T_p , a_0 to S , E_{fl} , a_0 the representative wave conditions that will be used as input in the process-based numerical model are selected.

2.1.5. 5th test KM-05

The penultimate test case KM-05, concentrates at incorporating results obtained from the binning input reduction methods while simultaneously counterbalancing an issue associated with the over-representation of low-energetic wave characteristics, in the wave climate (de Queiroz et al., 2019). For this purpose, a novel binning wave schematization method (Papadimitriou et al., 2020) based on filtering of sea states considered unable to initiate sediment motion in the nearshore and then obtaining representative wave conditions based on the calculation of the sediment Pick-up Rate (van Rijn, 1986; van Rijn et al., 2019) is the centerpiece of this test. The distinct steps of this methodology will be briefly outlined below, for a more detailed overview the reader is referred to Papadimitriou et al. (2020):

1. Given a time series of offshore sea state wave characteristics (H_s , T_p , MWD), calculation of the critical Shields parameter θ_{cr} , the non-dimensional threshold for the initiation of sediment motion, is carried out for each individual wave record.
2. Wave characteristics at a characteristic depth (at around $h = 8-10$ m) are obtained by utilizing a PMS wave model (Chondros et al., 2021). After obtaining the wave climate in the nearshore, a “1-1” correspondence between each wave component offshore and the wave characteristics at the characteristic depth is established. This characteristic depth should provide a good representation of nearshore wave characteristics, hence it usually reaches values between 8–10 m (Kraus et al., 1998).
3. Calculation of the depth of closure (h_{in}) defined as the seaward limit of the littoral zone (Hallermeier, 1980; Houston, 1995) follows. For instance, Hallermeier (1980) formula reads:

$$h_{in} = 2.28H_{s,12h/y} - 68.5 \left(\frac{H_{s,12h/y}^2}{gT_{p,12h/y}^2} \right) \quad (5)$$

where $H_{s,12h/y}$ and $T_{p,12h/y}$ are the significant wave height and peak wave period exceeded for 12 hours per year, calculated at the characteristic depth specified in step 2.

4. The root mean square wave orbital velocity signal near the bed is extracted at the depth of closure.
5. For each wave record the bed shear stress due to waves $\tau_{b,w}$ and ultimately the Shields parameter θ is obtained
6. If $\theta < \theta_{cr}$ the wave record is eliminated since it does not contribute to sediment motion. Through the “1-1” correspondence established in step 2, the respective wave record of the offshore time-series is disposed of.
7. Calculation of the sediment Pick-up rate P_{in} (van Rijn et al., 2019) through Eq. (6) for each wave record at the depth of closure. Also, the cumulative Pick-up rate

P for the aforementioned wave record is determined.

$$P_{in} = 0.00033\rho_s[(s - 1)gd_{50}]^{1/2}D_*^{0.3}f_D \left[\left(\frac{\theta - \theta_{cr}}{\theta} \right) \right]^{1.5} \quad (6)$$

where P_{in} is the sediment Pick-up rate, $f_D = 1/\theta$ is a damping factor for high-velocity magnitudes ($\theta > 1.0$), d_{50} is the median sediment diameter and D_* is the dimensionless sediment grain diameter.

8. The wave records are divided into classes with respect to wave direction and significant wave height. Each class in both wave direction and significant wave heights is characterized by an equal fraction of the cumulative Pick-up rate and can be described by a set of wave characteristics.
9. Utilizing once again the “1-1” correspondence of the offshore and nearshore sea state wave characteristics, a set of representative conditions is obtained through extrapolation at the offshore dataset.

The pick-up rate method was shown to be efficient in further accelerating morphodynamic simulations by reducing the effective size of the dataset while retaining accuracy in model results (Papadimitriou et al., 2020). For test KM-05, the representatives obtained through the implementation of the Pick-up rate method were used as the initial centers for the KM algorithm utilizing the same procedure described in KM-02, effectively coercing the algorithm to commence the iterative procedure by the highly energetic centroids obtained through the Pick-up rate method.

2.1.6. 6th test KM-06

Lastly, a test case denoted as KM-06, comprised of a modification to test KM-04, was set up. The centerpiece of this modified test was the application of a comprehensive filtering procedure taking advantage of the employment of the PMS wave model for the propagation of individual wave characteristics and estimation of longshore transport rates and the wave energy flux at the breaking point. The distinct steps of the methodology applied in KM-06 are shown below and illustrated as a flow chart in Figure 1:

1. A dataset consisting of offshore sea state wave characteristics is obtained.
2. A simulation utilizing a PMS wave model is executed for each wave condition.
3. A particular row/column of the computation grid considered representative of the coastline geometry and bathymetry of the study area is predefined.
4. The point where initiation of breaking occurs is located for the predefined row/column of the computational grid specified in the previous step.
5. Non-breaking waves are noted since they are considered unable to produce adequate longshore transport for sediment motion and then eliminated, effectively reducing the total amount of wave characteristics. It should be stated that non-breaking waves denote sea states with particularly small values of significant wave height, which given the specific numerical grid resolution do not dissipate their energy due to bathymetric breaking. For this case, a spatial discretization step of 2.5 m was used to satisfy the CFL stability criterion (Courant et al., 1967) in the PMS-SP model, lead-

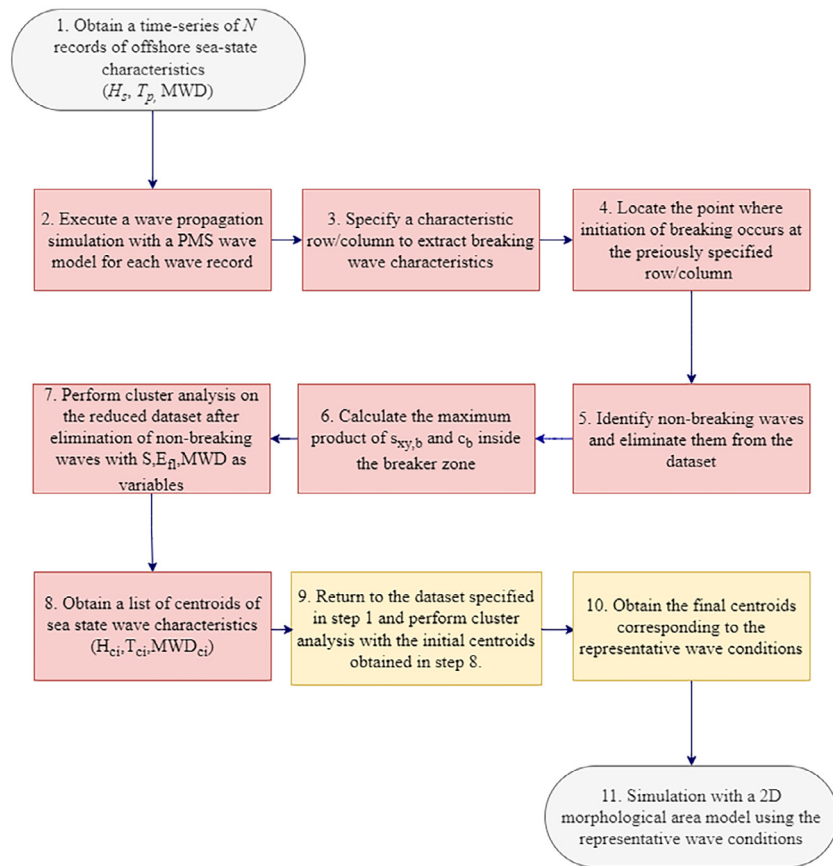


Figure 1 Flow chart of the methodological procedure applied in KM-06 to obtain the representative wave conditions.

ing to a corresponding minimum water depth of about 0.45 m.

6. Inside the breaker zone, and specifically shoreward the depth where wave breaking is initiated (see step 4), the maximum product of the shear radiation stress component $s_{xy,b}$ and wave celerity c_b is computed and then the longshore sediment transport S through Eq. (3) and wave energy flux E_{fl} through Eq. (2) are calculated.
7. A reduced dataset of S , E_{fl} , a_0 is given as input to the KM algorithm in order to obtain the resulting centroids.
8. The centroids obtained at step 7 are transformed to H_{mo} , T_p , a_0 taking into consideration that each individual wave record belongs uniquely in each cluster.
9. The representatives calculated in the previous step are used as initial centroids for the non-reduced dataset of offshore sea state wave characteristics (see step 1) and another instance of KM algorithm is utilized to obtain new centroids.
10. The centroids obtained at step 9, corresponding to the final representative wave conditions are obtained.
11. The wave representatives are set as input to the process-based numerical model, to perform the morphological evolution simulation.

2.1.7. Concatenated overview of the examined tests

A complete list of the examined scenarios carried out for the purpose of this research, denoting important aspects

of the KM algorithm configuration is compiled and shown in Table 1.

Note should be taken about the number and the sequencing of the representative wave conditions selected within the context of this research. Both parameters significantly affect the process-based model performance (Benedet et al., 2016; Daly et al., 2014; de Queiroz et al., 2019) due to the non-linear response of the sediment transport to the wave forcing. In this study and for all examined test cases the predefined number of representatives was kept constant at 12, which was found to be a good quantity in representing wave climates with duration at the order of 365 days (Benedet et al., 2016). This number was further validated (de Queiroz et al., 2019), with extensive testing on the duration of the wave climate and the number of representatives.

Regarding the sequencing of the reduced set of wave conditions obtained through the cluster analysis, random ordering was undertaken, known to provide a good representation of the natural variability of the wave climate (Benedet et al., 2016; Walstra et al., 2013). However, recognizing that random perturbation of the cluster centroids obtained through tests KM-01 to KM-06 can lead to a majorly different ordering of the representatives and significantly affect performance evaluation, an effort to reduce this effect was undertaken. Performing a random ordering of the obtained representatives for case KM-01, for the subsequent tests the ordering with the closest similarity between the examined test and KM-01 was obtained by imple-

Table 1 Overview of the examined Input Reduction cases and applied configurations for the cluster analysis.

Test	Input Variables	Cluster Initialization Method	Applied weights
KM-01	H_{mo}, T_p, a_0	K-Means++	-
KM-02	H_{mo}, T_p, a_0	Energy Flux method centroids	-
KM-03	H_{mo}, T_p, a_0	K-Means++	Energy flux of individual waves
KM-04	S, E_{fl}, a_0	K-Means++	-
KM-05	H_{mo}, T_p, a_0	Pick-up rate method centroids	-
KM-06	S, E_{fl}, a_0 H_{mo}, T_p, a_0	K-Means++ Centroids from previous instance of the algorithm	-

menting the well-known Kuhn-Munkres optimization algorithm (Munkres, 1957) for the assignment problem. Specifically, the most similar centroids with regards to the normalized H_{mo}, T_p, a_0 values with respect to the KM-01 case were calculated for each test KM-02 through KM-06 and then ordered accordingly. Although the representatives obtained through the different tests still exhibit differences, it is the authors’ belief that implementation of the Kuhn-Munkres algorithm can ultimately minimize the effect of sequencing between the consecutive tests and ensure that the performance evaluation of model results can largely be attributed to the enhancements to the KM algorithm proposed herein.

2.2. Theoretical background of numerical models

Within the scope of this research, a 2D composite model, namely MIKE21 Coupled Model FM (DHI, 2014) was utilized for the simulation of wave propagation, hydrodynamic circulation, sediment transport and morphological bed evolution. In addition, a robust wave model (Chondros et al., 2021; Papadimitriou et al., 2020) based on the parabolic approximation of the Mild Slope Equation was employed as an integral part of the cluster analysis and methodology in test KM-04 and KM-06 respectively. Moreover, the specific model considers nonlinear amplitude dispersion effects and treats the propagation of uni-directional irregular waves and thus can produce accurate results in the nearshore. Nevertheless, it should be mentioned that parabolic approximation models are restricted to cases where wave reflection is not dominant and standing wave patterns are not present, due to their inability to simulate back-scattering waves. In the following sections, the governing equations and main features of the abovementioned numerical models are presented.

2.2.1. The MIKE21 Coupled Model FM suite

For the annual prediction of the bed evolution, the process-based numerical model MIKE 21 Coupled Model FM (DHI, 2014) was used for the detailed description of hydrodynamics, waves, and sediment transport rates. The model has been used extensively in a variety of coastal engineering applications, with and without the presence of coastal protection structures (Afentoulis et al., 2017; Drønen et al., 2011; Gad et al., 2018; Kaergaard et al., 2014).

The MIKE21 Coupled model FM suite includes several complementary numerical models and tools three of which were used for the purpose of this research:

- MIKE21 SW (DHI, 2009a), a 3rd generation spectral wave model based on the evolution of the wave action-density spectrum, suited for the propagation and transformation of waves in the coastal zone.
- MIKE21 HD (DHI, 2009b), a depth-averaged hydrodynamic model based on the Reynolds averaged Navier-Stokes equations of motion (RANS), for the description of the nearshore circulation.
- MIKE21 ST (DHI, 2009c), a sand transport and morphology updating model used to calculate sediment transport rates and ultimately the morphological bed evolution.

The three models are directly coupled, allowing for the interaction between waves and currents and the effect of bed level changes in waves and hydrodynamics. The calculations are performed in an unstructured finite element mesh, allowing for flexibility in calculations and a more precise representation of the coastline and complex topography features. The governing equations of each respective model will be presented briefly below.

MIKE 21 SW model (DHI, 2009a) is a 3rd generation spectral wave model suited for the propagation of waves in the oceanic scale and in nearshore areas. The governing equation of the model is based on the principle of conservation of the wave action-balance (Komen et al., 1994) which reads in Cartesian coordinates:

$$\frac{\partial N}{\partial t} + c_x \frac{\partial N}{\partial x} + c_y \frac{\partial N}{\partial y} + c_\sigma \frac{\partial N}{\partial \sigma} + c_\theta \frac{\partial N}{\partial \theta} = \frac{S}{\sigma} \tag{7}$$

where $N(x, y, \sigma, \theta, t)$ is the wave action density, c_x, c_y are the propagation velocities in the spatial domain, c_σ is the propagation velocity in the frequency domain, c_θ is the propagation velocity in the directional domain, S denotes source and sink terms (e.g. generation due to wind, white-capping dissipation, non-linear wave interactions, depth-induced breaking) and σ is the wave intrinsic angular frequency. All the aforementioned transfer velocities are computed according to the linear wave theory (Komen et al., 1994).

The hydrodynamic model MIKE21 HD (DHI, 2009b) is based on the solution of the depth-integrated shallow water equations, expressed by the continuity and momentum

equations in the Cartesian space:

$$\frac{\partial h}{\partial t} + \frac{\partial h\bar{u}}{\partial x} + \frac{\partial h\bar{v}}{\partial y} = hS \quad (8)$$

$$\begin{aligned} \frac{\partial h\bar{u}}{\partial t} + \frac{\partial h\bar{u}^2}{\partial x} + \frac{\partial h\bar{u}\bar{v}}{\partial y} \\ = f\bar{v}h - gh\frac{\partial\eta}{\partial x} - \frac{h}{\rho}\frac{\partial p_a}{\partial x} - \frac{gh^2}{2\rho}\frac{\partial\rho}{\partial x} + \frac{\tau_{sx}}{\rho} - \frac{\tau_{bx}}{\rho} \\ - \frac{1}{\rho}\left(\frac{\partial S_{xx}}{\partial x} + \frac{\partial S_{xy}}{\partial y}\right) + \frac{\partial}{\partial x}(hT_{xx}) + \frac{\partial}{\partial y}(hT_{xy}) + hu_sS \end{aligned} \quad (9)$$

$$\begin{aligned} \frac{\partial h\bar{v}}{\partial t} + \frac{\partial h\bar{u}\bar{v}}{\partial x} + \frac{\partial h\bar{v}^2}{\partial y} \\ = f\bar{u}h - gh\frac{\partial\eta}{\partial y} - \frac{h}{\rho}\frac{\partial p_a}{\partial y} - \frac{gh^2}{2\rho}\frac{\partial\rho}{\partial y} + \frac{\tau_{sy}}{\rho} - \frac{\tau_{by}}{\rho} \\ - \frac{1}{\rho}\left(\frac{\partial S_{xy}}{\partial x} + \frac{\partial S_{yy}}{\partial y}\right) + \frac{\partial}{\partial x}(hT_{xy}) + \frac{\partial}{\partial y}(hT_{yy}) + hv_sS \end{aligned} \quad (10)$$

Where h is the total depth of the water column, \bar{u} and \bar{v} are the depth-averaged velocity components in the x and y direction respectively, η is the surface elevation, f is the Coriolis parameter, ρ is the water density, S_{xx} , S_{yy} , S_{xy} , are components of the radiation stress tensor, p_a is the atmospheric pressure, S being the magnitude of point sources, with u_s , v_s being the velocity vectors of a point discharge and T_{xx} , T_{yy} , T_{xy} denoting lateral stresses including viscous, turbulent friction and differential advection.

MIKE 21 ST model (DHI, 2009c) calculates the sediment transport rates and the morphological bed evolution either in a pure current case, or under the combined effect of waves and currents.

For the case of wave- and current-induced sediment transport, these rates are calculated by linear interpolation on an externally formed sediment transport table. The core of this utility is a quasi-three-dimensional sediment transport model (STPQ3D). The model calculates the instantaneous and time-averaged hydrodynamics and sediment transport in the two horizontal directions.

An integral quantity of the bed level evolution is the rate of bed level change $\frac{\partial z}{\partial t}$ calculated at the element cell centers of the computational mesh. This parameter is obtained by solving the well-known equation of sediment continuity, called the Exner equation:

$$\frac{\partial z}{\partial t} = -\frac{1}{(1-n)}\left(\frac{\partial q_x}{\partial x} + \frac{\partial q_y}{\partial y} - \Delta S\right) \quad (11)$$

where n is the sediment porosity, q_x , q_y are the total load sediment transport rates in the x and y direction respectively and ΔS is a sediment source or sink term. The new bed level is then obtained by a forward-marching scheme.

2.2.2. The PMS-SP wave model

In order to calculate the nearshore wave characteristics in tests KM-04 and KM-06, a Parabolic Mild Slope model is implemented, utilizing its accuracy in prescribing the wave field in mildly sloping sea bottoms and its computational efficiency. In particular, the wave model PMS-SP is an extended version of the model presented in Chondros et al. (2021) based on the work of Kirby and Dalrymple (1983) who derived a parabolic equation, in the form

of a cubic Schrödinger differential equation, governing the complex amplitude, of the fundamental frequency component of a Stokes wave. The parabolic equation and its range of validity was further improved (Dalrymple and Kirby, 1988) by developing approximations based on minimax principles in order to allow for large-angle propagation and rendering the approximation suitable for large-scale applications.

The model treats the generation and propagation of uni-directional irregular waves, by solving the governing equation for each wave component separately and ultimately performing linear superposition to obtain the wave characteristics. Waves are generated considering either a Jonswap (Hasselmann et al., 1973), TMA (Bouws et al., 1985), or Pierson-Moskowitz (Pierson and Moskowitz, 1964) spectrum and distinction into discrete wave components is carried out by dividing the spectrum into equal energy bands. Additionally, the model incorporates non-linear dispersion characteristics, in order to improve results in the nearshore area, which can be obtained by introducing an approximate non-linear amplitude dispersion relationship (Zhao and Anastasiou, 1993). Energy dissipation due to bottom friction is also incorporated (Putnam and Johnson, 1949). The model's computations are performed in a regular grid and the finite difference method is utilized to discretize the model equations. It is mentioned that the PMS-SP wave model was selected instead of the MIKE21 SW wave model for wave propagation in the nearshore in the context of the examined KM tests, due to its relative computational efficiency. This is further exemplified by the enhancements made in the framework of this research which further facilitated the easier post-processing of results.

Since the PMS-SP model is tasked with the calculation of radiation-stress components and wave celerities at the breaking point, the incorporation of wave energy dissipation due to bathymetric breaking becomes a noteworthy aspect. Energy dissipation (D) due to wave breaking is calculated in the model through the formulation of Janssen and Battjes (2007) which reads:

$$D = \frac{3\sqrt{\pi}B}{16} \frac{\bar{f}\rho g H_{rms}^3}{h} \left[1 + \frac{4}{3\sqrt{\pi}} \left(R^3 + \frac{3}{2}R \right) \exp(-R^2) - \text{erf}(R) \right] \quad (12)$$

where B is a calibration coefficient, H_{rms} is the root-mean-square wave height, h is the water depth, \bar{f} is the spectrum mean frequency and $R = H_m/H_{rms}$ with H_m being the maximum wave height obtained through Miche's criterion (Miche, 1951). The model is based on the work of Baldock et al. (1998), improving the latter's behavior near the waterline by achieving the elimination of singularities after the point of saturation (Battjes and Janssen, 2009). The incorporation of Eq. (12) is expected to improve the depth-induced energy dissipation in the model, replacing the original formulation of Battjes and Jansen (1978) which was included in the original model developed by Chondros et al. (2021).

To validate the model performance in simulating wave breaking for uni-directional irregular waves the experiment on wave propagation and breaking on plane beach with a slope of 1:20 (Mase and Kirby, 1992) was reproduced. Herein, model results will be compared to the measurements corresponding to the first case of said experiment.

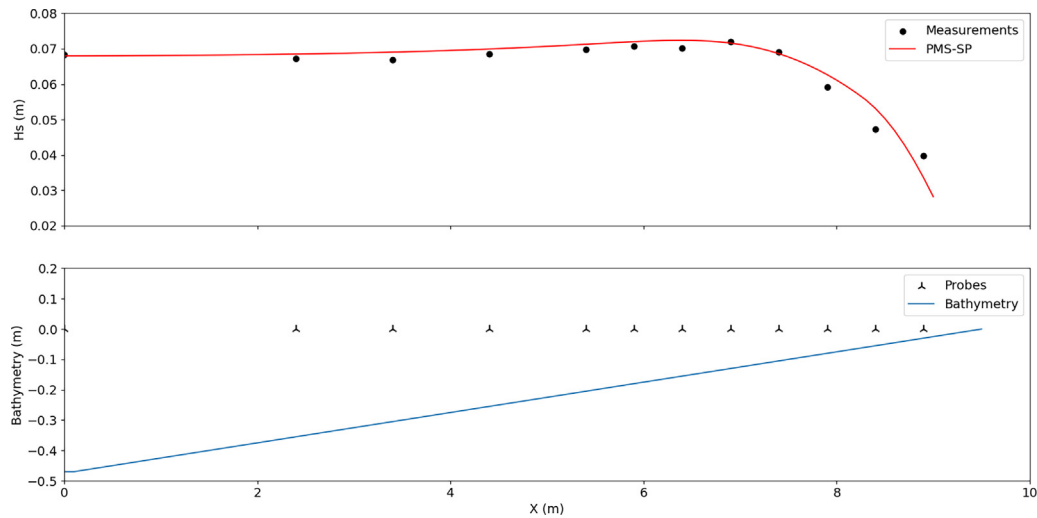


Figure 2 Computed (solid red line) and measured (circular markers) values of test 1 for the Mase and Kirby (1992) experiments along with the bathymetry (solid blue line) and probe positions (markers).

In the experimental layout, waves propagate for 10 m on a bed with a constant water depth of 0.47 m, before propagating up a sloped beach starting at $x = 0$ m. The free surface was measured by 12 probes located at 0, 2.4, 3.4, 4.4, 5.4, 5.9, 6.4, 6.9, 7.4, 7.9, 8.4, 8.9 m respectively. Waves were generated through a Pierson-Moskowitz source function with a peak frequency $f_p = 0.6$ Hz and a spectral wave height $H_{m0} = 0.068$ m. In the numerical model, the spectrum was discretized using 50 wave frequencies.

The numerical model results concerning the computed significant wave heights compared to the experimental measurements are illustrated in Figure 2. It is shown that the model is capable of reproducing accurately the effect of wave shoaling and captures quite well the starting point of wave dissipation due to wave breaking. At the last two probes, a discrepancy between measurements and model results can be attributed to the inability of the model to predict wave setup near the coastline. Considering all the above, model results are comparable and in excellent agreement with those presented in (Chawla et al., 1998) who also utilized a spectral version of a parabolic mild slope wave model, further validating the ability of the PMS-SP model in simulating wave dissipation due to depth-induced breaking on a mildly sloping bed.

3. Model setup and implementation

3.1. Study area

Evaluation of the KM algorithm’s-obtained representative conditions was carried out using the MIKE21 Coupled Model FM suite in the coast located in the close vicinity of the port of Rethymno, on the island of Crete, Greece (Papadimitriou et al., 2020). The area of interest, shown in Figure 3, includes the previously mentioned port, located at the northern end of Crete within the homonymous bay and the adjacent coastal area eastward and a coastline of approximately 4 km in length. The coastal bed is comprised mostly of fine sand, with a median sediment diameter of

$d_{50} = 0.15$ mm, which was set as a constant for the morphological simulations. Being a highly urbanized area, commercial, administrative, cultural and tourist activities are concentrated along the north coast where the city is located. Consequently, a year-to-year prediction of the bed evolution and ultimately the displacement of the shoreline is of particular interest to the scientific community and the public.

3.2. Offshore wave characteristics and computational mesh

To force the 3rd generation spectral wave model MIKE21 SW, time series of wave characteristics, namely spectral wave height, peak wave period and mean wave direction, were obtained at the north boundary of the computational mesh, from the Copernicus Marine Service (CMEMS) database for a time range covering 01/1993–12/2019. For this purpose, the regional package MED-SEA_MULTIYEAR_WAV_006_012 (Korres et al., 2019), a multi-year wave hindcast product composed of hourly wave parameters at $1/24^\circ$ horizontal grid resolution was utilized. The KM algorithm configurations were examined for a time series covering a full year (365 days) of wave records, extending from 01/01/2012 to 01/01/2013. A Morfac value (Lesser, 2009) of 50 was used for all simulations in order to obtain reasonable computational times. For each examined test, the process-based model results were compared to a brute force simulation containing the full extent of the extracted time series. The wave climate was rather diverse, containing both mild- and extreme-wave sea states, with a minimum wave height of 0.09 m and a maximum wave height of 4.66 m. From an initial filtration of the waves that exit the computational domain (generated from SE, S and SW directions) and therefore have no effect on the morphological bed evolution, the dataset was reduced from 8762 hourly changing wave records to 8219. The wave rose plot of the full time-series utilized as input in the brute force simulation is shown in Figure 4.



Figure 3 The coastal zone where the MIKE21 Coupled Model FM was implemented, superimposed with the location of the prefecture of Rethymno, relative to the island of Crete (top right).

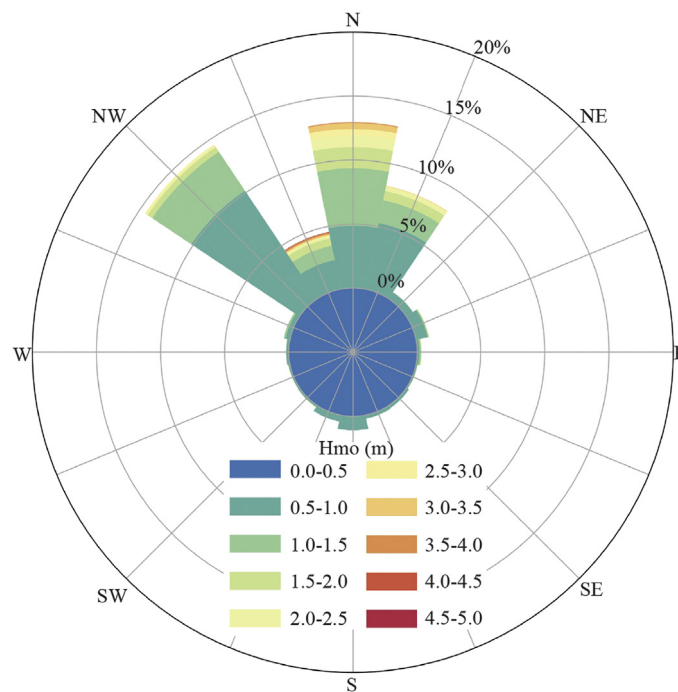


Figure 4 Wave rose plot for the dataset containing records of 365 days.

An unstructured finite element mesh was constructed for the purpose of the composite model simulations. Three separate mesh density levels were used for the discretization of the domain, with the coarser area being near the offshore and the lateral wave boundaries, and the denser one covering an extend of 3.5 km long and 10.0 km wide. A third density level was established extending at about 250 m offshore the western coastline which was a particular area of interest. For the solid boundaries, a vertice-adaptive mesh

generation scheme allowed the construction of relatively small finite elements, allowing for a more detailed representation of the bathymetric variations in shallow water areas. Regarding the dimensions of the interior triangular elements, they are characterized by a mean nominal length of about 100 m, with the largest element size being 293 m and the minimum 0.71 m. The north offshore open boundary coincided with the point where offshore sea state wave characteristics were extracted from the CMEMS database.

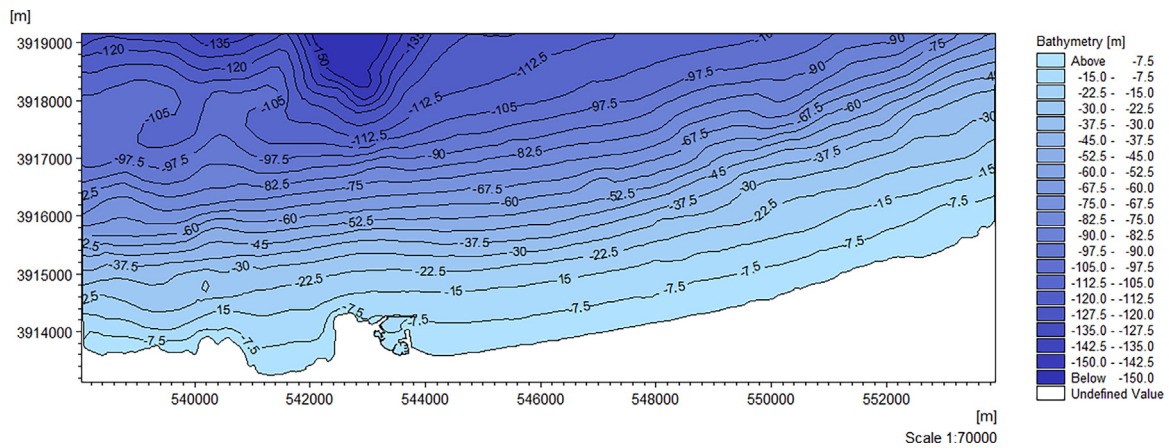


Figure 5 Contour map of the bathymetric computational domain of the study area of Rethymno, Crete, Greece.

The bathymetry of the study area is showcased in Figure 5 while the unstructured finite element mesh of the model is shown in Figure 7.

3.3. Obtained representative wave conditions

In this subsection, an overview of the 12 representative wave conditions obtained through the cluster analysis will be given. Although clustering algorithms utilize three variables as input for the purpose of wave schematization, a 2-D scatter plot in terms of wave height and wave incidence angle for all tests is shown in Figure 6 for a more comprehensive representation. It should be noted that in Figure 6 wave incidence angles are given with respect to the shore normal, with -90° denoting waves generated from the west sector and 90° denoting waves generated from the east.

Regarding the obtained representatives for KM-01 it can be observed that due to the form of the dataset, some obtained centroids are closely located (e.g. at angles of wave incidence located near -40°). For tests KM-02, KM-05 and KM-06, which use previously obtained representatives as initial centers, cluster centroids are distributed in a broader area, and a shift is observed to more energetic wave representatives. Special attention should be paid to test KM-03, namely the one containing weights related to the wave energy flux during the algorithm execution, which as seen in Figure 6, leads to a significant shift of all the obtained centroids to more energetic conditions compared to all the other tests. Clusters in KM-04 are more distinctively defined which can be caused by the shift of clustering variables from H_{m0} , T_p , a_0 to S , E_{fl} , a_0 . Finally, tests KM-05 and KM-06 in which two filtering methodologies for low-energy sea states were applied, lead to a similar pattern regarding the distribution of wave representatives in the wave height/wave incidence angle plane.

Although not evident directly in Figure 6, a major parameter in the calculations is the frequency of occurrence (f_i) of each representative, which is calculated by dividing the number of members of each cluster by the total amount of the dataset. As a showcase, in Table 2, the representatives obtained through KM-02 and the respective ones through KM-05 are presented.

It can be observed that most respective representatives of the two tests showcased in Table 2 above are quite similar (with the biggest difference observed at cluster 9, marked with bold fonts in Table 2). However, in general, KM-05 representatives are characterized by a higher frequency of occurrence of the more energetic sea-states (e.g. cluster 6) compared to KM-02 and in turn milder wave conditions have a lower frequency of occurrence (e.g. cluster 1). This can in part be attributed to the elimination of low-energy-wave sea states due to the criterion of incipient motion, integral to the implementation of the Pick-up rate method, which coerces the KM algorithm to initiate the iterative procedure from essentially more energetic centroids. Therefore, tests that include a filtering procedure and utilize previously calculated initial centroids tend to have an increased frequency of occurrence for more energetic wave events. Hence, it is considered that the frequency of occurrence is a parameter directly influencing the composite model (i.e. MIKE 21 CM FM) performance and accuracy of the results.

3.4. Model performance evaluation

In order to evaluate the performance of the 2D morphological area model, various statistical metrics can be calculated (Sutherland et al., 2004). The performance of a morphological model can ultimately be assessed by estimating its bias, accuracy and skill. The most commonly used measure of the latter quantity is the Brier Skill Score (BSS) which has been implemented in a plethora of morphological modeling applications (Knaapen and Jouxtra, 2012; Sutherland et al., 2004; van Rijn et al., 2003). It is calculated through the following relationship:

$$BSS = 1 - \frac{MSE(Y, X)}{MSE(B, X)} = 1 - \frac{\langle (Y - X)^2 \rangle}{\langle (B - X)^2 \rangle} \quad (13)$$

where Y denotes the predicted (modeled) quantity, X denotes a measured quantity, corresponding to the brute force simulation for the present study due to lack of measurements, and B is a baseline prediction, usually representing the initial bathymetry. Additionally, the square brackets denote averaged quantities over the computational domain. In Table 3 the classification scores for the BSS to estimate the

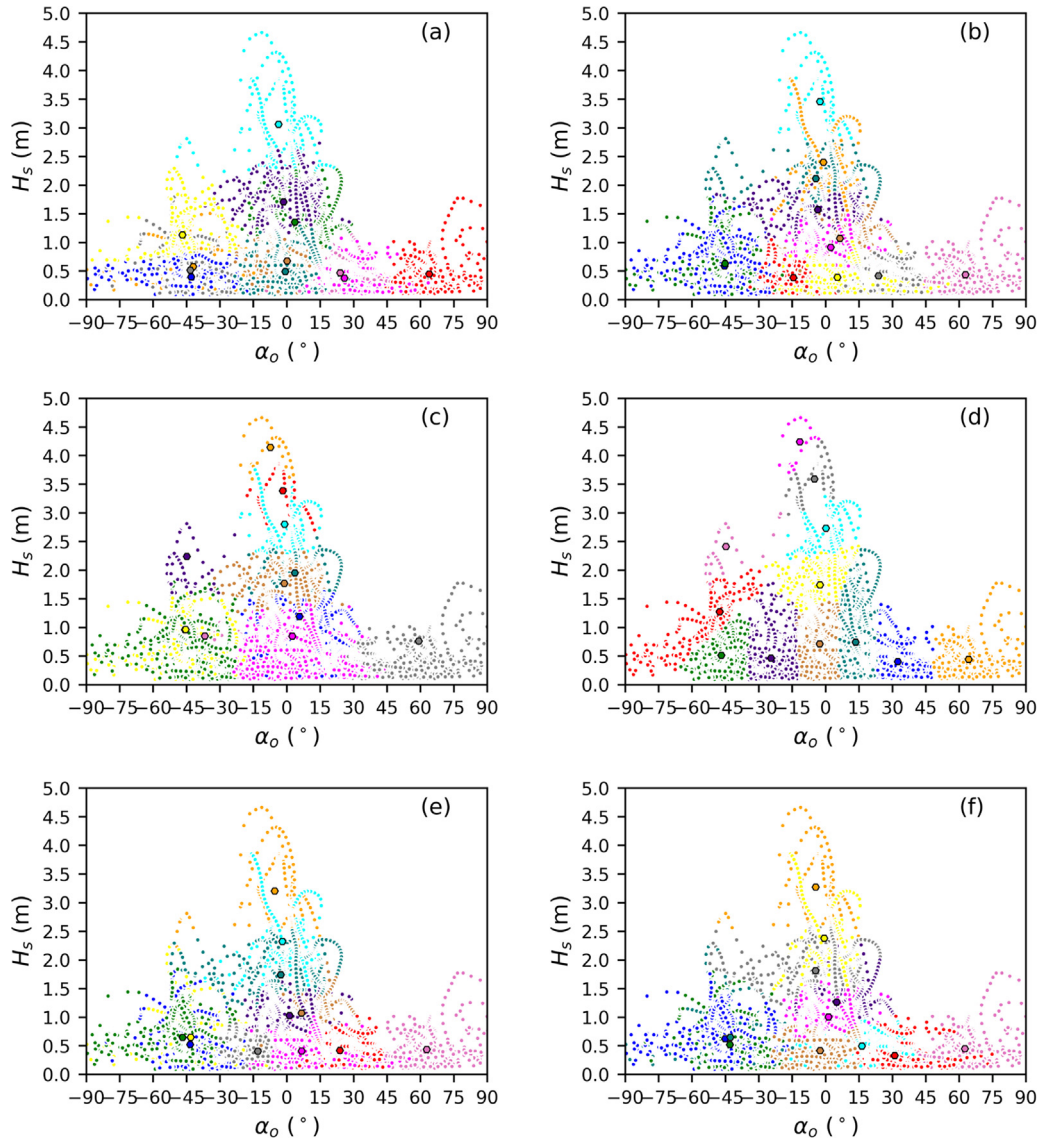


Figure 6 Obtained clusters and representative wave conditions for the: (a) KM-01, (b) KM-02, (c) KM-03, (d) KM-04, (e) KM-05 and (f) KM-06 test cases.

Table 2 Comparison of the obtained representative wave characteristics from KM-02 and KM-05 cases.

Cluster	KM-02				KM-05			
	H_{mo} [m]	T_p [s]	α_0 [°]	f_i [%]	H_{mo} [m]	T_p [s]	α_0 [°]	f_i [%]
1st	0.58	3.88	-45.35	19.36	0.52	3.18	-43.32	11.62
2nd	0.63	6.75	-45.12	11.77	0.64	5.40	-46.73	15.06
3rd	0.38	4.92	-14.41	8.65	0.65	7.78	-43.06	5.15
4th	2.40	3.18	-0.94	1.70	2.32	3.37	-1.94	2.08
5th	0.39	3.52	5.36	11.23	0.41	3.61	6.73	11.86
6th	3.46	6.83	-2.48	1.39	3.20	6.75	-5.38	1.98
7th	0.41	5.83	23.80	11.50	0.42	5.86	23.88	11.33
8th	0.91	4.34	2.36	9.83	1.02	4.36	1.29	9.78
9th	2.11	6.60	-4.34	3.21	0.40	4.84	-12.93	9.27
10th	1.57	5.17	-3.46	7.12	1.74	5.79	-2.62	7.73
11th	0.43	5.92	62.88	5.57	0.43	5.92	62.88	5.57
12th	1.07	6.87	6.47	8.68	1.07	6.84	6.65	8.57

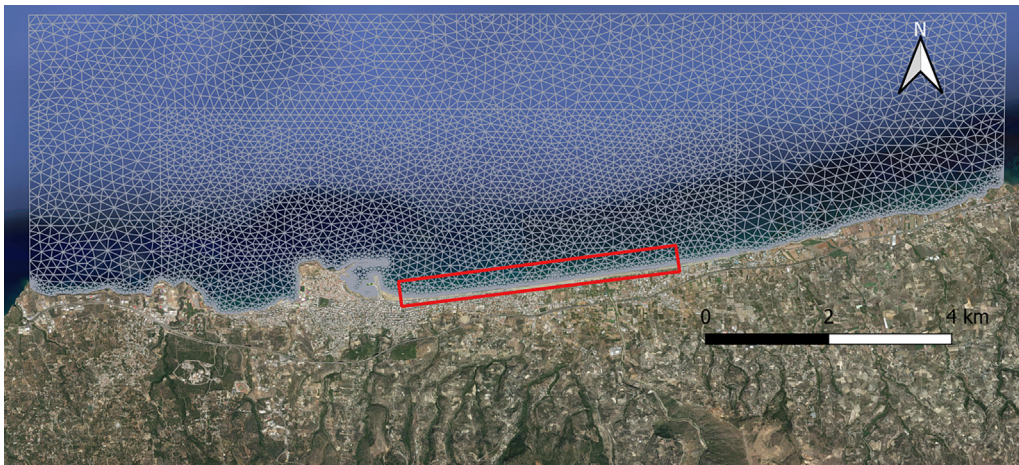


Figure 7 Finite element mesh showcasing the area (within the closed polygon) where the morphological model results will be evaluated.

Table 3 Classification table for the Brier Skill Score (Sutherland et al., 2004).

	BSS
Excellent	1.0–0.5
Good	0.5–0.2
Reasonable/fair	0.2–0.1
Poor	0.1–0.0
Bad	<0.0

performance of a given morphological evolution model are shown:

An additional metric was also utilized to evaluate the model’s performance, the Normalized Mean Square Error (NMSE), a metric to assess the differences between the measured and modeled values, calculated by the following equation.

$$NMSE(Y, X) = \frac{MSE(Y, X)}{\bar{Y}\bar{X}} \quad (14)$$

where the overbar denotes averaged quantities.

It is noted that a normalized error metric is preferred in this assessment, since if the computed bed levels by the brute force simulation are significant, even a relatively small underprediction or overprediction by the KM test simulations can exhibit large values of the non-normalized error metrics.

Performance evaluation of the morphological model was carried out for an area extending close to 450 m offshore (at a maximum depth of about 9 m) the eastern coastline adjacent to the port. It should be noted, that for the particular dataset the depth of closure (Houston, 1995) is about 5.5 m signifying that the largest portion of the sediment transport occurs shoreward this depth. This area (enclosed by the polygon shown in Figure 7) was the main focus of the evaluations since it consists mostly of a sandy uniform bed and is of high interest to the public due to the concatenation of tourist and economic activities at this location.

4. Results and discussion

In this section, the results obtained by the MIKE21 CM-FM composite model will be presented and analyzed for all the examined tests with respect to the different configurations of the KM algorithm.

The morphological bed evolution obtained from the brute force simulation is shown in Figure 8. Zones of accretion can be observed along the examined coastline along with some accretion at the lee breakwater of the port. Additionally, accumulation of sediment can be observed at the port entrance while an extended erosion zone is located south of the port entrance. Some erosion zones can also be observed at shallow depths extending from the middle of the computational mesh until the eastern boundary. It should be noted that model calibration for the brute force simulation due to the absence of bed-level measurements in the study area is not feasible, however, it is considered that the process of keeping the same model parametrization between the brute force and test simulations can provide a fair evaluation of the performance of the KM algorithm examined herein.

The bed evolution at an annual time scale, obtained at the end of the numerical simulations for tests KM-01 through KM-06 is depicted in Figure 9. The results will first be visually compared to the brute force simulation to evaluate the capability of each test in reproducing the morphological changes induced by the full set of offshore sea state characteristics.

Regarding case KM-01, the general morphological response is deemed similar to the one obtained from the brute force simulation. Although the accretion at the coastline of interest is reproduced, the magnitude of the bed level changes is underestimated, whilst the erosion areas just a few meters offshore are overestimated both in length and magnitude. Additionally, the erosion zone southward of the port entrance is present in the process-model results, albeit it is once again underestimated in magnitude. The same conclusions can be drawn for case KM-02, although more alternating zones between erosion and accretion are observed throughout the shallow areas of the computational mesh.

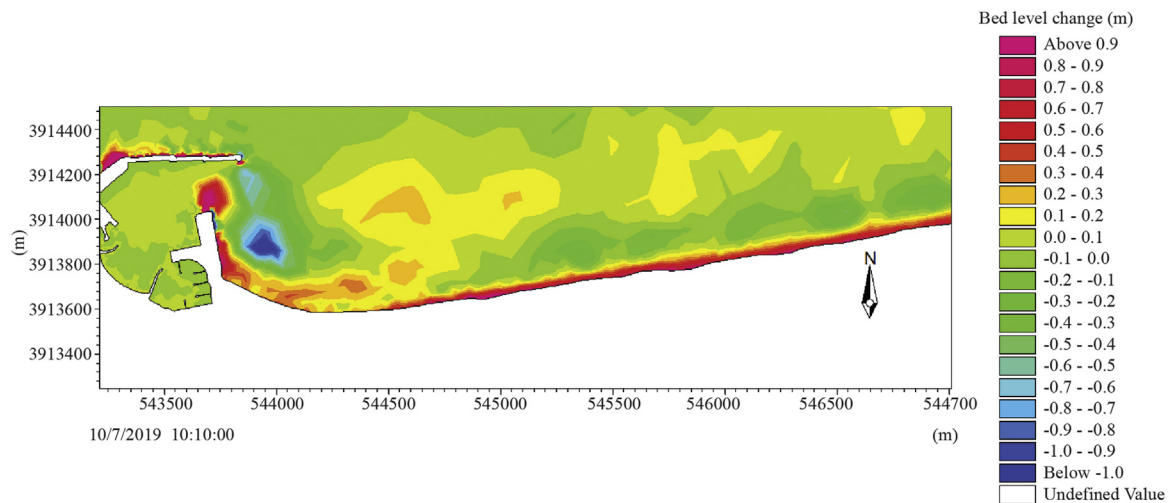


Figure 8 Morphological bed evolution obtained from the brute force simulation containing the full extent of the wave records.

Test KM-03 seems to lead to the best results regarding the visual inspection of the morphological evolution related to the brute force simulation results. Interestingly, despite the fact that this test is associated with the more energetic representatives, in turn, the morphological changes do not exhibit extreme variations. This can be attributed to the fact that the extreme sea states have small frequencies of occurrence and that the morphological response of the particular study area is not driven exclusively by these events. To expand on this, the obtained representatives of the particular KM-03 test shown in Figure 6, do not lead to the best representation of the cluster members throughout, since the centroids are shifted to unrealistically large values for the milder sea states.

Concerning case KM-04 a persistent underestimation of the intensity of the morphological changes is present throughout the computational mesh. Particularly evident is the absence of an elongated accretion zone at the port's lee breakwater. The transformation of clustering variables can be the cause of this effect, since non-breaking waves that have oblique incidence with respect to the coastline normal, can significantly affect the clustering analysis results. In general, though, the morphodynamic patterns of KM-04 are deemed acceptable compared to the reference simulation.

KM-05 seems to offer a good reproduction of the morphological evolution obtained from the brute force simulation. Specifically, this test is associated with morphological changes of the same magnitude as the brute force simulation, capturing the intensity of the accretion zone at the coast of interest quite satisfactorily, although some differences in the patterns of erosion and accretion zones compared to the brute force simulation are noticeable. As with the previously examined scenarios though, the erosion zone near the port entrance is once again underestimated. Similar morphological bed evolution results are obtained in the KM-06 case which operates in a similar manner, i.e. centroid initialization specified by a thorough methodological approach and filtering of low-energy sea states. Small differences in the accretion/erosion patterns can be observed in which each test is superior to the other, for example, KM-05 gives a better reproduction of the results along the sandy

coastline whereas KM-06 captures the accretion at the lee breakwater in a more satisfying manner.

To further illustrate the differences between the brute force simulation and each of the KM tests, Figure 10 shows the bed level computed by the brute force simulation (X) subtracted from the respective bed level of each KM test (Y). It is noted that the positive values of this difference signify an overprediction of the bed level by the KM tests, while negative values denote underprediction. Observing Figure 10, it can be deduced that KM-05 test, followed by KM-06 has the best performance compared to the other tests, as far as the magnitude and patterns of the observed bed level changes are concerned.

As has been previously mentioned, model evaluation will be carried out for the area enclosed within the polygon shown in Figure 7, to ultimately assess in a more precise manner the performance of each test and evaluate the efficiency of the KM clustering algorithm as an input reduction technique. A compiled list of the calculated BSS and NMSE values is shown in Table 4. In the same Table, the model runtime reduction compared to the Brute Force simulation is also depicted. For reference, the brute force simulation was completed after 8.9 days (on an Intel Core i7-4770 processor) while the KM-01 test simulation was completed in about 6.38 days. This is attributed to the smaller spin-up times of the model due to the significantly smaller number of wave boundary conditions compared to the brute force simulation. It should be noted that the MIKE21 CM FM operated in the online coupling mode, considering the constant interaction between waves, hydrodynamics and morphodynamics at each model time step. If the so-called "Morphostatic" approach is selected instead, in which the distinct simulations forced with the wave representative conditions are executed sequentially (offline coupling), then the model-run time reduction is significantly larger and can reach up to 450% (Papadimitriou et al., 2023) for the particular case study.

All tests that were examined for the purpose of this research are deemed as "Excellent" with respect to the BSS classification (Sutherland et al., 2004) shown in Table 3, which further validates the findings from visual inspection of the morphological bed evolution analyzed above. The

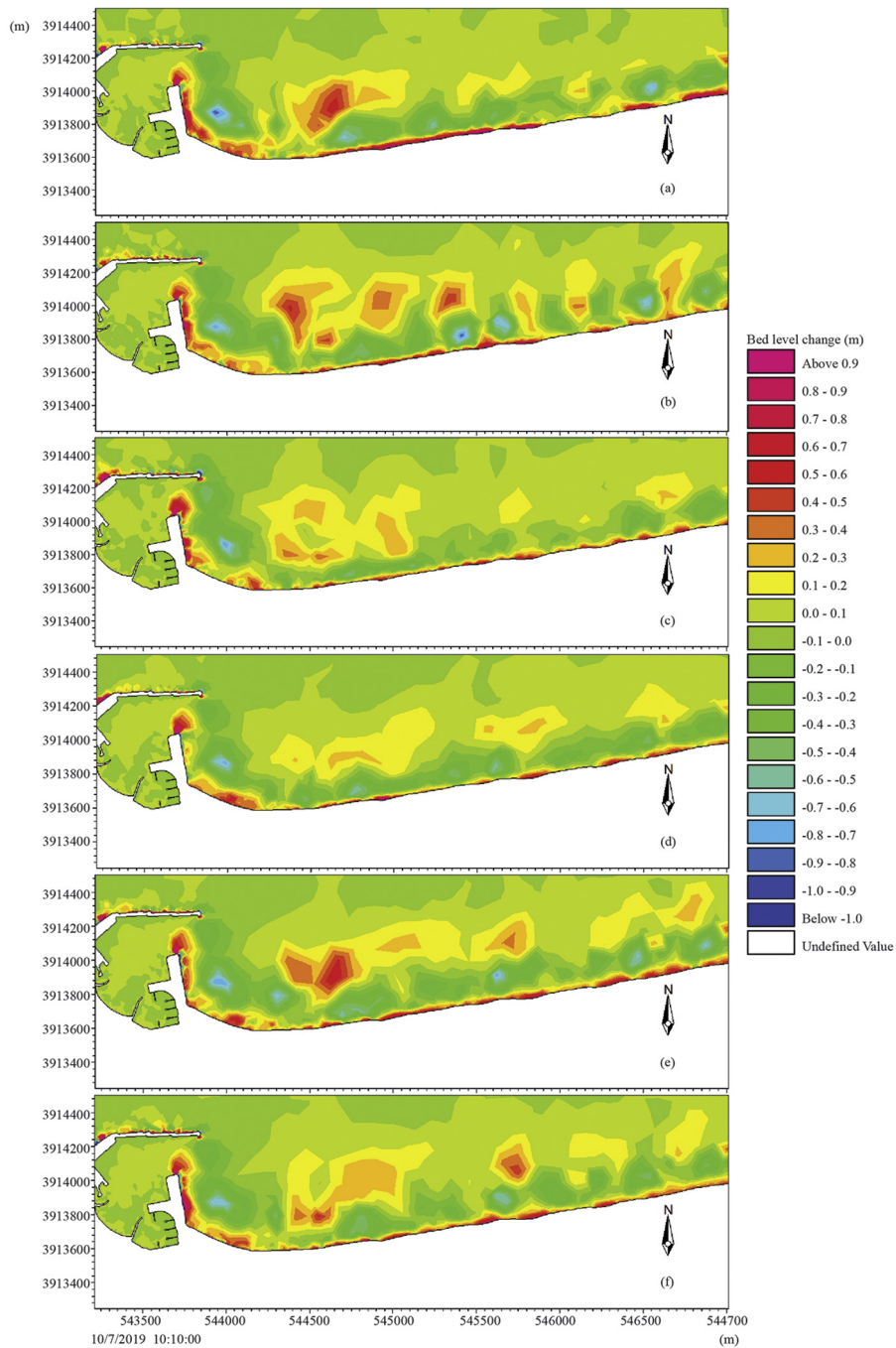


Figure 9 Morphological bed evolution simulation results for tests KM-01 (a), KM-02 (b), KM-03 (c), KM-04 (d), KM-05 (e), KM-06 (f).

Table 4 Statistical measures of model bias, skill and performance for all examined test cases.

	KM-01	KM-02	KM-03	KM-04	KM-05	KM-06
BSS	0.63	0.64	0.65	0.66	0.71	0.68
NMSE(Y,X)	0.063	0.062	0.060	0.063	0.055	0.057
Model run-time reduction (%)	28.22	23.25	25.05	23.01	21.95	21.62

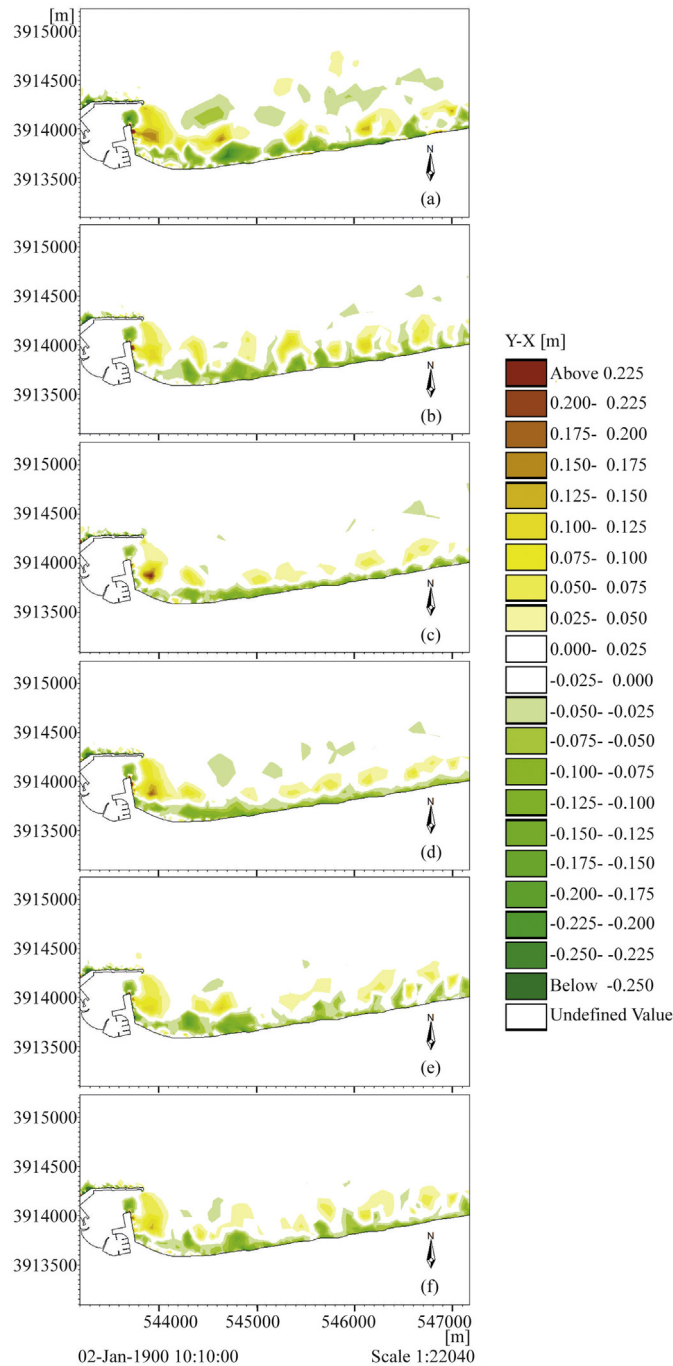


Figure 10 Relative difference of the predicted bed levels (Y) for tests KM-01 (a), KM-02 (b), KM-03 (c), KM-04 (d), KM-05 (e), KM-06 (f) compared to the brute force simulation (X).

same conclusion can be drawn for the NMSE values, which are considered relatively small, with each test also exhibiting a marginal improvement compared to the default test of KM-01. Test KM-02 offers a rather inconsequential improvement in terms of BSS compared to the default setup of the KM algorithm presented in KM-01. Both tests essentially perform similarly since they overestimate the contribution of low-energy sea states, signified by a relatively high frequency of occurrence for the corresponding clusters. KM-03 tests offer a slight improvement in the statistical metrics compared to the previous two tests, which should in part

be attributed to the increased weights of the high-energy sea states. However, it is noted that despite the shift to significantly more energetic representative wave conditions compared to other tests, the performance increase of KM-03 is barely noticeable. This implies that the frequencies of occurrence (f_j) should be rescaled, in order to avoid overly increasing the contribution of the more energetic representatives.

Test KM-04 exhibits a marginal improvement of performance, which signifies that for the particular study area, swapping clustering variables from H_{m0} , T_p , MWD to S , E_{ft} ,

MWD leads to an improvement of model results. Additionally, a further improvement is achieved in KM-06, which operates using the same clustering variables, albeit utilizing a filtering procedure to eliminate non-breaking waves from the dataset, considered unable to produce significant morphological changes. It should be noted that for the study area in question and the particular dataset, non-breaking waves corresponded to about 23% of the total amount of data, a percentage that is regarded to affect cluster formation significantly. To further support this, the best-performing test was found to be KM-05 which once again utilizes cluster initialization obtained from a binning input reduction method in conjunction with a filtering methodology based on the criterion of incipient sediment motion.

In both KM-05 and KM-06, the effective reduction of the dataset ultimately leads to a shift of higher frequencies of occurrence for the more energetic representative wave conditions. This parameter is considered to be vital in obtaining more accurate results since even a small percentile increase significantly affects the obtained morphological evolution at an annual scale. By applying a filtering methodology, the issue inherently present in clustering algorithms, related to the overestimation of mild sea states' contribution to the morphological bed evolution (de Queiroz et al., 2019) is somewhat alleviated, leading to a significant performance increase of the process-based model. Even though some differences in the erosion and accretion patterns in these tests were located with respect to the brute force simulation, these tests capture the magnitude of the bed level changes to a satisfying degree thus leading to an increase of the BSS values. Finally, it should be stated that model performance can also be affected by the use of Morfac values employed to speed up the simulations due to the non-linear response of the morphology to each wave forcing condition. With regard to the complexity of the Pick-up rate method, integral for test KM-05, it is considered and proposed that the methodological approach of KM-06 can be safely applied in coastal engineering applications producing satisfying results of bed level evolution for coasts where waves are the main forcing factor driving the sediment transport. Despite the lower obtained BSS values in relation to the proposed enhancements, the use of the default implementation of the K-Means algorithm (test KM-01) is justified for use in coastal engineering applications. The reduced level of interference required for the selection of the representative sea states is especially alluring since it requires minimal user input compared to the more complex tests of KM-02 through KM-06.

5. Conclusions

In the present research, a thorough investigation of the capability of utilizing the K-Means clustering algorithm for wave schematization purposes and prediction of the morphological bed evolution in the medium term was undertaken. Various tests were carried out, aiming to enhance the performance of the algorithm and concert the classic binning input reduction methods with the newly tested clustering algorithm. All tests were implemented using the process-based model MIKE21 Coupled Model FM for the calculation of wave propagation, current and sediment transport regime.

The examined enhancements of the algorithm can be divided vaguely into the following categories, (a) a default case of the algorithm with minimal user intervention (test KM-01), (b) two cases concerning binning input reduction methods with clustering techniques (test KM-02 and KM-05), (c) utilization of weights in the clustering analysis (test KM-03), (d) alteration of clustering input variables (test KM-04 and KM-06) and (e) two cases concerning the application of initial filtration of sea states unable to induce substantial morphological changes and thus reducing the contribution of milder sea states (test KM-05 and test KM-06). From the obtained results all tests were deemed as “Excellent” with respect to the commonly used metric of BSS (Sutherland et al., 2004) measuring morphological model performance thus validating the utilization of clustering algorithms as wave input reduction methods.

The best-performing tests were found to be the ones associated with filtration of the previously mentioned lowly energetic wave records from the dataset, which alleviates the disadvantage of clustering algorithms to overestimate the contribution of said sea states to the morphological bed evolution. When combined with initial centroid selection linked with quantities related to the longshore sediment transport (such as the sediment Pick-up rate or bulk longshore transport rates) the algorithm is coerced to initiate the iterative procedure from “smartly” selected centroids, further improving model results.

Consequently, the K-Means algorithm is deemed to be a valuable tool which can be utilized for the purpose of reducing the input offshore sea state wave characteristics and alleviating numerical burden from the demanding process-based model simulations, especially when combined with comprehensive filtering methodologies. For the filtering procedures presented in this research, a uni-directional random wave version of a Parabolic Mild Slope wave model was employed, which is highly robust and suitable for the accurate simulation of nearshore wave transformations. Simpler alternatives of these more complex methodologies can also be utilized, albeit with a small expected penalty in model accuracy, ultimately providing fast and efficient solutions for coastal modelers desiring to obtain a good representation of the inter-annual morphological evolution of complex coastal areas.

Future research should concentrate on further evaluating the performance of the K-Means clustering algorithm's configuration with special attention given to the contribution of wave sequencing on the results, which was systematically minimized for the purpose of this research by applying an optimization algorithm. The ability to observe the movement of each centroid during the iterations when providing externally calculated values can probably be used to introduce some reproducibility of wave chronology to the analysis by dividing the wave climate in “winter” and “summer” profiles respectively.

Declaration of competing interests

The authors declare that they have no known competing financial interests or personal relationships that could have appeared to influence the work reported in this paper.

Acknowledgements

The authors gratefully acknowledge Nikolaos Martzikos and Anastasios Metallinos of the National Technical University of Athens for their valuable comments and suggestions that helped in the improvement of the manuscript. Acknowledgements are also due to DHI and especially Elias Moussoulis for the free-of-charge provision of the MIKE21 software products in the context of Andreas Papadimitriou's PhD dissertation.

References

- Afentoulis, V., Kragiopolou, E., Skarlatou, E., Moschos, E., Lykou, A., Makropoulos, C., Tsoukala, V., 2017. Coastal Processes Assessment Under Extreme Storm Events Using Numerical Modelling Approaches. *Environ. Process.* 4, 731–747.
- Afentoulis, V., Papadimitriou, A., Belibassakis, K., Tsoukala, V., 2022. A coupled model for sediment transport dynamics and prediction of seabed morphology with application to 1DH/2DH coastal engineering problems. *Oceanologia* 64 (3), 514–534. <https://doi.org/10.1016/j.oceano.2022.03.007>
- Arthur, D., Vassilvitskii, S., 2007. K-means++: The advantages of careful seeding. In: *Proceedings of the Annual ACM-SIAM Symposium on Discrete Algorithms*.
- Bailard, J.A., 1985. Simplified model for longshore sediment transport. In: *Proceedings of the Coastal Engineering Conference*. ASCE, 1454–1470. <https://doi.org/10.9753/icce.v19.99>
- Baldock, T.E., Holmes, P., Bunker, S., Van Weert, P., 1998. Cross-shore hydrodynamics within an unsaturated surf zone. *Coast. Eng.* 34, 173–196. [https://doi.org/10.1016/S0378-3839\(98\)00017-9](https://doi.org/10.1016/S0378-3839(98)00017-9)
- Battjes, J.A., Janssen, J.P.F.M., 1978. Energy loss and set-up due to breaking of random waves. In: *Proceedings of the 16th International Conference on Coastal Engineering*. Hamburg, Germany.
- Battjes, J.A., Janssen, T.T., 2009. Random wave breaking models – history and discussion. In: *Proceedings of the 31st Coastal Engineering Conference*. Hamburg, Germany. https://doi.org/10.1142/9789814277426_0002
- Benedet, L., Dobrochinski, J.P.F., Walstra, D.J.R., Klein, A.H.F., Ranasinghe, R., 2016. A morphological modeling study to compare different methods of wave climate schematization and evaluate strategies to reduce erosion losses from a beach nourishment project. *Coast. Eng.* 112, 69–86. <https://doi.org/10.1016/j.coastaleng.2016.02.005>
- Bezdek, J.C., 1981. *Pattern Recognition with Fuzzy Objective Function Algorithms*. Springer, New York. <https://doi.org/10.1007/978-1-4757-0450-1>
- Bouws, E., Günther, H., Rosenthal, W., Vincent, C., 1985. Similarity of the wind wave spectrum in finite depth water: 1. Spectral form. *J. Geophys. Res. Oceans* 90, 975–986. <https://doi.org/10.1029/JC090iC01p00975>
- Brown, J.M., Davies, A.G., 2009. Methods for medium-term prediction of the net sediment transport by waves and currents in complex coastal regions. *Cont. Shelf Res.* 29, 1502–1514. <https://doi.org/10.1016/j.csr.2009.03.018>
- Camus, P., Mendez, F.J., Medina, R., Cofiño, A.S., 2011. Analysis of clustering and selection algorithms for the study of multivariate wave climate. *Coast. Eng.* 58, 453–462. <https://doi.org/10.1016/j.coastaleng.2011.02.003>
- Chawla, A., Özkan-Haller, T.H., Kirby, J.T., 1998. Spectral model for wave transformation over irregular bathymetry. *J. Waterw. Port Coast. Ocean Eng.* 124 (4). [https://doi.org/10.1061/\(ASCE\)0733-950X\(1998\)124:4\(189\)](https://doi.org/10.1061/(ASCE)0733-950X(1998)124:4(189))
- Chondros, M., Metallinos, A., Memos, C., Karambas, T., Papadimitriou, A., 2021. Concerted nonlinear mild-slope wave models for enhanced simulation of coastal processes. *Appl. Math. Model.* 91, 508–529. <https://doi.org/10.1016/j.apm.2020.08.027>
- Copernicus Marine Service, n.d., <https://marine.copernicus.eu/> (accessed 11/10/2022).
- Courant, R., Friedrichs, K., Lewy, H., 1967. On the Partial Difference Equations of Mathematical Physics. *IBM J. Res. Dev.* 11, 215–234. <https://doi.org/10.1147/rd.112.0215>
- Dalrymple, R.A., Kirby, J.T., 1988. Models for very wide-angle water waves and wave diffraction. *J. Fluid Mech.* 192, 33–50. <https://doi.org/10.1017/S0022112088001776>
- Daly, C.J., Bryan, K.R., Gonzalez, M.R., Klein, A.H.F., Winter, C., 2014. Effect of selection and sequencing of representative wave conditions on process-based predictions of equilibrium embayed beach morphology. *Ocean Dynam.* 64, 863–877. <https://doi.org/10.1007/s10236-014-0730-9>
- de Queiroz, B., Scheel, F., Caires, S., Walstra, D.J., Olij, D., Yoo, J., Reniers, A., de Boer, W., 2019. Performance evaluation of wave input reduction techniques for modeling inter-annual sandbar dynamics. *J. Mar. Sci. Eng.* 7, 148. <https://doi.org/10.3390/jmse7050148>
- de Vriend, H.J., Zyserman, J., Nicholson, J., Roelvink, J.A., Péchon, P., Southgate, H.N., 1993. Medium-term 2DH coastal area modelling. *Coast. Eng.* 21, 193–223. [https://doi.org/10.1016/0378-3839\(93\)90050-1](https://doi.org/10.1016/0378-3839(93)90050-1)
- DHI, 2014. *Coupled Model FM (MIKE 21/3 FM). User Guide*. Danish Hydraulic Institute.
- DHI, 2009a. *Spectral Wave Module. Scientific Documentation*. Danish Hydraulic Institute.
- DHI, 2009b. *21&3 Flow Model FM, Hydrodynamic and Transport Module, Scientific Documentation*. Danish Hydraulic Institute.
- DHI, 2009c. *Flow Model FM Sand Transport Module, Scientific Documentation*. Danish Hydraulic Institute.
- Drønen, N., Kristensen, S., Taaning, M., Elfrink, B., Deigaard, R., 2011. Long term modeling of shoreline response to coastal structures. In: *Proceedings of the Coastal Sediments Conference*. Miami, Florida, USA, 2–6 May 2011. https://doi.org/10.1142/9789814355537_0073
- ERA5-INTERIM, 1959–present. ERA5-INTERIM: hourly data on single levels from 1959 to present, [dataset]. <https://cds.climate.copernicus.eu/cdsapp#!/dataset/reanalysis-era5-single-levels?tab=overview/> (accessed 27/12/2022).
- Fairley, I., Lewis, M., Robertson, B., Hemer, M., Masters, I., Horrillo-Caraballo, J., Karunarathna, H., Reeve, D.E., 2020. A classification system for global wave energy resources based on multivariate clustering. *Appl. Ener.* 262, 114515. <https://doi.org/10.1016/j.apenergy.2020.114515>
- Gad, F.-K., Hatiris, G.-A., Loukaidi, V., Dimitriadou, S., Drakopoulou, P., Sioulas, A., Kapsimalis, V., 2018. Long-Term Shoreline Displacements and Coastal Morphodynamic Pattern of North Rhodes Island. Greece. *Water* 10, 849. <https://doi.org/10.3390/w10070849>
- Guha, S., Rastogi, R., Shim, K., 2001. CURE: An efficient clustering algorithm for large databases. *Inf. Syst.* 26, 35–58. <https://doi.org/10.1145/276305.276312>
- Hallermeier, R.J., 1980. A profile zonation for seasonal sand beaches from wave climate. *Coast. Eng.* 4, 253–277. [https://doi.org/10.1016/S0306-4379\(01\)00008-4](https://doi.org/10.1016/S0306-4379(01)00008-4)
- Hasselmann, K., Barnett, T.P., Bouws, E., Carlson, H., Cartwright, D.E., Enke, K., Ewing, J.A., Gienapp, H., Hasselmann, D.E., Kruseman, P., Meerburg, A., Mller, P., Olbers, D.J., Richter, K., Sell, W., Walden, H., 1973. Measurements of wind-wave growth and swell decay during the Joint North Sea Wave Project (JONSWAP). *Ergänzungsheft zur Deutschen Hydrographischen Zeitschrift Reihe A(8) (12)*, 95.

- Houston, J.R., 1995. Beach-fill volume required to produce specific dry beach width. *Coast. Eng. Technical Note CETN II-32*. US Army Corps Eng. Waterw. Exp. Station, Vicksburg, Mississippi.
- Janssen, T.T., Battjes, J.A., 2007. A note on wave energy dissipation over steep beaches. *Coast. Eng.* 54, 711–716. <https://doi.org/10.1016/j.coastaleng.2007.05.006>
- Kaergaard, K., Mortensen, S.B., Kristensen, S.E., Deigaard, R., Teasdale, R., Hunt, S., 2014. Hybrid shoreline modelling of shoreline protection Schemes, Palm Beach, Queensland, Australia. In: Proceedings of the 34th Coastal Engineering Conference. Seoul, Korea 15–20 June 2014. <https://doi.org/10.9753/icce.v34.sediment.23>
- Kamphuis, J.W., 1991. Alongshore Sediment Transport Rate. *J. Waterw. Port Coast. Ocean Eng.* 117, 624–640. [https://doi.org/10.1061/\(asce\)0733-950x\(1991\)117:6\(624\)](https://doi.org/10.1061/(asce)0733-950x(1991)117:6(624))
- Kelpšaitė-Rimkienė, L., Parnell, K.E., Žaromskis, R., Kondrat, V., 2021. Cross-shore profile evolution after an extreme erosion event—Palanga, Lithuania. *J. Mar. Sci. Eng.* 9, 1–15. <https://doi.org/10.3390/jmse9010038>
- Kirby, J.T., Dalrymple, R.A., 1983. A parabolic equation for the combined refraction diffraction of Stokes waves by mildly varying topography. *J. Fluid Mech.* 136, 453–466. <https://doi.org/10.1017/S0022112083002232>
- Knaapen, M.A.F., Joustra, R., 2012. Morphological acceleration factor: usability, accuracy and run time reductions. In: Proceedings of the XIXth TELEMAC-MASCARET User Conference. Oxford, UK 18–19 October 2012.
- Komar, P., Inman, D., 1970. Longshore sand transport on beaches. *J. Geophys. Res.* 75, 5914–5927. <https://doi.org/10.1029/jc075i030p05914>
- Komen, G.J., Cavaleri, L., Donelan, M., Hasselmann, K., Hasselmann, S., Janssen, P.A.E.M., 1994. Dynamics and Modelling of Ocean Waves. Cambridge University Press, Cambridge. <https://doi.org/10.1017/CBO9780511628955>
- Korres, G., Ravdas, M., Zacharioudaki, A., 2019. Mediterranean Sea Waves Hindcast (CMEMS MED-Waves) [dataset]. https://doi.org/10.25423/CMCC/MEDSEA_HINDCAST_WAV_006_012
- Kraus, N.C., Larson, M., Wise, R.A., 1998. Depth of Closure in Beach-fill Design. *Coast. Eng. Technical Note CETN, II-40*. US Army Coast. Hydraul. Lab., Corps Eng. Waterw. Exp. Station, Vicksburg, Mississippi.
- Lesser, G.R., 2009. An Approach to Medium-term Coastal Morphological Modelling PhD thesis. Delft University of Technology, Netherlands.
- MacQueen, J., 1967. Some methods for classification and analysis of multivariate observations. In: Proceedings of the 5th Berkeley Symp. Math. Stat. Probab., 1, 281–297.
- Martzikos, N., Afentoulis, V., Tsoukala, V., 2018. Storm clustering and classification for the port of Rethymno in Greece. *Water Util. J.* 20, 67–79.
- Mase, H., Kirby, J.T., 1992. Hybrid frequency-domain KdV equation for random wave transformation. In: Proceedings of the 12th Coastal Engineering Conference. Venice, Italy, October 4–9 1992. <https://doi.org/10.1061/9780872629332.035>
- Miche, M., 1951. Le pouvoir réfléchissant des ouvrages maritimes exposés à l'action de la houle. *Annales de Ponts et Chaussées Technical Report*.
- Munkres, J., 1957. Algorithms for the assignment and transportation problems. *J. Soc. Ind. Appl. Math.* 5, 32–38.
- Papadimitriou, A., Panagopoulos, L., Chondros, M., Tsoukala, V., 2020. A wave input-reduction method incorporating initiation of sediment motion. *J. Mar. Sci. Eng.* 8. <https://doi.org/10.3390/JMSE8080597>
- Papadimitriou, A., Tsoukala, V., Karambas, T., 2023. Revisiting and enhancing the concept of equivalent wave heights. In: Proceedings of the 2nd International Conference Design, Management of Port, Coastal and Offshore Works (DMPCO 2023). Thessaloniki, Greece, May 24–27 2023.
- Pedregosa, F., Varoquaux, G., Gramfort, A., Michel, V., Thirion, B., Grisel, O., Blondel, M., Prettenhofer, P., Weiss, R., Dubourg, V., Vanderplas, J., Passos, A., Cournapeau, D., Brucher, M., Perrot, M., Duchesnay, E., 2011. Scikit-learn: Machine Learning in Python *JMLR* 12, 2825–2830.
- Pierson, W.J., Moskowitz, L., 1964. A proposed spectral form for fully developed wind seas based on the similarity of S. A. Kitaigorodskii. *J. Geoph. Res.* 69, 5181–5190.
- Putnam, J.A., Johnson, J.W., 1949. The dissipation of wave energy by bottom friction. *Eos Trans. AGU* 30, 67–74. <https://doi.org/10.1029/TR030i001p00067>
- Roelvink, D., Reniers, A., 2012. A guide to modeling coastal morphology, 1st edition Word Scientific, Singapore. <https://doi.org/10.1142/9789814304269>
- Splinter, K.D., Golshani, A., Stuart, G., Tomlinson, R., 2011. Spatial and Temporal Variability of Longshore Transport Along Gold Coast, Australia. In: Proceedings of the 32nd Coastal Engineering Conference, Shanghai, China. <https://doi.org/10.9753/icce.v32.sediment.95>
- Sutherland, J., Peet, A.H., Soulsby, R.L., 2004. Evaluating the performance of morphological models. *Coast. Eng.* 51, 917–939. <https://doi.org/10.1016/j.coastaleng.2004.07.015>
- Tsiaras, A.-C., Karambas, T., Koutsouvela, D., 2020. Design of Detached Emerged and Submerged Breakwaters for Coastal Protection: Development and Application of an Advanced Numerical Model. *J. Waterw. Port Coast. Ocean Eng.* 146, 04020012. [https://doi.org/10.1061/\(asce\)jww.1943-5460.0000566](https://doi.org/10.1061/(asce)jww.1943-5460.0000566)
- Tsoukala, V., Chondros, M., Kapelonis, Z., Martzikos, N., Lykou, A., Belibassakis, K., Makropoulos, C., 2016. An integrated wave modelling framework for extreme and rare events for climate change in coastal areas – the case of Rethymno, Crete. *Oceanologia* 58 (2), 71–89. <https://doi.org/10.1016/j.oceano.2016.01.002>
- van Duin, M.J.P., Wiersma, N.R., Walstra, D.J.R., Van Rijn, L.C., Stive, M.J.F., 2004. Nourishing the shoreface: observations and hindcasting of the Egmond case, The Netherlands. *Coast. Eng.* 51, 813–817. <https://doi.org/10.1016/j.coastaleng.2004.07.011>
- van Rijn, L.C., 1986. Sediment pick-up functions. Applications of sediment Pick-up function. *J. Hydraul. Eng.* 112, 867–874. [https://doi.org/10.1061/\(ASCE\)0733-9429\(1984\)110:10\(1494\)](https://doi.org/10.1061/(ASCE)0733-9429(1984)110:10(1494))
- van Rijn, L.C., Bisschop, R., van Rhee, C., 2019. Modified Sediment Pick-Up Function. *J. Hydraul. Eng.* 145 (1), 060180171–060180176. [https://doi.org/10.1061/\(ASCE\)HY.1943-7900.0001549](https://doi.org/10.1061/(ASCE)HY.1943-7900.0001549)
- van Rijn, L.C., Waslra, D.J.R., Grasmeijer, B., Sutherland, J., Pan, S., Sierra, J.P., 2003. The predictability of cross-shore bed evolution of sandy beaches at the time scale of storms and seasons using process-based profile models. *Coast. Eng.* 47, 295–327. [https://doi.org/10.1016/S0378-3839\(02\)00120-5](https://doi.org/10.1016/S0378-3839(02)00120-5)
- Walstra, D.J.R., Hoekstra, R., Tonnon, P.K., Ruessink, B.G., 2013. Input reduction for long-term morphodynamic simulations in wave-dominated coastal settings. *Coast. Eng.* 77, 57–70. <https://doi.org/10.1016/j.coastaleng.2013.02.001>
- Zhao, Y., Anastasiou, K., 1993. Economical random wave propagation modelling taking into account non-linear amplitude dispersion. *Coast. Eng.* 20, 59–83. [https://doi.org/10.1016/0378-3839\(93\)90055-D](https://doi.org/10.1016/0378-3839(93)90055-D)

Available online at www.sciencedirect.com

ScienceDirect

journal homepage: www.journals.elsevier.com/oceanologia

ORIGINAL RESEARCH ARTICLE

Coverage estimation of benthic habitat features by semantic segmentation of underwater imagery from South-eastern Baltic reefs using deep learning models

Andrius Šiaulys^{a,*}, Evaldas Vaičiukynas^b, Saulė Medelytė^a,
Kazimieras Buškus^b

^a Marine Research Institute, Klaipėda University, Klaipėda, Lithuania

^b Faculty of Informatics, Kaunas University of Technology, Kaunas, Lithuania

Received 10 July 2022; accepted 17 December 2023

Available online 4 January 2024

KEYWORDS

Underwater video;
Epibenthos;
Mosaicking;
Segmentation;
Computer vision,
PSPNet;
ResNet;
Baltic Sea

Abstract Underwater imagery (UI) is an important and sometimes the only tool for mapping hard-bottom habitats. With the development of new camera systems, from hand-held or simple “drop-down” cameras to ROV/AUV-mounted video systems, video data collection has increased considerably. However, the processing and analysing of vast amounts of imagery can become very labour-intensive, thus making it ineffective both time-wise and financially. This task could be simplified if the processes or their intermediate steps could be done automatically. Luckily, the rise of AI applications for automatic image analysis tasks in the last decade has empowered researchers with robust and effective tools. In this study, two ways to make UI analysis more efficient were tested with eight dominant visual features of the Southeastern Baltic reefs: 1) the simplification of video processing and expert annotation efforts by skipping the video mosaicking step and reducing the number of frames analysed; 2) the application of semantic segmentation of UI using deep learning models. The results showed that the annotation of individual frames provides similar results compared to 2D mosaics; moreover, the reduction of frames by 2–3 times resulted in only minor differences from the baseline. Semantic segmen-

* Corresponding author at: Marine Research Institute, Klaipėda University, Klaipėda, Lithuania.

E-mail address: andrius.siaulys@ku.lt (A. Šiaulys).

Peer review under the responsibility of the Institute of Oceanology of the Polish Academy of Sciences.



<https://doi.org/10.1016/j.oceano.2023.12.004>

0078-3234/© 2023 Institute of Oceanology of the Polish Academy of Sciences. Production and hosting by Elsevier B.V. This is an open access article under the CC BY-NC-ND license (<http://creativecommons.org/licenses/by-nc-nd/4.0/>).

tation using the PSPNet model as the deep learning architecture was extensively evaluated, applying three variants of validation. The accuracy of segmentation, as measured by the intersection-over-union, was mediocre; however, estimates of visual coverage percentages were fair: the difference between the expert annotations and model-predicted segmentation was less than 6–8%, which could be considered an encouraging result.

© 2023 Institute of Oceanology of the Polish Academy of Sciences. Production and hosting by Elsevier B.V. This is an open access article under the CC BY-NC-ND license (<http://creativecommons.org/licenses/by-nc-nd/4.0/>).

1. Introduction

Renewable energy installations, oil and gas drilling, maritime shipping and fishing, ecosystem surveillance and biodiversity conservation, aquaculture production, and a variety of other uses are becoming more common and increasing the need for maritime space. The need for maritime space necessitates integrated planning and management strategies based on sound scientific understanding and accurate seabed mapping (Smith and Cardoso, 2020), with underwater images (Urta et al., 2021) being one of the most widely used seabed mapping materials. The main advantage of underwater imagery is its cost-effectiveness and simplicity, which allow for the rapid collection of large volumes of data with a variety of underwater cameras, from relatively simple handheld GoPros or “drop-down” cameras to more advanced ROV and AUV-mounted filming systems. There are several applications and platforms designed or utilized for underwater imagery analysis, such as BIGLE 2.0 (Langenkämper et al., 2017), CPCe (Kohler and Gill, 2006), Image J (Ferreira and Rasband, 2012), PhotoQuad (Trygonis and Sini, 2012), and broad-scale projects ongoing collecting huge amounts of video material, e.g., MAREANO (Buhl-Mortensen et al., 2015), yet only a small part of the information is being extracted due to labour-intensive and time-consuming analysis procedures. A promising way to process large amounts of images is computer-aided analysis, i.e., conversion of raw seabed video to 2D mosaics (Casoli et al., 2021; Šaškov et al., 2015), annotation and image segmentation (Martin-Abadal et al., 2018; Piechaud et al., 2019; Šiaulyš et al., 2021), and quantification of segmentation results (Buškus et al., 2021).

Automatic segmentation of underwater imagery, compared to other types of image analysis, is a relatively new and challenging research direction. According to a survey (Gracias et al., 2017), the first publications on the seabed segmentation task (also termed seafloor classification) appeared 25 years ago and are still scarce, the common ground between them being the use of “hand-crafted” image features and traditional machine learning algorithms, for example, random forest (Rimavičius et al., 2018). Novel deep learning architectures of neural networks could be the enabling technologies to replace image features and analyse images more effectively, accurately, and quickly than ever before. Initial efforts to apply deep learning to UI concern corals (Alonso et al., 2019) and other broad categories such as fish, plants, divers, or stones (Islam et al., 2020; Liu and Fang, 2020), mostly from independent photographs and with little preoccupation with the sea floor. Other studies have shown that seafloor videos could be converted into 2D mo-

saics (multiple frames that are stitched together into a single still image), which can later be used for efficient visual analysis (Medelytė et al., 2022a; Šaškov et al., 2015) with applications of deep learning models (Buškus et al., 2021). However, the mosaicking of seabed videos is a labour-intensive process, requiring specific software and professional knowledge (Li et al., 2019), with some prerequisites for video material as well (stable distance from the seabed, homogeneous lighting, no fast-moving objects, etc.), which can be unachievable in rough open seas or very dynamic coastal areas.

In this study, two ways of making UI analysis more efficient were tested on eight dominant visual features of the SE Baltic reefs: 1) the simplification of video processing and expert annotation effort by skipping the video mosaicking step and reducing the frames analysed, and 2) the application of semantic segmentation of UI using deep learning models for automatic estimates of seabed visual features. Estimations were done both manually, by obtaining expert annotations, and automatically, by training a deep learning convolutional architecture on the annotated data. Experiments measure segmentation success and accuracy of automated visual coverage estimates through three types of validation: two-fold cross-validation, leave one out validation, and hold-out validation.

2. Material and methods

2.1. Underwater imagery data

Underwater videos were filmed in the coastal and offshore reefs of Lithuanian marine waters in the South-Eastern Baltic Sea at eight locations (Figure 1). Underwater video filming was carried out 1 m above the seabed, at depths of 4–8 m in the coastal area and 30–40 m offshore. The underwater videos in the coastal area were collected by SCUBA divers with a handheld GoPro underwater camera and “drop-down” type camera system equipped with an analog camera with 700 TV lines (TVL) resolution for live view and a digital camera (Panasonic HX-A500) that recorded the seabed at high resolution (1280 × 720 px). Offshore data was collected using an ROV-mounted Full HD (1920 × 1080) resolution camera with a lighting system consisting of 16 bright LEDs in 4 × 4 stations. In total, coastal data consists of five 10 m transects: SM02-1, SM02-2, SM07-1, SM07-2 and SM08; (the latter being divided into two segments), while offshore data consists of two 30 s long video clips (DE01-1, DE01-2), which are accessible through the Mendeley cloud-based repository (Medelytė et al., 2022b).

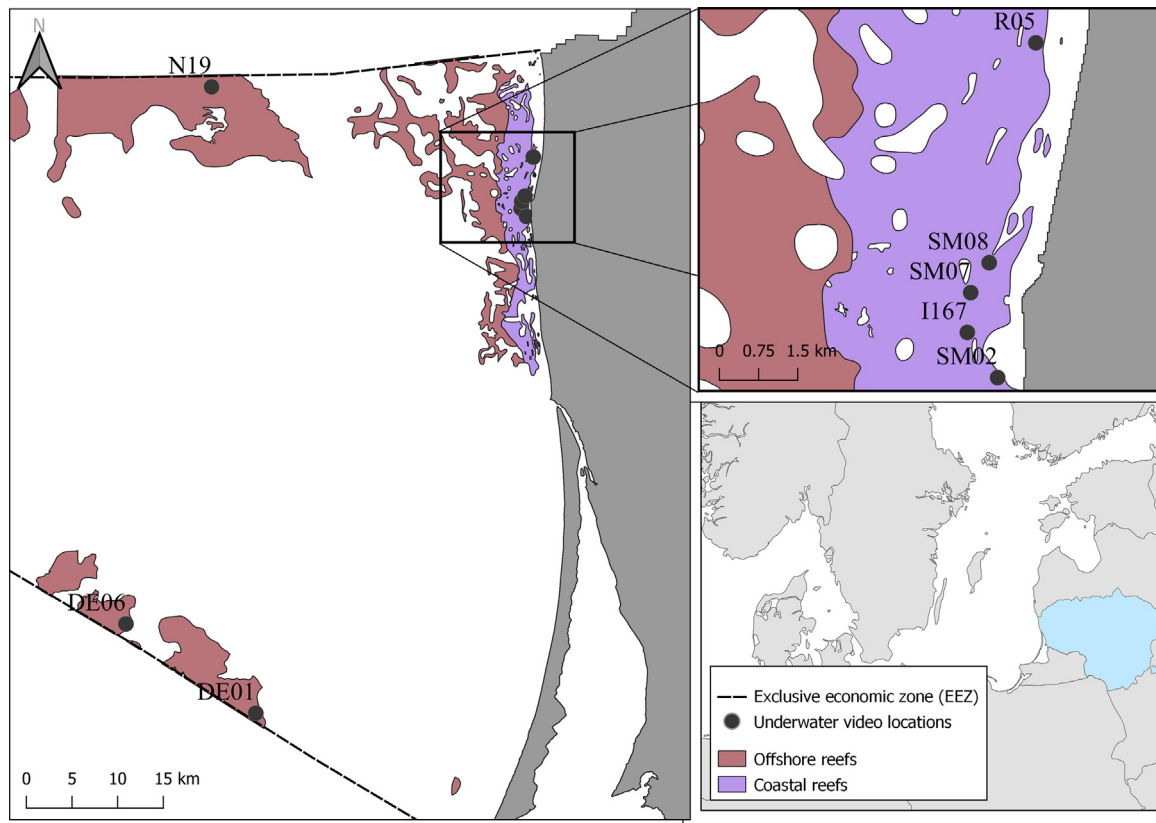


Figure 1 Underwater video sampling sites in South-Eastern Baltic Sea reefs.

For the validation of models, additional video data from four transects was used: R05, DE06, I167 and N19.

Ten video mosaics were created using a method developed by Rzhano and Mayer (2004) while following steps outlined by Šaškov et al. (2015) and Šiaulys et al. (2021). The underwater mosaicking process is not always possible due to difficult weather conditions in open seas, since the “drop-down” camera is lifted by waves, resulting in an unstable camera distance from the bottom and thus complicating the frame-to-frame pairwise registration process needed for smooth mosaic construction. To address this issue, an experiment was carried out to test how the accuracy of biological and geological feature extraction changes when analysing mosaics and individual frames, i.e., whether it is possible to avoid the mosaicking step for accurate image analysis by analysing only frames. The frames were selected in such a way that adjacent frames did not overlap but were not too far apart (Figure 2), resulting in 148 extracted frames.

2.2. Extraction of frames

For the frame sampling approach, experts assigned a specific number of frames, typically 12–16, for each video transect, and equally spaced frames of 960×540 size were extracted using a command-line ffmpeg tool (Tomar, 2006). Additionally, seeking to obtain better quality representative frames, a complex sampling strategy was introduced: 1) Each video frame was converted to a high-dimensional feature vector of 1280 elements by using ImageNet pre-

trained EfficientNet deep convolutional architecture (Tan and Le, 2019), the smallest and fastest EfficientNetB0 variant in the Python package image_embeddings. For example, DE01-2 video had 150 frames, and, after passing each frame through the model, we obtained a matrix of 150×1280 in size; 2) matrix obtained after converting frames to embeddings was further processed using sparse modelling for finding representative objects – Sparse Modelling Representative Selection (SMRS) algorithm (Elhamifar et al., 2012), using the authors’ Python code. Parameters used: $\alpha=5$, $\text{norm_type}=2$, $\text{thrS}=0.99$, $\text{thrP}=0.98$, $\text{max_iter}=5000$, $\text{step}=100$. This algorithm tries to find frames that are the most representative in a mathematical sense. 3) A representative frame that is closest to the frames selected by simple sampling is selected. Being close is defined here as smaller than 25% of the average distance between frames in simple sampling; 4) in a rare case, when no closest representative frames are detected, all frames around the corresponding frame (\pm average distance) from simple sampling are cut out into a smaller matrix, which is passed again to the SMRS algorithm, and steps 2–3 are repeated.

2.3. Manual annotation

All video mosaics and extracted frames of fixed size were annotated by 3 experts by drawing closed polygons (striving for pixel-level accuracy) using the Labelbox manual pixel-wise segmentation tool (Labelbox). Dominant features of the SE Baltic coastal and offshore reefs were selected for



Figure 2 An example of a 2D mosaic and separate frames from the same video transect.

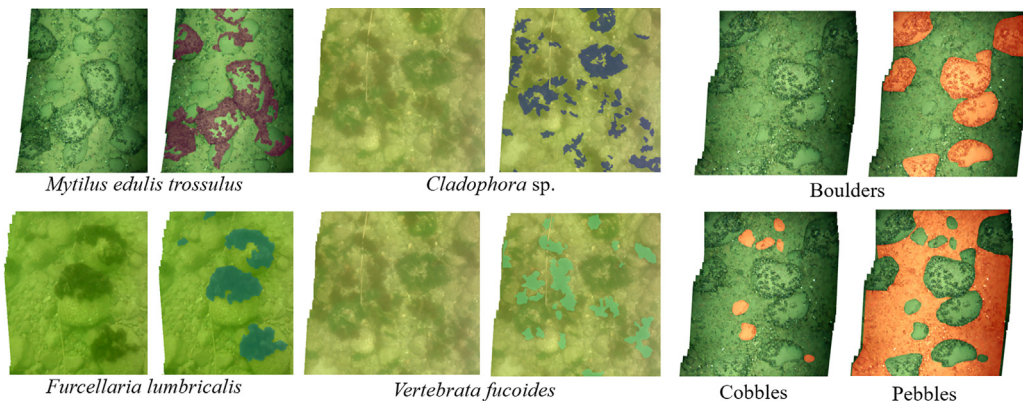


Figure 3 Annotated biological and geological features of SE Baltic coastal and offshore reefs.

annotation (see [Figure 3](#)). Selected biological features were red algae *Furcellaria lumbricalis* and *Vertebrata fucoides*, green algae *Cladophora* sp., blue mussel *Mytilus edulis trossulus*, geological features: boulders (>25 cm), cobbles (6–25 cm), pebbles (0.2–6 cm), and sand (<0.2 cm) according to the Wentworth scale ([Wentworth, 1922](#)). The summary of UI with mosaic sizes, number of frames, visual and modelled features is given in [Table 1](#).

2.4. Pre-processing of underwater imagery

For the deep learning model with convolutional architecture, training and testing data were made by patching together underwater images that were either in the form of large mosaics or representative frames. This was done using the sliding window principle. Training patches were augmented to maximize the amount of information available and to provide a simple form of regularization. For evaluation, the transects were split in half to achieve 2-fold cross-validation.

Due to the limitations of the available computational resources, both mosaics and frames were sliced into overlapping 288×288 -size patches. Overlap was the result of a sliding window or block processing idea with vertical and horizontal strides of 144 pixels. Due to the fact that mosaics contained a lot of white pixels, as a result of the mosaicking process, only patches with a minimum of 70% non-white

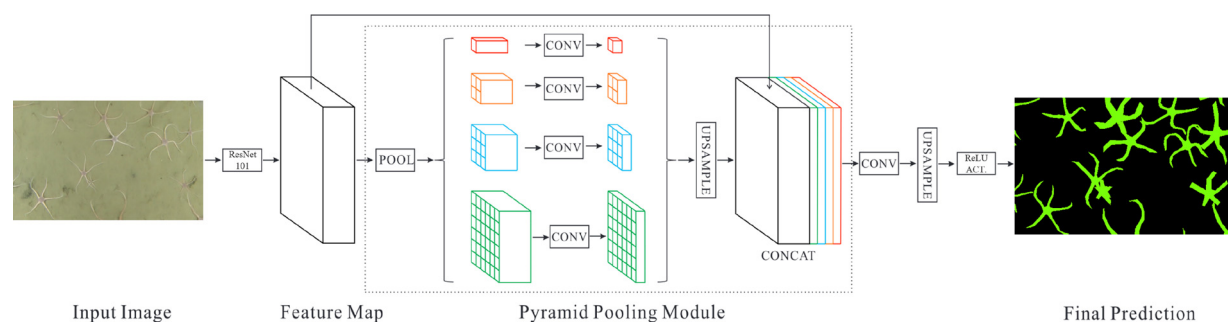
pixels were considered as input images. Additionally, to increase the amount of training data, a few traditional augmentation techniques, such as vertical and horizontal flip, and one marine-specific technique, removal of water scattering (RoWS) ([Chao and Wang, 2010](#)), were used on the prepared input image patches.

2.5. Deep learning model for semantic segmentation

In the experiments, we used a deep convolutional neural network with pyramid spatial pooling architecture – the PSPNet model ([Zhao et al., 2017](#)) – with ImageNet pre-trained ResNet-34 ([He et al., 2016](#)) as the backbone. The PSPNet architecture takes its name from the so-called Pyramid Pooling Module, which helps the model capture the global context within the segmented image, leading to more successful pixel annotations using global information present in the image ([Figure 4](#)). In a nutshell, this module captures different resolutions of the feature map, trying to identify and preserve the most important features from the feature map (output from the backbone model), combining both the downsampled, convoluted, and upsampled features and the original feature map (obtained from the backbone model) itself. The model was implemented using the Keras framework (version 2.3.1), running on the Tensorflow backend (version 2.1.0), with the

Table 1 Summary of the underwater imagery. MP corresponds to the size of imagery in megapixels. The last 4 transects were only for a final hold-out validation. Modelled features were used for deep learning experiments.

Transect	Mosaic size	Mosaic MP	Frames	Frames MP	Modelled features	Additional features
SM02-1	3671 × 8285	8.20	16	8.29	Boulders	Cladophora, Vertebrata, Cobbles, Pebbles, Sand
SM02-2	4693 × 7307	8.36	14	7.26	Boulders	Cladophora, Vertebrata, Cobbles, Pebbles, Sand
SM07-1	2434 × 8774	9.04	16	8.29	Furcellaria, Boulder	Cobbles, Pebbles, Sand
SM07-2	5021 × 5107	7.06	12	6.22	Furcellaria, Boulder	Cobbles, Pebbles, Sand
SM08-1	4191 × 5379	6.64	12	6.22	Furcellaria, Boulder	Cladophora, Vertebrata, Cobbles, Pebbles, Sand
SM08-2	4745 × 5379	6.85	12	6.22	Furcellaria, Boulder	Cladophora, Vertebrata, Cobbles, Pebbles, Sand
DE01-1	1580 × 5480	5.17	11	5.70	Mytilus, Boulder	Cobbles, Pebbles, Sand
DE01-2	2434 × 8774	6.56	11	5.70	Mytilus, Boulder	Cobbles, Pebbles, Sand
DE06-1	1495 × 7087	6.87	10	5.18	Mytilus, Boulder	Cobbles, Pebbles, Sand
R05-1	1656 × 7113	7.11	9	4.67	Furcellaria, Boulder	Cobbles, Pebbles, Sand
I167	—	—	15	7.78	Furcellaria, Boulder	Cobbles, Pebbles, Sand
N19	—	—	10	5.18	Mytilus, Boulder	Cobbles, Pebbles, Sand

**Figure 4** PSPNet model used for semantic segmentation. From Zhao et al. (2017) and Buškus et al. (2021).

help of the segmentation-models package (version 1.0.1) (Yakubovskiy, 2019). The models were trained for 50 epochs, with a batch size of 8 image patches.

2.6. Evaluation of model-based semantic segmentation

For training and testing the convolutional neural network model, we employed 2D mosaics and representative transect frames containing two biological and one geological feature (*F. lumbricalis*, *M. edulis trossulus*, and Boulders). The semantic segmentation task here was solved separately for each feature in a detection fashion. After a summary of manual annotation, the semantic segmentation task was evaluated by three types of validation schemes: 1) 2-fold transect-stratified cross-validation where each transect was

split in half and either all bottom parts or all top parts of transects were used for training; 2) leave one transect out validation where a single transect is used for testing while training on all the remaining transects; 3) hold-out validation had additional unseen imagery with features of interest collected and annotated as a way to stress-test the semantic segmentation task.

Stratification by transect in a 2-fold CV means that each transect is split in half -top and bottom parts – and training is performed on one part while testing on the other part. For example, after training on all the bottom parts of mosaics (or the first half of the corresponding frame set), testing is performed on all the top parts, and vice versa. Such a strategy guarantees that testing is performed on somewhat similar imagery to the one the model was trained on. However, the drawback is that smaller amounts of training data

(50/50% split instead of a more common 80/20%) and the count of feature instances (objects of interest) can differ to a large extent between the top and bottom parts of the transect.

The main benefit of the leave-one-out validation (LOO) strategy is the use of all available training data, but the drawback is the lack of stratification by transect, where in this strategy it is designed fully as the testing data. In this kind of validation model, usefulness can be fully investigated, but the testing data can differ from training due to visual differences between transects.

Due to the selected transects for the testing split, the hold-out validation strategy was the most challenging validation. The transects were recorded at different times and using different video recording equipment. Moreover, two of the four transects could not be stitched into mosaics because of poor image quality resulting from strong waves at the recording time. For those two challenging transects (I167 and N19), only the selection of representative video frames was possible.

The success of segmentation was determined by the intersection over union (IOU) metric, and estimates of visual coverage were calculated. This is a common metric in semantic image segmentation (Elbode et al., 2020), measuring segmentation success by comparing the ground truth with the prediction mask (that is, annotated and predicted image pixels), also known as the Jaccard index. The metric is defined as:

$$IOU = \frac{\text{true positive}}{\text{true positive} + \text{false negative} + \text{false positive}}$$

In addition, final prediction masks were used to estimate the visual coverage of the feature in question. The coverage itself was interpreted as a ratio between predicted or ground truth masks (that is, ‘active’ pixels) with only relevant pixels (excluding white pixels), in the mosaic setting and all pixels in the frame setting.

3. Results

Distinct benthic communities represented the sites chosen for this study. Coastal sites (SM) were dominated by macroalgae, while offshore sites (DE) were dominated by mussels (Figure 5). Three coastal sites were also different: The shallowest (4 m) SM02 site was dominated by the green algae *Cladophora* sp. (23.1±0.5%) and red algae *V. fucooides* (14.5±1.3%), with only a few thalli of *F. lumbricalis* (0.1%). On the contrary, the SM08 site was dominated by *F. lumbricalis* (49.4±10.1%) with only a few *Cladophora* sp. (3.1±3.2%) and *V. fucooides* (8.1±7.7%). At the SM07 site, only scarce patches of *F. lumbricalis* were present (10.8±1.5%). The substrate in all sites was dominated by coarse sediments: boulders (32.4–75.1%), cobble (2.8–16.8%), pebble (10.7–54.4%), while the sand fraction had the lowest share (7.8±6.2%).

3.1. Comparison of manual expert annotations

A comparison of 2D mosaic versus sampled frames with respect to expert-based manual annotations was done first. The possibility of sparsifying selected frames and using

Table 2 Average differences (± standard deviation) between expert coverage estimations of 2D mosaics (baseline) and frames for biological and geological visual features from all samples.

Feature	All frames	1/2 frames	1/3 frames
<i>F. lumbricalis</i>	4±2.8	3.9±2.2	5.5±3
<i>M. edulis trossulus</i>	1.6±1.2	3.3±2.1	1.7±2.2
<i>Cladophora</i> sp.	1.3±1	1.2±0.5	1.4±0.7
<i>V. fucooides</i>	2.7±3.6	2.7±3.5	4.4±5.6
Boulders	4.9±7.3	5.6±6.8	5.4±4.1
Cobble	2.1±1.9	2.2±1.8	2.8±1.5
Pebble	5.8±4.8	6±4.7	6.1±3.5
Sand	2.8±3.7	2.8±2.5	3.7±6.1

fewer images is evaluated with respect to coverage estimates. The accuracy was measured as the absolute difference from the mosaic coverage estimates (baseline) according to the following heuristic scale: 0–5% excellent, 5–10% good, 10–20% moderate, >20% bad.

As explained in Section 2.1, two methods for frame extraction from videos were used: simple and complex. For each video transect, we estimated the differences in coverage estimations (both for biological and geological visual features) from the baseline (mosaics) for both methods. The pairwise Wilcoxon signed-rank test showed that the simple method gives significantly lower baseline differences than the complex method (test statistic = 2.31 with continuity correction applied, p-value = 0.01). Thus, to make further analysis less complicated, only estimations of simple frame selection are provided further in this subsection.

The results have shown that, in general, the quality of visual evaluation does not suffer when analysing individual frames when comparing the differences between mosaics and frames (Table 2). Analysis of all frames had excellent accuracy and differed less than 5% from the baseline, except pebble (5.8%, good accuracy); excellent accuracy was also achieved from the analysis with a reduced number of frames, with the exception of boulders, which differed 5.4–5.6% from the baseline (good accuracy).

The differences from the baseline *F. lumbricalis* coverage estimates from all frames ranged from 1.3 to 7.0% in individual mosaics, indicating excellent to good accuracy. The reduction of frames provided similar results (Table 3). It is noticeable that in transects with lower coverage of *F. lumbricalis*, a higher accuracy was reached: transects with <20% coverage maintained excellent accuracy even with frame reduction, while transects with >40% coverage showed lower but still good accuracy.

The accuracy of boulder estimation from all frames was excellent in 6 out of 8 transects; in the other two transects from SM02 site, experts significantly overestimated the boulder class, resulting in moderate and bad accuracies (Table 4). The reduction of analysed frames resulted in similar accuracy in all transects except SM08-1, where the analysis of 1/3 frames resulted in increased differences from the baseline from 1.9 to 9.2%.

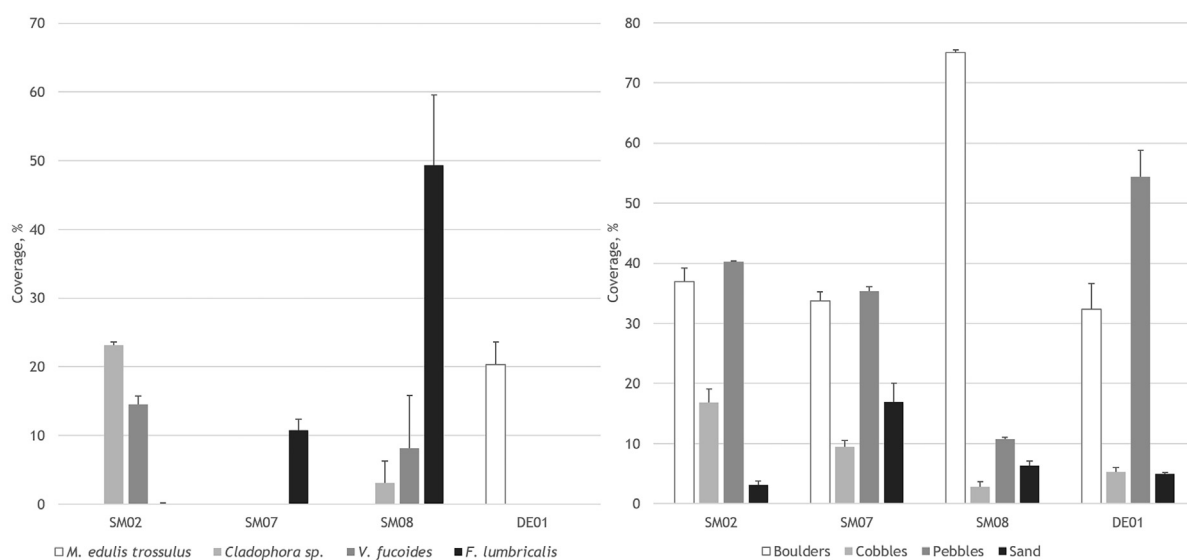


Figure 5 The percentage coverage of biological (*Furcellaria lumbricalis*, *Vertebrata fucooides*, *Cladophora* sp., *Mytilus edulis trossulus*) and geological (boulders, cobbles, pebbles and sand) visual features at research sites.

Table 3 Seabed visual coverage estimates (in %) of *F. lumbricalis* from the analysis of mosaics, all frames, half of frames and one third of frames. Note: Δ – differences from the mosaics (baseline).

<i>Furcellaria</i> transects	Mosaic	All frames	Δ	Coverage, %			
				1/2 frames	Δ	1/3 frames	Δ
SM07-1	9.7	8.4	1.3	8.9	0.8	7.3	2.4
SM07-2	11.8	10.0	1.9	7.9	3.9	8.4	3.5
SM08-1	42.2	47.8	-5.6	47.6	-5.4	50.1	-7.9
SM08-2	56.6	49.5	7.0	51.1	5.4	48.4	8.2

Table 4 The coverage (%) of boulders from the analysis of mosaics, all frames, half of frames and one-third of frames. Note: Δ – differences from the mosaics (baseline).

Boulder transects	Mosaic	All frames	Δ	Coverage, %			
				1/2 frames	Δ	1/3 frames	Δ
SM02-1	38.6	50.5	-11.9	50.6	-12.1	44.5	-5.9
SM02-2	35.5	55.8	-20.3	55.3	-19.8	48.8	-13.3
SM07-1	34.7	35.0	-0.2	32.4	2.4	29.7	5.1
SM07-2	32.6	32.4	0.2	31.8	0.8	34.7	-2.1
SM08-1	74.8	77.4	-2.7	80.0	-5.3	70.4	4.3
SM08-2	75.3	77.2	-1.9	74.4	0.9	84.5	-9.2
DE01-1	35.4	37.4	-2.0	37.5	-2.1	36.8	-1.4
DE01-2	29.4	29.8	-0.4	27.8	1.6	31.4	-2.0

3.2. Two-fold transect-stratified cross-validation

The segmentation success for the *F. lumbricalis* feature was very good, with the resulting IOU score in the 0.611–0.839 range (Table 5). Interestingly, the IOU score using frames was often higher than using mosaic, by 0.035 overall. Successful segmentation also resulted in accurate seabed visual coverage estimates (Table 6), where the estimate from expert annotations was 28.81%, the prediction of the model trained in mosaics was 28.57%, and the predictions from

models trained on frames were 27.55% and 27.92%. Individually, for separate transects, the difference between expert estimates on mosaic and models trained on frames did not exceed 8.5 percentage points.

The segmentation success for the *M. edulis trossulus* feature was moderate, with the resulting IOU score in the 0.560–0.699 range (Table 5). Frames performed similarly to mosaic with overall differences of -0.051 and 0.005 in the IOU score, but a simple sampling of frames provided more accurate coverage estimates. Poorer segmentation

Table 5 Segmentation performance, as measured by IOU score, using 2-fold and LOO validation for *F. lumbricalis*, *M. edulis trossulus* and boulders features in mosaic imagery or selected representative video frames (by simple or complex sampling).

Feature	Transect	Mosaic IOU		Simple Δ IOU		Complex Δ IOU	
		2-fold	LOO	2-fold	LOO	2-fold	LOO
<i>Furcellaria lumbricalis</i>	SM07-1	0.703	0.694	-0.015	-0.021	0.016	-0.043
	SM07-2	0.839	0.799	0.046	0.035	0.030	0.070
	SM08-1	0.661	0.628	-0.104	-0.127	-0.050	-0.099
	SM08-2	0.726	0.665	0.000	-0.047	0.028	-0.039
	Totals:	0.711	0.664	-0.035	-0.077	-0.035	-0.054
<i>Mytilus edulis trossulus</i>	DE01-1	0.671	0.486	-0.028	-0.113	0.064	-0.006
	DE01-2	0.560	0.600	-0.061	0.003	-0.050	0.005
	Totals:	0.613	0.549	-0.051	0.005	0.005	0.010
Boulders	DE01-1	0.670	0.551	-0.063	-0.112	0.012	-0.082
	DE01-2	0.649	0.601	-0.085	-0.074	-0.024	0.028
	SM07-1	0.582	0.566	-0.064	-0.024	0.060	0.022
	SM07-2	0.517	0.434	-0.111	-0.178	0.039	-0.015
	SM02-1	0.344	0.430	-0.256	-0.183	-0.091	-0.052
	SM02-2	0.297	0.279	-0.325	-0.264	-0.057	-0.117
	SM08-1	0.806	0.785	-0.016	-0.042	0.041	0.018
	SM08-2	0.790	0.776	-0.046	-0.057	0.014	-0.006
	Totals:	0.598	0.578	-0.108	-0.102	-0.003	-0.025

Table 6 Seabed visual coverage estimates, as measured in percentages, using 2-fold and LOO validation for *F. lumbricalis*, *M. edulis trossulus* and boulders features in mosaic imagery or selected representative video frames (by simple or complex sampling). Abbreviations: GT (ground-truth) – results of expert annotations; Δ DL – difference of model-based predictions (DL) from mosaic-wise ground-truth annotations (GT–DL).

Feature	Transect	Mosaic		Simple		Complex		
		GT	Δ DL	Δ DL	Δ DL			
		2-fold	LOO	2-fold	LOO	2-fold	LOO	
<i>Furcellaria lumbricalis</i>	SM07-1	9.75	0.31	-0.23	0.74	0.48	1.10	2.09
	SM07-2	11.91	0.86	1.26	2.66	3.11	1.45	2.89
	SM08-1	43.15	-0.68	-17.88	-5.89	-9.17	-5.19	-8.46
	SM08-2	57.48	0.41	13.07	8.41	6.82	6.82	4.42
	Totals:	28.81	0.24	-0.75	1.26	0.16	0.89	0.22
<i>Mytilus edulis trossulus</i>	DE01-1	22.83	0.76	9.92	3.62	7.59	7.07	11.18
	DE01-2	18.11	0.20	-0.82	1.86	-1.14	4.78	1.73
	Totals:	20.19	0.44	3.91	2.46	2.94	5.64	6.17
Boulders	DE01-1	29.65	4.09	7.87	-0.28	2.60	3.91	1.76
	DE01-2	35.60	2.62	5.73	1.49	2.14	4.44	0.18
	SM07-1	34.95	0.55	4.47	1.99	1.05	10.72	9.88
	SM07-2	32.82	9.36	13.74	3.28	5.76	15.30	16.00
	SM02-1	38.80	10.42	-4.85	-24.13	-24.14	3.76	-4.53
	SM02-2	35.40	8.57	13.56	-22.95	-11.66	10.78	6.15
	SM08-1	76.41	-3.59	-0.86	-6.59	-3.30	-0.53	-1.30
	SM08-2	76.55	-2.70	3.86	-7.70	-5.17	2.01	2.57
	Totals:	44.37	3.99	5.23	-7.72	-5.02	6.42	3.77

accuracy did not noticeably affect seabed visual coverage estimates (Table 6), where the estimate of expert annotations was 20.19%, prediction from model trained on mosaics was 19.75% and predictions from models trained on frames were 17.73% and 14.55%. Individually, for separate transects, the difference between the expert estimate on

the mosaic and the model trained on frames (from simple sampling) did not exceed 4 percentage points.

The segmentation success of the boulder feature was very varied, with much better results for simple frame sampling than using mosaics, with the resulting IOU score in the range 0.297–0.837 range (Table 5). Simple sampling

Table 7 Segmentation performance, as measured by IOU score, using hold-out validation for *F. lumbricalis*, *M. edulis trossulus* and boulders features in mosaic imagery or selected representative video frames by simple sampling.

Feature	Transect	Mosaic	Frames	Δ IOU
		IOU	IOU	
<i>Furcellaria lumbricalis</i>	R05-1	0.259	0.258	0.001
	I167	–	0.824	–
<i>Mytilus edulis trossulus</i>	DE06-1	0.061	0.075	–0.014
	N19	–	0.441	–
Boulders	R05-1	0.161	0.349	–0.188
	DE06-1	0.148	0.345	–0.197
	I167	–	0.453	–
	N19	–	0.143	–

provided the best segmentation accuracy overall, with an IOU score of 0.706. We suspect that such differences in IOU could be due to many objects in boulder class having poor visibility in the SM02_1 and SM02_2 mosaics, which also resulted in significant differences from expert annotations when using deep learning model predictions. The visual coverage estimates were markedly affected (Table 6), especially for SM02 and SM07 transects, where the overall estimate of the expert annotations was 44.37%, the prediction of the model trained on mosaics was 40.38% (underestimate of ~4 percentage points), and the predictions from models trained on frames were 52.09% (overestimate of ~7.7 percentage points) using simple and 37.95% (underestimate of ~6.4 percentage points) using complex frame sampling. Excluding too large overestimates of visual coverage using simple sampling of SM02 frames and underestimates using complex sampling of SM07-2 frames individually for separate transects, the difference between the expert estimate on the mosaic and model predictions did not exceed 11 percentage points.

3.3. Leave one transect out validation

The segmentation success for the *F. lumbricalis* feature was very good, with the resulting IOU score in the 0.628–0.799 range (Table 5). The IOU score was again higher for the *F. lumbricalis* feature using simple and complex frames sampling than using mosaic (overall by 0.077 and 0.054 respectively). Successful segmentation also resulted in accurate seabed visual coverage estimates (Table 6), where the estimate from expert annotations was 28.81%, the prediction of the model trained in mosaics was 29.56%, and predictions from models trained on frames were 28.65% and 28.59%. Individually, for separate transects, the difference between the expert estimate on the mosaic and the model trained on frames did not exceed 9.2 percentage points.

The segmentation success for the *M. edulis trossulus* feature was moderate, with the resulting IOU score in the 0.486–0.600 range (Table 5). Frames performed similarly to mosaic, with overall differences of 0.005 and 0.01 in the IOU score, but mosaic provided slightly more accurate coverage estimates. Poorer segmentation accuracy did not noticeably affect seabed visual coverage estimates (Table 6), where the estimate of expert annotations was 20.19%, prediction from model trained on mosaics was 16.28% and predictions

from models trained on frames were 17.25% and 14.02%. Individually, for separate transects, the difference between expert estimates on mosaic and models trained on frames did not exceed 11.2 percentage points.

The segmentation success of the boulder feature was very varied, with much better results for simple frame sampling than using mosaics, with the resulting IOU score in the 0.279–0.833 range (Table 5). Simple sampling provided the best segmentation accuracy overall, with an IOU score of 0.680. Similarly, for 2-fold CV results, we hypothesize that significant discrepancies in IOU may be related to the low visibility of several boulder-class objects in SM02-1 and SM02-2 mosaics, which also led to large differences between expert annotations and deep learning model predictions. The visual coverage estimates were markedly affected (Table 6), especially for SM02 and SM07 transects, where the overall estimate from expert annotations was 44.37%, the prediction from model trained in mosaics was 39.13% (underestimate of ~5.2 percentage points), and the predictions from models trained on frames were 49.38% (overestimate of ~5 percentage points) using simple and 40.60% (underestimate of ~3.8 percentage points) using complex frame sampling. Excluding too large overestimates of visual coverage using simple sampling of SM02 frames and underestimates using complex sampling of SM07-2 frames individually for separate transects, the difference between the expert estimate on the mosaic and model predictions did not exceed 16 percentage points.

3.4. Stress testing with hold-out validation

The segmentation success for the *F. lumbricalis* feature was poor for the R05-1 and excellent for the I167 transect (Table 7). Despite such different results, seabed visual coverage estimates were of acceptable accuracy (Table 8), deviating from ground-truth expert annotations by 6.7 percentage points for mosaic and just 3.4 or 0.93 percentage points for frames. Surprisingly, the frames outperformed the mosaic for the R05-1 transect. For comparison, the difference between expert annotations of mosaic and frames was 1.7 percentage points.

The segmentation success for the *M. edulis trossulus* feature was unacceptable for the DE06-1 and mediocre for the N19 transect (Table 7). Due to the low visual coverage in the DE06-1 transect (Table 8), where experts estimated

Table 8 Seabed visual coverage estimates, as measured in percentages, using hold-out validation for *F. lumbricalis*, *M. edulis trossulus* and boulders features in mosaic imagery or selected representative video frames by simple sampling. Abbreviations: GT (ground-truth) – results of expert annotations; DL (deep learning) – results of model-based predictions; Δ – difference from mosaic-wise ground-truth annotations (GT–DL). In case a mosaic was not available frame-based GT annotations were used.

Feature	Transect	Mosaic		Frames			
		GT	Δ DL	GT	Δ GT	DL	Δ DL
<i>Furcellaria</i>	R05-1	10.18	6.70	8.48	1.70	6.78	3.40
<i>lumbricalis</i>	I167	–	–	40.46	–	39.53	0.93
<i>Mytilus edulis</i>	DE06-1	7.76	7.24	8.40	–0.64	0.66	7.11
<i>trossulus</i>	N19	–	–	33.82	–	25.59	8.23
Boulders	R05-1	16.19	–51.23	32.13	–15.94	83.68	–67.49
	DE06-1	24.84	17.59	24.62	0.22	15.40	9.44
	I167	–	–	44.59	–	50.30	–5.71
	N19	–	–	51.09	–	32.13	18.96

7.76% in mosaics and 8.4% in frames (with a small overestimate of 0.64 percentage points), differences of ~7 percentage points are too large in this case. Basically, this means that the model could not predict lower amounts of *M. edulis trossulus* feature objects in the DE06-1 transect when trained on DE01-2 and DE01-1 transects, which had higher amounts. Meanwhile, the more successfully segmented N19 transect frames with higher amounts of *Mytilus* features had a seabed visual coverage estimate of 33.82% by experts and a 25.59% underestimate by the model (Table 8), where the difference of ~8 percentage points can be seen as a good result.

The segmentation success of the boulder feature was poor regardless of the transect but, interestingly, much better for frames than for mosaics (Table 7). However, the visual coverage for the R05-1 transect was unacceptably overestimated (Table 8), with the differences between the expert and the model being too large. Meanwhile, other transects showed better results, with the largest difference being ~19 percentage points.

5. Discussion

Our results have shown that in general, coverage estimations from mosaics and frames were very similar for all eight features, thus providing a few opportunities for more effective UI analysis. Using a set of representative frames from an underwater video may considerably reduce the time required for preprocessing raw data since mosaicking of seabed imagery can be labour-intensive and requires specific software or algorithms and professional knowledge, despite existing tools such as AutoStitch, APAP, and SPHP (Li et al., 2019). The most time-consuming step of mosaicking is manual registration of consecutive frames if automatic pair-wise registration of these frames is unsuccessful. This is often the case for Baltic Sea UI which is usually of limited quality (high turbidity, camera motion due to waves, motion of features, changing lighting, etc.). Also, the requirement of irregular manual intervention to mosaicking process makes a fully automated video analysis very complicated. Frames-based approach with a decreased number of analysed frames also provides a reasonable option

to reduce the efforts needed for UI annotation, considering that a single 100 m video transect, depending on the drift, can result in 100–150 individual frames. However, this approach has some implicit limitations. While the frame-based analysis may well substitute mosaicking for features that require coverage estimation (such as underwater vegetation, colonial fauna, and substrate types), this approach is less successful in estimating the number of individual organisms, especially if they are rare and scarce or moving during the video. We noticed that some individuals can be counted twice if they are partially annotated in two adjacent frames, or cannot be counted at all if they are located between adjacent frames (Figure 6). Furthermore, reducing the number of frames analysed in this case may lead to significant overestimations or underestimations, depending on whether or not a rare feature occurs in the analysed set of frames.

Surprisingly, complex sampling did not provide a clear advantage over simple sampling, with semantic segmentation performance always inferior (resulting in lower IOU values) and coverage estimations depending on the class analyzed (only with marginally better results for *F. lumbricalis* and boulder classes). Due to poorer segmentation results and negligible differences in coverage estimates, the introduced complex sampling cannot be recommended since it requires a large computational overhead while not providing better results. One of the reasons why complex sampling failed could be the high dimensionality of EfficientNet embeddings applied to short video segments, creating a curse of dimensionality challenge (Moghaddam et al., 2020) for the underlying SMRS algorithm.

Semantic segmentation gave moderate accuracy, as measured by the IOU score, but seabed coverage estimates obtained from predicted segmentations were overall quite accurate. Based on leave-one-out and two-fold transect stratified validations, the total absolute differences between expert annotations and model results were less than 6% and 8%, respectively, which is quite impressive considering the often higher variability of intra- and interobserver classification (Beijbom et al., 2015; Reeves et al., 2007). However, some individual transects resulted in high biases of up to 24% in absolute difference.



Figure 6 Double annotation of European flounder *Platichthys flesus* in two adjacent frames (top picture, DE01-1 transect) and misannotation of moon jelly *Aurelia aurita* between adjacent frames (bottom picture, SE07-1 transect).



Figure 7 The performance of deep learning models for the boulder class based on IOU scores from worst (left) to best (right) in SM02-1, SM07-1, DE01-2 and SM08-2 transects respectively.

The validation of the boulder class gave somewhat unexpected results. The best IOU scores were for SM08 transects where boulders were mostly overgrown by macroalgae *F. lumbricalis* and with hardly visible outlines, while transects with relatively easily outlined boulders gave lower IOU scores (Figure 7). This could be explained by the substrate preferences of different macroalgae species. For example, as stated by Bučas et al. (2007), in Lithuanian coastal reefs, perennial red algae *F. lumbricalis* (the dominant feature of SM08 transects) prefer the most stable substrate – boulders, while green algae *Cladophora* sp. (the dominant feature of SM02 transects) can overgrow both boulders and cobbles. This could suggest that during substrate classification, the model considers epibenthos and tends to assign over-

grown substrate to the boulder class rather than to cobble, whereas, in transects with scarce vegetation (SM07) or vegetation both on boulders and cobbles (SM02), the classification is less accurate. On the other hand, model results from the frame analysis were more accurate than from mosaics, showing that the framing approach is not only more effective for the annotation of UI but also more suitable for deep learning models.

Stress tests with hold-out validation, which were based on additionally annotated challenging test data, resulted in even worse model performance, with differences between experts and the model exceeding 50% for some transects. This could be explained by intentionally selecting videos with different image quality for the test

dataset. For example, I167 and N19 sites were filmed with a “drop-down” video system with noticeable wave action, while the light environment and image sharpness in R05-1, sediment composition, and colour palette in DE06-1 were also different. This emphasizes the importance of having a training dataset with a variety of filming equipment and environmental conditions. This seems especially important for the very dynamic environment of Lithuanian coastal reefs, which are under the influence of plume from the Curonian Lagoon (Vaičiūtė et al., 2012), regular upwelling events (Dabulevičienė et al., 2018), waves and currents, not to mention different cloudiness, all of which can determine different lighting, water colour, transparency/turbidity, camera motion, and other parameters that can influence the results of visual analysis.

6. Conclusions

Our study has shown that seabed coverage estimations from video mosaics and individual frames provided similar results, suggesting that the mosaicking step, often used for UI analysis, could be skipped if an approximate estimate of biological and geological features is sufficient. Moreover, results indicated that even a two- or three-fold decrease in the frames analysed still resulted in relatively accurate coverage estimates for most of the features. In general, coverage estimates from automatic segmentation with deep learning models gave very promising seabed coverage estimation results for all visual classes, despite moderate IOU scores. Frame-based results were often slightly worse than mosaic-based results, but these differences seem to be negligible. When comparing seabed visual coverage estimates from expert annotated mosaics with the estimates from model-based segmentation predictions, absolute differences did not exceed 11% in 2-fold transect-stratified cross-validation, 16% in the leave-one-transect-out validation scheme, and 19% in challenging hold-out validation overall. Interestingly, the largest differences were consistently obtained for the boulder feature, which had large percentages of objects, resulting in large visual coverage. Judging from observed biases differing with respect to the validation scheme, we could advise having more varied imagery, both in recording equipment and environmental conditions. Therefore, contrary to coverage estimates from expert annotation of frames recommendations, we do not recommend reducing the number of selected frames if the goal is to prepare underwater imagery for deep learning model training. Finally, this study has laid a solid stepping stone towards automatic recognition and estimation of SE Baltic hard bottom features from UI, which in the future could considerably facilitate reef monitoring and environmental status assessment.

Declaration of competing interest

The authors declare that they have no known competing financial interests or personal relationships that could have appeared to influence the work reported in this paper.

Acknowledgements

This study was supported by the project DEMERSAL “A deep learning-based automated system for seabed imagery recognition” funded by the Research Council of Lithuania under the agreement No. P-MIP-19-492.

References

- Alonso, I., Yuval, M., Eyal, G., Treibitz, T., Murillo, A.C., 2019. CoralSeg: Learning coral segmentation from sparse annotations. *J. Field Robot.* 36 (8), 1456–1477. <https://doi.org/10.1002/rob.21915>
- Beijbom, O., Edmunds, P.J., Roelfsema, C., Smith, J., Kline, D.I., Neal, B.P., Dunlap, M.J., Moriarty, V., Fan, T.Y., Tan, C.J., Chan, S., 2015. Towards automated annotation of benthic survey images: Variability of human experts and operational modes of automation. *PLOS One* 10 (7), e0130312. <https://doi.org/10.1371/journal.pone.0130312>
- Bučas, M., Daunys, D., Olenin, S., 2007. Overgrowth patterns of the red algae *Furcellaria lumbricalis* at an exposed Baltic Sea coast: the results of a remote underwater video data analysis. *Estuar. Coast. Shelf S.* 75 (3), 308–316. <https://doi.org/10.1016/j.ecss.2007.04.038>
- Buhl-Mortensen, L., Buhl-Mortensen, P., Dolan, M.F., Holte, B., 2015. The MAREANO programme—A full coverage mapping of the Norwegian off-shore benthic environment and fauna. *Mar. Biol. Res.* 11 (1), 4–17. <https://doi.org/10.1080/17451000.2014.952312>
- Buškus, K., Vaičiukynas, E., Verikas, A., Medelytė, S., Šiaulys, A., Šaškov, A., 2021. Automated quantification of brittle stars in seabed imagery using computer vision techniques. *Sensors* 21 (22), 7598. <https://doi.org/10.3390/s21227598>
- Casoli, E., Ventura, D., Mancini, G., Pace, D.S., Belluscio, A., Ardizzone, G., 2021. High spatial resolution photo mosaicking for the monitoring of coralligenous reefs. *Coral Reefs* 40 (4), 1267–1280. <https://doi.org/10.1007/s00338-021-02136-4>
- Chao, L., Wang, M., 2010. Removal of water scattering. In: International conference on computer engineering and technology IEEE, 2, 35. <https://doi.org/10.1109/ICCET.2010.5485339>
- Dabulevičienė, T., Kozlov, I.E., Vaiciute, D., Dailidienė, I., 2018. Remote sensing of coastal upwelling in the south-eastern Baltic Sea: Statistical properties and implications for the coastal environment. *Remote Sens.* 10 (11), 1752. <https://doi.org/10.3390/rs10111752>
- Eelbode, T., Bertels, J., Berman, M., Vandermeulen, D., Maes, F., Bisschops, R., Blaschko, M.B., 2020. Optimization for medical image segmentation: theory and practice when evaluating with dice score or Jaccard index. *IEEE T. Med. Imaging* 39 (11), 3679–3690. <https://doi.org/10.1109/TMI.2020.3002417>
- Elhamifar, E., Sapiro, G., Vidal, R., 2012. See all by looking at a few: Sparse modeling for finding representative objects. In: Proc. CVPR IEEE, 1600–1607. <https://doi.org/10.1109/CVPR.2012.6247852>
- Ferreira, T., Rasband, W., 2012. ImageJ user guide – IJ 1.46. URL: <https://imagej.net/docs/guide/> (accessed on 2 August 2023).
- Gracias, N., Garcia, R., Campos, R., Hurtos, N., Prados, R., Shihavuddin, A.S.M., Nicosevici, T., Elibol, A., Neumann, L., Escartin, J., 2017. Application challenges of underwater vision. In: López, A.M., Imiya, A., Pajdla, T., Álvarez, J.M. (Eds.), *Computer Vision in Vehicle Technology: Land, Sea & Air*. Wiley, Chichester, 133–160. <https://doi.org/10.1002/9781118868065.ch7>
- He, K., Zhang, X., Ren, S., Sun, J., 2016. Deep Residual Learning for Image Recognition. *Proc. CVPR IEEE*, 770–778. <https://doi.org/10.1109/CVPR.2016.90>

- Islam, M.J., Edge, C., Xiao, Y., Luo, P., Mehtaz, M., Morse, C., Enan, S.S., Sattar, J., 2020. Semantic segmentation of underwater imagery: Dataset and benchmark. *IEEE Int. C. Int. Robot.* 1769–1776. <https://doi.org/10.1109/iros45743.2020.9340821>
- Kohler, K.E., Gill, S.M., 2006. Coral Point Count with Excel extensions (CPCe): A Visual Basic program for the determination of coral and substrate coverage using random point count methodology. *Comput. Geosci.* 32 (9), 1259–1269. <https://doi.org/10.1016/j.cageo.2005.11.009>
- Labelbox. URL: <https://labelbox.com> (accessed 2 August 2023).
- Langenkämper, D., Zurowietz, M., Schoening, T., Nattkemper, T.W., 2017. Biigle 2.0-browsing and annotating large marine image collections. *Front. Mar. Sci.* 4, 83. <https://doi.org/10.3389/fmars.2017.00083>
- Li, Y., Randall, C.J., van Woesik, R., Ribeiro, E., 2019. Underwater video mosaicing using topology and superpixel-based pairwise stitching. *Expert Syst. Appl.* 119, 171–183. <https://doi.org/10.1016/j.eswa.2018.10.041>
- Liu, F., Fang, M., 2020. Semantic segmentation of underwater images based on improved Deeplab. *J. Mar. Sci. Eng.* 8 (3), 188. <https://doi.org/10.3390/jmse8030188>
- Martin-Abadal, M., Guerrero-Font, E., Bonin-Font, F., Gonzalez-Cid, Y., 2018. Deep semantic segmentation in an AUV for on-line *Posidonia oceanica* meadows identification. *IEEE Access* 6, 60956–60967. <https://doi.org/10.1109/ACCESS.2018.2875412>
- Medelytė, S., Šiaulys, A., Daunys, D., Włodarska-Kowalczyk, M., Węstawski, J.M., Olenin, S., 2022a. Application of underwater imagery for the description of upper sublittoral benthic communities in glaciated and ice-free Arctic fjords. *Polar Biol.* 45 (12), 1655–1671. <https://doi.org/10.1007/s00300-022-03096-3>
- Medelytė, S., Šiaulys, A., Vaičiukynas, E., Buškus, K., Šaškov, A., Olenin, S., 2022b. A fully-annotated imagery dataset of sublittoral benthic species in South Eastern Baltic Sea reefs. *Mendeley Data*, V1. <https://doi.org/10.17632/wsd42v8mk5.1>
- Moghaddam, S.H.A., Mokhtarzade, M., Beirami, B.A., 2020. A feature extraction method based on spectral segmentation and integration of hyperspectral images. *Int. J. Appl. Earth Obs.* 89, 102097. <https://doi.org/10.1016/j.jag.2020.102097>
- Piechaud, N., Hunt, C., Culverhouse, P.F., Foster, N.L., Howell, K.L., 2019. Automated identification of benthic epifauna with computer vision. *Mar. Ecol. Prog. Ser.* 615, 15–30. <https://doi.org/10.3354/meps12925>
- Reeves, B.R., Dowty, P.R., Wyllie-Echeverria, S., Berry, H.D., 2007. Classifying the seagrass *Zostera marina* L. from underwater video: an assessment of sampling variation. *J. Mar. Environ. Eng.* 9 (1), 1–15.
- Rimavičius, T., Gelžinis, A., Verikas, A., Vaičiukynas, E., Bačauskienė, M., Šaškov, A., 2018. Automatic benthic imagery recognition using a hierarchical two-stage approach. *Signal Image Video P* 12 (6), 1107–1114. <https://doi.org/10.1007/s11760-018-1262-4>
- Rzhanov, Y., Mayer, L., 2004. Deep-sea image processing, 647–652, *Oceans '04 MTS/IEEE Techno-Ocean '04* (IEEE Cat. No.04CH37600). <https://doi.org/10.1109/OCEANS.2004.1405498>
- Šaškov, A., Dahlgren, T.G., Rzhanov, Y., Schläppy, M.L., 2015. Comparison of manual and semi-automatic underwater imagery analyses for monitoring of benthic hard-bottom organisms at offshore renewable energy installations. *Hydrobiologia* 756, 139–153. <https://doi.org/10.1007/s10750-014-2072-5>
- Šiaulys, A., Vaičiukynas, E., Medelytė, S., Olenin, S., Šaškov, A., Buškus, K., Verikas, A., 2021. A fully-annotated imagery dataset of sublittoral benthic species in Svalbard. *Arctic. Data Br.* 35, 106823. <https://doi.org/10.1016/j.dib.2021.106823>
- Smith Menandro, P., Cardoso Bastos, A., 2020. Seabed mapping: A brief history from meaningful words. *Geosciences* 10 (7), 273. <https://doi.org/10.3390/geosciences10070273>
- Tan, M., Le, Q., 2019. EfficientNet: Rethinking model scaling for convolutional neural networks. In: *International Conference on Machine Learning*, 6105–6114. <https://doi.org/10.48550/arXiv.1905.11946>
- Tomar, S., 2006. Converting video formats with FFmpeg. *Linux J.* 2006 (146), 10. <https://www.linuxjournal.com/article/8517>
- Trygonis, V., Sini, M., 2012. photoQuad: a dedicated seabed image processing software, and a comparative error analysis of four photoquadrat methods. *J. Exp. Mar. Biol. Ecol.* 424 (425), 99–108. <https://doi.org/10.1016/j.jembe.2012.04.018>
- Urra, J., Palomino, D., Lozano, P., González-García, E., Farias, C., Mateo-Ramírez, Á., Fernández-Salas, L.M., López-González, N., Vila, Y., Orejas, C., Puerta, P., 2021. Deep-sea habitat characterization using acoustic data and underwater imagery in Gazul mud volcano (Gulf of Cádiz, NE Atlantic). *Deep-Sea Res. Pt. I* 169, 103458. <https://doi.org/10.1016/j.dsr.2020.103458>
- Vaičiūtė, D., Bucas, M., Bresciani, M., 2012. Validation of MERIS bio-optical products with *in situ* data in the turbid Lithuanian Baltic Sea coastal waters. *J. Appl. Remote Sens.* 6 (1), 063568. <https://doi.org/10.1117/1.JRS.6.063568>
- Wentworth, C.K., 1922. A scale of grade and class terms for clastic sediments. *J. Geol.* 30 (5), 377–392. <https://doi.org/10.1086/622910>
- Yakubovskiy, P., 2019. *Segmentation Models*. GitHub repository. URL: https://github.com/qubvel/segmentation_models (accessed on 2 August 2023).
- Zhao, H., Shi, J., Qi, X., Wang, X., Jia, J., 2017. Pyramid Scene Parsing Network. *Proc. CVPR IEEE* 6230–6239. <https://doi.org/10.1109/CVPR.2017.660>

Available online at www.sciencedirect.com

ScienceDirect

journal homepage: www.journals.elsevier.com/oceanologia

ORIGINAL RESEARCH ARTICLE

Influence of wind and waves on ambient noise and bubble entrainment depth in the semi-enclosed Baltic Sea

Agata Dragan-Górska^{a,*}, Natalia Gorska^a, Piotr Markuszewski^{b,c,d},
Zygmunt Klusek^a

^a Marine Physics Department, Institute of Oceanology, Polish Academy of Sciences, Sopot, Poland

^b Physical Oceanography Department, Institute of Oceanology, Polish Academy of Sciences, Sopot, Poland

^c Department of Environmental Science, Stockholm University, 10691 Stockholm, Sweden

^d Bolin Centre for Climate Research, Stockholm University, 10691 Stockholm, Sweden

Received 23 December 2022; accepted 16 December 2023

Available online 30 December 2023

KEYWORDS

Breaking waves;
Underwater ambient
noise;
Gas bubbles;
Semi-enclosed Baltic
Sea

Abstract Semi-enclosed, fetch-limited waters create unique conditions for wind wave development and breaking. Parameters of breaking waves influence bubble entrainment depth and associated noise, which is why they differ in semi-enclosed sea compared to open waters. While the established noise-wind speed relationship holds in oceanic conditions, it differs in land-constrained basins like the Baltic Sea. To explore noise level, bubble entrainment depth and wind speed relationships, we conducted noise and sub-surface bubble measurements, coupled with wind observations, in the selected area of the Baltic Sea during two consecutive summers. A novel method was employed to estimate bubble entrainment depth under conditions of strong backscatter. Model data of wave field parameters were employed to assess their influence on noise level and bubble entrainment depth. Results suggest stronger connections between noise level and wind speed, as well as wave height, compared to wave age and wind sea steepness. The same patterns hold true for the correlation between bubble entrainment depth and both wind speed and wave field parameters. The parameterized noise level-wind speed relationship differs from that obtained for oceanic conditions and also varies across measurement periods. Observed differences were shaped by varying wind-wave conditions, notably differences in wind speed, direction, wave height, and the presence of swell. The noise level-

* Corresponding author at: Marine Physics Department, Institute of Oceanology, Polish Academy of Sciences, Powstańców Warszawy 55, Sopot, Poland.

E-mail address: adgorska@iopan.pl (A. Dragan-Górska).

Peer review under the responsibility of the Institute of Oceanology of the Polish Academy of Sciences.



<https://doi.org/10.1016/j.oceano.2023.12.003>

0078-3234/© 2023 Institute of Oceanology of the Polish Academy of Sciences. Production and hosting by Elsevier B.V. This is an open access article under the CC BY-NC-ND license (<http://creativecommons.org/licenses/by-nc-nd/4.0/>).

bubble entrainment depth relation is reported for the first time for Baltic Sea conditions. For a thorough analysis of the influence of these factors on noise and bubbles, longer measurements under diverse wind-wave conditions are required to account for site-specific wave field characteristics.

© 2023 Institute of Oceanology of the Polish Academy of Sciences. Production and hosting by Elsevier B.V. This is an open access article under the CC BY-NC-ND license (<http://creativecommons.org/licenses/by-nc-nd/4.0/>).

1. Introduction

Wave breaking is responsible for the introduction of gas bubbles under the sea surface. Bubbles undergo complex volume oscillations and emit noise (Banner and Cato, 1988; Medwin and Beaky, 1989). They are not only the primary source of wind-dependent ambient noise in the ocean (Farmer and Vagle, 1988; Kerman, 1988), but they also play an important role in various processes related to the air-sea interface interactions, as heat and gas exchange, aerosol generation, momentum transfer from the wind to currents and many others.

The parameters of wind and breaking waves inherently affect the population of bubbles, influencing their entrainment depth (Graham et al., 2004; Wang et al., 2016) and impacting characteristics of underwater noise, such as its level and the shape of the frequency spectrum (Farmer and Lemon, 1984; Perrone, 1969; Wille and Geyer, 1984). The characteristics of the wind and wave fields significantly depend on the examined water body, especially on the proximity of the study site to the shoreline and its shape. In semi-enclosed areas and coastal regions with nearby shorelines and islands, they differ from those in the open ocean (Soomere, 2023). Therefore, it is reasonable to expect that the distance to the land also influences the spatial distribution of bubbles and characteristics of generated noise.

Pioneering measurements of underwater sound by Knudsen et al. (1948) have shown a correlation between ambient noise and sea state. Field measurements of Piggott (1964) and Shaw et al. (1978) led to the establishment of a well-known relationship between wind-driven ambient noise spectrum level $NSL(f)$ in the 100–25 000 Hz range and wind speed U , in the form:

$$\log(U) = m(f)NSL(f) + n(f) \quad (1)$$

where U is the wind speed in m/s, f is the frequency in Hz, $m(f)$ and $n(f)$ are coefficients and $NSL(f)$ is in dB re $1\mu\text{Pa}^2\text{Hz}^{-1}$.

Later studies have confirmed a strong correlation between ambient noise and wind speed (Lemon et al., 1984; Vagle et al., 1990). The proposed relationship was used in practice (*Wind Observations Through Ambient Noise, WOTAN*) to estimate oceanic winds through underwater noise (Vagle et al., 1990). However, the variability between coefficients $m(f)$ and $n(f)$ was observed (Farmer and Lemon, 1984; Klusek and Lisimenka, 2016; Vakkayil et al., 1996). It was suggested that the wind-noise relationship might be site- and frequency-dependent (Vagle et al., 1990).

Most of the aforementioned studies focused on the open ocean, where wave parameters (e.g. height, length) remain

unaffected by wind direction, and waves often develop under unlimited fetch conditions. In coastal or semi-enclosed waters, the direction of the wind is an important factor as it determines the fetch length and other characteristics of the wave field.

Not many attempts were made to verify the wind speed – ambient noise relation in the area where land proximity might influence wave breaking (Cato and Tavener, 1997; Kim and Choi, 2006; Poikonen and Madekivi, 2010; Reeder et al., 2011; Markuszewski et al., 2020). The proximity of land complicates the wind field, negatively affecting the correlation between wind speed and noise level (Cato and Tavener, 1997). Moreover, differences in ambient noise level and spectral characteristics of noise, in comparison to open waters, were observed (Cato, 2019; Ingenito and Wolf, 1989; Ramji et al., 2008).

Wind speed influences not just the noise level and the shape of the noise frequency spectrum, but also the depth of bubble entrainment (Thorpe, 1992). The relationship between entrainment depth and wind speed has been examined in various regions using up-looking echosounders (Crawford and Farmer, 1987; Strand et al., 2020; Wang et al., 2016). It has been demonstrated that both the character of the dependence and the bubble entrainment depths are site-specific.

Given that gas bubbles generated by breaking waves are the primary source of wind-dependent noise, it follows that the wave characteristics should also influence both the bubbles and the resulting noise. Initial measurements revealed a weak correlation between noise level and significant wave height (Farmer and Lemon, 1984; Felizardo and Melville, 1995; Perrone, 1969). However, removing the influence of swell improved correlations between wave height and ambient sea noise (Felizardo and Melville, 1995) and wave height and bubble entrainment depth (Strand et al., 2020). Limited research has explored relationships between noise, gas bubbles and other wave field parameters. A good correlation was found between the wave slope and the noise level (Felizardo and Melville, 1995; Rapp and Melville, 1990). The steepness of the wind sea affects the frequency of wave breaking (Banner et al., 2000) and, consequently, should also influence the noise and bubble entrainment depth. Steeper waves are characteristic of a developing sea (young waves), whereas less steep waves are typical of a mature sea (developed waves). A parameter that provides information about the state of wave development is the wave age. Bubble entrainment depth was found to decrease with the wave age (Graham et al., 2004; Thorpe, 1986; Wang et al., 2016), however, Gemmrich and Farmer (1999) stated that wave age alone may not fully represent wave-breaking conditions.

The semi-enclosed nature of the Baltic Sea results in unique characteristics of wind waves (Soomere, 2023), which may lead to distinctive properties of underwater noise, the depth of entrainment of gas bubbles, and their relationships with wind-wave field properties. On the one hand, this specificity refers to the morphometry of the sea (Leppäranta and Myrberg, 2009). This includes, firstly, the small size of the sea and thus the limited fetch length that controls the development of wind waves. Secondly, the Baltic Sea has a complex shape due to the diversity of its coastal environments and extensive archipelago areas. On the other hand, the specificity of predominant winds also plays a role. In this area, the winds have a multi-peak directional structure with strong anisotropy of wind directions (Karagali et al., 2014). The location of the Baltic Sea in the periphery of the highly variable North Atlantic storm track (Wickström et al., 2020), exposes it to abundant stormy winds (Pinto et al., 2007). This might result in winds blowing from unusual directions (Bierstedt et al., 2015), and can significantly impact the wind wave field properties.

The listed features lead to high spatio-temporal variability of wind and wave fields in the Baltic Sea, which are thus site-specific, opposite to many areas of the World Ocean. As a result, observations conducted in specific sea locations cannot be easily extrapolated to other areas. Hence it is of great importance to study underwater noise and gas bubble populations in particular areas of the Baltic Sea, as it might yield significantly diverse findings.

A recent study by Klusek and Lisimenka (2016) in a fetch-limited area of the semi-enclosed Baltic Sea has shown that ambient noise might also depend on the seasonally changing sound propagation conditions: presence and type of acoustic waveguide. The specific spatial features of the semi-enclosed Baltic Sea, including the presence of straits, bays, and islands, not only alter the wind-wave field but also impact sound propagation conditions. Noise measurements carried out in different areas of the Baltic Sea indicate the existence of significant differences in shape and levels of ambient noise spectra (Bagočius, 2013; Bagočius and Narščius, 2022; Grelowska, 2016; Grelowska and Kozaczka, 2020; Klusek and Lisimenka, 2016; Poikonen and Madekivi, 2010; Sigray et al., 2016).

The factors mentioned above stimulated our research, prompting us to choose the Gulf of Gdansk as our measurement site. Within this location, we aim to demonstrate how intricate wind-wave conditions impact both noise levels and the depth of gas bubbles entrained during the process of wave breaking.

2. Methods

2.1. Study site

The data used in the analysis were collected during two measurement campaigns conducted in the Gulf of Gdansk (southern Baltic Sea). The first experiment was carried out from 14 to 18 September 2005 (54.5917°N, 19.3583°E), while the second was conducted about a year later, from 3 to 6 October 2006 (54.5833°N, 19.4150°E). Later in the paper, whenever we use the term “in 2005” or “in 2006”, we are referring to these specific periods only, not the entire

years. The distance between both measurement points was approximately 2 NM. The depth at the measurement site was 79 m in 2005 and 75 m in 2006. The sea bottom in the area consists mostly of muddy sediments (Zachowicz et al., 2004).

The sound propagation conditions at the site were typical for the summer season. The conditions were determined by three distinct water layers: an upper mixed layer with a constant sound speed; seasonal thermocline with a rapidly decreasing sound speed (in the depth range: 20–40 m and 30–40 m for 2005 and 2006, respectively) and a deep water layer where the sound speed was slightly increasing with the depth, Figure 1b. This resulted in the creation of the weakly expressed mid-water acoustic waveguide with a sound speed minimum at a depth between 60–70 m and 43–55 m, respectively, during the first and second measurement campaign.

The air-sea temperature difference varied between -6°C and $+1.5^{\circ}\text{C}$ during 2005 measurements, and between -6.5°C and -2.5°C during 2006 measurements, defining atmospheric boundary layer conditions as generally unstable. The stability of the atmospheric boundary layer may influence wave height (Wille and Geyer, 1984) and depth of bubble clouds (Thorpe, 1982).

The wind direction has an influence on the wave field in the area of the semi-enclosed waters of the southern part of the Baltic Sea. The arrows in the Figure 1a present the distance from the study site to the nearest land (fetch length) as a function of the direction, which together with the wind speed and wind duration determines the size of waves (height and length). At the study site, waves are the highest when the wind is from NW through N to NE directions, and when the fetch reaches up to 600 km. While waves originate from the land (from E through S to W directions), fetch length ranges from 20 to 80 km, with an average value of 40 km.

2.2. Hydroacoustic measurements

2.2.1. Hydroacoustic buoy

The underwater ambient noise and acoustic backscatter measurements were performed using an autonomous hydroacoustic buoy (a prototype instrument). It was designed as a simple, self-sufficient system that can be deployed for up to a few days. The buoy consisted of a cylindrical pressure housing (0.3 m diameter and 1.0 m height) with electronics and battery set inside, two main hydroacoustic modules (active and passive), and a pressure sensor. The dominant design factor was the integration of the two hydroacoustic modules into one buoy.

The passive hydroacoustic module comprised two broadband omnidirectional hydrophones attached vertically on the side of the buoy (Figure 2a). The upper hydrophone was connected to a spherical float which held it at a desired depth. It was located in a subsurface layer at depths of 23 m (2005) and 21 m (2006), while the lower hydrophone was consistently placed 22 m below the upper one. Such an arrangement enabled to record a noise that originated from the local subsurface sources (upper hydrophone in the mixed layer) and from distant sources (lower hydrophone in the thermocline).

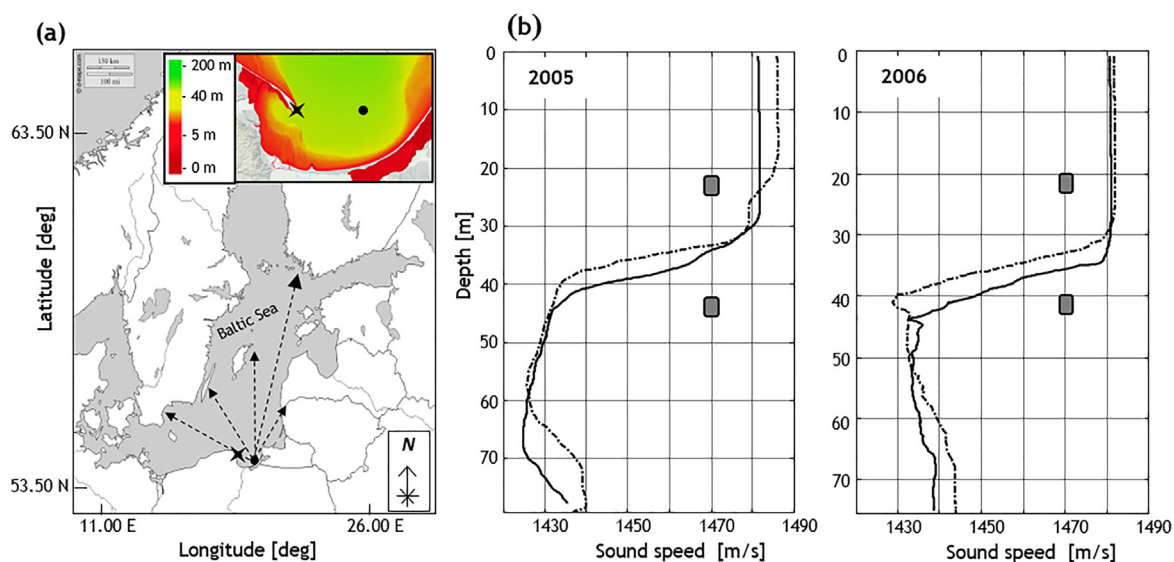


Figure 1 (a) Map of the study site. The measurement point is marked by a black dot, the land weather station is marked by a star and the arrows indicate the highest fetch length values depending on the direction. The enlarged section of a map contains bathymetric data (<https://emodnet.ec.europa.eu/>) marked by colour. (b) Sound speed depth profiles were obtained in 2005 and 2006 at the beginning (dotted line) and at the end (solid line) of each measurement campaign. The depth of the hydrophones is marked by grey rectangles.

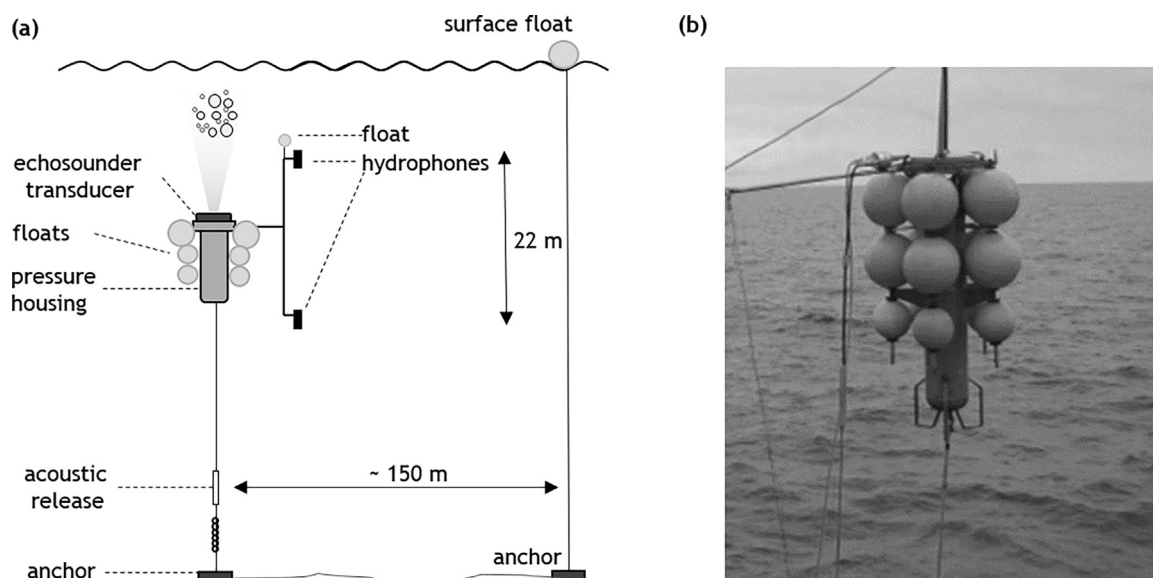


Figure 2 Measurement scheme (a) and a photograph of the hydroacoustic buoy just before deployment (b).

The active module was represented by Inverted Echo Sounder (IES), operated at 130 kHz frequency, mounted externally on the top side of the buoy. Hydrophones and echosounder were developed in cooperation between the Institute of Oceanology Polish Academy of Sciences and the Gdansk University of Technology.

The pressure sensor (ADZ-SML 20.0) calibrated by the manufacturer was capable of measuring pressure in the range of 0.06 to 6.00 MPa. Raw hydroacoustic data and pressure data were stored internally on a standard PC hard drive installed in the buoy.

The buoy was moored with an anchor and an acoustic release attached to the bottom of the pressure housing.

To facilitate locating the buoy after measurements, a second anchor with a surface float was used (Figure 2a). Deployments and recoveries were carried out from the r/v *Oceania*, which was anchored about a mile and a half from the buoy mooring during measurements. The buoyancy of the buoy and its stability were adjusted using 15 plastic spherical floats attached to the pressure cylinder. The total buoyancy of the system was approximately 135 liters and its total weight was 120 kg. The top part of the buoy, together with the face of the echosounder transducer, was submerged at a depth of approximately 37 m. The photograph of the buoy just before deployment is presented in Figure 2b.

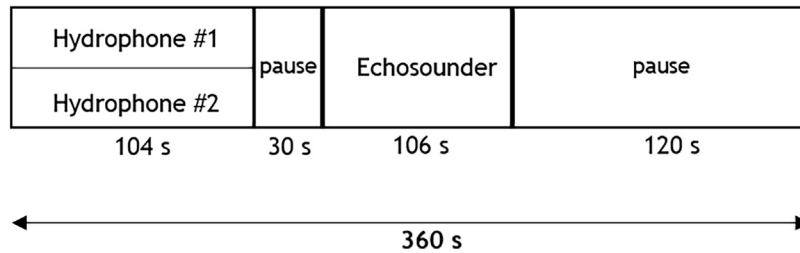


Figure 3 Diagram of the recording cycle.

2.2.2. Hydrophones

The custom-made hydrophones were calibrated in the laboratory and under in situ conditions with the Bruel & Kjaer 8104 hydrophone as a reference device. Both hydrophones, used in the measurements, are omnidirectional in the 350–14 000 Hz frequency range. The hydrophones were equipped with preamplifiers and high-pass filters (roll-off below 300 Hz) to reduce signal saturation due to low-frequency ship noise and hydrodynamic pressure from surface waves. Additionally, a low-pass filter was employed to prevent aliasing from high-frequency noise components. Signals were sampled by a 16-bit Analog-to-Digital converter with a sampling frequency of 32051 Hz and were stored on a hard drive.

In the paper, we focus on the underwater noise originating from the breaking of surface waves. Due to the layer structure of the seawater, surface-generated noise is most pronounced in the first top layer. A mid-water layer serves as an acoustic waveguide that captures both surface-generated noise and distant shipping sounds (Klusek and Lisimenka, 2016). Therefore, we analyze only the noise data recorded by the upper hydrophone located above the thermocline, in the subsurface top water layer.

2.2.3. Echosounder

The IES device was directed upward to measure backscattered echo from the surface and subsurface gas bubbles. Its –3 dB beam width was 7 degrees. The pulse length was 0.5 ms, which provided an echosounder vertical resolution of 0.37 m. The IES transmitted 2 pulses per 1 s. The backscattered signals were amplified with the time-varied gain function (TVG) to compensate for geometric spread and absorption losses. Their echo envelopes were then digitized with the frequency of 6 kHz with 10-bit resolution and stored on the hard drive. The echosounder was calibrated using the standard sphere method (Foote et al., 1987).

For the operating frequency of 130 kHz, the radius of the gas bubble that resonates at this frequency depends on its depth and varies over the range from about 25 μm at the sea surface to about 35 μm at 10-m depth (the greatest depth at which the bubbles were observed during the measurements).

2.2.4. Recording schedule

Acoustic data were recorded in 6-minute cycles as depicted in Figure 3. The cycle started with the work of the passive module. The noise was recorded by two hydrophones simultaneously for 104 s. After a 30-s pause the echosounder was working for a 106 s, transmitting a set of 128 pulses and registering backscattered signals. The cycle was ended by a 120-s pause.

2.3. Accompanied measurements

2.3.1. Environmental parameters

Environmental parameters were measured from the r/v *Oceania*. Data on wind speed and direction, air temperature and humidity were collected by the *Vaisala WXT510* weather station mounted on the ship’s bow. Measurements were performed from 1 to 4 times per minute. Weather station data were averaged in 6-minute intervals (corresponding to the acoustic measurement cycle) to enable comparison with hydroacoustic data. Averaging was performed using Circular Statistics Toolbox for MATLAB, based on formulas given by (Fisher, 1995).

The apparent values of the wind measured by the weather station were transformed into true values, using information about the speed and heading of the ship. Although the ship was anchored, it was yawing at a small speed of order of 0.1 m/s. In practice, the true values of the wind speed were the same as the apparent, unlike the true wind direction, which differed from the apparent one. In 2005, information about the heading of the ship was not logged (for technical reasons) and the wind direction was obtained from the closest land weather station of the Institute of Meteorology and Water Management (IMGW-PIB), located at Hel (54.6036°N, 18.8119°E), about 35 km west of the measurement site.

To check that the wind data from the land weather station is a decent approximation of the data recorded on the ship near the measurement site, we compared 2006 datasets: the true wind direction data collected on the ship and the data recorded by the land weather station. The mean difference between sea and land-measured wind direction is about 23°.

Before each deployment and recovery of the buoy, the temperature and salinity profiles were measured using a Valeport 606+ CTD profiler. The sound speed vertical profile was further calculated using the formula proposed by Chen and Millero (1977).

2.3.2. Wave model data

For the purpose of our analysis, we used wave model data from the Copernicus Marine Environment Monitoring Service’s (CMEMS) hindcast product BALTIC-SEA_REANALYSIS_WAV_003_015 (Baltic Sea Wave Hindcast, n.d.) available in the Copernicus Marine Service. The simulation was made and compiled using the wave model WAM (cycle 4.6.2) adopted to the Baltic Sea. The atmospheric forcing for the model is obtained from the European Centre for Medium-Range Weather Forecasts Reanalysis v5

(ECMWF's ERA5). The product is characterized by a spatial resolution of 1 nautical mile and a temporal resolution of 1 hour.

From the model we acquired the following wave parameters:

- significant wave height H_{sig} , (name of the variable in the model: spectral significant wave height) – defined as the average of the highest one-third of wave heights which in terms of spectral analysis is based on and comparable to zeroth spectral moment,
- wind wave height H_{ww} (name of the variable in the model: spectral significant wind wave height) is a spectral component referring to local wind-generated waves,
- swell wave height H_{sw} (name of the variable in the model: spectral significant primary swell wave height) is a spectral component referring to distant generated swell waves,
- wave period T_p (name of the variable in the model: wave period at spectral peak).

The use of each component of the wave field height (H_{sig} , H_{ww} , and H_{sw}) instead of only H_{sig} , should help us investigate their individual influence on the acoustic parameters. To increase the temporal resolution of modelled data linear interpolation was used. For hourly data, the interpolated values at 30-minute intervals were obtained by averaging the values of consecutive data points.

To describe the interaction between a wave field and the atmosphere we used a dimensionless parameter wave age W_a , defined as the ratio between wave phase velocity c_p and 10 m wind speed U_{10} :

$$W_a = \frac{c_p}{U_{10}} \quad (2)$$

where the wave phase velocity was obtained from the wave period T_p and gravitational acceleration g , by using the equation $c_p = gT_p(2\pi)^{-1}$. U_{10} was obtained from the wind speed measured on the ship. The parameter can be used to determine the dominance of swell waves over the wind waves in a particular wave field. According to the Pierson and Moskowitz spectrum, the wave age parameter allows the characterization of the sea state development as wind sea-dominated if $c_p/U_{10} < 1.2$, or as swell sea-dominated if $c_p/U_{10} > 1.2$ (Pierson and Moskowitz, 1964).

To assess wave breaking probability we used significant spectral peak steepness of the local wind sea (Banner et al., 2000), defined as:

$$\varepsilon = \frac{H_{ww}k_p}{2} \quad (3)$$

where H_{ww} is the wind wave height and k_p is the spectral wave number obtained from $k_p = 4\pi^2(gT_p^2)^{-1}$. The definition differs slightly from originally proposed by the authors (eq. 4.1 in Banner et al., 2000) but in principle, it fulfils the same conditions – reduction of the influence of background swell. In the further part of the text, we will use the term “wind sea steepness” to refer to the parameter ε , in order to emphasize that this parameter is related to the steepness of the wind wave field and not to the steepness of an individual wave.

2.4. Data analysis

The noise and backscatter data were processed in MATLAB with custom-written scripts.

2.4.1. Preprocessing

The noise records were first inspected for the presence of unwanted sounds such as shipping noise and precipitation. Contaminated noise records were identified and together with the corresponding echosounder data were excluded from further analysis. More details on noise preprocessing can be found in Klusek and Lisimenka (2016).

During the echogram overview, we noticed some corrupted backscatter profiles with anomalously higher energy than the proper backscatter echo signals. To address this issue, the 128-ping blocks of backscatter data were divided into 8-ping subsets. We identified and removed corrupted pings within each subset, finding no more than 4 incorrect pings in each. Next, the correct backscatter profiles were averaged within a single subset (averaging time – 4 s) and these data were used in further analysis. Due to the properties of the applied TVG, it was impossible to make an accurate conversion of an echo amplitude to backscattered strength (S_v), therefore the depth profiles of backscatter signals are presented in squared volts V^2 (linear scale) or dB re $1 V^2$ (logarithmic scale).

2.4.2. Computation of noise spectra

Each noise record was divided into 0.5-s nonoverlapping segments, the noise spectra were then computed using the FFT algorithm and averaged to obtain the mean noise spectrum. Subsequently, the mean noise spectrum level in one-third octave bands was calculated according to the equation:

$$NSL(f) = 10\log_{10} \frac{2 \int_{f_{min}}^{f_{max}} |S(f)|^2 df}{f_{max} - f_{min}} \quad (4)$$

where $NSL(f)$ is the noise spectrum level (dB re $1 \mu Pa^2 Hz^{-1}$) in the frequency band from f_{min} to f_{max} , f is the central frequency of the band, $S(f)$ is the one-sided noise spectrum based on the Fourier transform (of the time series converted to the acoustic pressure) (Ballou, 2013). Central frequencies f of the bands ranged from 350 to 12500 Hz.

2.4.3. Sea surface identification methods

As an initial step in processing IES data, we determined the distance from the echo sounder face to the sea surface h , crucial for accurately estimating the depth of bubble entrainment. The simplest technique to extract the sea surface location on the echogram, involves the use of an amplitude threshold. This method, however, only works adequately when the bubble density is low and the interface is clearly distinguishable on the echogram (Strand et al., 2020; Zedel, 1994). Previous research by Vagle and Farmer (1998) and Trevorrow (2003) reported difficulties in identifying the air-sea interface in case of high bubble densities.

Under high wind speed conditions, with dense bubble clouds present below the sea surface, the relatively high gain and limited dynamic range of the echosounder can lead to signal saturation in the bubbly layer before reaching the sea surface. As a consequence, the section of the echogram

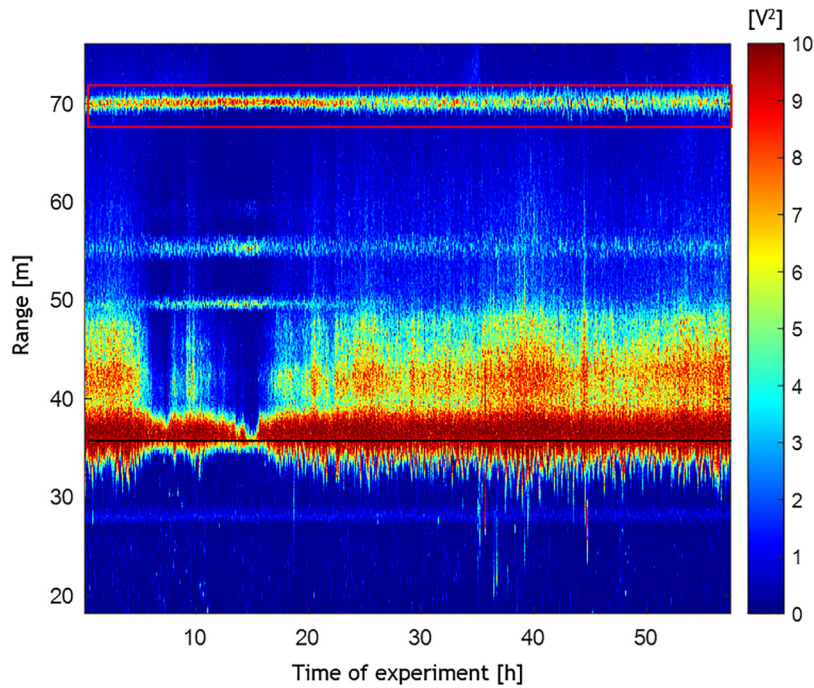


Figure 4 Echogram showing the method of sea surface determination based on the second reflection from the sea surface. The red rectangle marks the area of the second reflection and the black line corresponds to the sea surface obtained based on the second surface reflection, h . The colour scale is related to backscatter intensity (linear scale, squared volts [V^2]).

where we expected to find the highest echo signal value became broadened.

We applied the air-sea interface identification technique for high bubble densities proposed by [Trevorrow \(2003\)](#) and by [Gemmrich \(2010\)](#), but these methods did not yield satisfactory results with our data. Due to that, we proposed and implemented our own two-step method.

2.4.3.1. First step. In order to correctly interpret the echogram and facilitate the identification of the sea surface in areas of high backscatter, we utilized data from the pressure sensor and conducted an in-depth analysis of the echogram.

The time series of the hydrostatic pressure was analyzed, and the distance from the echosounder transducer to the sea surface h_p was estimated using the equation:

$$h_p = \frac{P_h - P_a}{\rho g} \quad (5)$$

where P_h – measured hydrostatic pressure, P_a – atmospheric pressure, ρ – water density and g is gravitational acceleration.

We assumed that the density of the medium was equal to the density of water. However, during wave breaking, bubble clouds create a two-phase mixture. The average density of the mixture is lower than that of pure water. Therefore, the obtained values of h_p are underestimated with regard to the true distance to the sea surface. Despite this, it still allows us to estimate the minimum range from the IES to the sea surface. In the previous work ([Dragan et al., 2010](#)), surface detection was completed at this point. In this study, we significantly enhanced the surface detection method, improving the accuracy of bubble entrainment depth estimations.

2.4.3.2. Second step. Accounting for the results of the first step, we conducted a careful examination of the echogram to improve the evaluation of the range from the echosounder face to the sea surface.

At a depth corresponding to approximately $2h_p$ ([Eq. \(5\)](#)), a pronounced local maximum in echoes was observed on the echogram (marked by a red rectangle in [Figure 4](#)). It was interpreted as a second reflection from the sea surface: the sound pulse emitted by the echosounder travelled to the sea surface and back to the transducer twice. Due to sound attenuation in water and bubbly layer, the signal amplitude corresponding to the second reflection was lower and owing to that – not clipped. We exploited this to determine the double distance from the echosounder to the sea surface. By focusing on the part of the echogram depicting the second reflection, the numerical gradient of each depth profile was calculated. Its first maximum was found and regarded as a double distance to the sea surface. The range from the transducer face to the sea surface, h_p (red line in [Figure 4](#)) was determined by halving this double distance.

The reliability of the applied method was verified by analyzing data recorded during low wind speed conditions, during which there were almost no gas bubbles near the air-water boundary. In the echogram, this is reflected as a narrower section of the maximum signal amplitude. The detailed inspection indicated that the sea surface identified using the second surface reflection, for most of the pulses corresponded to the maximum backscatter value in the depth profiles.

2.4.4. Estimation of bubble depth

In the next step, we remapped the echogram to a wave-following coordinate system ([Wang et al., 2016](#)). The new

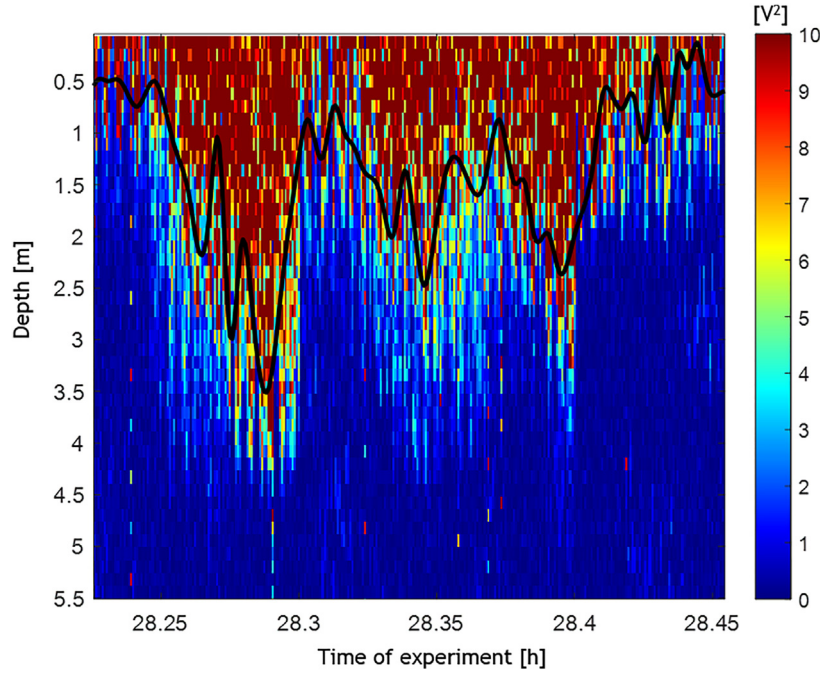


Figure 5 The echogram in a wave-following coordinate system. The vertical depth axis shows the distance from the sea surface downwards. The colour scale is related to backscatter intensity (linear scale, $[V^2]$). The black curve denotes the bubble entrainment depth obtained from the Otsu method.

echogram consists of depth profiles that have been truncated at the identified value of the sea surface h_p – [Figure 5](#). The depth axis is pointed downward from the sea surface, and the change of the bubble entrainment depth in time can be easily followed.

To determine bubble depth, we employed Otsu’s method ([Otsu, 1979](#)), widely utilized in image processing to perform automatic image thresholding. The outcome of the method is a threshold value that separates image pixels into two classes: foreground and background. It is accomplished by iterating through all the possible threshold values and calculating the variance of the values on each side of the threshold. The aim is to find the threshold value where the sum of foreground and background variance is at its minimum.

The implementation of the Otsu’s method in obtaining bubble entrainment depth values was as follows. The analysis was performed on non-averaged echograms – each data subset consisted of 128-backscattering depth profiles (related to a single measurement cycle) excluding corrupted ones, see [Section 2.4.1](#). For each depth profile, a 256-bin histogram of backscatter intensity was created and analyzed with the Otsu’s algorithm. As a result, we obtained a threshold value (varying in each depth profile), that indicated the boundary between backscatter values assigned to bubbles (foreground) and values assigned to the water column (background). Then, starting from the first sample of each depth profile and going down, we found the first sample with a value lower than the threshold. The preceding sample constituted the boundary between the subsurface bubbles and the water column and was assumed to be a bubble entrainment depth. To smooth the obtained boundary, the lower peak envelope was determined using spline interpolation over local maxima ([Figure 5](#), black curve).

To relate bubble entrainment depth to other measured parameters, its values were averaged over 6-minute periods. The obtained averaged values D_b , do not reflect the greatest depths to which bubbles were advected, and this information is essential and should be included in the analysis of bubble depth. Therefore, we decided to represent it by a value calculated as an average of 5% of the highest values falling into a singular averaging range (6-minute period), and denote it as D_{bMAX} . [Figure 6](#) shows an excerpt of the echogram with the red curve corresponding to the determined bubble entrainment depth, average bubble depth D_b (squares on a dashed line), and maximum bubble entrainment depth D_{bMAX} (asterisks on a dashed line).

3. Results

3.1. Time series of hydroacoustic, meteorological and wave data

[Figure 7](#) illustrates the time series of the analyzed variables. The wind speed U_{10} (plots (a) and (e), blue curve) and ambient noise level in 400–12500 Hz range, NL , (plots (a) and (e), orange curve) were measured. Average bubble entrainment depth D_b (blue curve, plots (b) and (f)) and maximum bubble entrainment depth, D_{bMAX} (orange curve, plots (b) and (f)), were estimated based on the echosounder backscatter depth profiles (see [Section 2.4.4](#)). Significant wave height H_{sig} (black dashed curve) and its components: wind waves height H_{ww} (blue curve) and primary swell waves height H_{sw} (orange curve) – plots (c) and (g), were obtained from Baltic Sea Wave Hindcast (see [Section 2.3.2](#)). Wave age W_a (plots (d) and (h)) was calculated from [Eq. \(2\)](#).

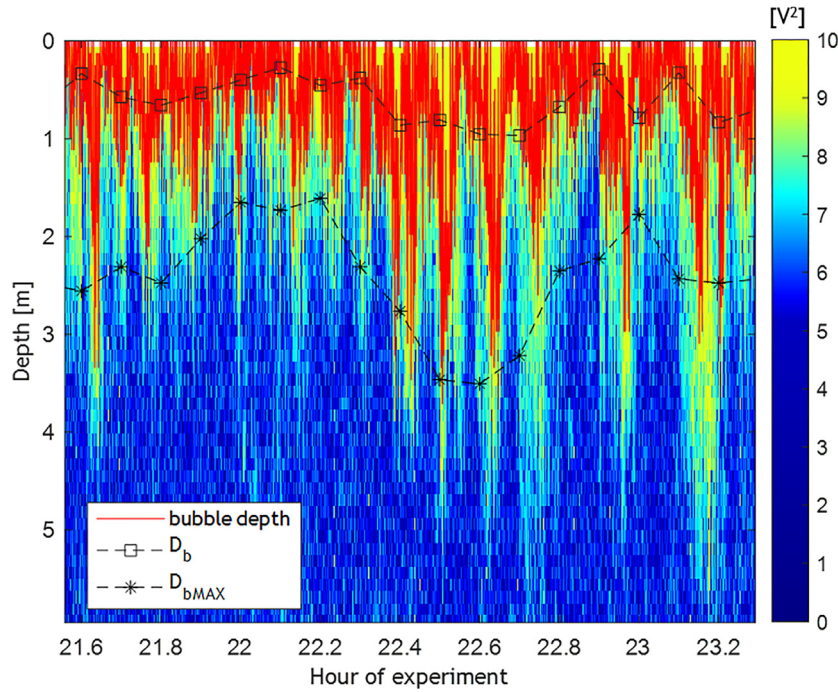


Figure 6 Excerpt from the echogram (corresponds to 2006 dataset) with plotted bubble entrainment depth obtained with Otsu’s method (solid red line), average bubble depth D_b (dashed line with square markers), and maximum bubble entrainment depth D_{bMAX} (dashed line with asterisks). The colour scale is related to the backscatter intensity (linear scale, $[V^2]$).

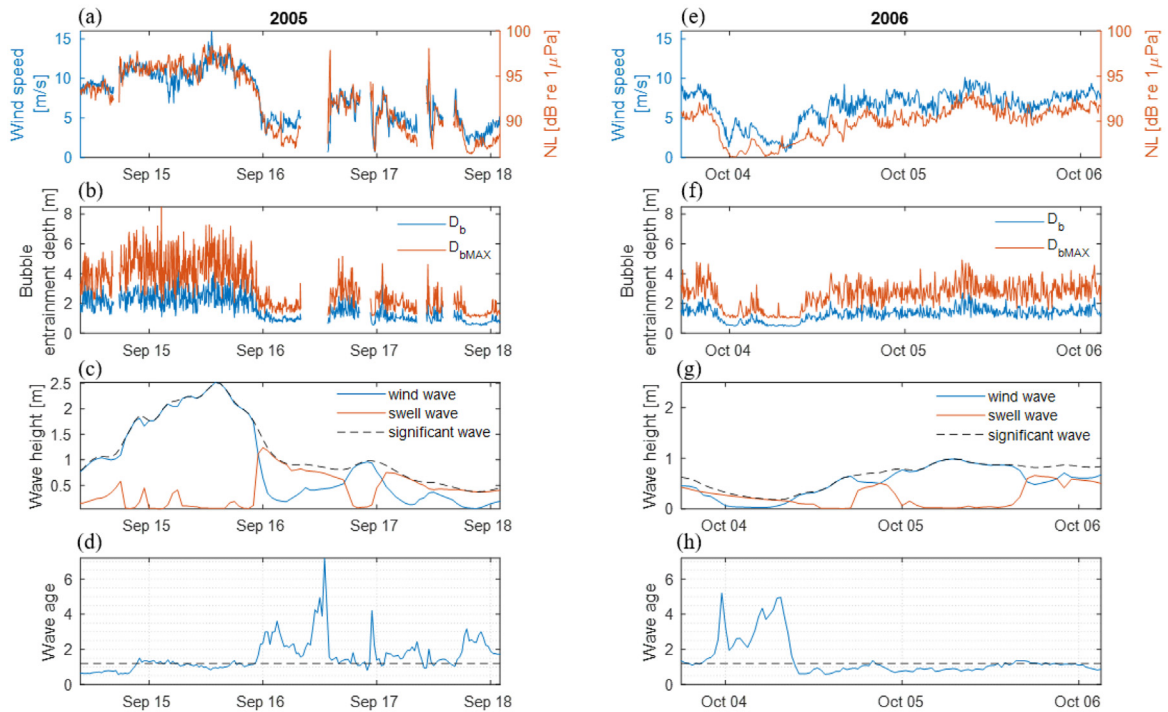


Figure 7 Time series of September 2005 (left panel) and October 2006 (right panel) data. Plots (a) and (e) show wind speed U_{10} (left axis, blue colour) and ambient noise level NL (right axis, orange colour). Plots (b) and (f) demonstrate average bubble entrainment depth D_b (blue colour) and maximum bubble entrainment depth, D_{bMAX} (orange colour). Significant wave height H_{sig} (black dashed curve) and its components: wind waves height H_{ww} (blue curve) and swell waves height H_{sw} (orange curve) are presented in plots (c) and (g), and wave age, W_a – plots (d) and (h), where dashed horizontal lines indicate the value of $W_a = 1.2$ – the boundary between the sea state dominated by wind sea and dominated by swell sea.

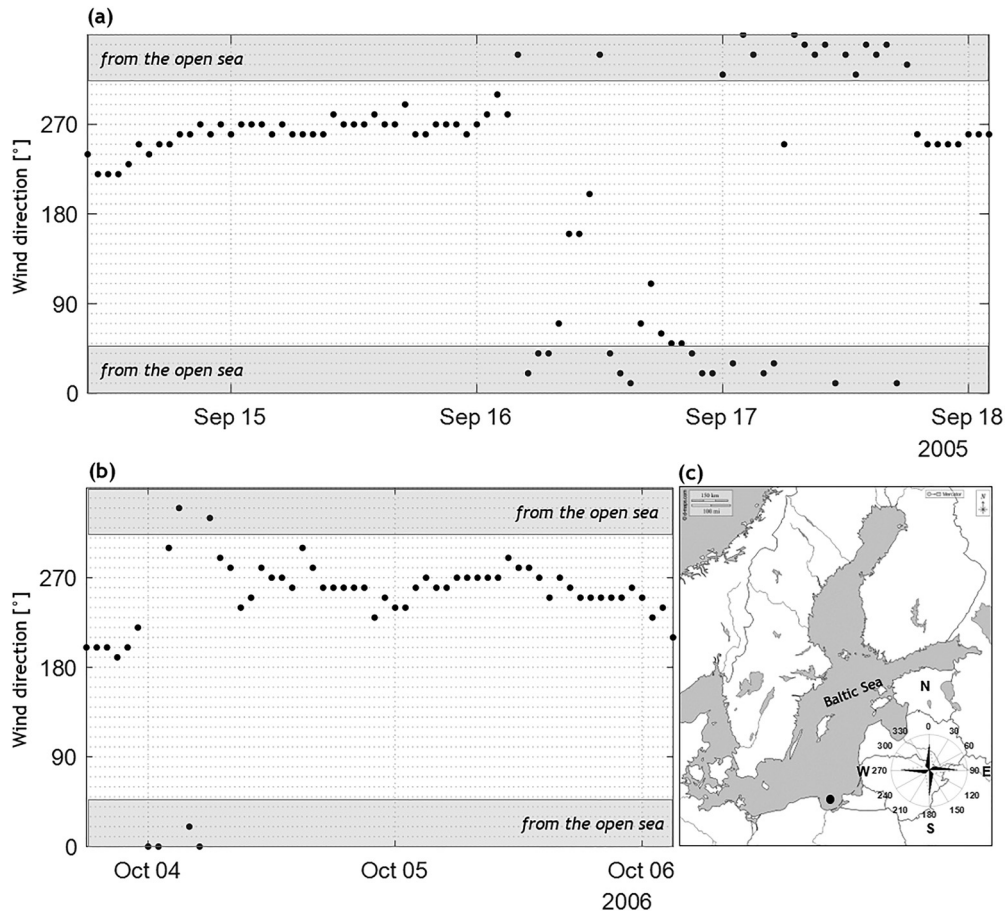


Figure 8 Wind directions – plots (a) and (b). Grey shading on plots (a) and (b) relate to wind from the northeast sector (from the open sea). Plot (c) shows a map with a wind rose and the measurement site marked by a dot.

The data shown on plots (a), (b), (e) and (f) are presented with a 6-minute time resolution, corresponding to a single measuring cycle. Data on plots (c), (d), (g), (h) are presented in 30-minute intervals, aligning with the time resolution of the used wave model. Gaps in the plots of the 2005 time series are due to the exclusion of contaminated data during the data preprocessing (see Section 2.4.1).

The two measurement campaigns differed in the range of particular parameters. In 2005, the wind speed ranged from 1 to approximately 15 m/s (plot (a), blue curve), while in 2006, the wind speed did not exceed 10 m/s (plot (e), blue curve). The corresponding time series of ambient noise levels had an approximate dynamic range of 10 dB in 2005 (plot (a), orange curve) and 5 dB in 2006 (plot (e), orange curve).

In 2005, the average bubble entrainment depth D_b ranged between 0.5 m and 5.0 m and maximum values of D_{bMAX} reached a value of 8.5 m. In 2006, variability of D_b was almost two times lower than in 2005 (up to 2.7 m) and D_{bMAX} reached a value of 5.0 m.

In general, for each year, the variability trends of measured and estimated time series of: U_{10} , NL and D_b and D_{bMAX} appear to be strictly correlated (Figure 7a,b,e,f). However, as is shown in plots (c) and (g), the modelled wind wave height (both H_{ww} and H_{sig}) does not precisely align with the changes of the aforementioned parameters.

Figure 7c demonstrates the complex relationship between the height of the wind wave, swell wave, and their

resultant – significant wave height in 2005. From the onset of measurements until September 16, H_{sig} was almost equal to H_{ww} and the accompanying swell waves were low. The progressive increase of the significant wave height in that period was likely attributed to the moderate and consistently increasing wind speeds that persisted for over first 24 hours of measurements. The decrease in wind speed around midnight on September 16 led to a decrease in the height of the wind waves, while waves associated with the swell were still present which resulted in the value of $H_{sig} \sim 1$ m. In the latter part of the observations, the height of the wind waves did not exceed 1 m, with the intermittent presence of the swell waves.

During 2006 measurements, the situation remained more stable, with the wind wave height of less than 1 m. Low swell wave was present occasionally and was not higher than 0.66 m.

In 2005, during the initial period of measurements (until September 16), the waves were classified as young ($W_a < 1.2$), subsequently transitioning to the developed. Meanwhile, in 2006, apart from a period of approximately 8 hours starting on October 4, the wave field predominantly exhibited characteristics of a developing wind wave system.

Figure 8 illustrates the wind direction observed during the 2005 (plot (a)) and 2006 (plot (b)) measurements, along with a map of the Baltic Sea, including the wind rose (plot (c)). Both years were dominated by the winds from the

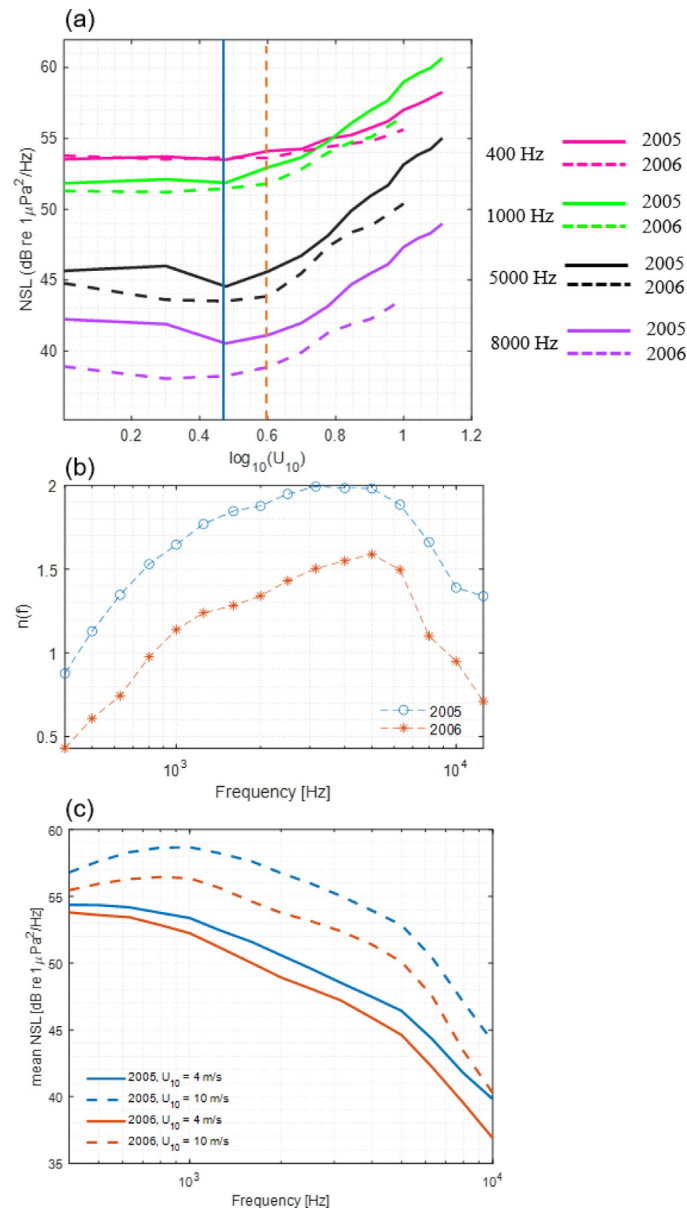


Figure 9 (a) Noise spectrum level $NSL(f)$ in selected one-third octave bands obtained in 2005 (solid lines) and 2006 (dashed lines), plotted against the logarithm of the wind speed (U_{10}), U_{10} is in [m/s]; central frequencies of particular bands are specified in the legend; (b) frequency dependence of the coefficient $n(f)$ from Eq. (1) for – 2005 (blue circles) and 2006 (orange asterisks); (c) mean noise spectrum level determined by averaging all noise spectra levels falling within wind speed bins of 1 m/s width. The curves labelled as 4 m/s (solid lines) and 10 m/s (dashed lines), correspond to the data obtained at wind speeds ranging from 3 to 4 m/s, and from 9 to 10 m/s, respectively. Data collected in 2005 are represented by the blue colour and data collected in 2006 are represented by the orange colour.

southwest sector (from the land), which is typical for this period of the year in the Gulf of Gdansk (Herman, 2022). The grey shading on the plots highlights the range of directions associated with wind from the northeast sector (from the open sea). Such winds were observed for 33% of the study period in 2005 and 10% in 2006.

3.2. Relationship between noise spectrum level and the wind speed

Noise spectrum levels $NSL(f)$ in selected one-third octave bands with central frequencies 400, 1000, 5000 and 8000 Hz,

are plotted against the logarithm of the wind speed U_{10} in Figure 9a. Solid lines represent 2005 data, dashed lines – 2006 data. Colours correspond to frequency bands described in the legend.

Figure 9a reveals the existence of two regimes differing in the dependence of the $NSL(f)$ on the wind speed. The boundary between these regimes is shown by a vertical line – solid blue for 2005 data and dashed orange for 2006 data. It corresponds to 3 m/s and 4 m/s for the years 2005 and 2006, respectively. In both years, for lower wind speeds (to the left from the vertical lines), the $NSL(f)$ was fairly constant within this wind speed range. However, the

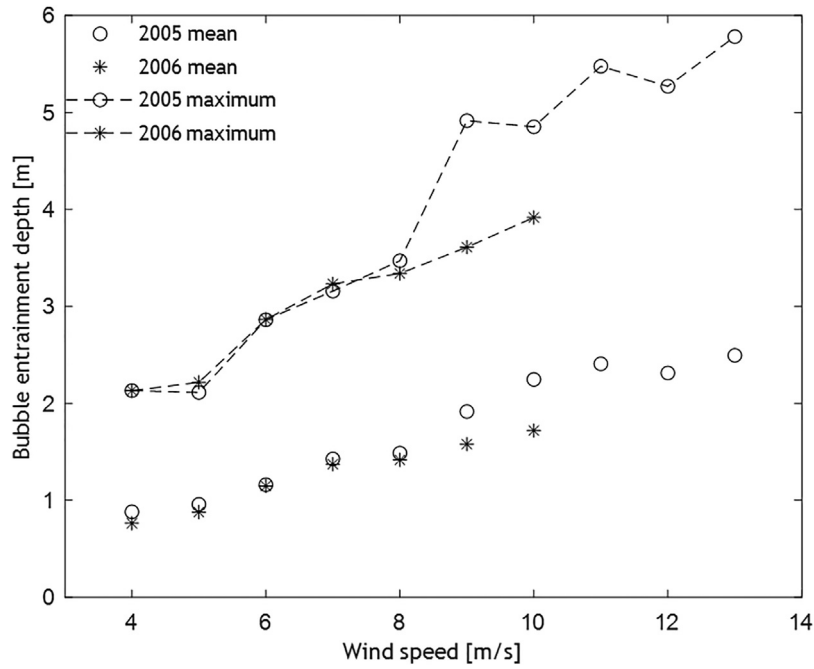


Figure 10 Average bubble entrainment depth (circles and asterisks) and maximum bubble entrainment depth (circles and asterisks on dashed lines) obtained in 1 m/s wind speed bins in 2005 (circles) and 2006 (asterisks).

$NSL(f)$ values were higher in 2005 compared to the corresponding values in 2006. The difference between the measurement years becomes more pronounced as the frequency increases. As we focus on processes related to and dependent on wind speed, and since the noise spectrum level below the threshold is wind-independent, further in the paper we consider only data corresponding to $U_{10} \geq 4$ m/s.

For higher wind speeds (to the right of the vertical lines in plot (a)), $NSL(f)$ increased with wind speed and was higher in 2005 (solid lines for 2005 data overlap with dashed lines for 2006 data). The rate of increase of the noise level represented by the coefficient $n(f)$, Eq. (1), is frequency dependent (Figure 9b). The maximum values of $n(f)$ are in the mid-frequency range, starting from $f = 2500$ Hz in 2005 and $f = 3150$ Hz in 2006, and extending up to $f = 5000$ Hz in both years. The $n(f)$ values were generally higher in 2005 by 0.4 to 0.64 in comparison to 2006 data.

The variability of $n(f)$ in the frequency domain implies that the energy contribution of individual noise bands to the total ambient noise level was changing with wind speed. For instance, during calm winds, noise in the lowest frequency band ($f = 400$ Hz) had a more significant impact on the ambient noise compared to the higher frequency band ($f = 1000$ Hz). However, as the wind speed increased, this relationship reversed, with the higher frequency band playing a more dominant role and contributing more to the overall noise level (Figure 9a). The change in the contribution resulted in the wind-dependent shape of the noise spectrum, as demonstrated in Figure 9c. The figure shows mean noise spectrum levels determined by averaging all noise spectra levels falling within wind speed bins of 1 m/s width. The averaging was conducted on a linear scale, not logarithmic. The curves, labelled as 4 m/s (solid lines) and 10 m/s (dashed lines), correspond to the data obtained at

wind speeds ranging from 3 to 4 m/s and from 9 to 10 m/s, respectively. The mean noise spectrum level in both wind speed bins is in general higher in 2005 than in 2006. At 4 m/s, the difference in mean noise spectrum level between years depended on frequency and was on average 1.5 dB, while at 10 m/s the difference reached 3.0 dB. The mean noise spectrum level slope within the frequency range of 1000 – 5000 Hz remained constant, with -3.0 dB/octave at a wind speed of 4 m/s and -2.5 dB/octave at a wind speed of 10 m/s, regardless of the measurement year.

To determine in which frequency band noise followed changes in wind speed the most, Pearson's correlation coefficient of $NSL(f)$ and $\log_{10}(U_{10})$ time series was calculated. In 2005, the correlation between noise spectrum level and wind speed was almost frequency-independent, with correlation coefficients oscillating around 0.9. Data from the following year show lower and more variable values of correlation coefficients. In 2006, the highest values ($R = 0.78$) were obtained in the central frequency range from 800 Hz to 1600 Hz and the lowest value occurred at $f = 12000$ Hz ($R = 0.67$).

Among these frequencies, the $NSL(f)$ at $f = 1250$ Hz demonstrated the strongest correlation with wind speed in both studied periods. Thus, we further examined the dependence of the noise spectrum level on wind speed specifically at this frequency. Using the regression method the best-fit curves were obtained. Slopes of the curves are $n(1250 \text{ Hz}) = 1.77$ for 2005 and $n(1250 \text{ Hz}) = 1.24$ for 2006, indicating that the dependence of the $NSL(1250 \text{ Hz})$ on the U_{10} is:

$$NSL(1250 \text{ Hz}) = 10 \cdot 1.77 \cdot \log_{10} U_{10} + 40.69, \text{ for 2005} \quad (6a)$$

$$NSL(1250 \text{ Hz}) = 10 \cdot 1.24 \cdot \log_{10} U_{10} + 43.33, \text{ for 2006} \quad (6b)$$

This results in 2.8 dB difference in $NSL(1250 \text{ Hz})$ between both years.

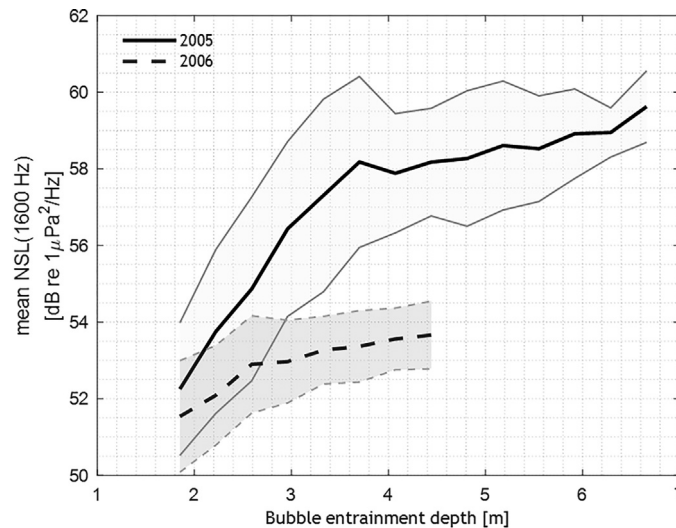


Figure 11 The mean noise spectrum level $NSL(1600\text{ Hz})$ calculated in bins of maximum bubble entrainment depth of 0.37 m bin width. Solid lines refer to 2005 data and dashed lines to 2006 data. The shaded area corresponds to the standard deviation.

3.3. Bubble entrainment depth at different wind speeds

The dependence of the average and maximum bubble entrainment depth on the wind speed is presented in Figure 10. Average and maximum values were calculated based on all the determined values of bubble entrainment depth (represented by the red curve in Figure 6): from each single 6-minute measurement cycle, 128 values of bubble entrainment depth and one value of the wind speed were obtained. The average and maximum values were calculated from non-overlapping wind speed bins of 1 m/s width. The 1 m/s bin width is small enough to display the relation between variables with appropriate accuracy, and large enough to contain a sufficient number of observations (it was not less than 22 observations within an individual bin) to compute an average value. The average bubble entrainment depth was determined by averaging values falling within particular wind speed bins. For instance, the bin labelled 10 m/s included data obtained at wind speeds ranging from 9 to 10 m/s. The maximum bubble entrainment depth values were calculated as the mean of 5% of the highest values within each bin.

In both years, the average D_b (circles and asterisks) and maximum D_{bMAX} (circles and asterisks on the dashed lines) values of the bubble entrainment depth increased with wind speed across the entire range. Up to the $U_{10} = 8$ m/s, both parameters exhibited a similar increase in wind speed in both years but above this wind speed, the differences became more significant. Specifically, at $U_{10} = 10$ m/s, the average bubble entrainment depth was by 0.53 m higher in 2005 than in 2006 and the maximum bubble entrainment depth was by 0.93 m higher in 2005 than in 2006.

At the highest wind speed common to both years, $U_{10} = 10$ m/s, bubbles were observed at a maximum depth of 4.85 m and 3.92 m in 2005 and 2006, respectively. Meanwhile, the average bubble entrainment depth was 2.25 m in 2005 and 1.72 m in the following year.

3.4. Bubble entrainment depth and underwater noise

To relate the underwater noise to bubble entrainment depth, we first calculated the Pearson correlation coefficients of D_b and D_{bMAX} with the noise spectrum level $NSL(f)$ at each central frequency.

In 2005, both D_b and D_{bMAX} were correlated equally well with $NSL(f)$ – the correlation coefficients ranged from 0.69 to 0.73 over the entire range of central frequencies. The maximum correlation coefficients between noise spectrum level and D_b were obtained for frequencies 800 Hz and 1000 Hz, while between noise spectrum level and D_{bMAX} , in the frequency range from 800 Hz to 1600 Hz.

In 2006, the correlation between bubble entrainment depth and $NSL(f)$ was weaker compared to 2005. The correlation coefficients for D_b ranged from 0.53 to 0.60 peaking at frequencies 1600, 5000 and 10000 Hz. The correlation coefficients were lower for D_{bMAX} (from 0.44 to 0.54), with the maximum value obtained at 1600 and 5000 Hz.

In order to establish the relationship between noise spectrum level and maximum bubble entrainment depth, the $NSL(f)$ values were averaged within maximum bubble entrainment depth bins. The bin width was selected to match the vertical resolution of the echosounder and was set to 0.37 m. Each bin contained a minimum of 10 data points. Prior to averaging, $NSL(f)$ was converted to pressure units, then averaged, and the resulting average value was logarithmically transformed. Figure 11 illustrates the relation between mean $NSL(f)$ at 1600 Hz and maximum bubble entrainment depth. The frequency 1600 Hz represents the central frequency of the one-third octave band which exhibited a strong correlation with the maximum bubble entrainment depth in both measurement periods.

In both years, the dependence of $NSL(1600\text{ Hz})$ on the maximum bubble entrainment depth can be divided into two distinct ranges, each exhibiting a different rate of increase in the mean noise spectrum level. In the range of smaller bubble entrainment depths, the $NSL(1600\text{ Hz})$ in-

creased at a faster rate compared to the greater entrainment depths.

The boundary between the two ranges was around 3.7 m, while in 2006 it was approximately 2.6 m. In the range of low D_{bMAX} , the $NSL(1600\text{ Hz})$ increased by 3 dB/m in 2005 and 1.5 dB/m in 2006. For greater D_{bMAX} , the increase was 0.5 dB/m in both years. The standard deviation was generally higher for the data from 2005 (1–2.5 dB re $1\mu\text{Pa}^2/\text{Hz}$) in comparison to the data collected in 2006 (0.75–1.5 dB re $1\mu\text{Pa}^2/\text{Hz}$).

4. Discussion

4.1. Factors influencing noise level

The generation of wind-driven noise depends on several factors, including wind speed and characteristics of the agitated sea surface, such as the height of breaking waves or the frequency of breaking events (Ding and Farmer, 1994; Felizardo and Melville, 1995; Means and Heitmeyer, 2002). The relationship between noise spectrum level and wind speed is presented in Section 3.2 and Figure 9a and will be further explored in Section 4.1.1. The influence of the wave field parameters on the noise level will be examined in Section 4.1.2.

4.1.1. Wind speed

It is widely recognized that the relationship between $NSL(f)$ and $\log_{10}U_{10}$ is linear (Equations (6a) and (6b)) at wind speed not exceeding 15 m/s. However, depending on the year of measurement, the noise level increased with the wind speed at different rates, as expressed by the $n(f)$ (Figure 9b). Several studies conducted in various reservoirs provided values of $n(f)$ in the range 2–5 (Evans et al., 1984; Klusek, 1977; Klusek and Lisimenka, 2007; Lemon et al., 1984; Poikonen and Madekivi, 2010; Vagle et al., 1990; Vakkayil et al., 1996; Wille and Geyer, 1984). However, in most cases, the value is approximately 2. In the mentioned studies, the coefficients $n(f)$ were determined across various marine areas, each characterized by distinct sound propagation conditions, surface water temperature, presence of surfactants, etc. Consequently, a direct comparison of the $n(f)$ coefficients becomes challenging.

Our results show that the coefficient $n(f)$ changes with frequency in a similar way in both years, but its values are higher in 2005 than in 2006 across all frequencies. The maximum value of $n(f) = 2$ obtained in 2005 is consistent with most of the reported values. The maximum value of $n(f)$ obtained from the 2006 data is lower and is approximately 1.6, indicating that ambient noise level increased slower with the wind speed than in the previous year.

The studies concluded that the coefficient $n(f)$ depends on the measurement site, more precisely on the sound propagation conditions including e.g. vertical sound speed profile, water depth, bottom sediment type. On the other hand, the obtained difference in $n(f)$ between 2005 and 2006 could not result from the indicated factors as the measurements were carried out under approximately the same conditions.

One of the probable explanations for this lower rate of increase (in the 2006 dataset) is the presence of shipping

noise. In the data preprocessing stage, we removed the subsets of data where the presence of ship noise was evident. However, the detection of all unwanted sources of sound is not always feasible. Occurrence of ships effects in higher low-frequency noise levels at lower wind speed and thus less steep slope of $NSL - \log_{10}U_{10}$ relationship (lower $n(f)$).

4.1.2. Wave field parameters

The influence of the wave field parameters on the noise level (NL) can be investigated by analyzing Figure 12a–d. These figures present noise level data (NL) plotted against significant and wind wave height (H_{sig} and H_{ww}) – plot (b), wave age (W_a) – plot (c) and wind sea steepness (ε) – plot (d). The illustration is restricted to the wind speed range of 4–10 m/s. The lower limit determines the minimum wind speed at which individual waves may break. The upper limit, on the other hand, determines the maximum wind speed value from the range common to both measurement periods.

4.1.2.1. Relationship between the wind speed U_{10} and the noise level NL . Figure 12a confirms the linear relation between the NL and the logarithm of U_{10} , within the wind speed range of 4–10 m/s. The linear correlation coefficients for the 2005 and 2006 datasets are 0.88 and 0.77, respectively. The NL exhibited higher values in 2005 than in 2006 within the chosen wind speed range. This might suggest that additional factors, including those related to the wave field, may influence underwater noise generation. These factors will be considered below.

4.1.2.2. Impact of the significant wave height H_{sig} and wind wave height H_{ww} on the noise level NL . Figure 12b (left and right columns respectively) reveals that the noise level increases with significant wave height (H_{sig}) and wind wave height H_{ww} . The correlation coefficient between the NL and H_{sig} was 0.62 in 2005 and 0.75 in 2006. Meanwhile, the correlation coefficient for NL and H_{ww} was higher (0.84) in 2005 and lower (0.60) in 2006. It is worth noting that in 2005, the NL exhibited a stronger correlation with H_{ww} than with H_{sig} .

The lower correlation between NL and H_{sig} compared to the correlation of NL and H_{ww} may be attributed to a larger scatter of NL values with respect to H_{sig} (Figure 12b, left panel) than with respect to H_{ww} (Figure 12b, right panel). For instance, at H_{sig} approximately 1 m, the scatter of NL was around 6 dB, whereas such a large scatter was not observed for the NL vs. H_{ww} relationship.

To comprehend this pronounced scatter, it is important to remind that H_{sig} combines both the local wind-sea and distant swell-sea components of the wave field. During 2005, there were periods with a significant swell contribution to the values of H_{sig} (solid orange vs. dotted black curves in Figure 7c). The same value of H_{sig} may be due to various combinations of wind speed and wave field conditions. For instance, an H_{sig} of approximately 1 m was linked to two distinct time periods that displayed different relationships between wind speed and swell waves. The first period (during the first 8 hours of the 2005 measurements, refer to the left panel of the Figure 7) was distinguished by high wind speed $U_{10} = 10\text{ m/s}$ (Figure 7a) and low swell waves $H_{sw} \sim 0.25\text{ m}$. During the second one (the beginning of September 16, 2005) the wind speed was below 5 m/s, which is close to the threshold for wave breaking, and the swell wave height was around 1 m.

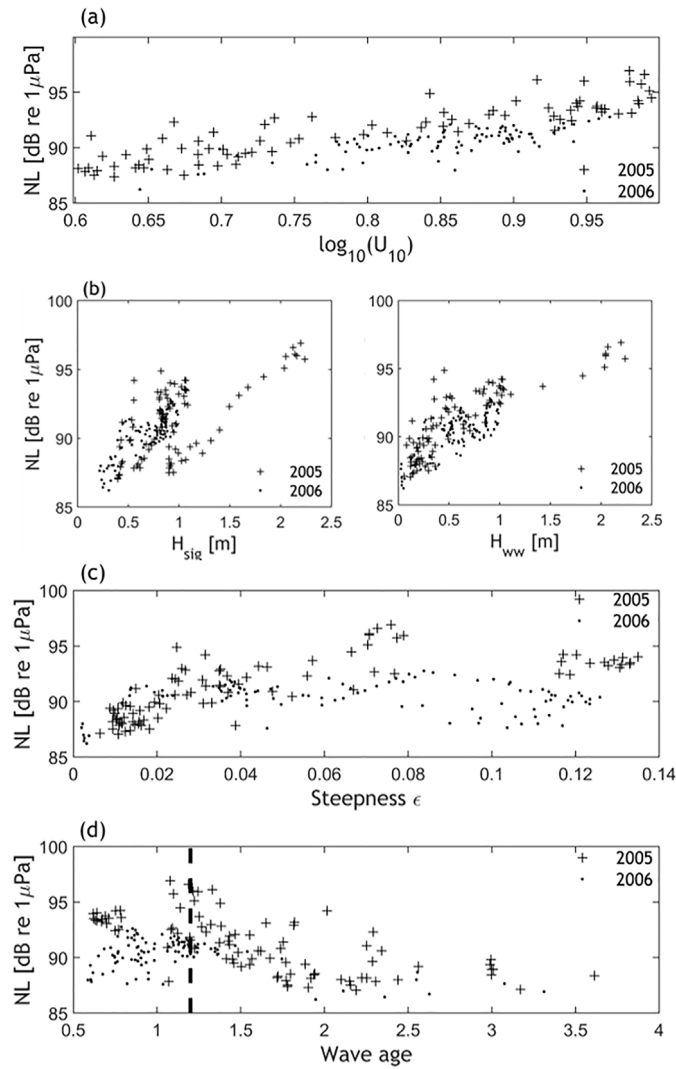


Figure 12 Noise level (NL) plotted against: the logarithm of the wind speed $\log(U_{10})$, U_{10} in [m/s] – plot (a), significant H_{sig} and wind H_{ww} wave height – plot (b), left and right panels respectively, wind sea steepness ϵ – plot (c) and wave age W_a – plot (d).

The two periods differed in NL values, with NL significantly higher in the first one than in the second period (see Figure 7a). Various wind speeds and swell wave conditions affecting the NL could explain the scatter in NL data and potentially weaken the correlation.

4.1.2.3. Impact of the wind sea steepness on the noise level NL . Figure 12c illustrates that NL increases with the wind sea steepness in 2005 ($R=0.68$) and that there is no such correlation in the 2006 dataset ($R = -0.14$). Banner et al. (2000) found that the probability of wave breaking increases close to quadratically for $\epsilon > 0.055$. This might result in a higher number of breaking waves and thus in higher noise level.

What is interesting, is that in 2005 dataset there are two distinct groups of data based on the range of ϵ . In the first subset of data (for ϵ ranging from 0.01 to 0.08), there is a noticeable increase in NL as the wind sea steepness increases. However, in the second group of data (for ϵ ranging from 0.12 to 0.14), the NL values are similar to the NL values observed under conditions when the wind sea steepness was

two times lower. Hence, it seems that the wind sea steepness is not the only factor affecting the noise level.

4.1.2.4. Impact of the wave age on the noise level NL . Figure 12d shows that in 2005 noise level was inversely proportional to the wave age ($R = -0.65$). The younger the waves ($W_a < 1.2$), the higher the probability of wave breaking, the larger possible number of breaking events, and the higher the noise level becomes. However, there is no such clear relation in 2006 ($R = -0.04$).

4.1.2.5. Reasons for the difference in NL between measurement periods. We aim to understand the difference in noise level between the two measurement periods, considering the aforementioned factors. Despite the relatively short duration of our measurements, we encountered a reasonably diverse range of wind and wave conditions that exhibited differences between the two measurement periods.

As it was demonstrated, the noise level increased linearly with the logarithm of wind speed and with wind wave height. Upon further examination of the U_{10} and H_{ww} (not shown here), differences between the two periods in both

parameters were revealed. Throughout the entire measurement period of 2005, 27% of the wind speed values exceeded 10 m/s and 38% of the H_{ww} values exceeded 1 m, while in 2006, such high values of both wind speed and wave height were not observed. Moreover, Figure 12b shows that in the wind speed range common to both measurement periods (4–10 m/s), wind wave height in 2005 was found to be even twice as high as in 2006. The higher values of U_{10} and H_{ww} observed in 2005 could have contributed to a higher noise level compared to 2006.

The noise level seems to be indirectly related to both the wave age and to the wind sea steepness. In the range of young waves ($W_a < 1.2$), there is no clear relation between NL and the W_a , especially for the data from 2006. For instance, the NL recorded in 2005, corresponding to W_a values in the range of 0.6–0.8 (Figure 12d), is associated with the beginning of the measurements, during which relatively high wind speeds ($U_{10} \sim 10$ m/s) and $H_{sig} \sim 1$ m were observed. For the same wave development stage, the corresponding NL values obtained in 2006 were lower, as both the wave height and the wind speed were lower during that period. This indicates that the difference in noise level is more influenced by the wave height and wind speed than by the wave age.

The lack of correlation between W_a and NL in 2006 may be attributed to the limited variability of wave field conditions during that period, as approximately 67% of all W_a were concentrated below $W_a = 1.2$, indicating the predominance of young waves (Figure 12d). In 2005, young wave field conditions were observed for 40% of the measurement period. Such distribution of values might have influenced the obtained correlations between NL and W_a .

The wind sea steepness (ε) was not a significant factor that could have influenced the difference in noise levels between the two periods. The range of ε was comparable in both years, since steep wave field ($\varepsilon > 0.055$) was observed for 45% of the time in 2005 and 50% in 2006.

We aim to take into consideration an additional factor – the wind direction. During 2005, the wind originated from the N to NE direction for approximately 35% of the time. At the location of measurements, this direction is associated with long fetch conditions. However, due to the short duration of the northerly wind and high variability in wind direction, such wind-wave conditions were rather insufficient for the development of long, energetic waves originating from the open sea. However, the wind conditions might have facilitated the approaching of swell waves from the north – which we observed, and a complex interaction with the local wind-wave system – which is out of our scope. Northerly winds appeared occasionally in the 2006 dataset, only when the wind speed was less than 5 m/s.

The variation in noise level between the years could have been influenced by a combination of specific wind and wave conditions prevailing during the measurements in 2005. During the first period of measurements (up to the end of September 15), the wind speed gradually increased, and the wind direction changed very slowly. As a result, the wave field became more developed and continued to be agitated even after the wind had ceased, making it more susceptible to wind action (Hwang, 2008). Consequently, in the second part of the measurements (from 15:00 of September 16 up to the end), the noise level recorded when wind wave height

spanned the range from 0.2 m to 1 m was regularly higher in 2005 than in 2006. The swell wave higher than 0.2 m was present for 91% of the period.

The influence of swell and its direction relative to the wind wave direction might have also played a role. During both measurement campaigns in the Baltic Sea, the difference in the direction of swell wave and wind wave was in the range 0–100 degrees. Further analysis of the dependence of particular wind, wave and acoustic parameters on the directional difference, revealed no obvious trends. The interaction between the swell wave system and the wind wave system is still not well understood. Field measurements (Hwang et al., 2011; Vincent et al., 2020) indicated that wind-wave generation is altered when the swell is present. Laboratory experiments (Chu et al., 1992; Donelan, 1987) revealed that when swell direction aligns with the wind wave direction, it reduces the growth of wind waves, while swell in the opposite direction intensifies their growth, potentially increasing the likelihood of wave breaking. Hwang (2008) found that in mixed seas, the swell has a complex effect on the wave spectrum, dependent on wave length. On the other hand, (Arduin et al., 2007) observed that in the ocean, moderate swell opposing the wind does not significantly affect wind wave growth.

Our data show that the highest influence on the noise level (and bubble depth) has wind speed (U_{10}) and wind wave height (H_{ww}). The wind sea steepness as well as the wave age influence the noise level but to a lower extent. The presence of swell modulates the growth of wind waves and thus affects the process of wave breaking. However, its exact effect remains unclear.

The obtained results confirm the need to consider not only wind speed but also fetch conditions in ambient noise estimated wind speed or in the assessment of processes occurring at the air-water boundary.

4.2. Factors influencing bubble entrainment depth

4.2.1. Wind speed

Wind speed affects not only noise level and shape of the noise spectrum but also bubble entrainment depth (Thorpe, 1992). Measurements by Wang et al. (2016) conducted at the site of 73 m water depth, have shown linear dependence between bubble depth and wind speed up to 10 m/s, and non-linear above this wind speed range. Their estimation of bubble depth was derived from backscatter profiles obtained with 208 kHz echosounder, and was based on the threshold value method. The acquired bubble depth corresponds to our maximum bubble entrainment depth (D_{bMAX}). The reported shape of the bubble depth – wind speed relation is in line with our results obtained in 2005, but the transition from linear to non-linear dependence occurs in our data at $U_{10} = 8$ m/s (Figure 10, circles on dashed line). The bubble depth-wind speed relationship obtained based on the 2006 data, is linear in an entire wind speed range (4–10 m/s), but it is not possible to verify if the relation changes at higher wind speeds, as suggested by Wang et al. (2016). Strand et al. (2020) used a 70-kHz echosounder to observe gas bubbles at over 250 m depth site. They reported a linear bubble depth-wind speed relation for wind speed ranging from 4 to 17 m/s, even though bubble depth was estimated in a similar way

as by Wang et al. (2016). The reason for the different forms of the relation might be associated with different sounding frequencies used in the mentioned studies. This might suggest that the parameters of gas bubble populations strongly depend on sound propagation conditions and the size of observed gas bubbles.

Crawford and Farmer (1987) in semi-enclosed, deep oceanic water (~ 1000 m), at $U_{10} = 10$ m/s, using an echosounder operating at 119 kHz, found bubbles at an average depth of 4–5 m and a maximum depth of 8 to 12 m. This is about two times deeper compared to our results (Figure 10). The authors suggest the possible impact of Langmuir circulation on the high value of bubbles depth and their spatial distribution. Wang et al. (2016) at the same wind speed ($U_{10} = 10$ m/s) in oceanic shallow waters (depth 73 m), observed bubbles penetrating the water column to about 7 m. Reported greater depths of bubbles are associated with site properties (e.g. salinity, sound speed profile) and wave field conditions.

4.2.2. Wave field parameters

It was expected to find a strong correlation between bubble entrainment depth and underwater noise level (correlation coefficients equal to 0.84 and 0.81 in 2005 and 2006, respectively), as gas bubbles are the primary factor in noise generation during wave breaking. Our focus concentrates on the relationship between D_b and U_{10} as the scatter plots depicting the bubble entrainment depth (D_b) and wave variables exhibit patterns similar to those observed for the ambient noise level (NL) and wave variables (Figure 12).

The results of our measurements indicate a strong correlation between the bubble entrainment depth and wind speed in both measurement periods. The linear correlation coefficients were 0.86 (2005) and 0.70 (2006). Within the wind speed range up to $U_{10} = 8$ m/s, the values of D_b in both years were comparable (Figure 13a). However, for higher U_{10} values - inside dashed rectangle in the Figure 13a, the bubble entrainment depth was generally greater in 2005 compared to 2006 (as indicated by crosses being above the dots). The relationships resemble those presented in Figure 10 (section Results), where average bubble entrainment depth was calculated within 1 m/s wind speed bins, based on the bubble entrainment depths obtained in 6-minute intervals. To enable a straightforward comparison of D_b acquired through measurements (at 6-minute intervals) with modelled data (at 30-minute intervals), the mean bubble depth in Figure 13 was calculated as a mean value from 30-minute intervals.

To interpret the aforementioned dependence, we employed the formula proposed by Graham et al. (2004), which links wave field parameter H_{sig} and wind-wave parameter W_a with bubble entrainment depth, D_b . The formula indicates that bubble entrainment depth is proportional to H_{sig}/W_a . Later in the text, we denote H_{sig}/W_a ratio as D . Figure 13b illustrates the dependence of the D calculated from the modelled data H_{sig} and W_a , on the wind speed – for 2005 (crosses) and 2006 (dots) conditions.

The dependence of the D on U_{10} reveals a similar feature as the D_b on U_{10} (Figure 13a). In both years, D is comparable within the wind speed range from 4 m/s to 8 m/s, while for higher U_{10} , D is higher in 2005 compared to 2006.

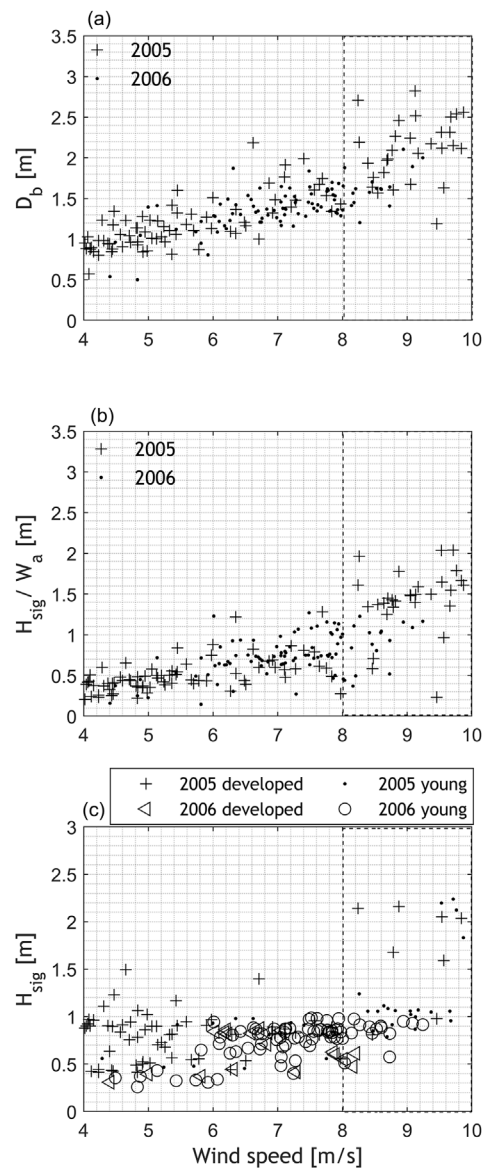


Figure 13 (a) D_b plotted against wind speed, (b) $D = H_{sig}/W_a$ plotted against wind speed. In plots (a) and (b) crosses correspond to 2005 data and dots to 2006 data. Plot (c) presents the relation between significant wave height (H_{sig}) and wind speed depending on wave field conditions: developed wave field conditions are marked by crosses (2005) and triangles (2006), young wave field conditions are marked by dots (2005) and circles (2006). Dashed rectangle indicates the highest wind speed range.

In order to understand this dependence we consider the scattering plot H_{sig} vs U_{10} (Figure 13c). The information about the wave stage development (wave age) is also presented. It is evident that for the majority of the data points in the higher wind speed domain (marked by the dashed rectangle), the significant wave height (H_{sig}) values were higher in 2005 compared to 2006. Young waves ($W_a < 1.2$, dots and circles) were prevailing in both years. Under such conditions, while the denominator of $D = H_{sig}/W_a$ is comparable in both years, the numerator is higher in 2005, leading to higher values of D in 2005.

In the lower wind speed range, we observed that in 2005 predominantly higher developed waves were present ($W_a > 1.2$, crosses) in contrast to 2006 where lower young waves ($W_a < 1.2$, circles) dominated. In that case, higher H_{sig} and higher W_a give a similar ratio to lower H_{sig} and lower W_a , which results in comparable values of D in both years.

The bubble entrainment depth obtained under the same wind speed conditions differs between the years. As shown in the above analysis, it depends not only on the wind speed but also on wave parameters – wave height (H_{sig}) and wave age (W_a).

4.3. Relation between bubble entrainment depth and noise spectrum level

Concurrent observations of bubbles penetrating the water column and the noise level generated in this process revealed that, at shallow entrainment depths, the noise level increased faster than when the bubbles were at greater depths (Figure 11). This could be attributed to the attenuation of noise by larger bubble clouds, which under higher wind speeds form at greater depths within the water column. The shape of the obtained relation between bubble depth and mean noise spectrum level was similar in both years. However, it differed in values and in depth where bubbles started to attenuate sound. The noise level recorded during the presence of bubbles at a depth of 2.5 m differs in both years by 2 dB re $1 \mu\text{Pa}^2/\text{Hz}$. This difference reached 4.5 dB re $1 \mu\text{Pa}^2/\text{Hz}$ at a depth of 4 m. A possible explanation for this difference may be that not only the depth of bubbles affects the noise level, but also their volume and the frequency of wave-breaking events. A greater number of breaking waves, which can entrain bubbles at a particular depth, would cause a higher noise level but might not influence observed bubble depth.

5. Conclusions

Measurements of ambient noise and estimations of bubbles entrainment depth were conducted in the semi-enclosed, fetch-limited area of the Baltic Sea, during two consecutive summer periods, under the same sound propagation conditions but under distinct wind-wave field conditions.

The outcomes of this study are meaningful due to the semi-enclosed character of the Baltic Sea, where parameters of breaking wind waves, the primary source of underwater noise, might diverge from those of the open ocean. This affects the underwater noise as well as the depth of bubble entrainment.

Considering the site-sensitivity of the wind-wave field in the Baltic Sea, the local approach to the study of noise and bubbles created during breaking of waves should be applied here. From this perspective, our study in the selected area of the sea during two measurement periods makes important contribution to understanding underwater noise generation by breaking wind waves in the Baltic Sea.

The main obtained results include:

1. The relationship between noise level and wind speed was parametrized for the selected study site in the Baltic

Sea. It has been demonstrated that the slope of the dependence differs from those obtained in previous studies concerning both open sea and semi-enclosed basins.

2. It has been shown that the correlations of noise level with wind speed and with wind wave height (in 2005) and significant wave height (in 2006) were higher than with wave age and wind sea steepness. The same conclusion holds for the correlation of bubbles entrainment depth with wind speed and with wind wave field parameters, for both years.
3. It is worth mentioning that in 2005 the correlation of noise level with wind wave height was higher than with significant wave height, while the opposite was true for 2006. This discrepancy might possibly be related to the stronger impact of the swell in 2005 compared to 2006.
4. The higher noise level across the entire wind speed range and the larger bubble entrainment depth for wind speed higher than 8 m/s in 2005, were attributed to the prevailing higher wind speeds and wind wave heights at the beginning of the 2005 campaign. The comparable bubble entrainment depth values at lower wind speeds in both measurement periods could be attributed to both the higher significant wave height in 2005 and the presence of older wind waves during summer period of that year.
5. The introduction of the new method to extract the sea surface from the echogram and to estimate the depth of bubble entrainment in conditions of a strong backscatter from bubble clouds, allows us to relate bubble depth to wind speed and to noise level. The noise level-bubble entrainment depth relationship is reported for the first time for the Baltic Sea.

The study provides grounds for making some recommendations:

1. Wind direction and related fetch length should be considered in future studies in semi-enclosed areas. These two parameters might influence the wind wave field and subsequently alter underwater noise characteristics.
2. The findings of this study underline the fact that site-dependent factors should be considered in order to reliably infer wind speed or gas bubble parameters from ambient noise measurements.
3. More accurate determination of the influence of wave field on ambient noise and gas bubble characteristics requires longer observations not only of ambient noise and gas bubbles but also of wave parameters, collected under variable wind-sea conditions. Additionally, considering the impact of swell on noise level and on bubble entrainment depth is also important.

Declaration of competing interest

The authors declare that they have no known competing financial interests or personal relationships that could have appeared to influence the work reported in this paper.

Acknowledgments

This work was supported by the [State Committee for Scientific Research](#) (project No. 6 PO4E 029 16); the

Polish National Agency for Academic Exchange under the Bekker Program (decision PPN/BEK/2019/1/00043/DEC/1); and the Polish Academy of Sciences statutory activity.

We are pleased to acknowledge Dr. Aliaksandr Lisimenka for field data acquisition and many valuable discussions. We kindly thank the crew of the r/v *Oceania* for all technical assistance and safety care during the cruise.

References

- Arduhin, F., Herbers, T.H.C., Watts, K.P., van Vledder, G.P., Jensen, R., Graber, H.C., 2007. Swell and Slanting-Fetch Effects on Wind Wave Growth. *J. Phys. Oceanogr.* 37, 908–931. <https://doi.org/10.1175/JPO3039.1>
- Bagočius, D., 2013. Underwater noise level in Klaipėda Strait. Lithuania. *Baltica* 26, 45–50. <https://doi.org/10.5200/baltica.2013.26.05>
- Bagočius, D., Narščius, A., 2022. The underwater sound levels of Lithuanian marine harbour. *Mar. Pollut. Bull.* 185, 114335. <https://doi.org/10.1016/j.marpolbul.2022.114335>
- Ballou, G., 2013. *Handbook for sound engineers*. Taylor & Francis, 1748 pp.
- Baltic Sea Wave Hindcast, n.d., E.U. Copernicus Marine Service Information (CMEMS). Marine Data Store (MDS). <https://doi.org/10.48670/moi-00014> (accessed on 8-05-2023).
- Banner, M.L., Babanin, A.V., Young, I.R., 2000. Breaking Probability for Dominant Waves on the Sea Surface. *J. Phys. Oceanogr.* 30, 3145–3160. [https://doi.org/10.1175/1520-0485\(2000\)030<3145:BPFDWO>2.0.CO;2](https://doi.org/10.1175/1520-0485(2000)030<3145:BPFDWO>2.0.CO;2)
- Banner, M.L., Cato, D.H., 1988. Physical Mechanisms of Noise Generation by Breaking Waves – A Laboratory Study. In: *Sea Surface Sound*. Springer, Netherlands, Dordrecht, 429–436. https://doi.org/10.1007/978-94-009-3017-9_31
- Bierstedt, S.E., Hünicke, B., Zorita, E., 2015. Variability of wind direction statistics of mean and extreme wind events over the Baltic Sea region. *Tellus A* 67, 29073. <https://doi.org/10.3402/tellusa.v67.29073>
- Cato, D.H., 2019. Surface generated underwater noise in open and enclosed waters. In: *Proceedings of the Acoustics*. Cape Schanck, Victoria, Australia, 1–7.
- Cato, D.H., Tavener, S., 1997. Ambient sea noise dependence on local, regional and geostrophic wind speeds: Implications for forecasting noise. *Appl. Acoust.* 51, 317–338. [https://doi.org/10.1016/S0003-682X\(97\)00001-7](https://doi.org/10.1016/S0003-682X(97)00001-7)
- Chen, C., Millero, F.J., 1977. Speed of sound in seawater at high pressures. *J. Acoust. Soc. Am.* 62, 1129–1135. <https://doi.org/10.1121/1.381646>
- Chu, J.S., Long, S.R., Phillips, O.M., 1992. Measurements of the interaction of wave groups with shorter wind-generated waves. *J. Fluid. Mech.* 245, 191–210.
- Crawford, G.B., Farmer, D.M., 1987. On the spatial distribution of ocean bubbles. *J. Geophys. Res.* 92, 8231. <https://doi.org/10.1029/JC092iC08p08231>
- Ding, L., Farmer, D.M., 1994. Observations of Breaking Surface Wave Statistics. *J. Phys. Oceanogr.* 24, 1368–1387. [https://doi.org/10.1175/1520-0485\(1994\)024<1368:OBSWS>2.0.CO;2](https://doi.org/10.1175/1520-0485(1994)024<1368:OBSWS>2.0.CO;2)
- Donelan, M., 1987. The effect of swell on the growth of wind waves. *Johns Hopkins APL Tech. Dig.* 8, 18–23.
- Dragan, A., Klusek, Z., Lisimenka, A., 2010. Ambient noise, bubble clouds and wind speed relationships. In: *Proceedings of the 10th European Conference on Underwater Acoustics ECUA 2010*, 662–668.
- Evans, D.L., Watts, D.R., Halpern, D., Bourassa, S., 1984. Oceanic winds measured from the seafloor. *J. Geophys. Res.* 89, 3457. <https://doi.org/10.1029/JC089iC03p03457>
- Farmer, D.M., Lemon, D.D., 1984. The Influence of Bubbles on Ambient Noise in the Ocean at High Wind Speeds. *J. Phys. Oceanogr.* 14, 1762–1778. [https://doi.org/10.1175/1520-0485\(1984\)014<1762:TIOBOA>2.0.CO;2](https://doi.org/10.1175/1520-0485(1984)014<1762:TIOBOA>2.0.CO;2)
- Farmer, D.M., Vagle, S., 1988. On the determination of breaking surface wave distributions using ambient sound. *J. Geophys. Res.* 93, 3591. <https://doi.org/10.1029/JC093iC04p03591>
- Felizardo, F.C., Melville, W.K., 1995. Correlations between Ambient Noise and the Ocean Surface Wave Field. *J. Phys. Oceanogr.* 25, 513–532. [https://doi.org/10.1175/1520-0485\(1995\)025<0513:CBANAT>2.0.CO;2](https://doi.org/10.1175/1520-0485(1995)025<0513:CBANAT>2.0.CO;2)
- Fisher, N.I., 1995. *Statistical analysis for circular data*. Cambridge Univ. Press, 269 pp.
- Foote, K.G., Knudsen, H.P., Vestnes, G., MacLennan, D.N., Simmonds, E.J., 1987. Calibration of acoustic instruments FDR fish density estimation: a practical guide. ICES Cooperative Research Report 144.
- Gemmrch, J., 2010. Strong turbulence in the wave crest region. *J. Phys. Oceanogr.* 40, 583–595. <https://doi.org/10.1175/2009JPO4179.1>
- Gemmrch, J.R., Farmer, D.M., 1999. Observations of the Scale and Occurrence of Breaking Surface Waves. *J. Phys. Oceanogr.* 29, 2595–2606. [https://doi.org/10.1175/1520-0485\(1999\)029<2595:OOTSAO>2.0.CO;2](https://doi.org/10.1175/1520-0485(1999)029<2595:OOTSAO>2.0.CO;2)
- Graham, A., Woolf, D.K., Hall, A.J., 2004. Aeration Due to Breaking Waves. Part I: Bubble Populations. *J. Phys. Oceanogr.* 34, 989–1007. [https://doi.org/10.1175/1520-0485\(2004\)034<0989:ADTBWP>2.0.CO;2](https://doi.org/10.1175/1520-0485(2004)034<0989:ADTBWP>2.0.CO;2)
- Grelowska, G., 2016. Study of Seasonal Acoustic Properties of Sea Water in Selected Waters of the Southern Baltic. *Pol. Marit. Res.* 23, 25–30. <https://doi.org/10.1515/pomr-2016-0004>
- Grelowska, G., Kozaczka, E., 2020. Changes in conditions of acoustic wave propagation in the Gdansk deep as an effect of climate changes in the Baltic Sea region. *Mar. Pollut. Bull.* 160, 111660. <https://doi.org/10.1016/j.marpolbul.2020.111660>
- Herman, A., 2022. Pogoda i klimat Zatoki Puckiej. In: *Bolalek, J., Burska, D. (Eds.), Zatoka Pucka, Tom I Aspekty Geologiczne i Fizyczne*. Wydawnictwo Uniwersytetu Gdańskiego, Gdańsk, 159–175.
- Hwang, P.A., 2008. Observations of swell influence on ocean surface roughness. *J. Geophys. Res.-Oceans* 113, C12024. <https://doi.org/10.1029/2008JC005075>
- Hwang, P.A., García-Nava, H., Ocampo-Torres, F.J., 2011. Observations of Wind Wave Development in Mixed Seas and Unsteady Wind Forcing. *J. Phys. Oceanogr.* 41, 2343–2362. <https://doi.org/10.1175/JPO-D-11-044.1>
- Ingenito, F., Wolf, S.N., 1989. Site dependence of wind-dominated ambient noise in shallow water. *J. Acoust. Soc. Am.* 85, 141–145. <https://doi.org/10.1121/1.397722>
- Karagali, I., Peña, A., Badger, M., Hasager, C.B., 2014. Wind characteristics in the North and Baltic Seas from the QuikSCAT satellite. *Wind Energy* 17, 123–140. <https://doi.org/10.1002/we.1565>
- Kerman, B.R., 1988. Sea surface sound: natural mechanisms of surface generated noise in the ocean. In: *Series C: Math. Phys. Sci.*, vol. 238. Kluwer Academic, Dordrecht, Boston, London, 652 pp.
- Kim, B.-C., Choi, B.K., 2006. Variation of underwater ambient noise observed at IORS station as a pilot study. *Ocean Sci. J.* 41, 175–179. <https://doi.org/10.1007/BF03022422>
- Klusek, Z., 1977. Directivity of the noise field in the Southern Baltic Sea. *Stud. Mater. Oceanol. KBM PAN* 17, 83–106.
- Klusek, Z., Lisimenka, A., 2016. Seasonal and diel variability of the underwater noise in the Baltic Sea. *J. Acoust. Soc. Am.* 139, 1537–1547. <https://doi.org/10.1121/1.4944875>
- Klusek, Z., Lisimenka, A., 2007. Ambient sea noise in the Baltic Sea. In: *Proceedings of the 2nd International Conference and Exhibition on Underwater Acoustic Measurements: Technologies and Results*, Crete, Greece, 625–632.

- Knudsen, V.O., Alford, R.S., Emling, J.W., 1948. Underwater ambient noise. *J. Mar. Res.* 7, 410–429.
- Lemon, D.D., Farmer, D.M., Watts, D.R., 1984. Acoustic measurements of wind speed and precipitation over a continental shelf. *J. Geophys. Res.* 89, 3462. <https://doi.org/10.1029/JC089iC03p03462>
- Leppäranta, M., Myrberg, K., 2009. *Physical Oceanography of the Baltic Sea*. Springer, Berlin, Heidelberg, 378 pp. <https://doi.org/10.1007/978-3-540-79703-6>
- Markuszewski, P., Klusek, Z., Nilsson, E.D., Petelski, T., 2020. Observations on relations between marine aerosol fluxes and surface-generated noise in the southern Baltic Sea. *Oceanologia* 62 (4), 413–427. <https://doi.org/10.1016/j.oceano.2020.05.001>
- Means, S.L., Heitmeyer, R.M., 2002. Surf-generated noise signatures: A comparison of plunging and spilling breakers. *J. Acoust. Soc. Am.* 112, 481–488. <https://doi.org/10.1121/1.1491256>
- Medwin, H., Beaky, M.M., 1989. Bubble sources of the Knudsen Sea noise spectra. *J. Acoust. Soc. Am.* 86, 1124–1130. <https://doi.org/10.1121/1.398104>
- Otsu, N., 1979. A Threshold Selection Method from Gray-Level Histograms. *IEEE T. Syst. Man Cyb.* 9, 62–66. <https://doi.org/10.1109/TSMC.1979.4310076>
- Perrone, A.J., 1969. Deep-Ocean Ambient-Noise Spectra in the Northwest Atlantic. *J. Acoust. Soc. Am.* 46, 762–770. <https://doi.org/10.1121/1.1911759>
- Pierson, W.J., Moskowitz, L., 1964. A proposed spectral form for fully developed wind seas based on the similarity theory of S. A. Kitaigorodskii. *J. Geophys. Res.* 69, 5181–5190. <https://doi.org/10.1029/JZ069i024p05181>
- Piggott, C.L., 1964. Ambient Sea Noise at Low Frequencies in Shallow Water of the Scotian Shelf. *J. Acoust. Soc. Am.* 36, 2152–2163. <https://doi.org/10.1121/1.1919337>
- Pinto, J.G., Ulbrich, U., Leckebusch, G.C., Spanghel, T., Reyers, M., Zacharias, S., 2007. Changes in storm track and cyclone activity in three SRES ensemble experiments with the ECHAM5/MPI-OM1 GCM. *Clim. Dynam.* 29, 195–210. <https://doi.org/10.1007/s00382-007-0230-4>
- Poikonen, A., Madekivi, S., 2010. Wind-generated ambient noise in a shallow brackish water environment in the archipelago of the Gulf of Finland. *J. Acoust. Soc. Am.* 127, 3385–3393. <https://doi.org/10.1121/1.3397364>
- Ramji, S., Latha, G., Rajendran, V., Ramakrishnan, S., 2008. Wind dependence of ambient noise in shallow water of Bay of Bengal. *Appl. Acoust.* 69, 1294–1298. <https://doi.org/10.1016/j.apacoust.2007.09.001>
- Rapp, R.J., Melville, W.K., 1990. Laboratory measurements of deep-water breaking waves. *Philos. T. R. Soc. S.-A* 331, 735–800. <https://doi.org/10.1098/rsta.1990.0098>
- Reeder, D.B., Sheffield, E.S., Mach, S.M., 2011. Wind-generated ambient noise in a topographically isolated basin: A pre-industrial era proxy. *J. Acoust. Soc. Am.* 129, 64–73. <https://doi.org/10.1121/1.3514379>
- Shaw, P.T., Watts, D.R., Rossby, H.T., 1978. On the estimation of oceanic wind speed and stress from ambient noise measurements. *Deep Sea Res.* 25, 1225–1233. [https://doi.org/10.1016/0146-6291\(78\)90015-2](https://doi.org/10.1016/0146-6291(78)90015-2)
- Sigray, P., Andersson, M., Pajala, J., Laanearu, J., Klauuson, A., Tegowski, J., Boethling, M., Fischer, J., Tougaard, J., Wahlberg, M., Nikolopoulos, A., Folegot, T., Matuschek, R., Verfuss, U., 2016. BIAS: A Regional Management of Underwater Sound in the Baltic Sea. In: Popper, A., Hawkins, A. (Eds.). *The Effects of Noise on Aquatic Life II. Advances in Experimental Medicine and Biology*, vol. 875. Springer, New York, NY. https://doi.org/10.1007/978-1-4939-2981-8_126
- Soomere, T., 2023. Numerical simulations of wave climate in the Baltic Sea: a review. *Oceanologia* 65 (1), 117–140. <https://doi.org/10.1016/j.oceano.2022.01.004>
- Strand, K.O., Breivik, Ø., Pedersen, G., Vikebø, F.B., Sundby, S., Christensen, K.H., 2020. Long-Term Statistics of Observed Bubble Depth Versus Modeled Wave Dissipation. *J. Geophys. Res.-Oceans* 125, e2019JC015906. <https://doi.org/10.1029/2019JC015906>
- Thorpe, S.A., 1992. Bubble clouds and the dynamics of the upper ocean. *Q. J. Roy. Meteor. Soc.* 118, 1–22. <https://doi.org/10.1002/qj.49711850302>
- Thorpe, S.A., 1986. Measurements with an Automatically Recording Inverted Echo Sounder; ARIES and the Bubble Clouds. *J. Phys. Oceanogr.* 16, 1462–1478. [https://doi.org/10.1175/1520-0485\(1986\)016\(1462:MWAARI\)2.0.CO;2](https://doi.org/10.1175/1520-0485(1986)016(1462:MWAARI)2.0.CO;2)
- Thorpe, S.P., 1982. On the clouds of bubbles formed by breaking wind-waves in deep water, and their role in air-sea gas transfer. *Philos. T. R. Soc. S.-A* 304, 155–210. <https://doi.org/10.1098/rsta.1982.0011>
- Trevorrow, M.V., 2003. Measurements of near-surface bubble plumes in the open ocean with implications for high-frequency sonar performance. *J. Acoust. Soc. Am.* 114, 2672. <https://doi.org/10.1121/1.1621008>
- Vagle, S., Farmer, D.M., 1998. A comparison of four methods for bubble size and void fraction measurements. *IEEE J. Oceanic Eng.* 23, 211–222. <https://doi.org/10.1109/48.701193>
- Vagle, S., Large, W.G., Farmer, D.M., 1990. An Evaluation of the WOTAN Technique of Inferring Oceanic Winds from Underwater Ambient Sound. *J. Atmos. Ocean. Tech.* 7, 576–595. [https://doi.org/10.1175/1520-0426\(1990\)007\(0576:AETWT\)2.0.CO;2](https://doi.org/10.1175/1520-0426(1990)007(0576:AETWT)2.0.CO;2)
- Vakkayil, R., Graber, H.C., Large, W.G., 1996. Oceanic winds estimated from underwater ambient noise observations in SWADE. In: *OCEANS 96 MTS/IEEE Conference Proceedings. The Coastal Ocean - Prospects for the 21st Century*. IEEE, 45–51. <https://doi.org/10.1109/OCEANS.1996.572450>
- Vincent, C.L., Graber, H.C., Collins, C.O., 2020. Effect of Swell on Wind Stress for Light to Moderate Winds. *J. Atmos. Sci.* 77, 3759–3768. <https://doi.org/10.1175/JAS-D-19-0338.1>
- Wang, D.W., Wijesekera, H.W., Jarosz, E., Teague, W.J., Pegau, W.S., 2016. Turbulent Diffusivity under High Winds from Acoustic Measurements of Bubbles. *J. Phys. Oceanogr.* 46, 1593–1613. <https://doi.org/10.1175/JPO-D-15-0164.1>
- Wickström, S., Jonassen, M.O., Vihma, T., Uotila, P., 2020. Trends in cyclones in the high-latitude North Atlantic during 1979–2016. *Q. J. Roy. Meteor. Soc.* 146, 762–779. <https://doi.org/10.1002/qj.3707>
- Wille, P.C., Geyer, D., 1984. Measurements on the origin of the wind-dependent ambient noise variability in shallow water. *J. Acoust. Soc. Am.* 75, 173–185. <https://doi.org/10.1121/1.390411>
- Zachowicz, J., Kramarska, R., Uściniowicz, S., 2004. The southern Baltic Sea—test field for international co-operation. *Przełąd Geologiczny* 52, 738–743.
- Zedel, L., 1994. Deep Ocean Wave Measurements Using a Vertically Oriented Sonar. *J. Atmos. Ocean. Tech.* 11, 182–191. [https://doi.org/10.1175/1520-0426\(1994\)011\(0182:DOWMUA\)2.0.CO;2](https://doi.org/10.1175/1520-0426(1994)011(0182:DOWMUA)2.0.CO;2)

Available online at www.sciencedirect.com

ScienceDirect

journal homepage: www.journals.elsevier.com/oceanologia

ORIGINAL RESEARCH ARTICLE

Soft postglacial cliffs in Poland under climate change

Grzegorz Różyński*, Grzegorz Cerkowniak*

Institute of Hydro-Engineering, Polish Academy of Sciences, Gdańsk, Poland

Received 25 January 2023; accepted 10 January 2024

Available online 3 February 2024

KEYWORDS

Baltic Sea;
Sea level rise;
Soft cliffs;
Mixed sediments;
Extreme events

Abstract The paper presents the results of the simulations of soft cliff erosion in Poland under future sea level rise. Two locations were investigated: one situated on the Wolin island, and the second near the town of Ustka. The cliffs will be suffering enhanced erosion for a number of reasons. First, the adopted sea level rise of 0.7 m results in a direct attack on cliff foot, leading to enhanced erosion with rates being roughly twice as high as that occurring without the rise. A high rate of erosion can persist because the cliff cannot reconfigure itself by moving landward and will permanently remain exposed to wave attack even under milder regimes. Second, the wave climates in the Baltic Sea release most energy in close shoreline proximity. Third, longer storm event durations can lead to ‘erosion saturation’, but this result requires further investigations, which will include alongshore effects induced by local bathymetry and longshore currents, ignored in 1-D simulations. Finally, the granulometry was found less important; finer grains offer less resistance to depletion, leading to greater erosion. The results demonstrate the need for vast follow-up research: (1) detailed mapping of the bathymetry near cliffs in order to properly reproduce alongshore redistribution of sediment during storms and achieve better estimates of cliff erosion, (2) detailed mapping of cliff lithology in order to properly reproduce their sediment composition and thus achieve better estimates of built-in susceptibility to erosion, (3) preparation of 2-D modeling suites for improved assessment of the rates of erosion of cliffs subjected to sea level rise.

© 2024 Institute of Oceanology of the Polish Academy of Sciences. Production and hosting by Elsevier B.V. This is an open access article under the CC BY-NC-ND license (<http://creativecommons.org/licenses/by-nc-nd/4.0/>).

* Corresponding authors at: Institute of Hydro-Engineering, Polish Academy of Sciences, 7 Kościarska, 80–328 Gdańsk, Poland.

E-mail addresses: grzegorz@ibwpan.gda.pl (G. Różyński), grzegorzcerkowniak@ibwpan.gda.pl (G. Cerkowniak).

Peer review under the responsibility of the Institute of Oceanology of the Polish Academy of Sciences.



<https://doi.org/10.1016/j.oceano.2024.01.003>

0078-3234/© 2024 Institute of Oceanology of the Polish Academy of Sciences. Production and hosting by Elsevier B.V. This is an open access article under the CC BY-NC-ND license (<http://creativecommons.org/licenses/by-nc-nd/4.0/>).

1. Introduction

1.1. Rationale of the study

BALTEX Assessment of Climate Change for the Baltic Sea Basin – [BACC II \(2015\)](#) identified key elements of climate change in the Baltic Sea basin. Despite large uncertainties it was generally accepted that: 1) a distinct growth of air temperature in all seasons, driven by rising greenhouse gases (GHG) emissions, will persevere; 2) based on the Special Report on Emission Scenarios (SRES) A1B and A2 the summer sea surface temperature (SST) is expected to increase by ca. 2°C in the southern and 4°C in the northern parts of the Baltic Sea; 3) a severe decrease in sea-ice cover is expected; 4) a mild increase of annual mean storm surges of 10 cm was estimated; 5) for the SRES A1B scenario, the sea level was estimated to rise by 0.7 m (± 0.3 m) until the end of the 21st century; for AR5 scenarios, the projections fall between 0.26 and 0.82 m, [IPCC AR5 Synthesis Report \(2014\)](#).

Recent observations generally concur with these predictions. Moreover, erosion also became more widespread and severe: (1) almost two-thirds of Polish coastal dunes are eroded ([Pruszek and Zawadzka, 2005](#)), and nearly 75% of the sandy coast with low-lying hinterland is flood-prone ([Łabuz, 2012](#)); (2) almost 75% of German sandy coasts are threatened by erosion ([Sterr, 2008](#)); (3) over 65% of the Latvian coast is eroded ([Eberhards, 2003](#)); the situation is similar in Lithuania, Latvia, and Estonia ([Milerienė et al., 2008](#)); (4) about 40% of the Russian Neva Bay has been affected by heavy erosion events in recent years ([Ryabchuk et al., 2011](#)). In the context of the above-mentioned studies, the current one investigates the resilience of soft cliffs in Poland subjected to climate change, as they are very likely to be susceptible to intensive future erosion due to the combined effects of ‘static’ sea level rise, storm surges and wave action. Hence, the analysis of these impacts is the main aim of the study. The literature review reveals a complex character of cliff erosion. A very comprehensive description of erosion processes in cliffs is provided by [USGS Professional Paper 1693 \(2004\)](#). They noted that the majority of cliffs along today’s coastlines are relatively young geologic features, having formed after the most recent ice age. Next, they pointed to the key role of marine processes, namely the rise of water level and wave action being fundamental in that they operate from the inception through the mature stages of coastal cliff evolution; active cliffs, i.e. those eroded by water levels and waves can be further modified by terrestrial processes, producing multiple complex effects. For this reason, coastal cliffs can display a wide range of form and stability. Among terrestrial processes, the [USGS Professional Paper 1693 \(2004\)](#) points to surface runoff and groundwater as the main drivers of cliff evolution. Surface runoff resulting from rainfalls both softens and sculpts broad areas of a cliff face because of the tractive force that water exerts on the erodible surface. Fresh-water sheet flow generally causes only a small amount of coastal-cliff retreat, but concentrated runoff can carve gullies that deeply indent the cliff. On the contrary, strong enough groundwater discharge can dislodge grains from a cliff face – a process known as seepage erosion. Concentrated discharge around plant roots and animal burrows causes cave-like piping. Consequently, groundwa-

ter flow also can be concentrated along structural discontinuities such as joints, decreasing the outcrop-scale (rock-mass) strength and destabilizing a cliff. Another process contributing to cliff erosion is weathering. The [USGS Professional Paper 1693 \(2004\)](#) noted that the cliffs are exposed to severe weathering environment if they experience repeated wetting by salt spray or surface runoff, interspersed with periods of drying and heating. Also, the weathering process is accentuated if the surface material is fractured. The next group of processes is related to ice action. The ice developing at sea can be pushed against the bluff of a cliff and impair its integrity. On the other hand, it prevents cliff face from wave action. Hence, the role of sea-ice is very complicated producing both positive (protection) and negative (erosion) effects. By contrast, the role of ice developed within a cliff can have a direct impact on its recession, particularly when the ice melts; solar-induced melting of near-surface interstitial ice and the inability of the meltwater to infiltrate the underlying frozen soil can lead to high water content and reduced strength of a thin surficial layer of bluff material. The last group of terrestrial processes fostering cliff erosion includes gravity induced phenomena: slope instability, slope failure and coastal landslides, [USGS Professional Paper 1693 \(2004\)](#). Slope instability is a condition that initiates a process called slope failure that creates an object called a landslide. Landslides have many forms: a fall (detachment and free descent), a topple (forward rotation and tumbling), a slide or slump (shear deformation along a single or a few planar or curved rupture surfaces), and a spread (movement of competent beds atop water-bearing layers of sediment).

The above-mentioned broad groups of processes controlling cliff erosion are well represented along the Baltic Sea cliffs in Poland. [Kostrzewski et al. \(2021\)](#) summarized earlier research efforts, see e.g. [Subotowicz \(1982\)](#), [Kostrzewski and Zwoliński \(1986, 1995\)](#), [Kostrzewski et al. \(2015\)](#), and highlighted several key phenomena. The autumn and winter storm surges initiating abrasive processes in cliffs were mentioned as a primary driver of cliff retreat: during high sea water levels waves remove loose colluvium from under the undercut cliff foot, whereas the associated wave-driven currents re-distribute it in both longshore and cross-shore direction. When undercuts are large enough the cliff slides and a new colluvium is formed. Second, mass spring movements of cliffs are triggered by de-freezing of topsoil and disappearance of ice cover, cf. e.g. [Winowski \(2008\)](#); the melting ice contributes to soaking of cliff massif and shallow sediment slides that land on a beach and are further reconfigured by waves. Third, the cliff body dries up in summer and fine sand particles are removed by wind. On the contrary, intensive summer rainfalls can trigger severe erosion; the most optimum conditions for such events occur when the rainfall over 14 consecutive days exceeds 90 mm and the rainfall over two consecutive days exceeds 40 mm, cf. [Winowski \(2015\)](#). Moreover, [Winowski \(2015\)](#) introduced the concept of a ‘high morphogenetic potential event’, i.e. a sudden landslide of cliff face. Six such episodes were identified between 1973 and 2009 on the Wolin island – they occurred in October 1973, November 1995, 2001 and 2006, June–July 2006 and April 2008. Despite the pivotal role of storm surges the most interesting conclusion was that optimum conditions for land-

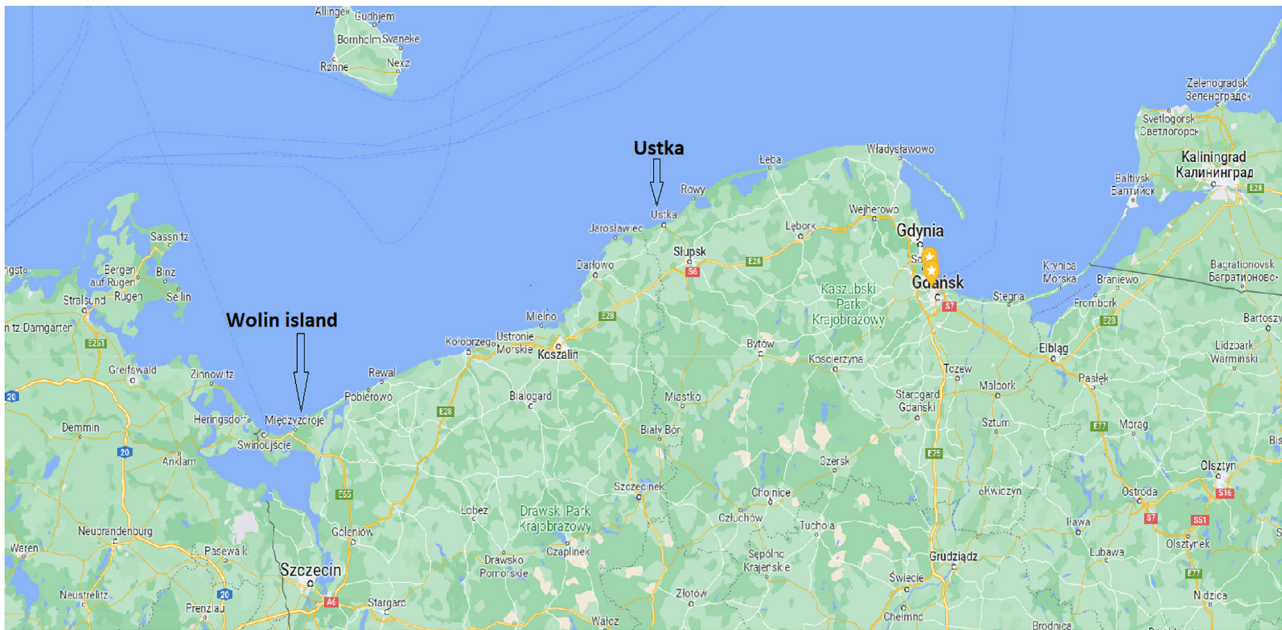


Figure 1 Polish coast and locations of past and current studies.

slide episodes occur when the surge exceeds 90 cm (i.e. sea level reaches 590 cm with respect to the Amsterdam datum) and its 24-hour amplitude is greater than 1.4 m – 9 such situations occurred between 1973 and 2009. In this way, [Winowski et al. \(2015\)](#) pointed to the existence of joint extreme events driven by both rainfalls and storms occurring at the same time. Consequently, [Terefenko et al. \(2018\)](#), basing on the study of cliff retreat at Międzyzdroje, found another important clue, namely the clustered storms, when quickly succeeding storms produce enhanced erosion: intensive erosion occurs since no beach recovery is possible between almost overlapping storms, and gentle undercuts formed during an initial event become subject to further degradation by wave energy of next events. As a result, the cliff face is likely to suffer a large landslide event. The complexity of the behavior of cliffs was also noticed by [Florek et al. \(2008\)](#), whose research approach was based on measurements taken along a number of closely located transects. They found that: (1) the rate of retreat varies significantly at almost neighboring transects – e.g. from 0.37 m/yr at km 230.3 of the National Chainage to 2.22 m/yr at km 230.5, (2) cliffs made of eolic or limno-glacial sands were found to be particularly erosion-prone, (3) the amount of clayey sediments in cliff massifs plays a very important and underestimated role in their evolution, (4) there is no simple relationship between sedimentological composition of cliffs and their rate of retreat. In all, the literature review demonstrates the very high complexity of cliff evolution. Thus, their investigations are a serious research challenge.

1.2. Study locations

Two locations were selected for the analysis. One is situated on the Wolin island in the westernmost part of the Polish coast and contains two cross-shore profiles at km 404 and 410 of the National Coastal Chainage cf. [Figure 1](#). It

forms a strip of the highest cliffs in Poland. Also, it was a subject of many past research studies, which are relatively well documented in the literature. The second site is situated east and west of Ustka harbor at km 231 and 235 of the Chainage respectively, cf. [Figure 1](#). From strictly geological point of view, coastal formations there feature very large sandy dunes. However, from the point of view of coastal engineering, they are so high that their evolution resembles the behavior of typical cliffs because terrestrial processes described in the Introduction become important due to the size of those large sandy formations. Thus, the choice of that site was done in order to compare the results of computations for a cliff with complex sedimentary composition incl. cohesive stratum (Wolin island) with more homogeneous, predominantly sandy formations at Ustka.

2. Material and methods

2.1. Site description

The Wolin island location corresponds to Sheet No. 3 at km 410 and to No. 4 at km 404 of the [Geodynamic Map of Polish Baltic Sea Coastal Region \(2007\)](#). The associated geological cross-shore profile at about km 409.8 of the Chainage describes sedimentological composition of cliffs on the Wolin island, see [Figure 2](#). It demonstrates that the contact layer of the cliff with seawater is made of postglacial till and sand, which is about 15 m thick. It is topped by sands and gravels, reaching a height of 95 m or so. Marine sand is present only in a residual form in the foreshore and near the shoreline.

The locations in the vicinity of Ustka harbor correspond to Sheet No. 25 of the Geodynamic Map for both km 231 and 235. The associated geological cross-shore profile at about km 231.5 of the Chainage, provides a description of local lithology at this transect, cf. [Figure 3](#). It shows that the cliff is made of eolic sand and is ca. 10 m high. In general, the

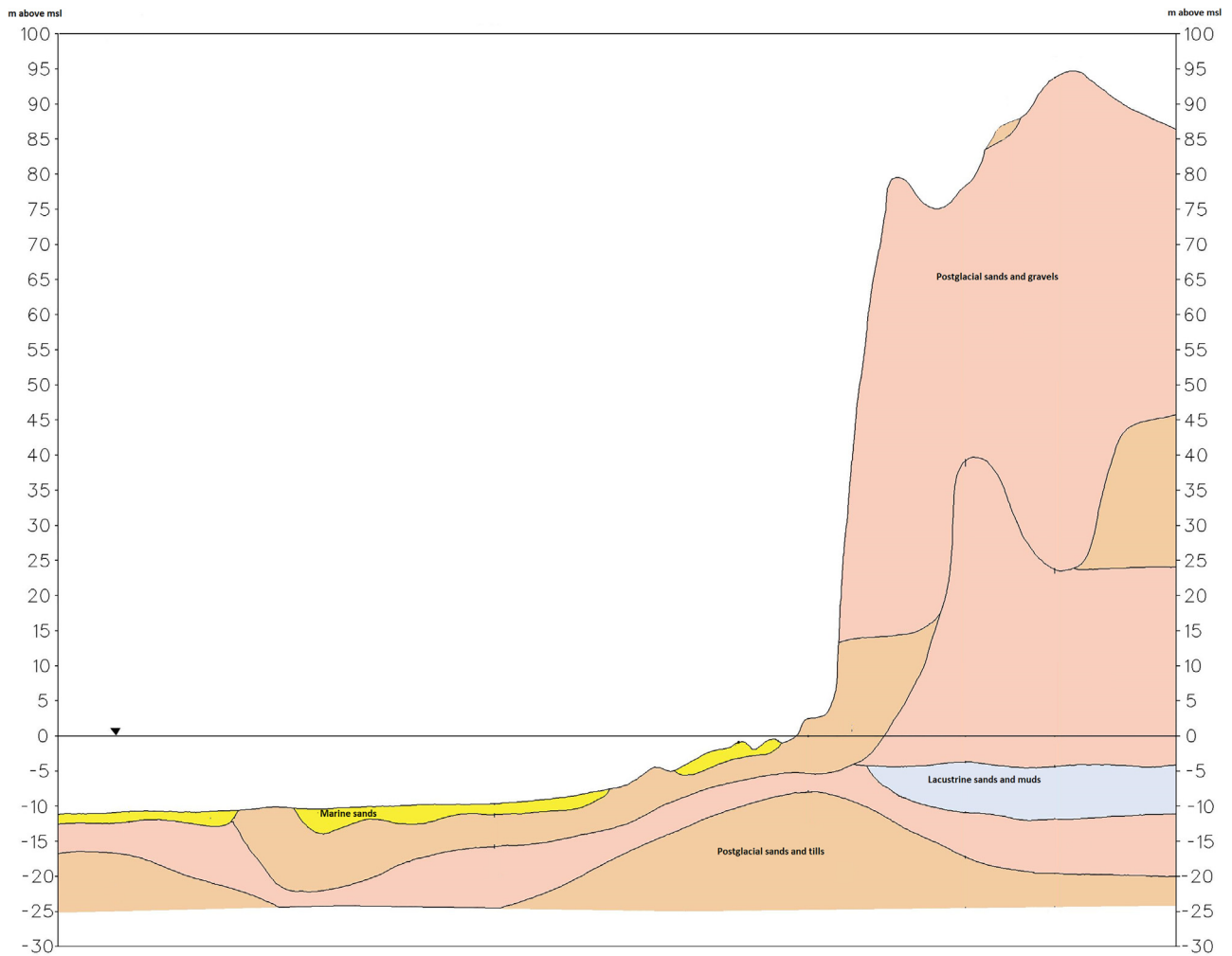


Figure 2 Location Wolin island: geological transect at km 409.8 of Nat. Coastal Chainage – extracted from geological cross-shore profile of Sheets No. 3, 4 of [Geodynamic Map of Polish Baltic Sea Coastal Region \(2007\)](#).

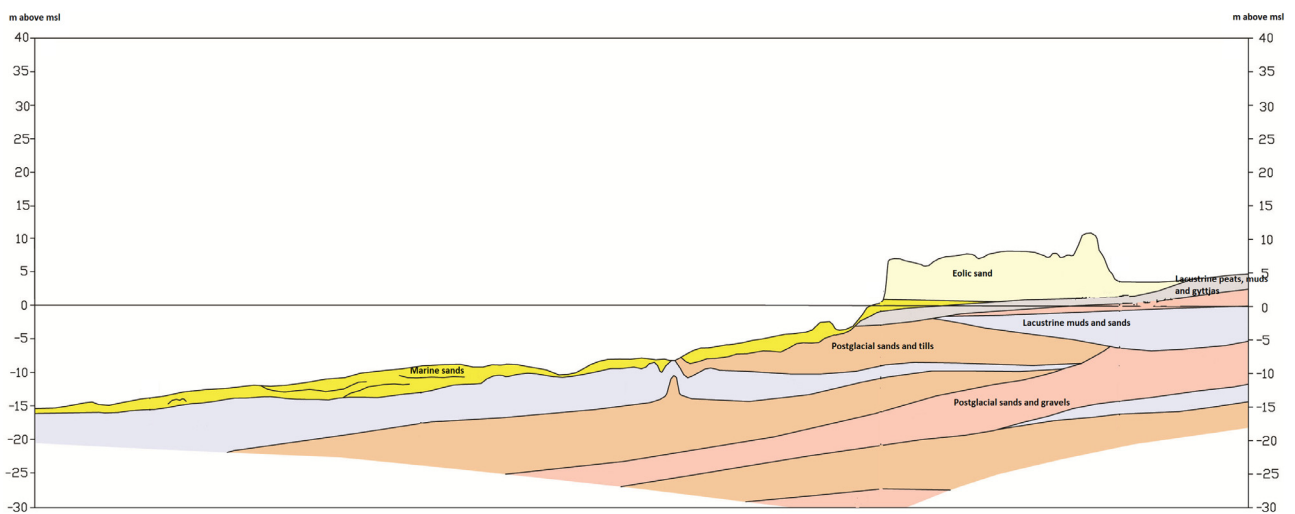


Figure 3 Location Ustka: geological transect at km 231.5 of Nat. Coastal Chainage – extracted from geological cross-shore profile of Sheet No. 25 of [Geodynamic Map of Polish Baltic Sea Coastal Region \(2007\)](#).

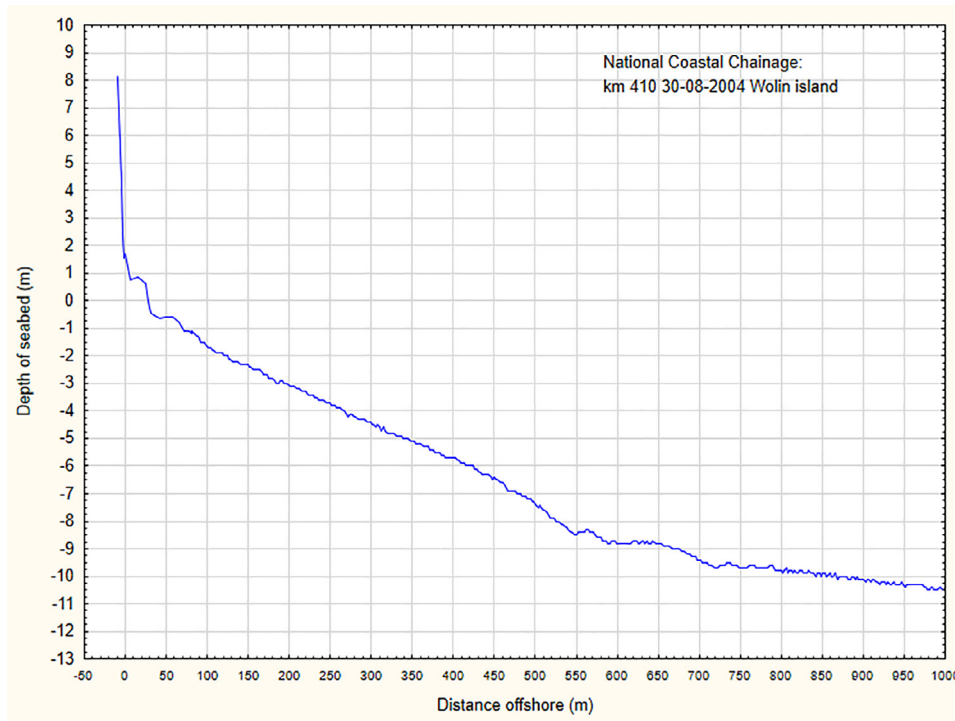


Figure 4 Bathymetric profile at km 410 from August 2004, source – Maritime Office in Szczecin.

cliff rests on postglacial tills and sands and residual marine sand is present in the foreshore. It therefore demonstrates that due to the presence of cohesive sediments, the system should have a tendency toward sand scarcity and be prone to erosion.

2.2. Bathymetric data

The simulations of shoreline change, executed at km 410, 404, 235 and 231 were based on shoreline bathymetry transects, measured by coastal authorities and presented in Figures 4–7 respectively.

Figure 4 shows that the cliff at km 410 practically has no protection against wave action because of the absence of nearshore bars. The beach is very narrow and a small hump in the vicinity of the shoreline indicates a colluvium that can provide elementary protection against waves attacking the cliff body head-on. Nevertheless, the cliff is prone to substantial erosion: the absence of bars suggests a large offshore migration of fine sediment particles, corroborating conclusions by Winowski (2015), who noticed that substantial cliff collapse events occur when a rapid change in seawater level of at least 140 cm occurs over a short time of 24 hours or so. This should produce a significant offshore directed cross-shore current that is able to wash away finer particles beyond the nearshore zone. The amount of such particles is high enough for the nearshore bars not to develop in close shoreline proximity. Another indication of sand scarcity is the perfectly linearly sloping bottom from 1 to 9 m depth of the seabed.

The situation is slightly different at km 404 – see Figure 5. The cliff is somewhat protected by two nearshore bars. The beach is almost non-existent and there is a step of the height of ca. 1 m situated very close to the shoreline,

which gradually transforms into the cliff slope. It, therefore, appears that the percentage of fine particles at km 404 is somewhat smaller in relation to sand volume and to the situation at km 410 because there are enough coarser grains to provide rudimentary protection of cliff foot by nearshore bars. On the other hand, the practical absence of the beach shows that the exposure to erosion during storms is still high. The seabed is sloping linearly up to ca. 9 m depth, showcasing sand scarcity.

Figure 6 illustrates the bathymetry from July 2006 at km 235, that is west of Ustka harbor. We can see two small nearshore bars and a narrow and steep beach. At about 1 m above msl there is a small shelf (colluvium), rapidly turning into the cliff slope. Further offshore the seabed inclines in a perfectly linear manner, indicating certain sand scarcity in the nearshore region.

Figure 7 illustrates the bathymetry at km 231, from April 2006, which is east of Ustka harbor breakwaters. The beach hardly exists and there are no nearshore bars. The seabed slopes steeply from the depth of 6 to 2 m. At about 1000 m offshore a large underwater seabed form is located – it sits too deep to function like a nearshore bar (depth of crest of 7 m), perhaps with the exception of the mightiest storms. In all, this configuration points to very significant exposure to erosion. It remains to be investigated whether sandy sediments can accumulate between the shoreline and the large underwater bulge, or they are washed away by longshore currents instantly. In all, both transects near Ustka harbor also show sediment scarcity and exposure to erosion.

2.3. Software and simulations

The simulations of cliff response to extreme events, including the effects of climate change, were executed using

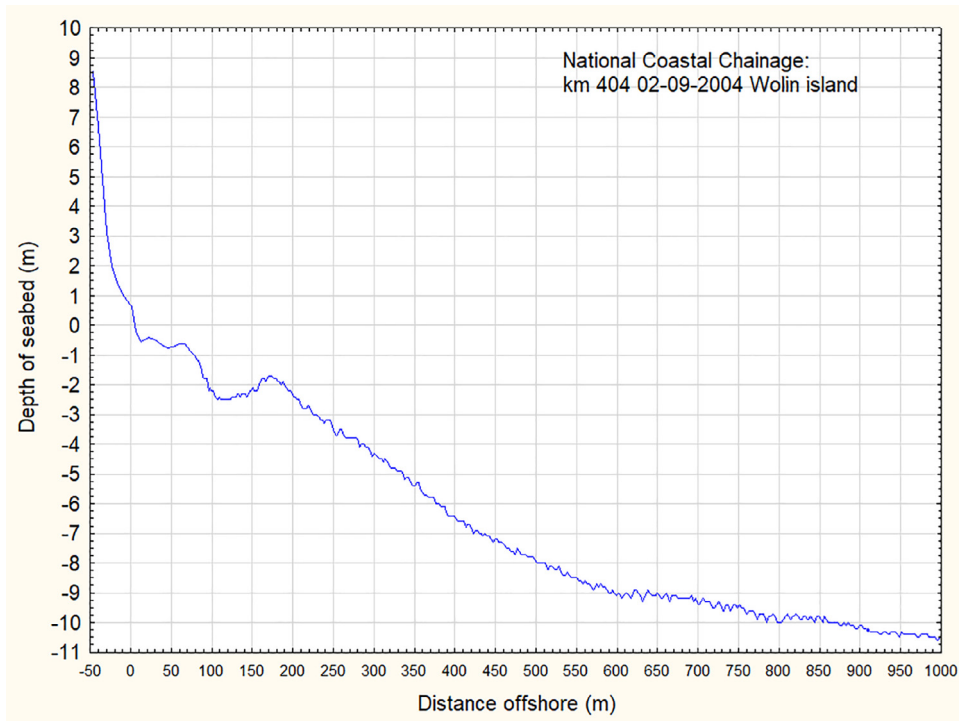


Figure 5 Bathymetric profile at km 404 from September 2004, source – Maritime Office in Szczecin.

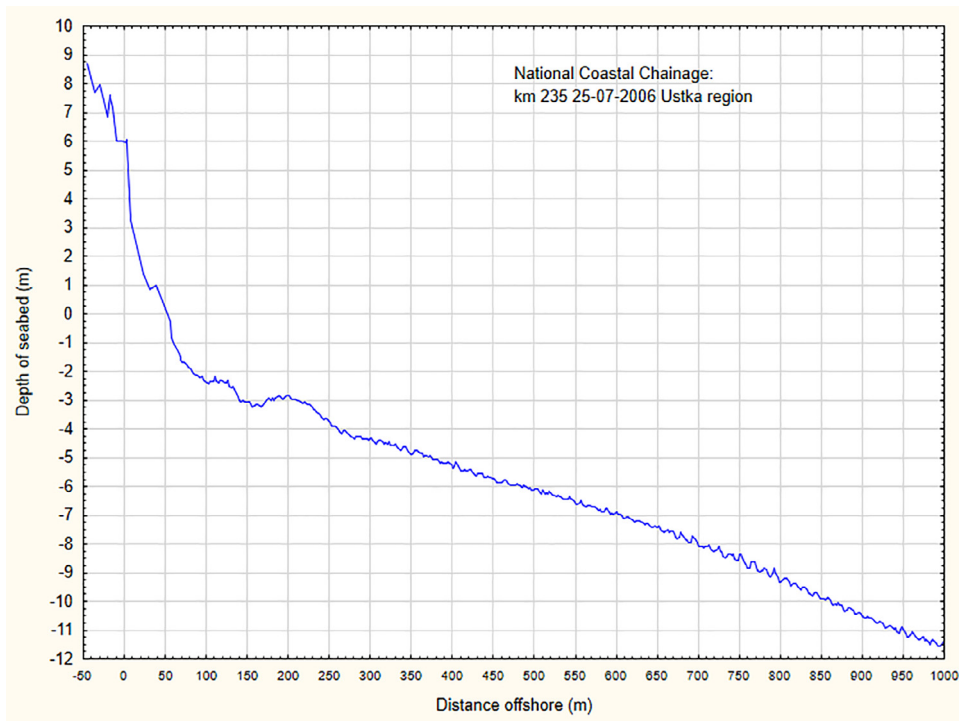


Figure 6 Bathymetric profile at km 235 from July 2006, source – Maritime Office in Słupsk.

the XBeach package. This package is basically intended to simulate erosion impacts on dunes. Its application to cliff face/foot is intended only to simulate direct consequences of wave action and instantaneous storm surge with and without the inclusion of static (climate-driven) sea level rise. For this reason, the simulations do not include possible land-

slide events triggered and induced by undercut cliff foot by waves. This is an obvious significant limitation of the study, which is concentrated on the most important drivers of cliff erosion, as defined by [UGSS Professional Paper 1693 \(2004\)](#). In particular, the erosion surplus caused by static sea level rise is investigated. In this context, it should be

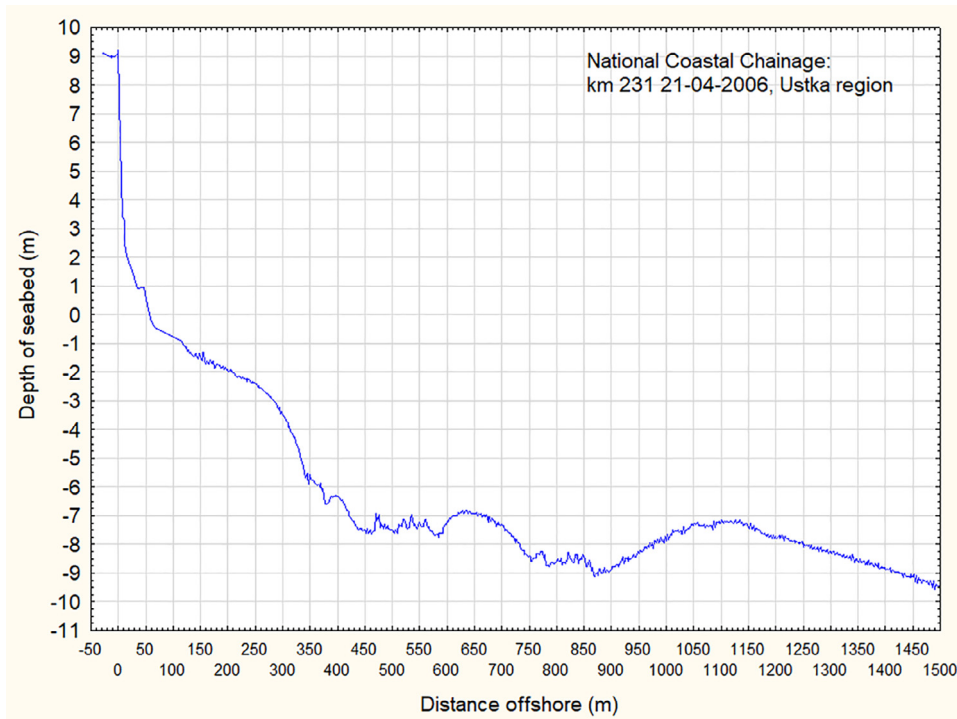


Figure 7 Bathymetric profile at km 231 from April 2006, source – Maritime Office in Słupsk.

expected that possible landslides triggered by foot erosion can be much greater than the currently observed events. Therefore, the simulations executed herein should be integrated with simulations of landslides, including the determination of tipping points, whose exceedance will result in a landslide event. Thus, the current efforts point to future integrated analyses combining coastal engineering and slope stability studies. This large latter group of disciplines may involve the effects of groundwater and surface runoff as well to achieve better accuracy of results.

For all simulations a westerly wave approach was assumed, reflecting the prevailing wave approach; hence the angle between the studied beach profiles and the azimuth of the wave approach was set at 30°. This obliquity was also introduced to reduce unrealistic zones of sediment depletion/deposition, usually observed for shore normal wave approach in the absence of longshore sediment transport. Other general assumptions included:

- (1) the JONSWAP spectrum with default peak concentration coefficient of 3.3 and cosine power 2 s directional spreading model with $s = 20$;
- (2) maximum frequency range of 1 Hz, corresponding to the wave period $T = 1$ s;
- (3) minimum frequency range of 0 Hz and $T = \infty$;
- (4) Chezy bottom friction coefficient $c = 55$ was adopted, assuming that friction-induced wave energy dissipation is very small;
- (5) the wave approach sector of $\pm 45^\circ$ about the main westerly wave direction was defined; its directional resolution was coarsely parameterized with the bin angle of 20°, sufficient for 1-D simulations.

The simulations assumed conditions expected at the end of 21st Century. Thus, the sea level rise of 0.7 m was

Table 1 Hydrodynamic parameters used in simulations, after Boniecka et al. (2013).

Return period:	T_p (years)	20	50	100
Wave period:	T (s)	8.5	8.8	9.1
Wave length:	L (m)	95.6	100.35	105.07
Significant wave height:	H_s (m)	5.71	6.22	6.61

adopted, following BACC II (2015) all and one common storm surge of 1.3 m was assumed for all simulations, roughly corresponding to the return period of surges of 20 years, Wiśniewski and Wolski (2009) – the simulations were executed for two variants of elevated seawater table, that is 1.3 m and 2 m. The simulated storms analyzed events with the return periods of 20, 50 and 100 years. Their parameters were provided by Boniecka et al. (2013); the periods, lengths and significant heights of waves were determined using methodologies elaborated by e.g., British Standard Code of Practice for Maritime Structures (2000) or Dnv-Os-J101 (2011), cf. Table 1. The periods and lengths of the extreme waves do not differ significantly for those return periods, in contrast to the growth of significant wave height by almost 1 m for the return periods of 20 and 100 years, see Table 1. The saturation of wave period and length results from the fetch limited character of the marginal Baltic Sea. The duration of extreme events, again following the recommendations of the British Standard Code of Practice for Maritime Structures (2000) and Dnv-Os-J101 (2011), was set at 3 h. In addition to that the simulations for longer events of 6 h were executed as well in order to inspect potential limitations of the 1-D XBeach model – the so-called profile

response saturation, where the lack of longshore sediment migration, despite the assumed obliquity of wave approach leads to the saturated profile erosion before the end of such longer events. Simulations of longer events were also intended to include the anticipated effects of growing storminess as another consequence of climate change. Two variants of wave breaking index γ were assumed, namely 0.78, which is typical for steep and short waves in the Baltic Sea developing in fetch-limited conditions, and 0.53, commonly applied in most XBeach applications. The main underlying reason was to inspect the effect of wave energy dissipation concentrated near the cliff foot for $\gamma = 0.78$, producing greater erosion vs. milder and more cross-shore distributed dissipation occurring for $\gamma = 0.53$. The uncertainty related to insufficient knowledge of the composition of grains in the colluviums near the toes of the cliffs was parameterized by assuming two values of mean sediment diameter $D_{50} = 0.22$ mm and $D_{50} = 0.4$ mm. It is clear that it is a non-trivial simplification of the actual granulometry of sediments forming colluviums and cliff foot. Still, such an assumption was found acceptable at the current stage of research. In sum: 3 return periods of storm parameters, 2 variants of seawater table elevation, 2 variants of D_{50} , 2 variants of event duration, and 2 variants of wave breaking index applied to the morphology of 4 cross-shore transects resulted in the execution of 192 simulations.

3. Results

The simulations were analyzed in terms of key variables, i.e. seawater table elevation of 1.3 and 2.0 m, wave breaking index of 0.53 and 0.78, and mean grain size diameter of 0.22 mm and 0.4 mm, bearing in mind standard and extended event time of 3 and 6 hours respectively. For each of those parameters tables are presented and the results are illustrated graphically for each of the four profiles.

The role of water table elevation is presented in Table 2. In general, the role of sea level rise of 0.7 m above the storm surge of 1.3 m is very significant: the rate of erosion can increase twofold (with respect to storm surge only) during extreme events, particularly the longer ones. The only exception occurred at km 231 for finer grains ($D_{50} = 0.22$ mm) and smaller wave breaking index $\gamma = 0.53$, which is not typically used – in this case the rates of erosion were similar (1.0–2.5 m for 1.3 m vs 1.5–2.0 m for 2 m of seawater table elevation). The role of elongated event duration (6 vs. 3 hours) is also clearly visible: the rates of erosion for longer events are significantly greater. Table 2 does not discriminate among erosion rates induced by waves of different return periods (20, 50 and 100 years), because the differences are not significant: it is well shown in Figures 8, 9 for the profile at km 410. In general, the impact of climate change-induced sea level rise on intensified cliff erosion is very high and points to potential difficulties of future management of cliffs, should they be protected.

Table 3 demonstrates the role of wave-breaking index. We can see that for $\gamma = 0.78$ the retreat of cliffs after extreme events is significantly (that is twice or more) greater than for $\gamma = 0.53$ no matter the storm duration or seawater table elevation. It is related to a more concentrated release of wave energy near the cliff toes, as for $\gamma = 0.53$ the

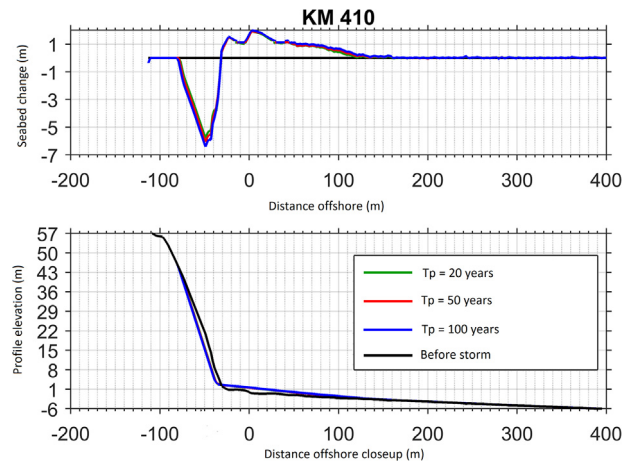


Figure 8 Response of cliff at km 410 to storm event for seawater table elevation 1.3 m, event duration 3 h, $D_{50} = 0.4$ mm and $\gamma = 0.78$.

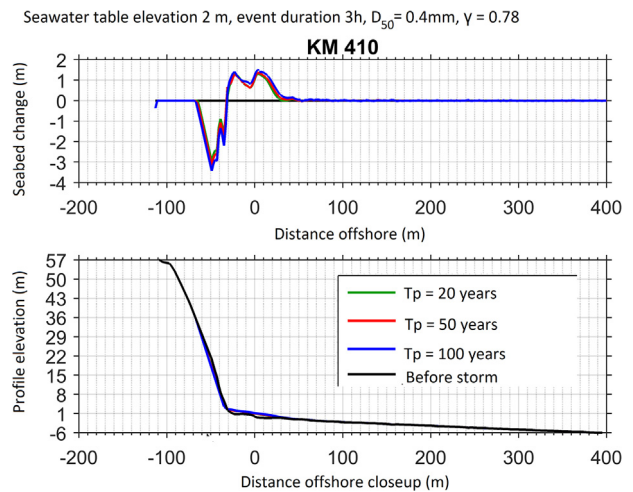


Figure 9 Response of cliff at km 410 to storm event for seawater table elevation 1.3 m, event duration 3 h, $D_{50} = 0.4$ mm and $\gamma = 0.78$.

spill-breaking process is initiated further offshore at greater nearshore depths of the seabed, whereas for $\gamma = 0.78$ the waves achieve greater steepness and generally plunge-break near the shoreline and cliff toe. This is generally consistent with observations of wave regimes in the marginal shelf Baltic Sea, where, due to limited fetch, the waves cannot achieve wavelengths typical for the oceans and remain steep and short. Plunge-breaking near the shoreline is enhanced by generally mildly sloping sea bottom in the nearshore region, where the bars are small or do not exist at all. Thus, the wave breaking concentrated near the shoreline will have adverse consequences for cliff erosion, adding to the exposure from sea level rise. This fact illustrates the key issue of cliff protection, should such schemes be considered: dispersion of concentrated fluxes of wave energy by coastal protection structures may be difficult from the engineering point of view; surely it is not possible without the erection of hard structures, which may be unacceptable from the perspective of nature-based solutions. The exam-

Table 2 Impact of seawater level elevation on cliff erosion.

Km 231	Event time 3 h				Event time 6 h			
	$D_{50} = 0.22$ mm		$D_{50} = 0.4$ mm		$D_{50} = 0.22$ mm		$D_{50} = 0.4$ mm	
	$\gamma = 0.53$	$\gamma = 0.78$	$\gamma = 0.53$	$\gamma = 0.78$	$\gamma = 0.53$	$\gamma = 0.78$	$\gamma = 0.53$	$\gamma = 0.78$
Seawater table elevation 1.3 m	1.0–2.5 m	1–2.2 m	0.2–0.4 m	1.0–1.6 m	1.0–2.4 m	2.5–5.8 m	0.6–1.5 m	2.2–5.0 m
Seawater table elevation 2 m	1.5–2 m	2.5–5.0 m	1.0–1.6 m	2.5–3.3 m	2.5–4.0 m	6.8 m	2.2–3.2 m	5.0–6.5 m
Km 235	Event time 3 h				Event time 6 h			
	$D_{50} = 0.22$ mm		$D_{50} = 0.4$ mm		$D_{50} = 0.22$ mm		$D_{50} = 0.4$ mm	
	$\gamma = 0.53$	$\gamma = 0.78$	$\gamma = 0.53$	$\gamma = 0.78$	$\gamma = 0.53$	$\gamma = 0.78$	$\gamma = 0.53$	$\gamma = 0.78$
Seawater table elevation 1.3 m	1.1–1.7 m	3.0–4.0 m	1.0–1.2 m	2.5–3.5 m	3.0–4.0 m	4.2 m	2.0–3.2 m	4.0 m
Seawater table elevation 2 m	2.5–3.5 m	3.5–3.8 m	2.2–3.0 m	2.0–3.2 m	3.8 m	4.2–4.8 m	3.5 m	3.2–4.5 m
Km 404	Event time 3 h				Event time 6 h			
	$D_{50} = 0.22$ mm		$D_{50} = 0.4$ mm		$D_{50} = 0.22$ mm		$D_{50} = 0.4$ mm	
	$\gamma = 0.53$	$\gamma = 0.78$	$\gamma = 0.53$	$\gamma = 0.78$	$\gamma = 0.53$	$\gamma = 0.78$	$\gamma = 0.53$	$\gamma = 0.78$
Seawater table elevation 1.3 m	0.6–0.8 m	1.2–2.0 m	0.4–0.6 m	1.0–1.6 m	2.4 m	4.0–4.5 m	1.5 m	3.5–4.0 m
Seawater table elevation 2 m	1.8 m	2.5–3.0 m	1.3–1.6 m	2.0–3.0 m	3.2–4.0 m	6.0 m	3.0 m	5.0 m
Km 410	Event time 3 h				Event time 6 h			
	$D_{50} = 0.22$ mm		$D_{50} = 0.4$ mm		$D_{50} = 0.22$ mm		$D_{50} = 0.4$ mm	
	$\gamma = 0.53$	$\gamma = 0.78$	$\gamma = 0.53$	$\gamma = 0.78$	$\gamma = 0.53$	$\gamma = 0.78$	$\gamma = 0.53$	$\gamma = 0.78$
Seawater table elevation 1.3 m	1.6 m	1.8–3.0 m	1.6 m	1.3–2.4 m	2.4–3.0 m	4.0–5.0 m	2.2 m	3.0–4.2 m
Seawater table elevation 2 m	2.2–3.0 m	3.0–3.8 m	2.0–2.4 m	3.0–3.2 m	3.2–4.5 m	5.5–6.0 m	3.2–3.5 m	5.0–5.8 m

Table 3 Impact of wave breaking index on cliff erosion.

Km 231	Event time 3 h				Event time 6 h			
	$z = 1.3 + 0.7 = 2$ (m)		$z = 1.3$ (m)		$z = 1.3 + 0.7 = 2$ (m)		$z = 1.3$ (m)	
	$D_{50} = 0.22$ mm	$D_{50} = 0.4$ mm	$D_{50} = 0.22$ mm	$D_{50} = 0.4$ mm	$D_{50} = 0.22$ mm	$D_{50} = 0.4$ mm	$D_{50} = 0.22$ mm	$D_{50} = 0.4$ mm
$\gamma = 0.53$	1.5–2.0 m	1.0–1.6 m	1.0–2.5 m	0.2–0.4 m	2.5–4.0 m	2.2–3.2 m	1.0–2.4 m	0.6–1.5 m
$\gamma = 0.78$	2.5–5.0 m	2.5–3.3 m	1.0–2.2 m	1.0–1.6 m	6.8 m	5.0–6.5 m	2.5–5.8 m	2.2–5.0 m
Km 235	Event time 3 h				Event time 6 h			
	$z = 1.3 + 0.7 = 2$ (m)		$z = 1.3$ (m)		$z = 1.3 + 0.7 = 2$ (m)		$z = 1.3$ (m)	
	$D_{50} = 0.22$ mm	$D_{50} = 0.4$ mm	$D_{50} = 0.22$ mm	$D_{50} = 0.4$ mm	$D_{50} = 0.22$ mm	$D_{50} = 0.4$ mm	$D_{50} = 0.22$ mm	$D_{50} = 0.4$ mm
$\gamma = 0.53$	2.5–3.5 m	2.2–3.0 m	1.1–1.7 m	1.0–1.2 m	3.8 m	3.5 m	3.0–4.0 m	2.0–3.2 m
$\gamma = 0.78$	3.5–3.8 m	2.0–3.2 m	3.0–4.0 m	2.5–3.5 m	4.2–4.8 m	3.2–4.5 m	4.2 m	4 m
Km 404	Event time 3 h				Event time 6 h			
	$z = 1.3 + 0.7 = 2$ (m)		$z = 1.3$ (m)		$z = 1.3 + 0.7 = 2$ (m)		$z = 1.3$ (m)	
	$D_{50} = 0.22$ mm	$D_{50} = 0.4$ mm	$D_{50} = 0.22$ mm	$D_{50} = 0.4$ mm	$D_{50} = 0.22$ mm	$D_{50} = 0.4$ mm	$D_{50} = 0.22$ mm	$D_{50} = 0.4$ mm
$\gamma = 0.53$	1.8 m	1.3–1.6 m	0.6–0.8 m	0.4–0.6 m	3.2–4.0 m	3 m	2.4 m	1.5 m
$\gamma = 0.78$	2.5–3.0 m	2.0–3.0 m	1.2–2.0 m	1.0–1.6 m	6 m	5 m	4.0–4.5 m	3.5–4.0 m
Km 410	Event time 3 h				Event time 6 h			
	$z = 1.3 + 0.7 = 2$ (m)		$z = 1.3$ (m)		$z = 1.3 + 0.7 = 2$ (m)		$z = 1.3$ (m)	
	$D_{50} = 0.22$ mm	$D_{50} = 0.4$ mm	$D_{50} = 0.22$ mm	$D_{50} = 0.4$ mm	$D_{50} = 0.22$ mm	$D_{50} = 0.4$ mm	$D_{50} = 0.22$ mm	$D_{50} = 0.4$ mm
$\gamma = 0.53$	2.2–3.0 m	2.0–2.4 m	1.6 m	1.6 m	3.2–4.5 m	3.2–3.5 m	2.4–3.0 m	2.2 m
$\gamma = 0.78$	3.0–3.8 m	3.0–3.2 m	1.8–3.0 m	1.3–2.4 m	5.5–6.0 m	5.0–5.8 m	4.0–5.0 m	3.0–4.2 m

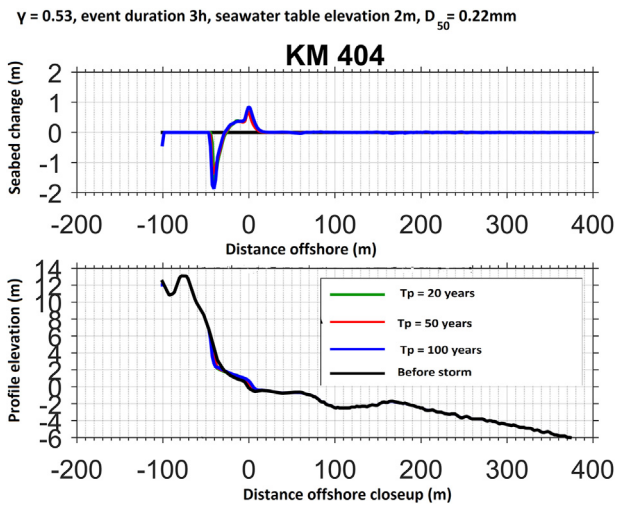


Figure 10 Response of cliff at km 404 to storm event for $\gamma = 0.53$, seawater table elevation 2 m, event duration 3 h and, $D_{50} = 0.22$ mm.

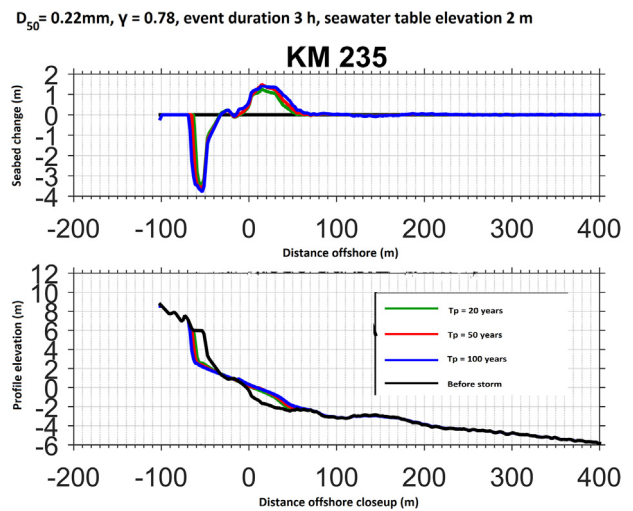


Figure 12 Response of cliff at km 235 to storm event for $D_{50} = 0.22$ mm, $\gamma = 0.78$, event duration 3 h and seawater table elevation 2 m.

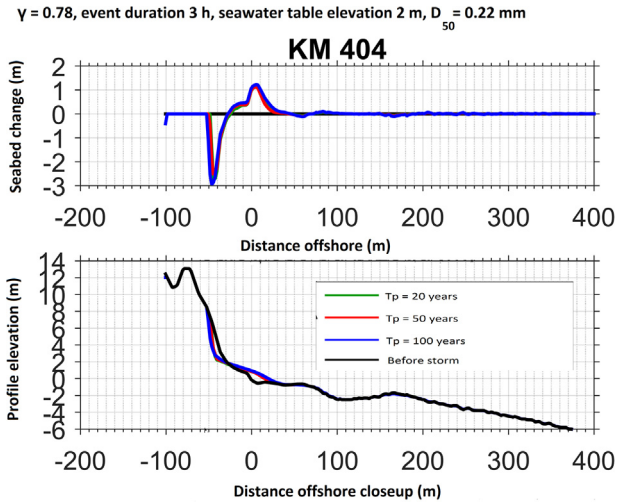


Figure 11 Response of cliff at km 404 to storm event for $\gamma = 0.78$, seawater table elevation 2 m, event duration 3 h and, $D_{50} = 0.22$ mm.

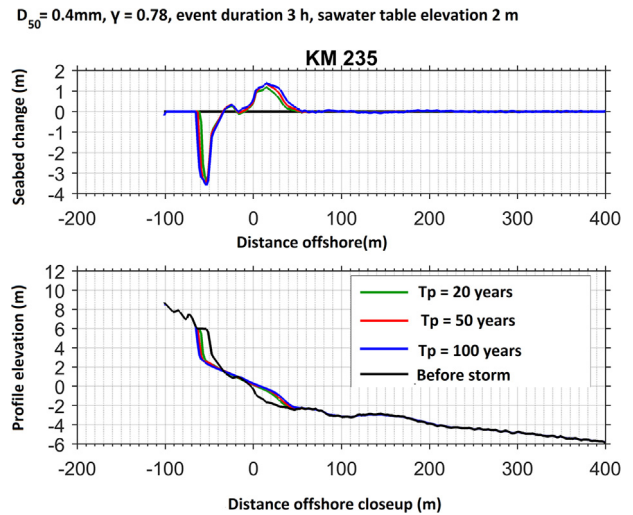


Figure 13 Response of cliff at km 235 to storm event for $D_{50} = 0.4$ mm, $\gamma = 0.78$, event duration 3 h and seawater table elevation 2 m.

ples of the role of wave breaking index are presented in Figures 10 and 11.

The impact of mean grain size D_{50} on the cliff erosion is presented in Table 4. As could be expected the retreat of cliff foot is greater for smaller D_{50} (0.22 mm), but it is not very significant – in most cases, it is greater by 1.0–1.5 m than for the coarser grains of 0.4 mm. The smallest differences were observed for larger wave breaking index ($\gamma = 0.78$) and longer storm duration (6 h). It can be interpreted as the ‘saturation’ of cliff retreat due to the fact that longshore processes were not incorporated in 1-D XBeach simulations, despite the assumed obliquity of the wave approach. Given the lack of notable nearshore bars in the nearshore area, the results point to the need for detailed determination of sediment composition in the colluviums in the vicinity of cliff toes. A more accurate assessment of sediment compositions should aid in more precise

follow-up simulations. Figures 12 and 13 are graphical representations of the apparently low significance of the role of D_{50} .

The last element related to cliff retreat is the event duration. Tables 2, 3, and 4 show that the rates of erosion for the shorter event of 3 hours demonstrated greater variability, whereas a saturation tendency for the longer event of 6 hours was observed, i.e. the simulated retreats mostly fell between 4 and 6 m. It definitely points to the limitations of a 1-D model, which established a dynamic equilibrium in the absence of longshore hydrodynamic parameters and the constant storm surge (seawater level) of either 1.3 or 2.0 m. Exemplary results of event duration significance are given in Figures 14 and 15.

Table 4 Impact of mean grain size D_{50} on cliff erosion.

Km 231	Event time 3 h				Event time 6 h			
	$z = 1.3 + 0.7 = 2$ (m)		$z = 1.3$ (m)		$z = 1.3 + 0.7 = 2$ (m)		$z = 1.3$ (m)	
	$\gamma = 0.53$	$\gamma = 0.78$	$\gamma = 0.53$	$\gamma = 0.78$	$\gamma = 0.53$	$\gamma = 0.78$	$\gamma = 0.53$	$\gamma = 0.78$
$D_{50} = 0.22$ mm	1.5–2.0 m	2.5–5.0 m	1.0–2.5 m	1.0–2.2 m	2.5–4.0 m	6.8 m	1.0–2.4 m	2.5–5.8 m
$D_{50} = 0.4$ mm	1.0–1.6 m	2.5–3.3 m	0.2–0.4 m	1.0–1.6 m	2.2–3.2 m	5.0–6.5 m	0.6–1.5 m	2.2–5.0 m
Km 235	Event time 3 h				Event time 6 h			
	$z = 1.3 + 0.7 = 2$ (m)		$z = 1.3$ (m)		$z = 1.3 + 0.7 = 2$ (m)		$z = 1.3$ (m)	
	$\gamma = 0.53$	$\gamma = 0.78$	$\gamma = 0.53$	$\gamma = 0.78$	$\gamma = 0.53$	$\gamma = 0.78$	$\gamma = 0.53$	$\gamma = 0.78$
$D_{50} = 0.22$ mm	2.5–3.5 m	3.5–3.8 m	1.1–1.7 m	3.0–4.0 m	3.8 m	4.2–4.8 m	3.0–4.0 m	4.2 m
$D_{50} = 0.4$ mm	2.2–3.0 m	2.0–3.2 m	1.0–1.2 m	2.5–3.5 m	3.5 m	3.2–4.5 m	2.0–3.2 m	4.0 m
Km 404	Event time 3 h				Event time 6 h			
	$z = 1.3 + 0.7 = 2$ (m)		$z = 1.3$ (m)		$z = 1.3 + 0.7 = 2$ (m)		$z = 1.3$ (m)	
	$\gamma = 0.53$	$\gamma = 0.78$	$\gamma = 0.53$	$\gamma = 0.78$	$\gamma = 0.53$	$\gamma = 0.78$	$\gamma = 0.53$	$\gamma = 0.78$
$D_{50} = 0.22$ mm	1.8 m	2.5–3.0 m	0.6–0.8 m	1.2–2.0 m	3.2–4.0 m	6 m	2.4 m	4.0–4.5 m
$D_{50} = 0.4$ mm	1.3–1.6 m	2.0–3.0 m	0.4–0.6 m	1.0–1.6 m	3.0 m	5 m	1.5 m	3.5–4.0 m
Km 410	Event time 3 h				Event time 6 h			
	$z = 1.3 + 0.7 = 2$ (m)		$z = 1.3$ (m)		$z = 1.3 + 0.7 = 2$ (m)		$z = 1.3$ (m)	
	$\gamma = 0.53$	$\gamma = 0.78$	$\gamma = 0.53$	$\gamma = 0.78$	$\gamma = 0.53$	$\gamma = 0.78$	$\gamma = 0.53$	$\gamma = 0.78$
$D_{50} = 0.22$ mm	2.2–3.0 m	3.0–3.8 m	1.6 m	1.8–3.0 m	3.2–4.5 m	5.5–6.0 m	2.4–3.0 m	4.0–5.0 m
$D_{50} = 0.4$ mm	2.0–2.4 m	3.0–3.2 m	1.6 m	1.3–2.4 m	3.2–3.5 m	5.0–5.8 m	2.2 m	3.0–4.2 m

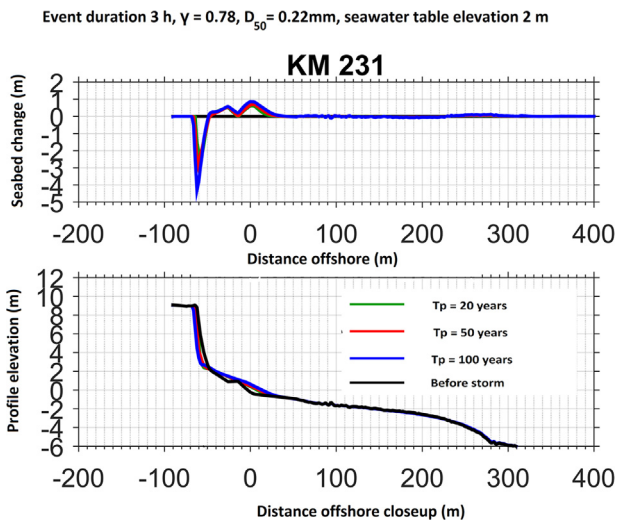


Figure 14 Response of cliff at km 231 to storm event for event duration 3 h, seawater table elevation 2 m, $D_{50} = 0.22$ mm and $\gamma = 0.78$.

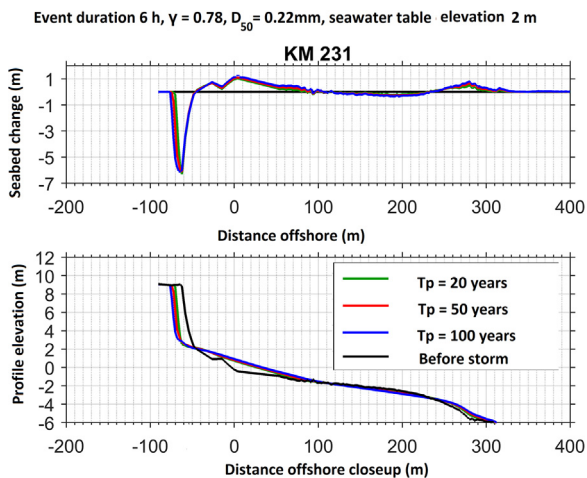


Figure 15 Response of cliff at km 231 to storm event for event duration 6 h, seawater table elevation 2 m, $D_{50} = 0.22$ mm and $\gamma = 0.78$.

4. Discussion

The role of sea level rise appears to be the most important element impacting the future evolution of cliffs on the Polish Baltic Sea coast. The simulations, juxtaposed in Table 2 and illustrated by Figures 8 and 9 showed that in the presence of that rise the cliffs will be undergoing fast retreat because the cliff toes will be exposed to permanent wave attack. Thus, one should expect enhanced acceleration of the retreat in the coming decades with respect to recent observations. Hence, maintenance of the cliffs, which remain unprotected nowadays, should start being considered; if left unprotected the fast retreat may result in the loss of important environmental features of active cliffs – both seascape/landscape qualities as well as ecosystem services. On the other hand, any protection measures should be constructed in such a way that the cliffs will remain active, and their key aim will be the reduction of erosion. There-

fore, low-crested structures together with periodically repeated beach fills should be considered in the longer perspective. However, one should keep in mind that such structures somewhat violate the paradigm of nature-based solutions. Thus, in order to minimize the volume of unnatural materials the cores of low-crested structures should be made of geo-bags, covered by large stones (boulders), not natural for the Polish soft cliffs. In this way, the boulders would be the only non-natural component of the protection structures, being only a small fraction of their total volume.

The value of wave breaking index γ turned out to be another vital aspect of the results. They are juxtaposed in Table 3 and illustrated in Figures 10–11. The high value of 0.78 is associated with the character of wave climates in the Baltic Sea that develop in conditions of limited fetch. Such waves are steep and short and they release their energy in closer proximity to the shoreline (and cliff toe). Delayed release of wave energy, concentrated near the shoreline, exacerbates the rates of cliff erosion, in particular when nearshore bathymetries are largely featureless – without or only with very tiny nearshore bars. Such morphologies point to sand deficit, which will be discussed later. Concentrated wave energy releases generate additional difficulties in case low-crested protection schemes are considered: on the one hand they should only reduce wave energy dissipation to ensure the active status of cliffs, on the other hand, those structures must be robust enough to resist rapid bursts of high-intensity energy fluxes, induced by artificial underwater structures. Finally, it should be recalled that smaller values of wave breaking index (e.g. 0.53) are encountered on oceanic beaches. Such waves are generated in unlimited fetch conditions, are much longer and thus much more energetic. They would probably rapidly destroy soft cliffs on the Polish coast, so concentrated wave energy release near cliff toes, however adverse for the conditions of cliffs, is an inherent feature of beach processes in the Baltic Sea basin.

The role of the mean diameter of grain size D_{50} turned out to be surprisingly of secondary importance, at least in the XBeach simulations of cliff erosion. The results are juxtaposed in Table 4 and illustrated in Figures 12–13. It may be related to the fact that high-energy hydrodynamic regimes, occurring during extreme events, usually produce similar retreats of cliff toes. Nevertheless, such results indicate the necessity of in-depth studies of the granulometric composition of cliffs. The looming modeling difficulties concern significant fractions of cohesive sediments in cliff massifs. They probably lose most of their cohesion as a result of (1) permanent contact with water, and (2) collapse of the upper sub-stratum forming loosely compacted colluvium with residual strength parameters. As will be demonstrated in the next paragraph more precise determination of cliff lithology will serve for better reproduction of the aftermaths of extreme events with 2-D modelings, incorporating the impacts of longshore sediment migration.

2-D migration of sediments, eroded from the cliffs during extreme events, is also related to the next element of the modeling of aftermaths of extreme events, namely the event duration. Simulations results can be traced in Tables 2, 3, and 4 and are illustrated in Figures 14 and 15. The most important outcome is the saturation of cliff retreat and profile reconfiguration, induced by the restrictions

of 1-D model, despite the assumed obliquity of the wave approach. This is another indication toward incorporation of a more complex 2-D modeling framework, already identified in the analysis of the surprisingly low impact of D_{50} . However, another aspect needs to be considered, namely the evolution of hydrodynamics after the peak of extreme events. Apart from decaying wave heights, the drop of sea-water table elevation must be incorporated, since the fast drop of that table will induce significant offshore migration of finer particles, eroded from cliff bodies. Hence, the main outcome of the study is the need for follow-up simulations of storm recession patterns. In connection with more accurate identification of granulometric composition of cliffs they will provide much more accurate assessments of cliff retreat under climate change embracing both offshore and longshore sediment migration and the resulting segregation of portions of sediment eroded away and remaining in the nearshore region. Such simulations will be consistent with Winowski (2015), who noticed enhanced retreat of cliffs when a storm is followed by a rapid fall of seawater table. They should also explain why the cross-shore bathymetric transects are generally featureless – exacerbating the exposure to erosion.

The last element impacting the rates of cliff retreat due to extreme events is the return period of those events. The simulations have shown that events with a return period of 20 years produce almost the same consequences as those whose return periods are 50 and 100 years. First, it is caused by rather non-vital growth of wave parameters, associated with such events. Second, it is definitely related to the limitations of 1-D models, described before. One important aspect of the simulations though, is that the cliffs turned out to be very sensitive to storm surges combined with sea level rise, so the sequence of smaller extreme events, whose recurrence period is closer to 1–5 years, may be much more impactful. This issue is another avenue of follow-up research, which should incorporate the period of storm recession and include both offshore and longshore sediment migration.

The results show that XBeach simulations are applicable to other soft cliffs. However, one should always keep in mind the limitations illustrated in the description of XBeach package applied herein. Nevertheless, it appears that XBeach simulations can serve as 1st step of postulated integrated simulations, involving slope stability analyses of a cliff face undercut by extreme events under the sea level rise regime. This 2nd group of simulations could serve as 2nd stage of comprehensive studies on cliff retreat under climate change.

5. Conclusions and recommendations

1. The role of sea level rise exacerbating the conditions of cliffs seems pivotal: the performed simulations show that it is the most important factor in the enhanced retreat of cliffs. It appears that the protection of cliffs may be ultimately enforced by sea level rise.
2. The role of the wave breaking index is important, as its high-value results in the release of wave energy near the shoreline. Therefore, it also works in favor of enhanced cliff erosion. Moreover, it will be a critical factor in the design of future protection structures (low-

crested breakwaters) that should reduce the wave impact, but simultaneously do not stop natural cliff evolution completely.

3. The role of sediment composition turned out to be less significant. However, in connection with event duration, the results clearly show the limitations of 1-D modeling frameworks. Therefore, follow-up simulations should be executed including aftermaths of extreme events, such as the rapid drop of water elevation and longshore sediment migration.
4. The role of the recurrence period of extreme events was found rather insignificant. Therefore, more impactful events should be investigated: they may consist of a sequence of less powerful extreme events with recurrence periods in the range of 1–5 years. Such sequences should be analyzed in conjunction with their aftermath, described above.
5. The results show that XBeach simulations can be applicable to other soft cliffs. On the other hand, the complexity and multitude of marine and terrestrial phenomena that shape the evolution of cliffs point to future research avenues. They should aim at integrated research in which XBeach simulations could be the 1st and the associated analyses of cliff slope stability the 2nd step of investigations. The former will describe the coastal component that initiates cliff retreat, whereas the latter will provide information on extended, terrestrial effects resulting from that initial erosion driven by marine forces. Thus, collaboration among hydraulic and civil engineers and researchers is postulated.

Declaration of competing interest

The author declares that they have no known competing financial interests or personal relationships that could have appeared to influence the work reported in this paper.

References

- BACC II – BALTEX Assessment of climate Change for the Baltic Sea Basin, 2015. Second Assessment of Climate Change for the Baltic Sea Basin. The BACC II Author Team. Regional Climate Studies. Springer, Cham, Heidelberg, New York, Dordrecht, London. <https://doi.org/10.1007/978-3-319-16006-1>
- Boniecka, H., Gajda, A., Gawlik, W., Marcinkowski, T., Olszewski, T., Szmytkiewicz, M., Skaja, M., Szmytkiewicz, P., Chrzastowska, N., Piotrowska, D., 2013. Monitoring and investigation of the current condition of the coastal zone: assessment of the effectiveness of coastal protection schemes implemented under the long-term “Programme of Coastal Protection”. Maritime Institute in Gdańsk, 250 Technical Rep. No. 6793 (in Polish).
- British Standard Code of Practice for Maritime Structures, 2000. British Standard Code of practice for Maritime structures Part 1. General Criteria. The British Standards Institution, London BS 6349: Pt. 1.
- Dnv-Os, 2011. Design of Offshore Wind Turbine Structures. Det Norske Veritas, Bærum.
- Eberhards, G., 2003. The sea coast of Latvia. Morphology Structure. Coastal Processes. Risk zone. Forecast. Coastal Protection and Monitoring. Latvijas Universitate, Riga, Latvia.

- Florek, W., Kaczmarzyk, J., Majewski, M., Olszak, I.J., 2008. Lithological and extreme event control of changes in cliff morphology in the Ustka region. *Landform Analysis* 7, 53–68 (in Polish).
- Geodynamic Map of Polish Baltic Sea Coastal Region, 2007. Sheets 3, 4 and 25. Polish Nat. Geol. Inst., Warsaw.
- IPCC AR5 Synthesis Report, 2014. https://www.ipcc.ch/site/assets/uploads/2018/02/SYR_AR5_FINAL_full.pdf (accessed 14th June 2021).
- Kostrzewski, A., Zwoliński, Z., 1986. Operation and morphologic effects of present-day morphogenetics processes modelling the cliffed coast of Wolin Island, N.W. Poland. In: Gardiner, V. (Ed.), *International Geomorphology*. John Wiley and Sons, New York, 1231–1252.
- Kostrzewski, A., Zwoliński, Z., 1995. Present-day morphodynamics of the cliff coasts of Wolin Island. *J. Coastal Res.* 22 (Sp. Iss), 293–303.
- Kostrzewski, A., Zwoliński, Z., Winowski, M., Tylkowski, J., Samołyk, M., 2015. Cliff top recession rate and cliff hazards for the sea coast of Wolin Island (Southern Baltic). *Baltica* 28 (2), 109–120.
- Kostrzewski, A., Musielak, S., Furmańczyk, K., Dudzińska-Nowak, J., Osadczuk, K., Winowski, M., Wolski, T., Zwoliński, Z., 2021. Chapter 10. The current evolution of South Baltic coastal relief. In: Zwoliński, Z. (Ed.), *Contemporary transformations of Poland's relief*. Bogucki Wydawnictwo Naukowe, Poznań, 575–619, (in Polish). <https://doi.org/10.12657/9788379863822-10>
- Łabuz, T., 2012. Coastal response to climatic changes: discussion with emphasis on southern Baltic Sea. *Landform Anal* 21, 43–55.
- Milerienė, R., Gulbinskas, S., Blazauskas, N., Dailidienė, I., 2008. Geological indicators for integrated coastal zone management. In: *US/EU-Baltic International Symposium, 27–28 May 2008, Tallinn, Estonia*, 1–4.
- Pruszek, Z., Zawadzka, E., 2005. Vulnerability of Poland's coast to sea level rise. *Coast Eng. J.* 47, 131–155.
- Ryabchuk, D., Kolesov, A., Chubarenko, B., Spiridonov, M., Kurennoy, D., Soomere, T., 2011. Coastal erosion processes in the eastern Gulf of Finland and their links with long-term geological and hydrometeorological factors. *Boreal Environ. Res.* 16, 117–137.
- Sterr, H., 2008. Assessment of vulnerability and adaptation to sea level rise for coastal zone of Germany. *J. Coastal Res.* 24, 380–393.
- Subotowicz, W., 1982. *Cliff lithodynamics*. Ossolineum Publ., Gdańsk (in Polish).
- Terefenko, P., Giza, A., Paprotny, D., Kubicki, A., Winowski, M., 2018. Cliff Retreat Induced by Series of Storms at Miedzyzdroje (Poland). *J. Coastal Res.* 85, 181–185. <https://doi.org/10.2112/SI85-037.1>
- USGS Professional Paper, 2004. *Formation, Evolution, and Stability of Coastal Cliffs – Status and Trends*. U.S. Department of the Interior, U.S. Geological Survey, 129.
- Winowski, M., 2008. Geomorphological effects of ice melt on Wolin island cliffs. *Landform Analysis* 9, 222–225 (in Polish).
- Winowski, M., 2015. The activity of landslides on the cliffcoast on the Wolin Island under the influence of hydrometeorological events with high morphogenetic potential (Bay of Pomerania – Southern Baltic). *Landform Analysis* 28, 87–102 (in Polish). <https://doi.org/10.12657/landfana.028.007>
- Wiśniewski, B., Wolski, T., 2009. Catalogues of sea level storm surges and falls and extreme water levels on the Polish coast. *Marine Acad. Publ., Szczecin*, 156 pp. (in Polish).

Available online at www.sciencedirect.com

ScienceDirect

journal homepage: www.journals.elsevier.com/oceanologia

ORIGINAL RESEARCH ARTICLE

Knowledge Transfer Platform FindFISH – Numerical Forecasting System for the Marine Environment of the Gulf of Gdańsk for Fisheries

Lidia Dzierzbicka-Głowacka^{a,*}, Maciej Janecki^a, Dawid Dybowski^a,
Artur Nowicki^a, Agata Zaborska^a, Piotr Pieckiel^b, Michał Wójcik^{b,c},
Tomasz Kuczyński^b, Jacek Wittbrodt^d

^a Institute of Oceanology, Polish Academy of Science, Sopot, Poland

^b Maritime Institute – Gdynia Maritime University, Gdynia, Poland

^c Gdańsk University of Technology, Gdańsk, Poland

^d The Association of Marine Fishermen – Producers' Organization in Władysławowo, Poland

Received 1 September 2023; accepted 30 January 2024

Available online 19 February 2024

KEYWORDS

Sustainable fishing;
Numerical modeling;
Forecasting habitat

Abstract Fast access to expert knowledge is very valuable, especially in the context of decision-making. Fishermen can use this knowledge to diagnose hydrological and hydrochemical conditions in which fish stocks should be the most abundant. In response to this need, a digital service has been developed. It is a service created within the FindFISH project, which provides the results of all developed models: hydrodynamic, biochemical, and *Fish* – for selected commercially caught fish species (herring, sprats, cod, and flounder). Our research revealed that the FindFISH service can enhance fishing efficiency and quality by approximately 40%, significantly increasing expected profits. In practical applications, we observed a 50% to 70% concordance between the fishing grounds recorded by fishermen and those identified by the FindFISH Platform. The website runs dynamically in operational mode, allowing visualization of forecasts in the form of maps, time series, spatial data, and tables.

© 2024 Institute of Oceanology of the Polish Academy of Sciences. Production and hosting by Elsevier B.V. This is an open access article under the CC BY-NC-ND license (<http://creativecommons.org/licenses/by-nc-nd/4.0/>).

* Corresponding author at: Institute of Oceanology, Polish Academy of Sciences, Powstańców Warszawy 55, 81–712 Sopot, Poland.

E-mail address: dzierzb@iopan.pl (L. Dzierzbicka-Głowacka).
Peer review under the responsibility of the Institute of Oceanology of the Polish Academy of Sciences.



Production and hosting by Elsevier

<https://doi.org/10.1016/j.oceano.2024.01.004>

0078-3234/© 2024 Institute of Oceanology of the Polish Academy of Sciences. Production and hosting by Elsevier B.V. This is an open access article under the CC BY-NC-ND license (<http://creativecommons.org/licenses/by-nc-nd/4.0/>).

1. Introduction

The *FindFISH Knowledge Transfer Platform* is a response to the main problem identified in the fisheries sector, which is the reduction in the profitability of fishing. Additional issues include increasing operating costs incurred by fishermen, the need for fishermen to embark on longer and farther fishing trips in search of fish, the capture of low-value or small quantities of fish, conducting activities on the brink of profitability due to rising costs, the limitation of fishing quotas, and the associated difficulties.

The Polish fishing industry appears to be looking for efficient approaches in this area at the moment. As a result of increasing nutritional awareness among Poles, there is a growing trend in fish consumption (European Commission, 2009). New technologies enable meeting the growing demand, but at the same time significantly increase the pressure on fishing supply. As a result, many fish resources are overexploited, posing a threat to the marine ecosystem of which fish are an integral part (Fousiya et al., 2023; Kemp et al., 2023; Laghari et al., 2022).

Each individual fish stock is part of a larger and complex marine ecosystem, whose functioning is difficult to predict, and providing a precise description of its functioning is a challenging task. Factors influencing fish resources in the marine environment include rapid technological advancements, the use of modern equipment and high-quality apparatus, marine pollution, the development of coastal cities, and global warming (Fousiya et al., 2023; Laghari et al., 2022). The scale and pace of environmental changes in the marine environment make it difficult for researchers to control and create ecosystem models, i.e., models of marine living organisms.

Fishermen have extensive practical knowledge of fish resource behavior, which is difficult to acquire through other means, and their experience becomes significant when contextualized in scientific research for the study of marine ecosystem dynamics.

The fishing industry is often accused of environmental destruction, excessive fishing, and the decline in seabird and marine mammal populations. Imposed bans elicit an understandable reluctance among fishermen to cooperate with environmental scientists. Unfortunately, the lack of research and mutual information only increases the level of risk assessed based on expert opinions.

In recent years, it seems that the barriers between fishermen and scientists, who previously regarded each other with mutual mistrust, are beginning to diminish. Fishermen spend much more time at sea than scientists, such as hydrobiologists or ecophysicists. Scientists should consider the practical experiences and information provided by fishermen in their research. In turn, as fishermen learn how scientists arrive at their conclusions, they will be able to trust the research results.

The costs associated with industrial fishing continue to increase. One way to limit these costs is by using technological developments in the localization of fish shoal and the estimation of their size. Specialized electronic devices that help fishing operations are used for shoal localization, biomass estimation, fish size and quantity assessment, monitoring of trawl and fishing net parameters, monitoring fish behavior, and assessing the nature and structure of

the seabed and sediment. The diversity of devices allows equipment selection for different types of vessels and fishing methods.

The development of sonar technology used in fisheries has made significant advances over the past two decades. It is estimated that the use of modern sonars brings about tangible economic savings, both in terms of fuel consumption and shorter fishing time, by approximately 25% (European Commission, 2009; Nakayama et al., 2023). However, this endeavor remains expensive and currently difficult to implement, as not every fishing vessel is equipped with such devices as sonars, echo sounders, or acoustic cameras. Furthermore, not every skipper has sufficient knowledge of sonar technology and the experience necessary to interpret echograms to benefit from their use. However, conducting in situ measurements for the purpose of precise diagnosis of the marine environment in real-time is impossible due to the high cost of such monitoring.

The Common Fisheries Policy (CFP) (European Commission, 2009) is not solely concerned with creating regulations that limit fishing in terms of quantity. Its objective is also to establish quality standards (known as technical measures) that protect fish populations and the ecosystems they inhabit. The common denominator connecting all these measures is the fact that they aim to make fishing more selective.

Selective fishing is a challenging task that depends largely on the specific conditions prevailing in a given region at sea. The proposed numerical method, the *FindFISH Platform* presented in this study, is intended to be a helpful tool for fishermen to solve the aforementioned problems for the purpose of effective planning of fishing trips.

The specific environmental conditions of the Gulf of Gdańsk influence its ecosystem (Dzierzbicka-Głowacka et al., 2011). The occurrence of fauna typical for a low-salinity environment is characteristic of this region. In addition, regular spring-summer algal blooms have become a significant environmental and economic problem. More than thirty species of phytoplankton found in the Baltic Sea are classified as harmful to human health (Öberg, 2017). The investigation of the constantly evolving environment presents a significant obstacle for researchers from diverse scientific disciplines. While emerging technical solutions facilitate the work of scientists, they do not provide an ideal solution.

Numerical modelling is significantly more efficient than field studies using buoys, ships, or satellite measurements. This explains the widespread use of mathematical models and computer simulations as new methods to understand the governing principles of the natural world in the digital age. This particularly applies to issues at the intersection of several disciplines, which is the norm in oceanographic research.

Numerical modelling of hydrodynamic and biochemical phenomena in the aquatic environment is a complex task. It is necessary to consider various factors, such as the inflow of nutrient-rich freshwater from rivers and the inflow of saltwater from the North Sea. Input data for the model, such as information on river inflows, atmospheric data, and boundary conditions, must be of high quality. These are the main forcing factors of the model and their quality significantly influences the accuracy and alignment

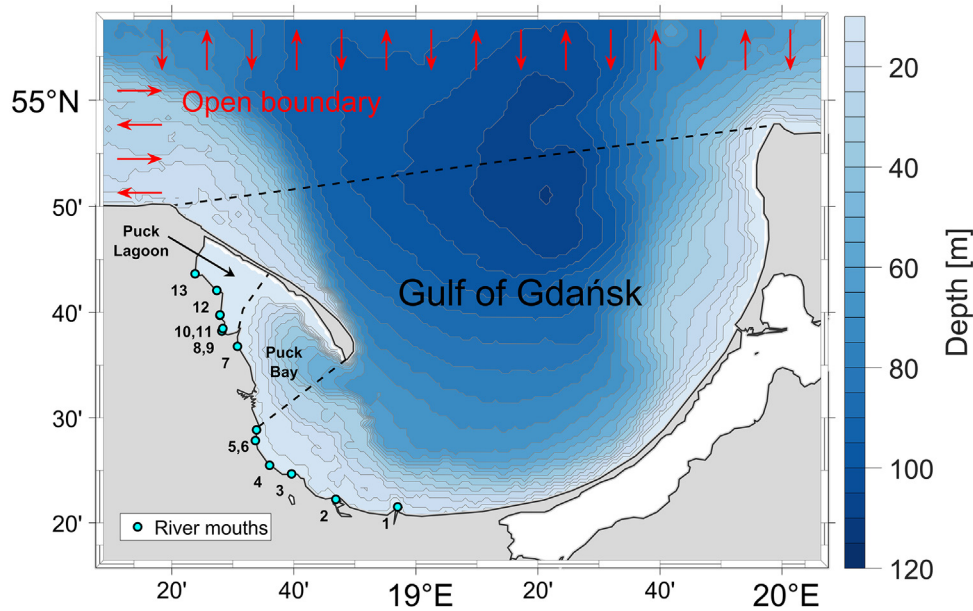


Figure 1 *EcoFish* model domain (including the *Fish Module*) with bathymetry. Points 1 to 13 represent the mouths of rivers included in the model.

of the obtained results with reality. Due to the highly dynamic nature of the environment, only simultaneous environmental/observational and numerical studies can provide the most reliable picture of the actual state of the studied aquatic area. High-resolution results in terms of time and space can provide local-scale information on the formation of eddies, mixing of waters with different densities, or the occurrence of intrusions. Additionally, studying basic parameters of the aquatic environment and the processes occurring within it forms the basis for generating new research hypotheses and disseminating knowledge to build cooperation between entities operating in the scientific and socio-economic spheres.

The construction of the *FindFISH Knowledge Transfer Platform* through the Numerical System for Predicting the Environmental Conditions of the Gulf of Gdańsk for Fisheries is based on *in situ* research, environmental data (physicochemical and hydrometeorological), quantitative and qualitative data on fishing, and numerical modelling of hydrodynamic, physicochemical, and biological parameters in the Gulf of Gdańsk region (Figure 1).

The primary goal of this research was to develop and validate the *FindFISH* digital service, a sophisticated platform that integrates hydrodynamic, biochemical, and fish models for selected commercially important fish species such as herring, sprats, cod, and flounder. This service, designed to operate dynamically in real-time, provides crucial data visualizations including maps, time series, and spatial data that assist fishermen in identifying the most abundant fishing grounds under prevailing hydrological conditions.

By leveraging expert knowledge and advanced modeling techniques, the *FindFISH* platform aims to significantly increase the quality and quantity of fish catches, thereby improving the profitability of fishing operations. Moreover, it seeks to contribute to the sustainable management of marine resources by enabling more targeted and efficient fishing practices, reducing unnecessary by-

catch, and minimizing the ecological impact on marine ecosystems.

2. Material and methods

The work within the project was divided into five main stages and implemented in three blocks: environmental research, numerical work, and IT tasks (Figure 2) (Dzierzbicka-Głowacka et al., 2018).

2.1. Assessment of the Gulf of Gdańsk environmental condition

In the first stage, an assessment of the environmental condition of the Gulf of Gdańsk was conducted (Kuczyński et al., 2023; Zaborska et al., 2023, 2019). It was carried out through the analysis of the current (as of the date of the study) chemical and ecological state of the Gulf, with a focus on the ichthyofauna, based on existing and newly acquired data obtained within the project.

2.2. Fishing expeditions

The second stage of the study consisted of fishing expeditions (Krzemień and Wittbrodt, 2023). During these voyages, environmental measurements were conducted using specialized instruments, specifically the Midas CTD+ instrument from Valeport, United Kingdom. The objective was to gather physicochemical data, primarily water temperature, salinity, and dissolved oxygen levels. These data, along with notes from fishing logs and other information provided by the captains, such as meteorological data, quantitative and qualitative catch results, observations, and comments, were then used to determine habitat preferences of selected fish species and develop the *Fish Module*. Further-

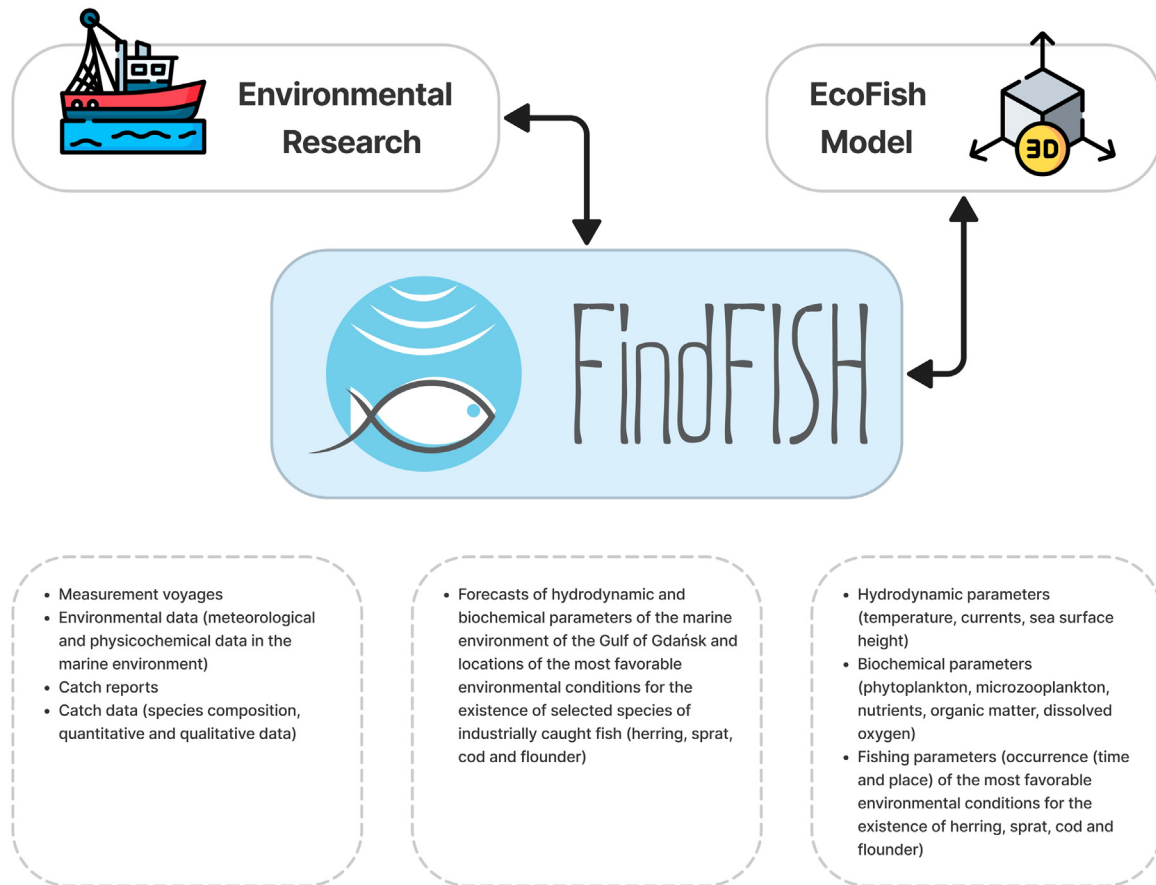


Figure 2 Structure of the FindFISH platform.

more, these data were used for the validation of the ecohydrodynamic model of the Gulf of Gdańsk – *EcoFish*. In addition to catch results, the fishermen were required to provide supplementary information in the surveys, including:

- Vessel name
- Date and time of deployment and retrieval of the fishing gear (start time for towed gear)
- Fishing square
- Deployment positions of the fishing gear (initial and final positions for towed gear)
- Wind speed and direction
- Cloud cover
- Precipitation
- Air temperature and sea surface temperature
- Sea state (wave height)

2.3. Habitat preferences of selected fish species

Analysis of data obtained during fishing expeditions allowed determination of habitat preferences for commercially harvested fish species in the Gulf of Gdańsk (Pieckiel et al., 2023). A total of 2,857,288 records, acquired with the CTD instrument, were used in the analysis. These records were derived from datasets comprising a single instrument deployment for each respective fish species, with the following numbers:

- 44 records for cod (*Gadus morhua*)
- 61 records for flounder (*Platichthys flesus*)
- 202 records for herring (*Clupea harengus*)
- 156 records for sprat (*Sprattus sprattus*)

Water parameters were measured using the MIDAS CTD+ instrument mounted on the fishing trawl. The analyzed data were based on four parameters measured by the instrument:

- Pressure
- Conductivity
- Temperature
- Dissolved oxygen (Table 5.1)

Salinity was converted using Valeport Software Ltd.’s software with a resolution of 0.01 and an accuracy level of ± 0.02 .

All the investigated parameters were analyzed using the boxplot method with varied filtering applied. The next step involved analyzing the correlation between the values of the investigated parameters and the catch sizes of individual fish species. For each parameter, the median value was calculated for each fishing series, representing the prevailing conditions at the fish concentration locations, based on the most frequently occurring value in the filtered dataset for each series. This analysis was performed using Pearson’s correlation and analysis of variance (ANOVA).

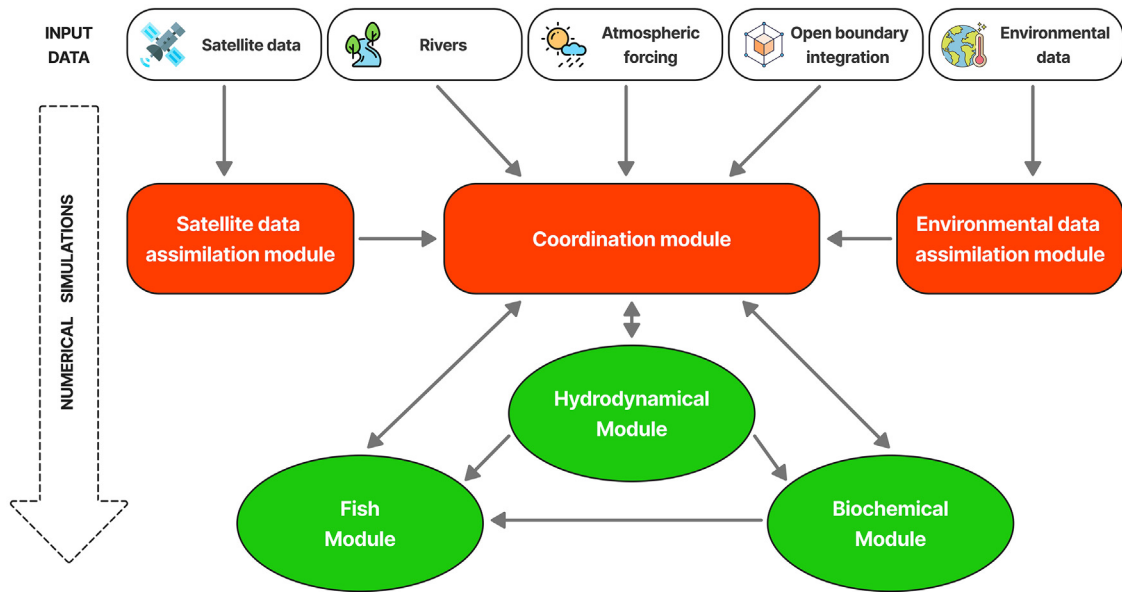


Figure 3 Diagram of the *EcoFish* ecohydrodynamic model with the *Fish Module*.

Principal component analysis (PCA) was performed on the entire dataset, aiming to identify the most significant parameters determining commercial catches. Median values for each fishing trip were prepared for the test, using data filtered from the dataset based on fishing depths below 15 meters. The data underwent Hellinger transformation using the Vegan package version 2.6-2 (Piecki et al., 2023).

2.4. The *EcoFish* model

The *EcoFish* model is a three-dimensional predictive ecohydrodynamic model of the Gulf of Gdańsk (Janecki et al., 2023b,c; Janecki and Dzierzbicka-Głowacka, 2023; Nowicki et al., 2023a,b). It was developed in the third stage of the project and consists of three main modules: hydrodynamic (Janecki et al., 2022, 2021), biochemical (Janecki et al., 2023a), and *Fish Module* (Janecki et al., 2023a; Janecki and Dzierzbicka-Głowacka, 2023) (Figure 3). The *EcoFish* model, along with the *Fish Module*, enables the monitoring of the marine environment and the tracking and prediction of changes occurring within it. It also allows determining the most favorable environmental conditions for the habitat of specific commercially harvested fish species in the study area.

Additionally, the *EcoFish* model includes modules for input and output data processing, data assimilation from various sources, and a coordinating module for operational mode (Janecki et al., 2022, 2021). Satellite data on sea surface temperature and chlorophyll *a* concentration, assimilated in the *EcoFish* model, are obtained from the *SatBałtyk* database (www.satbaltyk.pl; Woźniak et al., 2011a,b).

Meteorological data with a 72-hour forecast are retrieved from the UM Interdisciplinary Centre for Mathematical and Computational Modelling of the University of Warsaw (ICM UW) weather model and used in the *3D CEMBS* and *EcoFish* models as atmospheric forcing.

The *EcoFish* model is based on the source code of the Parallel Ocean Program (POP) model, which was also

used to develop the *3D CEMBS* ecosystem model of the Baltic Sea (www.cembs.pl; Dzierzbicka-Głowacka et al., 2013a,b). Data from the operational *3D CEMBS* model are used in real-time to determine the boundary conditions at the water-water interface in the *EcoFish* model. The horizontal resolution of the *EcoFish* model is 575 m; and it has 26 vertical layers (levels), each with a thickness of 5 m.

2.5. The *Fish Module*

Implementation of the *Fish Module* required the use of fuzzy logic (Janecki and Dzierzbicka-Głowacka, 2024). Fuzzy logic is a generalization of classical two-valued logic, where a range of intermediate values exists between the states of 0 (false) and 1 (true), representing the degree of membership of an element in a set. Fuzzy systems encompass techniques and methods that handle imprecise, uncertain, or vague information. They allow for describing phenomena with multiple meanings that cannot be captured by classical theory and two-valued logic. These systems process knowledge symbolically and encode it in the form of fuzzy rules. A fuzzy system is applicable here because the presence of fish is influenced by many interconnected factors and it is not possible to rely solely on individual environmental parameters.

The programming work for creating the *Fish Module* (Janecki and Dzierzbicka-Głowacka, 2023) was carried out using software from the Matlab environment, specifically the “Fuzzy Logic Toolbox” extension. Initially, the boundary values of parameters determining optimal conditions for the habitat of the investigated fish species (herring, sprat, cod, and flounder) were established. For this purpose, data describing the environmental preferences of fish in the study area (Gulf of Gdańsk) were utilized. These data were specified within the project (Piecki et al., 2023) based on fishing records, literature data, and expert knowledge. They include information on recorded fishing grounds, the time

of occurrence, catch sizes, and environmental parameter values (temperature, salinity, depth, and dissolved oxygen concentration).

Next, validation was conducted to verify whether the temperature, salinity, and oxygen data derived from the *EcoFish* model exhibited sufficient agreement with the measurement data to serve as input for the *Fish Module*. Details regarding the validation of physical variables (temperature and salinity) are presented in the articles (Janecki et al., 2021, 2023c). Details regarding the validation of dissolved oxygen concentration are provided in the articles (Janecki et al., 2023a,b).

Subsequent work focused on the *Fish Module* itself. A rule base was created for reasoning in the fuzzy system, and a set of membership functions was developed for each species considered. After parameterization and calibration of the entire system, the correctness of the results provided by the *Fish Module* needed to be verified. For this purpose, the Habitat Suitability Index (HSI) parameter was validated by graphically comparing the values obtained from the *Fish Module* with catch performance results from oceanographic-fishing voyages conducted on the *r/v Baltica* by the National Marine Fisheries Research Institute (Radtke et al., 2017; 2018a,b; 2019a,b; 2020a,b; 2021) and fishing expeditions carried out within the *FindFISH* project.

2.6. The *FindFISH* Platform

Finally, as part of the fourth stage, the visualization of measurement data from sondes and fishing operations, quantitative and qualitative data, and results from the *EcoFish* model and the *Fish Module* was performed. These data were presented in the form of tables, charts, and maps on the *FindFISH Platform* ([FindFISH project's website, 2023](#)), which was developed within the project (Biernaczyk et al., 2023). The platform provides real-time access to forecasts of hydrodynamic and biochemical parameters, as well as the locations of the most favorable environmental conditions for the habitat of specific commercially harvested fish species in the Gdańsk Bay.

2.7. *FindFISH* testing

The fifth stage involved testing the functionality of the *FindFISH* numerical system. The efficiency of the voyages using the *FindFISH* numerical system was compared with those without it by comparing the results of the *Fish Module* with actual fishing outcomes. The test results helped determine whether the system is a useful source of information for fishermen, scientists, and fisheries administrators, and whether its use leads to improved performance and increased competitiveness (Dzierzbicka-Głowacka et al., 2023).

The final step is the implementation of the *FindFISH Platform* for operational use, which includes both the technical aspects of launching the platform by IT personnel on the target server and its introduction for use by fishermen on their fishing boats.

3. Results and discussion

3.1. Assessment of the environmental state of the Gulf of Gdańsk

3.1.1. Ecological assessment

Fish species in the Gulf of Gdańsk constitute a crucial element of the entire Baltic Sea ecosystem. The taxonomic composition of the ichthyofauna in the study area includes freshwater, marine, brackish, and migratory species. Each of these groups of organisms has specific preferences regarding environmental conditions. The Gulf of Gdańsk does not have a strictly marine or freshwater character, and most fish species occurring in these waters exhibit a wide range of tolerance to prevailing conditions. The spatial distribution of specific fish assemblages in the Gulf of Gdańsk is also related to the presence of typical habitats formed by both abiotic and biotic elements. Abiotic factors include, among others, temperature, salinity, dissolved oxygen, and components of non-living habitat. Another important factor influencing the occurrence of certain species is the food base. Fish species have specific dietary preferences and group themselves in areas where food of suitable quality and quantity is available, both in the water column (zooplankton) and on the seabed (zoobenthos) (RDSM, 2012, as amended). In addition to natural factors, anthropogenic factors also influence the ichthyofauna of the Gulf of Gdańsk, which are consequences of human activities. One of the primary factors of this kind is fishing, which directly affects the stocks of commercially harvested fish and indirectly impacts other components of the ecosystem through trophic interactions. Other anthropogenic factors are associated with the input of various substances into marine waters, leading to negative changes related to overall water trophic conditions, such as eutrophication.

Based on the projected trends for selected factors, the environmental state of the Gulf of Gdańsk was assessed in relation to the ichthyofauna (Table 1).

The Gulf of Gdańsk is one of the most exploited fishing areas in Polish marine waters (Piecki, 2013). The main target species of fishing here are cod, flounder, herring, and sprat. In the 1970s and 1980s, significant quantities of freshwater fish, such as pike and roach, were also caught, mainly in the Puck Bay. The bay encompasses both spawning areas for many fish species and habitats for fry development and feeding. In addition to the commercially exploited marine fish species, numerous protected fish species occur here, benefiting from the diversity of habitats created by the specific biotic and abiotic conditions of this region. Despite the concentration of various sectors related to maritime ports in Gdynia and Gdańsk, which are among the most important ports in the Baltic Sea, as well as intensive fishing activities, the Gulf of Gdańsk stands out among Polish marine areas for its exceptional natural values. These values are not only due to fish resources, but also due to plant formations, waterbird populations, and marine mammals, whose aggregations are concentrated at the mouth of the Vistula River (Grusza, 2009). However, despite its high natural values and the inclusion of a significant part of the Gulf of Gdańsk in the area-based nature protection forms of "Natura 2000", a weak overall ecological state of the waters is observed, and

Table 1 Forecasted trends for factors influencing the ichthyofauna in the Gulf of Gdańsk (Kuczyński et al., 2023).

Factor	Trend
Natural	
Temperature	Negative – temperature will increase, affecting the reproductive success of certain fish species, facilitating the spread of invasive species that may negatively impact food competition and pose a direct threat to native fauna. Seasonal changes will disrupt the development of marine organisms.
Salinity	Neutral – salinity will not change significantly and will not have a negative impact on the overall reproductive success of all fish species.
Dissolved oxygen	Negative – hypoxic and anoxic areas will expand, resulting in increased mortality of eggs and fry and prompting fish to migrate from key feeding areas.
Food base	Negative – the food base will change and diminish, becoming insufficient in quantity, and changes in quality will affect fish condition.
Habitats	Negative – the habitat area will decrease, and the prevailing conditions in the habitats will change, unable to support the development of all fish species and provide sufficient resources for exploitation.
Anthropogenic	
Pollution	Neutral – concentrations of polluting substances will decrease, which may alleviate the effects of their impact on fish organisms, but new hazardous substances may emerge.
Eutrophication	Neutral – currently observable effects of increased trophic conditions in the basin will not intensify and there will be no degradation of natural habitats for the ichthyofauna.
Fishing	Negative – fishing activities at levels preventing natural recruitment of new fish generations, and the capture of undersized individuals of various species negatively affect the populations of other animal species.

the forecast for the well-being of the ichthyofauna in the coming years is not favorable. A detailed description of the ecological assessment of the Gulf of Gdańsk is presented in the paper by Kuczyński et al. (2023).

3.1.2. Chemical status assessment

The Gulf of Gdańsk is not a highly polluted area with chemical substances; on the contrary, the levels of many pollutants are below the permissible threshold values, indicating a good environmental state. Monitoring of the abiotic and biotic elements of the ecosystem shows that the concentrations of PCBs, PAHs, dioxins, and chlorinated pesticides in marine waters have been decreasing over the past decade, which is consistent with global trends (Zaborska et al., 2019). However, a decreasing trend is not observed for all investigated compounds. For example, concentrations of heavy metals measured in recent years are not lower than those measured in the 1970s and 1980s. A decrease in the concentrations of selected heavy metals (Cd, Hg, Pb) has been observed in fish tissues, while the concentrations of other metals (Cu, Zn, As) have increased (Polak-Juszczak, 2013). Additionally, the concentration of EC may increase or, at least, remain at a constant level. This is due to the wide use of these compounds and the inefficiency of current wastewater treatment technologies in their removal. The most polluted areas in the Gulf of Gdańsk are the Vistula River mouth, where large amounts of pollutants transported from the catchment area through the Vistula River accumulate, and the semi-enclosed area of the Puck Bay (Puck Lagoon), with numerous point sources of pollution and limited water exchange. Among the compounds discussed (Zaborska et al., 2023, 2019), the greatest threat to the Gulf of Gdańsk appears to be posed by brominated compounds, tin-organic compounds, and substances from the group of emerging pollutants.

Although restrictions and bans on the use of most of the pollutants discussed have led to a decrease in their concentrations in the Gulf of Gdańsk, future scenarios may vary. This is due to the potential re-release of pollutants resulting from surface runoff, seepage water supply, and/or resuspension of previously deposited contaminants in the seabed. According to climate models, the Baltic Sea region will experience changes in precipitation patterns, prolonged droughts, and an increase in both frequency and magnitude of floods (Bełdowska et al., 2015; Helsinki Commission, 2013). Floods, in particular, can serve as significant secondary sources of pollution (Saniewska et al., 2014); therefore, additional pollutant loads from land sources can be expected in the future. Furthermore, human activities (e.g., hydroengineering works) and previously unknown sources of pollution (e.g., shipwrecks and chemical ammunition) may contribute to increased pollutant concentrations in certain areas of the Gulf of Gdańsk.

A modern approach to monitoring programs should include the assessment of ecological risk using integrated indicators, such as integrated biomarkers and predictive models. Most “emerging” pollutants can affect marine organisms even at very low concentrations. The impact of pollutants on the hormonal system can lead to reproductive disorders, developmental changes, and ultimately long-term infertility and species extinction. In the case of the Gulf of Gdańsk, the first signs of reproductive disorders, such as the occurrence of fish with both male and female gonads, have already been observed (Guellard et al., 2015). Moreover, pollutants are never present in the environment as single substances, but as mixtures of various compounds, which, even in small doses, can have a strong impact on organisms through synergistic or additive interactions with other substances and chronic exposure. Therefore, a holistic approach to studying the impact of pollutants on organisms is recommended during the assessment of the health status of

the ecosystem. This is also crucial for evaluating the actual risk posed by the mixture of chemicals present in the environment.

An important element of assessing the ecosystem status in the Gulf of Gdańsk would be the identification of areas particularly vulnerable to pollution, known as hotspots (e.g., sewage outflows, untreated wastewater, ports, river mouths, locations of sunken ammunition and shipwrecks) and the intensified and detailed monitoring of these areas. It is also essential to integrate measurements of chemical concentrations with biological effects measurements.

A detailed analysis of the chemical status of the Gulf of Gdańsk in terms of trace metal concentrations, radionuclides, and organic pollutants, based on long-term data, has been conducted and presented in the works by Zaborska et al. (2019, 2023).

3.2. Fishing expeditions

Between the years of 2018 and 2022, as part of the Find-FISH initiative, a total of 587 fishing expeditions were conducted utilizing MIDAS CTD+ instruments. During this period, fishing vessels (8-10 m long) carried out 280 trips, while larger trawlers (over 18 m in length) conducted 307 trips. Trawlers focused their fishing activities on pelagic species, such as sprat (*Sprattus sprattus*) and herring (*Clupea harengus*); as well as cod (*Gadus morhua*), until the complete ban on cod fishing in the eastern part of the Baltic Sea was implemented in July 2019 (Council Regulation (EU) 2019/1838). The fishing boats primarily targeted flounder (*Platichthys flesus*), and in periods when flounder was not available on the fishing grounds, they caught herring, sea trout, and perch. During fishing expeditions, a total of 4,780 kg of flounder were caught using static gear, and during research trawls, 1,440,958 kg of sprat, 850,427 kg of herring, and 22,861 kg of cod (during the period when it was allowed to be caught) were harvested.

3.3. Preferences of industrially caught fish in the Gulf of Gdańsk

The selected model species were the most intensively exploited fish species by Polish fishing between 2014 and 2021. In order of highest to lowest tonnage of landings, these species were (according to data from the Fisheries Monitoring Center in Gdynia):

- sprat (*Sprattus sprattus*),
- herring (*Clupea harengus*),
- flounder (*Platichthys flesus*),
- cod (*Gadus morhua*).

Salinity, temperature, and dissolved oxygen are crucial factors that determine the distribution of fish in the water column. In the study area, these relationships are particularly important for the modeled pelagic species such as herring and sprat (Akimova et al., 2016; Saraux et al., 2014), while the subsequent modeled species such as cod (Gollock et al., 2006; Tirsgaard et al., 2015) and especially the representative of flatfish – flounder (Cabral et al., 2021; Duthie and Houlihan, 1982; Fonds et al., 1992;

Hutchinson and Hawkins, 2004; Martinho et al., 2009) are less sensitive to these parameters. The Baltic Sea is an atypical marine basin with the lowest salinity worldwide, relatively shallow depths, and high water dynamics (ICES, 2018; Meier et al., 2022), making the results of the conducted analyses unique for the studied species compared to other water bodies around the world. The main objective of the project is to parameterize the analyzed factors for the fish shoals, for the adult form, within the size range allowed for commercial fishing.

The studied parameters (mainly temperature) are currently undergoing changes in the Baltic Sea basin associated with climate warming (Meier et al., 2022). Many studies focus on modelling the impact of these changes in the Baltic Sea on major fish resources such as herring and sprat (Bauer et al., 2019; Harvey et al., 2003; Maravelias et al., 2000; Tamm et al., 2018; Voss et al., 2011). The precise determination of values for the analyzed parameters, as in this study, has not yet been described in the Baltic Sea, which hinders comparative analyses. Currently, in many cases worldwide, this knowledge is based on mathematical models mainly relying on temperature and the correlation of water column temperature with air temperature, as in the case of studies by Freitas et al. (2021), making the data used here innovative.

In the presented study, the locations of fish shoals mainly concentrated in the water column layer with stabilized temperature values. For pelagic fish, these were most often the thermocline layers, while for other fish species, they were depths below the thermocline. In monthly resolution and during seasonal changes throughout the year, this parameter exhibited a high repeatability of values, oscillating around 5.8°C. In the autumn months, this parameter showed the highest variability due to significant water dynamics.

Salinity increases in the Baltic Sea in deep-water regions, which was also observed during conducted fishing expeditions, where the halocline was typically exceeded, and salinity above 11 was frequently observed. However, fishing activities primarily revolved around a salinity level of 7.9, and it was not a strategic parameter in the selection of fishing grounds.

The most common fishing depth was 48.09 m, but it was significantly dependent on the optimal temperature and varied throughout the year, reaching 65.7 m. Dissolved oxygen values also changed drastically from full saturation at 100% to extreme values dropping to 1%. However, the majority of fishing expeditions remained within the level of 78.1%. Both parameters exhibited high dynamic throughout the year. These parameters were also not strategic targets in the selection of fishing grounds.

The success of the fishing was mainly dependent on temperature, where a statistically significant correlation was observed between the decrease in temperature and the increase in the fish catch, especially for herring and sprat. The remaining analyzed parameters did not show such dependencies.

3.4. The EcoFish model

The numerical model is a tool that can be used to predict ecosystem properties in time and space with satisfactory ac-

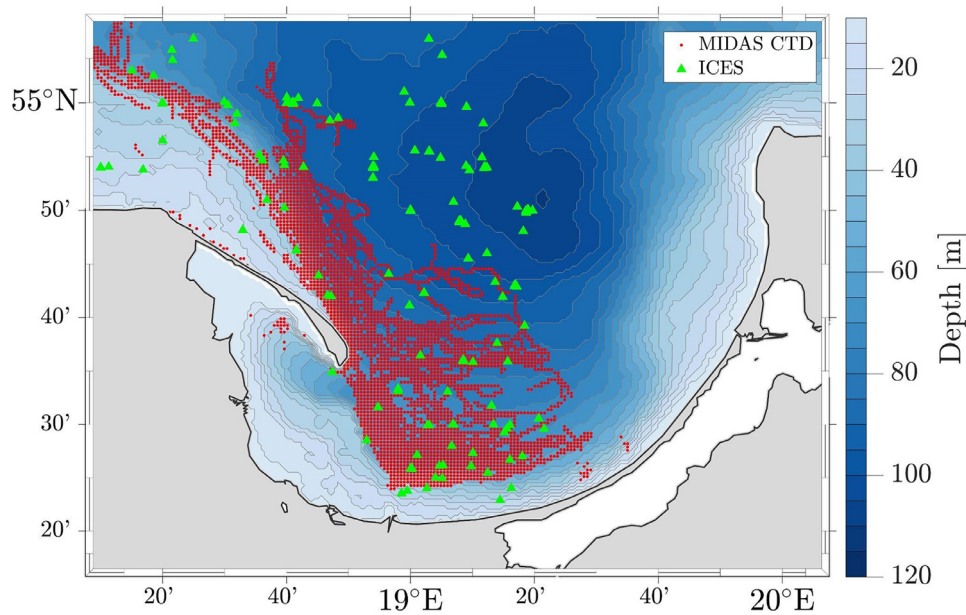


Figure 4 Locations of *in situ* data.

curacy. It can also be used to test hypotheses and assumptions and to conduct numerical experiments.

Hydrodynamic models enable the estimation of major physical parameters describing the marine environment, such as currents, water temperature, salinity, and others, such as mixed layer depth, turbulent diffusion coefficient, or sea surface height (SSH). The same applies to biochemical models, which allow for the determination of the state of the ecosystem in the studied area by considering additional parameters and their mutual interactions.

Starting from the global ecosystem model (Moore et al., 2001) and based on a regional model for the Baltic Sea (Dzierzbicka-Głowacka et al., 2013b), the implementation of the biochemical component was carried out in the *EcoFish* model for the Gulf of Gdansk. Basic parameters of the marine ecosystem were defined, including phytoplankton and zooplankton biomass, primary production, living and dead organic matter, chlorophyll *a* concentration, and dissolved oxygen (O_2), as well as chemical parameters such as nitrates (NO_3), phosphates (PO_4), and silicates (SiO_3).

The statistical validation of the *EcoFish* model was conducted to verify the accuracy of the results in terms of seasonal and spatial variability. To validate the hydrodynamic component of the *EcoFish* model, the results from a 7-year simulation from January 1, 2014, to December 31, 2020, preceded by a 2-year spin-up, were used. The experimental data source, used to validate the temperature and salinity of water in the *EcoFish* model, is the online hydrochemical database provided by the International Council for the Exploration of the Sea (ICES) and the data collected during fishing expeditions carried out as part of the FindFISH project (Figure 4).

The validation revealed that the results obtained from the *EcoFish* for temperature and salinity are in good agreement with *in situ* observations (Table 2).

Analyzing the 7-year simulation run of the *EcoFish* model (from January 2014 to December 2020), it is evident that

Table 2 Statistical comparison of modeled temperature and salinity with *in situ* data (Janecki et al., 2021, 2023c).

Database	Pearson's r	RMSE	STD	Bias
Temperature				
ICES	0.94	1.33°C	3.66°C	-0.36°C
MIDAS	0.87	1.83°C	3.57°C	-0.34°C
Salinity				
ICES	0.94	0.80	1.27	-0.01

the temperature of the Gulf of Gdansk undergoes significant seasonal variations, primarily influenced by changes in air temperature and solar radiation. These temperature fluctuations are largely shaped by convection and mixing processes driven by wind action. The influence of the Vistula River on the water temperature of the Gulf is also apparent, with its waters raising the temperature during spring and summer and lowering it in autumn. The lowest average surface water temperature values throughout the model domain occur in February. During this month, surface waters across the entire basin exhibit similar temperatures, with differences not exceeding 2.5°C. In the following months, surface water temperatures increase, most rapidly in the coastal zone. The highest spatial variations are observed in May and June, with differences reaching approximately 7°C. The highest average surface water temperatures occur in August.

The geographical location of the Gulf of Gdansk and its distinct bathymetry are significant factors in the variation in salinity. Significant differences in salinity distribution occur between the shallow coastal area and the deeper parts of the Gulf, which exhibit characteristics similar to open sea waters with a typical stratified structure of the Baltic Sea (including the presence of a halocline and thermocline). The

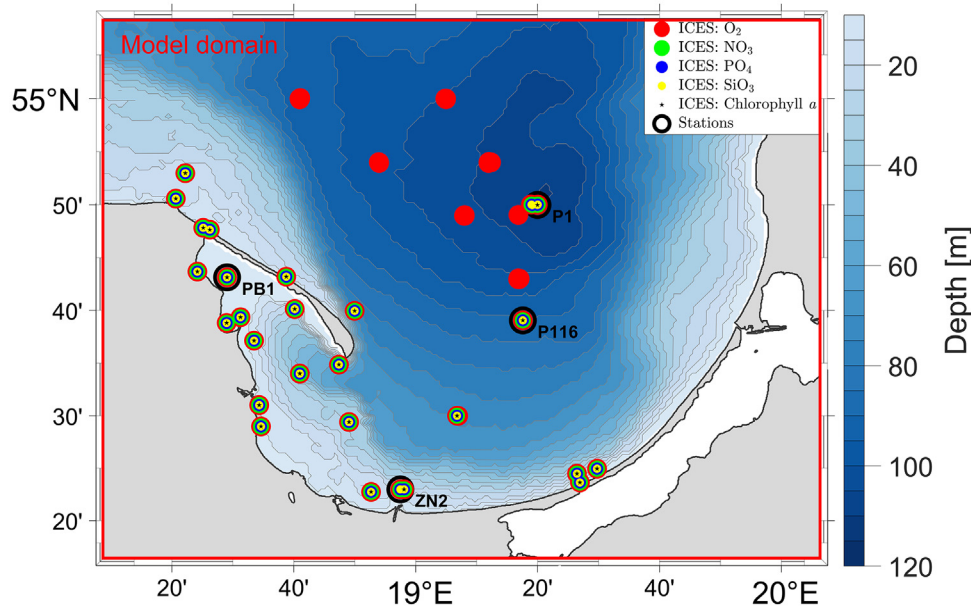


Figure 5 Locations of measurement points from the ICES database for the years 2017–2020 used for the validation of biochemical variables from the *EcoFish* model. (Source: [Janecki et al., 2023a](#), [Figure 1](#))

shallow coastal zone of the Gulf of Gdańsk is influenced by freshwater inflows from rivers and other surface runoff. The Vistula River has the greatest impact on salinity changes, as its massive volumes of freshwater (with an average flow exceeding $1000 \text{ m}^3 \text{ s}^{-1}$) cause salinity to decrease below 7. Its influence is also noticeable in the surface layer of the deep-water part of the Gulf of Gdańsk, primarily during spring, when river waters mix with seawater and are transported into the depths of the Gulf.

When analyzing the distribution of currents in the study domain, a distinctive area can be identified along the Hel Peninsula, where the strongest surface currents occur, often exceeding $20 \text{ cm} \cdot \text{s}^{-1}$. The prevailing current directions in this area depend on the season. Northwest currents are typically observed during the summer months, causing water to be pushed from the Gdańsk Basin towards the open sea and accompanied by the formation of coastal upwellings. In other months, southeast currents prevail in this region, transporting water towards the inner Gulf of Gdańsk. The distribution of surface currents near the mouth of the Vistula River is also peculiar, with the eastern current being the most common, dispersing the waters from the Vistula along the Gulf coast. The prolonged presence of this current restricts the extent of Vistula water dispersion and reduces the zone of freshwater mixing with seawater ([Janecki et al., 2021, 2023c](#)).

The accuracy of the results obtained from the biochemical component of the *EcoFish* model was verified by comparing them with *in situ* data. The ICES database was also used for this purpose. The majority of ICES data for the years 2017–2020 came from the shallow-water zone near Puck Bay and the southern part of the Gulf of Gdańsk. Only a small portion (mainly regarding dissolved oxygen) pertained to greater depths in the open sea ([Figure 5](#)).

The most important variable that needed validation was dissolved oxygen (O_2), as it is used as an input parameter for

the *Fish Module* ([Janecki and Dzierzbicka-Głowacka, 2023](#)). Furthermore, we verified nitrate (NO_3), phosphate (PO_4), silicate (SiO_3), and chlorophyll *a* concentration sum of three phytoplankton groups implemented in the *EcoFish*. The model simulation for which the validation was conducted covered the period 2017–2020.

In the *EcoFish* model, all depth levels have a thickness of 5 m. However, the experimental data from ICES had non-uniform sampling density in the water column (e.g., 0 m, 1 m, 2.5 m, 4 m, 5 m, 10 m, 20 m). As a result, some ICES measurements corresponded to the same *EcoFish* model value, or an ICES measurement was taken at a depth on the boundary of two adjacent model levels. This led to unnatural distortion of the validation results. To eliminate the negative impact of non-uniform sampling density, interpolation (and extrapolation) between the *EcoFish* model levels with a step of 0.1 m was applied. Among the available interpolation and extrapolation methods, the Piecewise Cubic Hermite Interpolation (PCHIP) was chosen, which interpolates both the function and its first derivative ([Janecki et al., 2023a](#)). [Table 3](#) presents the final results of the comparison between the *EcoFish* model (biochemical component) and the experimental data available from ICES.

The *EcoFish* model has a tendency to systematically overestimate (for oxygen, nitrates, and phosphates) and underestimate (for chlorophyll *a* and silicates) the results. However, these values do not deviate significantly from the experimental data and are acceptable after careful examination of the underlying causes (see: [Janecki et al., 2023b](#); [Janecki and Dzierzbicka-Głowacka, 2023](#)).

The *EcoFish* numerical model is a key component of the “*Knowledge Transfer Platform – FindFISH*” service, which provides information on hydrodynamic and biochemical variables for the Gulf of Gdańsk region. Through numerical simulations derived from the *EcoFish* model and results for temperature, salinity, and dissolved oxygen, the

Table 3 Statistical comparison of the biochemical variables from the *EcoFish* model with ICES data for the period 2017–2020.

Parameter	ICES			EcoFish		Comparison	
	N	Mean	STD	Mean	STD	RMSE	<i>r</i>
O ₂ [mmol m ⁻³]	3329	306.32	102.58	325.17	56.78	70.86	0.75
NO ₃ [mmol m ⁻³]	2370	2.47	2.80	4.25	4.12	3.77	0.46
PO ₄ [mmol m ⁻³]	2592	0.69	0.82	1.21	0.48	0.63	0.65
SiO ₃ [mmol m ⁻³]	2610	17.99	13.07	10.64	7.18	10.32	0.62
Chlorophyll <i>a</i> [mg m ⁻³]	972	3.84	3.01	2.89	2.44	2.77	0.50

Fish Module (Janecki and Dzierzbicka-Głowacka, 2023) operates by utilizing these variables and employing fuzzy logic methodology to create maps of the most favorable environmental conditions for commercially harvested fish species in the Gulf of Gdańsk region, namely herring, sprat, cod, and flounder.

Validation of the most important physical variables (Janecki et al., 2021, 2023c) and biochemical variables (Janecki et al., 2023a,b) of the *EcoFish* model ensures that the results of numerical simulations are consistent with the measurement data, thus providing a reliable set of input data for the *Fish Module* (Janecki and Dzierzbicka-Głowacka, 2023).

3.5. The *Fish Module*

Following the stages of implementation, parameterization, and testing, the *Fish Module* was launched on the project server. In conjunction with the operational *EcoFish* model, this allowed for the creation of forecasts (and reanalyses) for the most favorable environmental conditions (HSI) for all species considered in the project, with certain limitations for flounder (only from July to November).

Due to the lack of access to detailed numerical catch data for herring, sprat, cod, and flounder in the Gulf of Gdańsk region (other than that collected in the project), the validation of the *Fish Module* was conducted through a graphical comparison of the HSI results with the fishing efficiency maps for these four species presented in the bimonthly journal “Wiadomości Rybackie” by the National Marine Fisheries Research Institute (Radtke et al., 2017, 2018a,b, 2019a,b, 2020a,b). To assess the alignment of the results obtained from the *Fish Module* with the catch efficiencies recorded during oceanographic-fishing expeditions in an accessible manner, the validation results are presented in Table 4.

Good/very good alignment (green cells) is the category assigned when at least 60% of the locations with observed fishing efficiencies from oceanographic expeditions align with the HSI values indicated by the FindFISH system. Moderate alignment (yellow cells) was defined for 40% to 60% while poor/unsatisfactory alignment (red cells) was used when less than 40% of the locations align with the HSI values from FindFISH.

The cumulative result of the validation conducted for the years 2017–2020 can be considered very good. This implies that in the majority of expeditions, the environmental conditions determined by the *Fish Module* are in line with the catch efficiencies. The best results were achieved for her-

ring and cod. Due to the lack of data regarding flounder preferences from December to June, it was not possible to verify the accuracy of the *Fish Module*'s performance for this species during winter trips.

The subsequent validation step related to the *Fish Module* involved calculating catch efficiencies obtained during fishing expeditions conducted within the FindFISH project. These were determined by relating the reported catch compositions and weights from fishing surveys to the time the fishing gear was immersed at the depth where effective fishing occurred.

The average HSI values for all analyzed fishing expeditions conducted in this manner were compared to the catches' efficiencies (Figure 6). Analyzing this comparison reveals that for sprat, herring, and cod, there is a certain threshold HSI value below which successful catches do not occur, except for occasional exceptions. This indicates that the system correctly identifies areas with favorable environmental conditions for the habitat of these three species, and fishermen should select routes where HSI > 0.5 for herring and sprat, and HSI > 0.4 for cod.

In assessing the relationship between the Habitat Suitability Index (HSI) and catch efficiency, we've also performed a linear regression analysis based on the data presented in Figure 6. This analysis quantified the increase in fishing efficiency relative to the mean HSI score for sprat, herring and cod. Specifically, for sprat, there was an increase of 150 kg per hour for every 0.1 increase in HSI score. For herring, the increase was 180 kg per hour per 0.1 HSI, and for cod, an even more pronounced improvement of 240 kg per hour per 0.1 HSI was observed. It is evident that choosing the highest HSI values helps to achieve the most favorable catch efficiencies.

This comprehensive quantitative analysis of information collected during fishing expeditions, juxtaposed with modeled HSI values, demonstrates that the system accurately identifies areas with fishing potential. It also highlights the utility of the FindFISH Knowledge Transfer Platform in such a way that choosing fishing routes in areas with favorable environmental conditions for the habitat of the species can positively impact fishing efficiency and reduce the costs associated with fishing operations (Janecki and Dzierzbicka-Głowacka, 2023).

3.6. Web portal

The results from the ecosystem model of the Gulf of Gdańsk *EcoFish*, the *Fish Module*, and data from the instruments and fishing surveys are available on the FindFISH website

Table 4 A comparison between results obtained from the *Fish Module* and oceanographic-fishing expeditions. Red cells denote poor or unsatisfactory alignment. Yellow cells represent satisfactory alignment. Green cells indicate good or very good alignment. Grey cells signify a lack of data.

Name	Expedition date	Sprat	Cod	Herring	Flounder
2017-1Q	09.02 - 08.03 2017				
2017-4Q	13.11 - 03.12 2017				
2018-1Q	07.02 - 02.03 2018				
2018-4Q	14.11 - 01.12 2018				
2019-1Q	12.02 - 07.03 2019				
2019-4Q	11.11 - 29.11 2019				
2020-1Q	04.02 - 03.03 2020				
2020-4Q	12.11 - 02.12 2020				

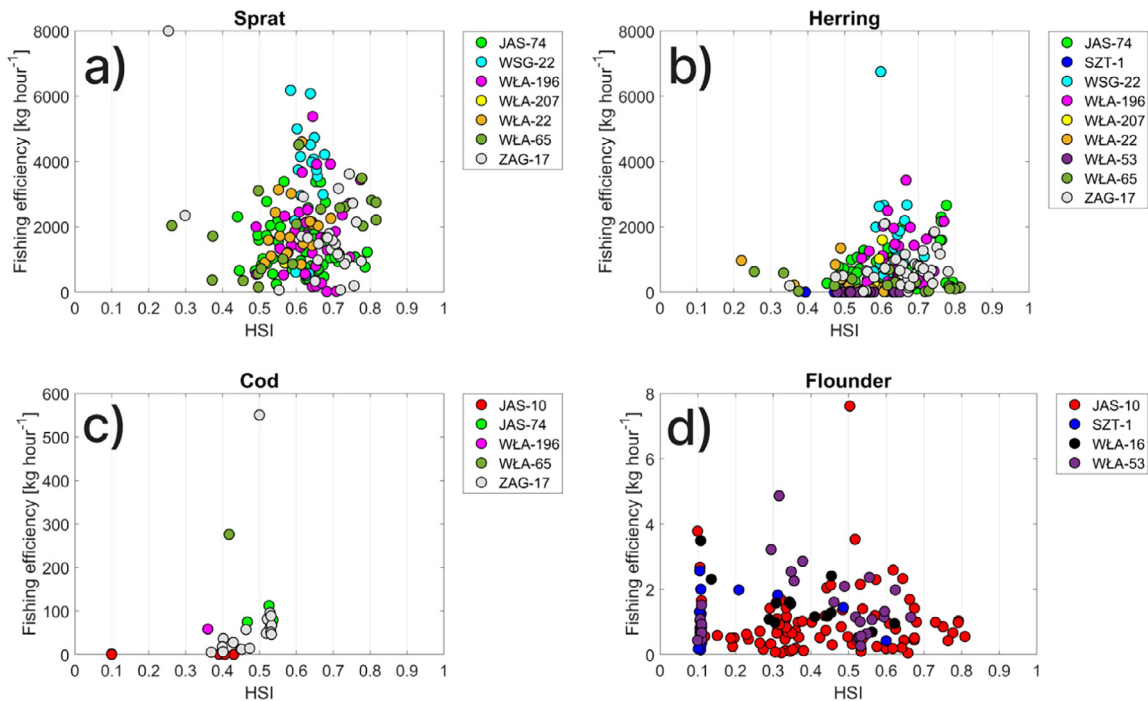


Figure 6 Relationship between the fishing efficiencies of sprat, herring, cod, and flounder and the average HSI values.

(www.findfish.pl) through the “FindFISH Service” tab on the navigation bar after selecting “Model data” or “Measurement data” (Figure 7).

3.6.1. The “Model data” service

The time period covered by the *FindFISH* service starts in January 2017, up to the latest 48-hour forecast. For all model products (Figure 8A) and variables (Figure 8B), users can generate raster maps (Figure 8C) for individual depths that represent the vertical level of the model. In addition, it is possible to create time (Figure 8D1) and spatial (Figure 8E) series for fixed periods in a selected location (af-

ter determining or indicating the desired latitude and longitude), as well as model data tables (Figure 8D2) for the selected parameter (Figure 8B).

There are the following ways of presenting model data within the *FindFISH* Service:

- a) Spatial distribution (map): This is the default form of results presentation available in the “Map data” tab.
- b) Spatial distribution (vertical section): Option available in the “Map data” tab. The “Vertical section” button allows you to select two locations on the map. After selection, a 2D plot is created with the spatial variation of the pa-

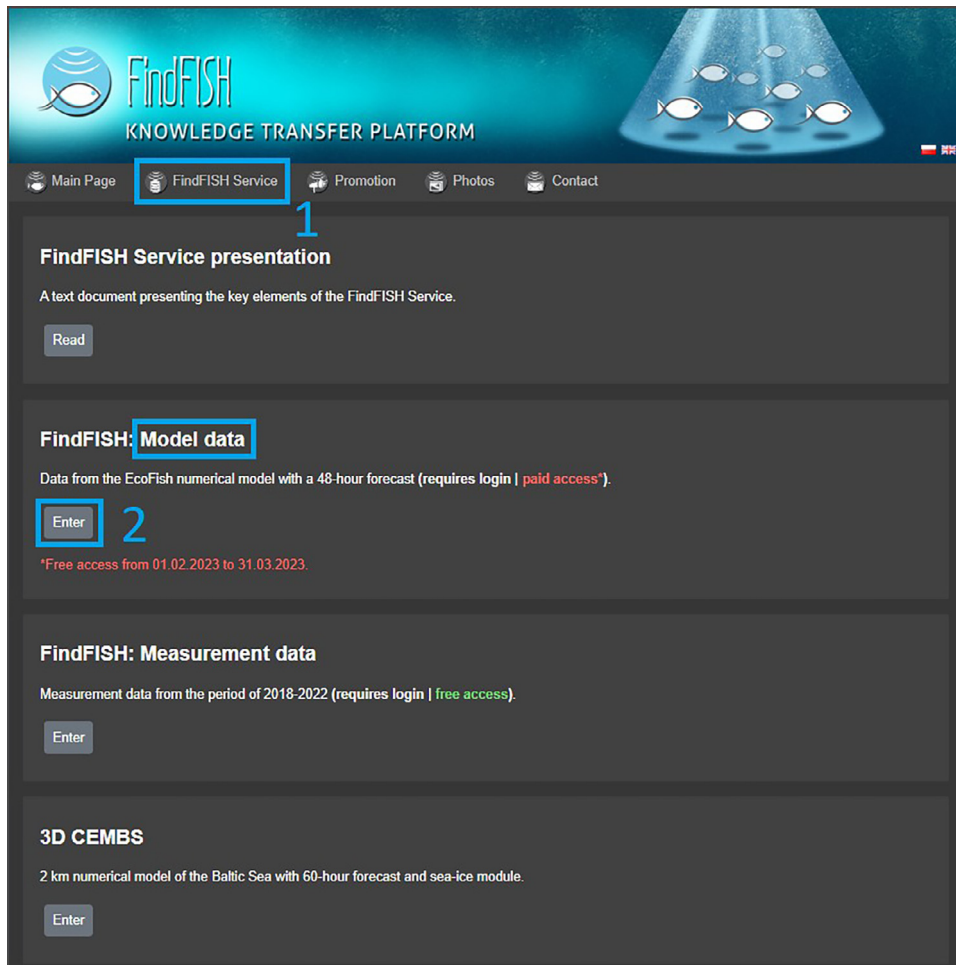


Figure 7 FindFISH project website and “Model Data” service selection page.

- parameter between the selected locations from the surface to the bottom (This option is available only for 3D variables).
- c) Point time series (graph): Option available in the “Point data” tab. Select the location, depth, start and end date and press the “Graph” button. A graph is created showing the variability of the parameter at a selected location and time period.
 - d) Point time series (table): Option available in the “Point data” tab. Select the location, depth, start and end date, and press the “Table” button. A table is created with the parameter values at the selected location for consecutive days in the time period.

Through the “EcoFish Model – Hydrodynamical Module” service, forecasts of the following parameters are available: water temperature, salinity, sea level, and currents, with a 48-hour forecast of these parameters. Moreover, through the “EcoFish Model – Biochemical Module” service, forecasts of the following parameters are available: chlorophyll *a* concentration, nitrates, ammonia, phosphates and silicates, dissolved oxygen, dissolved organic carbon, phytoplankton, and microzooplankton biomass.

Through the “Fish Module” service, presenting under what hydrological conditions fisheries for herring, sprat,

cod, and flounder should be the most abundant in resources, the following fields (with a 48-hour forecast) are available: maximum HSI in the water column, depth for maximum HSI $> 0.9/0.8/0.7$, depth for maximum HSI in the water column and HSI at the selected depth.

The service also gives the possibility of presenting data in a vertical section (limited to 3D variables). This is done by selecting two locations on the map. As a result, a 2D plot is created with spatial variation for the selected parameter between the selected locations from the surface to the bottom.

3.7. Fishing expeditions to verify the functionality of the *FindFISH* system

The FindFISH Platform is expected to be successfully used by fishery’s information services and ship captains. It will help reduce the time spent searching for fishing grounds, lower the costs incurred by the fleet or investors, maximize fishing success, and improve the profitability of investments in the fisheries sector.

The gradual implementation agreement of the landing obligation, also known as the discard ban, is considered one of the most significant and crucial changes introduced un-

der the Common Fisheries Policy reform. It is a response to the widespread belief across the European Union that discarding caught fish into the sea, where they often perish, constitutes unacceptable waste from moral, biological-ecological, and economic perspectives. Although everyone agrees on the need to avoid wasting caught fish, implementing the catch ban by fishermen remains a challenging task. The FindFISH Platform can potentially reduce the amount of discards by using numerical modeling results, guiding fishermen to areas with environmental conditions favorable for the existence of specific fish species.

The application of the FindFISH Platform will improve the efficiency of work at sea, not only for fishermen but also for entities in the tourism sector, maritime services, scientists, ecologists, and government agencies. Furthermore, the FindFISH Platform can contribute to supporting sustainable fisheries and fostering the development of a smart economy in marine sectors (the so-called blue economy).

By combining mathematical modeling with actual fishing data (qualitative and quantitative assessment - a task carried out by the ZRM-OP), the profitability of fishing can

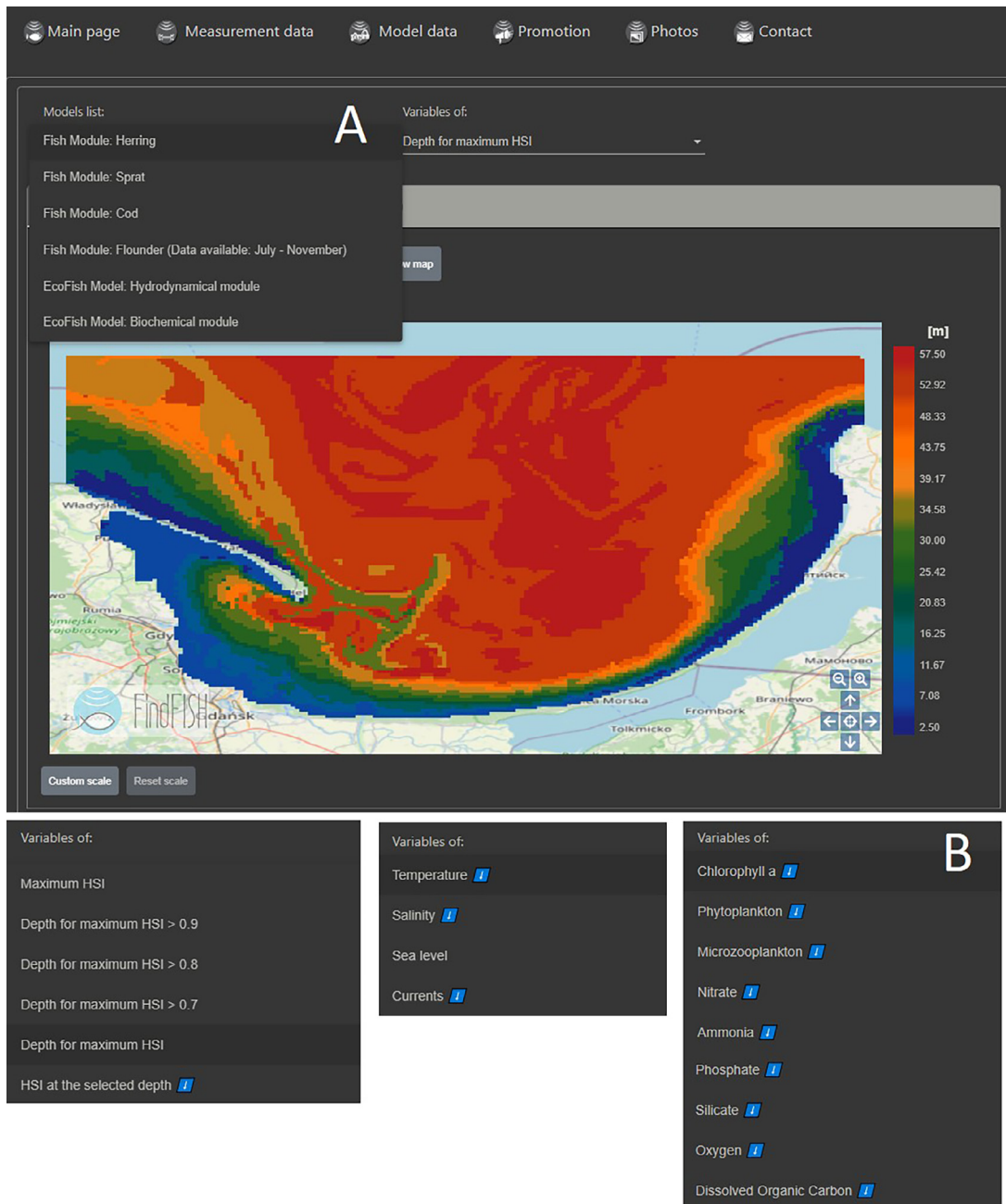


Figure 8 The FindFISH project website after selecting the “Model data” service. Selection of the model list (A) and hydrodynamic and biochemical variables (B). The FindFISH project website after selecting the “Model data” service. Results in the form of maps (C), graphs (D1) and tables (D2), for the selected point on the map (D) and for the selected time period, as well as for 3D variables in the form of vertical section between two selected points (E).

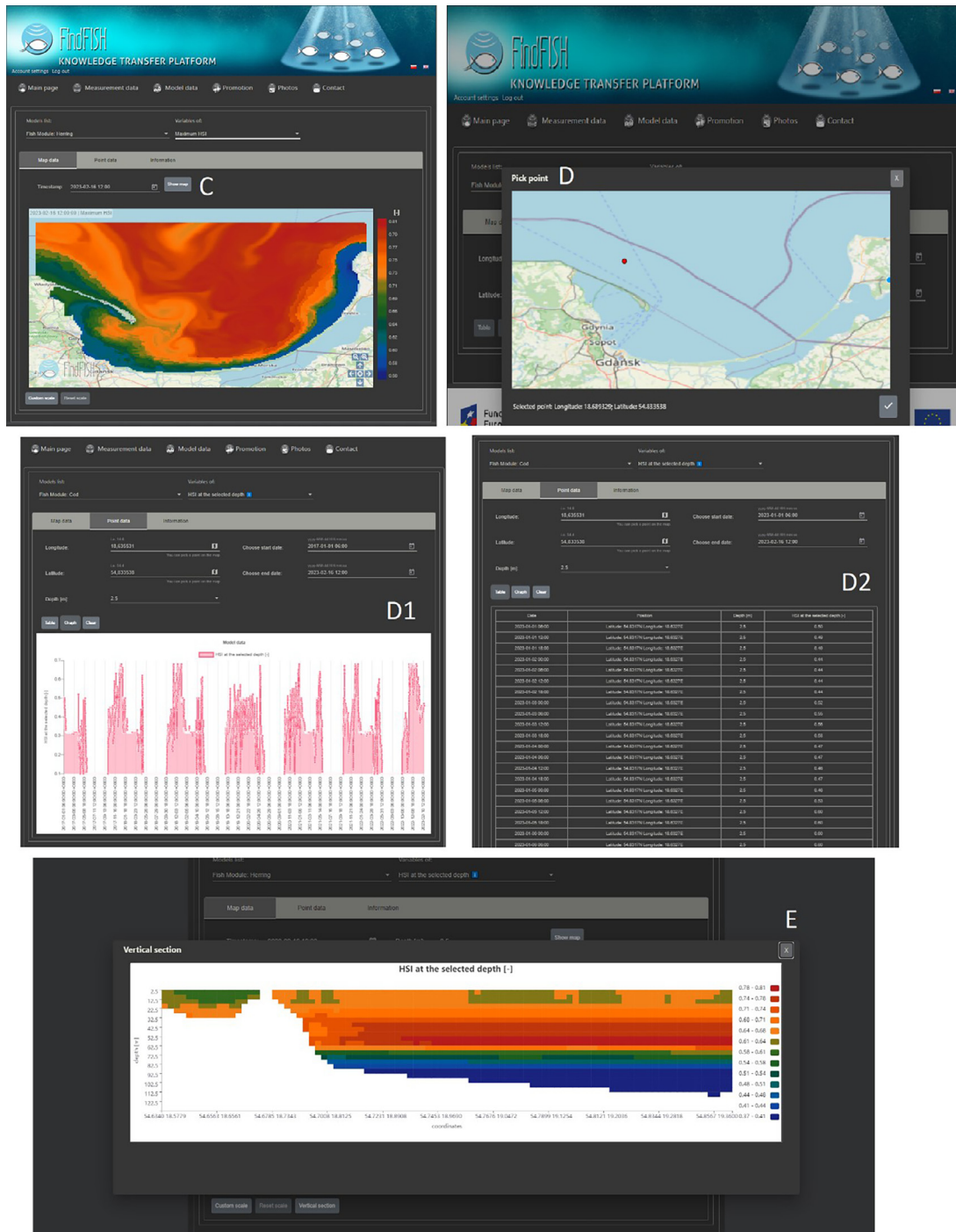


Figure 8 Continued.

be positively affected. With limited fishing quotas, fishermen are interested in qualitative rather than quantitative catches. According to the authors, using the platform can increase fishing efficiency and quality by approximately 40% (with a pessimistic approach), thus proportionally increasing expected profits.

The fifth stage of the project involved tests of the FindFISH numerical system. To verify the functionality of the FindFISH system, fishing expeditions were conducted, during which individual evaluations were collected from skip-

pers and vessel managers. The effectiveness of voyages using the FindFISH numerical system was compared with voyages without its use by comparing the results of the Fish Module with actual fishing outcomes. Based on the conducted research and fishing trips, it was established that in 50% to 70% of cases (depending on a specie), the fishing grounds recorded by the fishermen (using towed gear) in the open waters of the Gulf of Gdańsk coincided with or were close to the locations identified by the FindFISH Platform. These percentages were derived using the Habitat Suitabil-

ity Index (HSI) as the primary criterion for identifying potential fishing locations. Sites with HSI values greater than 0.4 for cod, and 0.5 for sprat and herring, were considered favorable. In transitional waters, where set gear was used, coverage ranging from 40% to 50% was observed.

The transitional water area in the coastal zone is highly challenging for modeling due to the significant dynamics of hydrodynamic and biochemical processes, heavily influenced by both initial and coastal conditions of the model, as well as microscale structures present in such basins.

The website (www.findfish.pl) was used to verify the automatic creation of maps of the hydrodynamic and biochemical parameters of the marine environment in the Gulf of Gdańsk, as well as parameters describing the Habitat Suitability Index (HSI), which is the occurrence of the most favorable environmental conditions for industrially harvested fish species in the studied area. This was done based on the EcoFish numerical model with the Fish Module running in operational mode.

4. Conclusions

The *FindFISH Platform* is a significant advancement in fishing technology, offering a comprehensive solution that blends historical data, environmental observations, and user feedback to optimize fishing operations. This platform promises substantial economic and ecological benefits:

- **Fuel Savings and Operational Cost Reductions:** Based on operational data, the *FindFISH Platform* can reduce overall operational costs by 5–15%. This is achieved through more efficient fishing routes and strategies, leading to considerable fuel savings, especially for vessels undertaking longer voyages.
- **Time Efficiency and Enhanced Fish Quality:** The platform can reduce trawling time by an approximate 25%, as precise location predictions lead to more efficient fishing. This also results in about 20% reduction in the time from catch to port, significantly improving the freshness and quality of the catch.
- **Environmental Benefits:** The *FindFISH* service aids in decreasing the environmental impact of fishing. Reduced trawling time means less disturbance to marine ecosystems and a reduction in bycatch.
- **Profitability and Compliance:** By aiding in targeted fishing, the platform ensures compliance with fishing quotas and increases the profitability of catches, as fishermen can focus on commercially valuable species.

These estimates were developed based on the experiences and feedback of fishermen who have used the platform, as well as an analysis of various factors that influence the costs of fishing operations. The detailed impact of the *FindFISH Platform* on cost reductions will become more evident in the upcoming years, as increasing numbers of fishermen adopt the system and provide feedback on its effectiveness.

The *FindFISH Platform* is not only a tool for fishermen but also a conduit for knowledge transfer between scientific institutions and the fishing industry. Its potential impact spans several sectors:

- **Innovation in Fishing Practices:** The platform's advanced modeling techniques and real-time environmental data position it as a unique and innovative tool in the market, with no direct competition currently in the Gulf of Gdańsk region.
- **Competitive Advantage for Users:** Fishermen using the *FindFISH* service can expect significant improvements in operational efficiency and catch quality, giving them a competitive edge in the market.
- **Wider Sectoral Impact:** The platform's benefits extend to the fish processing and transportation industries, environmental monitoring, and even tourism, by providing comprehensive data on marine conditions.

In summary, the *FindFISH Platform* is a transformative tool, poised to revolutionize the fishing industry in the Gulf of Gdańsk. It offers a suite of benefits that include cost savings, enhanced efficiency, improved catch quality, and environmental sustainability, all of which contribute to a more profitable and responsible fishing sector.

5. Summary

The *FindFISH Platform*, designed for fishermen, aims to enhance fishing efficiency and reduce environmental impact. This tool, a first of its kind, uses a numerical method to forecast marine conditions in the Gulf of Gdańsk, aiding in locating optimal fishing grounds. Targeting a diverse market, *FindFISH* promises profitability and reduced operational costs for the fishing industry, while ensuring sustainability and environmental protection. The platform is developed through a collaboration between scientific institutes and a fishermen's association, integrating real-time data and eco-hydrodynamic models. It is expected to benefit not just fishermen but also various stakeholders, promoting sustainable fishing practices and aiding in marine environment protection.

Declaration of competing interest

The authors declare that they have no known competing financial interests or personal relationships that could have appeared to influence the work reported in this paper.

Acknowledgments

The project “Knowledge transfer platform *FindFISH* – Numerical Forecasting System for the Marine Environment of the Gulf of Gdańsk for Fisheries” (no. RPPM.01.01.01-22-0025/16-00) is co-financed from the European Regional Development Fund (ERDF) under the Regional Operational Program for the Pomeranian Voivodeship for 2014–2020, Priority Axis 01. Commercialization of knowledge, Measure 01.01. Expansion through innovation, Sub-measure 01.01.01. Expansion through innovation.

Calculations were carried out at the Academic Computer Centre in Gdańsk.

References

- Akimova, A., Núñez-Riboni, I., Kempf, A., Taylor, M.H., 2016. Spatially-Resolved Influence of Temperature and Salinity on Stock and Recruitment Variability of Commercially Important Fishes in the North Sea. *PLOS ONE* 11, e0161917. <https://doi.org/10.1371/journal.pone.0161917>
- Bauer, B., Horbowy, J., Rahikainen, M., Kulatska, N., Müller-Karulis, B., Tomczak, M.T., Bartolino, V., 2019. Model uncertainty and simulated multispecies fisheries management advice in the Baltic Sea. *PLOS ONE* 14, e0211320. <https://doi.org/10.1371/journal.pone.0211320>
- Beldowska, M., Jędruch, A., Stupkowska, J., Saniewska, D., Saniewski, M., 2015. Macrophyta as a vector of contemporary and historical mercury from the marine environment to the trophic web. *Environ. Sci. Pollut. Res.* 22, 5228–5240. <https://doi.org/10.1007/s11356-014-4003-4>
- Biernaczyk, J., Głowacki, R., Kubiak, K., Piotrowski, P., Wosek, S., Wójcik, M., 2023. Architektura oraz technologie wykorzystane podczas tworzenia Platformy FindFISH. Platforma Transferu Wiedzy FindFISH. Wydawnictwo Uniwersytetu Morskiego w Gdyni, Gdynia.
- Cabral, H., Drouineau, H., Teles-Machado, A., Pierre, M., Lepage, M., Lobry, J., Reis-Santos, P., Tanner, S.E., 2021. Contrasting impacts of climate change on connectivity and larval recruitment to estuarine nursery areas. *Prog. Oceanogr.* 196, 102608. <https://doi.org/10.1016/j.pocean.2021.102608>
- Duthie, G.G., Houlihan, D.F., 1982. The effect of single step and fluctuating temperature changes on the oxygen consumption of flounders, *Platichthys flesus* (L.): Lack of temperature adaptation. *J. Fish Biol.* 21, 215–226. <https://doi.org/10.1111/j.1095-8649.1982.tb04001.x>
- Dzierzbicka-Głowacka, L., Jakacki, J., Janecki, M., Nowicki, A., 2013a. Activation of the operational ecohydrodynamic model (3D CEMBS) – the hydrodynamic part. *Oceanologia* 55 (3), 519–541. <https://doi.org/10.5697/oc.55-3.519>
- Dzierzbicka-Głowacka, L., Janecki, M., Nowicki, A., Jakacki, J., 2013b. Activation of the operational ecohydrodynamic model (3D CEMBS) – the ecosystem module. *Oceanologia* 55 (3), 543–572. <https://doi.org/10.5697/oc.55-3.543>
- Dzierzbicka-Głowacka, L., Kuliński, K., Maciejewska, A., Jakacki, J., Pempkowiak, J., 2011. Numerical modelling of POC dynamics in the southern Baltic under possible future conditions determined by nutrients, light and temperature. *Oceanologia* 53 (4), 971–992.
- Dzierzbicka-Głowacka, L., Nowicki, A., Janecki, M., Szymczycha, B., Piotrowski, P., Piekiel, P., Łukasiewicz, G., 2018. Structure of the FindFish Knowledge Transfer Platform. *Fisher. Aquat. Life* 26, 193–197. <https://doi.org/10.2478/aopf-2018-0021>
- Dzierzbicka-Głowacka, L., Wittbrodt, J., Łukasiewicz, G., 2023. Ocena działania usługi FindFISH. Platforma Transferu Wiedzy FindFISH. Wydawnictwo Uniwersytetu Morskiego w Gdyni, Gdynia.
- European Commission, 2009. Wspólna polityka rybołówstwa – podręcznik użytkownika. Urząd Oficjalnych Publikacji Wspólnot Europejskich, Luksemburg.
- FindFISH project's website. FindFISH project's website [WWW Document]. www.findfish.pl.
- Fonds, M., Cronie, R., Vethaak, A.D., Van Der Puyl, P., 1992. Metabolism, food consumption and growth of plaice (*Pleuronectes platessa*) and flounder (*Platichthys flesus*) in relation to fish size and temperature. *Neth. J. Sea Res.* 29, 127–143. [https://doi.org/10.1016/0077-7579\(92\)90014-6](https://doi.org/10.1016/0077-7579(92)90014-6)
- Fousiya, A.A., Malik, J.N., Chakraborty, S., 2023. Climatic Variability and Anthropogenic Forcing on Marine Ecosystems: Evidence from the Lakshadweep Archipelago. In: Jayaraju, N., Sreenivasulu, G., Madakka, M., Manjulatha, M. (Eds.), *Coasts, Estuaries and Lakes: Implications for Sustainable Development*. Springer International Publishing, Cham, 93–108. https://doi.org/10.1007/978-3-031-21644-2_6
- Freitas, C., Villegas-Ríos, D., Moland, E., Olsen, E.M., 2021. Sea temperature effects on depth use and habitat selection in a marine fish community. *J. Animal Ecol.* 90, 1787–1800. <https://doi.org/10.1111/1365-2656.13497>
- Gollock, M.J., Currie, S., Petersen, L.H., Gamperl, A.K., 2006. Cardiovascular and haematological responses of Atlantic cod (*Gadus morhua*) to acute temperature increase. *J. Exp. Biol.* 209, 2961–2970. <https://doi.org/10.1242/jeb.02319>
- Grusza, G., 2009. Atlas of Polish marine area bottom habitats: environmental valorization of marine habitats. Broker-Innowacji.
- Guellard, T., Sokotowska, E., Arciszewski, B., 2015. First report on intersex in invasive round goby *Neogobius melanostomus* from the Baltic Sea (Gulf of Gdańsk, Poland). *Oceanologia* 57 (1), 102–106. <https://doi.org/10.1016/j.oceano.2014.09.004>
- Harvey, C.J., Cox, S.P., Essington, T.E., Hansson, S., Kitchell, J.F., 2003. An ecosystem model of food web and fisheries interactions in the Baltic Sea. *ICES J. Mar. Sci.* 60, 939–950. [https://doi.org/10.1016/S1054-3139\(03\)00098-5](https://doi.org/10.1016/S1054-3139(03)00098-5)
- Helsinki Commission, 2013. Baltic Sea Environment Proceedings No. 129B. Helsinki.
- Hutchinson, S., Hawkins, L.E., 2004. The relationship between temperature and the size and age of larvae and peri-metamorphic stages of *Pleuronectes flesus*. *J. Fish Biol.* 65, 448–459. <https://doi.org/10.1111/j.0022-1112.2004.00462.x>
- ICES, 2018. Baltic Sea Ecoregion – Ecosystem Overview. *Ecosystem Overviews*.
- Janecki, M., Dybowski, D., Dzierzbicka-Głowacka, L., 2023a. The influence of biochemical parameters on primary production in the Gulf of Gdańsk region: A model study. *Oceanologia* 65 (4), 517–533. <https://doi.org/10.1016/j.oceano.2023.05.001>
- Janecki, M., Dybowski, D., Jakacki, J., Nowicki, A., Dzierzbicka-Głowacka, L., 2021. The Use of Satellite Data to Determine the Changes of Hydrodynamic Parameters in the Gulf of Gdańsk via EcoFish Model. *Remote Sens.* 13, 3572. <https://doi.org/10.3390/rs13183572>
- Janecki, M., Dybowski, D., Nowicki, A., Dzierzbicka-Głowacka, L., 2023b. Analiza dynamiki zmienności parametrów biochemicznych w rejonie Zatoki Gdańskiej za pomocą modelu EcoFish. Platforma Transferu Wiedzy FindFISH. Wydawnictwo Uniwersytetu Morskiego w Gdyni, Gdynia.
- Janecki, M., Dybowski, D., Nowicki, A., Jakacki, J., Dzierzbicka-Głowacka, L., 2023c. Analiza parametrów fizycznych wód Zatoki Gdańskiej za pomocą modelu numerycznego EcoFish. Platforma Transferu Wiedzy FindFISH. Wydawnictwo Uniwersytetu Morskiego w Gdyni, Gdynia.
- Janecki, M., Dybowski, D., Rak, D., Dzierzbicka-Głowacka, L., 2022. A New Method for Thermocline and Halocline Depth Determination at Shallow Seas. *J. Phys. Oceanogr.* 52, 2205–2218. <https://doi.org/10.1175/JPO-D-22-0008.1>
- Janecki, M., Dzierzbicka-Głowacka, L., 2023. Moduł Fish – mapowanie najkorzystniejszych warunków środowiskowych dla bytowania ryb badanych gatunków poławianych przemysłowo w rejonie Zatoki Gdańskiej. Platforma Transferu Wiedzy FindFISH. Wydawnictwo Uniwersytetu Morskiego w Gdyni, Gdynia.
- Janecki, M., Dzierzbicka-Głowacka, L., 2024. Fish Module - A prognostic tool for modeling the optimal environmental conditions for fish Image 1. *Appl. Soft Comput.* 153, 111302. <https://doi.org/10.1016/j.asoc.2024.111302>
- Kemp, P.S., Subbiah, G., Barnes, R., Boerder, K., O'Leary, B.C., Stewart, B.D., Williams, C., 2023. The future of marine fisheries management and conservation in the United Kingdom:

- Lessons learnt from over 100 years of biased policy. *Mar. Policy* 147, 105075. <https://doi.org/10.1016/j.marpol.2022.105075>
- Krzemień, G., Wittbrodt, J., 2023. Wyprawy rybackie – realizacja rejsów pomiarowych przez kutry i łodzie rybackie. Platforma Transferu Wiedzy FindFISH. Wydawnictwo Uniwersytetu Morskiego w Gdyni, Gdynia.
- Kuczyński, T., Piecki, P., Barańska, A., Olenych, M., 2023. Analiza stanu ekologicznego Zatoki Gdańskiej na podstawie ichtiofauny. Platforma Transferu Wiedzy FindFISH. Wydawnictwo Uniwersytetu Morskiego w Gdyni, Gdynia.
- Laghari, M.Y., Ghaffar, A., Mubeen, M., 2022. Climate Change a Great Threat to Fisheries. In: Jatoi, W.N., Mubeen, M., Ahmad, A., Cheema, M.A., Lin, Z., Hashmi, M.Z. (Eds.), *Building Climate Resilience in Agriculture: The Theory, Practice and Future Perspective*. Springer International Publishing, Cham, 131–142. https://doi.org/10.1007/978-3-030-79408-8_9
- Maravelias, C.D., Reid, D.G., Swartzman, G., 2000. Modelling Spatio-Temporal Effects of Environment on Atlantic Herring, *Clupea harengus*. *Environ. Biol. Fish.* 58. <https://doi.org/10.1023/a:1007693732571>
- Martinho, F., Dolbeth, M., Viegas, I., Teixeira, C.M., Cabral, H.N., Pardal, M.A., 2009. Environmental effects on the recruitment variability of nursery species. *Estuar. Coastal Shelf Sci.* 83, 460–468. <https://doi.org/10.1016/j.ecss.2009.04.024>
- Meier, H.E.M., Kniebusch, M., Dieterich, C., Gröger, M., Zorita, E., Elmgren, R., Myrberg, K., Ahola, M.P., Bartosova, A., Bonsdorff, E., Börgel, F., Capell, R., Carlén, I., Carlund, T., Carstensen, J., Christensen, O.B., Dierschke, V., Frauen, C., Frederiksen, M., Gaget, E., Galatius, A., Haapala, J.J., Halkka, A., Hugelius, G., Hünicke, B., Jaagus, J., Jüssi, M., Käyhkö, J., Kirchner, N., Kjellström, E., Kuliński, K., Lehmann, A., Lindström, G., May, W., Miller, P.A., Mohrholz, V., Müller-Karulis, B., Pavón-Jordán, D., Quante, M., Reckermann, M., Rutgersson, A., Savchuk, O.P., Stendel, M., Tuomi, L., Viitasalo, M., Weisse, R., Zhang, W., 2022. Climate change in the Baltic Sea region: a summary. *Earth Syst. Dynam.* 13, 457–593. <https://doi.org/10.5194/esd-13-457-2022>
- Moore, K., Doney, S., Kleypas, A., Glover, M., Fung, Y., 2001. An intermediate complexity marine ecosystem model for the global domain. *Deep-Sea Res. Pt. II* 49 (1–3), 403–462. [https://doi.org/10.1016/S0967-0645\(01\)00108-4](https://doi.org/10.1016/S0967-0645(01)00108-4)
- Nakayama, S.-I., Suyama, S., Fuji, T., Hashimoto, M., 2023. Estimating relative gear efficiency of surface trawl nets using comparative trawl survey data. *Fish. Sci.* 89, 725–730. <https://doi.org/10.1007/s12562-023-01712-7>
- Nowicki, A., Janecki, M., Dybowski, D., Dzierzbicka-Głowacka, L., 2023a. Automatyczny system kontroli modelu EcoFish w trybie operacyjnym. Platforma Transferu Wiedzy FindFISH. Wydawnictwo Uniwersytetu Morskiego w Gdyni, Gdynia.
- Nowicki, A., Janecki, M., Dzierzbicka-Głowacka, L., 2023b. Asymilacja danych satelitarnych oraz środowiskowych w modelu EcoFish. Platforma Transferu Wiedzy FindFISH. Wydawnictwo Uniwersytetu Morskiego w Gdyni, Gdynia.
- Öberg, J., 2017. Cyanobacteria blooms in the Baltic Sea. HELCOM Baltic Sea Environment Fact Sheets.
- Piecki, P., 2013. Zagrożenia dla przedmiotów ochrony obszarów Natura 2000 - Rybołówstwo (No. 6760). Wydawnictwa Wewnętrzne Instytutu Morskiego w Gdańsku, Gdańsk.
- Piecki, P., Dziaduch, D., Dzierzbicka-Głowacka, L., Kalarus, M., 2023. Cooperation between the fishery sector and science: CTD probe measurements during fishing catches on the feeding grounds of herring (*Culpea harengus*) and sprat (*Sprattus sprattus*) in the south-eastern part of the Baltic Sea. *Oceanologia*, article in press. <https://doi.org/10.1016/j.oceano.2023.10.001>
- Polak-Juszczak, L., 2013. Trace elements in the livers of cod (*Gadus morhua* L.) from the Baltic Sea: levels and temporal trends. *Environ. Monit. Assess.* 185, 687–694. <https://doi.org/10.1007/s10661-012-2584-2>
- Radtke, K., Wodzinowski, T., Ścics, I., 2017. Najnowsze wyniki badań z rejsu r.v. Baltica (09.02–08.03.2017 r.). *Wiadomości Rybackie MIR-PIB*.
- Radtke, K., Wodzinowski, T., Wójcik, I., 2021. Wyniki badań oceanograficzno-rybackiego rejsu r.v. Baltica na przełomie listopada i grudnia 2020 roku. *Wiadomości Rybackie MIR-PIB*.
- Radtke, K., Wodzinowski, T., Wójcik, I., 2020a. Wyniki badań oceanograficzno-rybackich r.v. Baltica w rejsie jesiennym 2019 r. *Wiadomości Rybackie MIR-PIB*.
- Radtke, K., Wodzinowski, T., Wójcik, I., 2020b. Wyniki badań oceanograficzno-rybackich r.v. Baltica w rejsie zimowym 2020 r. *Wiadomości Rybackie MIR-PIB*.
- Radtke, K., Wodzinowski, T., Wójcik, I., 2019a. Wyniki badań oceanograficzno-rybackich r.v. Baltica w rejsie jesiennym w 2018 r. *Wiadomości Rybackie MIR-PIB*.
- Radtke, K., Wodzinowski, T., Wójcik, I., 2019b. Wyniki oceanograficzno-rybackiego rejsu r.v. Baltica zrealizowanego w lutym i marcu 2019 r. *Wiadomości Rybackie MIR-PIB*.
- Radtke, K., Wodzinowski, T., Wójcik, I., 2018a. Podsumowanie oceanograficzno-rybackich wyników z rejsu zimowego r.v. Baltica w 2018 roku. *Wiadomości Rybackie MIR-PIB*.
- Radtke, K., Wodzinowski, T., Wójcik, I., Ścics, I., 2018b. Wyniki badań demersalnego rejsu r.v. Baltica – jesień 2017. *Wiadomości Rybackie MIR-PIB*.
- RDSM, 2012. *Wstępna ocena stanu środowiska wód morskich polskiej strefy Morza Bałtyckiego (2005-2010)*.
- Saniewska, D., Betdowska, M., Betdowski, J., Jędruch, A., Saniewski, M., Falkowska, L., 2014. Mercury loads into the sea associated with extreme flood. *Environ. Pollut.* 191, 93–100. <https://doi.org/10.1016/j.envpol.2014.04.003>
- Saraux, C., Fromentin, J.-M., Bigot, J.-L., Bourdeix, J.-H., Morfin, M., Roos, D., Beveren, E.V., Bez, N., 2014. Spatial Structure and Distribution of Small Pelagic Fish in the Northwestern Mediterranean Sea. *PLOS ONE* 9, e112111. <https://doi.org/10.1371/journal.pone.0111211>
- Tamm, O., Maasikamäe, S., Padari, A., Tamm, T., 2018. Modelling the effects of land use and climate change on the water resources in the eastern Baltic Sea region using the SWAT model. *CATENA* 167, 78–89. <https://doi.org/10.1016/j.catena.2018.04.029>
- Tirsgaard, B., Svendsen, J.C., Steffensen, J.F., 2015. Effects of temperature on specific dynamic action in Atlantic cod *Gadus morhua*. *Fish. Physiol. Biochem.* 41, 41–50. <https://doi.org/10.1007/s10695-014-0004-y>
- Voss, R., Hinrichsen, H.-H., Quaas, M.F., Schmidt, J.O., Tahvonen, O., 2011. Temperature change and Baltic sprat: from observations to ecological-economic modelling. *ICES J. Mar. Sci.* 68, 1244–1256. <https://doi.org/10.1093/icesjms/fsr063>
- Woźniak, B., Bradtke, K., Darecki, M., Dera, J., Dudzińska-Nowak, J., Dzierzbicka-Głowacka, L., Ficek, D., Furmańczyk, K., Kowalewski, M., Krężel, A., Majchrowski, R., Ostrowska, M., Paszkuta, M., Stoń-Egiert, J., Stramska, M., Zapadka, T., 2011a. SatBałtyk – A Baltic environmental satellite remote sensing system – an ongoing project in Poland. Part 1: Assumptions, scope and operating range. *Oceanologia* 53 (4), 897–924. <https://doi.org/10.5697/oc.53-4.897>
- Woźniak, B., Bradtke, K., Darecki, M., Dera, J., Dudzińska-Nowak, J., Dzierzbicka-Głowacka, L., Ficek, D., Furmańczyk, K., Kowalewski, M., Krężel, A., Majchrowski, R., Ostrowska, M., Paszkuta, M., Stoń-Egiert, J., Stramska, M., Zapadka, T., 2011b. SatBałtyk – A Baltic environmental satellite remote sensing system – an ongoing project in Poland. Part 2: Practical applicability and preliminary results. *Oceanologia* 53 (4), 925–958. <https://doi.org/10.5697/oc.53-4.925>
- Zaborska, A., Siedlewicz, G., Szymczycha, B., Dzierzbicka-Głowacka, L., Pazdro, K., 2019. Legacy and emerging pollutants

in the Gulf of Gdańsk (southern Baltic Sea) – loads and distribution revisited. *Mar. Pollut. Bull.* 139, 238–255. <https://doi.org/10.1016/j.marpolbul.2018.11.060>

Zaborska, A., Szymczycha, B., Siedlewicz, G., Saghravani, S.R., Pajda, B., Pazdro, K., 2023. Analiza stanu chemicznego środowiska

Zatoki Gdańskiej w zakresie stężeń metali śladowych, radionuklidów i zanieczyszczeń organicznych w oparciu o wieloletnie dane. Platforma Transferu Wiedzy FindFISH. Wydawnictwo Uniwersytetu Morskiego w Gdyni, Gdynia.

Available online at www.sciencedirect.com

ScienceDirect

journal homepage: www.journals.elsevier.com/oceanologia

ORIGINAL RESEARCH ARTICLE

The zooplankton community of Baltic Sea ports: diversity and seasonal dynamics

Bartosz Witalis^a, Anna Iglukowska^{b,*}, Marta Ronowicz^c,
Agata Weydmann-Zwolicka^d, Piotr Kukliński^c

^aNational Marine Fisheries Research Institute, Gdynia, Poland

^bUniversity of Gdańsk, Faculty of Biology, Department of Evolutionary Genetics and Biosystematics, Laboratory of Biosystematics and Ecology of Aquatic Invertebrates, Gdańsk, Poland

^cInstitute of Oceanology Polish Academy of Sciences, Marine Ecology Department, Sopot, Poland

^dUniversity of Gdańsk, Faculty of Oceanography and Geography, Department of Marine Biology and Biotechnology, Laboratory of Plankton Biology, Gdynia, Poland

Received 8 February 2023; accepted 2 February 2024

Available online 26 February 2024

KEYWORDS

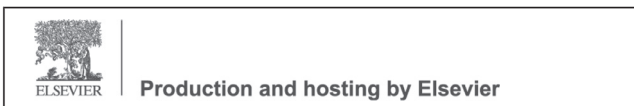
Seasonal dynamics;
Plankton diversity;
Copepoda;
Invasive species;
Gulf of Gdańsk

Abstract In this study, we investigated zooplankton composition and seasonal dynamics, as well as the influence of selected environmental factors on the zooplankton community in three ports on the Polish Baltic coast: Władysławowo, Gdynia and Gdańsk. Our aim was to determine whether harbours' heavy traffic, chemical pollution and physical disturbances affect the zooplankton community, and whether new nonindigenous planktonic species occur in these habitats. Forty three zooplankton taxa were found in all three ports; however, it is important to note that no new nonindigenous species were observed in the port basins. The most influential environmental factors affecting the zooplankton community were: seawater temperature (17% of explained zooplankton variability) and transparency (4%), which were related to seasonal changes. *Acartia* spp. (although of different development stages) was the dominant taxon during the study, and the examined ports/seasons differed in the presence and proportions of less abundant taxa: the autumn and winter assemblages were dominated by *Acartia* spp. nauplii, the spring assemblage by numerous Polychaeta larvae, while Cirripedia nauplii and early development stages of *Eurytemora affinis* were particularly abundant in summer. In addition,

* Corresponding author at: Faculty of Biology, Department of Evolutionary Genetics and Biosystematics, Laboratory of Biosystematics and Ecology of Aquatic Invertebrates, University of Gdańsk, Wita Stwosza 59, 80–308 Gdańsk, Poland.

E-mail addresses: bwitalis@mir.gdynia.p (B. Witalis), anna.iglikowska@ug.edu.pl (A. Iglukowska), martar@iopan.pl (M. Ronowicz), agata.weydmann@ug.edu.pl (A. Weydmann-Zwolicka), kuki@iopan.pl (P. Kukliński).

Peer review under the responsibility of the Institute of Oceanology of the Polish Academy of Sciences.



<https://doi.org/10.1016/j.oceano.2024.02.001>

0078-3234/© 2024 Institute of Oceanology of the Polish Academy of Sciences. Production and hosting by Elsevier B.V. This is an open access article under the CC BY-NC-ND license (<http://creativecommons.org/licenses/by-nc-nd/4.0/>).

changes in salinity (2% explained variability) had a particular impact on the zooplankton community and especially on the assemblage of Gdańsk Port, which was influenced by freshwater inflow from the Motława and Dead Vistula rivers. Our study has clearly shown that, despite severe physical and chemical disturbances in all studied ports, the composition and seasonal dynamics of the zooplankton community were similar to those of the Gulf of Gdańsk outside the ports.

© 2024 Institute of Oceanology of the Polish Academy of Sciences. Production and hosting by Elsevier B.V. This is an open access article under the CC BY-NC-ND license (<http://creativecommons.org/licenses/by-nc-nd/4.0/>).

1. Introduction

The ports of the southern Baltic Sea are highly disturbed environments under substantial anthropogenic impact. Intense shipping, repair and handling activities, as well as constant transformation of coastlines, are among the typical characteristics of this heavily exploited marine habitat (Bolatek and Radke, 2010). The threats from intense shipping include accidental (or intentional) spillage of pollution and hazardous materials, such as petroleum products, mineral oils, anti-fouling paints and other chemicals (Filipkowska et al., 2011; Neira et al., 2011; Radke et al., 2008). Surprisingly, these highly inhospitable environments are not a “biological desert”, and a wide variety of aquatic organisms can adapt to their specific habitat (Witalis et al., 2021).

Zooplankton is a vital component of marine ecosystems, contributing to energy flow, organic carbon turnover, and trophic network functioning (e.g., Lampert, 1997), especially mesozooplankton, primarily calanoid copepods, which play a significant role (e.g., Möllmann et al., 2003). As with other temperate waterbodies, the Baltic Sea experiences seasonal changes in plankton occurrence and developmental stages (e.g., Musialik-Koszarowska et al., 2019). However, highly modified port areas likely disrupt the natural cycles of marine organisms, including zooplankton. The Baltic Sea has lower biodiversity than similar latitude seas (Elmgren and Hill, 1997; Ojaveer et al., 2010), housing a mix of marine, brackish, and freshwater species, including highly adaptable opportunistic taxa, relics from its geological history, and an increasing number of invasive species (Leppäkoski et al., 2002; Ojaveer et al., 2010; Snoeijs-Leijonmalm et al., 2017). The low salinity of the sea is considered the most influential factor determining its low biodiversity (Remane, 1934; Remane and Schlieper, 1971; Snoeijs-Leijonmalm et al., 2017; Telesh and Khlebovich, 2010). Other factors influencing species diversity include young geological age (≈ 8000 years: Lass and Matthäus, 2008), oxygen deficiency and anoxic conditions causing dead zones at the seafloor (Ekau et al., 2010), eutrophication (Leppäkoski et al., 1999), and anthropogenic disturbance such as overexploitation (e.g., Casini et al., 2008; Suikkanen et al., 2013).

Baltic seaports face the challenge of transporting non-indigenous species (NIS) since these ports serve as gateways for NIS introduction, with an estimated 225 alien species entering the Baltic Sea through ballast waters, hulls, underwater ship elements, and rivers (AquaNIS, 2015: www.corpi.ku.lt/databases/index.php/aquanis (accessed

2023-12); Ojaveer et al. 2017; Snoeijs-Leijonmalm et al., 2017). To address this issue, the Baltic Sea region signed the BWM 2004, an International Convention for the Control and Management of Ships’ Ballast Water and Sediments (IMO, 2004). However, continuous biomonitoring of port areas is necessary to ensure effective protection against the colonization of new nonindigenous organisms, which may turn out to be possible threats to native biota.

The major goal of this study was to compare the zooplankton community in three Baltic Sea port basins with different levels of anthropogenic disturbances and environmental characteristics, such as salinity gradients and the exchange of seawater with the open sea. Therefore, the main objectives of the present study were: 1) to assess and compare the biodiversity of zooplankton communities in the highly disturbed habitats of the southern Baltic Sea ports; 2) to reveal the influence of environmental conditions, including water temperature, salinity and water transparency, on species composition and seasonal zooplankton dynamics in the examined ports; and finally, 3) to reveal the possible presence of new nonindigenous plankton species in port basins, which are highly exposed to potential colonization.

2. Material and methods

2.1. Study area

The Baltic Sea (Figure 1) is a large (385,000 km²) brackish sea, which is characterized by a strong salinity gradient, with the highest values observed in the southwestern part in Kattegat (S: 27) and the lowest in the northernmost basin of the Bothnian Bay (S: < 1). Due to intense anthropogenic exploitation of the catchment area, the Baltic Sea is heavily polluted and suffers from progressing eutrophication (Helcom, 2009). The degradation of large biomass of phytoplankton leads to the utilization of oxygen, thus creating hypoxic, or even anoxic, conditions near the bottom (e.g., Conley et al., 2009). Furthermore, the weak mixing of water masses contributes to the formation of a sulfidic zone below the halocline (Fonselius, 1970; Laine et al., 1997).

Coordinates of sampling stations, depths and dates of material collection, and type of cargo on each wharf are presented in Supplementary material available online. In each port, three stations were selected: inner, middle and outer, which reflects their distance from the port entrance (Figure 1). It was assumed that, depending on location within a port area, sampling stations differed in their envi-

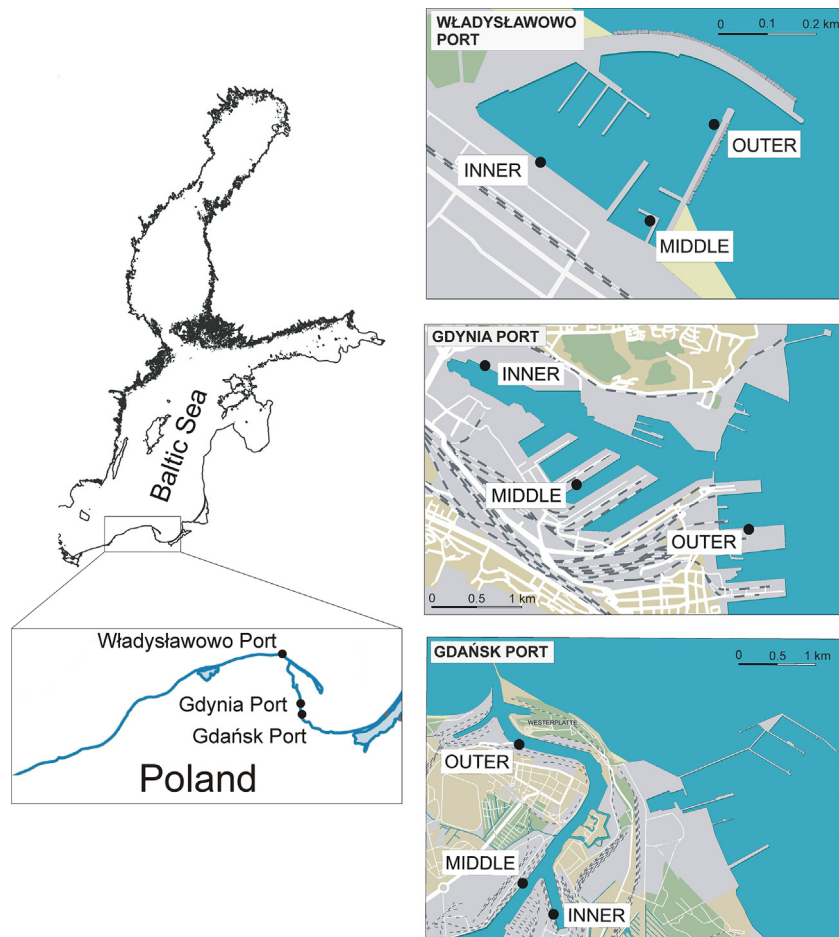


Figure 1 Map of the studied Southern Baltic Sea ports and location of sampling stations within each port: inner, middle and outer, which reflects their distance from the port entrance (more details in Supplementary material available online).

ronmental dynamics, such as traffic intensity, type of cargo (Supplementary material available online) and level of pollution (Pustelnikovas et al., 2007; Radke et al., 2008, 2012, 2013).

2.1.1. Port of Władysławowo

Władysławowo Port, situated on the southern Baltic coast near the Hel Peninsula (Figure 1), serves as a typical fishing port with passenger and sailing quays. It is protected by two breakwaters, and primarily facilitates local cargo reloading. The port accommodates fishing cutters (≈ 80 boats) and serves cruise ships during the summer season. Additionally, it houses a ship-repair yard and a fish processing plant and is an important local centre of sea fishing. In contrast, the larger Gdańsk and Gdynia Ports have more significant international shipping, industrial, and urban infrastructure impacts.

2.1.2. Port of Gdynia

Gdynia Port is relatively young (established in 1922) and occupies a smaller area (972 ha) than Gdańsk Port but is also characterized by the intense traffic of vessels with international range. Both ports, Gdańsk and Gdynia, are surrounded by densely human-populated city infrastructure. The wide entrance to Gdynia Port ensures easy access of ships to

the sea, but also facilitates water mass exchange with the nearby Gulf of Gdańsk, although the port basin is protected by breakwaters, which reduces storm surges and, to some extent, prevents mixing by sea currents (Radke et al., 2013). In the port of Gdynia, a variety of chemicals and metallurgical products and other types of cargo are transhipped; furthermore, at the outer quay, the Stena Line Ferries are served (for more details see Table 1 in Witalis et al., 2021).

2.1.3. Port of Gdańsk

The Port of Gdańsk is one of the oldest (established in the 10th century), largest and deepest ports in the Baltic Sea. Generally, the port consists of two separate areas, i.e. the northern (outer) port, located on the coast of the Gulf of Gdańsk, and the inner port situated near the Motława River and Dead Vistula River; in this study, only the inner port has been investigated. The surface of the inner port area is 3248 ha and the length of transshipment quays is 2455 m. The port is visited by ships, which have an international range and can serve all types and sizes of vessels, with a variety of transshipment cargo (Supplementary material available online). There are also several shipyards in the port of Gdańsk. Because Gdańsk Port is located near the rivers' mouth, the hydrological conditions

Table 1 Results of multivariate PERMANOVA with three main factors: fixed 'Port', 'Season', and 'Station' nested within 'Port', as well as their interactions; based on the square-root transformed abundance structure of zooplankton taxa and Bray-Curtis coefficient resemblance matrix. Statistically significant factors are bolded.

Factor	df	SS	Variation [%]	MS	Pseudo-F	P (perm)	Unique perms
Port	2	9060.7	5.1	4530.4	4.690	0.004	824
Season	3	62046.0	34.6	20682.0	29.214	0.001	998
Station (Port)	6	5781.2	3.2	963.5	0.539	1.000	996
Port x Season	6	13303.0	7.4	2217.2	3.152	0.001	994
Station (Port) x Season	18	12511.0	7.0	695.1	0.389	1.000	997
Residuals	42	75104.0	41.9	1788.2			
Total	77	179100	100.0				

of this area are strongly affected by an inflow of riverine waters.

2.2. Sampling procedure

Zooplankton samples were collected directly from the quays in the ports of Władysławowo, Gdynia and Gdańsk (Figure 1), from January to December 2011, with monthly coverage. In each port, three stations, differing in their distance from the port entrance, were examined (Figure 1 and Supplementary material available online). Sampling was performed using a plankton WP-2 net, with a mesh size of 100 μm , an opening diameter of 19 cm and net trawl length of 80 cm, as recommended by Helcom (2021). The WP-2 net was operated vertically (from near the bottom to the surface, Supplementary material available online), once at each station. The haul was considered a quantitative catch, which collected all zooplankton development stages, i.e., adults and juveniles. To measure *in situ* seawater temperature and salinity values, a mini CTD probe (model SD204) was used. The CTD probe was lowered to the bottom manually and then pulled up to the surface, and measurements were recorded in intervals of 1.0 m. The CTD probe was also employed to estimate the depth of each station (Supplementary material available online), which was necessary to calculate the number of zooplankton individuals (n) to volume-based units ($n\text{ m}^{-3}$). The transparency of seawater was tested with a Secchi disc, and followed the standard procedure, during which the disc was lowered slowly down in the water to the limit of visibility on a calibrated rope. This procedure was repeated twice at each station. After collection, zooplankton samples were immediately preserved in a 4% borax-buffered formalin-seawater solution and then transported to the laboratory for further analyses. In certain winter months (December and March in Gdańsk and Gdynia Ports and February in Władysławowo Port), the sampling failed due to the freezing of port basins. Furthermore, sample collection was not performed in July in Władysławowo Port because of the prohibited access to that area, due to renovation works on the wharf.

2.3. Laboratory analyses

Taxonomic identification and counting procedures were carried out according to the Guidelines for Monitoring of Mesozooplankton by Helcom (2021). Most zooplankton specimens

were identified to the species level using a stereomicroscope (OLYMPUS SZX12, magnification: $1.6 \times 15 \times 90$). In the case of copepods, development stages were determined as follows: nauplii (npl.), copepodites CI-III and CIV-V, as well as adults (males and females). Juvenile organisms of other zooplankton taxa (juv.) were also recorded and identified to the genus or higher taxonomic level. For taxon identification, the keys by Telesh and Heerkloss (2002, 2004) and Razouls et al. (2005–2017) were used.

2.4. Data processing and statistical analysis

To examine the potential effects of the studied environmental factors on the zooplankton community composition and taxa richness in the Baltic Sea ports, multivariate analyses were performed. Because the data did not show a normal distribution (Shapiro-Wilk test: $p < 0.05$), for the numerical analyses a nonparametric PERMANOVA (permutational multivariate analysis of variance) procedure was used (Anderson, 2001). In the multivariate PERMANOVA three factorial design, two fixed factors were used, i.e., port (three levels: Władysławowo, Gdynia and Gdańsk), and season (four levels: winter, spring, summer and autumn), as well as one factor, 'station', nested in 'port' (three levels: inner, middle and outer). PERMANOVA was computed on the basis of the Bray-Curtis resemblance matrix, and prior to analysis, all data were square-root transformed. Additionally, individual taxa contributions to the observed similarity pattern were tested using SIMilarity PERcentages (SIMPER). The SIMPER procedure allows us to assess which taxa were principally responsible for the grouping of zooplankton assemblages within the studied ports and seasons.

The impact of measured environmental variables (i.e., seawater temperature, transparency and salinity) on the zooplankton community was examined with distance-based linear modelling (DistLM). DistLM detects the main patterns of dependence between the Bray-Curtis similarity matrix of zooplankton abundance and environmental data to reveal the most influential variables, driving an observed diversity structure. Relationships between environmental data and the abundance of zooplankton taxa were displayed in the ordination space of dbRDA (distance-based redundancy analysis), which is a part of the DistLM procedure. The PERMANOVA, SIMPER and DistLM analyses were performed using the PRIMER 7 statistical package (Clarke and Gorley, 2015) with the PERMANOVA+ add on (Anderson et al., 2008).

3. Results

3.1. Salinity, water temperature and transparency in the examined port basins

The examined southern Baltic Sea ports faced seasonal changes typical for temperate regions, although with slight differences between them (Figure 2). Władystawowo Port experienced the coldest seawater temperature (1.43°C) in February and the warmest temperature (18.05°C) in August. Salinity reached its minimum (5.11) in February and its maximum (7.32) in November. The lowest transparency was recorded in February (0.8 m), while the highest was observed in November (3.40 m) (Figure 2).

In Gdynia Port, the lowest seawater temperature (0.19°C) occurred in January, while the highest (17.80°C) was observed in August. Salinity levels were lowest (1.27) in December and highest (7.22) in January. The lowest transparency was noted in April (1.6 m), and the highest occurred in November (4.10 m) (Figure 2).

In Gdańsk Port, seawater temperature varied seasonally, ranging from -0.06°C (min. in February 2011) to 18.73°C (max. in August). Salinity exhibited less variability, with levels ranging from 2.12 (min. in December) to 7.07 (max. in January). The lowest water transparency was in

February (0.7 m), while the highest was in November (3.6 m) (Figure 2).

3.2. Zooplankton community structure and seasonal dynamics

3.2.1. Species abundance and diversity

In this study, 43 taxa were recorded in all three ports, of which 25 were identified to the species level, and the remaining taxa were identified to higher taxonomic groups. Generally, at all three ports, similar taxa richness was found, and the lowest mean taxa number was observed in winter (14 taxa m⁻³ ± 2.78 SD), while the highest was observed in summer (21 taxa m⁻³ ± 3.89). Similar patterns, consistent across all three ports, of zooplankton abundance were noted, with the highest values in summer (mean abundance in summer months 54,347 ind. m⁻³ ± 54,497) and the lowest in winter (mean abundance in winter months 2,601 ind. m⁻³ ± 1,537). The most numerous zooplankton groups in Władystawowo Port were meroplanktonic larvae (51%) and calanoid copepods (46%), whereas in Gdynia Port the most abundant were rotifers (45%). In Gdańsk Port calanoid copepods showed the highest numbers, with the share at 58% of the total abundance of this port. The constant (though less abundant) component of all port assemblages was the copepod *Pseudocalanus elongatus*. It is

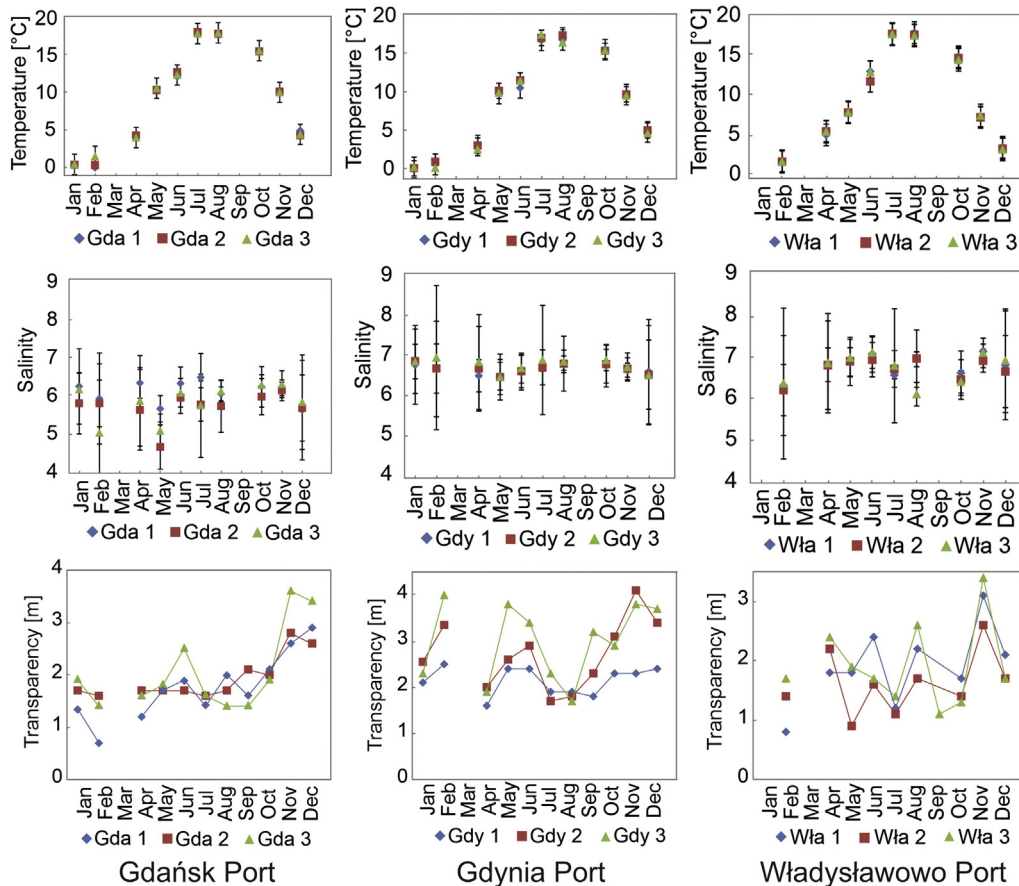


Figure 2 Seasonal changes of seawater temperature, salinity and transparency (mean values from the bottom to the surface ± standard deviations) in the water column of the Baltic Sea ports and stations. GDA/GDY/WŁA 1 = inner, GDA/GDY/WŁA 2 = middle, GDA/GDY/WŁA 3 = outer station.

worth noting that no new nonindigenous species were found in any of the examined ports and stations.

3.2.2. Spatial and temporal structure of the zooplankton community

Multivariate PERMANOVA revealed statistically significant differences between the sampling seasons and ports, and their interactions (Table 1), but the most important factor influencing zooplankton assemblages was connected to seasonal changes in species composition and abundance, which was confirmed by the highest proportion of zooplankton variation explained by the ‘season’ factor alone (34.7%).

The results of the SIMPER analysis indicated taxa characteristic for each season. In winter, the zooplankton community was dominated by *Acartia* spp. (*A. bifilosa*, *A. longiremis* adults, and *Acartia* nauplii and copepodites CI-CV), which contributed to the differentiation of this group. The spring assemblage was characterized by higher numbers of Polychaeta larvae and lower shares of *Acartia* nauplii and *Synchaeta monopus* individuals than the summer and autumn assemblages. The most influential for separation of the summer assemblage was the high share of Cirripedia larvae, although the occurrence of relatively high numbers of *Acartia* nauplii and early copepodites was also significant. The autumn assemblage differed from the others in a particularly high *Acartia* nauplii abundance and a higher share of *Acartia tonsa* adults when compared to other seasons (Table 2).

3.2.3. Factors influencing community structure

The DistLM model performed for all samples explained 23.4% of the total variation in the zooplankton community, with 21.4% of the variation explained by the first two axes of dbRDA (Figure 3). The dbRDA diagram allowed us to distinguish three zooplankton assemblages: winter, spring-autumn and summer (Figure 3). The most influential environmental variable was seawater temperature (16.7% of explained zooplankton variability), followed by water transparency and salinity (Table 3). High seawater temperatures indicated the summer samples on the right side of the RDA plot, whereas low temperatures separated the winter samples on the left side of the diagram (Figure 3). Samples characterized by high seawater transparency (i.e., collected in winter and autumn) were located in the upper sector of the RDA plot, while spring and summer samples – showing low transparency of water – can be found in the bottom part of the diagram (Figure 3). Although salinity appeared to be statistically significant in the DistLM model, it explained only 2% of the observed variation (Table 3), which contributed to the separation of samples from Gdańsk Port, which was slightly less saline, from the remaining samples (Figure 2, Supplementary material available online).

Multivariate PERMANOVA revealed statistically significant differences between the studied ports in terms of zooplankton composition; the ports were responsible for 5.1% of the variation in zooplankton data (Table 1). Furthermore, the interaction between factors ‘port’ and ‘season’ was also significant and explained 7.4% of the observed variability in the abundance structure of taxa. It is worth noting that the zooplankton species abundance structure in Władysławowo Port significantly differed from the zooplankton communities in the ports of Gdynia and Gdańsk (Table 4). The SIMPER

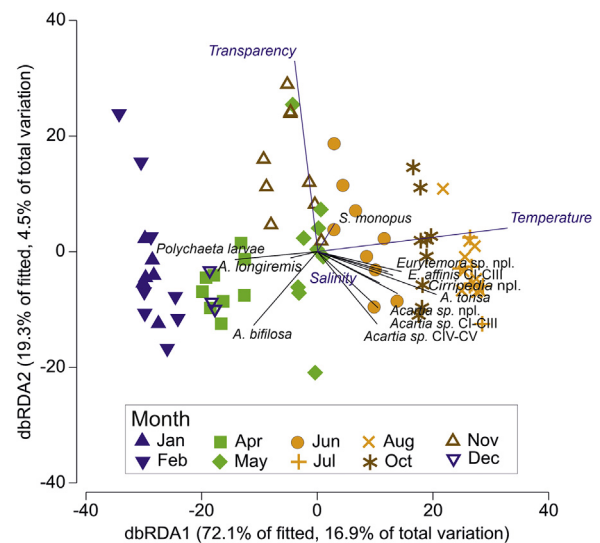


Figure 3 Ordination plot of distance-based redundancy analysis (dbRDA) created on the basis of distance-based linear modeling (DistLM), showing relationships between the abundance of zooplankton taxa and continuous environmental predictors i.e. seawater temperature, transparency and salinity, with vector overlay of Pearson’s correlations of taxa (restricted to those having $> \pm 0.4$). Purple symbols = winter samples, green symbols = spring samples, orange symbols = summer samples and brown symbols = autumn samples. Environmental factors were not measured in March (due to the freezing of port basins), and in September (due to instrument failure).

analysis indicated taxa, that were primarily responsible for the distinctiveness of zooplankton assemblages in the examined ports (Table 2). Interestingly, differentiation was not influenced by the dominance of any particular taxon, but it was determined by the presence/share of less abundant taxa. In each studied port, the constant dominant was *Acartia* spp. (all development stages, including adults, earlier copepodites and nauplii). The most influential taxa responsible for the distinctiveness of the Władysławowo Port assemblage were harpacticoid copepods, *Eurytemora affinis* copepodites and Polychaeta larvae (Table 2). In the Gdynia Port, the higher numbers of Polychaeta and Cirripedia larvae contributed to the differentiation of this assemblage, whereas the Gdańsk Port was characterized by higher shares of *S. monopus* and *E. affinis* specimens.

4. Discussion

4.1. Species abundance and richness in the Ports of Władysławowo, Gdynia and Gdańsk

A total of 43 zooplankton taxa were found in all examined ports (33 in Władysławowo Port, 34 in Gdynia Port and 31 in Gdańsk Port), which is a similar, or slightly lower, species richness when compared to other Baltic ports, e.g. Muuga – Estonia (44 taxa: Ojaveer et al., 2015), Riga – Latvia (32 taxa: Strake et al., 2015), Liepaja – Latvia (34 taxa: Strake et al., 2015), and in the earlier investigation from Gdynia Port (35 taxa: Normant et al., 2015). Previous

Table 2 Summary of the key zooplankton species identified by SIMPER analysis as primarily responsible for the distinctiveness of assemblage at each port (upper panels) and season (lower panels) separately; with a cut-off at 70%.

Taxa	Mean abundance	Mean similarity	Contribution [%]	Cumulative contribution
PORTS				
Gdańsk Port assemblage (mean similarity: 37.68)				
<i>Acartia</i> sp. npl.	48.78	9.35	24.8	24.8
<i>Acartia</i> sp. CI-CIII	21.23	4.37	11.61	36.41
<i>Acartia</i> sp. CIV-CV	18.00	3.50	9.30	45.71
<i>S. monopus</i>	39.64	2.91	7.72	53.43
<i>E. affinis</i> CI-CIII	29.84	2.34	6.21	59.64
<i>E. affinis</i> CIV-CV	17.03	1.66	4.42	64.06
<i>E. affinis</i> npl.	25.41	1.58	4.19	68.24
Polychaeta larvae	25.36	1.51	4.02	72.26
Gdynia Port assemblage (mean similarity: 35.77)				
<i>Acartia</i> sp. npl.	47.19	8.03	22.45	22.45
<i>Acartia</i> sp. CI-CIII	25.21	4.37	12.22	34.67
<i>Acartia</i> sp. CIV-CV	16.04	2.89	8.08	42.75
<i>S. monopus</i>	39.28	2.37	6.64	49.39
Polychaeta larvae	29.65	2.05	5.74	55.13
<i>T. longicornis</i> CIV-CV	8.70	1.41	3.94	59.07
Cirripedia npl.	23.43	1.35	3.77	62.84
<i>T. longicornis</i> ad.	7.29	1.11	3.11	65.96
<i>A. bifilosa</i> ad.	6.72	1.11	3.10	69.05
<i>E. affinis</i> ad.	5.69	1.00	2.80	71.85
Władysławowo Port assemblage (mean similarity: 32.73)				
<i>Acartia</i> sp. npl.	33.90	8.67	26.48	26.48
<i>Acartia</i> sp. CI-CIII	19.60	3.94	12.04	38.52
<i>Acartia</i> sp. CIV-CV	14.63	2.84	8.67	47.19
Harpacticoida indet.	21.63	2.82	8.63	55.82
<i>E. affinis</i> CIV-CV	7.62	1.49	4.54	60.36
Polychaeta larvae	23.50	1.45	4.44	64.80
<i>E. affinis</i> ad.	7.30	1.45	4.43	69.23
<i>A. tonsa</i> ad.	20.04	1.34	4.08	73.31
SEASONS				
Winter assemblage (mean similarity: 58.36)				
<i>Acartia</i> sp. npl.	34.22	20.28	34.75	34.75
<i>A. bifilosa</i> ad.	11.98	5.65	9.68	44.43
<i>Acartia</i> sp. CIV-CV	12.39	5.63	9.65	54.08
<i>Acartia</i> sp. CI-CIII	11.71	5.55	9.50	63.58
<i>A. longiremis</i> ad.	9.70	4.30	7.36	70.94
Spring assemblage (mean similarity: 51.00)				
Polychaeta larvae	88.93	19.28	37.79	37.79
<i>Acartia</i> sp. npl.	34.47	7.29	14.30	52.09
<i>Acartia</i> sp. CI-CIII	22.74	5.77	11.31	63.40
<i>S. monopus</i>	32.39	4.26	8.35	71.75
Summer assemblage (mean similarity: 37.32)				
Cirripedia npl.	84.77	6.70	17.94	17.94
<i>Acartia</i> sp. npl.	59.13	6.38	17.10	35.04
<i>Acartia</i> sp. CI-CIII	24.93	2.47	6.61	41.65
<i>A. tonsa</i> ad.	32.58	2.40	6.42	48.06
<i>S. monopus</i>	63.71	2.32	6.22	54.29
<i>E. affinis</i> CI-CIII	36.69	2.13	5.69	59.98
<i>E. affinis</i> npl.	33.28	2.06	5.51	65.50
<i>Acartia</i> sp. CIV-CV	19.86	1.93	5.17	70.67
Autumn assemblage (mean similarity: 42.24)				
<i>Acartia</i> sp. npl.	41.16	7.47	17.68	17.68
<i>A. tonsa</i> ad.	33.67	5.57	13.19	30.87
<i>Acartia</i> sp. CI-CIII	26.09	5.28	12.49	43.37
<i>Acartia</i> sp. CIV-CV	20.44	4.29	10.15	53.51
Cirripedia npl.	12.33	2.60	6.15	59.67
<i>S. monopus</i>	13.77	2.36	5.58	65.25
<i>E. affinis</i> CI-CIII	9.24	2.25	5.33	70.57

Table 3 Summary of sequential DistLM test searching for relationships between the abundance of zooplankton taxa and environmental variables (seawater temperature, transparency and salinity). Statistically significant variables are bolded.

Environmental variable	R ²	SS (trace)	Pseudo-F	p-value	Prop.	Cumulative variation explained	Res. df
Temperature	0.16702	29913.0	15.239	0.0001	0.167	0.167	76
Transparency	0.21194	8045.0	4.2749	0.0001	0.045	0.212	75
Salinity	0.23443	4028.2	2.174	0.0207	0.022	0.234	74

Table 4 Results from multivariate PERMANOVA post-hoc t-test for the studied ports (GDA – Gdańsk, GDY – Gdynia, WŁA – Władysławowo). The PERMANOVA test was based on square-root transformed abundances of taxa and Bray-Curtis coefficient resemblance matrix. Statistically significant values are bolded.

Port	Abundance structure of taxa		
	t	p-value	perms
GDA & GDY	1.671	0.095	10
GDA & WŁA	2.161	0.001	60
GDY & WŁA	2.512	0.001	60

research conducted in the Gulf of Gdańsk (but not in any port area) revealed lower species richness, i.e., from 24 to 30 taxa (Bielecka et al., 2000b; Józefczuk et al., 2003), although the difference in taxa number in the present study can be ascribed to the differences in sampling effort, e.g., the number of sampling stations. The study revealed statistically significant differences in the abundance structure of taxa among the studied ports and stations, although they explained only 4.7% and 3.2% (respectively) of the observed zooplankton variability (Table 1). Obvious factors driving these differences could be higher salinity in Władysławowo Port and higher anthropogenic impact, including ship traffic and human-mediated pollution, in Gdańsk and Gdynia Ports than in Władysławowo Port.

Our results proved that three environmental variables (i.e., seawater temperature, transparency and salinity) had a significant impact on the observed abundance structure of zooplankton taxa in the examined ports (Table 3). However, all three abiotic factors together had relatively low explanatory power (23%), which suggests that there are also other variables not included in our study (such as chlorophyll *a* or oxygen concentrations) that likely influence the zooplankton community throughout the year.

Seawater temperature and transparency seemed to be mainly responsible for temporal variability in zooplankton community structure (i.e., seasonal differences among zooplankton assemblages), whereas salinity contributed to spatial differences in the examined zooplankton community (variation between the ports). In Gdańsk Port, the mean salinity was approximately 1 unit lower than that in other ports during the year. A similar investigation conducted in Vistula Lagoon (located 25 km from Gdańsk Port) suggested that changes in salinity at a one-unit level could be sufficient to affect the density and structure of a zooplankton community, although not its diversity (Paturej and

Gutkowska, 2015). In this study, we found that the taxonomic composition slightly differed between the particular ports. The SIMPER analysis showed that the differentiation of zooplankton was not influenced by dominant species but was determined by the share of less abundant taxa (Table 2).

Similar dominant taxa compositions were observed in all studied ports and stations, most likely due to the homogeneity of hydrographic conditions, primarily temperature and salinity. However, some variations in zooplankton abundance were noted (Supplementary material available online). The Gdańsk Port exhibited slightly higher density, potentially attributed to its connection with the Dead Vistula River, allowing species preferring low salinity conditions (e.g., *Eudiatomus gracilis*) to enter. Sea currents and the influx of water masses from the open sea also influenced the differences in species abundance between Władysławowo Port and both Gdańsk and Gdynia Ports (Table 4), creating more favourable conditions for certain zooplankton species.

It is worth noting that no new nonindigenous (NIS) or invasive species were recorded in the examined ports during the investigation. Furthermore, relatively new studies (e.g., Dzierzbicka-Głowacka et al., 2014) could not detect new invasion events in the Gulf of Gdańsk. However, earlier reports indicated the presence of nonindigenous species such as *Cercopagis pengoi* (Bielecka et al., 2000b) and *Mnemiopsis leidyi* (Janas and Zgrundo, 2007) in the study area, but they had not been detected in this study. The sampling campaign was conducted in 2011 when ballast water management recommendations were likely implemented to a limited extent. The international Ballast Water Management Convention (BWM) was signed in 2004 (IMO, 2004), entered into force in 2017, and was ratified in Poland in 2019. Guidelines for voluntary ballast water exchange were issued in 2008, but adherence to these recommendations by shipowners remains uncertain. Our one-year study period may not provide comprehensive information on potential introduction processes in the port basins, highlighting the need for continuous, long-term monitoring to detect early-stage invasion events.

Comparison with other seaport surveys reveals variations in sampling efforts, with higher efforts generally yielding increased zooplankton abundance and taxa richness (e.g., Shaikh et al., 2021; Vidjak et al., 2019). However, a diversified research methodology (differences in net mesh sizes, sampling frequency, sample size, differences in data processing, etc.) was a serious limitation of the above comparison. The common characteristics of all reviewed port investigations were the presence of numerous and diversified zooplankton communities and the inherent appearance of nonindigenous species (Table 5, Vidjak et al., 2019).

Table 5 Comparison with similar survey carried out in seaports of the Gulf of Finland (maximum abundance, dominant taxa in assemblage and NIS = nonindigenous species).

Region	Ports	Depth [m]	Mesh size [μm]	Sampling frequency times/year	Number of samples	Max abundance/dominance	NIS	Reference	Remarks
Baltic Sea, Gulf of Finland	Ust-Luga, Kronshadt	6-18	50, 100	3	6	125,500 ind. m^{-3} / <i>Eurytemora affinis</i> , <i>Cercopagis pengoi</i>	<i>Cercopagis pengoi</i> , <i>Eurytemora carolleeae</i> , <i>Acartia tonsa</i> , <i>Acanthocyclops americanus</i>	Alekseev & Sukhikh 2023	Only data for ports used. Study contains also data for river, temporary pools and benthic taxa
Southern Baltic Sea	Władystawowo, Gdynia, Gdańsk	5-12.8	100	12	108	28,697 ind. m^{-3} (Gdańsk)/ <i>Acartia</i> sp., <i>Eurytemora affinis</i> , <i>Synchaeta monopus</i> , Polychaeta larvae	<i>Acartia tonsa</i> , <i>Amphibalanus improvisus</i> larvae	This study	Taxa dominance seasonally dependent

4.2. Seasonal variability in zooplankton assemblages

4.2.1. General description

This investigation clearly showed that the species composition and abundance of zooplankton in all studied ports were highly seasonal (Figure 3, Table 2). Such seasonal fluctuation patterns of zooplankton are generally well documented in the Gulf of Gdańsk (Bielecka et al., 2000a; Dzierzbicka-Głowacka et al., 2014; Mudrak and Żmijewska, 2007; Musialik-Koszarowska et al., 2019) and other localities in the southern Baltic Sea (Möllmann et al., 2000; Wiktor, 1990). However, our study revealed the undisturbed course of seasonal changes in the zooplankton community in heavily exploited port basins, proving the possibly high resistance of the community to multiple stressors. Indeed, each season was characterized by a unique zooplankton assemblage (Table 2). Clear seasonality observed in the Ports of Władystawowo, Gdynia and Gdańsk was mainly a consequence of temperature changes, and despite severe anthropogenic pressure, the seasonal patterns of examined zooplankton port assemblages resembled the adjacent marine environment. Generally, the genus *Acartia* contributed a high share of the zooplankton community throughout the year. It consisted of species belonging to eurythermal *A. bifilosa* present all year round, thermophilous *A. tonsa* dominating in summer and autumn months, and psychrophilic *A. longiremis* dominating during winter months. Similar seasonal fluctuations in these species are known from other studies conducted in the southern Baltic Sea (Mudrak and Żmijewska, 2007; Żmijewska et al., 2000). According to Line (1984), *Acartia* spp. are characterized by a long reproduction season (March–December) and a high number of generations per year (up to seven). However, the tendency to build up the maximum abundance of assemblage in summer months was apparent in these mostly thermophilic species (Chojnacki, 1984).

4.2.2. Summer assemblage

The summer months were characterized by sudden and intense development of zooplankton, as the number of species and their abundances exhibited the highest levels. In summer, the most characteristic taxa were copepods *Acartia tonsa* and their nauplii, *Eurytemora affinis* and Cirripedia nauplii, which reached their abundance peaks in this time of the year. However, in Władystawowo Port, the maximum levels occurred one month earlier (i.e., May–July) than in Gdańsk and Gdynia Ports (Supplementary material available online). Möllmann et al. (2000) found differences in the maximum biomasses of zooplankton between the Bornholm Basin (July) and the Gdańsk Deep (August–September), and this observation was explained by the earlier appearance of phytoplankton blooms in the Bornholm Basin, being a food supply for the growing zooplankton community. Indeed, the observed differences in water transparency can be considered an indirect indication of phytoplankton density since low transparency was found in May–July in the Władystawowo Port, and in August–September in the Gdańsk and Gdynia Ports (Figure 2). Cirripedia larvae are typical components of zooplankton communities during warmer months in the Gulf of Gdańsk

(Mudrak and Żmijewska, 2007; Żmijewska et al., 2000) as well as in other regions, such as Svalbard, because these larvae are strongly related to algal food availability (Walczńska et al., 2019; Weydmann-Zwolicka et al., 2021). Moreover, in summer, numerous occurrences of copepods were recorded in the investigated ports, similar to the adjacent areas of the southern Baltic Sea (Figiela et al., 2016; Musialik-Koszarowska et al., 2019). In the central Baltic Sea, Möllmann et al. (2000) observed considerable numbers of cladocerans in summer, whereas in the studied port basins, this group exhibited relatively low abundances.

4.2.3. Autumn assemblage

In autumn, a sudden reduction in taxa number and abundance was observed when compared to the summer assemblage. The autumn assemblage was distinctive in a relatively high number of *A. tonsa* adults, abundant *Acartia* juveniles (nauplii and copepodites) and a higher number of Cirripedia nauplii. Similar autumn abundance peaks (September and November) of Cirripedia nauplii were also recorded in the Gulf of Gdańsk outside the port area (Bielecka et al., 2000a). In autumn, environmental characteristics resembled those in spring with moderate seawater temperatures and transparency, although differences in taxa composition were apparent.

4.2.4. Winter assemblage

In the southern Baltic ports, species richness and number of individuals were generally low in winter (Supplementary material available online). The winter assemblage was characterized by the predominance of consecutive developmental stages of *Acartia* spp., from nauplii throughout copepodites CI-CV to adult individuals of *A. biflosa* and *A. longiremis*. Viitasalo et al. (1995) found the thermal optimum for *Acartia longiremis* within cooler temperatures, and our observations seem to confirm this trend, since *A. longiremis* adults showed the maximum number in February and afterwards decreased in abundance until July. In Gdańsk Port, the adults of *A. biflosa* appeared in January, together with the earliest copepodites of this genus.

4.2.5. Spring assemblage

Based on the results of dbRDA and SIMPER analyses, the spring zooplankton assemblage was characterized by numerous Polychaeta larvae, *Acartia* spp. nauplii and rotifers. This assemblage was explained by moderate values of seawater temperatures and transparency. In the studied ports, the dominant rotifer was *Synchaeta monopus*, which showed the highest abundance in May and June (Supplementary material available online). For comparison, in the coastal waters of the Gulf of Gdańsk, the highest numbers of rotifers (*Synchaeta* spp.) were observed in May (Dippner et al., 2000; Józefczuk et al., 2003; Mudrak-Cegiołka et al., 2013), whereas in the northern Baltic Sea (SW coast of Finland), *Synchaeta* spp. peaked in June but generally exhibited high abundance until October (Viitasalo et al., 1995).

5. Conclusions

- The zooplankton community in the investigated ports of the southern Baltic Sea was rich in taxa (43), and com-

parable to the taxa richness of other southern Baltic seaports e.g., Muuga, Riga, and Liepaja. No nonindigenous or invasive species were recorded in the examined ports.

- The taxa composition and seasonal zooplankton dynamics in the examined port basins resembled the zooplankton community inhabiting ambient habitats outside the ports, i.e., the Gulf of Gdańsk and the Baltic Proper.
- Significant differences in the zooplankton community structure among the ports and seasons were recorded. However, the examined ports/seasons were similar in the dominance of *Acartia* spp. (although of different development stages) but differed in the presence and proportions of less abundant taxa, especially during the productive season: Polychaeta larvae and rotifers were abundant in spring (especially *Synchaeta monopus*); Cirripedia nauplii and early development stages of the copepod *Eurytemora affinis* were numerous in summer.
- The main abiotic factors regulating the dynamics of zooplankton community natural cycles were seawater temperature and transparency, which are related to changing seasons, although they were also likely modified by biological factors, i.e., algal blooms, which provided a food base for the developing zooplankton community.

Declaration of competing interest

The authors declare that they have no known competing financial interests or personal relationships that could have appeared to influence the work reported in this paper.

Acknowledgments

This study received funding from the statutory activity of the Institute of Oceanology Polish Academy of Sciences and from the National Marine Fisheries Research Institute. We would like to thank Edyta Białowąs, Katarzyna Dorosz, Katarzyna Hlebowicz-Wojciechowska and Daria Mróz for facilitating access to port areas and logistic support. Authors are also thankful to Katarzyna Dmoch for confirming species identification.

Supplementary materials

Supplementary material associated with this article can be found, in the online version, at <https://doi.org/10.1016/j.oceano.2024.02.001>.

References

- Anderson, M.J., 2001. A new method for non-parametric multivariate analysis of variance. *Austral Ecol* 26, 32–46. <https://doi.org/10.1111/j.1442-9993.2001.01070.pp.x>
- Anderson, M.J., Gorley, R.N., Clarke, K.R., 2008. PERMANOVA+ for PRIMER: Guide to Software and Statistical Methods. PRIMER-E, Plymouth, UK.

- AquaNIS, 2015. Information system on Aquatic Non-Indigenous and Cryptogenic Species. World Wide Web electronic publication. www.corpi.ku.lt/databases/aquanis. Version 2.36+. Accessed 2023-12.
- Bielecka, L., Gaj, M., Mudrak, S., Żmijewska, M.I., 2000a. The seasonal and short-term variability of zooplankton taxonomic composition in the shallow coastal area of the Gulf of Gdańsk. *Oceanol. Hydrobiol. Stud.* 29, 57–76.
- Bielecka, L., Żmijewska, M.I., Szyborska, A., 2000b. A new predatory cladoceran *Cercopagis (Cercopagis) pengoi* (Ostroumov 1891) in the Gulf of Gdańsk. *Oceanologia* 42 (3), 371–374.
- Bolatek, J., Radke, B., 2010. Aspects of pollution in the harbours located near the river mouth using the example of the Gdańsk and Klaipėda harbours. *Prace i Studia Geograficzne* 44, 249–265 (in Polish with English abstract).
- Casini, M., Lövgren, J., Hjelm, J., Cardinale, M., Molinero, J.C., Kornilovs, G., 2008. Multi-level trophic cascades in a heavily exploited open marine ecosystem. *Proc. Royal Soc. B* 275, 1793–1801. <https://doi.org/10.1098/rspb.2007.1752>
- Chojnacki, J., 1984. Quantitative occurrence of Copepoda in Southern Baltic inshore waters. *Crustaceana Supplement* 126–136.
- Clarke, K.R., Gorley, R.N., 2015. PRIMER V7: User manual/tutorial, PRIMER – E, Plymouth.
- Conley, D.J., Björck, S., Bonsdorff, E., Carstensen, J., Destouni, G., Gustafsson, B.G., Hietanen, S., Kortekaas, M., Kuosa, H., Meier, H.E.M., Müller-Karulis, B., Nordberg, K., Norrko, A., Nürnberg, G., Pitkänen, H., Rabalais, N.N., Rosenberg, R., Savchuk, O.P., Slomp, C.P., Voss, M., Wulff, F., Zillén, L., 2009. Hypoxia-related processes in the Baltic Sea. *Environ. Sci. Technol.* 43, 3412–3420. <https://doi.org/10.1021/es802762a>
- Dippner, J.W., Kornilovs, G., Sidrevics, L., 2000. Long-term variability of mesozooplankton in the central Baltic Sea. *J. Marine Syst.* 25, 23–31. [https://doi.org/10.1016/S0924-7963\(00\)00006-3](https://doi.org/10.1016/S0924-7963(00)00006-3)
- Dzierzbicka-Głowacka, L., Kalarus, M., Musialik-Koszrowska, M., Lemieszek, A., Żmijewska, M.I., 2014. Seasonal variability in the population dynamics of the main mesozooplankton species in the Gulf of Gdańsk (southern Baltic Sea): Production and mortality rates. *Oceanologia* 57 (1), 78–85. <https://doi.org/10.1016/j.oceano.2014.06.001>
- Ekau, W., Auel, H., Pörtner, H.O., Gilbert, D., 2010. Impacts of hypoxia on the structure and processes in pelagic communities (zooplankton, macro-invertebrates and fish). *Biogeosciences* 7, 1669–1699. <https://doi.org/10.5194/bg-7-1669-2010>
- Elmgren, R., Hill, C., 1997. Ecosystem function at low biodiversity – the Baltic example. *Mar. Biodivers.* 319–336.
- Figiela, M., Musialik-Koszrowska, M., Nowicki, A., Lemieszek, A., Kalarus, M., Druet, C., 2016. Long-term changes in the total development time of Copepoda species occurring in large numbers in the Southern Baltic Sea – numerical calculations. *Oceanol. Hydrobiol. Stud.* 45, 1–10. <https://doi.org/10.1515/ohs-2016-0001>
- Filipkowska, A., Kowalewska, G., Pavoni, B., Łęczyński, L., 2011. Organotin compounds in surface sediments from seaports on the Gulf of Gdańsk (southern Baltic coast). *Environ. Monit. Assess.* 182, 455–466. <https://doi.org/10.1007/s10661-011-1889-x>
- Fonselius, S.H., 1970. On the stagnation and recent turnover of the water in the Baltic, Fishery board of Sweden. *Hydrographic Department Göteborg*, 22, 533–544.
- Helcom, 2009. Eutrophication in the Baltic Sea – an integrated thematic assessment of the effects of nutrient enrichment and eutrophication in the Baltic Sea region. In: *Baltic Sea Environment Proceedings 115B*, Helsinki.
- Helcom, 2021. Guidelines for monitoring of mesozooplankton. Manuals and Guidelines, Helcom. Available at: <https://helcom.fi/wp-content/uploads/2019/08/Guidelines-for-monitoring-of-mesozooplankton.pdf>.
- IMO, 2004. International Convention for the control and management of Ships' Ballast Water and Sediments. International Maritime Organization, London.
- Janas, U., Zgrundo, A., 2007. First record of *Mnemiopsis leidyi* A. Agassiz, 1865 in the Gulf of Gdańsk (southern Baltic Sea). *Aquat. Invasions* 2, 450–454. <https://doi.org/10.3391/ai.2007.2.4.18>
- Józefczuk, A., Guzera, E., Bielecka, L., 2003. Short-term and seasonal variability of mesozooplankton at two coastal stations (Gdynia, Sopot) in the shallow water zone of the Gulf of Gdańsk. *Oceanologia* 45 (2), 317–336.
- Laine, A.O., Sandler, H., Andersin, A.B., Stigzelius, J., 1997. Long-term changes of macrozoobenthos in the Eastern Gotland Basin and the Gulf of Finland (Baltic Sea) in relation to the hydrographical regime. *J. Sea Res.* 38, 135–159.
- Lampert, W., 1997. Zooplankton research: the contribution of limnology to general ecological paradigms. *Aquat. Ecol.* 31, 19–27. <https://doi.org/10.1023/A:1009943402621>
- Lass, H.-U., Matthäus, W., 2008. General oceanography of the Baltic Sea. In: Feistel, R., Nausch, G., Wasmund, N. (Eds.), *State and evolution of the Baltic Sea 1952–2005*. John Wiley & Sons, Inc., Hoboken, N.J., 5–44.
- Leppäkoski, E., Gollasch, S., Gruszka, P., Ojaveer, H., Olenin, S., Panov, V., 2002. The Baltic a sea of invaders. *Can. J. Fish. Aquat. Sci.* 59, 1175–1188. <https://doi.org/10.1139/f02-089>
- Leppäkoski, E., Helminen, H., Hänninen, J., Tallqvist, M., 1999. Aquatic biodiversity under anthropogenic stress: an insight from the Archipelago Sea (SW Finland). *Biodivers. Conserv.* 8, 55–70. <https://doi.org/10.1023/A:1008805007339>
- Line, R.J., 1984. On reproduction and mortality of zooplankton (Copepoda) in the South-eastern, Eastern and North-eastern Baltic. *Articles on biological productivity of the Baltic Sea* 2, 265–274.
- Möllmann, C., Kornilovs, G., Sidrevics, L., 2000. Long-term dynamics of main mesozooplankton species in the central Baltic Sea. *J. Plankton Res.* 22, 2015–2038. <https://doi.org/10.1093/plankt/22.11.2015>
- Möllmann, C., Köster, F., Kornilovs, G., Ludvigs, S., 2003. Interannual variability in population dynamics of calanoid copepods in the Central Baltic Sea. *ICES Mar. Sci. Symposia* 219, 220–230.
- Mudrak, S., Żmijewska, M., 2007. Spatio-temporal variability of mesozooplankton from the Gulf of Gdańsk (Baltic Sea) in 1999–2000. *Oceanol. Hydrobiol. Stud.* 36, 3–9. <https://doi.org/10.2478/v10009-007-0007-4>
- Mudrak-Cegiołka, S., Beldowska, M., Jędruch, A., 2013. Zooplankton w badaniach rtęci w strefie przybrzeżnej Zatoki Gdańskiej. In: Falkowska, L. (Ed.), *Rtęć w środowisku: identyfikacja zagrożeń dla zdrowia człowieka*. Wydawnictwo Uniwersytetu Gdańskiego, Gdańsk, 165–170.
- Musialik-Koszrowska, M., Dzierzbicka-Głowacka, L., Weydmann, A., 2019. Influence of environmental factors on the population dynamics of key zooplankton species in the Gulf of Gdańsk (southern Baltic Sea). *Oceanologia* 61 (1), 17–25. <https://doi.org/10.1016/j.oceano.2018.06.001>
- Neira, C., Mendoza, G., Levin, L.A., Zirino, A., Delgadillo-Hinojosa, F., Porrachia, M., Deheyne, D.D., 2011. Macrobenthic community response to copper in Shelter Island Yacht Basin, San Diego Bay, California. *Mar. Pollut. Bull.* 62, 701–717. <https://doi.org/10.1016/j.marpolbul.2011.01.027>
- Normant, M., Bielecka, L., Dmochowska, B., Dumnicka, E., Dziubińska, A., Jakubowska, M., Kobos, J., Łądkowska, H., Marszewska, L., Zgrundo, A., 2015. Detailed sampling results of the Port of Gdynia (Poland). In: Ruiz, M., Karhu, J., Backer, H. (Eds.), *Testing monitoring methods for non-indigenous species in ports (Balsam project – work package 4)*. Baltic Marine Environment Protection Commission, HELCOM, Helsinki, 31–55.

- Ojaveer, H., Jaanus, A., MacKenzie, B.R., Martin, G., Olenin, S., Radziejewska, T., Telesh, I., Zettler, M.L., Zaiko, A., 2010. Status of Biodiversity in the Baltic Sea. *PLoS ONE* 5, e12467. <https://doi.org/10.1371/journal.pone.0012467>
- Ojaveer, H., Olenin, S., Narščius, A., Florin, A.B., Ezhova, E., Golasch, S., Jensen, K.R., Lehtiniemi, M., Minchin, D., Normant-Saremba, M., Stråke, S., 2017. Dynamics of biological invasions and pathways over time: a case study of a temperate coastal sea. *Biol. Invasions* 19, 799–813.
- Ojaveer, H., Põllumäe, A., Jaanus, A., Kotta, I., 2015. Detailed sampling results of the Port of Muuga Harbour, Port of Tallin (Estonia). In: Ruiz, M., Karhu, J., Backer, H. (Eds.), *Testing monitoring methods for non-indigenous species in ports (Balsam project - work package 4)*. Baltic Marine Environment Protection Commission, HELCOM, Helsinki, 9–16.
- Paturej, E., Gutkowska, A., 2015. The effect of salinity levels on the structure of zooplankton communities. *Arch. Biol. Sci.* 67, 483–492. <https://doi.org/10.2298/ABS140910012P>
- Pustelnikovas, O., Dembska, G., Szefer, P., Radke, B., Bolalek, J., 2007. Distribution of migration (state) forms of microelements in the sediments of the ports of Klaipėda and Gdańsk. *Oceanol. Hydrobiol. Stud.* 36, 129–149. <https://doi.org/10.2478/v10009-007-0032-3>
- Radke, B., Łęczyński, L., Wasik, A., Namieśnik, J., Bolalek, J., 2008. The content of butyl- and phenyltin derivatives in the sediment from the Port of Gdańsk. *Chemosphere* 73, 407–414. <https://doi.org/10.1016/j.chemosphere.2008.05.020>
- Radke, B., Piketh, S., Wasik, A., Namieśnik, J., Dembska, G., Bolalek, J., 2013. Aspects of pollution in Gdansk and Gdynia Harbours at the coastal zone of the South Baltic Sea. *TransNav: International Journal on Marine Navigation and Safety of Sea Transportation* 7, 11–18. <https://doi.org/10.1016/10.12716/1001.07.01.01>
- Radke, B., Wasik, A., Jewell, L.L., Piketh, S., Pączek, U., Gatuszka, A., Namieśnik, J., 2012. Seasonal changes in organotin compounds in water and sediment samples from the semi-enclosed Port of Gdynia. *Sci. Total Environ.* 441, 57–66. <https://doi.org/10.1016/j.scitotenv.2012.09.006>
- Razouls, C., de Bovée, F., Kouwenberg, J., Desreumaux, N., 2005–2017. Diversity and Geographic Distribution of Marine Planktonic Copepods. <http://copepodes.obs-banyuls.fr/en> (accessed on 14.02.2019).
- Remane, A., 1934. *Die Brackwasserfauna: Mit besonderer Berücksichtigung der Ostsee*. *Verh. Dtsch. Zool. Ges.* 36, 34–74.
- Remane, A., Schlieper, C., 1971. *Biology of Brackish Water. Die Binnengewässer Vol. XXV. E. Schweizerbartsche Verlagsbuchhandlung, Stuttgart.*
- Shaikh, S.M.S., Tagde, J.P., Singh, P.R., Dutta, S., Sangolkar, L.N., Kumar, M.S., 2021. Impact of Port and harbour activities on plankton distribution and dynamics: A multivariate approach. *Mar. Pollut. Bull.* 165, 112105. <https://doi.org/10.1016/j.marpolbul.2021.112105>
- Snoeijs-Leijonmalm, P., 2017. Patterns of diversity. In: Snoeijs-Leijonmalm, P., Schubert, H., Radziejewska, T. (Eds.), *Biological Oceanography of the Baltic Sea*. Springer Science and Business Media, 123–192. https://doi.org/10.1007/978-94-007-0668-2_4
- Strake, S., Alberte, M., Barda, L., Labucis, A., Labuce, A., Perkons, V., 2015. Detailed sampling results of the Port of Liepaja and Port of Riga (Latvia). In: Ruiz, M., Karhu, J., Backer, H. (Eds.), *Testing monitoring methods for non-indigenous species in ports (Balsam project – work package 4)*. Baltic Marine Environment Protection Commission, HELCOM, Helsinki, 17–30.
- Suikkanen, S., Pulina, S., Engström-Öst, J., Lehtiniemi, M., Lehtinen, S., Brutemark, A., 2013. Climate change and eutrophication induced shifts in northern summer plankton communities. *PLoS one* 8, e66475. <https://doi.org/10.1371/journal.pone.0066475>
- Telesh, I., Heerkloss, R., 2002. *Atlas of Estuarine Zooplankton of the Southern and Eastern Baltic Sea. Part I Rotifera*. Verlag Dr. Kovac, Hamburg, 89 pp.
- Telesh, I., Heerkloss, R., 2004. In: *Atlas of Estuarine Zooplankton of the Southern and Eastern Baltic Sea. Part II: Crustacea*. Verlag Dr. Kovac, Hamburg, 118 pp.
- Telesh, I.V., Khlebovich, V.V., 2010. Principal processes within the estuarine salinity gradient: a review. *Mar. Pollut. Bull.* 61, 149–155. <https://doi.org/10.1016/j.marpolbul.2010.02.008>
- Vidjak, O., Bojanić, N., de Olazabal, A., Benzi, M., Brautović, I., Camatti, E., Hure, M., Lipej, L., Lučić, D., Pansera, M., Pečarević, M., Pestorić, B., Pigozzi, S., Tirelli, V., 2019. Zooplankton in Adriatic port environments: Indigenous communities and non-indigenous species. *Mar. Pollut. Bull.* 147, 133–149. <https://doi.org/10.1016/j.marpolbul.2018.06.055>
- Viitasalo, M., Vuorinen, I., Saesmaa, S., 1995. Mesozooplankton dynamics in the northern Baltic Sea: implications of variations in hydrography and climate. *J. Plankton Res.* 17, 1857–1878. <https://doi.org/10.1093/plankt/17.10.1857>
- Walczyńska, K.S., Søreide, J.E., Weydmann-Zwolicka, A., Ronowicz, M., Gabrielsen, T.M., 2019. DNA barcoding of Cirripedia larvae reveals new knowledge on their biology in Arctic coastal ecosystems. *Hydrobiologia* 837, 149–159. <https://doi.org/10.1007/s10750-019-3967-y>
- Weydmann-Zwolicka, A., Balazy, P., Kukliński, P., Søreide, J.E., Patuła, W., Ronowicz, M., 2021. Meroplankton seasonal dynamics in the high Arctic fjord: comparison of different sampling methods. *Prog. Oceanogr.* 190, 102484. <https://doi.org/10.1016/j.pocean.2020.102484>
- Wiktor, K., 1990. Zooplankton. In: Majewski, A. (Ed.), *Zatoka Gdańska*, Wydawnictwo Geologiczne, Warszawa, 380–401.
- Witalis, B., Iglowska, A., Ronowicz, M., Kukliński, P., 2021. Biodiversity of epifauna in the ports of Southern Baltic Sea revealed by study of recruitment and succession on artificial panels. *Estuar. Coast. Shelf Sci.* 249, 107107. <https://doi.org/10.1016/j.ecss.2020.107107>
- Żmijewska, M.I., Niemkiewicz, E., Bielecka, L., 2000. Abundance and species composition of plankton in the Gulf of Gdańsk near the planned underwater outfall of the Gdańsk-Wschód (Gdańsk-East) sewage treatment plant. *Oceanologia* 42 (3), 335–357.

Available online at www.sciencedirect.com

ScienceDirect

journal homepage: www.journals.elsevier.com/oceanologia

ORIGINAL RESEARCH ARTICLE

Variability of chlorophyll *a* concentration in surface waters of the open Baltic Sea

Malgorzata Stramska*, Jaromir Jakacki

Institute of Oceanology, Polish Academy of Sciences, Sopot, Poland

Received 2 December 2022; accepted 27 February 2024

Available online 12 March 2024

KEYWORDS

Baltic Sea;
Remote sensing;
Annual cycles;
Chl variability

Abstract In situ, satellite and reanalysis data from numerical models were used to study the characteristic features of Chl variability in the Baltic Sea. The analysis is focused on the years 2003–2020 when regular observations of ocean color with the MODIS AQUA are available. In the Baltic Sea, there is a pronounced annual cycle in physical conditions in the water column, driven by seasonal cycles in atmospheric forcing. The seasonal cycle of Chl concentration does not conform to the picture known from classical models, with low phytoplankton concentration when nutrients are low. In contrast, in the Baltic Sea, the concentration of Chl is high even during the summer months when nutrients are depleted. This can be explained by a continuous supply of nutrients by runoff from land, as well as by a significant contribution to primary production by phytoplankton able to survive in environment poor in dissolved nutrients. There is also a considerable interannual variability in Chl. There are many possible cause/effect interactions involved, but the data series are still too short to make clear which of them are the most important. The most striking event was a spring bloom in 2008.

© 2024 Institute of Oceanology of the Polish Academy of Sciences. Production and hosting by Elsevier B.V. This is an open access article under the CC BY-NC-ND license (<http://creativecommons.org/licenses/by-nc-nd/4.0/>).

1. Introduction

The main focus of this paper is surface chlorophyll *a* concentration (Chl) in the Baltic Sea. Various available historical data sets are used to discuss this variability on annual and interannual time scales. In order to discuss the forcing for the observed patterns in Chl, a piece of background information on selected environmental variables such as the sea surface temperature (SST), nutrients, and meteorological data is also presented.

It is well documented that phytoplankton communities in the oceans respond to environmental conditions (e.g.,

* Corresponding author at: Institute of Oceanology, Polish Academy of Sciences, Powstańców Warszawy 55, Sopot 81–712, Poland.

E-mail address: mstramska@wp.pl (M. Stramska).

Peer review under the responsibility of the Institute of Oceanology of the Polish Academy of Sciences.



Production and hosting by Elsevier

Dutkiewicz et al., 2020; Stramska and Dickey, 1993, 1994; Sverdrup, 1953). For example, phytoplankton concentration in temperate and boreal climate zones varies seasonally. In early spring, phytoplankton grows rapidly in response to increasing sunlight taking advantage of accumulated nutrients, whereas low nutrient concentrations limit phytoplankton biomass later in the season. The onset and the intensity of the blooms vary interannually in response to atmospheric forcing. This general pattern of phytoplankton dynamics has been described in the past also in the Baltic Sea (Wasmund et al., 1998). It has been postulated, that nutrient loads tend to control species abundance and diversity (e.g., Chorus and Spijkerman, 2021). Significant interannual variability of phytoplankton blooms has been also observed and investigated using modeling approach (Beltran-Perez and Waniek, 2021, 2022).

The Baltic Sea is a brackish inland sea located in northern Europe. The sea includes deeper basins separated by shallow sills, and is characterized by latitudinal gradients in temperature and salinity (Leppäranta and Myrberg, 2009). The water salinity and density strongly depend on freshwater runoff from rivers and water exchange with the North Sea. Considerable input of freshwater from rivers decreases seawater salinity and maintains a permanent two-layer salinity structure in the Baltic Sea. Spatial distribution of salinity is characterized by large gradients between the surface water layer and the saltier bottom layer, and between the northern and the western area, where water exchange between the Baltic Sea and the North Sea takes place (Leppäranta and Myrberg, 2009). Most of the time, there is only a weak inflow of dense and salty water into the Baltic Sea from the North Sea (through the Danish Straits, Skagerrak, and Kattegat). The intensity of this inflow can at times increase significantly. Such episodes, called the Major Baltic Inflows (MBI), depend on weather patterns controlling the sea-level difference between the Baltic and the North Seas (Matthäus and Franck, 1992; Mohrholz, 2018; Stramska and Aniskiewicz, 2019).

The ecosystem of the Baltic Sea has been under anthropogenic stress for many decades (HELCOM, 2009). This is directly related to the significant input of nutrients and various pollutants due to human activities. Large summer blooms in the Baltic Sea, often dominated by just a few species of filamentous cyanobacteria have been observed (Kahru and Elmgren, 2014, Löptien and Dietze, 2022). Eutrophication is a major environmental problem in the Baltic Sea (e.g. Håkanson and Bryhn, 2008, Savchuk and Wulff, 2007). For managing this marine region, it is crucial to develop a better understanding of the primary biogeochemical processes playing major roles in shaping the environment. However, addressing biogeochemical variability and quantitative description of processes is a challenging task due to the complexity of the system. The best strategy in this type of research is to use in parallel a number of approaches, such as biogeochemical modeling, satellite monitoring, in situ observations, and laboratory experiments with phytoplankton. Each of these approaches has its stronger points and weaknesses. The coupled physical-biogeochemical models struggle with the proper representation of biogeochemical processes in numerical expressions. In the real ocean, most processes governing the interactions between biogeochemical compartments are very

Table 1 Geographical positions of in situ stations.

Station	Latitude	Longitude
BY5	55.25°N	15.98°E
BY10	56.63°N	19.58°E
BCSIII	55.55°N	18.40°E

complex, vary in space and time and some of them are still poorly known (e.g., Dutkiewicz, 2020; Munkes et al., 2021; Stramska et al., 2020). These potential sources of errors limit the applicability of the models for future projections, till the times when model parameters and equations can be better determined. Nevertheless, even if the models do not always agree with observations, they are a useful tool for testing our understanding of marine biogeochemical processes. Satellite observations of ocean color and water temperature are another important source of information, but they allow us to monitor only the surface layer of the sea and there are large gaps in data series due to the clouds. Finally, although in situ observations are necessary for a checkup of indirect observations and modeling efforts, they are very time-consuming and costly. Unfortunately, it is only possible to collect in situ data at a limited number of stations and dates.

The main goal of this paper is to present the results of the re-analysis of the existing data sets for the Baltic Sea and to describe the characteristic patterns in Chl variability. Our analysis is focused on the years 2003–2020 when regular observations of ocean color with the MODIS AQUA are available. Our approach is based on the presentation of satellite and in situ observations, as well as some modeling results. A more detailed discussion of the quantitative intercomparison of the data sets was published before (Stramska et al., 2021). In the present paper, our main focus is to show what information can be gained from the existing data sets to achieve a better understanding of the Chl dynamics and the shortcomings in our knowledge of the physical-biogeochemical state of the Baltic Sea.

2. Material and methods

This article is based on an analysis of oceanographic data sets obtained from different sources and, unless stated otherwise, covers the 18-year-long (2003–2020) time interval. We used satellite and model-derived data, as well as data from historical in situ observations, as explained below.

2.1. In situ Chl, SST, and nutrients

In situ data were downloaded from public databases of the International Council for the Exploration of the Sea (ICES Dataset on Ocean Hydrography, <https://ocean.ices.dk>). For this work, we decided to use data from three stations located in the open sea and representative of the Baltic Proper. The geographical positions of these stations are listed in Table 1 and displayed in Figure 1. In situ data discussed in this paper include the surface chlorophyll *a* concentration (Chl), sea surface temperature (SST), as

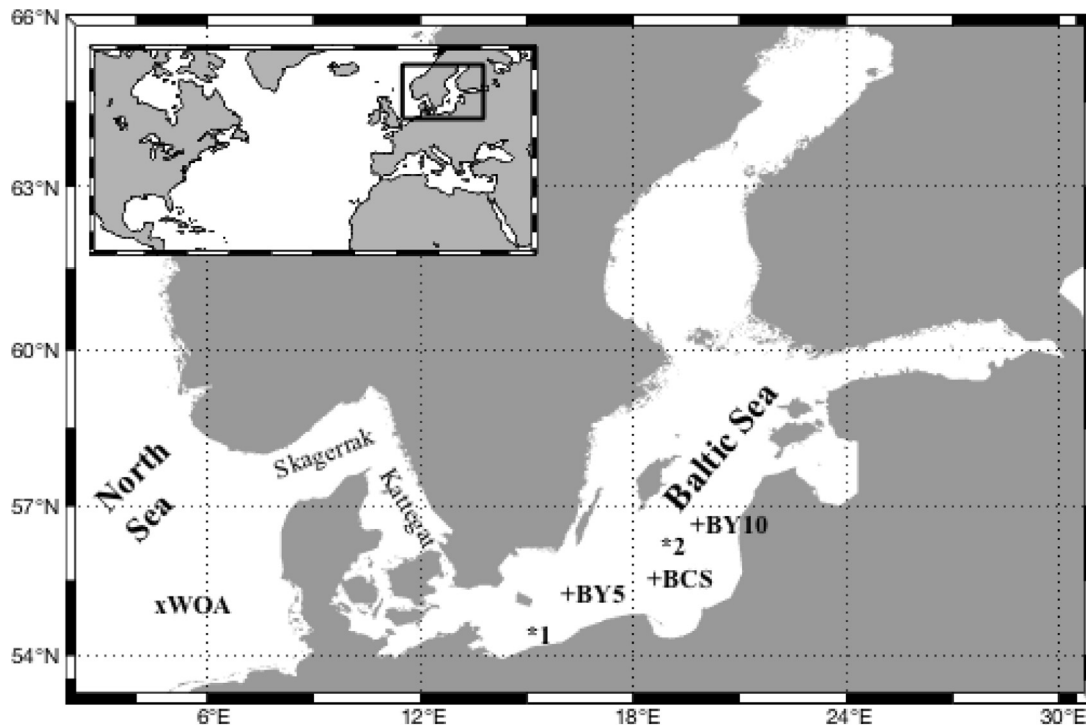


Figure 1 Map showing the geographical location of the Baltic Sea. The crosses indicate the positions of the in situ stations (BY5, BY10, and BCSIII), stars indicate the positions of the NCEP gridpoints, and x is the position of the WOA gridpoint.

well as concentrations of dissolved inorganic phosphate (PHOS), nitrate (NTRA), and nitrite (NTRI). The results are quite similar for station BY10 and BCSIII, therefore data for station BY10 are not always shown. Sampling was carried out according to HELCOM protocols (<https://helcom.fi/helcom-at-work/publications/manuals-and-guidelines/>). Usually, data were collected monthly or two times in a given month, but sometimes data were missing or collected more often.

2.2. Satellite Chl, Z_{eu} , and SST

Satellite ocean color data presented in this paper include surface chlorophyll *a* concentration (Chl) and euphotic depth (Z_{eu}) from MODIS AQUA obtained from NASA's Ocean Color Web (www.oceancolor.gsfc.nasa.gov/; reprocessing version 2021). The variability of Chl concentration is discussed using the standard MODIS retrievals (Bailey et al., 2006; Seegers et al., 2018; Scott and Werdell, 2019). The euphotic depth data product (Z_{eu}) was based on the algorithm described in Lee et al. (2007). Recall, that the euphotic depth is defined as the depth where photosynthetic available radiation (PAR) is 1% of its surface value. Our analysis is based on Level 3 MODIS Aqua data, which were binned on an equal-area grid with a nominal 4 km × 4 km resolution. The standard ocean color data processing procedures applied by NASA to derive their data products such as remote sensing reflectance, Chl, and Z_{eu} involve atmospheric correction and removal of pixels with land, ice, clouds, or heavy aerosol load prior to calculation of ocean color data products.

The satellite SST data series used in this paper are part of the National Oceanic and Atmospheric Administra-

tion (NOAA) daily Optimum Interpolation SST data set. The dOISST.v2 data are available at the National Centers for Environmental Information (NCEI) website (ncei.noaa.gov), under the name "NOAA Optimum Interpolation 1/4 Degree Daily Sea Surface Temperature (OISST) Analysis, Version 2" (with doi:10.7289/V5SQ8XB5). The same data are also distributed at the Physical Oceanography Distributed Active Archive Center (PODAAC) of the Jet Propulsion Laboratory, NASA. The dOISST.v2 data set has been approved by the NOAA Climate Data Record (CDR) program as an operational Climate Data Record (CDR). It meets the definition of CDR put forward by the National Research Council (2004), as it is of sufficient length, consistency, and continuity to determine climate variability. These global daily SST records (one daily value for each pixel), with a spatial resolution of 0.25° by 0.25°, have been based on the Advanced Very High Resolution Radiometer (AVHRR) infrared satellite measurements (Pathfinder from September 1981 through December 2005, operational AVHRR from January 2006). The final global data set has been derived by combining satellite SST retrievals with SST observations from ships and buoys, and proxy SSTs generated from sea ice concentrations. A full description of data processing methods and comparisons between the NOAA dOISST.v2 and in situ data can be found in (Banzon et al., 2014, 2016). Note, that the infrared satellite remote sensing SST algorithms can provide either a skin SST if they are based on radiative transfer models or a subskin SST if in situ observations have been used to adjust satellite retrievals. In the dOISST.v2 data set the bias correction of the satellite data has been based on data from ships and buoys, therefore it should be interpreted as the bulk SST (Reynolds et al., 2007). In order to apply the correction for bias, the satellite data have been classified into daytime

and nighttime bins and corrected separately using in situ data. Then, all the data have been reanalyzed jointly using the optimum interpolation (OI) procedure. The final data represent the daily mean bulk SST values representative for the top 1-m surface water layer.

2.3. Model Chl, SST, and MLD

The model SST, mixed layer depth (MLD), and surface Chl data used in our analysis have been extracted from the Baltic Sea biogeochemical reanalysis data set (BAL-TICSEA_REANALYSIS_BIO_003_012) provided by the Copernicus Marine Environment Monitoring Service's (CMEMS) Baltic Monitoring and Forecasting Centre (BAL MFC). These reanalysis data have been derived using the ice-ocean NEMO (Nucleus for European Modelling of the Ocean) model (Axell et al., 2019; Pemberton et al., 2017). NEMO was coupled with the biogeochemical model SCOBI (Swedish Coastal and Ocean Biogeochemical model). The horizontal grid resolution is approximately 2 nautical miles (latitude 0.03333 degrees; longitude 0.05556 degrees), and there are 56 water depth levels. The reanalysis applies the Localized Singular Evolutive Interpolated Kalman (LSEIK) filter for the assimilation of observational data (Nerger et al., 2005). In this paper, SST and Chl data from the years 2003–2019 are used at grid points located at the shortest possible distance from the in situ stations. Data originate from the uppermost available model depth level (~1.5 m). The model also provided estimates of the mixed layer depth (MLD). The mixed layer of the ocean is the layer near the ocean surface with vertically quasi-homogeneous water properties such as temperature, salinity, and density (Kraus et al., 1988; Lorbacher et al., 2006; Niiler and Kraus, 1977). The intense vertical turbulent mixing near the surface is the cause of the observed vertical uniformity. More details on the model setup and performance can be found in the PRODUCT USER MANUAL Baltic Sea Biogeochemical Reanalysis Product (BALTIC SEA_REANALYSIS_BIO_003_012, CMEMS-BAL-PUM-003-012 version 2) (doi:10.48670/moi-00012 at data.marine.copernicus.edu).

2.4. NCEP data

To discuss atmospheric forcing, we used meteorological data from the NOAA–CIRES Climate Diagnostic Center NCEP/NCAR (National Centers for Environmental Prediction and National Center for Atmospheric Research) Reanalysis 1 Project, which applies a state-of-the-art analysis/forecast system to assimilate global meteorological data from various available sources (including satellite data) from 1948 to the present. In particular, we utilized the latent and sensible heat flux estimates, along with the net longwave and net shortwave radiation estimates, to calculate the net heat flux at the sea surface. We also used the wind stress data. NCEP data have coarser spatial resolution than the satellite data described above and are provided on a 2.5° x 2.5° spatial grid. For our work, we used the daily NCEP data from two grid points located in the middle of the Baltic Sea (near station BY5: NCEP grid point at 56.1893°N, 15°E; near station BCSIII: NCEP grid point at 56.1893°N, 18.75°E, see Figure 1). From these data, we calculated monthly and multiyear mean values presented in the Results section.

2.5. River runoff data

On average, the mean river discharge into the Baltic Sea is about 10 times larger than the net freshwater flux from precipitation minus evaporation at the sea surface (Leppäranta and Myrberg, 2009). Therefore, the runoff from rivers is an important component of the freshwater budget. Rivers bring into the Baltic Sea large amounts of dissolved organic matter, suspended sediments and nutrients; therefore, they have a profound effect on the ecosystem of the sea (Babin et al., 2003; Kowalczyk, 1999; Wozniak et al., 2018). The river discharge undergoes significant seasonal and interannual variability. The information about rivers presented in our paper is based on the daily time series of discharge estimated by the HYPE model provided by the Swedish Meteorological and Hydrographical Institute (SMHI) (<http://hypeweb.smhi.se/europehype/time-series/>). The model has been extensively validated by authors with in situ data. According to the information provided on the E-HYPE home website, the model development procedure involves a stepwise, simultaneous calibration applied to 116 representative upstream sites with river discharge observations, manual and remote sensing snow observations and evapotranspiration. Full description of the HYPE model and results from model validation are given in (Donnelly et al., 2016). Using model output, we calculated daily sums of water and N discharged to the Baltic Sea by the 90 largest rivers, and from such data series, we derived multiyear monthly means presented in the Results section.

2.6. World Ocean Atlas data

To discuss water properties, we also used the World Ocean Atlas 2018 data (WOA 2018, www.ncei.noaa.gov) provided by the National Ocean and Atmospheric Administration (NOAA) National Centers for Environmental Information (NCEI, www.ncei.noaa.gov). The WOA consists of a climatology of fields of in situ ocean properties objectively analyzed for the World Ocean (Boyer et al., 2018; Garcia et al., 2018). In this paper, we present climatological monthly means of MLD and nitrate for a selected grid point located at 55°N, 4.5°E (North Sea).

3. Results

3.1. Time series

Example time series analyzed in the paper are shown in Figure 2 and 3 for stations BY5 and BCSIII, respectively. The data are plotted for May in the years 2003–2011. In panels (a) of Figures 2 and 3, time series of modeled mixed layer depth (MLD) are compared with satellite-derived euphotic depth (Z_{LEE}). Recall, that the euphotic depth is defined as the water depth where underwater photosynthetically available radiation (PAR) decreases to 1% from its surface value (Mobely, 1994; Morel, 1988). The mixed layer depth (Kraus et al., 1988; Lorbacher et al., 2006; Niiler and Kraus, 1977) is used to estimate the depth of the surface water layer where phytoplankton is being mixed. In classical phytoplankton models, if the mixed layer depth is deeper

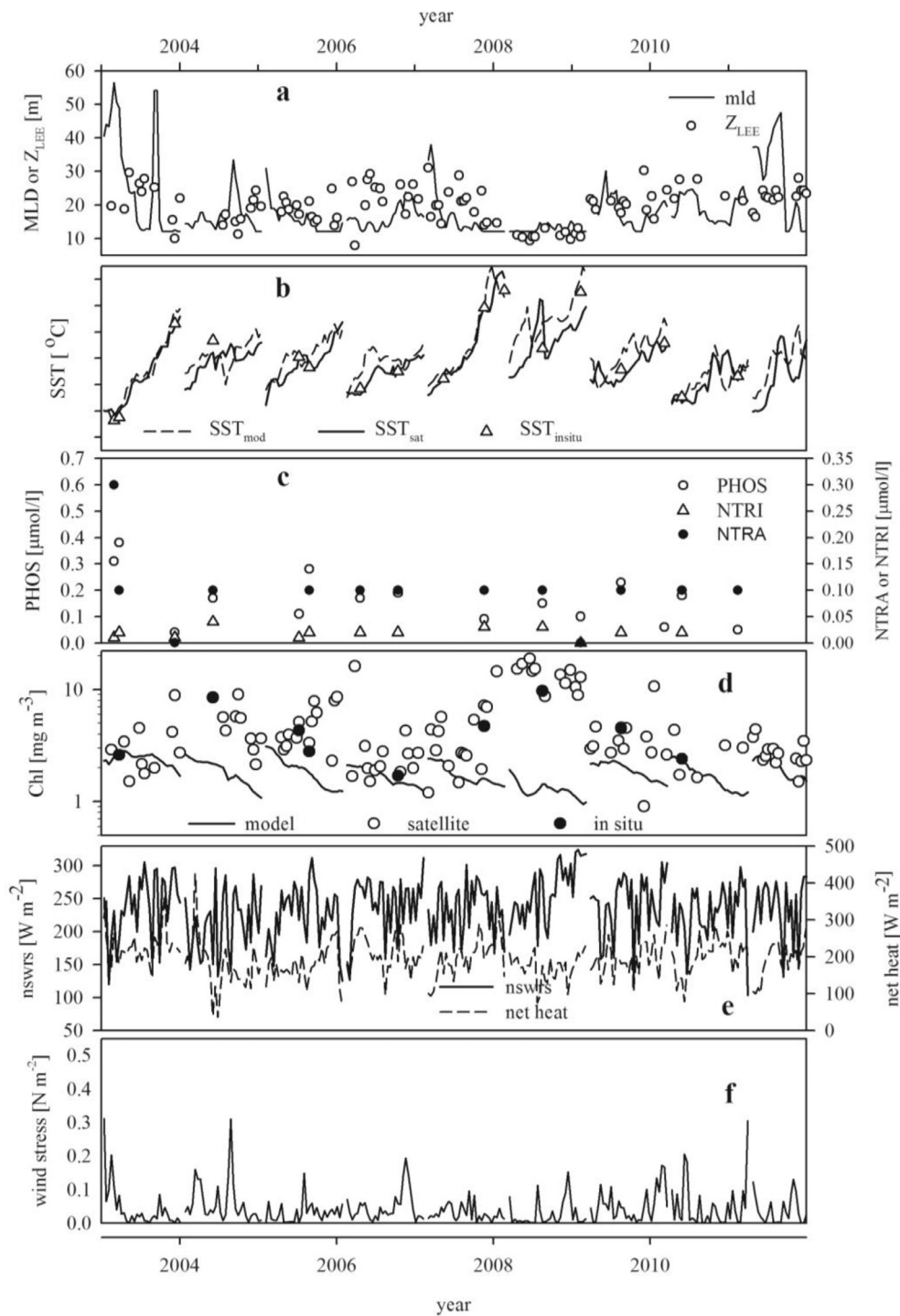


Figure 2 Daily time series at station BCSIII in the months of May 2003–2011: (a) the mixed layer depth (MLD) estimated from numerical model and the euphotic depth (Z_{LEE}) estimated from satellite data; (b) sea surface temperature from model (SST_{mod}), satellite (SST_{sat}), and in situ ($SST_{in\ situ}$) determinations; (c) in situ nutrient concentrations: nitrate (NTRA), nitrite (NTRI), and phosphates (PHOS); (d) model, in situ and satellite derived chlorophyll *a* concentrations (Chl); (e) the net heat flux and the net shortwave radiation flux (nswrs); (f) the wind stress. Data shown in panels (e) and (f) are from NCEP data grid point located at 56.1893°N, 18.75°E.

than the euphotic zone the growth of the phytoplankton can be limited by too low average light energy available for photosynthesis (Sverdrup, 1953). The time series shown in Figures 2a and 3a indicate some variability in both variables, MLD and Z_{LEE} . In general, at station BY5 Z_{LEE} is more

often deeper than MLD, than it is observed at station BCSIII. SSTs from in situ measurements, the model and satellite estimates are compared in panels (b). The data indicate that every year a consistent increase in SST is observed during the month of May. For each station, there is a reason-

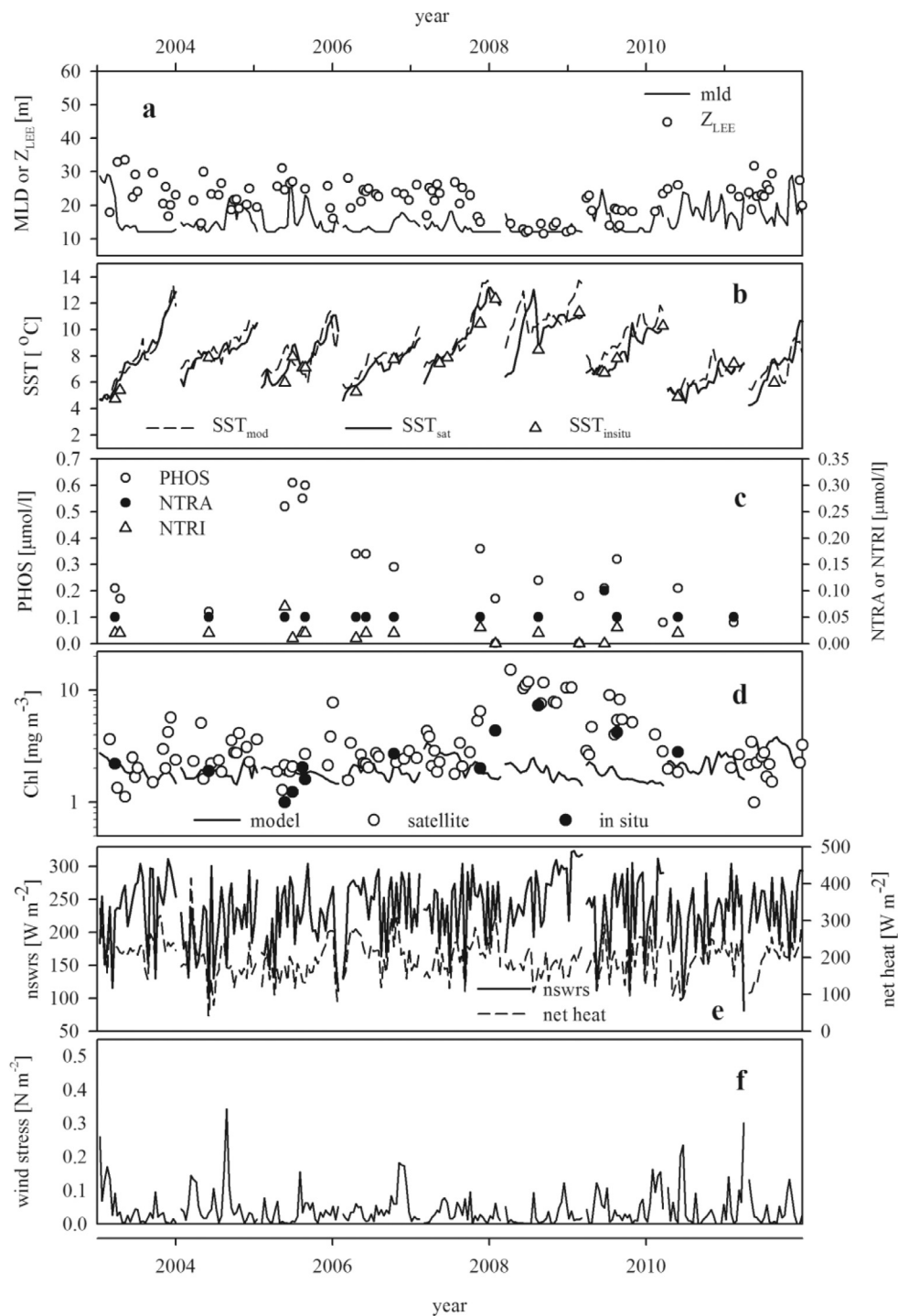


Figure 3 The same as in [Figure 2](#), but data are shown for station BY5. Data in panels (e) and (f) are from NCEP data grid point located at 56.1893°N, 15°E.

able agreement between different kinds of SST estimates. In panels (c) of [Figures 2](#) and [3](#), the in situ determinations of nutrient concentrations are displayed. As can be seen, nutrient concentrations in the Baltic Sea are already low in May. There is some spatial variability, and nitrates are somewhat higher at station BCSIII than at station BY5, but general seasonal depletion of nutrients is observed at both stations. Panels (d) present Chl from the model, in situ, and satellite

determinations. In situ, Chl determinations are often higher at station BCSIII (and BY10 not shown) than at station BY5. Model Chl predictions are at times significantly lower than the in situ data, more often so at station BCSIII. The important point is that both, the *in situ* and satellite data, indicate that high Chl values were reached in year 2008 at both stations, despite low nutrient concentration. This feature has been entirely missed by model simulations. Finally,

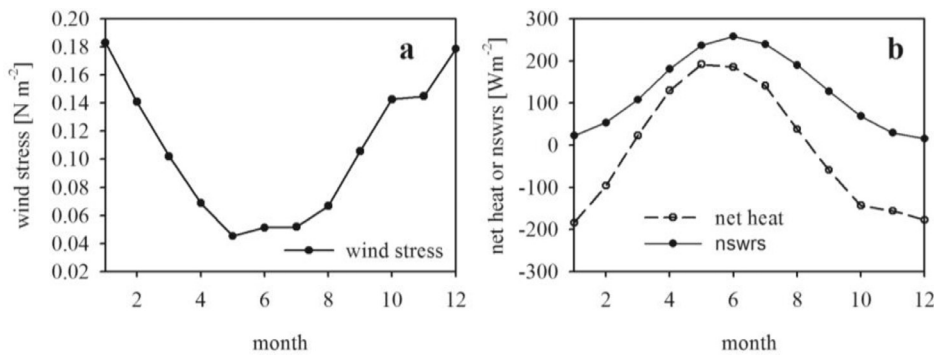


Figure 4 Monthly averaged (a) wind stress (b) net heat and net shortwave radiation flux (nswrs), based on NCEP data at grid point near station BCSIII (averaged in 2003–2020).

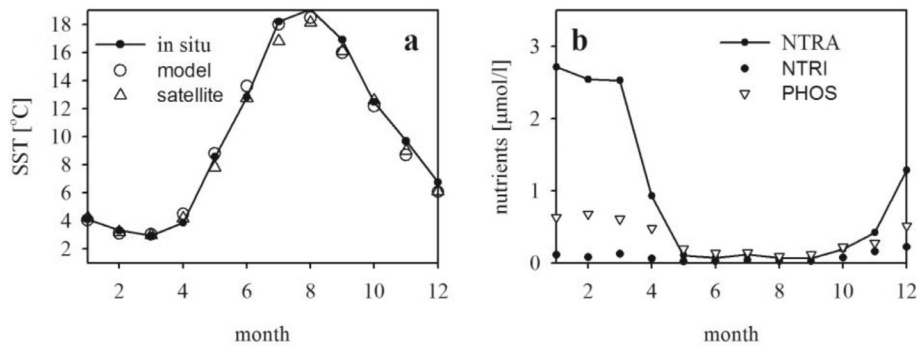


Figure 5 Monthly averaged (a) SST and (b) nutrient concentrations at station BCSIII, based on data from 2003–2020.

in panels (e) of Figures 2 and 3, the net shortwave radiation flux (nswrs) and the net heat flux are shown, while in panels (f) the wind stress is displayed. As can be seen, there is a significant variability in the daily values of the net shortwave radiation flux in May, with the daily values changing between about 100 and 325 $W m^{-2}$. Daily net heat flux varies between 36 and 424 $W m^{-2}$. Wind stress at this time of the year is usually rather low, below 0.3 $N m^{-2}$. We will come back to the discussion of Figures 2 and 3 later in this paper.

3.2. Seasonal cycle

Physical conditions in the Baltic Sea are undergoing a distinct seasonal cycle, and this is reflected in phytoplankton dynamics. We will first use the historical data sets to briefly illustrate the physical and meteorological situation in the Baltic Sea. Figure 4 displays NCEP data at a grid point located near station BCSIII. As can be seen in Figure 4, atmospheric forcing is characterized by strong winds during the fall/winter months with maximum wind stress in December–January, decreasing to minimum values in the summer (May–July). The net heat flux also displays an evident annual pattern, which is in large part driven by the annual cycle in solar insolation, as expected at these latitudes.

Figure 5 shows the annual cycle of SST (panel a) and nutrient concentration (b) at station BCSIII. Similar patterns were observed at stations BY5 and BY10 (not shown). As we can see in Figure 5, the minimum monthly SST is observed in March and the maximum in August. Nutrients become depleted in the spring and remain at very low values through-

out the summer. Their concentrations increase in the late fall to reach maximum values in winter (January and February), when the water column becomes mixed due to stormy weather and when primary production (PP) becomes limited by low light levels.

Figure 6 shows the annual cycle in the mixed layer depth, the euphotic depth, and Chl at stations BCSIII, BY5, and BY10. As expected, the MLD reaches a maximum in the winter (December–January), and a minimum in the summer (July). The range of MLD variability is the smallest at station BY5, where the maximum monthly MLD in the winter (30 m) is about 10–15 meters less than at stations BCSIII and BY10 (40–45 m). Comparison of the MLD with the euphotic depth indicates that MLD becomes about the same as Z_{eu} at station BY5 in April, while at stations BCSIII and BY10 this happens in May. This suggests that spring phytoplankton blooms might have, on average, better conditions to develop somewhat earlier in the season at station BY5 than at the two other stations. At all stations, the monthly MLD has similar values as Z_{eu} till September, while in October MLD again significantly exceeds the Z_{eu} . Satellite data indicate that the annual variability of Z_{eu} is rather weak. This is in agreement with the fact known from the literature, that Baltic Sea waters are turbid at all months, due to high concentrations of dissolved organic matter and suspended sediments (Babin et al., 2003; Kowalczyk, 1999). Among the data sets discussed in this paper, the biggest difficulty is the interpretation of Chl data (Figure 6c–f). Previous comparisons of Chl estimates from different sources showed that in the Baltic Sea, there is still a quite large uncertainty in these estimates (e.g., Stramska et al., 2021). Figure 6 shows that on

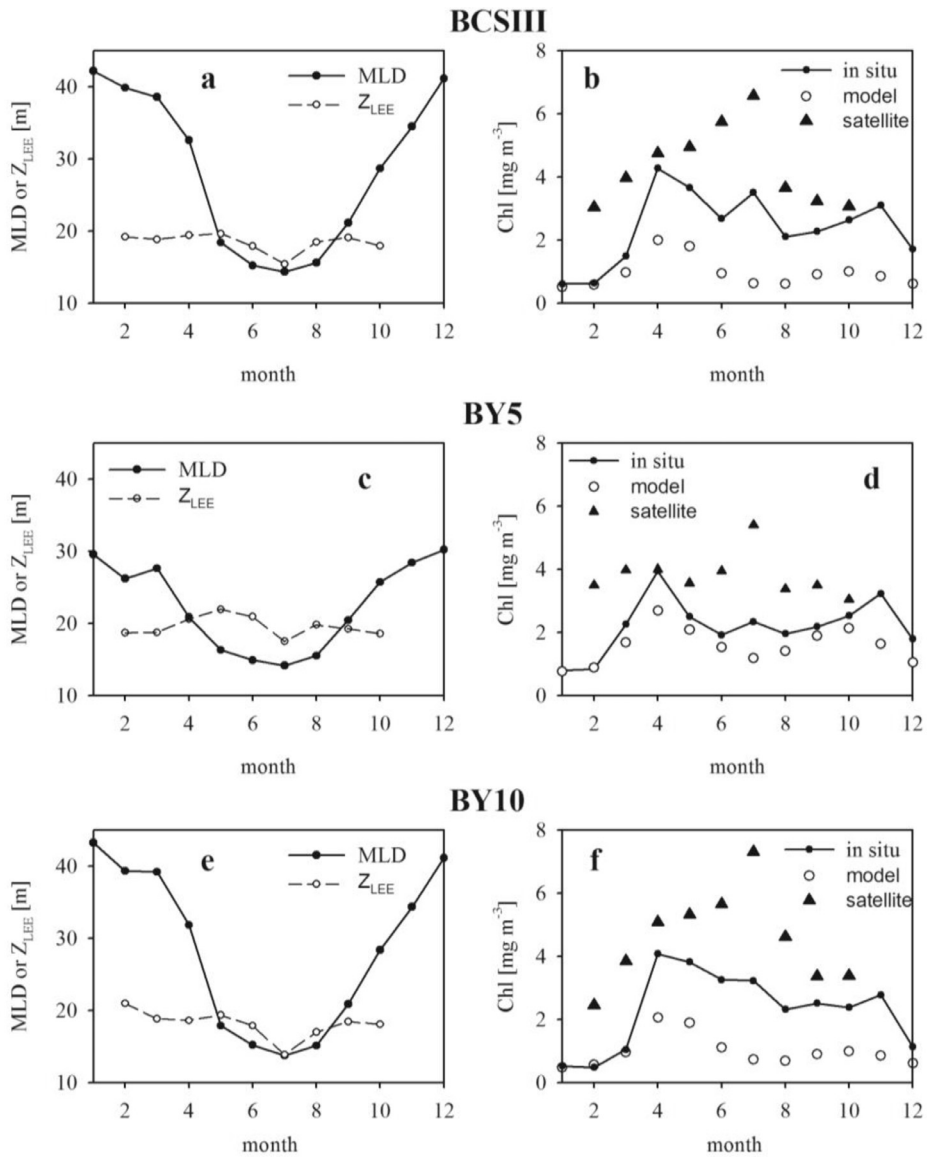


Figure 6 Monthly averaged: (a) (c) (e) the mixed layer and the euphotic depths; (b) (d) (f) Chl estimates. Data in top, middle and bottom panels are for station BCSIII, BY5, and BY10, respectively.

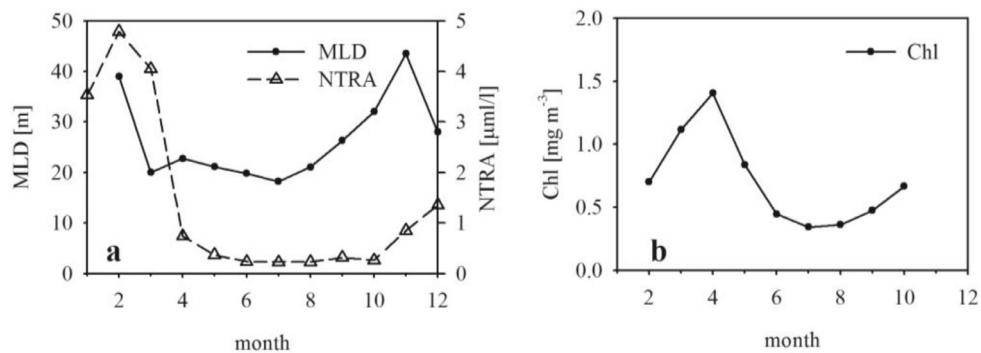


Figure 7 Monthly averaged (a) mixed layer depth and nitrate concentration (NTRA) based on the WOA data in the North Sea (55.5°N, 4.5°E). (b) Chl concentration at the same location derived from MODIS. Data in panels (a) and (b) were averaged in 2003–2018.

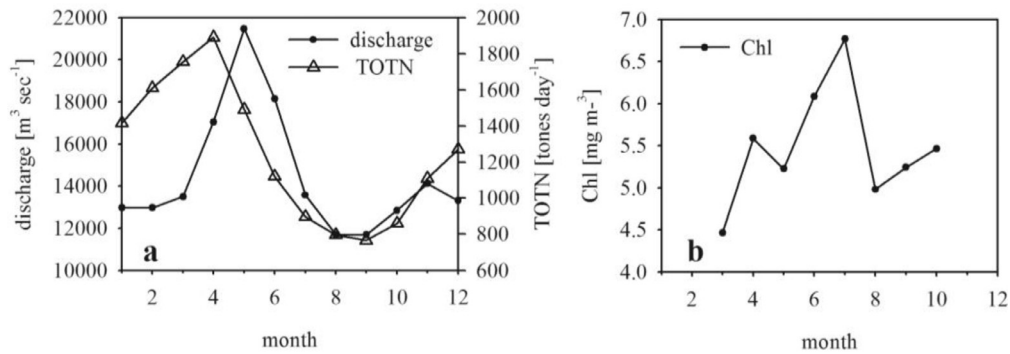


Figure 8 River water and N discharge into the Baltic Sea, based on model data from 2003–2020 (a), large scale monthly Chl *a* from MODIS averaged in 2003–2020 (b).

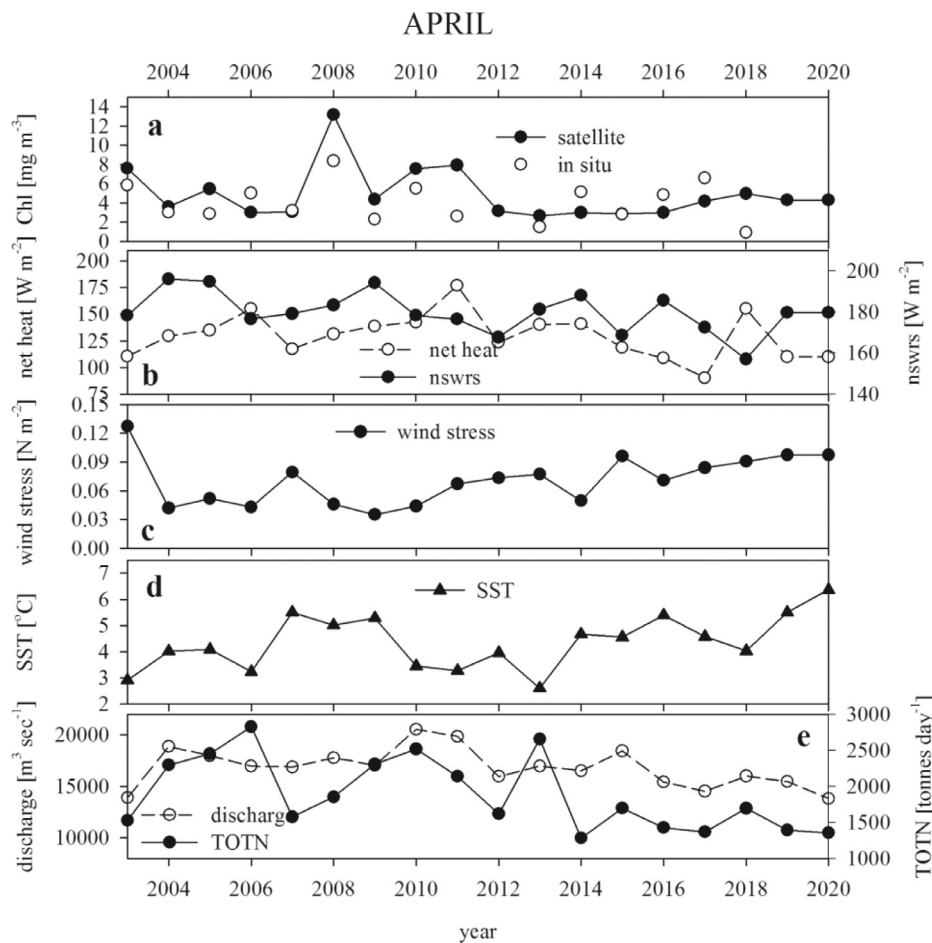


Figure 9 Time series of monthly averaged data for the month of April in 2003–2020 at station BCSIII: satellite and in situ Chl (a), net heat and nswrs fluxes (b), wind stress (c), sea surface temperature (d), discharge of water and N from rivers into the Baltic Sea (e).

average, the lowest monthly mean Chl concentrations were obtained from the model. Standard satellite Chl retrievals were generally higher than the in situ estimates. More detailed quantification of these differences can be found in [Stramska et al. \(2021\)](#). In the present paper we want to see if, despite divergences in the absolute Chl values in various data sets, any characteristic patterns in the temporal Chl variability can be substantiated. For example, when we

visually examine the data sets displayed in [Figure 6c,d,f](#), we notice that both in situ and satellite Chl were generally the lowest in December, January and February, but remained relatively high from early spring till October. Probably the most interesting observation is that such high Chl values are observed even in the months when nutrients are depleted (compare with [Figure 5](#)). This is in contrast with the long-established perception of the phytoplankton blooms, where

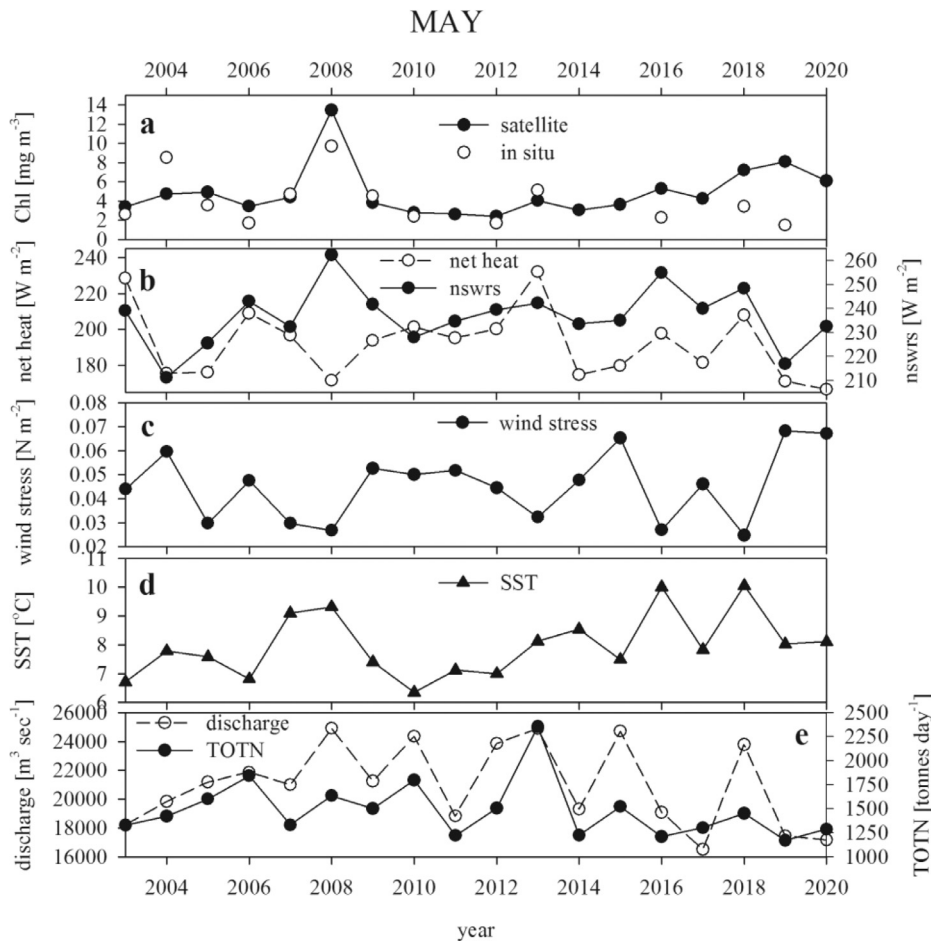


Figure 10 As in Figure 9, but data are shown for the month of May in 2003–2020.

depletion of nutrients is equivalent to a seasonal decrease of Chl.

To illustrate this point we present in Figure 7a the monthly climatology of MLD and NTRA for the North Sea. These data are from the World Ocean Atlas 2018 (WOA2018, ncei.noaa.gov) (Boyer et al., 2018; Garcia et al., 2018; Locarnini et al., 2018, 2019). In addition, Figure 7b shows the multiyear monthly climatology of Chl (based on MODIS Aqua data oceandata.sci.gsfc.nasa.gov/directaccess/MODIS-Aqua). The data indicate that open North Sea waters are characterized by a springtime peak in phytoplankton concentrations, the pattern is similar to that one described as classical phytoplankton blooms (Fasham et al., 1990; Sverdrup, 1953; Wroblewski et al., 1989). Key mechanisms underlying this phytoplankton cycle can be summarized as follows. In the winter, phytoplankton growth is light-limited, due to low solar angles and deep surface mixed layers. In the spring, water stratification, higher solar angles, and longer day length cause greater light availability for photosynthesis, enhancing phytoplankton growth rates. Nutrient limitation is an accepted reason for the decline of the blooms in late spring/summer, despite the high light availability.

Comparing Figures 5 and 6 with Figure 7 we can note significant differences between the patterns observed in the North and Baltic Seas. The situation in the Baltic Sea does

not conform to the classical phytoplankton cycle described in the literature, and despite low nutrient levels, we observe Chl of 2 mg m^{-3} and more in the summer. Importantly, this notion is supported by both the in situ and the satellite observations, regardless of the differences in the absolute Chl values in each data set.

How can one explain this seemingly bizarre observation that in the Baltic Sea phytoplankton can grow when nutrients are depleted? First, in the Baltic Sea, there are phytoplankton species able to take up N_2 from the atmosphere. N_2 fixing filamentous cyanobacteria (such as *Aphanizomenon flos-aquae*, *Nodularia spumigena*, *Anabaena*) contribute significantly to the primary production (PP) in the Baltic Sea (Kahru et al., 2020; Löptien and Dietze, 2022). Accordingly, a succession of phytoplankton species during an annual cycle in the Baltic Sea can be summarized as follows (Hjerne et al., 2019). Early spring (March, April) blooms are usually dominated by diatoms. When nutrient concentrations decrease, motile phytoplankton (e.g. diverse dinoflagellates) develop, thanks to the fact that it is capable of migrating vertically and using nutrients from deeper water layers. Picocyanobacteria also have an advantage at low nutrient concentrations in comparison to larger phytoplankton. Due to their small size (less than $1 \mu\text{m}$) and large surface-volume ratio, their uptake of nutrients is more efficient. Finally, when dissolved inorganic nitrogen becomes depleted,

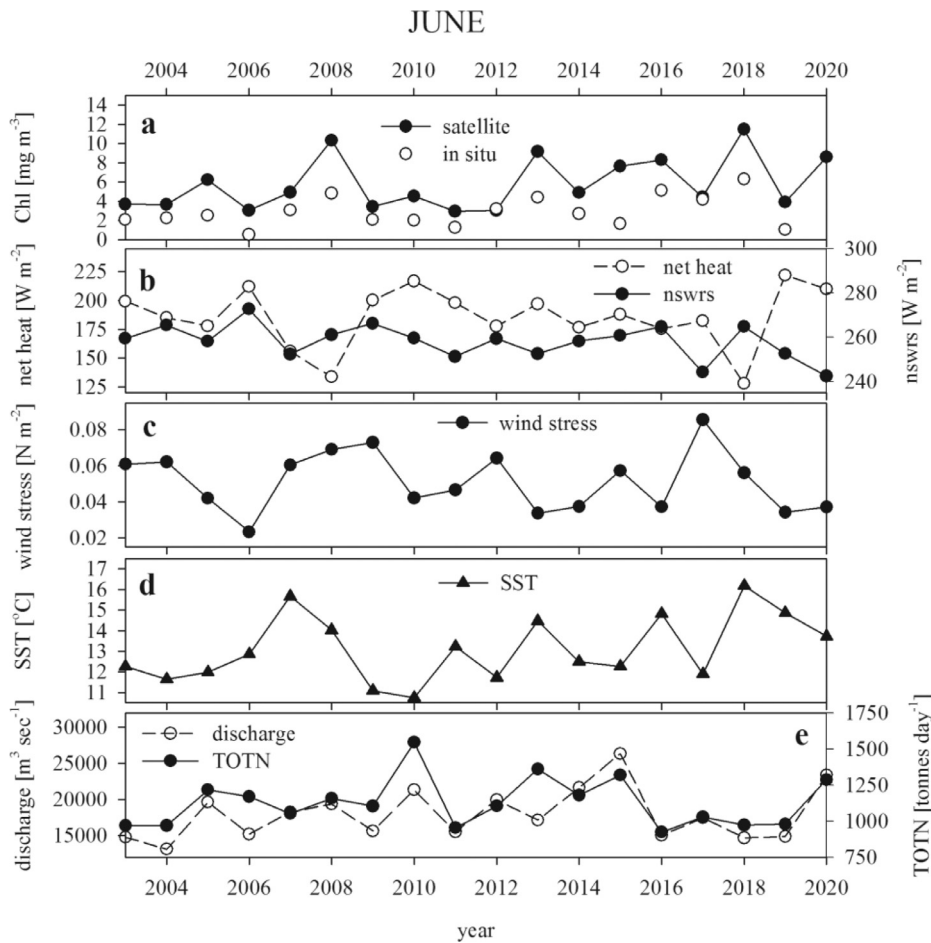


Figure 11 As in Figure 9, but data are shown for the month of June in 2003–2020.

nitrogen fixation by diazotrophic cyanobacteria (primarily *Nodularia spumigena* and *Aphanizomenon* sp.) allows them to gain advantage and to form extensive blooms in July and August. As a result, diazotrophic cyanobacteria supply the fixed nitrogen to other components of the Baltic ecosystem. Research on cyanobacteria and responses of their growth rates to environmental conditions has intensified in recent years (see Munkes et al., 2021 and references therein), but it is still not well understood what is their exact contribution to the total PP and how much nitrogen they supply at different times of the year and regions in the Baltic Sea.

Another justification for the observed high Chl in the Baltic Sea in the late spring-summer may be the existence of a continuous supply of nutrients from surrounding land. Delivery of nutrients from land includes nutrients discharged by rivers and transported directly from the coast to the sea (non-point runoff). Non-point runoff is difficult to estimate, but in Figure 8 we present an estimate of the water runoff from rivers and how much N is carried by rivers into the Baltic Sea. Using these data, it is possible to make a simplified estimate of the surplus of nutrients in the MLD due to the delivery by rivers. In our simple calculations we assume that nutrients discharged by rivers are quickly mixed over the entire Baltic Sea, but remain within the surface mixed layer. Taking an approximate area of the Baltic Sea as 380000 km², assuming MLD of 10 m and an average delivery of 1800 tones of N per day in May (see Figure 8a),

allows us to estimate that about 0.0338 μmoles of N which is added daily to each liter of water. If we assume an MLD of 5 m, which is often observed in the late spring, it would amount to 0.0676 μmoles of N per liter of surface water. This is not a very large amount, but over the time interval of one month, it adds up to about 2 μmoles l⁻¹, which is about the same magnitude as the decrease in nitrate concentration observed between March and April due to spring phytoplankton bloom (Figure 5b). Note, that the findings described here should be treated as an underestimate, as they do not take into account the non-point runoff of N from land or transport by upwellings. In the future, a numerical model will have to be used to simulate the transport and mixing of nutrients in the Baltic Sea waters.

The results presented above support the notion that significant modifications in the numerical models of phytoplankton in the Baltic Sea are required. As we can see in Figure 5 the modeled Chl does not reflect well the observed seasonal cycle of Chl in the Baltic Sea. The reasons for why phytoplankton models do not perform well in the Baltic Sea (and in general) are discussed comprehensively in Munkes et al. (2021). The authors discuss the problem by evaluating and comparing five cyanobacteria models. Four of the models are coupled to full ocean circulation models (model CEMBS: Nowicki et al., 2016; model ECOSMO II: Daewel and Schrum, 2017; model ERGOM: Neumann and Schernewski, 2005, 2008; and model SCOB1: Meier et al.,

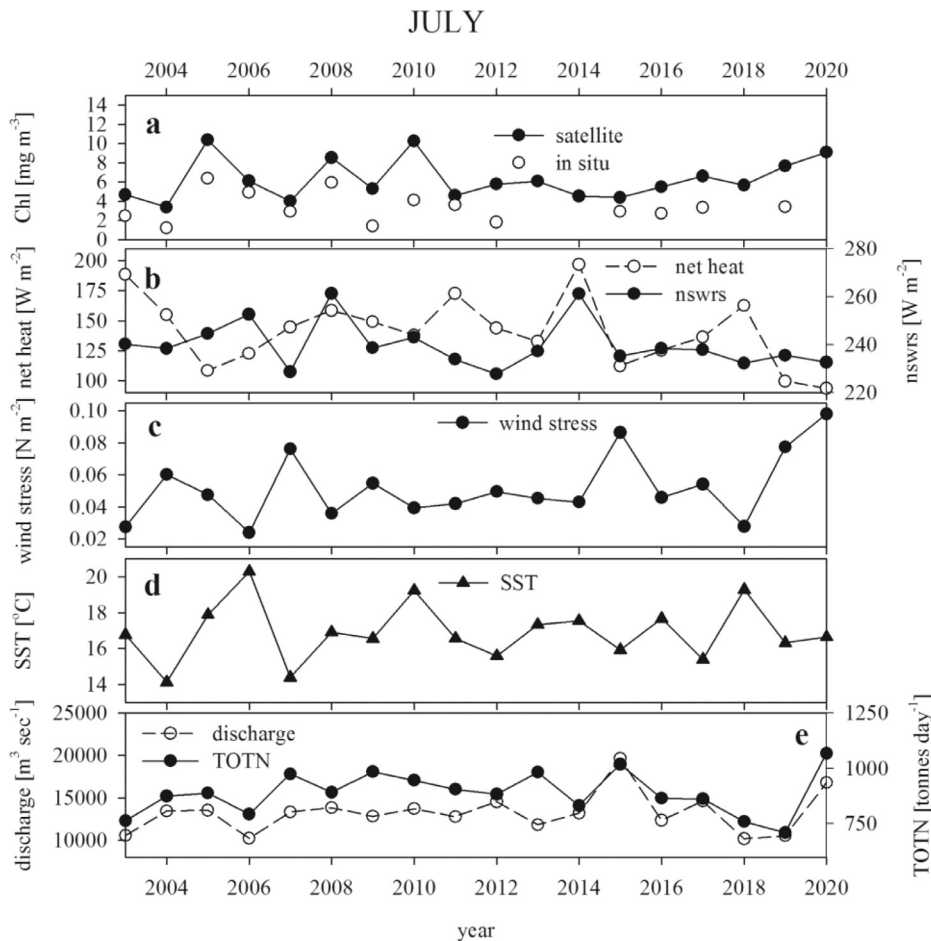


Figure 12 As in Figure 9, but data are shown for the month of July in 2003–2020.

2011). The fifth one is a box model BALTSEM, developed to support the Baltic Marine Environment Protection Commission – Helsinki Commission (HELCOM) and to develop the HELCOM Baltic Sea Action Plan (Savchuk et al., 2018). Munkes et al. (2021) show that the evaluated models differ substantially in the formulation of biogeochemical processes, due to a large uncertainty in quantitative understanding of these processes. The relationships were being adjusted based on simple empirical field correlations, valid only in certain situations. The authors conclude that a thorough understanding of the physiological responses of phytoplankton to environmental conditions is still lacking. Model assumptions and a mathematical formula, determined with a limited number of observations but encompassing multiple variables and interactions, may likely break under changing environmental conditions. Our results also suggest that improvements in the model formulations are necessary. This can be reached by suitable experimental design for in situ and laboratory biological studies in order to constrain model parameters.

3.3. Interannual variability

Time series of the monthly averaged Chl (panel a), net heat and shortwave radiation fluxes (b), wind stress (c), sea surface temperature (d), and water and N discharge by

rivers (e) in the most productive months (April–September) are displayed in Figures 9–14. The most striking example of interannual anomaly was observed in April–May 2008 (Figures 9 and 10). We can see that in May of 2008, Chl concentration was a few times higher than in the same month of the other years. Unusually high Chl values were recorded in *in situ* and satellite data at all stations (BY5, BY10, and BCSIII), but they were not achieved in the phytoplankton model (Figures 2 and 3). Based on in situ observations, this phytoplankton bloom was attributed to alternate-stage *Prymnesium polylepis* (Prymnesiales, Haptophyta) (Hajdu et al., 2015; Majaneva et al., 2012). Species of Prymnesiales have been reported before to form blooms in the Baltic Sea, for example in the Skagerrak and Kattegat region in 1988, 1989, 1994, and 1995. In 1988 such bloom became toxic and killed 900 tons of farmed fish on the coast of Denmark, Sweden and Norway (Skjoldal and Dundas, 1991). An evaluation of the environmental conditions reported during the development of this bloom has been attempted by Hajdu et al. (2015). Our data (Figures 2–3, and 10) support their conclusions, and indicate that the unusually high Chl concentrations observed in 2008 were associated with relatively low wind stress and high SST in comparison to other years. In addition, abnormally high values of the net shortwave radiation, the highest from all the years considered, were observed. This means that phytoplankton cells present

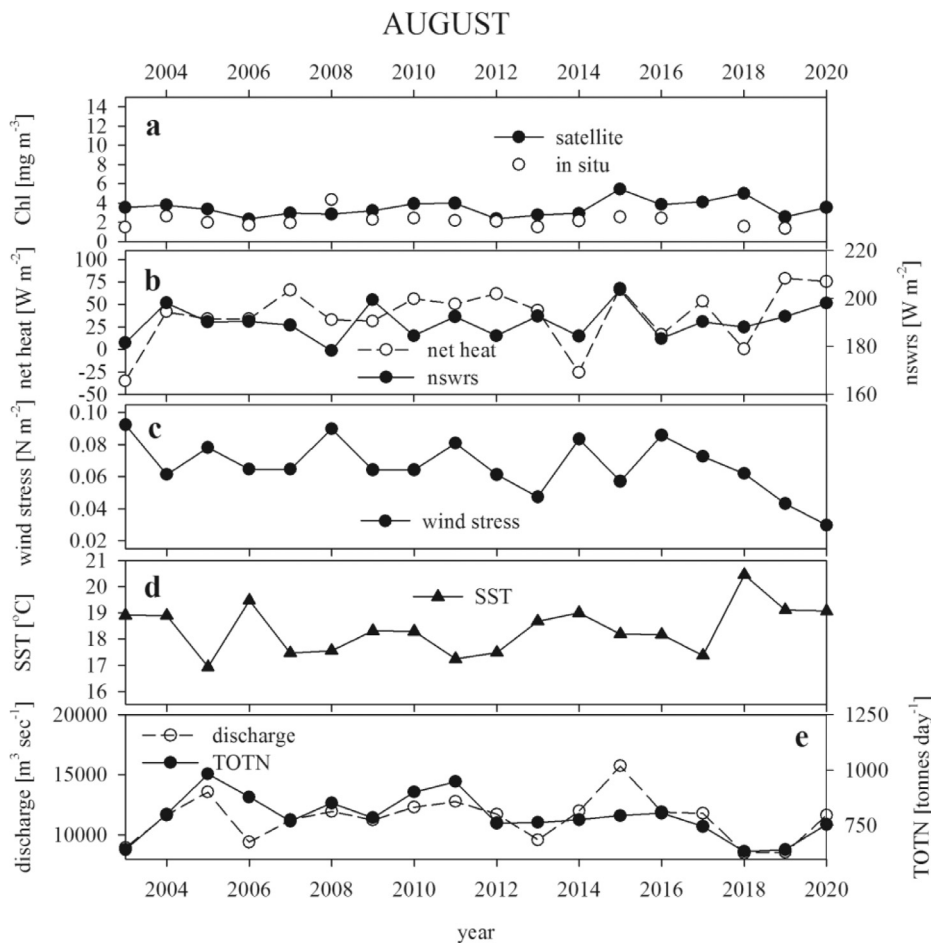


Figure 13 As in Figure 9, but data are shown for the month of August in 2003–2020.

in the surface mixed layer were exposed to extraordinarily high solar irradiances. However, such conditions may be favorable to many phytoplankton types, and it is not clear why the competition between different phytoplankton types was gained in 2008 by Pymnesiales.

If we analyze Figures 11–14, we note that the interannual variability of Chl in all the other month displayed is also evident, although the anomalies are not as spectacular as that in the spring of 2008. The summer phytoplankton communities are strongly influenced by low inorganic nitrogen concentrations. As a consequence, small-sized and motile phytoplankton types dominate primary production, followed by intense blooms of large nitrogen-fixing cyanobacteria (*Nodularia spumigena* and *Aphanizomenon* sp.). These blooms are known to develop in well-stratified surface waters, under conditions of high temperature and high solar insolation. It is also believed that the growth of cyanobacteria is favored by a low DIN/DIP ratio (low dissolved inorganic nitrogen but not limiting dissolved inorganic phosphate). In such conditions, diazotrophic cyanobacteria have an advantage over other phytoplankton types, but quantitative relationships between these factors are still unknown and it is not possible to predict the magnitude and the distribution of the annual occurrence of cyanobacteria production and accumulations in different basins of the Baltic Sea.

Our understanding of cyanobacteria blooms is hampered by observational difficulties, due to the fact that cyanobacterial blooms are extremely patchy (Kutser, 2004). Cyanobacterial concentrations often vary by more than 2 orders of magnitude over the distance of meters. Their surface accumulation and vertical structure is often destroyed by research vessels, therefore in situ measurements can be erroneous. The proof of concept study by Kutser (2004) compared radiometrically calibrated hyperspectral images from Hyperion (30-m spatial resolution) with in situ ship data to show that the patchiness of cyanobacterial blooms is one of the reasons why quantitative comparisons between in situ and satellite data during cyanobacteria blooms are difficult. Visible and near-infrared satellite sensors used routinely for monitoring the oceans have much coarser spatial resolution (~1 km) than Hyperion. In addition, they do not have sufficient spectral resolution to allow to distinguish cyanobacteria from different spectral signatures of other seawater components. Nevertheless, with some assumptions simplified satellite methods have been developed to monitor cyanobacteria blooms in the Baltic Sea (Kahru and Elmgren, 2014; Kahru et al., 2020). These approaches allow us to estimate the spatial area of the blooms, based on the expectation that high reflectance of the sea surface in the open sea in sum-

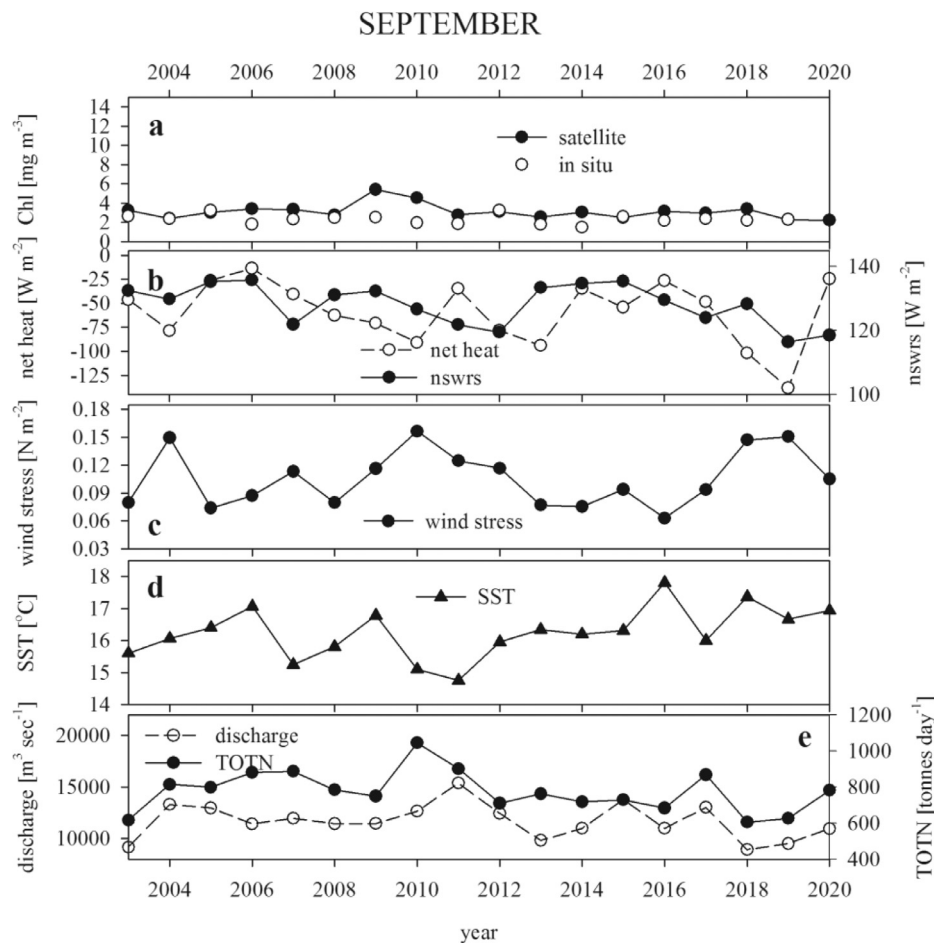


Figure 14 As in [Figure 9](#), but data are shown for the month of September in 2003–2020.

mer months indicates a high probability of cyanobacteria accumulations.

4. Conclusions

In this manuscript, we presented an analysis of the long-term data sets of Chl (in situ, satellite and model). The results indicate that:

- In the Baltic Sea, there is a remarkable annual cycle in physical conditions in the water column, driven by seasonal cycle in atmospheric forcing.
- The seasonal cycle of Chl concentration does not conform to the pattern known from classical models, with low phytoplankton concentration when nutrients are low.
- In the Baltic Sea, the concentration of Chl is high even during the summer months when nutrients are depleted. This can be explained by a continuous supply of nutrients by runoff from land, as well as by the significant contribution to primary production by phytoplankton able to survive in an environment poor in dissolved nutrients.
- There is a significant interannual variability in Chl. There are many possible cause/effect interactions involved, but the data series are still too short to make clear which of them are the most important.
- Unfortunately, the annual cycle and the interannual variability in Chl observed in in situ and satellite data are

not well reflected in biogeochemical numerical models. This supports the notion that the expressions included in the models to represent biological processes in the Baltic Sea will have to be better constrained in the future.

Declaration of competing interest

The authors declare that they have no known competing financial interests or personal relationships that could have appeared to influence the work reported in this paper.

Acknowledgments

This research was funded by the National Science Center in Poland (contract number: 2017/25/B/ST10/00159 entitled: “Numerical simulations of biological-physical interactions and phytoplankton cycles in the Baltic Sea”). Partial support comes from the statutory funds of the Institute of Oceanology of the Polish Academy of Sciences (IO PAN).

References

- Axell, L., Huess, V., Derval, C., 2019, PUM for the Baltic Sea Biogeochemical Reanalysis Product, E.U. Copernicus Marine Service In-

- formation [Online]. Available at: <http://marine.copernicus.eu/documents/PUM/CMEMS-BAL-PUM-003-012.pdf>.
- Babin, M., Stramski, D., Ferrari, G.M., Claustre, H., Bricaud, A., Obolensky, G., et al., 2003. Variations in the light absorption coefficients of phytoplankton, non-algal particles, and dissolved organic matter in coastal waters around Europe. *J. Geophys. Res.* 108, 3211. <https://doi.org/10.1029/2001JC000882>
- Bailey, S.W., Werdell, P.J., 2006. A multi-sensor approach for the on-orbit validation of ocean color satellite data products. *Remote Sens. Environ.* 102, 12–23.
- Banzon, V.F., Smith, T.M., Chin, T.M., Liu, C., Hankins, W., 2016. A long-term record of blended satellite and in situ sea surface temperature for climate monitoring, modeling and environmental studies. *Earth Syst. Sci. Data* 8, 165–176.
- Banzon, V.F., Reynolds, R.W., Stokes, D., Xue, Y.A., 2014. 1/4 o spatial resolution daily sea surface temperature climatology based on a blended satellite and in situ analysis. *J. Clim.* 27, 8221–8228.
- Beltran-Perez, O.D., Waniek, J.J., 2021. Environmental window of cyanobacteria bloom occurrence. *J. Marine Syst.* 224, 103618. <https://doi.org/10.1016/j.jmarsys.2021.103618>
- Beltran-Perez, O.D., Waniek, J.J., 2022. Inter-annual Variability Of Spring And Summer Blooms In The Eastern Baltic Sea. *Front. Mar. Sci.* 9, 928633. <https://doi.org/10.3389/fmars.2022.928633>
- Boyer, T. P., Garcia, H. E., Locarnini, R. A., Zweng, M.M., Mishonov, A. V., Reagan, J. R., Weathers, K. A., Baranova, O.K., Seidov, D., Smolyar, I.V., 2018. World Ocean Atlas, NOAA National Centers for Environmental Information. <https://accession.nodc.noaa.gov/NCEI-WOA18>
- Chorus, I., Spijkerman, E., 2021. What Colin Reynolds could tell us about nutrient limitation, N:P ratios and eutrophication control. *Hydrobiologia* 848, 95–111. <https://doi.org/10.1007/s10750-020-04377>
- Daewel, U., Schrum, C., 2017. Low-frequency variability in the North Sea and Baltic Sea identified through simulations with the 3-D coupled physical–biogeochemical model ECOSMO. *Earth Syst. Dynam.* 8, 801–815. <https://doi.org/10.5194/esd-8-801-2017>
- Donnelly, C.H., Andersson, J.C.M., Arheimer, B., 2016. Using flow signatures and catchment similarities to evaluate the E-HYPE multi-basin model across Europe. *Hydrol. Sci. J.* 61, 255–273.
- Dutkiewicz, S., Cermeno, P., Jahn, O., Follows, M.J., Hickman, A.E., Taniguchi, D.A.A., Ward, B.A., 2020. Dimensions of marine phytoplankton diversity. *Biogeosciences* 17, 609–634. <https://doi.org/10.5194/bg-17-609-2020>
- Fasham, M.J.R., Ducklow, H.W., McKelvie, S.M., 1990. A nitrogen-based model of plankton dynamics in the oceanic mixed layer. *J. Mar. Res.* 48, 591–639.
- Garcia, H.E., Weathers, K., Paver, C.R., Smolyar, I., Boyer, T.P., Locarnini, R.A., Zweng, M.M., Mishonov, A.V., Baranova, O.K., Seidov, D., Reagan, J.R., 2018. World Ocean Atlas Vol. 4: Dissolved Inorganic Nutrients (phosphate, nitrate and nitrate+nitrite, silicate). In: Mishonov, A. (Ed.), NOAA Atlas NESDIS, 84, 35 pp.
- Hajdu, S., Gorokhova, E., Larsson, U., 2015. In-Depth Analysis of an Alternate-Stage Pymnesium Polylepis (Haptophyta) Bloom and Long-Term Trends in Abundance of Pymnesiales Species in the Baltic Sea. *Mar. Ecol. Prog. Ser.* 526, 55–66. <https://doi.org/10.3354/meps11242>
- Håkanson, L., Bryhn, A.C., 2008. Eutrophication in the Baltic Sea; Present situation, Nutrient transport, Processes, Remedial strategies. In: Environmental Science and Engineering; Subseries: Environmental Science. Springer-Verlag, Berlin, Heidelberg, 261 pp.
- HELCOM, 2009. Eutrophication in the Baltic Sea – an integrated thematic assessment of the effects of nutrient enrichment and eutrophication in the Baltic Sea region. *Baltic Sea Environ. Proc.* 115B, 148 pp.
- Hjerne, O, Hajdu, S, Larsson, U, Downing, AS, Winder, M., 2019. Climate Driven Changes in Timing, Composition and Magnitude of the Baltic Sea Phytoplankton Spring Bloom. *Front. Mar. Sci.* 6, 482. <https://doi.org/10.3389/fmars.2019.00482>
- Kahru, M., Elmgren, R., Kaiser, J., Wasmund, N., Savchuk, O., 2020. Cyanobacterial blooms in the Baltic Sea: correlations with environmental factors. *Harmful Algae* 92, 101739. <https://doi.org/10.1016/j.hal.2019.101739>
- Kahru, M., Elmgren, R., 2014. Multidecadal time series of satellite-detected accumulations of cyanobacteria in the Baltic Sea. *Biogeosciences* 11, 3619–3633. <https://doi.org/10.5194/bg-11-3619-2014>
- Kowalczuk, P., 1999. Seasonal variability of yellow substance absorption in the surface layer of the Baltic Sea. *J. Geophys. Res.* 104, 30047–30058. <https://doi.org/10.1029/1999JC900198>
- Kraus, E.B., Bleck, R., Hanson, H.P., 1988. The Inclusion of a Surface Mixed Layer in a Large-scale Circulation Model. In: Ni-houl, J.C.J., Jamart, B.M. (Eds.), *Small Scale Turbulence and Mixing in the Ocean*. Elsevier, Amsterdam, 51–62.
- Kutser, T., 2004. Quantitative detection of chlorophyll in cyanobacterial blooms by satellite remote sensing. *Limnol. Oceanogr.* 49, 2179–2189.
- Lee, Z.-P., Weidemann, A., Kindle, J., Arnone, R., Carder, K.L., Davis, C., 2007. Euphotic Zone Depth: Its Derivation and Implication to Ocean-Color Remote Sensing. *J. Geophys. Res.* 112, C03009. <https://doi.org/10.1029/2006JC003802>
- Leppäranta, M., Myrberg, K., 2009. Physical Oceanography of the Baltic Sea. Springer-Praxis Book Series in Geophysical Sciences. Springer, Chichester, UK, 378 pp.
- Locarnini, R.A., Mishonov, A.V., Baranova, O.K., Boyer, T.P., Zweng, M.M., Garcia, H.E., Reagan, J.R., Seidov, D., Weathers, K., Paver, C.R., Smolyar, I., 2018. World Ocean Atlas Vol. 1: Temperature. In: Mishonov, A. (Ed.), NOAA Atlas NESDIS, 81, 52 pp.
- Locarnini, R.A., Boyer, T.P., Mishonov, A.V., Reagan, J.R., Zweng, M.M., Baranova, O.K., Garcia, H.E., Seidov, D., Weathers, K.W., Paver, C.R., Smolyar, I.V., 2019. World Ocean Atlas Vol. 5: Density. In: Mishono, A. (Ed.), NOAA Atlas NESDIS, 41 85.
- Löptien, U., Dietze, H., 2022. Retracing cyanobacteria blooms in the Baltic Sea. *Sci. Rep.* 12, 10873. <https://doi.org/10.1038/s41598-022-14880-w>
- Lorbacher, K., Dommenges, D., Niiler, P.P., Köhl, A., 2006. Ocean Mixed Layer Depth: A Subsurface Proxy of Ocean-Atmosphere Variability. *J. Geophys. Res.* 111, C07010. <https://doi.org/10.1029/2003JC002157>
- Majaneva, M., Rintala, J.M., Hajdu, S., Hällfors, S., Hällfors, G., Skjevik, A.T., Gromisz, S., Kownacka, J., Busch, S., Blomster, J., 2012. The extensive bloom of alternate-stage Pymnesium polylepis (Haptophyta) in the Baltic Sea during autumn—spring 2007–2008. *Eur. J. Phycol.* 47, 310–320.
- Matthäus, W.W., Franck, H., 1992. Characteristics of major Baltic inflows – A statistical analysis. *Cont. Shelf Res.* 12, 1375–1400.
- Meier, H.E.M., Eilola, K., Alroth-Rosell, E., 2011. Climate-related changes in marine ecosystems simulated with a three-dimensional coupled physical-biogeochemical model of the Baltic Sea. *Clim. Res.* 48, 31–55. <https://doi.org/10.3354/cr00968>
- Mobley, C.D., 1994. Light and Water. Radiative Transfer in Natural Waters. Acad. Press, San Diego, California.
- Mohrholz, V., 2018. Major Baltic Inflow Statistics – Revised. *Front. Mar. Sci.* 5, 384. <https://doi.org/10.3389/fmars.2018.00384>
- Morel, A., 1988. Optical modeling of the upper ocean in relation to its biogenous matter content (case I waters). *J. Geophys. Res.* 93, 10749–10768.
- Munkes, B., Löptien, U., Dietze, H., 2021. Cyanobacteria blooms in the Baltic Sea: a review of models and facts. *Biogeosciences* 18, 2347–2378. <https://doi.org/10.5194/bg-18-2347-2021>

- National Research Council, 2004. *Climate Data Records from Environmental Satellites: Interim Rep.* Nat. Acad. Press, Washington, DC, USA.
- Nerger, L., Hiller, W., Schröter, J., 2005. A Comparison of Error Subspace Kalman Filters. *Tellus series a-dynamic meteorology and oceanography* A57 (5), 715–735. <https://doi.org/10.1111/j.1600-0870.2005.00141.x>
- Neumann, T., Schernewski, G., 2005. An ecological model evaluation of two nutrient abatement strategies for the Baltic Sea. *J. Marine Syst.* 56, 195–206. <https://doi.org/10.1016/j.jmarsys.2004.10.002>
- Neumann, T., Schernewski, G., 2008. Eutrophication in the Baltic Sea and shifts in nitrogen fixation analysed with a 3D ecosystem model. *J. Marine Syst.* 74, 592–602. <https://doi.org/10.1016/j.jmarsys.2008.05.003>
- Niiler, P.P., Kraus, E.B., 1977. *One-dimensional Models of the Upper Ocean.* In: Kraus, E.B. (Ed.), *Modelling and Predictions of the Upper Layers of the Ocean.* Pergamon Press, Oxford, 143–172.
- Nowicki, A., Rak, D., Janecki, M., Dzierzbicka-Głowacka, L., 2016. Accuracy assessment of temperature and salinity computed by the 3D Coupled Ecosystem Model of the Baltic Sea (3D CEMBS) in the Southern Baltic. *J. Oper. Oceanogr.* 9, 67–73. <https://doi.org/10.1080/1755876x.2016.1209368>
- Pemberton, P., Löptien, U., Hordoir, R., Höglund, A., Schimanke, S., Axell, L., Haapala, J., 2017. Sea-ice evaluation of NEMO-Nordic 1.0: a NEMO-LIM3.6-based ocean-sea-ice model setup for the North Sea and Baltic Sea. *Geosci. Model Dev.* 10, 3105–3123. <https://doi.org/10.5194/gmd-10-3105-2017>
- Reynolds, R.W., Smith, T.M., Liu, C., Chelton, D.B., Casey, K.S., Schlax, M.G., 2007. Daily high-resolution-blended analyses for sea surface temperature. *J. Clim.* 20, 5473–5496. <https://doi.org/10.1175/2007JCLI1824.1>
- Savchuk, O.P., 2018. Large-Scale Nutrient Dynamics in the Baltic Sea, 1970–2016. *Front. Mar. Sci.* 5, 1–20. <https://doi.org/10.3389/fmars.2018.00095>
- Savchuk, P.O., Wulff, F., 2007. Modeling the Baltic Sea eutrophication in a decision support system. *AMBIO* 36, 141–148.
- Scott, J.P., Werdell, P.J., 2019. Comparing level-2 and level-3 satellite ocean color retrieval validation methodologies. *Opt. Express* 27, 30140–30157.
- Seegers, B.N., Stumpf, R.P., Schaeffer, B.A., Loftin, K.A., Werdell, P.J., 2018. Performance metrics for the assessment of satellite data products: an ocean color case study. *Opt. Express* 26. <https://doi.org/10.1364/OE.26.007404>
- Skjoldal, H. R., Dundas, I., 1991. *Chrysochromulina polylepis* bloom in the Skagerrak and Kattegat in May-June 1988: Environmental conditions, possible causes, and effects. ICES Cooperative Research Reports (CRR). Report. <https://doi.org/10.17895/ices.pub.5524>
- Stramska, M., Aniskiewicz, P., 2019. Satellite Remote Sensing Signatures of the Major Baltic Inflows. *Remote Sens.* 11, 954. <https://doi.org/10.3390/rs11080954>
- Stramska, M., Dickey, T., 1993. Phytoplankton bloom and the vertical thermal structure of the upper ocean. *J. Mar. Res.* 51, 819–842.
- Stramska, M., Dickey, T., 1994. Modeling phytoplankton dynamics in the northeast Atlantic during the initiation of the spring bloom. *J. Geophys. Res.* 99, 10241–10253.
- Stramska, M., Konik, M., Aniskiewicz, P., Jakacki, J., Darecki, M., 2021. Comparisons of Satellite and Modeled Surface Temperature and Chlorophyll Concentrations in the Baltic Sea with In Situ Data. *Remote Sens.* 13, 3049. <https://doi.org/10.3390/rs1315304>
- Stramska, M., Stoń-Egiert, J., Ostrowska, M., 2020. Towards modeling growth rates of cyanobacteria in the Baltic Sea. *Estuar. Coast. Shelf Sci.* 242, 106853. <https://doi.org/10.1016/j.ecss.2020.106853>
- Sverdrup, H.U., 1953. On conditions for the vernal blooming of phytoplankton. *ICES J. Mar. Sci.* 18, 287–295. <https://doi.org/10.1093/icesjms/18.3.287>
- Wasmund, N., Nausch, G., Matthäus, W., 1998. Phytoplankton spring blooms in the southern Baltic Sea: spatio-temporal development and long-term trends. *J. Plankton Res.* 20, 1099–1117.
- Wozniak, S.B., Sagan, S., Zablocka, M., Ston-Egiert, J., Borzycka, K., 2018. Light scattering and backscattering by particles suspended in the Baltic Sea in relation to the mass concentration of particles and the proportions of their organic and inorganic fractions. *J. Marine Syst.* 182, 79–96. <https://doi.org/10.1016/j.jmarsys.2017.12.005>
- Wroblewski, J.S., 1989. A model of the spring bloom in the North Atlantic and its impact on ocean optics. *Limnol. Oceanogr.* 34, 1563–1572.

Available online at www.sciencedirect.com

ScienceDirect

journal homepage: www.journals.elsevier.com/oceanologia

ORIGINAL RESEARCH ARTICLE

Distribution and biogeochemical perspectives of nutrients in the Eastern Equatorial Indian Ocean

Madhusudan Paul^a, Prasun Sanyal^a, Rishmita Mukherjee^a,
Vandana Kumari Gupta^a, Sneha Bakshi^a, Avanti Acharya^a,
Trishneeta Bhattacharya^{b,d}, Kunal Chakraborty^b,
Sandip Kumar Mukhopadhyay^{a,c,*}

^aDepartment of Marine Science, University of Calcutta, Kolkata, India

^bIndian National Centre for Ocean Information Services (INCOIS), Ministry of Earth Sciences, Government of India, Hyderabad, India

^cMinistry of Earth Sciences, Government of India, New Delhi, India

^dFaculty of Ocean Science and Technology, Kerala University of Fisheries and Ocean Studies, Kochi, India

Received 22 March 2023; accepted 27 February 2024

Available online 16 March 2024

KEYWORDS

Eastern Equatorial
Indian Ocean;
Nutrients;
Preformed nutrients;
Nitrate deficit

Abstract The seasonal reversal of ocean circulation associated with seasonal change in the direction of prevailing winds and the occurrence of several anomalous events in the Eastern Equatorial Indian Ocean (EEIO) make this region dynamic and complex in terms of its biogeochemical characteristics. Two multidisciplinary cruises were conducted to measure nutrients and associated physicochemical parameters across the water column (up to 1000 m) of the EEIO during boreal summer and winter monsoons to understand the distribution of nutrients and their spatio-temporal variability from a biogeochemical perspective. The seasonality in the thermohaline structure of the region is indistinct except for surface salinity drop during summer monsoon due to more precipitation on-site and in adjoining areas. Low concentrations of chlorophyll at the surface and in the deep chlorophyll maxima represent the oligotrophic

* Corresponding author at: Scientist-F, Ocean Sciences and Technology Division, Ministry of Earth Science (Headquarters), Government of India, Prithvi Bhavan, Lodhi Road, New Delhi: 110003 (recently at the Department of the Marine Science of the University of Calcutta, India).
E-mail address: Sandip.m@gov.in (S.K. Mukhopadhyay)

Peer review under the responsibility of the Institute of Oceanology of the Polish Academy of Sciences.



<https://doi.org/10.1016/j.oceano.2024.02.005>

0078-3234/© 2024 Institute of Oceanology of the Polish Academy of Sciences. Production and hosting by Elsevier B.V. This is an open access article under the CC BY-NC-ND license (<http://creativecommons.org/licenses/by-nc-nd/4.0/>).

nature of this region. Surface water was found nutrient-depleted (0.03–0.4 μM Nitrate, 0.02–0.13 μM Phosphate). The maxima of vertical profiles of nitrate and phosphate were recorded at a shallower depth (150–200 m) when compared to its maxima in usual oceanic conditions, but a silicate maximum was recorded in deeper water. In the surface and upper mixed layer paucity of nutrients resulted in low N:P and N:Si ratios. Therefore, nitrogen limitation is evident. The overall ratio of N:P yielded a mean value of 15.33 and matched with the representative literature value for the Indian Ocean. The minimum oxygen values (<50 μM) in the deep water (150–200 m) indicated a hypoxic condition. No signature of denitrification and a moderate nitrate deficit were observed in deep waters. The negative values of Nitrate anomaly (N-tracer) at 50–100 m depth were attributed to a Watermass influenced by denitrification. The prevailing oligotrophic condition caused limited synthesis of organic matter and subsequently little decomposition in deep water. The maxima in the apparent oxygen utilization (AOU) profile are confined to 150 to 200 m depth and represent the most active zone for regeneration that is limited to shallow depth. Regenerated nutrients reached maxima at shallower depth and primarily control material cycling in this region. Supply of nitrate to the surface water based on the preformed values of prevailing water mass was primarily by Bay of Bengal water. According to the findings of this study, preformed nitrate concentrations between 100 and 200 metres below the surface were found very low, indicating that Indonesian Through Flow (ITF) has little impact on the distribution of nutrients in this area.

© 2024 Institute of Oceanology of the Polish Academy of Sciences. Production and hosting by Elsevier B.V. This is an open access article under the CC BY-NC-ND license (<http://creativecommons.org/licenses/by-nc-nd/4.0/>).

1. Introduction

Dissolved nutrients in the oceans play a pivotal role in sustaining life through their involvement in the complex marine biogeochemical cycling processes. Among the nutrients, nitrogen and phosphorous are most important for marine primary production, but other nutrients like silicate, iron etc. are also significant in the oceanic carbon assimilation processes. These non-conservative constituents of seawater are consumed in the photic zone to support primary production for synthesizing organic matter, which is recycled in the water column, supporting grazing and food chains. The vertical distribution of nutrients in the ocean is determined by their uptake and release, physical processes related to shallow and deep vertical mixing and background or preformed concentration advected with the water masses present horizontally. The ocean being in a steady state and dynamic equilibrium, the combined effect of the above factors, builds up the nutrient levels at regional scales which are measured as representative in situ concentration and determine the characteristics of the water column. An insight into the vertical distribution of nutrients in a particular oceanic region reveals important information related to the biogeochemical significance of the region and the internal regulatory process causing such distribution. Oceanic phytoplankton fix around 50 Pg C per annum which is 40% of the global carbon fixation and they regulate the carbon pump of the ocean as well as the CO_2 content of the atmosphere (Bristow et al., 2017; Falkowski, 1994). The sunlit surface layer is the most important region for primary production in the ocean and the abundance of nutrients here (mainly nitrate) determines the fertility of the surface ocean. The potential for primary production determines the trophic status of the region, which controls the supply and availability of organic matter in the oceanic water column particularly in the surface and mixed layer.

The available organic matter sets the potential for recycling and is broken down to regenerate nutrients as well as other by-products. Following the above utilization and regeneration of nutrients, in general, oceanic surface water is nutrient-depleted and marginally increases downward in the photic zone. Below the photic zone nutrient concentrations abruptly increase through biotic respiration, which remineralizes nutrients that reach maxima in the thermocline region and typically remain stable downward as the organic matter gets exhausted. This chemical mass balance is very important in oceanic systems to understand the biogeochemical processes and corresponding changes in nutrient biogeochemistry in the water column. The relative and proportionate involvement of nutrients in the above-mentioned biological cycle establishes a stoichiometric relation (N:P ratio) among the nutrients. The molar ratio of N:P during assimilation or remineralization is typically 16:1, which is similar to the N:P ratio in phytoplankton at large spatial and temporal scales (Anderson and Sarmiento, 1994; Karl et al., 1992; Redfield 1934, 1958). Deviation from this stoichiometric ratio can give insights into the nutrient limitation, carbon sequestration, organic remineralization and input-output balance of the nitrogen cycle in the water column (Gruber and Sarmiento, 1997; Moore et al., 2013; Sigman and Boyle, 2000; Singh et al., 2015). In general, in subsurface waters, N:P ratio >16:1 indicates nitrogen gain via fixation, while deep-water values <16:1 represent a deficit in nitrate due to denitrification (Codispoti et al., 2001). Moreover, the status of the marine N cycle can be determined with the help of quasi-conservative tracers N^* (N tracer) which is a linear combination of nitrate and phosphate (Deutsch et al., 2001; Gruber and Sarmiento, 1997). A negative N tracer indicates nitrate deficit through the denitrification process, whereas a positive N tracer indicates nitrogen input via nitrogen fixation. The mean global N tracer value is reported to be approximately $-3.5 \mu\text{M}$, indicating

mean ocean water is deficient in NO_3^- by $\sim 10\%$ relative to PO_4^{3-} . In the Pacific Ocean N tracer is negative throughout the water column and decreases with depth, while the Atlantic has an excess of nitrate (N tracer $> 1 \mu\text{M}$) throughout much of the thermocline (100–800 m) and returns toward the global mean values in deep waters (Deutsch and Weber, 2012; Gruber and Sarmiento, 1997). In general, at the surface, both nutrients are strongly depleted and N tracer values are close to zero (Deutsch and Weber, 2012).

Large-scale nutrient distribution in the ocean is influenced by the global circulation pattern (Broecker et al., 1999) through which water masses are positioned at different depths and their preformed nutrient values build up background concentration at regional. A preformed nutrient is defined as the concentration of a nutrient originally present in a water parcel at the source just before the water mass was formed. Preformed nitrate and preformed phosphate have been traditionally used as a conservative tracer to identify water masses involved in global thermohaline circulation (Abell et al., 2005; Broecker, 1974; Broecker et al., 1985). Moreover, preformed nutrients can be used as a proxy for net remineralization of particulate organic matter (POM) and for nutrient biogeochemistry. The vertical mixing of the water column is primarily driven by two processes: wind stress, which induces the formation of eddies and gyres, and thermohaline circulation, which involves the upwelling and downwelling of water. Such vertical movements caused depletion and enrichment of nutrients in certain parts of the water column. The enrichment of surface layer nutrients through upwelling enhances productivity and has enormous significance in the global carbon cycle.

The Eastern Equatorial Indian Ocean (EEIO) is characterized by strong atmospheric convection resulting in large air-sea heat exchange over the Indian Ocean warm pool (Hori et al., 2016; Schott et al., 2009). Several atmospheric anomalous events like Madden–Julian Oscillation (MJO), Indian Ocean Dipole (IOD), El Niño–Southern Oscillation (ENSO) control the dynamics of this region and the subsequent response of the ocean towards these phenomena make this region unique and complex. Moreover, seasonal reversal of wind patterns and associated currents largely influence the biogeochemical pump operating in the region (Schott et al., 2001). All these physical forcing processes have a significant impact on the regional biogeochemistry. The thermohaline structure and circulation pattern are unique in this region and have been studied extensively, but information related to the biogeochemistry of nutrients is not sufficiently available in the literature. Moreover, this region receives important water masses like Indonesian Throughflow (ITF), Indian central water mass, Arabian Sea water mass and Bay of Bengal water mass. The influence of these water masses particularly Pacific waters on the nutrient distribution and water column biogeochemical processes is a matter of great significance.

So, it is evident that the understanding of the distribution of nutrients in the highly dynamic equatorial Indian Ocean is essential to have a clear perception of the biogeochemical cycle. This study is focused on the understanding the distribution of nutrients in the EEIO covering spatio-seasonal variability and highlighting their significance on the

biogeochemical perspectives of this region. In addition, the thermohaline structure of this region and the influence of water masses on the nutrient characteristics have been addressed.

2. Study area

This study was planned to understand the distribution of nutrients and their biogeochemical dynamics in this region. Two multidisciplinary cruises (SSD 025 and SSD 044) were undertaken occupying a north-south transect i.e., from 5°N to 11.2°S along 91°E to 101.9°E during boreal summer and from 5°N to 8.4°S along 91°E to 100°E during boreal winter (Figure 1). The area south of the Andaman Sea, bordering Indonesia was taken as a representative of the Eastern Equatorial Indian Ocean. The eastern Indian Ocean is so far the least studied region in the Indian Ocean as well as in the world ocean. It has some unique characteristics which make this region different from others. It is the part of Indo-Pacific warm pool; this region has a major impact on the global conveyor belt. In this region Indian Ocean meets the Pacific Ocean through Indonesian through flow. Moreover, it is the region of intense Air-Sea exchange which has a direct impact on global climate.

3. Material and methods

Two multidisciplinary cruises were undertaken in *r/v Sindhu Sadhana* during boreal summer (July–August 2016) and winter (November–December 2017) bearing cruise numbers SSD_025 and SSD_044, respectively. A total of 253 water samples at 16 CTD stations during July–August (Boreal Summer monsoon) and 235 water samples in 14 CTD stations during November–December (Boreal Winter monsoon) were collected during these expeditions.

Water samples were collected from different depths covering the upper 1000 m of the water column using a rosette sampler fitted with Niskin bottles and seabird CTD with temperature, salinity sensors and fluorometer for chlorophyll-*a* measurement.

From each Niskin bottle water samples were collected in BOD bottles with Penny-head Stopper (125 ml) and in two sets of HDPE bottles for dissolved oxygen and nutrients analyses. Dissolved oxygen was analyzed onboard using the Winkler method with the help of a Metrohm auto-titrator unit (model no. 865 Dosimat plus) with a precision of ± 0.013 ml/L. One set of nutrient samples was analysed onboard for nitrate ($\pm 0.1 \mu\text{M}$ in the range of 0–5 μM , $\pm 0.2 \mu\text{M}$ in the range 5–10 μM , and $\pm 0.5 \mu\text{M}$ in the higher concentration range), nitrite ($\pm 0.02 \mu\text{M}$), phosphate (relative precision $\pm 15\%$ at the low level 0.2 μM , at the medium level 0.9 μM $\pm 5\%$ and at the high level 2.8 μM $\pm 2\%$) and silicate (precisions of $\pm 4\%$ at 4.5 μM , $\pm 2.5\%$ at 45 μM and $\pm 6\%$ at the 150 μM level) following standard analytical methods (Grasshoff et al., 2009). Duplicate samples for nutrients were stored at -20°C . In the shore laboratory, 20% of the preserved samples were analysed for all the above-mentioned nutrients randomly using an auto-analyzer to crosscheck the accuracy of the analytical method. The relative error for both measurements in the same sample was

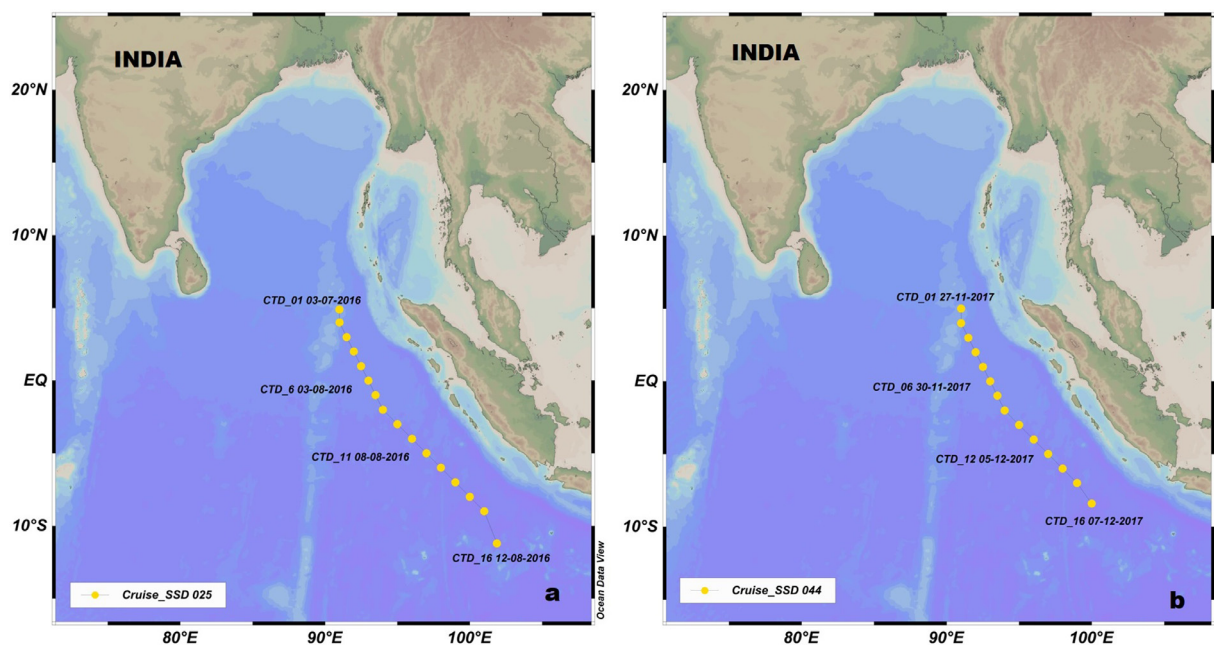


Figure 1 Map showing sampling stations (a) during July–August, 2016 (Cruise SSD_025, Boreal Summer) and (b) November–December, 2017 (Cruise SSD_044, Boreal Winter).

found to be below 1.5%. Based on the results of the biogeochemical parameters several indices were calculated as given below.

Apparent Oxygen Utilization (AOU) was calculated as the difference between saturation oxygen concentration and observed in situ oxygen concentration according to Garcia and Gordon (1992) and following the modification reported in the Weiss (1970) solubility equations and Benson and Krause (1984) solubility coefficients.

Regenerated nutrients (nitrate and phosphate) were calculated as the difference between observed nutrients and preformed nutrients using the following equation,

$$N_{pf} = N_m - (AOU/R_{-O_2/N}),$$

where N_{pf} is the preformed value, N_m is the measured nitrate concentration, AOU is the apparent oxygen utilization, and $R_{-O_2/N}$ is the stoichiometric ratio of oxygen consumption to nitrate regeneration during respiration of sinking POM (Abell et al., 2005; Park, 1967).

The nitrate anomaly (N-tracer) was calculated using the following equation (Deutsch et al., 2001; Gruber and Sarmiento, 1997):

$$N - \text{tracer} = \text{Nitrate} - 16 \times \text{Phosphate} + 2.9 \mu\text{mol kg}^{-1}.$$

Temperature and salinity were recorded using respective sensors fitted to the Sea-bird CTD system. Initially, all the cast data were recovered from Seasave V 7.23.2 and further processing was performed using Seabird data processing V 7.23.2 software following standard protocol. Salinity values were calculated through conductivity. After calibration, the accuracy for conductivity was found to be ± 0.00025 S/m. The temperature sensed by CTD probes was also calibrated following standard procedures and accuracy of measurement was found to be $\pm 0.001^\circ\text{C}$. All the plots and profiles have been made using Ocean Data View software (Schlitzer and Mieruch-Schnülle, 2019).

4. Results

4.1. Thermohaline structure and distribution of relevant variables of water column (1000 m)

Depth profiles of temperature and salinity in the EEIO during summer monsoon (SM) and winter monsoon (WM) are shown in Figure 2. An overlap of temperature profiles during both monsoons indicates that seasonal differences in the temperature distribution in the upper 1000 m of the water column are negligible. However, salinity profiles indicate that the upper 400 m of the water column exhibit a seasonal difference with lower surface salinity being recorded during SM (32.1–34.15) than WM (33.54–34.76). Vertical plots showing distributions of temperature and salinity during both monsoons are presented in Figure 2. The thermocline (D23) goes deeper (~ 120 m) at the equator, which is further extended to both sides covering 4°N – 4°S and 2°N – 7°S during SM and WM, respectively. The uplift of the thermocline is evident both north and south of the equator during both seasons with the shallowest (~ 60 m) depth at beyond 7°S during the WM. Shoaling of isotherm (23°C) is evident on both sides of the equator particularly 5°N (~ 90 m), 4°S to 6°S (~ 100 m) and beyond 8°S (80–90 m) during summer, while during winter it was prominent beyond 7°S (~ 60 m). Surface salinity at the equator and both the north and south sides was observed to be slightly higher during the WM than in the SM. The vertical distribution of DO in the EEIO during SM and WM is shown in Figure 3a–c. Surface waters exhibited values over $200 \mu\text{M}$ during both seasons and the depth of the oxycline (characterized by the isoline of $110 \mu\text{M}$) exhibited large spatial variability over both the northern and southern regions of the EEIO. Oxycline follows the thermocline in these regions i.e., it deepens and shoals on both at the equator during both seasons.

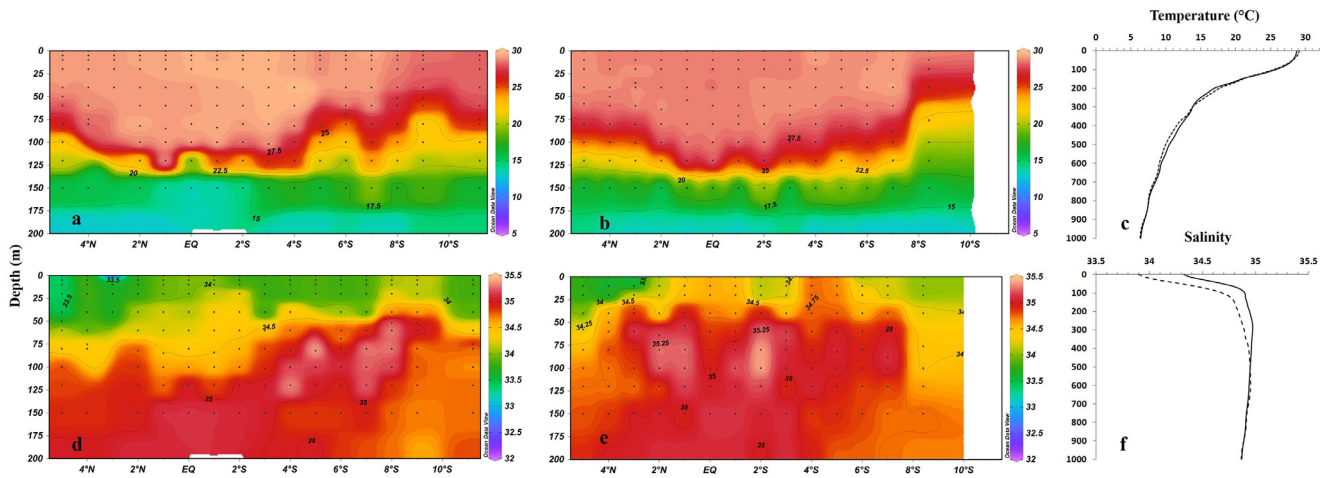


Figure 2 Vertical distribution (200 m) and depth profiles (1000 m) of temperature and salinity in the EEIO. Where, (a) and (b) represents temperature during summer monsoon and winter monsoon, (d) and (e) represents salinity during summer and winter monsoon, (c) and (f) represents depth profiles of temperature and salinity respectively. The dashed (continuous) line represents profiles for summer (winter) monsoon.

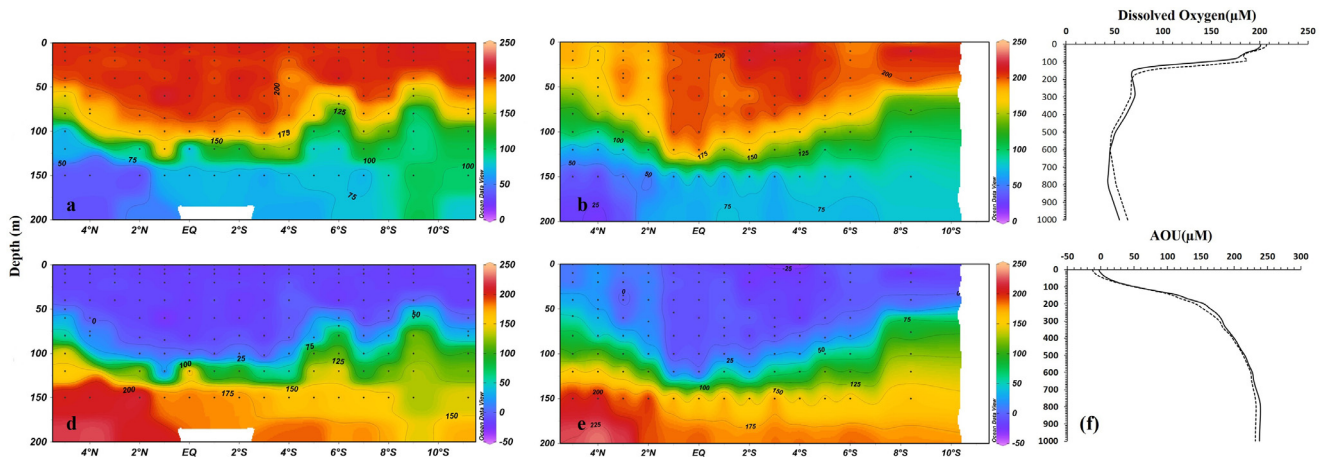


Figure 3 Vertical distribution (200 m) and depth profiles (1000 m) of dissolved oxygen (μM) and AOU (μM). (a) and (b) represents, dissolved oxygen during summer and winter monsoon respectively, (c) depth profile of dissolved oxygen. (d) and (e) AOU during summer and winter monsoon, (f) depth profile of AOU. The dashed (continuous) line represents profiles for summer (winter) monsoon.

The Θ -S diagram shows a scattered nature encompassing the thermohaline variability at sampling points on both sides of the equator. The Θ -S diagram and DO overlay on Θ -S are presented in Figure 4a–b). A high salinity water mass was found to exist within the depth range 50–130 m between 3°S–8°S during SM which was seen to extend to 3°N to 2°S during the WM Figure 3d–e). Southward to 8°S low salinity surface and subsurface water mass with lower subsurface temperature are evident. A low oxygen ($<50 \mu\text{M}$) water mass was found below 120 m between 5°N–2°N during both seasons, which was also recorded to have high salinity.

Chlorophyll-*a* in the EEIO during SM and WM is presented in Figure 5a–b. Near-surface waters of EEIO exhibit low concentrations of chlorophyll-*a* during both monsoons. The deep chlorophyll maximum (DCM) with chlorophyll-*a* values ranging from 0.75 to 1.0 mg/m^3 was restricted to 50–75 m during both the monsoon seasons. A prominent and continuous DCM was recorded during the WM in contrast

to SM. During SM chlorophyll-*a* concentration was found to be low and discontinuous (0.2–0.75 mg/m^3 except at 9°S) compared to WM where chlorophyll-*a* concentration was marginally higher and continuous (0.3–0.8 mg/m^3 , maximum $\sim 1 \text{ mg}/\text{m}^3$ at 4–5°N). At the equator, chlorophyll concentration in the DCM was found to be very low ($<0.25 \text{ mg}/\text{m}^3$).

The vertical distribution of nitrite in the water column is presented in Figure 5c–d. Throughout the water column, very low concentrations (0–0.1 μM) were observed, except at depths between 50–100 m where higher concentrations ($\sim 0.2 \mu\text{M}$) were observed. The nitrite maximum zone (50–100 m) with high nitrite concentration (0.5–0.75 μM) was observed at 4°N, 4–5°S, 7°S, 9°S during SM and 4–3°N, 3–7°S during WM, while at the equator nitrite concentration at such depths was found to be much lower during both the seasons. An association of nitrite maxima and DCM is clearly visible in this region.

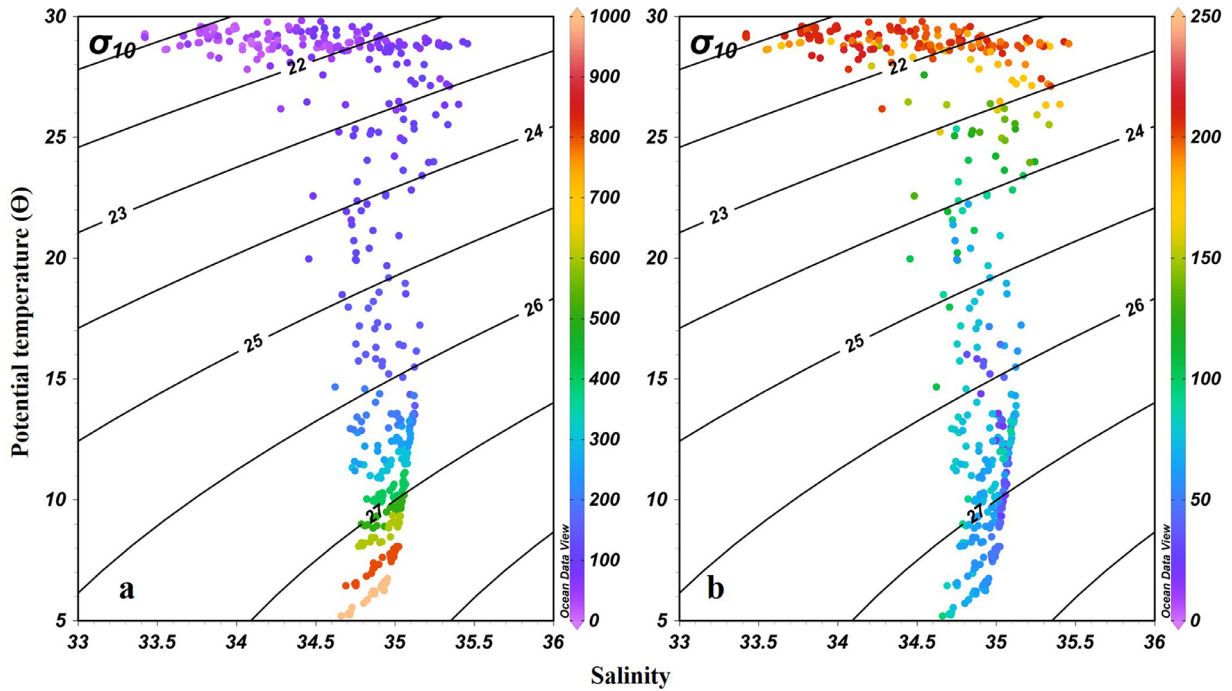


Figure 4 Potential temperature – salinity (Θ -S) diagram of EEIO overlaid with (a) depth (m), (b) dissolved oxygen (μM).

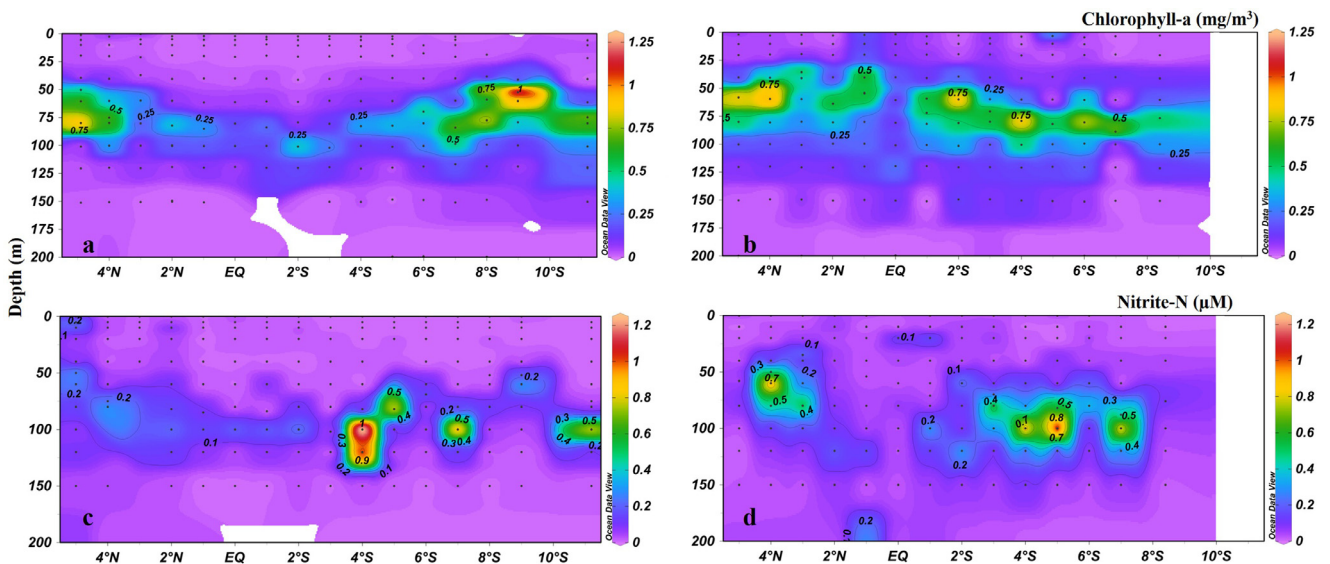


Figure 5 Vertical distribution of chlorophyll-a (mg/m^3) and Nitrite up to 200 m depth, where (a), (c) represents summer monsoon and (b), (d) represents winter monsoon respectively.

4.2. Distribution of nutrients and their ratios

Depth profiles of nutrients (nitrate, phosphate and silicate) are shown in Figure 6. The surface water in this region was found to be strongly depleted in nutrients with less than $1 \mu\text{M}$ nitrate, $0.1\text{--}0.5 \mu\text{M}$ phosphate and $\sim 1.5 \mu\text{M}$ silicate in the upper 50 m during both seasons. Nutrient values start increasing in the depth interval 100–200 m. A similar observation was made by Harms et al. (2019) in their study in the southern Indian Ocean ($2.98^\circ\text{--}8.81^\circ\text{S}$), where they found increasing nutrient concentrations from 90 m and

maxima of $>20 \mu\text{M}$ for nitrate and $>1.5 \mu\text{M}$ for phosphate in the thermocline zone before they attain their maxima at greater depth. Nitrate concentration was recorded to be around $10\text{--}18 \mu\text{M}$ at 100–200 m, $30\text{--}35 \mu\text{M}$ at 200–700 m and stabilized at a maximum value of around $40 \mu\text{M}$ below 700 m. Phosphate concentration at the depth of 50–200 m was found to be $0.5\text{--}1 \mu\text{M}$ during SM, whereas during WM it was slightly lower ($0.4\text{--}0.8 \mu\text{M}$). Further down (200–600 m), phosphate concentration ranged between $1.75\text{--}2.25 \mu\text{M}$ and $1.5\text{--}2.25 \mu\text{M}$ during SM and WM respectively. However, during WM north of the equator phosphate concentration

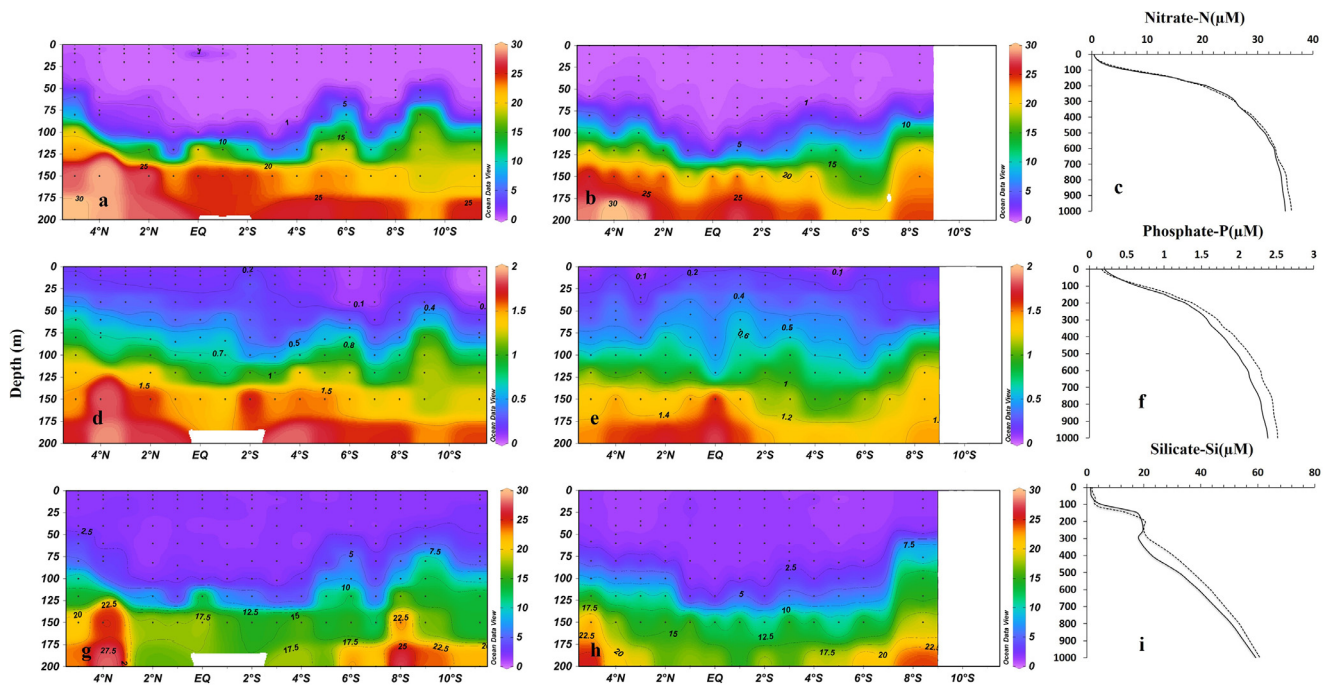


Figure 6 Vertical distribution (200 m) and depth profiles of nitrate (a,b,c), phosphate (d,e,f) and silicate (g,h,i), where, (a,d,g) represents summer and (b,e,h) represents winter monsoon, respectively. The dashed (continuous) line represents profiles for summer (winter) monsoon.

was lower ($1.5\text{--}2\ \mu\text{M}$) within the depth range 200–600 m, except between $2\text{--}3^\circ\text{N}$ (phosphate concentration $> 2.25\ \mu\text{M}$). Beyond 700 m phosphate concentration was found to vary between $2.25\text{--}3.0\ \mu\text{M}$ during both seasons.

The silicate concentration increased to $20\text{--}30\ \mu\text{M}$ within the depth range of 200–400 m from low near-surface values and continued to rise to 1000 m, reaching up to $60\ \mu\text{M}$. The maximum values for silicate were observed in deeper waters, unlike nitrate or phosphate. Marginally higher nutrient values during WM, particularly for phosphate and silicate, were recorded during SM below the MLD (Figure 6f,i).

The distribution of the nutrients on both sides of the equator did not exhibit any distinct heterogeneity. The nutricline is observed to be at shallower depths going further away from the equator. The uplift and shoaling of nutricline is uniformly noticed for all nutrients at $4^\circ\text{--}6^\circ\text{S}$ and $8^\circ\text{--}10^\circ\text{S}$ and 5°N to 4°N during summer season. During winter monsoon nitrate and silicate, distribution showed equivalent trends of shoaling from 5°N to 2°N and beyond 8°S , however, a diffused pattern of shoaling is recorded on both sides of the equator in the contours of phosphate.

The scatter plot of silicate vs. nitrate is presented in Figure 7c. The regression line showed an exponential fit ($R^2 = 0.9363$). It is evident that in the concentration range up to approx. $35\ \mu\text{M}$ for both the nutrients maintained more or less $\text{N}:\text{Si} = 1$. However, beyond $35\ \mu\text{M}$ concentration though the increase in nitrate values is minimal silicate abruptly increases to attain much higher values in deep water.

Figure 7b shows the scatter plot of NO_3^- and PO_4^{3-} by combining data from both the seasons. The $\text{N}:\text{P}$ ratio can be discerned from this plot as the slope of the regression line that was to be 15.33 ($R^2 = 0.846$) (excluding near-surface

values). Near-surface waters exhibit a very low $\text{N}:\text{P}$ ratio as both the nutrients in the near-surface are only sparingly available. Also, the concentration of NO_3^- at low ratios of $\text{N}:\text{P}$ in the surface layer during both seasons goes to zero before $\text{PO}_4^{3-}\text{-P}$. At higher values of NO_3^- and PO_4^{3-} the $\text{N}:\text{P}$ values show in general, a positive deviation from the regression line except for a few points at the maximum range which showed a negative deviation.

The $\text{N}:\text{P}$ ratio in the EEIO during both monsoons is presented in Figure 7a. In general, the ratio showed lower values in the upper layer up to 100 m but stabilized to around 15:1 beyond that point to further deep waters. The profiles for both seasons were found to be overlapping within the mixed layer and up to 200 m but a marginally lower ratio (14:1) was recorded during SM in the deeper waters with higher nutrient concentrations. The deficiency in the stoichiometric levels of nitrate was further analyzed by computing quasi-conservative tracer N^* (N tracer) and the vertical profile is shown in Figure 7d. N tracer showed positive values in the deep waters beyond 200 m with the highest values ($1\ \mu\text{M}$ during SM and $3.5\ \mu\text{M}$ during WM) at around 300 m depth. However, N tracer was negative (0 to $-2\ \mu\text{M}$ during SM and 0 to $-1.5\ \mu\text{M}$ during WM) in the upper layers.

4.3. Apparent oxygen utilization, nutrient re-mineralization and conservative tracers

To get an insight into the organic matter mineralization and its impact on the distribution of nutrients, the variation of Apparent Oxygen Utilization (AOU) across the depth is presented in Figure 3d–f. Surface water AOU during both monsoons ($0\text{--}60$ m and at equator ~ 100 m) was found to be negative except for the region between 5°N to 3°N where AOU

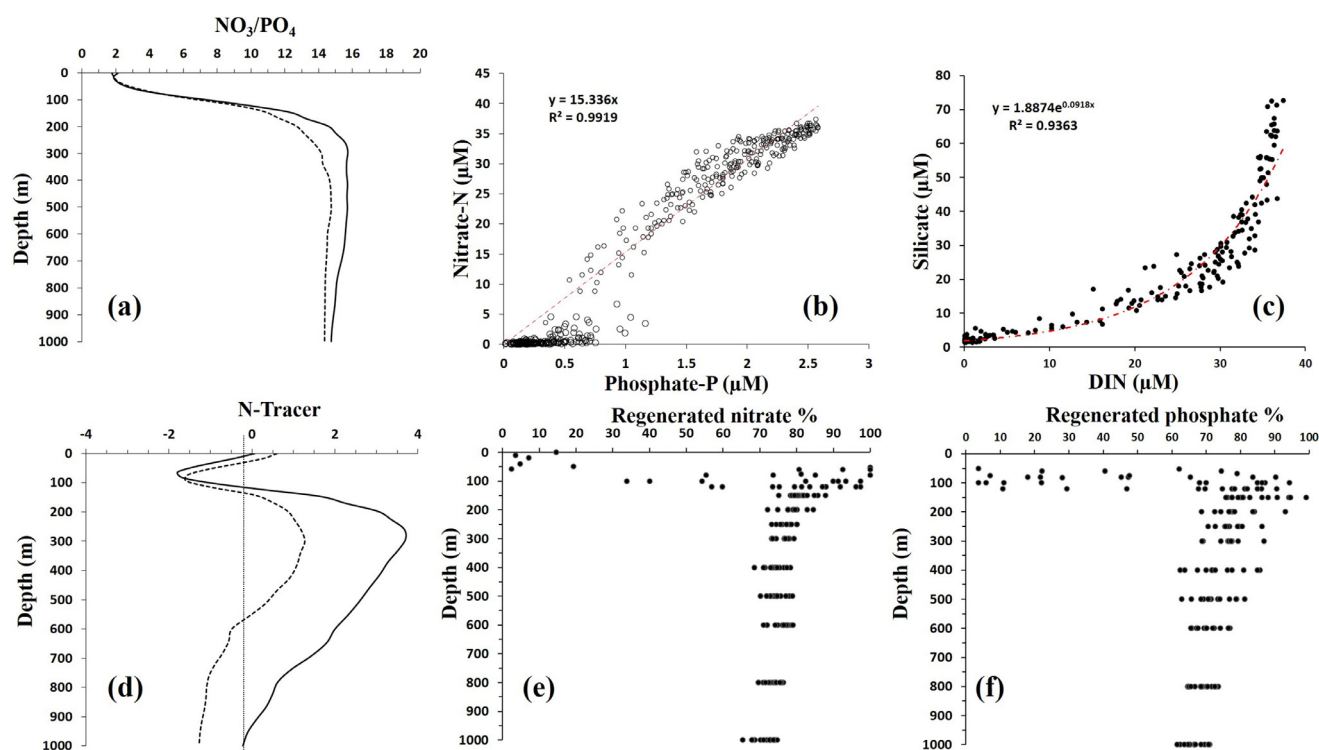


Figure 7 Depth profiles of (a) NO_3/PO_4 ratio, (b) scattered plot of nitrate Vs phosphate, (c) scattered plot of silicate vs. dissolved inorganic nitrogen (DIN), (d) depth profile of N tracer, (e) profiles of regenerated fractions of nitrate, (e) Profiles of regenerated fractions of phosphate in the EEIO to 1000 m depth.

was found to be higher during the WM. Below the mixed layer (>150 m) AOU values were found to vary between $150\text{--}200\ \mu\text{M}$ and high values were found much deeper ($200\text{--}250$ m) at the equator. The low oxygen zone below 120 m between $5^\circ\text{N}\text{--}2^\circ\text{N}$ showed the highest AOU values ($> 200\ \mu\text{M}$).

Considering the relationship of oxygen consumption to nutrient regeneration caused by biological oxidation and adopting the proposed ratio of 1:16:106:138 for P:N:C:O, insight could be gained into the recycling of the nutrients in the water column. The vertical distribution of the regenerated fractions of nitrate and phosphate is shown in Figure 7e–f. The maxima in regenerated nitrate and phosphate were found within the depth range $60\text{--}120$ m and sigma- θ range 23–24 indicating an active zone for mineralization of POM. The regeneration of nutrients continued further downwards maintaining around 80% of the maximum value.

The regenerated part of the nutrients being subtracted from the measured values represents preformed nutrient concentrations and such values across different isopycnal attributes the ambient nutrient concentration of the water masses before it had sunk at its origin. At the surface (BBW) preformed nitrate and phosphate are found $1.747\pm 0.5\ \mu\text{M}$ and $0.270\pm 0.05\ \mu\text{M}$ respectively. Whereas at MLD (ITF) it is found low (performed nitrate, $0.944\pm 0.4\ \mu\text{M}$ and $0.504\pm 0.08\ \mu\text{M}$) compared to the surface. The preformed nutrients (nitrate and phosphate) values and their ratios with measured nutrient concentration along with other relevant characteristics of the water masses present in the EEIO are presented in Table 1. The ratio of measured to preformed nitrate and phosphate values was found 0.51

and 0.97 for the BBW surface water. However, such ratios increase to 7.3 for nitrate and 1.4 for phosphate at the mixed layer contributed by ITF. Beyond the mixed layer, this ratio for both nutrients was stabilized between 3.5 to 4.5 for the water masses present in such depths.

5. Discussion

5.1. Water masses and productivity status

The observed thermal structure of the water column and lack of seasonality is typical for the equatorial region. The low salinity recorded in the surface layer during SM is driven by high precipitation and freshening by advection of low salinity waters from the Bay of Bengal (BoB) (Perigaud et al., 2003; Vinayachandran and Nanjundiah, 2009). The seasonality in the surface DO distribution can be attributed mainly to the semi-annual changes in physical forcing over this region. Well-oxygenated surface water is mainly from the Bay of Bengal water (BBW) which is less saline and transported to EEIO by Ekman transport from the north-eastern Bay of Bengal (Mamayev, 1975; Sengupta et al., 2006, 2013). Surface water DO values typical for the equatorial region which further stabilized to moderate values within 200 m depth indicate slow oxygen loss and a slow mineralization of organic matter. The deeper thermocline at the equator and subsequent upliftment (shallower) towards the north and south direction is caused and maintained by the tropical instability waves as well as equatorial waves (Evans et al., 2009). The similar variability in

Table 1 Representing the preformed water masses along with the physico-chemical properties in the Eastern Equatorial Indian Ocean (EEIO).

Water-mass	Temperature (°C)	Salinity	Dissolved Oxygen (μM)	Density (Sigma-θ)	Nitrate (μM)	Phosphate (μM)	Preformed Nitrate (μM)	Preformed phosphate (μM)
BBW (Bay of Bengal Water-mass)	27–30	33.5–34.5	180–225	21–22	0.90±0.5	0.26±0.07	1.74±0.5	0.27±0.05
ITF (Indonesian Through Flow waters)	22–25	34.5–35	100–130	23–23.5	6.86±2.3	0.68±0.11	0.94±0.4	0.50±0.08
ICW (Indian Central Water-mass)	6–15	35–35.1	25–50	25.7, 26.9, 27.1, 27.3	29.46±3.7	2.02±0.29	7.62±0.3	0.42±0.02
NICW (North Indian Central water-mass)	6–15	35–35.1	25–50	25.7, 27.1, 26.9	29.46±3.7	2.02±0.29	7.59±0.2	0.56±0.063
AAMW (Australasian Mediterranean water)	4–20	34.6–34.9	75–100	25.7, 27.3	34.57±0.35	2.34±0.03	7.59±0.2	0.56±0.3

the distribution of oxycline is primarily influenced by the variable thermocline and hydrodynamic settings of the region. Near-surface water (0–50 m) was found to be low saline and well oxygenated (180–225 μM) and based on the θ-S characteristics it was identified as the Bay of Bengal water (BBW). Whereas, from the literature, we found the mixed layer water (Sigma-θ 23–23.5) is influenced by ITF waters from south of Java (Emery and Meincke, 1986; Makarim Salvienty et al., 2019). At about 100 m DO concentration was found to be high (75–100 μM) and low (25–50 μM) at the same density levels (Sigma-θ 25–27.5) indicating the presence of different water masses at the same depth. At the northern terminal (5°N–1°N) of our sampling points, we found low DO (25–50 μM) corresponding to high salinity (35–35.1) between 200–800 m depths which resembles the characteristics of North Indian Central Water mass (NICW). South of 1°N, DO concentration was seen to increase (75–100 μM) and the corresponding salinity decreased (34.6–34.9) which resembled the θ-S characteristics of the Australasian Mediterranean water (AAMW). The Water-Masses prevailing in the EEIO have been described in the literature (Mamayev 1975; Sengupta et al., 2006, 2013; Sverdrup et al., 1942; Tomczak and Godfrey, 2003; You and Tomczak, 1993) and their characteristics like salinity, temperature, density and DO have been assigned in Figure 4a–b. A similar kind of salinity and water-mass distribution in this region was shown by Tomczak and Godfrey (2003). The upper layer of the water column in the EEIO comprises NICW, ICW, and AAMW which were identified in a different range of sigma-θ levels (25.7, 26.7, 26.9, 27.1, and 27.3) (You and Tomczak, 1993).

The low chlorophyll-*a* concentration both at the surface and the DCM is indicative of an oligotrophic ocean with low productivity potential. Such a condition subsequently would cause less regenerated nutrients at depths due to a lower supply of organic matter for remineralization. Previous studies have reported primary productivity in this region to be below 73–90 gC m⁻² yr⁻¹ compared to the equatorial Pacific (180 gC m⁻² yr⁻¹) and other regions of upwelling (180–3600 gC m⁻² yr⁻¹) (Millero, 2013).

5.2. Trophic status and biogeochemical perspectives of nutrients

Surface waters of the EEIO contain very low nitrate (from 0.03 to 0.4 μM) and phosphate (from 0.02 to 0.5 μM), which further implies that oligotrophic conditions prevail at the surface resulting in limited primary production. Concentrations below 0.7 μM for nitrate and 0.3 μM for phosphate produce nitrate and phosphate deficit cells and thereby reduce primary productivity (Millero, 2013). Moreover, nitracline (1 μM isoline corresponding to 0.4 μM of phosphate) extended from ~50 m to 100 m reinstates very low (oligotrophic) nutrient concentration in the mixed layer. Surface waters of this region being of BoB origin, which was also reported to be oligotrophic at both the eastern and the western parts (Sarma et al., 2016) contribute further to the oligotrophy in the EEIO. Such oligotrophic status of the BoB is the result of strong salinity-controlled stratification in the near-surface due to large precipitation during SM and subsequent huge freshwater inputs from various rivers (Ganges,

Brahmaputra, Godavari, Irrawadi, Mahanadi, Krishna, etc.) (Rao et al., 1994; Shetye et al., 1991; Shetye, 1993; Unger et al., 2003). Moreover, the riverine inputs are reported to be deficient in nutrients and particularly inorganic nitrogen was found to be almost (91%) exhausted in the riverine supply before entering BoB (Sarma et al., 2016). In the near-surface waters of the equatorial Indian Ocean along 77°E and 83°E Sardessai et al. (2010) also reported low nitrate and phosphate concentrations within the ranges 0.01–1.77 μM and 0.02–3 μM , respectively. In the equatorial Pacific similar oligotrophic status of the surface water was reported by Rodier (1997). The very low N:P ratio in the surface layer represents insufficiency of both nutrients indicating oligotrophic condition and similar observations were reported by several researchers previously (Deutsch et al., 2007; Sarmiento and Gruber 2006). Moreover, extremely low values of nitrate at the surface as well as low N:P and N:Si ratios indicate nitrogen limitation in the upper layer (0–50 m) of EEIO (Painter et al., 2017). Depth profiles of nitrate and phosphate during SM and WM exhibit an increasing trend in the concentration of both nutrients below the surface layer indicating the effect of organic matter respiration and mineralization nutrients in the thermocline and deeper waters. The maxima values of nutrients (35–40 μM nitrate and 2.25–3.0 μM phosphate) at shallower depth (200–300 m) could be the result of limited supply and early exhaustion of organic matter in the water column as well as shallow thermocline in the oligotrophic equatorial region.

The classical N:Si:P ratio (Redfield, 1934, 1958) is 16:15:1, which is maintained through the biological particulate cycle involving the consumption and release of nutrients. The nitrate vs. silicate scatter plot showed uniform values for both nutrients in the first part of the cluster dots till nitrate levels reached maxima indicating their similarity in the biochemical composition of particulates and the nature of the re-mineralization process. However, after exhaustion of the nitrogenous matter decomposition, the nitrate levels became stable but through sustained siliceous matter decomposition, the silicate levels increased resulting in an exponential trend for cluster dots at high values of both nutrients.

The nitrogen metabolism processes occurring in the water column like nitrogen fixation, nitrification and denitrification, influence such ratios to vary from standard value. The regression line of the N:P plot (Figure 7b) had a slope of 15.33, which is close to the Redfield ratio and matches with the overall Indian Ocean representative values (Millero, 2013). A cluster of low N:P values is found along the axis of phosphate till its 0.5 μM concentration point having negligible nitrate which clearly exhibits nitrogen limitation in the surface layer. In the depth profile of N:P very low and varying values are recorded in the surface mixed layer indicating the low concentration of these nutrients and their uptake in the photic zone for primary production. However, the value of N:P was stabilized to the mean value at around 100 m and the same is maintained in the deep waters beyond that point, which represents the lack of influence of the characteristic nitrogen metabolism process on the N:P values in the region. The marginally lower N:P values in deep waters during SM caused due to slightly higher phosphate concentration observed during summer though nitrate values remained unchanged season-

ally. Such disparity may be the result of higher decomposition of organo-phosphorous compounds yielding more phosphate during summer favoured by the marginal difference in temperature at such depths.

In general, positive deviation of N:P ratios from the regression line (Figure 7b) at higher values of both nutrients in the deep waters indicates the sufficiency of nitrate and ruled out its utilization as the oxidant for organic matter mineralization or could be caused by changes in preformed nutrients. Deviation from the Redfield stoichiometric ratio has been reported by many researchers for different basins like the Arabian Sea (Codispoti et al., 2001; Sen Gupta et al., 1976), subtropical Southern Indian Ocean (Harms et al., 2019), Eastern Indian Ocean (Sardessai et al., 2010). The nitrogen metabolism processes occurring in the water column like nitrogen fixation, nitrification and denitrification, influence such ratios to vary from standard value. The observed N:P ratio at such depths in the case of the Arabian Sea was reported to be 12.81 and attributed to the denitrification process (Codispoti et al., 2001; Harms et al., 2019; Sen Gupta et al., 1976). Positive N tracer values beyond 100 m to deep waters during both seasons also underline the sufficiency of nitrate. However, during summer N tracer values are negative below 600 m but much above the range of values ($<-3 \mu\text{M kg}^{-1}$) reported for water column denitrification in the oxygen minimum zones of the Arabian Sea, eastern tropical north and south Pacific (Gruber and Sarmiento, 1997). The oxygen values at such depth of EEIO varied around 50 μM , which further ruled out utilization of nitrate for organic matter mineralization. The nitrite values in the water column recorded very low levels and carry no signature of nitrite accumulation in the hypoxic deep waters. At the depth of around 100 m just below the DCM, a prominent peak at a low range in the profile of nitrite, corresponding to the ubiquitous primary nitrite maximum, is known to arise from the oxidation of NH_4^+ and/or excretion by phytoplankton (Lomas and Lipschultz, 2006). At the depth of the DCM (50–100 m) N tracer showed negative values indicating a deficit in nitrate in the well-oxygenated mixed layer. This deficit may be attributed to the prevailing water masses at such depth with an influence of the Arabian Sea denitrified waters. A similar observation highlighting the influence of the water mass on N tracer in the Southern Ocean was made by Harms et al. (2019).

5.3. Nutrient regeneration and preformed nutrients in water masses

The mixed layer and the DCM have negatively impacted AOU with low to moderate values which reinstate the limited organic matter synthesis and subsequently lower its availability in the water column in the EEIO. Such features led to low or moderate intensity of organic matter recycling in the water column and thereby lesser AOU values in the deep waters. The maximum regenerated nutrients observed within 150–200 m depths is the most active mineralization zone, which indicates early and shallow depth regeneration occurring in this region. Such shallow depth regeneration has also been reported by Ono et al. (2001) in the Bermuda Atlantic time series study (BATS), where they

found the highest remineralization rate at ~120 m depth. Laufkötter et al. (2017) mentioned shallower regeneration in low latitudes and deeper regeneration in higher latitudes while explaining the impact of oxygen and temperature on remineralization of organic matter. At the depth of regeneration maxima, both nitrate and phosphate concentrations are primarily (80–100%) contributed by regenerated forms. This indicates that regenerated nutrients play a significant role in controlling the primary production in the region. The preformed or background nutrients showed differential contributions in the water column of the region. The measured-to-preformed ratio (0.51) of nitrate in the surface water indicates a significant contribution of nitrate in the prevailing water mass, which, based on the thermohaline characteristics, has been assigned as BBW. Though BBW has been reported to be nutrient-depleted, particularly of nitrogen (Sarma et al., 2016), such a low level acts as a source of nitrates to the nutrient-poor surface layers of EEIO. However, this contribution of phosphate to the surface water was found to be insignificant. The very low level of preformed nutrients there, by the high measured-to-preformed ratio in the deeper water column (100–200 m), signifies the extensive regeneration of nutrients and negligible contribution through prevailing water mass. The thermohaline characteristics of the water mass at such depth ($\text{Sigma-}\Theta = 23\text{--}24$) indicate the presence of Indonesian Through Flow waters (ITF), which enter through Lombok Strait and maintain prolonged northwestward flow within the South Java Current. The ITF spreading in the Indian Ocean is mainly associated with the South Equatorial Current (SEC) (Gordon, 1997) but the circulation and interaction of ITF with the water masses and the current system in the Indian Ocean are poorly understood (Makarim et al., 2019). Makarim et al. (2019) also stated that ITF-source water in the mixed layer ($\text{Sigma-}\Theta = 23\text{--}23.5$) of off Sumatra is present at 70–90 m depth with 34.5–35 salinity and 22–25°C temperature. However, the ITF fraction in this region is very low (0.24). So, this region is impacted by ITF to a lesser degree. The low values of preformed nitrate in the less ITF-impacted water mass in this region point to the nitrogen being depleted or exhausted. Moreover, the complex and unique bathymetry of the narrow passages along the ITF pathways in the Indonesian Seas generates strong tidal mixing (Koch-Larrouy et al., 2007; Ray and Susanto, 2016; Sprintall et al., 2014), altering the Pacific water properties. The nutrient-depleted status of the upper thermocline water along the ITF outflow passages (Lombok, Ombai and Timor) has been reported by Taufiqurrahman et al. (2020). So, the influence of ITF on the nutrient values is insignificant or minor, however, this area is an active zone for organic matter decomposition, thus it can be hypothesized that some allochthonous supply of organic matter comes through ITF influencing augmented nutrient regeneration (Kehinde et al., 2023). Further down, the preformed values in the water masses were moderate and reached a stabilized ratio with measured nutrients reflecting their uniform contribution.

6. Conclusion

Based on our observation of nutrients and related physico-chemical parameters in the EEIO, we attempted to look into

the spatiotemporal variability of nutrients and some aspects of their biogeochemical cycling in the upper 1000 m water column. Surface water (0–50 m) in our study region (5°N to 11.2°S along 91°E to 101.9°E during Boreal summer and from 5°N to 8.4°S along 91°E to 100°E) was found to be oligotrophic, especially bio-limiting for nitrogen. Maximum values of all nutrients were observed at shallower depths compared to typical open ocean profiles. The regression line of the N:P plot has a slope of 15.33 consistent with previous reports from the Indian Ocean. Negative values of N tracer occurred between 50–100 m presumably due to an excess of phosphate over nitrate, a regional signature produced by denitrification in the Arabian Sea. A positive deviation in the N:P ratio at deep waters indicates sufficient nitrogen. Moreover, higher concentrations of regenerated nitrate and phosphate within the depth range of 150–200 m indicate shallow mineralization, which is a characteristic of less productive oligotrophic oceans. The influence of ITF on the nutrient values is found to be insignificant in this region. Moreover, it can be hypothesized that some allochthonous supply of organic matter coming through ITF influence augmenting nutrient regeneration.

Declaration of competing interest

The authors declare that they have no conflicts of interest. All applicable national and/or institutional guidelines for sampling, care, and experimental use of organisms for the study were followed.

Acknowledgements

We gratefully acknowledge the Ministry of Earth Sciences, Government of India for funding this research work under the project entitled “Biogeochemical Process and Paleocceanographic Studies of the Eastern Indian Ocean” (Sanction number: MoES/36/OOIS/Extra/34/2013 dated 28.04.2015). The authors are thankful to Dr. S.W.A. Naqvi for his kind valuable suggestions and recommendations during the preparation of the manuscript. We are extremely thankful to the Director and associated scientists of the National Institute of Oceanography, Goa for their support towards providing an opportunity to participate in both the cruises for undertaking this study.

References

- Abell, J., Emerson, S., Keil, R.G., 2005. Using preformed nitrate to infer decadal changes in DOM remineralization in the subtropical North Pacific. *Global Biogeochem. Cy.* 19 (1). <https://doi.org/10.1029/2004GB002285>
- Anderson, L.A., Sarmiento, J.L., 1994. Redfield ratios of remineralization determined by nutrient data analysis. *Global Biogeochem. Cy.* 8 (1), 65–80. <https://doi.org/10.1029/93GB03318>
- Benson, B.B., Krause Jr, D., 1984. The concentration and isotopic fractionation of oxygen dissolved in freshwater and seawater in equilibrium with the atmosphere 1. *Limnol. Oceanogr.* 29 (3), 620–632. <https://doi.org/10.4319/lo.1984.29.3.0620>
- Bristow, L.A., Mohr, W., Ahmerkamp, S., Kuypers, M.M., 2017. Nutrients that limit growth in the ocean. *Curr. Biol.* 27 (11), R474–R478. <https://doi.org/10.1016/j.cub.2017.03.030>

- Broecker, W.S., 1974. "NO", a conservative water-mass tracer. *Earth Planet. Sci. Lett.* 23 (1), 100–107. [https://doi.org/10.1016/0012-821X\(74\)90036-3](https://doi.org/10.1016/0012-821X(74)90036-3)
- Broecker, W.S., Takahashi, T., Takahashi, T., 1985. Sources and flow patterns of deep-ocean waters as deduced from potential temperature, salinity, and initial phosphate concentration. *J. Geophys. Res.* 90 (C4), 6925–6939. <https://doi.org/10.1029/JC090iC04p06925>
- Broecker, W., Matsumoto, K., Clark, E., Hajdas, I., Bonani, G., 1999. Radiocarbon age differences between coexisting foraminiferal species. *Paleoceanography* 14 (4), 431–436. <https://doi.org/10.1029/1999PA900019>
- Codispoti, L.A., Brandes, J.A., Christensen, J.P., Devol, A.H., Naqvi, S.W.A., Paerl, H.W., Yoshinari, T., 2001. The oceanic fixed nitrogen and nitrous oxide budgets: Moving targets as we enter the anthropocene. *Sci. Mar.* 65, 85–105. <https://doi.org/10.17615/ksfx-e447>
- Deutsch, C., Gruber, N., Key, R.M., Sarmiento, J.L., Ganachaud, A., 2001. Denitrification and N₂ fixation in the Pacific Ocean. *Global Biogeochem. Cy.* 15 (2), 483–506. <https://doi.org/10.1029/2000GB001291>
- Deutsch, C., Sarmiento, J.L., Sigman, D.M., Gruber, N., Dunne, J.P., 2007. Spatial coupling of nitrogen inputs and losses in the ocean. *Nature* 445, 164–167. <https://doi.org/10.1038/nature05392>
- Deutsch, C., Weber, T., 2012. Nutrient ratios as a tracer and driver of ocean biogeochemistry. *Ann. Rev. Mar. Sci.* 4, 13–141. <https://doi.org/10.1146/annurev-marine-120709-142821>
- Emery, W.J., Meincke, J., 1986. Global water masses-summary and review. *Oceanol. Acta* 9 (4), 383–391.
- Evans, W., Strutton, P.G., Chavez, F.P., 2009. Impact of tropical instability waves on nutrient and chlorophyll distributions in the equatorial Pacific. *Deep Sea Res. Pt. I* 56 (2), 178–188. <https://doi.org/10.1016/j.dsr.2008.08.008>
- Falkowski, P.G., 1994. The role of phytoplankton photosynthesis in global biogeochemical cycles. *Photosynth. Res.* 39 (3), 235–258. <https://doi.org/10.1007/BF00014586>
- Garcia, H.E., Gordon, L.I., 1992. Oxygen solubility in seawater: Better fitting equations. *Limnol. Oceanogr.* 37 (6), 1307–1312. <https://doi.org/10.4319/lo.1992.37.6.1307>
- Gordon, A.L., Ma, S., Olson, D.B., Hacker, P., Field, A., Talley, L.D., Wilson, D., Baringer, M., 1997. Advection and diffusion of Indonesian throughflow water within the Indian Ocean South Equatorial Current. *Geophys. Res. Lett.* 24 (21), 2573–2576. <https://doi.org/10.1029/97GL01061>
- Grasshoff, K., Kremling, K., Ehrhardt, M. (Eds.), 2009. *Methods of seawater analysis*. John Wiley & Sons.
- Gruber, N., Sarmiento, J.L., 1997. Global patterns of marine nitrogen fixation and denitrification. *Global Biogeochem. Cy.* 11 (2), 235–266. <https://doi.org/10.1029/97GB00077>
- Harms, N.C., Lahajnar, N., Gaye, B., Rixen, T., Dähnke, K., Ankele, M., Schwarz-Schampera, U., Emeis, K.C., 2019. Nutrient distribution and nitrogen and oxygen isotopic composition of nitrate in water masses of the subtropical southern Indian Ocean. *Biogeosciences* 16 (13), 2715–2732. <https://doi.org/10.5194/bg-16-2715-2019>
- Horii, T., Ueki, I., Ando, K., Hasegawa, T., Mizuno, K., Seiki, A., 2016. Impact of intraseasonal salinity variations on sea surface temperature in the eastern equatorial Indian Ocean. *J. Oceanogr.* 72 (2), 313–326. <https://doi.org/10.1007/s10872-015-0337-x>
- Karl, D.M., Letelier, R., Hebel, D.V., Bird, D.F., Winn, C.D., 1992. Trichodesmium blooms and new nitrogen in the North Pacific gyre. In: *Marine pelagic cyanobacteria: Trichodesmium and other diazotrophs*. Springer, Dordrecht, 219–237. https://doi.org/10.1007/978-94-015-7977-3_14
- Kehinde, O., Bourassa, M., Kranz, S., Landry, M.R., Kelly, T., Stukel, M.R., 2023. Lateral advection of particulate organic matter in the eastern Indian Ocean. *J. Geophys. Res.* 128 (5), e2023JC019723. <https://doi.org/10.1029/2023JC019723>
- Koch-Larrouy, A., Madec, G., Bouruet-Aubertot, P., Gerkema, T., Bessières, L., Molcard, R., 2007. On the transformation of Pacific Water into Indonesian Throughflow Water by internal tidal mixing. *Geophys. Res. Lett.* 34 (4). <https://doi.org/10.1029/2006GL028405>
- Laufkötter, C., John, J.G., Stock, C.A., Dunne, J.P., 2017. Temperature and oxygen dependence of the remineralization of organic matter. *Global Biogeochem. Cy.* 31 (7), 1038–1050. <https://doi.org/10.1002/2017GB005643>
- Lomas, M.W., Lipschultz, F., 2006. Forming the primary nitrite maximum: nitrifiers or phytoplankton? *Limnol. Oceanogr.* 51 (5), 2453–2467. <https://doi.org/10.4319/lo.2006.51.5.2453>
- Makarim, S., Sprintall, J., Liu, Z., Yu, W., Santoso, A., Yan, X.H., Susanto, R.D., 2019. Previously unidentified Indonesian Throughflow pathways and freshening in the Indian Ocean during recent decades. *Sci. Rep.* 9 (1), 1–13. <https://doi.org/10.1038/s41598-019-43841-z>
- Mamayev, O.I., 1975. *Temperature – Salinity Analysis of World Ocean Waters*. In: *Elsevier Oceanography Series*, 11. Elsevier Publ., Amsterdam, 374 pp.
- Millero, F.J., 2013. Descriptive oceanography. In: *Chemical Oceanography*. CRC Press, 21–74. <https://doi.org/10.1201/b14753-7>
- Moore, C.M., Mills, M.M., Arrigo, K.R., Berman-Frank, I., Bopp, L., Boyd, P.W., Galbraith, E.D., Geider, R.J., Guieu, C., Jaccard, S.L., Jickells, T.D., La Roche, J., Lenton, T.M., Mahowald, N.M., Marañón, E., Marinov, I., J Moore, K., Nakatsuka, T., Oschlies, A., Saito, M.A., Thingstad, T.F., Tsuda, A., Ulloa, O., 2013. Processes and patterns of oceanic nutrient limitation. *Nature Geosci* 6 (9), 701–710. <https://doi.org/10.1038/ngeo1765>
- Ono, T., Midorikawa, T., Watanabe, Y., Tadokoro, K., Saino, T., 2001. Temporal increases of phosphate and apparent oxygen utilization in the subsurface waters of western subarctic Pacific from 1968 to 1998. *Geophys. Res. Lett.* 28 (17), 3285–3288. <https://doi.org/10.1029/2001gl012948>
- Painter, S.C., Hartman, S.E., Kivimäe, C., Salt, L.A., Clargo, N.M., Daniels, C.J., Bozec, Y., Daniels, L., Allen, S., Hemsley, V.S., Moschonas, G., Davidson, K., 2017. The elemental stoichiometry (C, Si, N, P) of the Hebrides Shelf and its role in carbon export. *Prog. Oceanogr.* 159, 154–177. <https://doi.org/10.1016/j.pocean.2017.10.001>
- Park, K., 1967. Nutrient regeneration and preformed nutrients off Oregon. *Limnol. Oceanogr.* 12 (2), 353–357. <https://doi.org/10.4319/lo.1967.12.2.0353>
- Perigaud, C., McCreary Jr, J.P., Zhang, K.Q., 2003. Impact of inter-annual rainfall anomalies on Indian Ocean salinity and temperature variability. *J. Geophys. Res.* 108 (C10). <https://doi.org/10.1029/2002JC001699>
- Rao, C.K., Naqvi, S.W.A., Kumar, M.D., Varaprasad, S.J.D., Jayakumar, D.A., George, M.D., Singbal, S.Y.S., 1994. Hydrochemistry of the Bay of Bengal: possible reasons for a different water-column cycling of carbon and nitrogen from the Arabian Sea. *Mar. Chem.* 47 (3–4), 279–290. [https://doi.org/10.1016/0304-4203\(94\)90026-4](https://doi.org/10.1016/0304-4203(94)90026-4)
- Ray, R.D., Susanto, R.D., 2016. Tidal mixing signatures in the Indonesian seas from high-resolution sea surface temperature data. *Geophys. Res. Lett.* 43 (15), 8115–8123. <https://doi.org/10.1002/2016GL069485>
- Redfield, A.C., 1934. *On the proportions of organic derivatives in sea water and their relation to the composition of plankton*. Univ. Press, Liverpool, 76–192.
- Redfield, A.C., 1958. The biological control of chemical factors in the environment. *Am. Sci.* 46 (3), 205–221 230A. <http://www.jstor.org/stable/27827150>

- Rodier, M., 1997. Physical and nutrient variability in the upper equatorial Pacific associated with westerly wind forcing and wave activity in October 1994. *Deep Sea Res. Pt. II* 44 (9–10), 1783–1800. [https://doi.org/10.1016/S0967-0645\(97\)00023-4](https://doi.org/10.1016/S0967-0645(97)00023-4)
- Sardessai, S., Shetye, S., Maya, M.V., Mangala, K.R., Kumar, S.P., 2010. Nutrient characteristics of the water masses and their seasonal variability in the eastern equatorial Indian Ocean. *Mar. Environ. Res.* 70 (3–4), 272–282. <https://doi.org/10.1016/j.marenvres.2010.05.009>
- Sarma, V.V.S.S., Rao, G.D., Viswanadham, R., Sherin, C.K., Salisbury, J., Omand, M.M., Mahadevan, A., Murty, V.S.N., Shroyer, E.L., Baumgartner, M., Stafford, K.M., 2016. Effects of freshwater stratification on nutrients, dissolved oxygen, and phytoplankton in the Bay of Bengal. *Oceanography* 29 (2), 222–231. <https://www.jstor.org/stable/24862685>
- Sarmiento, J.L., Gruber, N., 2006. *Ocean Biogeochemical Dynamics*. Princeton Univ. Press, Princeton, NJ, 503 pp.
- Schlitzer, R., Mieruch-Schnülle, S., 2019. Bringing the Ocean Data View Software to the Web. In: *EGU General Assembly Conference Abstracts*, 6596.
- Schot, F., Xie, S.P., McCreary, J., 2009. Indian Ocean circulation and climate variability. *Rev. Geophys.* 47 (1). <https://doi.org/10.1029/2007RG000245>
- Schott, F.A., McCreary Jr, J.P., 2001. The monsoon circulation of the Indian Ocean. *Prog. Oceanogr.* 51 (1), 1–123. [https://doi.org/10.1016/S0079-6611\(01\)00083-0](https://doi.org/10.1016/S0079-6611(01)00083-0)
- Sen Gupta, R., Sankaranarayanan, V.N., De Sousa, S.N., Fondecarr, S.P., 1976. Chemical oceanography of the Arabian Sea: Part III – Studies on nutrient fraction and stoichiometric relationships in the northern and the eastern basins.
- Sengupta, D., Bharath Raj, G.N., Shenoi, S.S.C., 2006. Surface freshwater from Bay of Bengal runoff and Indonesian throughflow in the tropical Indian Ocean. *Geophys. Res. Lett.* (22) 33. <https://doi.org/10.1029/2006GL027573>
- Sengupta, S., Parekh, A., Chakraborty, S., Ravi Kumar, K., Bose, T., 2013. Vertical variation of oxygen isotope in Bay of Bengal and its relationships with water masses. *J. Geophys. Res.* 118 (12), 6411–6424. <https://doi.org/10.1002/2013JC008973>
- Shetye, S.R., Shenoi, S.S.C., Gouveia, A.D., Michael, G.S., Sundar, D., Nampoothiri, G., 1991. Wind-driven coastal upwelling along the western boundary of the Bay of Bengal during the southwest monsoon. *Cont. Shelf Res.* 11, 1397–1408. [https://doi.org/10.1016/0278-4343\(91\)90042-5](https://doi.org/10.1016/0278-4343(91)90042-5)
- Shetye, S.R., Gouveia, A.D., Shenoi, S.S.C., Sundar, D., Michael, G.S., Nampoothiri, G., 1993. The western boundary current of the seasonal subtropical gyre in the Bay of Bengal. *J. Geophys. Res.* 98 (C1), 945–954. <https://doi.org/10.1029/92JC02070>
- Sigman, D.M., Boyle, E.A., 2000. Glacial/interglacial variations in atmospheric carbon dioxide. *Nature* 407 (6806), 859–869. <https://doi.org/10.1038/35038000>
- Singh, A., Baer, S.E., Riebesell, U., Martiny, A.C., Lomas, M.W., 2015. C:N:P stoichiometry at the Bermuda Atlantic Time-series Study station in the North Atlantic Ocean. *Biogeosciences* 12 (21), 6389–6403. <https://doi.org/10.5194/bg-12-6389-2015>
- Sverdrup, H.U., Johnson, M.W., Fleming, R.H., 1942. *The Oceans: Their Physics, Chemistry, and General Biology*. Prentice-Hall, New York, 1087 pp.
- Sprintall, J., Gordon, A.L., Koch-Larrouy, A., Lee, T., Potemra, J.T., Pujiana, K., Wijffels, S.E., 2014. The Indonesian seas and their role in the coupled ocean–climate system. *Nature Geosci.* 7 (7), 487–492. <https://doi.org/10.1038/ngeo2188>
- Taufiqurrahman, E., Wahyudi, A.J., Masumoto, Y., 2020. The Indonesian Throughflow and its Impact on Biogeochemistry in the Indonesian Seas. *ASEAN J. Sci. Tech. Dev.* 37 (1), 29–35. <https://doi.org/10.29037/ajstd.596>
- Tomczak, M., Godfrey, J.S., 2003. *Regional oceanography: an introduction*. Daya Books.
- Unger, D., Ittekkot, V., Schäfer, P., Tiemann, J., Reschke, S., 2003. Seasonality and interannual variability of particle fluxes to the deep Bay of Bengal: influence of riverine input and oceanographic processes. *Deep Sea Res. Pt. II* 50 (5), 897–923. [https://doi.org/10.1016/S0967-0645\(02\)00612-4](https://doi.org/10.1016/S0967-0645(02)00612-4)
- Vinayachandran, P.N., Nanjundiah, R.S., 2009. Indian Ocean Sea surface salinity variations in a coupled model. *Climate Dynam.* 33 (2), 245–263. <https://doi.org/10.1007/s00382-008-0511-6>
- Weiss, R.F., 1970. The solubility of nitrogen, oxygen and argon in water and seawater. *Deep Sea Res. Oceanogr. Abs.* 17 (4), 721–735. [https://doi.org/10.1016/0011-7471\(70\)90037-9](https://doi.org/10.1016/0011-7471(70)90037-9)
- You, Y., Tomczak, M., 1993. Thermocline circulation and ventilation in the Indian Ocean derived from water mass analysis. *Deep Sea Res. Pt. I. Oceanogr. Res. Papers* 40 (1), 13–56. [https://doi.org/10.1016/0967-0637\(93\)90052-5](https://doi.org/10.1016/0967-0637(93)90052-5)

Available online at www.sciencedirect.com

ScienceDirect

journal homepage: www.journals.elsevier.com/oceanologia

ORIGINAL RESEARCH ARTICLE

Assessing the effect of coastal upwelling on the air temperature at the south-eastern coast of the Baltic Sea

Toma Dabulevičienė*, Laura Nesteckytė, Loreta Kelpšaitė-Rimkienė

Marine Research Institute, Klaipeda University, Klaipėda, Lithuania

Received 31 January 2023; accepted 6 March 2024

Available online 3 April 2024

KEYWORDS

Upwelling;
Baltic Sea;
Air temperature;
Satellite data;
Coastal meteorology

Abstract Coastal upwelling along the SE Baltic Sea coast is a common feature, especially during the warm season. It significantly lowers sea surface temperature (SST) in the coastal areas, and, therefore, may be responsible for modifying meteorological conditions in those coastal areas, where upwelling is most frequently observed. This study aims to assess the effect of coastal upwelling on the air temperature at the south-eastern coast of the Baltic Sea based on long-term period observations (2002–2021) from coastal hydrometeorological stations and satellite data. Overall, our study revealed that due to its high frequency and spatial extent, upwelling is responsible for lowering the mean summer season SST of the SE Baltic Sea coast by about 1°C. And even though upwelling is a short-term event, upwelling-induced SST drop results in cooling air temperatures in the coastal areas, i.e., the mean air temperatures during upwelling are typically 2–4°C lower than before. It was also observed that upwelling is favouring the development of advective fog. Thus, sudden changes in meteorological parameters during upwelling can have versatile effects on various socio-economic activities. The results of this study contribute to the understanding of upwelling feedback onto the lower atmosphere and, therefore, are important for advancing the accuracy of weather forecasts that are needed for coastal communities, including marine and coastal industries.

© 2024 Institute of Oceanology of the Polish Academy of Sciences. Production and hosting by Elsevier B.V. This is an open access article under the CC BY-NC-ND license (<http://creativecommons.org/licenses/by-nc-nd/4.0/>).

* Corresponding author at: Marine Research Institute, Klaipeda University, Universiteto ave. 17, 92294 Klaipėda, Lithuania. Tel.: +370-46-398782.

E-mail address: toma.dabuleviciene@ku.lt (T. Dabulevičienė).
Peer review under the responsibility of the Institute of Oceanology of the Polish Academy of Sciences.



Production and hosting by Elsevier

<https://doi.org/10.1016/j.oceano.2024.03.002>

0078-3234/© 2024 Institute of Oceanology of the Polish Academy of Sciences. Production and hosting by Elsevier B.V. This is an open access article under the CC BY-NC-ND license (<http://creativecommons.org/licenses/by-nc-nd/4.0/>).

1. Introduction

Coastal upwelling, i.e., a vertical flux of water moving upwards at the coast (Leppäranta and Myrberg, 2009), is a well-known oceanographic phenomenon. There are several upwelling systems existing throughout the global ocean, some of them are year-round features, while others occur on a seasonal basis (Kämpf and Chapman, 2016) whereas in other regions, a sporadic occurrence of wind-driven upwelling events might be observed (Rossi et al., 2014). Most pronounced regions of upwelling cover the coasts of Peru, Chile, the Arabian Sea, southwestern, southern, and eastern Africa, eastern New Zealand, and the California coast (Bakun, 1990; Garcia-Reyes et al., 2015; Mann and Lazier, 2005). Due to the uplift of nutrient-rich deeper waters to the surface (Ray et al., 2022), upwelling systems are associated with increased pelagic productivity (Jacox et al., 2018; Reddin et al., 2015) and can influence higher trophic levels directly through exposure to physical and chemical signatures of the deeper ocean (e.g., higher salinity, lower temperature, oxygen concentration, and pH) (Aguirre et al., 2018; Jacox et al., 2018). Sea surface temperature (SST) has a high impact on various atmospheric variables such as air temperature and wind speed (Holt et al., 2007). Through the upwelling-induced changes of SST, upwelling is also known to influence the coastal weather as the overlying air becomes chilled, contributing to the formation of fog banks (Diffenbaugh et al., 2004; Garrison, 2009). The intensification of fog development and onshore flow during the summer months due to upwelling may in turn lead to decreased temperatures and increased moisture flux over land (Snyder et al., 2003). On the other hand, cold upwelling waters also imply the reduction of evaporation, therefore, upwelling periods might be associated with precipitation decline (Ali et al., 2011; Aman et al., 2018). Major upwelling systems might even contribute to the development of a semi-arid/desert climate, as, e.g., is the case along the coast of the cold Peru-Chile Current, with upwelling being one of the factors controlling the climate of the Atacama Desert (Houston, 2006; Ritter et al., 2019).

Coastal upwelling is also quite frequently observed in the enclosed or semi-enclosed seas such as the Baltic Sea (Bychkova and Viktorov, 1987; Lehmann et al., 2012). The Baltic Sea, in particular, is located in moderate latitudes, where the temperature contrast varies significantly with the seasons. Thus, the upwelling varies from strong in the spring and summer to weak or non-existent in the winter in terms of SST changes (Mann and Lazier, 2005). The occurrence of upwelling in winter produces stronger records in salinity and currents than in water temperature (Suursaar, 2021). Several studies have shown that in the Baltic Sea “warm” wintertime upwelling exists, weakening ice formation and enhancing lake-effect precipitation (Kowalewska-Kalkowska and Kowalewski, 2019; Suursaar, 2021; Suursaar and Meitern, 2021). Although due to high cloudiness over the Baltic in winter and weaker thermal stratification winter upwelling is not as easily detected in thermal infrared satellite data as during the warm season (Kowalewska-Kalkowska and Kowalewski, 2019). During a warm season, Baltic Sea upwelling becomes frequently visible almost all along the coast, depending on prevailing wind conditions (Lehmann and Myrberg, 2008).

Baltic Sea coastal upwelling received considerable attention in the scientific literature (e.g., Bychkova and Viktorov, 1987; Dabuleviciene et al., 2018, 2020, 2023; Lehmann et al., 2012; Myrberg and Andrejev, 2003; Uiboupin and Laanemets, 2009; Zhurbas et al., 2008). According to previous studies, wind-driven coastal upwelling is an important mesoscale phenomenon of the Baltic Sea, especially during the warm season, redistributing heat and salt in the coastal regions (Laanemets et al., 2011) that might also drastically change the euphotic layer temperature and nutrient conditions (Vahtera et al., 2005). Upwelling was also found to trigger changes in the phytoplankton community, productivity, and species composition (Kratzer et al., 2011; Laanemets et al., 2004; Lips and Lips, 2010; Nommann et al., 1991), and to have an impact on the temporal dynamics of fish abundance and community composition (Dabuleviciene et al., 2023). In addition, the formation of upwelling fronts modifies the vertical stratification and turbulent regime in the marine-atmosphere boundary layer, resulting in a change in the surface wind stress and direction in the coastal zone (Gurova et al., 2013; Haapala, 1994; Kozlov et al., 2012; Sproson and Sahlee, 2014). It was also noted, that during the summer-time holiday season, coastal upwelling might also negatively impact tourist areas due to the rapid drop of water and air temperatures nearshore (Lehmann et al., 2012). In addition, sudden air temperature changes might have significant implications for human health, even increasing risks of non-external mortality (Guo et al., 2011).

However, despite the numerous studies of upwelling impact on the marine environment in the Baltic Sea, there is relatively little information regarding upwelling influence on coastal weather. Our focus here is, therefore, to analyse the coastal upwelling influence on meteorological conditions with the main focus on air temperature, and, consequently, its possible impacts on socio-economic activities in the coastal region.

2. Material and methods

2.1. Study site

The Baltic Sea is a landlocked shelf sea (Kuliński and Pempkowiak, 2011) connected to the North Sea via narrow Danish Straits. The coastal area of the Baltic Sea is typically quite shallow (20–40 m) and relatively large, thus playing a specific role here (Leppäranta and Myrberg, 2009). During the warm period, the sea is characterized by the development of pronounced vertical stratification with a strong seasonal thermocline from May to September.

Our study site covers part of the south-eastern (SE) Baltic Sea region and represents the Lithuanian Baltic Sea coastal waters (Figure 1).

As can be seen in Figure 1, the coastline of the study site (SE Baltic Sea) is oriented so that northerly and northeasterly winds favour upwelling development here, thus coastal upwellings are rather frequently observed in the region (e.g., Dabuleviciene et al., 2018; Lehmann and Myrberg, 2008; Lehmann et al., 2012). The Klaipeda Strait divides the Lithuanian coast of the Baltic Sea into two sections: a 51.03 km long section on the Curonian Spit

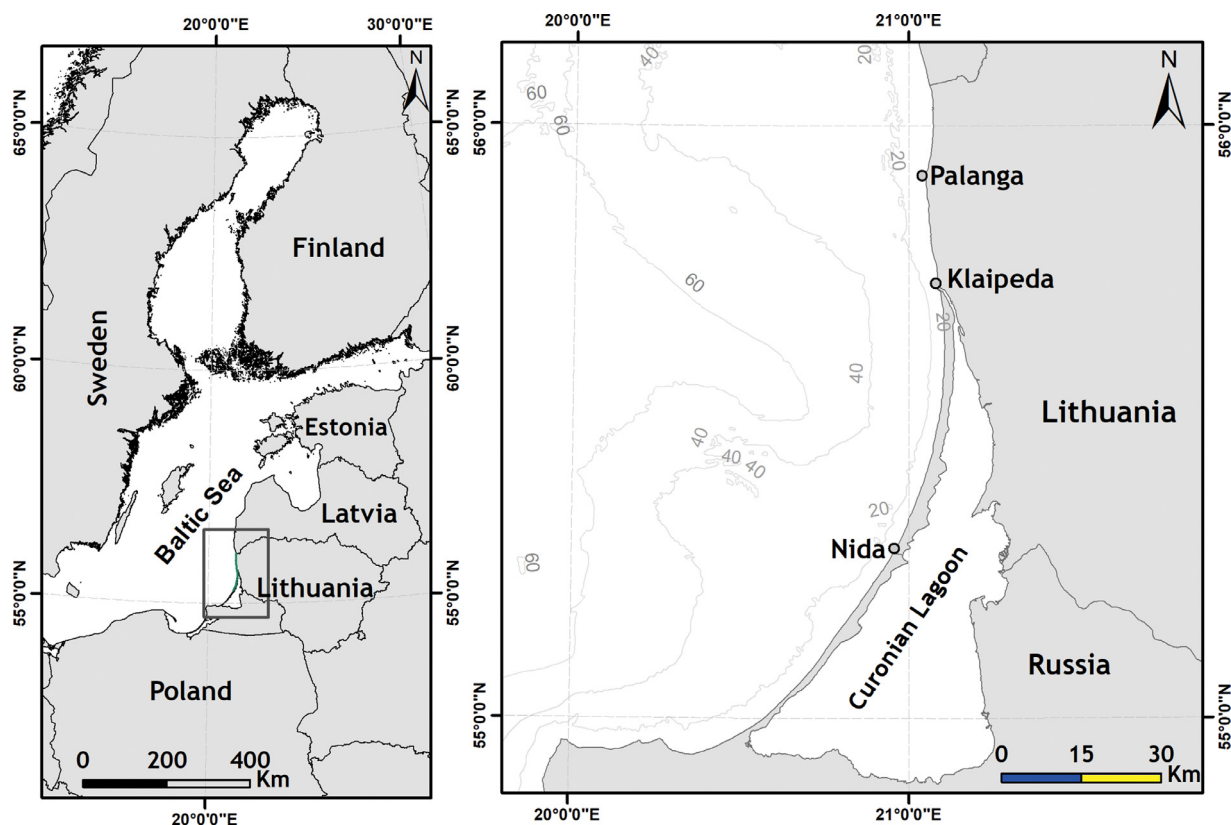


Figure 1 Map of the study site in the SE Baltic Sea.

(southern part) and a 38.49 km long mainland (northern) section (Bagdanavičiūtė et al., 2015). Curonian Spit coastline is oriented in the NE direction with an azimuth angle of 30°–45°, while the mainland coast is relatively straight and is oriented in the N direction.

According to the detailed upwelling study (Dabulevičienė et al., 2018), coastal upwelling at the SE Baltic Sea coast occurs about four times per warm (April–September) season covering about 16% of its duration. The majority of the events are observed between May and August peaking in July. The typical upwelling-induced SST drop here is about 2–6°C with the maximal values reaching up to 10–14°C.

2.2. Data analysis

In our study, we performed a joint analysis of remotely sensed sea surface temperature data from Terra/Aqua Moderate Resolution Imaging Spectroradiometer (MODIS) and in situ air temperature, wind, and fog data from hydrometeorological stations for the period of 2002–2021. Terra/Aqua MODIS Level 2 SST maps with a spatial resolution of about 1 km (Brown and Minnett, 1999) were obtained from the open-access NASA OceanColor website (<http://oceancolor.gsfc.nasa.gov/>). Satellite SST images were processed using the ESA BEAM and ArcGIS software. Upwelling events were identified using the 2°C threshold (temperature drop $\geq 2^\circ\text{C}$ relative to ambient waters) as described in previous studies (Dabulevičienė et al., 2018; Lehmann et al., 2012). In situ daily air temperature data were retrieved from three coastal hydrometeorological (HMS) stations along-

side the Lithuanian seashore (Nida, Klaipeda, and Palanga) and from Palanga Aviation meteorological station (Palanga AMS), which is located less than 2 km distance from the Baltic Sea coast. Additionally, fog data from Klaipeda HMS and Palanga AMS together with the information from Meteorological Aerodrome Reports (METAR) at Palanga Airport were used. For synoptical weather situation analyses surface pressure charts from the Deutscher Wetterdienst (https://www1.wetter3.de/archiv_dwd_dt.html) were also used. To assess the upwelling influence on the mean summer season (June–August) and monthly mean water temperatures we used all available satellite images with minimum cloud coverage covering 20 years of observations and identified SST images containing signatures of coastal upwelling. Visual inspection was used to eliminate cloud-covered images with about 1200 satellite images processed in total, from which 840 cloud-free satellite images were used to analyse SST variability during periods when no upwelling was present and with upwelling events included. Mean seasonal and monthly water temperatures were calculated with all available SST maps (denoted as “Mean monthly/summer SST” in Figure 2) and excluding upwelling-affected SST maps (denoted as “Mean monthly/summer SST (upwelling excluded)” in Figure 2).

For the assessment of upwelling influence on meteorological conditions air temperature data 3 days before the upwelling and during the period when upwelling was present at the location close to the coastal HMS (distance from the sea: Nida – 2000 m, Klaipeda – 400 m, Palanga – 1300 m) were used. The daily mean temperature was calculated from two available measurements (morning and afternoon)

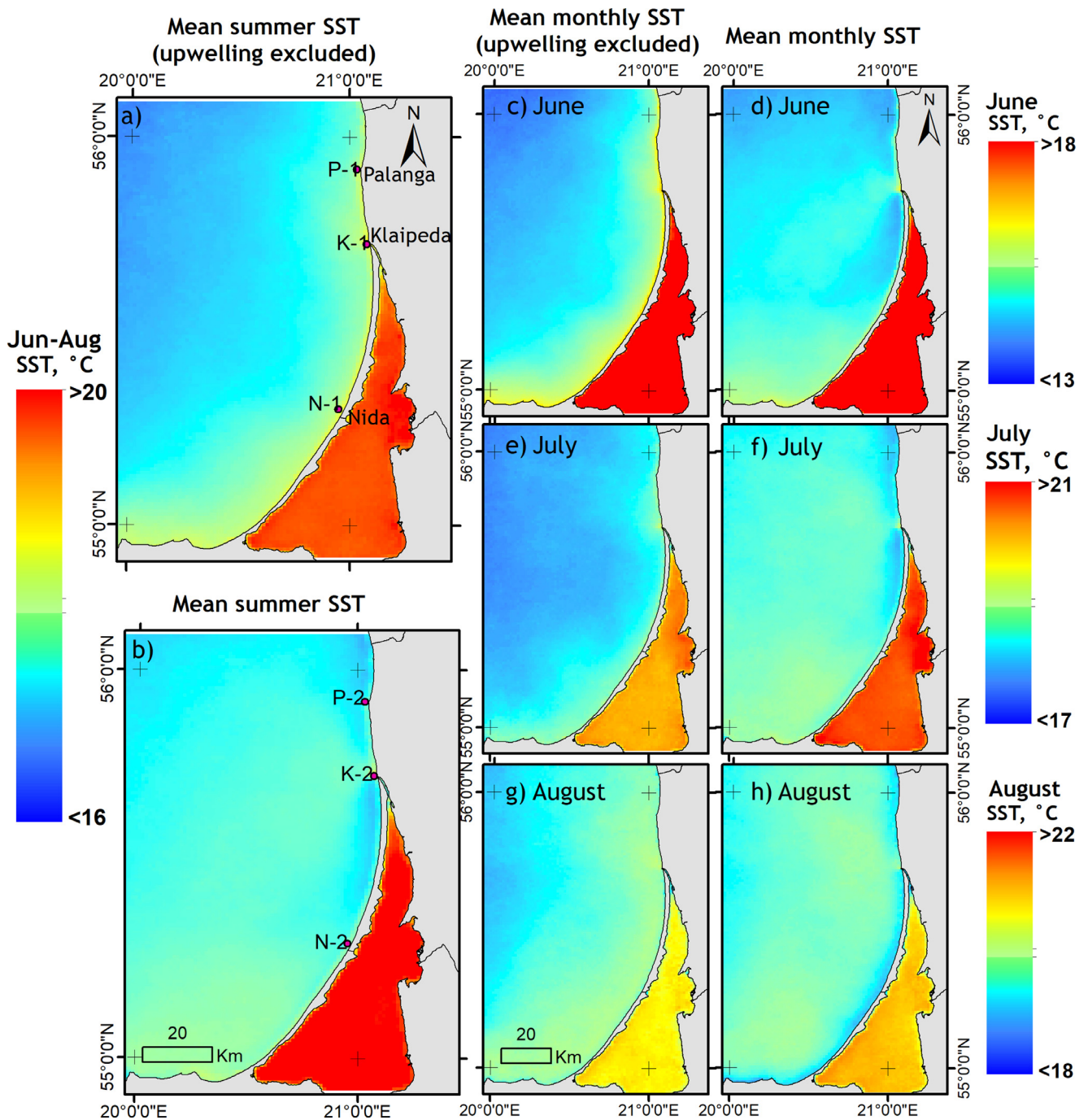


Figure 2 Seasonal (a–b) and monthly (c–h) mean SST of the SE Baltic Sea coast and Curonian Lagoon from MODIS Aqua/Terra 2002–2021.

per day. Upwelling-induced air temperature drop (ΔT_{air}) was defined as a difference between the mean air temperature 3 days before upwelling and mean air temperature during upwelling. 33 upwelling events were used in the analysis with 41 concurrent pairs of SST and air temperature measurements from three coastal stations analysed (events in May = 11, June = 9, July = 11, and August = 11). To better illustrate the upwelling influence on coastal weather several case studies were chosen for more detailed analysis. Wind speed and direction data sampled at a height of 10 m at the Nida, Klaipeda and Palanga coastal HMS were used

for the analysis of the upwelling-favourable meteorological conditions.

3. Results

3.1. Upwelling impact on coastal SST

A comparison of the mean seasonal and monthly SST values when upwellings were present, and excluding upwelling events was performed. Study results show that due to its

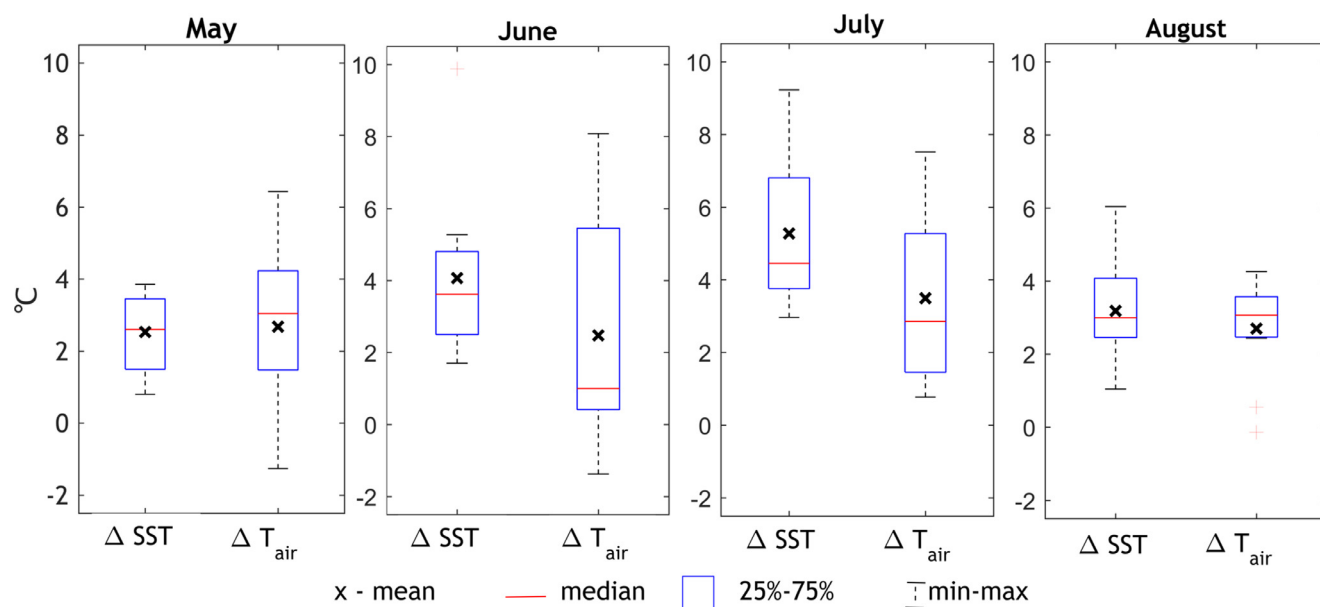


Figure 3 The minimum, maximum, mean, and median values of the air temperature difference and SST difference before and during upwelling in different months. Boxplots indicate 25–75% percentiles.

frequent nature and spatial extent upwelling has a sufficiently significant effect on the water temperature in the coastal areas (Figure 2a–h) reducing mean summer season SSTs. The difference between water temperatures derived at three sampling points (N-1, K-1, and P-1) when upwelling-affected SST maps were excluded and the mean SST values derived from all available multi-year summer months SST maps (sampling points N-2, K-2, and P-2) suggests that due to upwelling, SST was about 0.7–0.8°C lower at Nida and Palanga, while in Klaipeda the difference was smaller, about 0.2°C (Figure 2a–b). However, when analysing SST differences during different months we can see that for example, in June, SST differences were somewhat bigger and reached 1.2 and 2.9°C in Nida and Palanga, accordingly, when again, in Klaipeda, the difference was smaller, about 0.6°C.

3.2. Air temperature changes

Analysis of air temperatures before and during the upwelling event showed that upwelling-induced SST drop might result in the mean air temperature during upwelling being 2–4°C lower than before (Figure 3). In May and June mean difference between air temperature before and during upwelling (ΔT_{air}) was about 2.5°C, although in some cases air temperature during upwelling was recorded to be slightly higher than before, i.e., by about 0.5–1.5°C. The biggest SST and, consequently, air temperature drops were observed in July, with an average SST drop of around 5.3°C, and 3.5°C lower air temperatures during upwelling periods. In August SST and air temperature change during upwelling was slightly smaller, 3.2°C and 2.7°C, respectively.

However, there were particular cases when a significant drop in water temperature resulted in a much more pronounced lowering in air temperature. Figure 4, consisting of air and water temperature profiles and wind data at Klaipeda and Nida hydrometeorological stations together

with satellite SST maps, shows how an upwelling-induced significant drop in water temperature resulted in an air temperature drop. A more detailed analysis of this event shows that on 3 June water and air temperatures at Klaipeda HMS were relatively high, 20.7 and 21.3°C, accordingly, while at Nida both were lower, i.e., the average water temperature of 16°C and air temperature of 20.6°C. On 4 June a more significant drop in water temperature (from 16 to 11.5°C) was observed at Nida followed by an air temperature decrease to 15.5°C. Upwelling signatures were visible along the entire Lithuanian coastline, except near Klaipeda, where a warm water plume from the Curonian Lagoon was present (Figure 4c). However, even though on 4 June water temperature at Klaipeda HMS remained relatively high (19.7°C) due to warm plume waters, the upwelling-induced SST drop (SSTs as low as 9–12°C) in the surrounding coastal areas, not affected by the plume, already resulted in cooling of the air temperature, as air temperature records of 4 June showed. In situ water temperature records and satellite SST map on 5 June showed that the plume was no longer present at Klaipeda, and the opposite situation occurred, i.e., the inflow of upwelling-affected marine waters was influencing the northern part of the Lagoon (Figure 4c) followed by the further reduction of air temperature at Klaipeda. The daily average air temperatures reached only 10.3°C on 5 June with an even further reduction to 8.8°C on 6 June. The same pattern was observed at Nida, i.e., on 6 June water temperatures were as low as 9.8°C with a mean air temperature of only 11.1°C.

Upwelling favourable winds prevailed up until 13 June with some fluctuations to southerly directions observed on 7–8 June, which also resulted in water temperature, and, accordingly, air temperature variability (Figure 4a–b). Analysis of this upwelling case showed that an average (\pm standard deviation) SST 3 days before upwelling was $19.9 \pm 0.7^\circ\text{C}$ while during upwelling it was only $10.1 \pm 1.2^\circ\text{C}$, consequently, the air temperature decreased

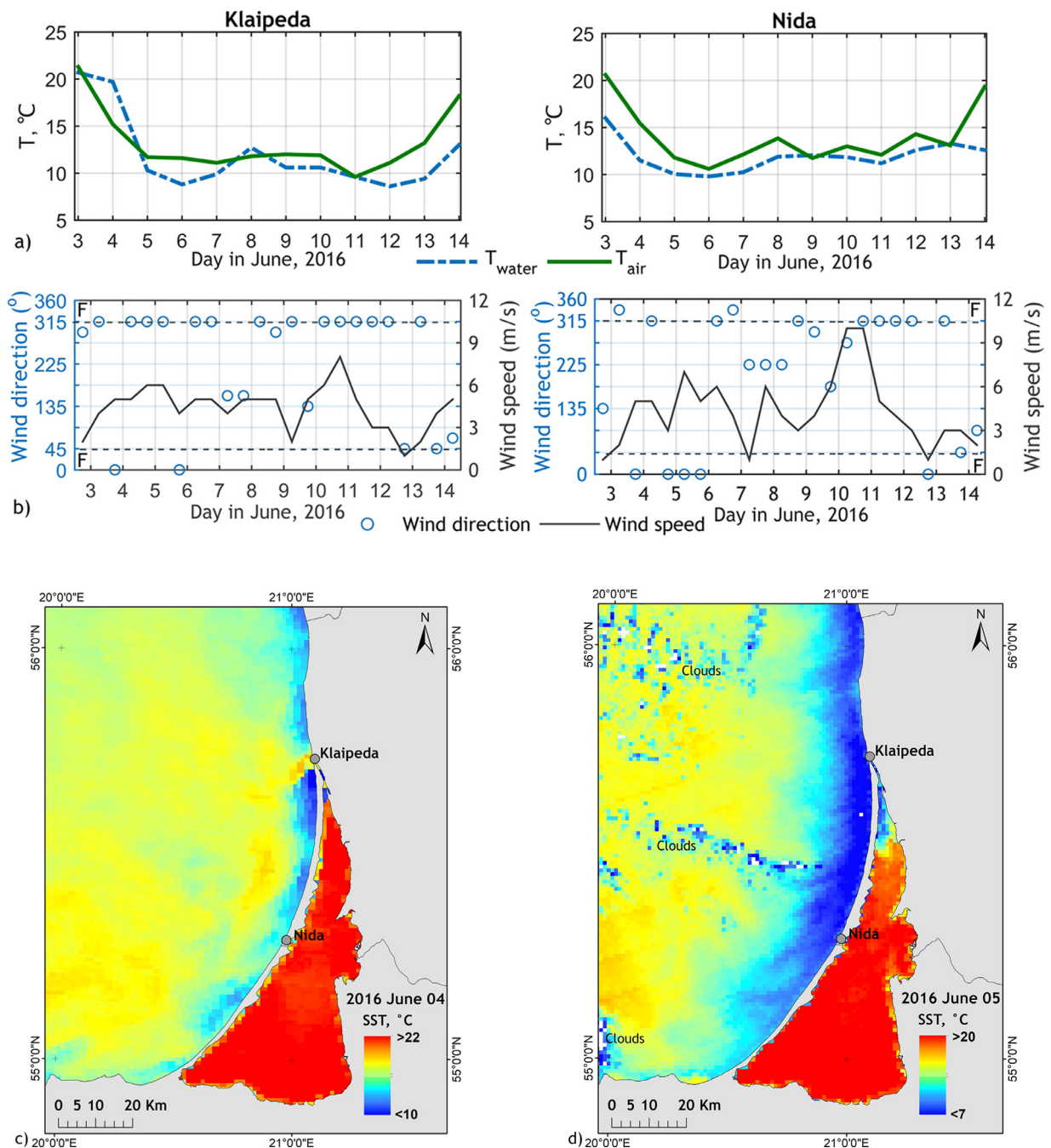


Figure 4 In situ water temperature (T_{water}), air temperature (T_{air}) and wind direction/speed changes recorded at Klaipeda and Nida hydrometeorological stations on June 2016 (a–b); and MODIS Aqua/Terra satellite SST maps of the SE Baltic Sea and Curonian Lagoon (c–d).

from $19.6 \pm 3.8^\circ\text{C}$ (3-days before upwelling average) to $11.6 \pm 0.9^\circ\text{C}$ during the upwelling period.

3.3. Case studies of different upwelling events

For the further analysis of the upwelling influence on air temperature, we investigated several case studies when upwelling was observed not along the entire coastline but only at certain sections (Figure 5) and compared air temperature and SST data at 3 coastal hydrometeorological stations. As can be seen from Figure 5 and Table 1, providing more de-

tailed characteristics of air temperature and SST during selected upwelling events, at the coastal stations, where upwelling was present not only SST, but the air temperatures were also lower. As expected, upwelling led to a decrease in air temperature. In addition, a more detailed analysis of these cases allowed us to better understand how local short-term SST changes are reflected in meteorological conditions.

In the July 2010 upwelling event (Figure 5a) it is seen that due to slightly different coastal orientation, the signatures of upwelling were observed at the coastal section

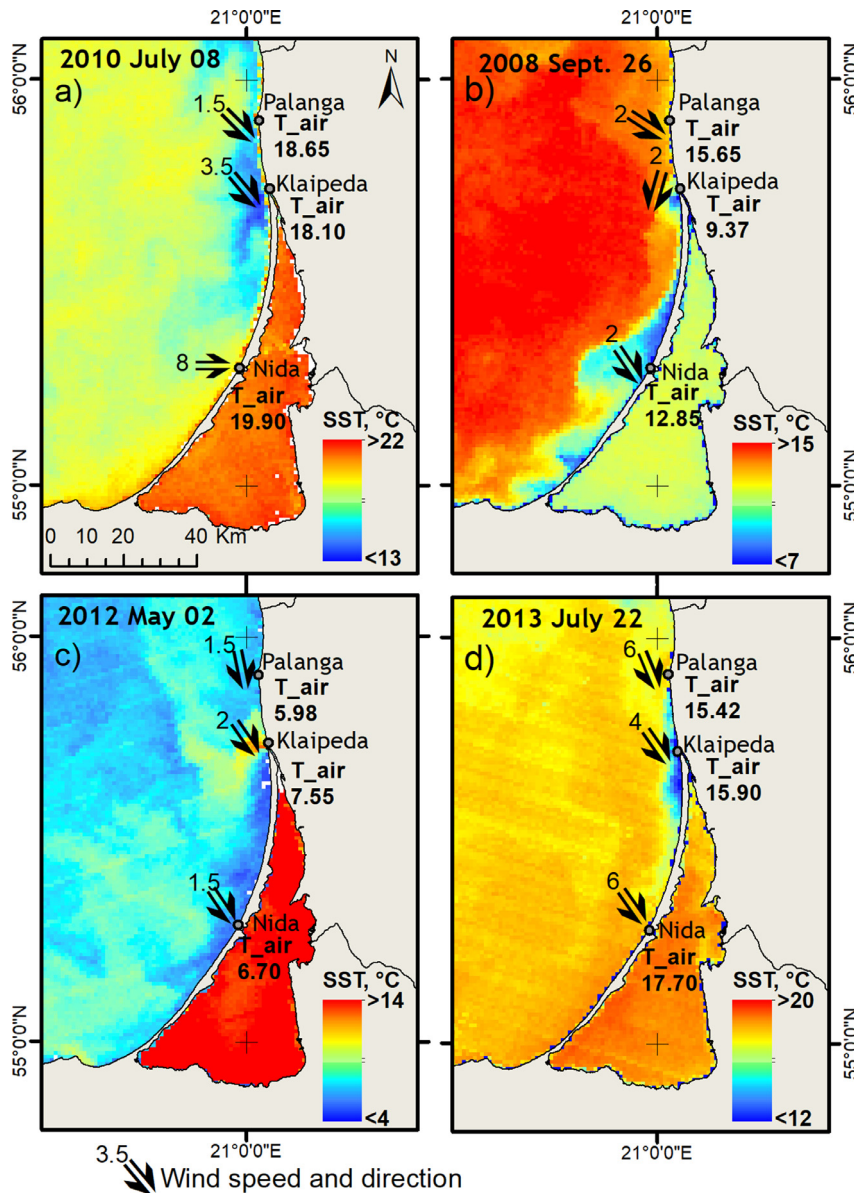


Figure 5 MODIS SST maps depicting different upwelling cases in the SE Baltic coast together with daily mean air temperatures (T_{air} , °C), and wind speed and direction at different locations.

in the vicinity of Klaipeda and Palanga, while they were not observed at Nida. In turn, SST in Klaipeda and Palanga was around 17°C, while in Nida it was around 20°C. The higher average air temperature was also observed at Nida coastal station. A similar situation was also observed in September 2008 (Figure 5b), where upwelling was present at Klaipeda and Nida, making water temperatures on average 2°C lower than in Palanga and much lower air temperature as well (Table 1). Another interesting upwelling case was recorded in May 2012 when a warm water plume from Curonian Lagoon was clearly evident in SST maps (Figure 5c). Such outflow of the water from the lagoon resulted in water temperatures at the Baltic Sea coast near Klaipeda to be around 2–4°C higher than at the upwelling affected areas south and north of Klaipeda Strait and, at the same time, observed air temperature at Klaipeda was on average about 2°C higher than in Nida or Palanga (Table 1).

During the case in July 2013, upwelling signatures were recorded at coastal areas near Klaipeda and Palanga (Figure 5d). A more detailed analysis of this event showed that SST values in the upwelling-affected waters were on average around 14°C with air temperatures of about 14–15°C at Klaipeda and Palanga. While at Nida, where upwelling was not present, average water and air temperatures were about 16°C and 17°C, accordingly (Table 1). The most significant drop in water temperature during this event was recorded on 24 July, reaching values as low as 12°C, thus favouring the formation of the marine fog. Observational evidence of the sea fog in this period was identified in the measurements in Klaipeda and Palanga HMS and Palanga AMS. The in situ data show that the mist, lowering visibility to 3000–5000 m at Klaipeda and to 1900–5000 m at Palanga was already recorded in Klaipeda and Palanga stations during the night-time from 23 to 24 July with relative



Figure 6 Photograph illustrating the fog during an upwelling event at Palanga coast on 24 July 2013 (©Alvydas Ziabkus, lrytas.lt).

Table 1 Descriptive statistics (mean±standard deviation) of air temperature (T_{air}) and SST during different upwelling events.

Date	Station	T_{air}	SST
23–26 09 2008	Nida	12.9±1.6	11.1±0.5
	Klaipeda	9.4±0.9	11.5±0.3
	Palanga*	15.7±1.2	13.4±0.3
04–09 07 2010	Nida*	21.4±1.6	19.9±0.6
	Klaipeda	19.9±1.8	17.3±2.4
	Palanga	20.4±0.9	16.9±0.9
01–03 05 2012	Nida	7.7±1.1	6.7±0.8
	Klaipeda*	9.82±2.0	10.5±0.6
	Palanga	8.1±2.3	8.3±1.1
22–25 07 2013	Nida*	17.2±1.1	15.8±1.3
	Klaipeda	14.6±1.3	14.2±1.6
	Palanga	14.7±1.7	14.3±0.5

* Locations, not affected by upwelling are indicated with asterisks.

humidity reaching 100% at the airport. On 24 July the warm air front moved across Lithuania and over the upwelling-affected Baltic Sea waters. As a result, thick advective fog began to form in the coastal areas (Figure 6). Meteorological Aerodrome Reports (METAR) from Palanga airport also showed that at 09:50 UTC the cloud base descended to as

low as 30 m and very thick fog with intensity from 800 m to 150 m was recorded in the airport.

4. Discussion

Frequent occurrence of upwelling events in the semi-enclosed basin, such as the Baltic Sea, may allow upwelling-induced SST changes to have significant feedback onto the lower atmosphere (Sproson and Sahlee, 2014). There are many papers briefly describing the Baltic Sea upwelling influence on meteorological conditions of a warm season through a decrease in air temperature, reduced wind speed, or increased frequency of summer fogs (Dabuleviciene et al., 2018; Lehmann et al., 2012; Leppäranta and Myrberg, 2009; Sproson and Sahlee, 2014; Suursaar, 2020). However, to our knowledge, not many detailed analyses on upwelling impacts on air temperature based on long-term observational data in the Baltic Sea exist. Therefore, our focus was to estimate the upwelling influence on air temperature during the warm season in the coastal areas of the SE Baltic Sea coast using both, in situ and satellite data.

Analysis of remotely-sensed SST data revealed that upwelling is responsible for lowering the seasonal mean SST of the SE Baltic Sea coast by about 1°C. However, during some upwelling events, short-term sea surface temperature drops might be very significant, resulting in very low SST

values, atypical for the given months. For example, during the major upwelling event that was recorded in July 2006, upwelling associated SST drop was reaching as low as 5–7°C in the upwelling core, as satellite SST data has shown, and even in the coastal stations' records the lowest temperatures recorded were 9.7°C in Klaipėda, 9.4°C in Palanga, and 7.5°C in Nida. This specific event was described in more detail by [Dabulevičienė et al. \(2018\)](#), demonstrating how the marine-atmosphere boundary layer (MABL) is adjusted to the sudden drop of water temperature, i.e., the cooling of the surface water resulted in an air temperature drop of around 10°C with the wind speed over the cold water in the upwelling region being significantly reduced as the MABL stratification became more stable.

The results of this study indicate that the typical air temperature drop during upwelling events is about 2.5–3.5°C and is in agreement with the numerical modelling results performed by [Sproson and Sahlee \(2014\)](#). In their study, analysing the importance of coastal upwelling to the mean summer conditions over the Baltic Sea, it was shown that in the active upwelling sites mean 2 m air temperature differences of up to 2°C might be observed with slightly, i.e., by up to 0.25 m s⁻¹ reduced wind speeds ([Sproson and Sahlee, 2014](#)). In this study, it is also briefly mentioned that the direct feedback on air temperature from the air-sea fluxes associated with coastal upwelling could also cause a change in the surface-specific humidity ([Sproson and Sahlee, 2014](#)). Cooling of the SST and the occurrence of hot air over the coastal area are conditions for fog appearance during the warm season ([Lewis, 2003](#); [Samelson et al., 2021](#)). This is what we have found analysing the coastal upwelling case that took place in July 2013, i.e., air humidity reaching up to 100% followed by a development of very thick advective fog in the coastal areas. This particular event received special attention in the media as well, and, according to the media article in *lytas.lt* ([Ziabkus, 2013](#)), very low visibility caused by sudden fog disturbed the work of lifeguards on the Palanga coast as it was impossible to monitor the water from the lifeguard coastal stations ([Figure 6](#)). Upwelling-induced sudden development of marine fog was also damping visibility, thus, causing dangerous situations for recreational fishermen, making it difficult to find a way back to the shore. In this case, even the rescue services had to be appointed.

In addition, the upwelling-favoured development of intense fog events could also have implications for the activities in the coastal airports. According to the Aeronautical Information Publication of Palanga Airport ([EYPA, 2022](#)), low visibility procedures are established for take-off at Palanga International Airport when the Runway Visual Range (RVR) value limitation is from 350 m to 250 m. Therefore, during this event, dangerous weather conditions for aviation with RVR reaching only 200 m were recorded at Palanga airport. In addition, such events may also disrupt operations in Port of Klaipėda, as in the case of dense fog, vessels are instructed to wait at Outer Roads until the entrance is permitted, also the pilot service is suspended ([Terminal Information Book, 2020](#)). Not considering upwelling-induced changes in the SST, air temperature, wind speed, and cloudiness can lead to inaccuracies in fog forecasting ([Samelson et al., 2021](#)). In turn, sudden and unforecasted fogs could have implications for the activities of

coastal airports and seaports more often when upwelling is present.

The analysis also showed that the distribution patterns of SST during upwelling along the Lithuanian coast might differ due to different coastal configurations and local hydrodynamical features. For example, the coastal section from Klaipėda to Palanga is oriented almost straight to the north while the Curonian Spit coast, where Nida station is located, is oriented slightly to the northeast. Consequently, during some cases, upwelling was observed not along the entire coastline. In addition, the coastal plume from the Curonian Lagoon is another common dynamic feature along the Lithuanian coast ([Vaičiute et al., 2012](#)). Therefore, upwelling fronts along the SE Baltic Sea coast might be quite often accompanied by the freshwater plume ([Dabulevičienė et al., 2020](#)), disturbing the continuity of upwelling at the SE Baltic Sea coast near Klaipėda. Accordingly, our results have shown that monthly mean and seasonal mean SSTs during summer months were higher in the Curonian Lagoon plume zone, diminishing the upwelling effect. Analysis of different upwelling cases also showed that upwelling-induced SST differences can result in local air temperature changes at sections of the coast that are affected versus unaffected by upwelling even if the distance between those sites is relatively short (20–40 km). Understanding the effect of coastal upwelling on meteorological conditions is also beneficial to advance the accuracy of coupled ocean-atmosphere forecast models and to improve weather forecasts.

Furthermore, even though coastal upwelling effects on air temperature are typically small, this can still have some versatile effects. For example, lower air and water temperatures can influence the summer holiday season and negatively impact particular touristy areas ([Lehmann et al., 2012](#)). A study by [Guo et al. \(2011\)](#) analysed the relationship between temperature and human health and found that air temperature changes of more than 3°C between neighbouring days, regardless of whether the change was negative or positive, could result in adverse impacts on human health. But, at the same time, lower air temperatures resulting from coastal upwelling may locally mitigate the overheating effects of heatwaves, which, under warming climates, started to occur in increasing intensity in Europe ([Suursaar, 2020](#)) having severe impacts on ecosystems and societies ([Rousi et al., 2022](#)).

5. Conclusions

In this study, the results of the coastal upwelling influence on meteorological conditions with a focus on air temperature in the SE Baltic Sea coast are presented. The analysis showed that coastal upwelling was responsible for lowering the mean summer season SST of the SE Baltic Sea coast by about 1°C, although, during distinct summer months, the upwelling effect can be even stronger lowering mean SSTs up to 3°C in some locations. It was also found that upwelling-induced SST drop results in cooling the air temperature, thus, mean air temperatures during upwelling were found to be on average 2–4°C lower than before, dropping down by up to 10°C during extreme upwelling events. The largest air temperature drop was observed during up-

welling events taking place in July. A more detailed analysis of separate upwelling cases also showed that upwelling favours the development of advective fog in the coastal areas. The results of this study contribute to the understanding of air temperature response to the sudden drop in water temperature, which is an important parameter for various socio-economic activities such as tourism, and even human health aspects. Insights on upwelling-favoured intensification of fog formation that were also discussed in this study are valuable for more accurate weather forecasts and are important for coastal communities, including marine and coastal industries.

Declaration of competing interest

The authors declare the following financial interests/personal relationships which may be considered as potential competing interests: Toma Dabuleviciene reports financial support was provided by European Social Fund.

Acknowledgements

This research was funded by the [European Social Fund](#) under the No [09.3.3-LMT-K-712](#) “Development of Competences of Scientists, other Researchers and Students through Practical Research Activities” measure. Grant agreement No [09.3.3-LMT-K-712-19-0115](#). The authors are grateful to the Lithuanian Hydrometeorological Service under the Ministry of Environment and Palanga Aviation meteorological station for providing the meteorological data and to the Marine Environmental Assessment Division of the Lithuanian Environmental Protection Agency for providing the in situ monitoring data. The authors are grateful to K. Myrberg for valuable scientific insights and are also grateful to S. Dalinkeviciute from the Lithuanian Hydrometeorological Service Forecast and Warning division for the consultations provided when analysing the synoptical situation.

References

Aguirre, C., Garcia-Loyola, S., Testa, G., Silva, D., Farias, L., 2018. Insight into anthropogenic forcing on coastal upwelling off south-central Chile. *Elementa-Sci. Anthropol.* 6, 59. <https://doi.org/10.1525/elementa.314>

Ali, K.E., Kouadio, K.Y., Zahiri, E.-P., Aman, A., Assamoi, A.P., Bourles, B., 2011. Influence of the Gulf of Guinea Coastal and Equatorial Upwellings on the Precipitations along its Northern Coasts during the Boreal Summer Period. *Asian J. Appl. Sci.* 4, 271–285. <https://doi.org/10.3923/ajaps.2011.271.285>

Aman, A., Toualy, E., Yoroba, F., 2018. On the Causes of the Minor Dry Season over the Coastal Region of the Northern Gulf of Guinea. *Atmos. Climate Sci.* 8, 121–133. <https://doi.org/10.4236/acs.2018.82009>

Bagdanavičiūtė, I., Kelpšaitė, L., Soomere, T., 2015. Multi-criteria evaluation approach to coastal vulnerability index development in micro-tidal low-lying areas. *Ocean Coast. Manage.* 104, 124–135. <https://doi.org/10.1016/j.ocecoaman.2014.12.011>

Bakun, A., 1990. Global Climate Change and intensification of coastal ocean upwelling. *Science* 247, 198–201. <https://doi.org/10.1126/science.247.4939.198>

Brown, O.B., Minnett, P.J., 1999. *MODIS Infrared Sea Surface Temperature Algorithm*. University of Miami, Coral Gables, FL, USA.

Bychkova, I., Viktorov, S., 1987. Use of satellite data for identification and classification of upwelling in the Baltic Sea. *Oceanology* 27 (2), 158–162.

Dabuleviciene, T., Jucevicius, D., Zolubas, T., Vaiciute, D., Nika, N., 2023. The Effect of Short-Term Upwelling Events on Fish Assemblages at the South-Eastern Coast of the Baltic Sea. *Water* 15. <https://doi.org/10.3390/w15030452>

Dabuleviciene, T., Vaiciute, D., Kozlov, I.E., 2020. Chlorophyll-a Variability during Upwelling Events in the South-Eastern Baltic Sea and in the Curonian Lagoon from Satellite Observations. *Remote Sens.* 12 (21), 3661. <https://doi.org/10.3390/rs12213661>

Dabuleviciene, T., Kozlov, I.E., Vaiciute, D., Dailidienė, I., 2018. Remote Sensing of Coastal Upwelling in the South-Eastern Baltic Sea: Statistical Properties and Implications for the Coastal Environment. *Remote Sens.* 10 (24), 1752. <https://doi.org/10.3390/rs10111752>

Diffenbaugh, N.S., Snyder, M.A., Sloan, L.C., 2004. Could CO₂-induced land-cover feedbacks alter near-shore upwelling regimes? *Proc. Natl. Acad. Sci. USA* 101, 27–32. <https://doi.org/10.1073/pnas.0305746101>

EYPA, 2022. AIP for LITHUANIA (section AD-2.EYPA) valid from 03 NOV 2022. Available online: https://www.oronavigacija.lt/a1/aip/004_03Nov2022/2022-11-03-AIRAC/html/eAIP/EY-AD-2.EYPA-en-GB.html (accessed 2023-01-26).

Garcia-Reyes, M., Sydeman, W.J., Schoeman, D.S., Rykaczewski, R.R., Black, B.A., Smit, A.J., Bograd, S.J., 2015. Under Pressure: Climate Change, Upwelling, and Eastern Boundary Upwelling Ecosystems. *Front. Mar. Sci.* 2, 109. <https://doi.org/10.3389/fmars.2015.00109>

Garrison, T., 2009. *Essentials of Oceanography*. Brooks/Cole, Cengage Learning, 384 pp.

Guo, Y., Barnett, A.G., Yu, W., Pan, X., Ye, X., Huang, C., Tong, S., 2011. A Large Change in Temperature Between Neighbouring Days Increases the Risk of Mortality. *PLOS One* 6, e16511. <https://doi.org/10.1371/journal.pone.0016511>

Gurova, E., Lehmann, A., Ivanov, A., 2013. Upwelling dynamics in the Baltic Sea studied by a combined SAR/infrared satellite data and circulation model analysis. *Oceanologia* 55 (3), 687–707. <https://doi.org/10.5697/oc.55-3.687>

Haapala, J., 1994. Upwelling and its Influence on Nutrient Concentration in the Coastal Area of the Hanko Peninsula, Entrance of the Gulf of Finland. *Estuar. Coast. Shelf Sci.* 38, 507–521. <https://doi.org/10.1006/ecss.1994.1035>

Houston, J., 2006. Variability of precipitation in the Atacama Desert: its causes and hydrological impact. *Int. J. Climatol.* 26, 2181–2198. <https://doi.org/10.1002/joc.1359>

Holt, T., Pullen, J., Blumberg, A.F., Bornstein, R.D., 2007. Atmospheric Response to Local Upwelling in the Vicinity of New York–New Jersey Harbor. *J. Appl. Meteorol. Climatol.* 46, 1031–1052. <https://doi.org/10.1175/jam2511.1>

Jacox, M.G., Edwards, C.A., Hazen, E.L., Bograd, S.J., 2018. Coastal Upwelling Revisited: Ekman, Bakun, and Improved Upwelling Indices for the US West Coast. *J. Geophys. Res.-Oceans* 123, 7332–7350. <https://doi.org/10.1029/2018jc014187>

Kämpf, J., Chapman, P., 2016. *Upwelling Systems of the World: A Scientific Journey to the Most Productive Marine Ecosystems*. Springer, Cham, 433 pp. <https://doi.org/10.1007/978-3-319-42524-5>.

Kowalewska-Kalkowska, H., Kowalewski, M., 2019. Combining Satellite Imagery and Numerical Modelling to Study the Occurrence of Warm Upwellings in the Southern Baltic Sea in Winter. *Remote Sens.* 11, 2982. <https://doi.org/10.3390/rs11242982>

Kozlov, I.E., Kudryavtsev, V.N., Johannessen, J.A., Chapron, B., Dailidienė, I., Myasoedov, A.G., 2012. ASAR imaging for coastal upwelling in the Baltic Sea. *Adv. Space Res.* 50, 1125–1137. <https://doi.org/10.1016/j.asr.2011.08.017>

- Kratzer, S., Ebert, K., Sørensen, K., 2011. Monitoring the Bio-optical State of the Baltic Sea Ecosystem with Remote Sensing and Autonomous In Situ Techniques. In: Harff, J., Björck, S., Hoth, P. (Eds.), *The Baltic Sea Basin. Central and Eastern European Development Studies (CEEDES)*. Springer, Berlin, Heidelberg. https://doi.org/10.1007/978-3-642-17220-5_20.
- Kuliński, K., Pempkowiak, J., 2011. The carbon budget of the Baltic Sea. *Biogeosciences* 8, 3219–3230. <https://doi.org/10.5194/bg-8-3219-2011>
- Laanemets, J., Kononen, K., Pavelson, J., Poutanen, E.L., 2004. Vertical location of seasonal nutriclines in the western Gulf of Finland. *J. Marine Syst.* 52, 1–13. <https://doi.org/10.1016/j.jmarsys.2004.03.003>
- Laanemets, J., Vali, G., Zhurbas, V., Elken, J., Lips, I., Lips, U., 2011. Simulation of mesoscale structures and nutrient transport during summer upwelling events in the Gulf of Finland in 2006. *Boreal Environ. Res.* 16, 15–26.
- Lehmann, A., Myrberg, K., 2008. Upwelling in the Baltic Sea – A review. *J. Marine Syst.* 74, S3–S12. <https://doi.org/10.1016/j.jmarsys.2008.02.010>
- Lehmann, A., Myrberg, K., Hoflich, K., 2012. A statistical approach to coastal upwelling in the Baltic Sea based on the analysis of satellite data for 1990–2009. *Oceanologia* 54 (3), 369–393. <https://doi.org/10.5697/oc.54-3.369>
- Leppäranta, M., Myrberg, K., 2009. *Physical Oceanography of the Baltic Sea*. Springer-Verlag, Berlin, Heidelberg. <https://doi.org/10.1007/978-3-540-79703-6>.
- Lewis, J., 2003. Sea fog off the California coast: Viewed in the context of transient weather systems. *J. Geophys. Res.* 108. <https://doi.org/10.1029/2002jd002833>
- Lips, I., Lips, U., 2010. Phytoplankton dynamics affected by the coastal upwelling events in the Gulf of Finland in July–August 2006. *J. Plankton Res.* 32, 1269–1282. <https://doi.org/10.1093/plankt/fbq049>
- Mann, K.H., Lazier, J.R.N., 2005. Vertical Structure in Coastal Waters: Coastal Upwelling Regions. In: *Dynamics of Marine Ecosystems*, Blackwell Publ., 118–161. <https://doi.org/10.1002/9781118687901.ch5>
- Myrberg, K., Andrejev, O., 2003. Main upwelling regions in the Baltic Sea – a statistical analysis based on three-dimensional modelling. *Boreal Environ. Res.* 8, 97–112.
- Nommann, S., Sildam, J., Noges, T., Kahru, M., 1991. Plankton distribution during a coastal upwelling event off Hiiu-maa, Baltic Sea – impact of short term flow field variability. *Cont. Shelf Res.* 11, 95–108. [https://doi.org/10.1016/0278-4343\(91\)90037-7](https://doi.org/10.1016/0278-4343(91)90037-7)
- Ray, S., Swain, D., Ali, M.M., Bourassa, M.A., 2022. Coastal Upwelling in the Western Bay of Bengal: Role of Local and Remote Windstress. *Remote Sens.* 14 (23), 4703. <https://doi.org/10.3390/rs14194703>
- Reddin, C.J., Docmac, F., O’Connor, N.E., Bothwell, J.H., Harrod, C., 2015. Coastal Upwelling Drives Intertidal Assemblage Structure and Trophic Ecology. *PLOS One* 10 (20), e0130789. <https://doi.org/10.1371/journal.pone.0130789>
- Ritter, B., Wennrich, V., Medialdea, A., Brill, D., King, G., Schneiderwind, S., Niemann, K., Fernández-Galego, E., Diederich, J., Rolf, C., Bao, R., Melles, M., Dunai, T.J., 2019. Climatic fluctuations in the hyperarid core of the Atacama Desert during the past 215 ka. *Sci. Rep.* 9, 5270. <https://doi.org/10.1038/s41598-019-41743-8>
- Rossi, V., Schaeffer, A., Wood, J., Galibert, G., Morris, B., Sudre, J., Roughan, M., Waite, A.M., 2014. Seasonality of sporadic physical processes driving temperature and nutrient high-frequency variability in the coastal ocean off southeast Australia. *J. Geophys. Res.-Oceans* 119, 445–460. <https://doi.org/10.1002/2013jc009284>
- Rousi, E., Kornhuber, K., Beobide-Arsuaga, G., Luo, F., Coumou, D., 2022. Accelerated western European heatwave trends linked to more-persistent double jets over Eurasia. *Nat. Commun.* 13, 3851. <https://doi.org/10.1038/s41467-022-31432-y>
- Samelson, R.M., de Zoeke, S.P., Skyllingstad, E.D., Barbour, P.L., Durski, S.M., 2021. Fog and low-level stratus in coupled ocean-atmosphere simulations of the northern California Current System upwelling season. *Mon. Weather Rev.* 149 (5), 1593–1617. <https://doi.org/10.1175/mwr-d-20-0169.1>
- Snyder, M.A., Sloan, L.C., Diffenbaugh, N.S., Bell, J.L., 2003. Future climate change and upwelling in the California Current. *Geophys. Res. Lett.* 30 (15), 1823. <https://doi.org/10.1029/2003GL017647>
- Sproson, D., Sahlee, E., 2014. Modelling the impact of Baltic Sea upwelling on the atmospheric boundary layer. *Tellus A* 66 (15), 24041. <https://doi.org/10.3402/tellusa.v66.24041>
- Suursaar, Ü., 2020. Combined impact of summer heat waves and coastal upwelling in the Baltic Sea. *Oceanologia* 62 (4 Pt. A), 511–524. <https://doi.org/10.1016/j.oceano.2020.08.003>
- Suursaar, Ü., 2021. Winter upwelling in the Gulf of Finland, Baltic Sea. *Oceanologia* 63 (3), 356–369. <https://doi.org/10.1016/j.oceano.2021.04.001>
- Suursaar, Ü., Meitern, H., 2021. Contribution of winter upwelling in the Gulf of Finland to lake-effect snow in Estonia. *Baltica* 34 (2). <https://doi.org/10.5200/baltica.2021.2.1>
- Terminal Information Book, 2020. Available online at: <https://bkt.lt/wp-content/uploads/2020/05/BKT-terminalo-informacine-knyga-2019-04-11-1.pdf> (accessed 2023-01-26).
- Uiboupin, R., Laanemets, J., 2009. Upwelling characteristics derived from satellite sea surface temperature data in the Gulf of Finland, Baltic Sea. *Boreal Environ. Res.* 14, 297–304.
- Vahtera, E., Laanemets, J., Pavelson, J., Huttunen, M., Kononen, K., 2005. Effect of upwelling on the pelagic environment and bloom-forming cyanobacteria in the western Gulf of Finland, Baltic Sea. *J. Marine Syst.* 58, 67–82. <https://doi.org/10.1016/j.jmarsys.2005.07.001>
- Vaičiūtė, D., Bresciani, M., Bučas, M., 2012. Validation of MERIS bio-optical products with in situ data in the turbid Lithuanian Baltic Sea coastal waters. *J. Appl. Remote Sens.* 6 (1), 063568. <https://doi.org/10.1117/1.JRS.6.063568>
- Zhurbas, V., Laanemets, J., Vahtera, E., 2008. Modeling of the mesoscale structure of coupled upwelling/downwelling events and the related input of nutrients to the upper mixed layer in the Gulf of Finland, Baltic Sea. *J. Geophys. Res.-Oceans* 113. <https://doi.org/10.1029/2007JC004280>
- Ziabkus, A., 2013. Baltijos jūrą užklojo tirštas rūkas, lrytas.lt. Available online: <https://www.lrytas.lt/zmones/pramogos/2013/07/24/news/baltijos-jura-uzklojo-tirstas-rukas-4950995> (accessed 2023-01-26).

Available online at www.sciencedirect.com

ScienceDirect

journal homepage: www.journals.elsevier.com/oceanologia

ORIGINAL RESEARCH ARTICLE

Phytoplankton pigments in the Baltic Sea – mathematical description of chlorophylls and carotenoids content in different seasons and regions

Joanna Stoń-Egiert^{a,*}, Mirosława Ostrowska^a, Roman Majchrowski^b

^a*Institute of Oceanology, Polish Academy of Sciences, Sopot, Poland*

^b*Institute of Geography, Pomeranian University in Słupsk, Słupsk, Poland*

Received 20 February 2023; accepted 27 March 2024

Available online 10 April 2024

KEYWORDS

Baltic Sea;
Chlorophylls;
Carotenoids;
Seasonal
approximations

Abstract This study aimed to trace the spatial and seasonal changes in pigment composition and to develop mathematical formulas to quantitatively describe their composition in different seasons in two regions: the open Baltic Sea region and the Gulf of Gdańsk. The analyses were carried out based on a 20-year database of empirical data from 1999 to 2018 obtained using the HPLC method. The proportion of chlorophyll *a* in the total content of pigments was stable irrespective of the season and region ($62\% \pm 5\%$). In summer and autumn, a higher total amount of photoprotective carotenoids (about 15–17% in total pigment content) than photosynthetic ones was recorded. The concentrations of marker pigments are related to periodic increases in the corresponding algal classes. The spring bloom dominated by diatoms and dinoflagellates results in 40% of fucoxanthin and 70% of peridinin in relation to their total content throughout all seasons. The highest percentage of chlorophyll *b* (up to 10% in open waters) and other pigments specific to green algae (neoxanthin, violaxanthin, lutein) were observed during summer and autumn. The 30% percentage of fucoxanthin confirms the occurrence of diatoms in autumn. The concentrations of groups and individual pigments have been determined as a function of chlorophyll *a* concentration. The best approximation results were obtained for the seasonal dependence of marker pigments for specific classes of algae. In summer and autumn – for chlorophyll *b* concentrations – zeaxanthin, fucoxanthin, alloxanthin and peridinin standard error factor ranges between 1.56 and 1.84.

© 2024 Institute of Oceanology of the Polish Academy of Sciences. Production and hosting by Elsevier B.V. This is an open access article under the CC BY-NC-ND license (<http://creativecommons.org/licenses/by-nc-nd/4.0/>).

* Corresponding author at: Institute of Oceanology, Polish Academy of Sciences, Powstańców Warszawy 55, 81–712 Sopot, Poland.
E-mail address: aston@iopan.pl (J. Stoń-Egiert).

Peer review under the responsibility of the Institute of Oceanology of the Polish Academy of Sciences.



<https://doi.org/10.1016/j.oceano.2024.03.003>

0078-3234/© 2024 Institute of Oceanology of the Polish Academy of Sciences. Production and hosting by Elsevier B.V. This is an open access article under the CC BY-NC-ND license (<http://creativecommons.org/licenses/by-nc-nd/4.0/>).

1. Introduction

Pigments are very important components of plant cells. Owing to various physicochemical properties, they absorb the solar energy necessary for photosynthesis and protect the photosynthetic apparatus of cells from photo-destruction. The composition and mutual proportions of pigments in the algae cells occurring in a given water body are closely related to environmental conditions, mainly to the spectral distribution of irradiance at depth (Babin et al., 1996; Kang et al., 2021; MacIntyre et al., 2002; Majchrowski et al., 2007; Stoń-Egiert et al., 2019; van Leeuwe et al., 2008; Woźniak et al., 2007; Woźniak and Dera, 2007).

In the marine environment, the spectral distribution of irradiance in different regions and at different depths is strongly influenced not only by seasonal variations of solar radiation but also by varying optical properties of seawater. The optimal use of the available light is enabled by a suitably adapted and characteristic for individual phytoplankton species pigments composition in their cells. The analysis of the composition and mutual proportions of pigments can therefore provide a lot of information characterizing not only the species composition of the phytoplankton community occurring in a given water body, but also allows estimation of its living conditions.

The importance of pigments as indicators of changes in the marine environment in the context of global climate change has been widely documented (Bode et al., 2015; Brierley and Kingsford, 2009; Häder and Gao, 2018; Richardson and Schoeman, 2004; Rousseaux and Gregg, 2015; Wernberg et al., 2011). Chlorophyll *a*, crucial in the photosynthesis process and present in all plant cells, is a good indicator of the total organic biomass in the water, while the presence of accessory pigments and their degradation products allows us to assess the physiological condition of the studied phytoplankton population. Pigments occur in algae cells in proportions and compositions characteristic of specific taxonomic classes, so based on their content, it is possible to infer the occurrence of specific classes of algae in a given water body (e.g. fucoxanthin in the case of diatoms, alloxanthin in the case of cryptophytes, or zeaxanthin with respect to cyanobacteria) (Jeffrey and Vesk, 1997; Roy et al., 2011).

As a result of the development of chromatographic techniques allowing the isolation, identification, and quantification of pigments in various ecosystems, the use of information on pigment concentrations to assess phytoplankton populations has become common in oceanographic research and possible on a larger scale than microscopic studies of species composition allowed (Mackey et al., 2002; Schlüter et al., 2016, 2018; Wänstrand and Snoeijs, 2006; Wright and Enden, 2000). Currently, based on the known concentrations of individual pigments, Phytoplankton Functional Types and the size structure of algae in different types of seawaters are successfully identified in oceans as well as in semi-closed seas, such as the Baltic and Mediterranean Sea (Brewin et al., 2010; Di Cicco et al., 2017; Hirata et al., 2008, 2011; IOCCG, 2014; Kramer and Siegel, 2019; Meler et al., 2020; Uitz et al., 2006). Owing to the use of programs like CHEMTAX (Mackey et al., 1996), relatively fast assessment of changes in marine biodiversity, re-

lated to changes in phytoplankton structure resulting from species expansion, has become possible (Goela et al., 2014; Latasa, 2007; Miranda-Alvarez et al., 2020; Wang et al., 2018).

Monitoring changes occurring in the marine environment is one of the most important issues of contemporary oceanology and requires appropriate measurement techniques. The source of data, which is increasingly used for such purposes, is satellite observation providing systematic information from large areas. Remote sensing methods make it possible to track phytoplankton blooms with high spatial and temporal resolution both in the waters of the World Ocean and coastal areas (Ciancia et al., 2021; Kahru and Elmgren, 2014; Kahru et al., 2016; Klemas, 2012; Kutser et al., 2006; Platt et al., 2009; Woźniak et al., 2016b). The characteristic optical properties of phytoplankton pigments are used in the remote methods of rapid assessment of surface ocean phytoplankton groups (Kramer and Siegel, 2019). The development of these methods requires the use of satellite algorithms linking the optical properties of waters with other characteristics of marine ecosystems. The accuracy of these remote methods depends on the accuracy of the developed algorithms and there is a pressing need for further validation across a wide variety of phytocoenoses. In the case of open ocean (Case 1) waters, remote methods for determining biogeochemical parameters are generally characterized by high accuracy (e.g. Dierssen, 2010; Dohan and Maximenko, 2010; Kowalczyk et al., 2010; Li et al., 2013). However, shelf and semi-enclosed seas are strongly influenced by external factors, such as the presence of non-covarying CDOM and sediment, which means that the application of ocean formulas to these regions leads to significant errors (Darecki et al., 2008; Ficek et al., 2011; Kratzer et al., 2017; Krężel et al., 2015; Ostrowska et al., 2022; Stramska and Zuzewicz, 2013; Woźniak, 2014; Woźniak et al., 2014; Woźniak et al., 2016a,b). Thus, the application of remote methods involves the necessity of developing individual mathematical formulas taking into account the specificity of the basin, the high dynamics of changes in hydrological conditions, and the significant influence of external factors. An example of such a water body is the Baltic Sea. Due to the limited water exchange with the North Sea and the inflow of river water masses, the salinity of the surface waters of the Baltic Sea fluctuates around 7 in the central part and around 4 in the river mouths. A consequence of the large influx of river masses is a high concentration of nutrients (HELCOM, 2009, 2018, 2018a; Pastuszak et al., 2018; Savchuk, 2018). Additionally, its geographical location in the temperate zone results in seasonal changes in hydrological and biological conditions. Phytocenosis of the Baltic Sea consists of organisms belonging mainly to the classes of cyanobacteria (blue-green algae), diatoms, dinophytes, cryptophytes, green algae, and occurring in smaller quantities organisms from euglenophytes, prasinophytes, and nanoplankton classes (HELCOM, 1997; Olenina et al., 2006; Stoń-Egiert et al., 2010).

In the Baltic Sea, the development of the biomass of phytoplankton organisms in the annual cycle shows 3 characteristic maxima (Thamm et al., 2004; Wasmund et al., 1996, 1998, 2011). The spring bloom of diatoms is caused

by an increase in temperature in the upper layers of the sea due to the increasing solar radiation and the presence of large amounts of nutrients accumulated during winter and brought to the surface during mixing processes. Gradually, along with a further increase in solar energy, it transforms into dinophyte blooms (Gasiūnaitė et al., 2005; Wasmund et al., 1998). Then there is a summer (July/August) increase in cyanobacteria biomass (Finni et al., 2001; Kahru et al., 2020; Mazur-Marzec et al., 2006; Stoń-Egiert and Ostrowska, 2022; Thamm et al., 2004; Wasmund et al., 2019) caused by thermal environmental conditions appropriate for the intensive cell growth of this autotrophic algae. In turn, the autumn bloom formed by thermophilic diatoms is caused by nutrient input from deeper sea layers as a result of intensive water mixing during this period (Wasmund et al., 1996, 2011; Wasmund and Ulig, 2003). Such dynamic seasonal changes in the composition and abundance of phytoplankton species in the Baltic Sea result in changes in the abundance and composition of algal pigments. This has been confirmed by systematic studies of the composition and resources of phytoplankton pigments in the waters of the Baltic Sea ecosystems conducted at the Institute of Oceanology of the Polish Academy of Sciences in Sopot since 1999 (Stoń-Egiert and Ostrowska, 2022). The 20-year database collected using HPLC techniques, containing data on concentrations of not only marker pigments of specific phytoplankton classes, but also other pigments from the chlorophyll and carotenoid groups provides the basis for qualitative and statistical analyses of quantitative changes in the composition of pigments in this basin. This work aims to use this 20-year database to develop mathematical formulas to quantitatively describe the composition of pigments in the Baltic Sea in different seasons and regions. Such analyses are of fundamental importance for the development and assessment of the accuracy of bio-optical models of the Baltic ecosystem, remote sensing methods estimating the total biomass of phytoplankton, determining the proportions between organisms of different classes of algae, and the amount of solar energy utilized in various processes in the sea (e.g. absorption, photosynthesis, fluorescence).

2. Material and methods

2.1. The geographical region of measurements

The investigations were focused on the Southern Baltic region. Measurement stations were localized in the Gulf of Gdańsk and the region of the open Baltic waters mostly in the Polish economic zone (Figure 1). Sampling was conducted during more than 100 scientific expeditions during 20 years of Baltic Sea explorations (from 1999 to 2018) in different seasons (see Table 1) mainly on board *r/v Oceania* but also on board the vessels: *r/v Baltica*, *r/v Oceanograf* and *Sonda 2*. Over 2400 collected samples of natural phytoplankton were analyzed.

2.2. Methodology of sampling and analysis

Seawater was sampled from the surface layer with an SBE32 Niskin bottle, then filtered through glass-fiber filters (Whatman GF/F; $\phi = 25$ mm). The filtration conditions were the same during all the cruises – the time of filtration under

gentle vacuum conditions did not exceed one hour, and the volume of filtered seawater depended on bio-hydrological conditions in different seasons. The filters were stored frozen in liquid nitrogen.

The pigment extraction method used mechanical grinding, and sonication (2 min., 20 kHz, Ultrasonic Homogenizer 4710 Series, Cole Parmer Instrument) of frozen filters in the presence of 90% acetone solution in dark conditions at 4°C for 2 hours (Parsons et al., 1984). Two types of chromatographic systems HP1100 (in years 1999–2009) and HP1200 (from 2010 to 2018) (Agilent, Perlan Technologies) were used to separate particular chlorophylls and carotenoids. In both systems diode array absorbance detectors (dad) recorded spectra in the range from 350 nm to 700 nm with a 1 nm step and 0.4 s time resolution. The calibration parameters were obtained for absorbance set at $\lambda = 440$ nm. The fluorescence detectors used to confirm the presence of chloropigments in extracts were set at excitation wavelength $\lambda_{ex} = 431$ nm and emission $\lambda_{em} = 660$ nm. Two types of C18 columns (dimensions 250 × 4 mm; particle size 5 μ m; pore size 100 Å) were used in the analysis: LichroCART™ Hypersil ODS (Merck) to separate pigments from the samples collected in 1999–2001, and LichroCART™ LiChrospher™ 100 RP18e (Merck) to the analysis conducted from 2002. The methodological details of chromatographic conditions, used solvents and adopted procedures (Barlow et al., 1993; Mantoura and Llewellyn, 1983), are described in Stoń-Egiert and Kosakowska (2002) and Stoń-Egiert and Kosakowska (2005). The calibration of both systems was conducted based on commercially available chlorophylls and carotenoids standard extracts isolated from reference strains of phytoplankton monocultures (The International Agency for ¹⁴C Determination DHI Institute for Water and Environment in Denmark). The parameters obtained for pigment standards, such as calibration curves, detection limits, and spectral shapes of absorption allowed both qualification and quantification of pigments present in samples with a precision error of 2.9% ± 1.5% and a recurrence error of 9.7% ± 6.4% (Stoń-Egiert et al., 2010).

This level of chromatographic performance allows characterization of 30 pigments which can be grouped with respect to their function to chlorophylls (chlorophyll *a*, chlorophyllide *a*, phaeophytin *a*, pheophorbide *a*; divinyl chlorophyll *a*, chlorophyll *b*, chlorophyll *c1c2*, chlorophyll *c3*), photosynthetic carotenoids PSC (peridinin, fucoxanthin, α -carotene, 19'hex-fucoxanthin, prasinoxanthin, canthaxanthin, echinenone, 19'but-fucoxanthin and astaxanthin); photoprotecting carotenoids PPC (diadinoxanthin, alloxanthin, zeaxanthin, lutein, neoxanthin, violaxanthin, β -carotene, diatoxanthin, myxoxanthophyll, antheraxanthin, aphanizophyll, gyroxanthin diester, crocoxanthin). For further analyses, the obtained pigment concentration data were grouped into subsets based on the measurement seasons: spring (number of a day in a year – Julian day from 79 to 171), summer (Julian day from 172 to 265), autumn (266–355) and winter (356–78).

2.3. Measurements of hydrological parameters

Profiles of hydrological parameters, such as temperature and salinity, were measured in situ routinely using Guildline

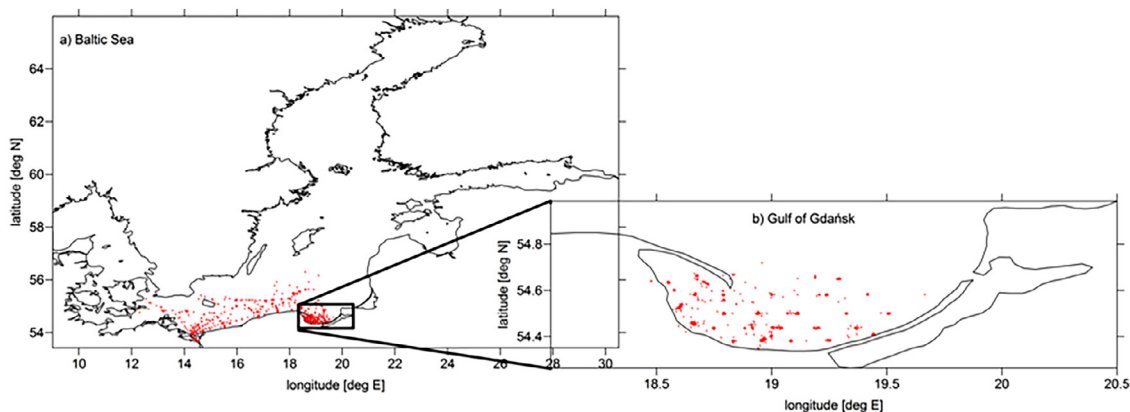


Figure 1 Location of the measuring stations at Southern Baltic region and Gulf of Gdańsk in years 1999–2018.

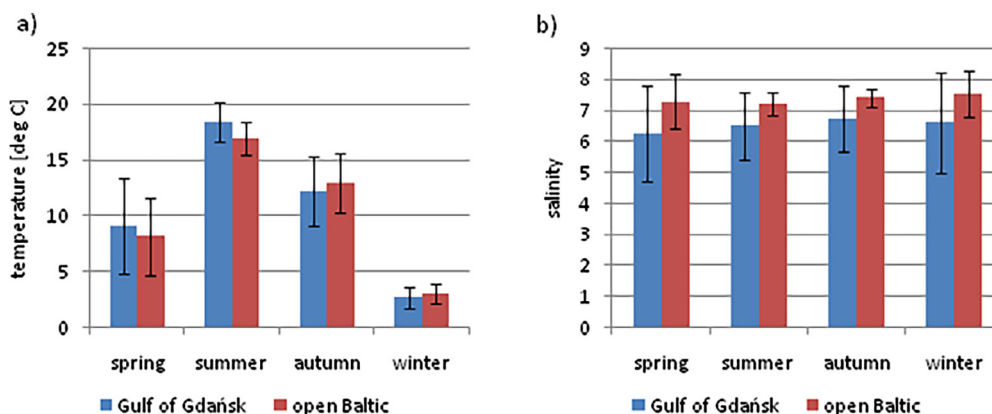


Figure 2 Mean values and standard deviations of temperature (a) and salinity (b) in the surface layer measured in Southern Baltic region and Gulf of Gdańsk in 1999–2018.

Table 1 Number of samples collected for HPLC pigment identification in surface layer waters of the Gulf of Gdańsk and the open Baltic region in 1999–2018.

Season	Number of a day in year (Julian day)	Number of samples		Total amount
		Gulf of Gdańsk	Open Baltic region	
spring	79–171	638	402	1040
summer	172–265	385	166	551
autumn	266–355	261	174	435
winter	356–78	225	162	387
Total		1509	904	2413

87104 or Sea-Bird SBE 9 probes during the cruises on *r/v Oceania*, and a Neil Brown Mark III probe during cruises on *r/v Baltica* and by Handylab salinometer. Figure 2 shows the surface values of the recorded hydrological parameters on an annual basis in the dataset covering the years 1999 to 2018.

3. Results

Based on chromatographic separations of phytoplankton samples collected in the period 1999 to 2018, the values

of phytoplankton pigment concentrations in particular seasons and regions of the Baltic Sea were obtained. Figure 3 shows the mean and standard deviation values of pigment concentrations in the region of the Gulf of Gdańsk and the open Baltic Sea in groups: chlorophylls (Figure 3a–b), photosynthetic carotenoids (Figure 3c–d), and photoprotective carotenoids (Figure 3e–f).

The dynamics of the changes in chlorophyll *a* concentration in different seasons (Figure 3a–b) reflect the changes in phytoplankton biomass during the annual cycle resulting from blooms of appropriate classes of algae, the physiological state of the cells, and their stage of development. In

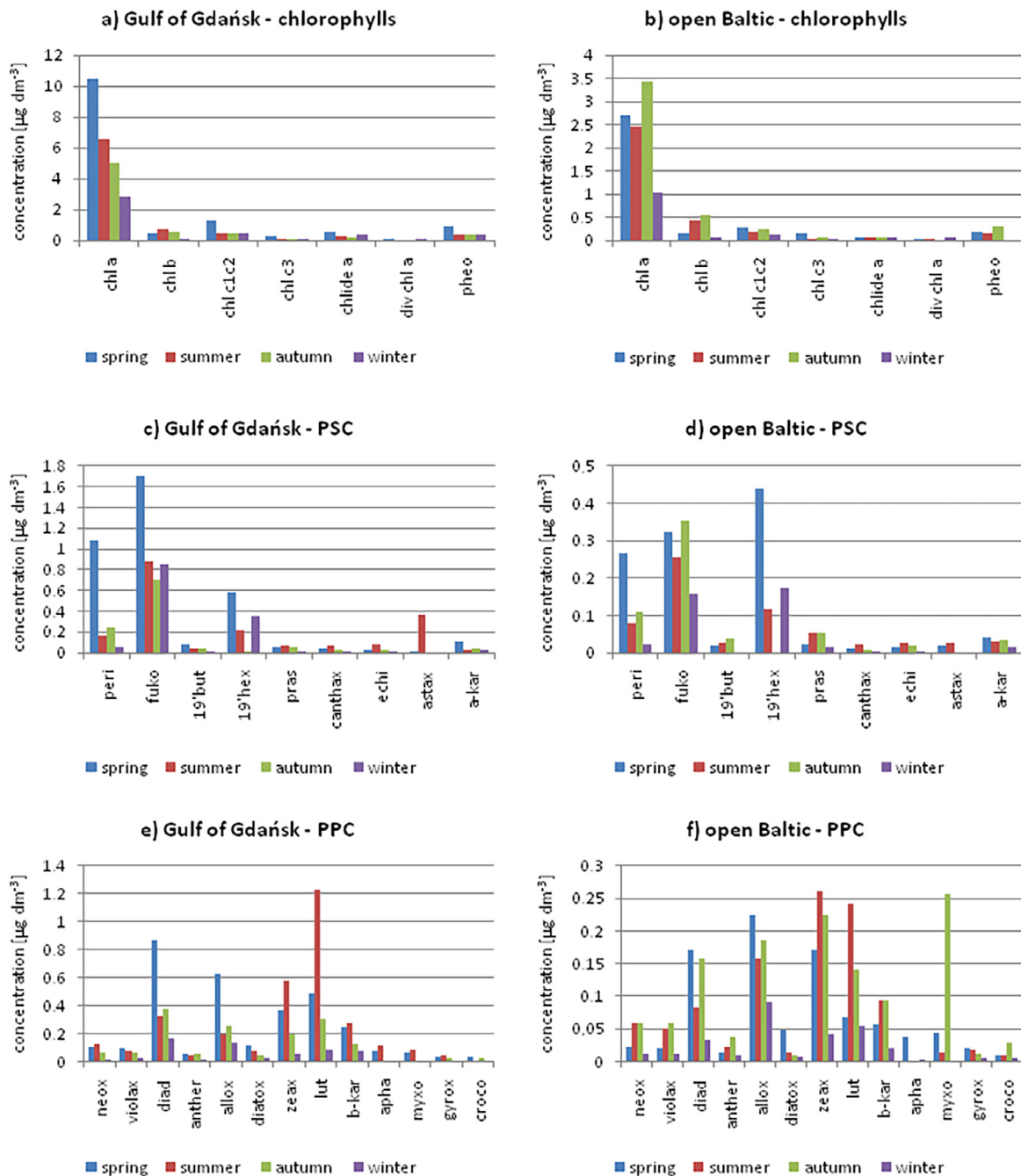


Figure 3 Values of mean concentrations of pigments identified in Gulf of Gdańsk (left panel) and open Baltic region (right panel): chlorophylls (a,b), photosynthetic carotenoids PSC (c, d) and photoprotective carotenoids PPC (e,f) in different seasons in 1999–2018.

the gulf area, the highest concentrations of chlorophyll *a* occurred in spring (mean $10.44 \pm 13.44 \mu\text{g dm}^{-3}$) and decreased throughout the year, reaching the lowest value in winter ($2.82 \pm 3.09 \mu\text{g dm}^{-3}$). In the open sea, however, the mean content of chlorophyll *a* was significantly lower than in the gulf waters. In spring and summer, in the open Baltic Sea, mean chlorophyll *a* concentrations were at a similar level ($2.69 \pm 3.3 \mu\text{g dm}^{-3}$ and $2.45 \pm 1.62 \mu\text{g dm}^{-3}$ respectively) and the highest mean values of this pigment were observed in autumn ($3.44 \pm 2.65 \mu\text{g dm}^{-3}$). The chlorophyllide *a*, one of the chlorophyll *a* derivatives, was identified

in 66% of the samples and its average concentration was 20–35 times lower compared to the average concentration of chlorophyll *a* in the study areas. Other derivatives of chlorophyll *a* or its decomposition products (divinyl chlorophyll *a*, pheophytin *a*, and pheophorbide *a*) occurred sporadically.

The chlorophyll pigments such as chlorophyll *b*, chlorophyll *c1c2*, and chlorophyll *c3*, absorbing solar radiation in other spectral ranges than chlorophyll *a* also showed spatial-seasonal variability. The highest mean concentrations of chlorophyll *b* were recorded in the gulf area in summer (0.74

$\pm 0.85 \mu\text{g dm}^{-3}$), while in the open sea area – in autumn ($0.54 \pm 0.71 \mu\text{g dm}^{-3}$). It is related to the increased growth of phytoplankton from the green algae group, in cells in which this pigment is present in amounts exceeding $> 10\%$ of the total content of other pigments in the cell.

The highest mean concentrations of pigments belonging to the group of chlorophyll *c* were identified in spring in gulf waters ($1.24 \pm 2.9 \mu\text{g dm}^{-3}$ – chlorophyll *c1c2* and $0.3 \pm 0.41 \mu\text{g dm}^{-3}$ – chlorophyll *c3*). During the other seasons in this area, it remained at similar levels (approximately $0.43 \mu\text{g dm}^{-3}$). In the Southern Baltic waters, the mean concentrations of these pigments were lower and did not exceed $0.29 \mu\text{g dm}^{-3}$ in the case of chl *c1c2* and $0.17 \mu\text{g dm}^{-3}$ with regard to chl *c3*.

In the group of photosynthetic carotenoids (PSCs), fucoxanthin was the most frequently identified in samples from both regions (Figure 3c–d). It constituted 50% (in open sea waters) to 58% (in gulf waters) of the total content of identified PSCs. The highest mean value of this pigment concentration was recorded in spring ($1.70 \pm 3.10 \mu\text{g dm}^{-3}$) in the gulf area, while in the other seasons, its mean content varied within the range of $0.71 \mu\text{g dm}^{-3}$ ($\pm 0.64 \mu\text{g dm}^{-3}$) up to $0.88 \mu\text{g dm}^{-3}$ ($\pm 1.92 \mu\text{g dm}^{-3}$). This is a result of blooms of diatoms that prefer low temperatures. In the open Baltic region throughout the year, its concentration was on average 4 times lower compared to the gulf waters. Both in spring and autumn, its mean concentrations were similar and amounted to $0.32 \pm 0.62 \mu\text{g dm}^{-3}$ and $0.35 \pm 0.32 \mu\text{g dm}^{-3}$, respectively. In the other seasons, they were lower and amounted to $0.25 \pm 0.27 \mu\text{g dm}^{-3}$ in summer and $0.16 \pm 0.33 \mu\text{g dm}^{-3}$ in winter.

Other photosynthetic pigments important in terms of frequency were peridinin representing 26–28% of total PSC and α -carotene representing 3 to 6% of total PSC. Their mean concentrations were lower compared to fucoxanthin content and also showed seasonal variation. The results of the analysis of spatial differentiation of peridinin indicated that its mean concentrations in the gulf waters were nearly 4 times higher than the mean concentrations recorded in the waters of the open sea. The average peridinin concentration was the highest in spring ($1.09 \pm 2.22 \mu\text{g dm}^{-3}$ in gulf and $0.27 \pm 0.63 \mu\text{g dm}^{-3}$ in open sea waters). The next increase in the average value of this pigment was recorded in the autumn ($0.25 \pm 0.92 \mu\text{g dm}^{-3}$ in the gulf area and $0.11 \pm 0.11 \mu\text{g dm}^{-3}$ in the waters of the open sea). In winter, the concentrations of this pigment were the lowest and amounted to $0.06 \pm 0.09 \mu\text{g dm}^{-3}$ in gulf and $0.02 \pm 0.05 \mu\text{g dm}^{-3}$ in the open sea waters. The mean concentration of α -carotene was 2 times higher in the gulf waters than in the open sea. Analogous to the previously discussed PSC – the highest average concentration was observed in spring: $0.11 \pm 0.04 \mu\text{g dm}^{-3}$ in gulf waters and $0.04 \pm 0.05 \mu\text{g dm}^{-3}$ in open sea region. In the remaining seasons, the average concentrations were at an even level and fluctuated within the range of 0.02 – $0.05 \mu\text{g dm}^{-3}$.

The remaining photosynthetic carotenoids occurred in small amounts, constituting from 2 to 7% of the total PSC content identified in the samples. The highest 19'hex-fucoxanthin concentrations were recorded in the waters of the Gulf of Gdańsk in spring ($0.57 \pm 0.63 \mu\text{g dm}^{-3}$). Prasinonanthin, canthaxanthin, and echinenone in summer and autumn were recorded in higher concentrations than in

other seasons. They made a small contribution to the total content of photosynthetic pigments, and their mean concentrations in bay waters were 1.2 to 6.6 times higher compared to those recorded in the open sea.

Seasonal-spatial variability was also noted in relation to the qualitative-quantitative characteristics of carotenoids belonging to the photoprotective group (PPC) (Figure 3e–f). Their mean concentration in gulf waters over the year was about 2–5 times higher than in open sea waters. Diadinoxanthin, alloxanthin, zeaxanthin, lutein, and β -carotene accounted for 10 to 30% of the total PPC content. In open water, alloxanthin and zeaxanthin constituted 27% of PPCs, while diadinoxanthin was 20%. In gulf waters, diadinoxanthin constituted 30% of the total content of PPC, while alloxanthin and zeaxanthin – approx. 21% each and were the dominant PPC carotenoids in this area. The highest mean concentrations of diadinoxanthin ($0.87 \pm 1.47 \mu\text{g dm}^{-3}$) and alloxanthin ($0.63 \pm 1.07 \mu\text{g dm}^{-3}$) were identified in the Gulf of Gdańsk area in spring. In the remaining seasons the content of these pigments was significantly lower, although, in both areas in the autumn, the second maximum of average concentrations of these pigments was observed, corresponding to the autumn increases in cryptophytes biomass (alloxanthin – marker), thermophilic diatoms and dinoflagellates, which are characteristic of the annual physiological cycle of phytoplankton. The contribution of the remaining compounds to the total content of PPC was significantly lower and did not exceed 7% as in the case of myxoxanthophyll in open waters and 5% in the case of aphanizophyll in gulf waters.

The seasonal distribution of the mean values of zeaxanthin, lutein, and β -carotene concentrations showed a similar distribution in the gulf waters, indicating spring and summer as the periods of higher mean concentrations of these compounds in the gulf waters, and summer and autumn in the waters of the open sea.

4. Discussion

The study of the physical, chemical and biological processes related to the development of phytoplankton in the seas and oceans often requires the use of complex and costly measurement methods and very specialized equipment. Hence, indirect methods using the still-developing knowledge of the mechanisms of these processes and their dependence on various environmental factors are searched for.

The development of mathematical formulas describing the dependence of these processes on external factors such as temperature and solar radiation as well as on the presence and concentration of dissolved and suspended substances in seawater enables not only qualitative but also advanced quantitative assessment of the condition and possible changes of the ecosystem. Such biophysical models of processes occurring in the sea are used, for example, in satellite algorithms. They allow tracking of complex phenomena occurring in the studied basins based on relatively easily measurable parameters. One of such parameters and at the same time an important indicator of the condition of the ecosystem, its trophicity, and phytoplankton biomass is the concentration of chlorophyll *a* in the water. Several easily available, relatively inexpensive, and accurate meth-

ods exist for determining the concentration of chlorophyll *a* (Aminot and Rey, 2001; Hagerthey et al., 2006; Holm-Hansen et al., 1965; Pinto et al., 2001; Welschmeyer, 1994) and the fact that it occurs in all plant cells have made it, especially for oceanic waters not subjected to terrestrial pressures, well correlated with both the concentrations of other seawater constituents and its optical properties. Therefore, chlorophyll *a* concentration is often used as an independent variable in mathematical descriptions of many processes in the marine environment. Analyses of the dependence of pigment concentration and composition in different seasons in the analyzed regions on chlorophyll *a* concentration are presented below. They are statistical and simplified compared to more complex analyses that take into account, for example, the influence of absolute levels and spectral distributions of solar radiation reaching phytoplankton cells (Babin et al., 1996; Gregg and Rousseaux, 2016; Majchrowski and Ostrwska, 2009; Majchrowski et al., 2007; Stoń-Egiert et al., 2019; Trees et al., 2000; Uitz et al., 2006, 2015; Woźniak and Dera, 2007). Nevertheless, as chlorophyll *a* concentration depends on many factors that shape phytoplankton habitat, such as temperature or the availability and spectral composition of light and nutrients availability, it can be assumed that these factors are taken into account indirectly. Such relationships based on one relatively easy-to-define variable may find some practical applications. In the case of the surface layer analyzed in this paper, the concentration of chlorophyll *a* can be determined with high accuracy based on satellite data which enables remote and fast quantitative assessment of the content of these groups of pigments in the analyzed phytocoenoses without the necessity to conduct point measurements with methods which make it possible to determine these pigments (e.g. HPLC).

Knowledge of the relationship between the concentrations of individual pigments or their functional groups and concentrations of chlorophyll *a* enables a preliminary assessment of the living conditions of phytoplankton populations and their optical properties. It makes it possible, for example, to determine what part of the absorbed energy was used by the plant in the photosynthesis process or otherwise dissipated by the photoprotective pigments. It is extremely important in the analysis and modeling of processes stimulated by solar energy taking place in the water column. It is of particular importance in coastal regions characterized by high productivity and variable optical conditions, resulting in, among other things, a stressful excess or deficit of solar energy. However, it should be remembered that in these regions the proximity to land, transport of substances from atmosphere, and human activity have a significant impact on marine ecosystems and often strongly modify the optical living conditions of marine phytocoenoses. Therefore, we are dealing with different ecosystems than in the case of the central regions of the oceans containing few substances of external origin. Therefore, the applicability of statistical relationships linking the concentration of chlorophyll *a* and the concentration of other pigments developed for ocean waters (Majchrowski, 2001) is limited to these regions. The accuracy of the estimates clearly decreases when applied to the Baltic waters (see Table 2). This can be observed in Figure 4 (column 1), where the empirical data of concentrations of individual groups of pigments in the Baltic Sea (chlorophylls

b, chlorophylls *c*, PPC, PSC) as a function of chlorophyll *a* concentration analyzed in this work (solid line) are shown against the relationships developed for oceanic waters by Majchrowski (2001) (dashed line). Both dependencies are in the form proposed by Majchrowski (2001):

$$C_i = A_i C_{chl a}^{B_i} \quad (1)$$

where:

- C_i – concentration of approximated pigment group *i* (chl *b*, chl *c*, PPC, PSC) [$\mu\text{g dm}^{-3}$],
- $C_{chl a}$ – concentration of chlorophyll *a* [$\mu\text{g dm}^{-3}$],
- A_i, B_i – numerical factors specific to individual pigment group.

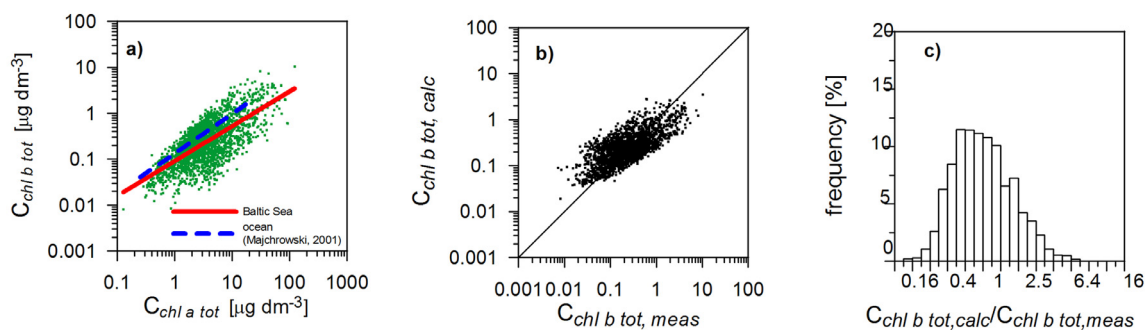
The factors A_i and B_i appointed for the Baltic Sea are shown in Table 3.

The errors in estimation of pigment groups concentrations in the Baltic using relationships developed for the oceans (Majchrowski, 2001) and using the local relationship developed in this study are presented in Table 2 and in Table 4. Due to the very wide, exceeding three orders, range of pigment concentration variability, the errors were determined using not only the arithmetic statistic standard but also the logarithmic transformation of data.

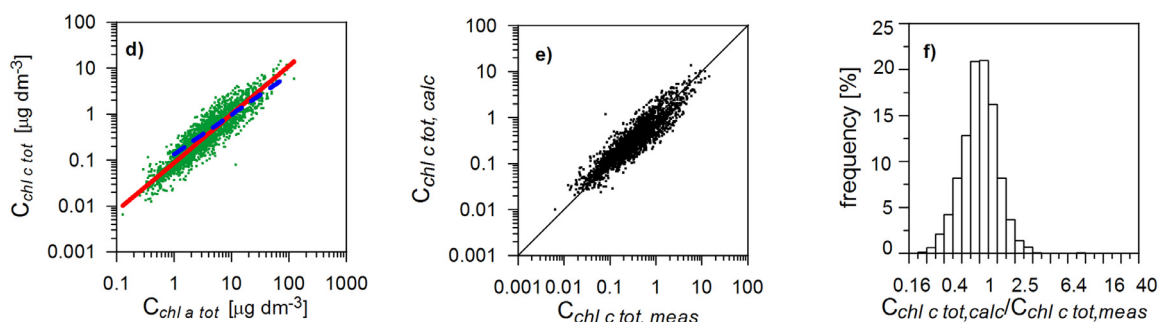
Figure 4 (middle and right panel) illustrates the comparison of the empirical data with values estimated based on the relationships developed for the Baltic Sea. The use of the local dependencies improved the quality of the estimation visible primarily in the significant reduction of systematic errors. The analyses of the Baltic Sea functioning, e.g. in periodic assessments of the condition of the Baltic Sea environment regularly performed by HELCOM (HELCOM, 2009, 2017, 2018), the division of this basin into sub-basins, whose ecosystems function under the influence of specific local conditions, is usually taken into account. These divisions include the morphology and hydrological conditions prevailing in different regions of this sea (Jakobsson et al., 2019). Using the collected dataset we carried out the analyses for two different neighbouring regions: the waters of the Gulf of Gdańsk and the open waters of the southern Baltic. In our analyses, we also considered the fact that the Baltic Sea lies in a climatic zone characterized by distinct seasonal variations of the occurring biological-hydrological conditions. Figure 5 shows the percentage of the five pigment groups in both these regions and in the different seasons. The proportion of chlorophyll *a* in the total content of pigments identified in both areas was relatively stable regardless of the season and amounted to approx. $62\% \pm 5\%$. In the case of the remaining groups of pigments, seasonal and regional changes in their participation in the total pigment content are visible.

However, these differences are more distinct between seasons than between regions. This is mainly due to the annual cycles of phytoplankton development and their succession that are characteristic of the Baltic Sea and which determine the presence of different pigment groups in the water column (Thamm et al., 2004; Wasmund et al., 1996, 1998, 2011). A clear increase in the average percentage of chlorophyll *b*, found in green algae cells, in both regions during the summer and autumn (6–7% in the gulf and about 10% in open waters of the total content of all identified pigments) was observed. In turn, in the summer and autumn,

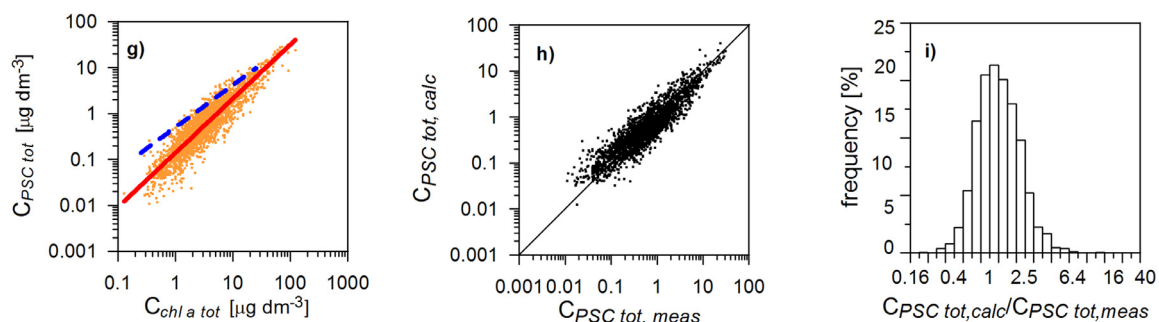
A) chlorophyll b



B) chlorophyll c tot



C) photosynthetic carotenoids PSC



D) photoprotectant carotenoids (PPC)

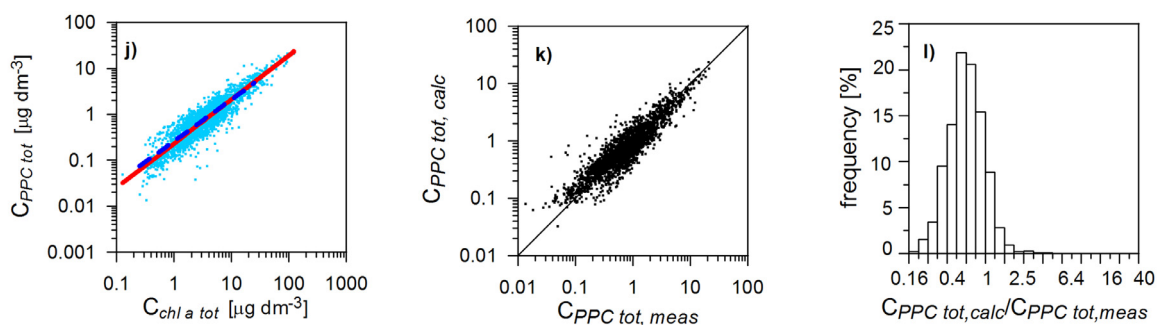


Figure 4 Concentration dependences of functional groups of pigments (respectively, chlorophyll b (A); chlorophylls c (B); photosynthetic carotenoids (C); photoprotecting carotenoids (D) on chlorophyll a concentration: a,d,g,j – comparison of empirical data with relationships obtained by Majchrowski (2001) (dashed line) and developed in this study (plain line); b,e,h,k – comparison of empirical data of pigments groups $C_{i,meas}$ and $C_{i,calc}$ approximated with the relevant equation for the Baltic Sea; c,f,i,l – histograms of the ratios $C_{i,meas}/C_{i,calc}$ for Baltic Sea.

Table 2 Errors of estimation the concentrations of functional groups of pigments (C_i): chlorophylls b ($C_{chl\ b\ tot}$), chlorophylls c ($C_{chl\ c\ tot}$), photosynthetic ($C_{PSC\ tot}$) and photoprotectant ($C_{PPC\ tot}$) carotenoids (approximations obtained by Majchrowski (2001) applied to Baltic datasets).

Pigments group	Arithmetic statistics		Logarithmic statistics			
	systematic error $\langle \varepsilon \rangle$ [%]	statistical error σ_ε [%]	systematic error $\langle \varepsilon \rangle_g$ [%]	standard error factor - x	statistical error σ_- [%]	σ_+
$C_{chl\ b\ tot}$	128.88	223.88	6.59E+01	2.15	-53.57	115.39
$C_{chl\ c\ tot}$	36.48	72.04	2.12E+01	1.64	-38.947	63.77
$C_{PSC\ tot}$	222.60	249.66	1.65E+02	1.83	-45.30	82.80
$C_{PPC\ tot}$	17.31	70.11	5.54E+00	1.55	-35.58	55.23

where

$\langle \varepsilon \rangle = (C_{i,calc} - C_{i,meas})/C_{i,meas}$ – relative error
 $C_{i,meas}$ · $C_{i,calc}$ – concentrations of pigment groups measured and calculated using appropriate formulas
 $\langle \varepsilon \rangle_g$ – arithmetic mean of errors
 $\langle \varepsilon \rangle_g$ – logarithmic mean of errors
 $\langle \varepsilon \rangle_g = 10^{[\langle \log(C_{i,calc} / C_{i,meas}) \rangle]} - 1$

$\langle \log(C_{i,calc} / C_{i,meas}) \rangle$ – mean of. $\log(C_{i,calc} / C_{i,meas})$.
 σ_ε – standard deviation of errors (statistical error)
 σ_{log} – standard deviation of $\log(C_{i,calc} / C_{i,meas})$
 $x = 10^{\sigma_{log}}$ – standard error factor
 $\sigma_+ = x - 1$ and $\sigma_- = (1/x) - 1$

Table 3 Parameterization coefficients (A_j , B_j) and determination coefficient (R^2) for estimation of concentrations of sum of: chlorophylls b ($C_{chl\ b\ tot}$), chlorophylls c ($C_{chl\ c\ tot}$), photosynthetic ($C_{PSC\ tot}$) and photoprotectant ($C_{PPC\ tot}$) carotenoids using Eq. (1) obtained for Baltic Sea data from period 1999–2018.

Pigments group	Number of data	Numerical value of coefficients		Determination coefficient R^2
		A_j	B_j	
$C_{chl\ b\ tot}$	2245	0.09162	0.75632	0.4925
$C_{chl\ c\ tot}$	2404	0.08796	1.05156	0.8472
$C_{PSC\ tot}$	2392	0.13930	1.17676	0.8263
$C_{PPC\ tot}$	2405	0.23201	0.95787	0.8325

Table 4 Relative errors of estimating the concentrations of: chlorophylls b ($C_{chl\ b\ tot}$), chlorophylls c ($C_{chl\ c\ tot}$), photosynthetic ($C_{PSC\ tot}$) and photoprotectant ($C_{PPC\ tot}$) carotenoids using Eq. (1) and numerical coefficients A_j , B_j given in Table 3.

Pigments group	Arithmetic statistics		Logarithmic statistics			
	systematic error $\langle \varepsilon \rangle$ [%]	statistical error σ_ε [%]	systematic error $\langle \varepsilon \rangle_g$ [%]	standard error factor - x	statistical error σ_- [%]	σ_+
$C_{chl\ b\ tot}$	36.45	130.00	3.25E-09	2.14	-53.25	113.92
$C_{chl\ c\ tot}$	10.94	58.70	-4.9E-08	1.57	-36.46	57.38
$C_{PSC\ tot}$	16.94	77.23	4.34E-08	1.72	-41.93	72.20
$C_{PPC\ tot}$	10.89	65.39	-1.4E-08	1.55	-35.35	54.69

The errors were calculated according the equations given in Table 2.

the total amount of photo-protective carotenoids (approx. 15–17% of the total amount of identified pigments) was higher than that of photosynthetic carotenoids (9–11% of the total amount of identified pigments) in both analyzed areas. It can be assumed that this is due to various functions performed in the photosynthetic apparatus: a higher concentration of protective carotenoids occurs in those seasons when intense solar radiation can cause photoinhibition.

During seasons characterized by lower light intensity, photosynthetic carotenoids predominate enabling efficient use of available solar radiation for photosynthesis of or-

ganic matter (Barlow et al., 2007; Marty et al., 2002; Stoń-Egiert et al., 2012). Figure 6 shows the dependence of the concentrations of individual pigment groups on chlorophyll a taking into account both analyzed regions and four seasons. Corresponding subsets of measurement data are highlighted in colors. For all these subsets, dependencies were determined using the formula (1). The coefficient values of Eq. (1) for the relationships determined for each pigment group for both regions and seasons and the errors of these estimates are presented in Table S01 in the Supplementary material.

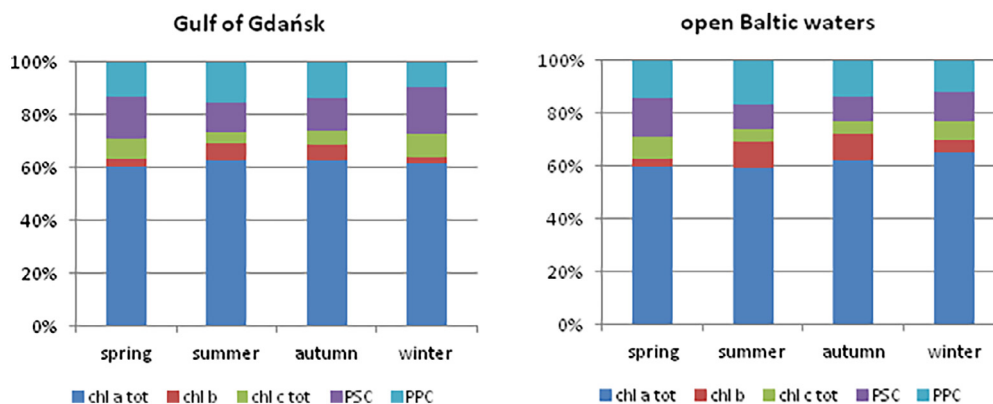


Figure 5 Mean percentage participations of functional pigment groups in the total content of identified pigments in the a) Gulf of Gdańsk and b) open Baltic waters determined for four seasons.

As can be seen in the figure (Figure 6, left panel), the concentrations of all pigments are significantly higher in the Gulf of Gdańsk than in open waters. However, for each of the four groups of pigments, it can be seen that the apparent differences in concentration levels do not significantly affect the nature of the analyzed relationship. Also, the error analysis does not indicate any improvement in the quality of estimation of these pigment concentrations while using the dependencies taking into account division into regions. On the other hand, the analysis of the dependences of the concentrations of pigment groups on the chlorophyll *a* content in different seasons confirms the different character of these dependences related to the seasons. In most cases, there is a clear decrease in the value of the *x* factor representing the systematic error in the logarithmic statistic (Table S01). Increasing the accuracy of indirect estimation of the concentration of different pigment groups in the phytoecosystems based on chlorophyll *a* concentration affects the accuracy of remote methods for determining the optical properties of the phytoecosystems. The use of the proposed relationships that take into account seasonal variation allows an approximate assessment of the absorption properties of the phytoplankton population in the study area, unfortunately, without the ability to distinguish its species composition, which would be justified when studying many other processes related to the use of solar radiation by phytoplankton cells. Attempts to remotely estimate the type of phytoplankton present in the studied reservoir use, among others, methods that determine the size structure of the phytoecosystems (e.g. Brewin et al., 2010; Di Cicco et al., 2017; Hirata et al., 2008, 2011; IOCCG, 2014; Kramer and Siegel, 2019; Meler et al., 2020; Uitz et al., 2006). There are also studies documenting the possibility of assessing the presence of cyanobacteria on the basis of the radiation signal in the appropriate spectral channels (Kahru and Elmgren, 2014; Malenovský et al., 2012; Woźniak et al., 2016a). Nevertheless, distinguishing the classes of occurring phytoplankton based on satellite observations of the marine environment is still an open task of modern oceanography. Development of model formulas allowing estimation of the content of individual pigments based on chlorophyll *a* concentration may contribute to the development of such methods using hyperspectral satellite radiometers. Especially in the context of the currently used

indirect methods of determining the species composition of phytoplankton populations based on the analysis of pigment composition determined, for example, by HPLC methods (Goela et al., 2014; Latasa, 2007; Mackey et al., 1996; Miranda-Alvarez et al., 2020; Wang et al., 2018). The clearly marked seasonally variable nature of the dependence of pigment groups, shown in Figure 6, is the result of the seasonal occurrence of individual pigments. The quantitatively dominant pigments in each season in the photosynthetic pigment group were fucoxanthin and peridinin, while in the photoprotective pigment group the dominant pigments were diadinoxanthin, alloxanthin, zeaxanthin, β -carotene, and lutein.

The seasonal variation in the percentage content of identified chlorophylls and carotenoids presented in Figure 7 strongly indicates the periodic dominance of marker pigments for individual phytoplankton groups, thus characterizing the composition of the phytoecosystems occurring in a given season. As mentioned before, the spring season in the Baltic Sea is dominated by the presence of diatoms and dinoflagellates (Thamm et al., 2004; Wasmund et al., 2011; Wasmund and Ulig, 2003), which results in the highest percentage of fucoxanthin (40% of the total identified quantity over the annual cycle) and peridinin (70% of the total identified quantity over the annual cycle) during this season. During summer, the Baltic phytoecosystems are characterized by the development of green algae biomass and cyanobacteria, consistent with the seasonal distribution of the percentage of characteristic pigments: neoxanthin, violaxanthin, lutein, chlorophyll *b* for green algae, and echinenone, astaxanthin, zeaxanthin – for cyanobacteria in comparison to the other seasons. On the other hand, the autumn phytoplankton population is mixed, although the occurrence of autumn diatom bloom (Wasmund and Ulig, 2003) has been documented over the years, and confirmed in the presented analyses of variation in fucoxanthin occurrence over the annual cycle.

To address the still open issue of modern oceanography, that is the differentiation of phytoplankton classes based on common and global satellite observations, an attempt was made to establish relationships between the pigments characteristic for particular classes of algae occurring seasonally in the Baltic Sea and trophic type represented by chlorophyll *a* concentration.

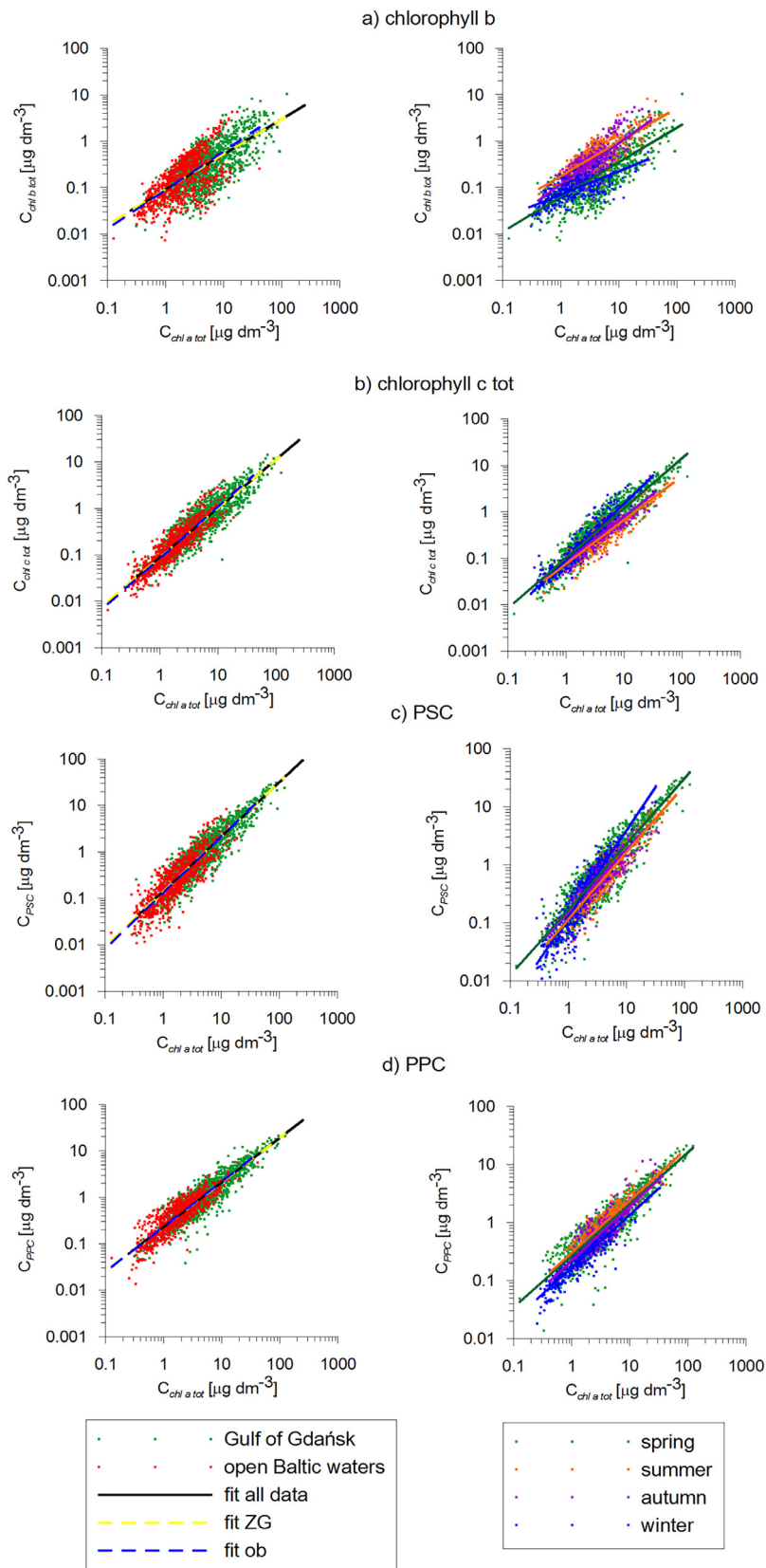


Figure 6 The relationships of functional groups of pigment concentrations (chlorophylls *b* (a), chlorophylls *c* (b), photosynthetic carotenoids (c), photoprotectant carotenoids (d)) on chlorophyll *a* concentrations determined for different regions (left panel) and seasons (right panel).

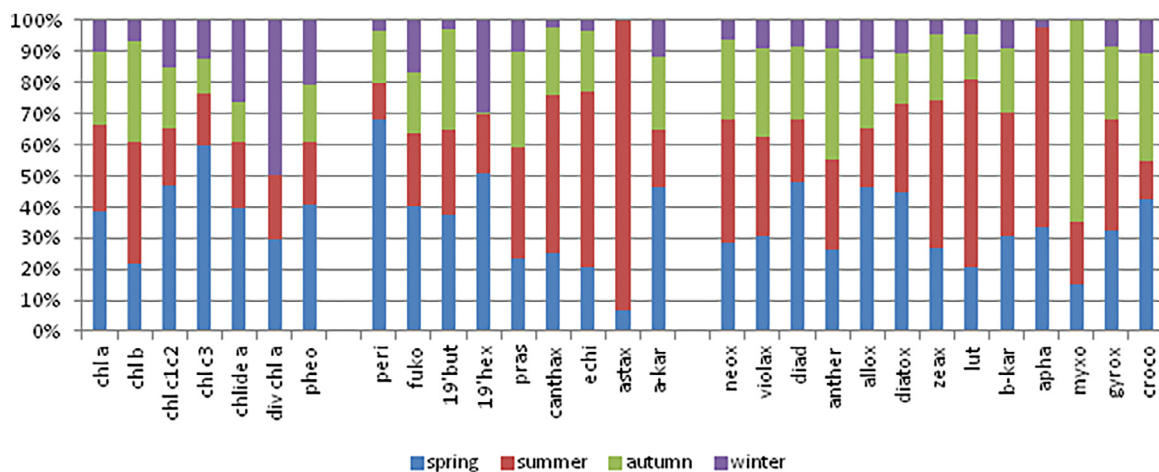


Figure 7 Mean percentage participations of individual pigments identified in each season in relation to their annual content in analysed period 1999–2018.

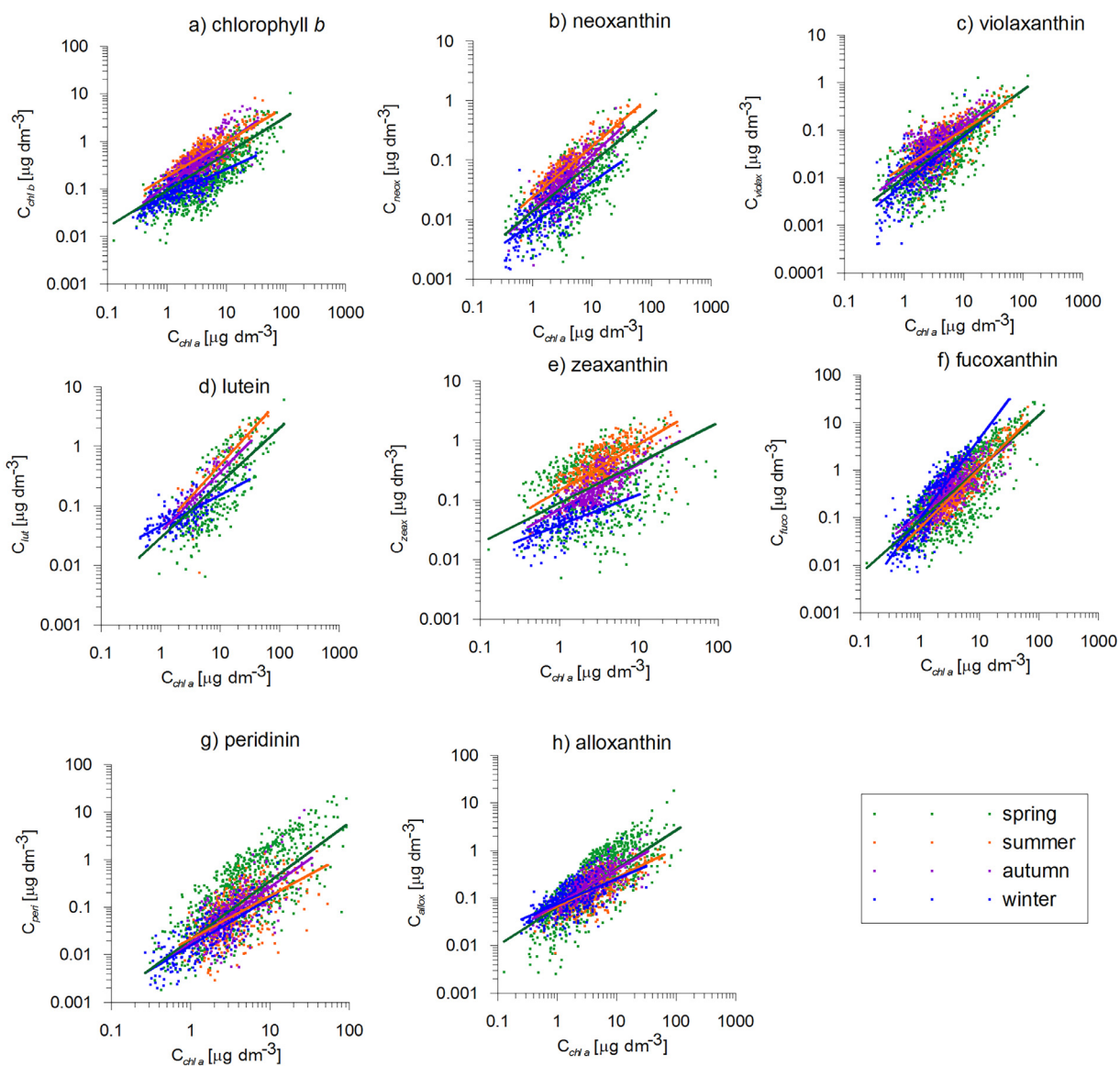


Figure 8 Seasonal relationships of concentrations of selected pigment markers of main algal groups occurring in Baltic Sea waters on chlorophyll a: a,b,c,d: green algae; e: cyanobacteria; f: diatoms; g: dinophytes; h: alloxanthin.

Table 5 Coefficients of relationship (1), A_i and B_i (obtained for Baltic Sea data from 1999-2018) and estimation errors of concentration of selected pigment markers of algal groups occurring seasonally in Baltic Sea waters.

	Parametrization			Errors of approximations						
	Number of data N	Coefficients of parametrization		Coefficient of determination R^2	Arithmetic statistics		Logarithmic statistics			
		A_i	B_i		systematic error $\langle \varepsilon \rangle$ [%]	statistical error σ_ε [%]	systematic error $\langle \varepsilon \rangle_g$ [%]	standard error factor - x	statistical error [%]	
									σ_-	σ_+
chlorophyll <i>b</i> - $C_{chl\ b}$										
All data	2245	0.092	0.773	0.507	35.23	126.79	4.19E-09	2.12	-52.75	111.66
Gulf of Gdańsk	1425	0.094	0.755	0.475	32.66	118.22	8.83E-09	2.07	-51.71	107.09
Southern Baltic	820	0.090	0.838	0.434	40.56	145.91	-6.9E-09	2.19	-54.35	119.08
spring	959	0.064	0.753	0.578	30.18	106.96	-2.3E-09	2.05	-51.32	105.40
summer	536	0.179	0.735	0.590	12.54	63.10	2.88E-08	1.60	-37.34	59.58
autumn	431	0.118	0.892	0.610	15.34	76.41	1.31E-08	1.67	-40.00	66.68
winter	319	0.070	0.567	0.536	9.83	48.86	-2.2E-09	1.55	-35.41	54.82
neoxanthin - C_{neox}										
All data	1559	0.014	0.818	0.518	43.26	170.82	1.26E-08	2.18	-54.17	118.20
Gulf of Gdańsk	958	0.014	0.807	0.488	39.04	142.22	1.74E-08	2.14	-53.37	114.47
Southern Baltic	601	0.013	0.886	0.441	50.95	221.25	-1.1E-08	2.24	-55.28	123.61
spring	506	0.010	0.765	0.525	46.18	161.59	-8.6E-10	2.35	-57.50	135.31
summer	418	0.024	0.853	0.763	7.37	44.84	1.36E-08	1.44	-30.68	44.27
autumn	418	0.014	0.929	0.608	17.85	85.33	9.72E-10	1.71	-41.54	71.06
winter	217	0.009	0.692	0.436	22.05	83.20	-6.6E-09	1.88	-46.74	87.74
violaxanthin - C_{violax}										
All data	2024	0.010	0.919	0.534	47.27	175.88	-2.9E-08	2.30	-56.48	129.76
Gulf of Gdańsk	1286	0.010	0.921	0.526	41.70	160.71	-1.2E-08	2.21	-54.71	120.81
Southern Baltic	738	0.010	1.017	0.448	56.59	200.23	1.05E-08	2.43	-58.93	143.49
spring	814	0.007	0.924	0.594	46.76	160.33	-2.3E-08	2.36	-57.71	136.44
summer	529	0.017	0.783	0.454	26.65	107.65	5.91E-09	1.92	-47.97	92.18
autumn	434	0.013	0.952	0.525	25.04	100.87	-7.7E-09	1.91	-47.78	91.49
winter	247	0.007	1.002	0.461	48.15	168.19	1.66E-08	2.40	-58.33	140.01
lutein - C_{lut}										
All data	639	0.029	0.922	0.618	39.64	153.05	8.15E-09	2.20	-54.49	119.74
Gulf of Gdańsk	522	0.028	0.951	0.619	41.42	163.90	1.57E-08	2.21	-54.79	121.17
Southern Baltic	117	0.038	0.478	0.268	24.07	94.23	1.51E-08	1.90	-47.41	90.16
spring	346	0.015	1.125	0.626	39.70	133.46	-9.7E-08	2.31	-56.71	131.02
summer	39	0.040	1.092	0.681	70.77	421.21	5.98E-08	2.01	-50.24	100.98
autumn	88	0.036	1.005	0.768	10.18	55.61	-7E-08	1.53	-34.47	52.60
winter	166	0.045	0.528	0.466	9.22	45.04	-5.8E-09	1.55	-35.45	54.93
zeaxanthin - C_{zeax}										
All data	1774	0.089	0.677	0.285	65.88	247.85	-7.5E-09	2.56	-60.96	156.14
Gulf of Gdańsk	995	0.106	0.610	0.198	66.57	233.60	-7.5E-09	2.59	-61.38	158.94
Southern Baltic	779	0.081	0.615	0.233	60.39	235.38	4.67E-09	2.48	-59.72	148.27
spring	713	0.112	0.326	0.077	88.34	273.71	-2.9E-08	3.00	-66.65	199.83
summer	512	0.144	0.781	0.498	16.86	95.13	-2.7E-08	1.68	-40.64	68.47
autumn	346	0.070	0.758	0.519	11.97	52.98	2.86E-09	1.63	-38.73	63.22

(continued on next page)

Table 5 (continued)

	Parametrization			Errors of approximations						
	Number of data N	Coefficients of parametrization		Coefficient of determination R^2	Arithmetic statistics		Logarithmic statistics			
		A_i	B_i		systematic error $\langle \varepsilon \rangle$ [%]	statistical error σ_ε [%]	systematic error $\langle \varepsilon \rangle_g$ [%]	standard error factor - x	statistical error [%]	
									σ_-	σ_+
winter fucoxanthin - C_{fuco}	203	0.038	0.513	0.419	10.88	55.75	1.3E-08	1.56	-35.95	56.12
All data	2373	0.087	1.111	0.641	49.48	197.42	-4.4E-08	2.29	-56.30	128.82
Gulf of Gdańsk	1491	0.102	1.051	0.571	56.13	229.12	1.89E-08	2.34	-57.27	134.05
Southern Baltic	882	0.078	1.062	0.564	36.52	133.85	1.21E-08	2.15	-53.51	115.12
spring	1020	0.082	1.086	0.613	73.38	249.69	5.36E-08	2.62	-61.82	161.89
summer	546	0.062	1.233	0.792	12.52	57.81	-6.3E-08	1.63	-38.66	63.02
autumn	434	0.115	0.997	0.581	20.96	79.65	1.52E-08	1.84	-45.54	83.61
winter peridinin - C_{peri}	373	0.098	1.672	0.758	39.94	149.62	-1.7E-08	2.18	-54.16	118.13
All data	1898	0.021	1.228	0.559	76.93	284.95	2.34E-08	2.87	-65.12	186.70
Gulf of Gdańsk	1219	0.019	1.251	0.508	87.28	326.50	2.02E-08	3.01	-66.82	201.37
Southern Baltic	679	0.022	1.270	0.538	57.79	191.91	4.96E-08	2.59	-61.45	159.41
spring	823	0.034	1.195	0.568	101.39	380.25	-4.2E-09	3.11	-67.84	210.90
summer	463	0.022	0.902	0.341	59.53	205.54	4.72E-09	2.50	-60.03	150.21
autumn	383	0.018	1.170	0.522	39.20	161.26	-5.1E-08	2.17	-53.90	116.90
winter alloxanthin - C_{allox}	229	0.016	1.003	0.554	27.37	91.10	-2.5E-08	2.04	-50.97	103.95
All data	2367	0.064	0.808	0.571	32.02	136.82	7.96E-09	2.01	-50.37	101.49
Gulf of Gdańsk	1478	0.061	0.801	0.508	33.44	130.79	-5.4E-09	2.09	108.67	-52.08
Southern Baltic	889	0.065	0.943	0.616	26.98	137.88	1.42E-10	1.86	85.57	-46.11
spring	1008	0.058	0.946	0.618	49.15	183.16	-7.1E-09	2.29	-56.42	129.45
summer	543	0.066	0.607	0.425	17.48	80.13	3.49E-09	1.72	-41.86	72.01
autumn	433	0.073	0.730	0.581	11.08	57.99	-2.8E-09	1.56	-35.97	56.17
winter	383	0.075	0.530	0.379	18.27	78.84	5.86E-09	1.77	-43.42	76.73

The errors were calculated according the equations given in Table 2.

Figure 8 presents the seasonal dependencies obtained for the selected pigment markers that indicate the presence of five phytoplankton classes predominant in the Baltic phytoecosystems. The coefficients of relationships for particular pigments and errors of these approximations are presented in Table 5. Similarly as in the case of analyses relating to groups of pigments, the introduction of the criterion of the season to the analyses allowed, for most of the pigments, to obtain correlations, characterizing in a more precise way the phytoplankton population developing at a given time. This is particularly evident in the case of pigments characteristic for classes of algae showing biomass growth in specific seasons of the year. For example, when estimating the concentrations of pigments characteristic of green algae (Figure 8a–d) (chlorophyll *b*, neoxanthin lutein violaxanthin) occurring in the highest concentrations in summer and autumn, errors are lower when using statistical relationships obtained for these seasons compared to relationships

determined without divisions into season (Table 5). A clear improvement in the accuracy of the approximation can be also noticed in the case of chlorophyll *b* ($R^2 = 0.6$ and 0.61 in summer and autumn, respectively, with the lowest standard error factor x of 1.6 and 1.66 obtained for these periods). On the other hand, the best mapping was obtained in the summer for neoxanthin ($x = 1.4$), while the relationship developed for the entire data set $x = 2.18$ (Table 5). The relationships obtained for zeaxanthin characteristic of cyanobacteria occurring in the Baltic Sea, especially in summer when they form toxic blooms, also show clear seasonal variation. Data presented in Figure 8e clearly shows that especially the dependence determined for the summer period takes into account relatively high concentrations of this pigment in comparison to other seasons, which indicates that the use of this criterion for grouping data is justified. The standard error factor x for the seasonal dependence of zeaxanthin concentration on chlorophyll *a* is lowest in summer and autumn

($x=1.68$ and 1.63) with a correlation factor of 0.51 and 0.52 (Table 5). Similarly, seasonal variation was observed for the remaining cyanobacteria-specific carotenoids: echinenone, canthaxanthin, aphanizophyll, and myxoxanthophyll (supplementary material, Figure S01, Table S02). In the case of fucoxanthin, the characteristic pigment of diatoms, the relationship obtained for the summer season was found to have the lowest error ($x=1.63$, $R^2=0.79$). An equally high accuracy of approximation was obtained for the autumn dependence ($x=1.84$). The spring and autumn dependences show a similar pattern even though the spring and autumn phytoecoenoses are characterized by developing in cold water (2–8°C) and thermophilic species of diatoms, respectively (Wasmund and Ulig, 2003). In the spring season, a significantly greater dispersion of measurement data was recorded due to different stages of development of phytoplankton cells.

The increase in dinophyte biomass in spring is clearly reflected by the seasonal dependence of peridinin concentration as a function of chlorophyll *a* (Figure 8g). The location of the group of points and the relationship describing them indicate an intensive increase in the concentration of this pigment in spring. This clearly supports the use of seasonal dependencies in estimating the concentration of this pigment, also in seasons in which the dinophytes are not dominant in the phytoecoenoses.

Seasonal variation can also be observed in the case of alloxanthin concentration (Figure 8h). This pigment is considered to be an indicator of the cryptophytes content in the phytoecoenoses, which accompanies the blooms of other phytoplankton species. The best accuracy of the dependence allowing the approximation of alloxanthin concentration was obtained for autumn ($x=1.56$), while not seasonally is burdened with the error of $x=2.05$ (Table 5).

The relationships obtained for the remaining non-marker pigments of algal groups identified in the 20-year database are presented in Supplementary Material in Fig.S01. As in the case of the approximation of the pigment groups, the respective tables contain the parameterization coefficients and errors in the arithmetic and logarithmic statistics (supplementary material, Table S02).

Pigments that are not as abundant in phytoplankton samples as indicator pigments like prasinoxanthin, 19'hex-fucoxanthin, and 19'but-fucoxanthin also showed clear seasonal relationships. The least seasonal variation was observed for pigments that are cell components of many algal classes such as chlorophyll *c1c2*, diadinoxanthin, α -carotene, or β -carotene.

5. Conclusions

The statistical analyses presented in this paper are based on a unique dataset of phytoplankton pigment concentrations in surface waters of two different regions of the Baltic Sea (open waters of the southern Baltic and Gulf of Gdańsk), collected over 20 years of research. The extensive data bank was obtained using HPLC technique and included more than 2400 measurements in different seasons. Covering a wide range of variability of the analyzed parameters, the data provided a good basis for determining seasonal regularities in the occurrence and mutual proportions of phytoplankton

pigments in both analyzed regions. The analyses were performed for the four main functional groups of pigments, distinguished based on similar absorption properties (chlorophylls *b* and *c*, photosynthetic and protective carotenoids) as well as for each of the identified pigments separately. They showed a clear seasonal variation in the pigment composition, in particular with regard to the indicator pigments. In both analyzed regions, both concentration and the percentage participation of pigment functional groups clearly increase in the periods in which the environmental conditions preferred by the related phytoplankton classes prevail.

The concentration of chlorophyll *a*, used as a universal biomass indicator, which is present in all plants and is crucial for photosynthesis, in both areas changes significantly in the annual cycle following the cycle of phytoplankton biomass development. The range of this variability is very wide and reaches three and in extreme cases even four orders of magnitude. On the other hand, its share in the total content of identified pigments is stable and, irrespective of season or region, amounts to approx. 62%. The content of chlorophyll *a* in the water, indirectly related to light conditions, temperature, and availability of nutrients, with high accuracy, can be determined directly based on satellite data. Therefore, its concentration was used as an independent variable in the statistical relationships developed to determine the concentrations of individual pigments and their groups in each season and region. These relationships take into account the specific conditions influencing the composition of phytoplankton pigments in the Baltic Sea, and thus allow the estimation of pigment concentrations with much higher accuracy than using similar relationships developed for oceanic waters.

The comparison of the results of the analyses in the studied regions clearly shows that both in the case of relationships developed for individual pigments and for the main four groups, the criterion of dividing the data set into seasons improves the accuracy of the estimation to a much greater extent than taking into account the division into regions. It is also worth noting that the higher level of pigments concentration in the Gulf of Gdańsk compared to the open waters of the southern Baltic does not change the nature of the determined relationships, which is reflected in the presented error analysis. This is due to the strong influence of seasonal changes on the composition of Baltic phytoecoenoses, phytoplankton development and the seasonal progression of dominant algal species. Thus, including seasonality in the analyses effectively captures the changing structure of the phytoplankton community in a way that is relevant for both areas.

The results obtained enable the qualitative and quantitative mapping of the phytoecoenoses, including distinguishing classes of Baltic Sea phytoplankton occurrence in different seasons thanks to the knowledge of chlorophyll *a* concentrations, which can now be determined by remote methods. Presented results can contribute to the development of methods of predicting other pigments from estimates of chlorophyll *a* from remote sensing e.g. by spectral analysis. They also make it possible to estimate the biomass of algae classes for which the relevant pigments are taxonomic markers. The application of the dependencies which take into account the seasonal occurrence of the given phyto-

plankton classes in the bio-optical models and formulas used in the development of satellite data may increase their accuracy.

The use of statistically developed dependencies that take into account local conditions affecting the composition of pigments in phytoplankton is a solution that should also be recommended for other water bodies. In the further stages of the work, the preliminary formulas will be developed and implemented in the mathematical descriptions of processes related to the distribution and utilization of solar energy in the Baltic ecosystems used in bio-optical models. We expect that this will contribute to their accuracy.

Declaration of competing interest

The authors declare that they have no known competing financial interests or personal relationships that could have appeared to influence the work reported in this paper.

Acknowledgements

This research was carried out within the resources dedicated to the statutory programme of the Institute of Oceanology of the Polish Academy of Sciences and financially supported by projects funded by the European Union through the European Regional Development Fund SatBaltik [POIG 01.01.02-22-011/09], eCUDO.pl [POPC.02.03.01-IP.01-00-0062/18]. We would like to thank our colleagues from IO PAS and the ship's crew for their help in collecting the water samples.

Supplementary materials

Supplementary material associated with this article can be found, in the online version, at <https://doi.org/10.1016/j.oceano.2024.03.003>.

References

Aminot, A., Rey, F., 2001. Chlorophyll *a*: Determination by spectroscopic methods. *ICES Tech. Mar. Environ. Sci.* 17. <https://doi.org/10.25607/OBP-278>

Babin, M., Sadoudi, N., Lazzara, L., Gostan, J., Partensky, F., Bricaud, A., Veldhuis, M., Morel, A., Falkowski, P.G., 1996. Photo-acclimation strategy of *Prochlorococcus* sp. and consequences on large scale variations of photosynthetic parameters, *Ocean Opt.* 13. In: *Proc. SPIE* 2963, 314–319. <https://doi.org/10.1117/12.266462>

Barlow, R.G., Mantoura, R.F.C., Gough, M.A., Fileman, T.W., 1993. Pigment signatures of the phytoplankton composition in the north-eastern Atlantic during the 1990 spring bloom. *Deep-Sea Res. II* 40 (1–2), 459–477. [https://doi.org/10.1016/0967-0645\(93\)90027-K](https://doi.org/10.1016/0967-0645(93)90027-K)

Barlow, R.G., Stuart, V., Lutz, V., Sessions, H., Sathyendranath, S., Platt, T., Kyewalyanga, M., Clementson, L., Fukasawa, M., Watanabe, S., Devred, E., 2007. Seasonal pigment patterns of surface phytoplankton in the subtropical southern hemisphere. *Deep-Sea Res. I* 54, 1687–1703. <https://doi.org/10.1016/j.dsr.2007.06.010>

Bode, A., Estévez, M.G., Varela, M., Vilar, J.A., 2015. Annual trend patterns of phytoplankton species abundance belie homogeneous taxonomical group responses to climate in the NE Atlantic upwelling. *Mar. Environ. Res.* 110, 81–91. <https://doi.org/10.1016/j.marenvres.2015.07.017>

Brewin, R.J.W., Sathyendranath, S., Hirata, T., Lavender, S.J., Barciela, R.M., Hardman-Mountford, N.J., 2010. A three-component model of phytoplankton size class for the Atlantic Ocean. *Ecol. Model.* 221, 1472–1483. <https://doi.org/10.1016/j.ecolmodel.2010.02.014>

Brierley, A.S., Kingsford, M.J., 2009. Impacts of Climate Change Review on Marine Organisms and Ecosystems. *Curr. Biol.* 19, R602–R614. <https://doi.org/10.1016/j.cub.2009.05.046>

Ciancia, E., Lacava, T., Pergola, N., Vellucci, V., Antoino, D., Satriano, V., Tramutoli, V., 2021. Quantifying the Variability of Phytoplankton Blooms in the NW Mediterranean Sea with the Robust Satellite Techniques (RST). *Remote Sens.* 13, 5151. <https://doi.org/10.3390/rs13245151>

Darecki, M., Ficek, D., Krężel, A., Ostrowska, M., Majchrowski, R., Woźniak, S.B., Bradtke, K., Dera, J., Woźniak, B., 2008. Algorithms for the remote sensing of the Baltic ecosystem (DE-SAMBEM). Part 2: empirical validation. *Oceanologia* 50 (4), 509–538.

Di Cicco, A., Sammartino, M., Marullo, S., Santoleri, R., 2017. Regional Empirical Algorithms for an Improved Identification of Phytoplankton Functional Types and Size Classes in the Mediterranean Sea Using Satellite Data. *Front. Mar. Sci.* 4, 126. <https://doi.org/10.3389/fmars.2017.00126>

Dierssen, H.M., 2010. Perspectives on empirical approaches for ocean color remote sensing of chlorophyll in a changing climate. *PNAS* 107 (40), 17073–17078. <https://doi.org/10.1073/pnas.0913800107>

Dohan, K., Maximenko, N., 2010. Monitoring ocean currents with satellite sensors. *Oceanography* 23 (4), 94–103. <https://doi.org/10.5670/oceanog.2010.08>

Ficek, D., Zapadka, T., Dera, J., 2011. Remote sensing reflectance of Pomeranian lakes and the Baltic. *Oceanologia* 53 (4), 959–970. <https://doi.org/10.5697/oc.53-4.959>

Finni, T., Kononen, K., Olsonen, R., Wallström, K., 2001. The history of cyanobacterial blooms in the Baltic Sea. *AMBIO: J. Hum. Environ.* 30 (4–5), 172–178. <https://doi.org/10.1579/0044-7447-30.4.172>

Gasiūnaitė, Z.R., Cardoso, A.C., Heiskanen, A.-S., Henriksen, P., Kauppila, P., Olenina, I., Pilkaitytė, R., Purina, I., Razinkovas, A., Sagert, S., Schubert, H., Wasmund, N., 2005. Seasonality of coastal phytoplankton in the Baltic Sea: Influence of salinity and eutrophication. *Estuar. Coast. Shelf Sci.* 65 (1–2), 235–252. <https://doi.org/10.1016/j.ecss.2005.05.018>

Goela, P.C., Danchenko, S., Icely, J.D., Lubian, L.M., Cristina, S., Newton, A., 2014. Using CHEMTAX to evaluate seasonal and interannual dynamics of the phytoplankton community off the South-west coast of Portugal. *Estuar. Coast. Shelf Sci.* 151, 112–123. <https://doi.org/10.1016/j.ecss.2014.10.001>

Gregg, W.W., Rousseaux, C.S., 2016. Directional and Spectral Irradiance in Ocean Models: Effects on Simulated Global Phytoplankton, Nutrients, and Primary Production. *Front. Mar. Sci.* 3, 240. <https://doi.org/10.3389/fmars.2016.00240>

Häder, D.P., Gao, K., 2018. *Aquatic Ecosystems in a Changing Climate*. CRC Press, Taylor & Francis Group.

Hagerthey, S.E., Louda, J.W., Mongkronsi, P., 2006. Evaluation of pigment extraction methods and a recommended protocol for periphyton chlorophyll *a* determination and chemotaxonomic assessment. *J. Phycol.* 42 (5), 1125–1136. <https://doi.org/10.1111/j.1529-8817.2006.00257.x>

HELCOM, 1997. *Manual for marine monitoring in the COMBINE programme of HELCOM, Part C. Programme for monitoring of eutrophication and its effects, Annex C-6, Phytoplankton species*

- composition, abundance and biomass. *Balt. Mar. Environ. Prot. Comiss.*, Helsinki 22 C6-1–C6-8.
- HELCOM, 2009. Eutrophication in the Baltic Sea – An integrated thematic assessment of the effects of nutrient enrichment and eutrophication in the Baltic Sea region. *Baltic Sea Environment Proc.* 115B, New York, NY.
- HELCOM, 2017. Manual for Marine Monitoring in the COMBINE Programme of HELCOM. Part C. Annex C-5. Phytoplankton Primary Production. <https://helcom.fi/media/publications/Manual-for-Marine-Monitoring-in-the-COMBINE-Programme-of-HELCOM.pdf>
- HELCOM, 2018. State of the Baltic Sea – Second HELCOM holistic assessment 2011–2016. In: *Baltic Sea Environment Proc.* 155. <https://helcom.fi/media/publications/BSEP155.pdf>
- HELCOM, 2018a. Sources and pathways of nutrients to the Baltic Sea. *Baltic Sea Environment Proc.* (153). <https://www.helcom.fi/wp-content/uploads/2019/08/BSEP153.pdf>
- Hirata, T., Aiken, J., Hardman-Mountford, N.J., Smyth, T.J., Barlow, R.G., 2008. An absorption model to determine phytoplankton size classes from satellite ocean colour. *Remote Sens. Environ.* 112, 3153–3159. <https://doi.org/10.1016/j.rse.2008.03.011>
- Hirata, T., Hardman-Mountford, N.J., Brewin, R.J.W., Aiken, J., Barlow, R.G., Suzuki, K., Isada, T., Howell, E., Hashioka, T., Noguci-Aita, M., Yamanaka, Y., 2011. Synoptic relationships between surface chlorophyll-a and diagnostic pigments specific to phytoplankton functional types. *Biogeosciences* 8, 311–327. <https://doi.org/10.5194/bg-8-311-2011>
- Holm-Hansen, O., Lorenzen, C.J., Holmes, R.W., Strickland, J.D.H., 1965. Fluorometric Determination of Chlorophyll. *ICES J. Mar. Sci.* 30 (1), 3–15. <https://doi.org/10.1093/icesjms/30.1.3>
- IOCCG, 2014. Phytoplankton functional types from space. In: Sathyendranath, S. (Ed.), *Reports of the International Ocean-Colour Coordinating Group, No. 15*. IOCCG, Dartmouth, Canada, 154.
- Jakobsson, M., Stranne, C., O'Regan, M., Greenwood, S.L., Gustafsson, B., Humborg, C., Weidner, E., 2019. Bathymetric properties of the Baltic Sea. *Ocean Sci.* 15, 905–924. <https://doi.org/10.5194/os-15-905-2019>
- Jeffrey, S.W., Vesk, M., 1997. Introduction to marine phytoplankton and their pigment signatures. In: Jeffrey, S.W., Mantoura, R.F.C., Wright, S.W. (Eds.), *Phytoplankton pigments in oceanography: guidelines to modern methods*. UNESCO Publ., Paris, 37–84.
- Kahru, M., Elmgren, R., 2014. Multidecadal time series of satellite-detected accumulations of cyanobacteria in the Baltic Sea. *Biogeosciences* 11, 3619–3633. <https://doi.org/10.5194/bg-11-3619-2014>
- Kahru, M., Elmgren, R., Kaiser, J., Wasmund, N., Savchuk, O., 2020. Cyanobacterial blooms in the Baltic Sea: Correlations with environmental factors. *Harmful Algae* 92, 101739. <https://doi.org/10.1016/j.hal.2019.101739>
- Kahru, M., Elmgren, R., Savchuk, O.P., 2016. Changing seasonality of the Baltic Sea. *Biogeosciences* 13, 1009–1018. <https://doi.org/10.5194/bg-13-1009-2016>
- Kang, J.-J., Min, J.-O., Kim, Y., Lee, C.-H., Yoo, H., Jang, H.-K., Kim, M.-J., Oh, H.-J., Lee, S.-H., 2021. Vertical Distribution of Phytoplankton Community and Pigment Production in the Yellow Sea and the East China Sea during the Late Summer Season. *Water* 13, 3321. <https://doi.org/10.3390/w13233321>
- Klemas, V., 2012. Remote Sensing of Algal Blooms: An Overview with Case Studies. *J. Coast. Res.* 28 (Suppl), 1A. <https://doi.org/10.2112/JCOASTRES-D-11-00051.1>
- Kowalczyk, P., Darecki, M., Zabłocka, M., Górecka, I., 2010. Validation of empirical and semi-analytical remote sensing algorithms for estimating absorption by Coloured Dissolved Organic Matter in the Baltic Sea from SeaWiFS and MODIS imagery. *Oceanologia* 52 (2), 171–196.
- Kramer, S.J., Siegel, D.A., 2019. How Can Phytoplankton Pigments Be Best Used to Characterize Surface Ocean Phytoplankton Groups for Ocean Color Remote Sensing Algorithms? *J. Geophys. Res.-Oceans* 124 (11), 7557–7574. <https://doi.org/10.1029/2019JC015604>
- Kratzer, S., Kowalczyk, P., Sagan, S., 2017. Bio-optical water quality assessment. In: Snoeijjs, P., Schubert, H., Radziejewska, T. (Eds.), *Biological Oceanography of the Baltic Sea*. Springer, 527–545.
- Kreżel, A., Bradtke, K., Herman, A., 2015. Use of satellite data in monitoring of hydrophysical parameters of the Baltic Sea environment. *Pol. Marit. Res.* 22 (3), 36–42. <https://doi.org/10.1515/pomr-2015-0054>
- Kutser, T., Metsamaa, L., Strömbeck, N., Vahtmäe, E., 2006. Monitoring cyanobacterial blooms by satellite remote sensing. *Estuar. Coast. Shelf Sci.* 67 (1–2), 303–312. <https://doi.org/10.1016/j.ecss.2005.11.024>
- Li, Z.-L., Tang, B.H., Wu, H., Ren, H., Yan, G., Wan, Z., Trigo, I.F., Sobrino, J.A., 2013. Satellite-derived land surface temperature: Current status and perspectives. *Remote Sens. Environ.* 131, 14–37. <https://doi.org/10.1016/j.rse.2012.12.008>
- Latasa, M., 2007. Improving estimations of phytoplankton class abundances using CHEMTAX. *Mar. Ecol. Prog. Ser.* 329, 13–21. <https://doi.org/10.3354/meps329013>
- MacIntyre, H.L., Kana, T.M., Anning, T., Geider, R.J., 2002. Photoacclimation of photosynthesis irradiance response curves and photosynthetic pigments in microalgae and cyanobacteria. *J. Phycol.* 38 (1), 17–38. <https://doi.org/10.1046/j.1529-8817.2002.00094.x>
- Mackey, D.J., Blanchot, J., Higgins, H.W., Neveux, J., 2002. Phytoplankton abundances and community structure in the equatorial Pacific. *Deep Sea Res. II* 49 (13–14), 2561–2582. [https://doi.org/10.1016/S0967-0645\(02\)00048-6](https://doi.org/10.1016/S0967-0645(02)00048-6)
- Mackey, M.D., Mackey, D.J., Higgins, H.W., Wright, S.W., 1996. CHEMTAX - a program for estimating class abundances from chemical markers: application to HPLC measurements of phytoplankton. *Mar. Ecol. Prog. Ser.* 144, 265–283. <https://doi.org/10.3354/meps144265>
- Majchrowski, R., 2001. The effect of lighting on the characteristics of light absorption by phytoplankton in the sea. *Stud. i rozpr., Pom. Akad. Pedag.* 1 (131) Słupsk (in Polish).
- Majchrowski, R., Ostrowska, M., 2009. Mathematical description of vertical algal accessory pigment distributions in oceans - a brief presentation. *Oceanologia* 51 (4), 561–580. <https://doi.org/10.5697/oc.51-4.561>
- Majchrowski, R., Stoń-Egiert, J., Ostrowska, M., Woźniak, B., Ficek, D., Lednicka, B., Dera, J., 2007. Remote sensing of vertical phytoplankton pigment distributions in the Baltic: new mathematical expressions. Part 2: Accessory pigment distribution. *Oceanologia* 49 (4), 491–511.
- Malenovský, Z., Rott, H., Cihlar, J., Schaeppman, M.E., García-Santos, G., Fernandes, R., Berger, M., 2012. Sentinels for science: Potential of Sentinel-1, -2, and -3 missions for scientific observations of ocean, cryosphere, and land. *Remote Sens. Environ.* 91–101. <https://doi.org/10.1016/j.rse.2011.09.026>
- Mantoura, R.F.C., Llewellyn, C.A., 1983. The rapid determination of algal chlorophyll and carotenoid pigments and their breakdown products in natural waters by reverse-phase high-performance liquid chromatography. *Anal. Chim. Acta* 151, 297–314. [https://doi.org/10.1016/S0003-2670\(00\)80092-6](https://doi.org/10.1016/S0003-2670(00)80092-6)
- Marty, J.C., Chiavérini, J., Pizay, M.D., Avril, B., 2002. Seasonal and interannual dynamics of nutrients and phytoplankton pigments in the western Mediterranean Sea at the DYFAMED time-series station (1991–1999). *Deep Sea Res. II* 49 (11), 1965–1985. [https://doi.org/10.1016/S0967-0645\(02\)00022-X](https://doi.org/10.1016/S0967-0645(02)00022-X)
- Mazur-Marzec, H., Kężel, A., Kobos, J., Piłński, M., 2006. Toxic Nodularia spumigena blooms in the coastal waters of the Gulf of Gdańsk: a ten-year survey. *Oceanologia* 48 (2), 255–273.

- Meler, J., Woźniak, S.B., Stoń-Egiert, J., 2020. Comparison of methods for indirectly estimating the phytoplankton population size structure and their preliminary modifications adapted to the specific conditions of the Baltic Sea. *J. Marine Syst.* 212, 103446. <https://doi.org/10.1016/j.jmarsys.2020.103446>
- Miranda-Alvarez, C., González-Silvera, A., Santamaría-del-Angel, E., López-Calderón, J., Godínez, V.M., Sánchez-Velasco, L., Hernández-Walls, R., 2020. Phytoplankton pigments and community structure in the northeastern tropical pacific using HPLC-CHEMTAX analysis. *J. Oceanogr.* 76, 91–108. <https://doi.org/10.1007/s10872-019-00528-3>
- Olenina, I., Hajdu, S., Edler, L., Andersson, A., Wasmund, N., Busch, S., Göbel, J., Gromisz, S., Huseby, S., Huttunen, M., Jaanus, A., Kokkonen, P., Ledaine, I., Niemkiewicz, E., 2006. Biovolumes and size-classes of phytoplankton in the Baltic Sea. *HELCOM Balt. Sea Environ. Proc.* (106) 144.
- Ostrowska, M., Ficek, D., Stoltmann, D., Stoń-Egiert, J., Zdun, A., Kowalewski, M., Zapadka, T., Majchrowski, R., Pawlik, M., Dera, J., 2022. Ten years of remote sensing and analyses of the Baltic Sea primary production (2010–2019). *Remote Sens. Appl. Soc. Environ.* 26, 100715. <https://doi.org/10.1016/j.rsase.2022.100715>
- Parsons, T.R., Maita, Y., Lalli, C.M., 1984. *A manual of chemical and biological methods for seawater analysis*. Pergamon Press, Oxford, 173 pp.
- Pastuszak, M., Bryhn, A.C., Håkanson, L., Stålnacke, P., Zalewski, M., Wodzinowski, T., 2018. Reduction of nutrient emission from Polish territory into the Baltic Sea (1988–2014) confronted with real environmental needs and international requirements. *Oceanol. Hydrobiol. Stud.* 1 47 (2), 140–166. <https://doi.org/10.1515/ohs-2018-0015>
- Pinto, A.M.F., Sperling, E., Moreira, R.M., 2001. Chlorophyll-*a* determination via continuous measurement of plankton fluorescence: methodology development. *Water Res.* 35 (16), 3977–3981. [https://doi.org/10.1016/S0043-1354\(01\)00102-6](https://doi.org/10.1016/S0043-1354(01)00102-6)
- Platt, T., Whitell, G.N., Zhai, L., Sathyendranath, S., Roy, S., 2009. The phenology of phytoplankton blooms: Ecosystem indicators from remote sensing. *Ecol. Modelling* 220 (21), 3057–3069. <https://doi.org/10.1016/j.ecolmodel.2008.11.022>
- Richardson, A.J., Schoeman, D.S., 2004. Climate impact on plankton ecosystems in the northeast Atlantic. *Science* 305 (5690), 1609–1612. <https://doi.org/10.1126/science.1100958>
- Rousseaux, C.S., Gregg, W.W., 2015. Recent decadal trends in global phytoplankton composition. *Glob. Biogeochemical Cy.* 29, 1674–1688. <https://doi.org/10.1002/2015GB005139>
- Roy, S., Llewellyn, C.A., Egeland, E.S., Johnsen, G., 2011. *Phytoplankton pigments, characterization, chemotaxonomy and applications in oceanography*. Cambridge Univ. Press, 845 pp.
- Savchuk, O.P., 2018. Large-scale nutrient dynamics in the Baltic Sea, 1970–2016. *Front. Mar. Sci.* 5, 95. <https://doi.org/10.3389/fmars.2018.00095>
- Schlüter, L., Behl, B., Striebel, M., Stibor, H., 2016. Comparing microscopic counts and pigment analyses in 46 phytoplankton communities from lakes of different trophic state. *Freshwater Biol.* 61, 1627–1639. <https://doi.org/10.1111/fwb.12803>
- Schlüter, L., David, G.S., Jørgensen, N.O.G., Podduturi, R., Tucci, A., Dias, A.S., da Silva, R.J., 2018. Characterization of phytoplankton by pigment analysis and the detection of toxic cyanobacteria in reservoirs with aquaculture production. *Aquaculture Environ. Interactions* 10, 35–48. <https://doi.org/10.3354/aei00256>
- Stoń, J., Kosakowska, A., 2002. Phytoplankton pigments designation – an application of RP-HPLC in qualitative and quantitative analysis. *J. Appl. Phycol.* 14 (3), 205–210. <https://doi.org/10.1023/A:1019928411436>
- Stoń-Egiert, J., Kosakowska, A., 2005. RP-HPLC determination of phytoplankton pigments – comparison of calibration results for two columns. *Mar. Biol.* 147 (1), 251–260. <https://doi.org/10.1007/s00227-004-1551-z>
- Stoń-Egiert, J., Lotocka, M., Ostrowska, M., Kosakowska, A., 2010. The influence of biotic factors on phytoplankton pigment composition and resources in Baltic ecosystems: new analytical results. *Oceanologia* 52 (1), 101–125. <https://doi.org/10.5697/oc.52-1.101>
- Stoń-Egiert, J., Majchrowski, R., Darecki, M., Kosakowska, A., Ostrowska, M., 2012. Influence of underwater light fields on pigment characteristics in the Baltic Sea – results of statistical analysis. *Oceanologia* 54 (1), 7–27. <https://doi.org/10.5697/oc.54-1.007>
- Stoń-Egiert, J., Majchrowski, R., Ostrowska, M., 2019. Distributions of photosynthetic and photoprotecting pigment concentrations in the water column in the Baltic Sea: an improved mathematical description. *Oceanologia* 61 (1), 1–16. <https://doi.org/10.1016/j.oceano.2018.08.004>
- Stoń-Egiert, J., Ostrowska, M., 2022. Long-term changes in phytoplankton pigment contents in the Baltic Sea: Trends and spatial variability during 20 years of investigations. *Cont. Shelf Res.* 236, 104666. <https://doi.org/10.1016/j.csr.2022.104666>
- Stramska, M., Zuzewicz, A., 2013. Comparison of primary productivity estimates in the Baltic Sea based on the DESAMBEM algorithm with estimates based on other similar algorithms. *Oceanologia* 55 (1), 77–100. <https://doi.org/10.5697/oc.55-1.077>
- Thamm, R., Schernewski, G., Wasmund, N., Neumann, T., 2004. *Spatial phytoplankton pattern in the Baltic Sea*. In: Schernewski, G., Wielgat, M. (Eds.), *Baltic Sea typology*. Coastline Rep., 4, 85–109.
- Trees, C.C., Clark, R.D.K., Bidigare, R., Ondrusek, M.E., Mueller, J.L., 2000. Accessory pigments versus chlorophyll *a* concentrations within the euphotic zone: A ubiquitous relationship. *Limnol. Oceanogr.* 45 (5), 1130–1143. <https://doi.org/10.4319/lo.2000.45.5.1130>
- Uitz, J., Claustre, H., Morel, A., Hooker, S.B., 2006. Vertical distribution of phytoplankton communities in open ocean: an assessment based on surface chlorophyll. *J. Geophys. Res.* 111 (C8), C08005. <https://doi.org/10.1029/2005JC003207>
- Uitz, J., Stramski, D., Reynolds, R.A., Dubranna, J., 2015. Assessing phytoplankton community composition from hyperspectral measurements of phytoplankton absorption coefficient and remote-sensing reflectance in open-ocean environments. *Remote Sens. Environ.* 171, 58–74. <https://doi.org/10.1016/j.rse.2015.09.027>
- van Leeuwe, M.A., Brotas, V., Consalvey, M., Forster, R.M., Gillespie, D., Jesus, B., Roggeveld, J., Gieskes, W.W.C., 2008. Photoacclimation in microphytobenthos and the role of xanthophyll pigments. *Europ. J. Phycol.* 43 (2), 123–132. <https://doi.org/10.1080/09670260701726119>
- Wang, L., Ou, L., Huang, K., Chai, C., Wang, Z., Wang, X., Jiang, T., 2018. Determination of the spatial and temporal variability of phytoplankton community structure in Daya Bay via HPLC-CHEMTAX pigment analysis. *J. Ocean. Limnol.* 36 (3), 750–760. <https://doi.org/10.1007/s00343-018-7103-z>
- Wasmund, N., Nausch, G., Gerth, M., Busch, S., Burmeister, C., Hansen, R., Sadkowiak, B., 2019. Extension of the growing season of phytoplankton in the western Baltic Sea in response to climate change. *Mar. Ecol. Prog. Ser.* 622, 1–16. <https://doi.org/10.3354/meps12994>
- Wasmund, N., Breuel, G., Edler, L., Kuosa, H., Olsonen, R., Schultz, H., Pys-Wolska, M., Wrzolek, L., 1996. *Baltic proper: Pelagic biology*. Third periodic assessment of the state of the marine environment of the Baltic Sea, 1989-93: background document. *Balt. Sea Environ. Proc.* 64B, HELCOM, 89–93.
- Wasmund, N., Nausch, G., Matthäus, W., 1998. Phytoplankton spring blooms in the southern Baltic Sea – spatio-temporal de-

- velopment and long-term trends. *J. Plankton Res.* 20 (6), 1099–1117. <https://doi.org/10.1093/plankt/20.6.1099>
- Wasmund, N., Uhlig, S., 2003. Phytoplankton trends in the Baltic Sea. *ICES J. Mar. Sci.* 60 (2), 177–186. [https://doi.org/10.1016/S1054-3139\(02\)00280-1](https://doi.org/10.1016/S1054-3139(02)00280-1)
- Wasmund, N., Tuimala, J., Suikkanen, S., Vandepitte, L., Kraberg, A., 2011. Long-term trends in phytoplankton composition in the western and central Baltic Sea. *J. Marine Sys.* 87, 145–159. <https://doi.org/10.1016/j.jmarsys.2011.03.010>
- Wänstrand, I., Snoeijs, P.J.M., 2006. Phytoplankton community dynamics assessed by ships-of-opportunity sampling in the northern Baltic Sea: A comparison of HPLC pigment analysis and cell counts. *Est. Coast. Shelf Sci.* 66 (1), 135–146. <https://doi.org/10.1016/j.ecss.2005.08.003>
- Welschmeyer, N.A., 1994. Fluorometric analysis of chlorophyll *a* in the presence of chlorophyll *b* and pheopigments. *Limnol. Oceanogr.* 39 (8), 1985–1992. <https://doi.org/10.4319/lo.1994.39.8.1985>
- Wernberg, T., Russell, B.D., Moore, P.J., Ling, S.D., Smale, D.A., Campbell, A., Coleman, M.A., Steinberg, P.D., Kendrick, G.A., Connell, S.D., 2011. Impacts of climate change in a global hotspot for temperate marine biodiversity and ocean warming. *J. Exp. Mar. Biol. Ecol.* 400 (1–2), 7–16. <https://doi.org/10.1016/j.jembe.2011.02.021>
- Woźniak, M., Bradtke, K., Darecki, M., Krężel, A., 2016a. Empirical model for phycocyanin concentration estimation as an indicator of cyanobacterial bloom in the optically complex coastal waters of the Baltic Sea. *Remote Sens.* 8 (3), 212. <https://doi.org/10.3390/rs8030212>
- Woźniak, S.B., Darecki, M., Zabłocka, M., Burska, D., Dera, J., 2016b. New simple statistical formulas for estimating surface concentrations of suspended particulate matter (SPM) and particulate organic carbon (POC) from remote-sensing reflectance in the southern Baltic Sea. *Oceanologia* 58 (3), 161–175. <https://doi.org/10.1016/j.oceano.2016.03.002>
- Woźniak, B., Dera, J., 2007. *Light Absorption in Sea Water*. Springer, New York, 454 pp.
- Woźniak, B., Majchrowski, R., Ostrowska, M., Ficek, D., Kunicka, J., Dera, J., 2007. Remote sensing of vertical phytoplankton pigment distributions in the Baltic: new mathematical expressions. Part 3: Nonphotosynthetic pigment absorption factor. *Oceanologia* 49 (4), 513–526.
- Woźniak, M., Bradtke, K.M., Krężel, A., 2014. Comparison of satellite chlorophyll *a* algorithms for the Baltic Sea. *J. Appl. Remote Sens.* 8 (1), 083605. <https://doi.org/10.1117/1.JRS.8.083605>
- Woźniak, S.B., 2014. Simple statistical formulas for estimating biogeochemical properties of suspended particulate matter in the southern Baltic Sea potentially useful for optical remote sensing applications. *Oceanologia* 56 (1), 7–39. <https://doi.org/10.5697/oc.56-1.007>
- Wright, S.W., van der Eenden, R.L., 2000. Phytoplankton community structure and stocks in the East Antarctic marginal ice zone (BROKE survey, January–March 1996) determined by CHEMTAX analysis of HPLC pigment signatures. *Deep Sea Res. II* 47 (12–13), 2363–2400. [https://doi.org/10.1016/S0967-0645\(00\)00029-1](https://doi.org/10.1016/S0967-0645(00)00029-1)

Available online at www.sciencedirect.com

ScienceDirect

journal homepage: www.journals.elsevier.com/oceanologia

SHORT COMMUNICATION

Apparent return of free-living *Fucus vesiculosus* to the Polish Baltic waters

Piotr Balazy*, Józef Wiktor, Agnieszka Tatarek, Jan Marcin Węślawski

Institute of Oceanology, Polish Academy of Sciences, Sopot, Poland

Received 21 December 2023; accepted 27 February 2024

Available online 12 March 2024

KEYWORDS

Underwater meadows;
Fucus mats;
Puck Lagoon;
Re-discovery

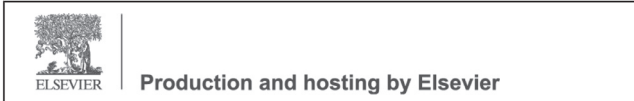
Abstract The underwater meadows of the Puck Bay, once thriving with eelgrass *Zostera marina*, bladderwrack *Fucus vesiculosus* and black carrageen *Furcellaria lumbricalis*, experienced a decline in water quality during the 1960s and 1970s due to untreated sewage pollution. This, together with commercial exploitation, led to the disappearance of bladderwrack in 1977, with unsuccessful attempts at reintroduction in the early 2000s. In December 2023, a SCUBA survey near Rzucewo revealed a numerous bladderwrack in a benthic free-living form after 46 years of absence. The algae were found between 1.7 and 2.7 m depth, loosely positioned on the seabed, often within *Z. marina* beds, and with blue mussels *Mytilus edulis* attached. This reappearance suggests a positive trend in seawater quality and overall state of the Puck Bay, especially when combined with recent recovery of other algae species. The apparent return of bladderwrack could enhance ecosystem functionality, benefiting fish recruitment, grazer and algal biomass. Further investigations on bladderwrack's reappearance are needed in order to verify whether this is the only ecotype currently present in the Puck Bay.

© 2024 Institute of Oceanology of the Polish Academy of Sciences. Production and hosting by Elsevier B.V. This is an open access article under the CC BY-NC-ND license (<http://creativecommons.org/licenses/by-nc-nd/4.0/>).

* Corresponding author at: Institute of Oceanology, Polish Academy of Sciences, Powstańców Warszawy 55, 81–712 Sopot, Poland.

E-mail address: balazy@iopan.pl (P. Balazy)

Peer review under the responsibility of the Institute of Oceanology of the Polish Academy of Sciences.



In the 1930s, and shortly after World War II, the underwater meadows of the inner Puck Bay consisting mostly of eelgrass *Zostera marina* and other members of Alismatales as well as Characeae, bladderwrack *Fucus vesiculosus* and black carrageen *Furcellaria lumbricalis* (Ciszewski et al., 1992), were widely spread covering the whole bottom in the euphotic zone of the Bay (Klekot, 1980). This ecosystem exhibited a complex structure and displayed a noteworthy density. The vertical range of underwater vegetation at some locations according to personal observations of people diving back then, due to high water transparency (reported 20 m visibility by Lakowitz (1907)), reached depths of sev-

<https://doi.org/10.1016/j.oceano.2024.02.004>

0078-3234/© 2024 Institute of Oceanology of the Polish Academy of Sciences. Production and hosting by Elsevier B.V. This is an open access article under the CC BY-NC-ND license (<http://creativecommons.org/licenses/by-nc-nd/4.0/>).

eral metres (Samsel, pers. comm.), or even down to 25+ m depth at the beginning of the 20th century (Pliński et al., 1992). Regrettably, the 1960s and 1970s witnessed a substantial decline in water quality due to the prolonged discharge of untreated municipal and industrial sewage. Consequently, the waters of Puck Bay experienced significant pollution and eutrophication (Pliński and Florczyk, 1984), leading to diminished light and oxygen conditions. The rapid growth of filamentous algae such as *Pylaiella littoralis*, which decomposed in huge quantities, made the situation even worse. The brief (several yearlong) but deleterious commercial exploitation of the *Furcellaria lumbri-calis* for agar-agar production at the Puck factory, involving the dredging of underwater meadows (Trokowicz and Andrulewicz, 2019), further contributed to the breakdown of this fragile ecosystem (Węstawski et al., 2013). These meadows, which sustained a diverse array of life, including phytophilic fish utilising them for breeding and shelter, underwent considerable degradation. By the early 1980s, underwater meadow occurrences were restricted to diminutive patches near Kuźnica and slightly larger ones in the vicinity of Ostonino and Rzucewo (Ciszewski et al., 1992; Klekot, 1980; Pliński, 1982). Concurrently, bladderwrack had completely vanished from the Puck Bay area. It was last observed in 1977 (Kruk-Dowgiatto, 1991). Subsequent experiments conducted in later years (Kruk-Dowgiatto and Ciszewski, 1994), involving the planting of eelgrass on sand transported from the mainland versus planting on a natural substrate, revealed that inadequate sediment oxygenation hindered the proper development of underwater meadows.

After that time stranded thalli of *F. vesiculosus* were recorded only sporadically on the Polish coast (Pliński et al., 1992), often after heavy storms with north wind directions, in the form of organisms washed ashore, originating most probably directly from Bornholm and Swedish coast, where it was still thriving (Nilsson et al., 2004). Recently however, there were a number of personal (e.g. Wiktor and Tatarek, Kotwicki, Kendzierska) and larger ‘citizen-science’ type observations (Kotwicki et al., in press) of *Fucus* sp. thalli not only at the open-sea coast but also inside the relatively sheltered Puck Bay. Despite these kinds of observations intensified (Kotwicki et al., in press), since the 1980s until recently the SCUBA surveys in various locations of the Puck Bay did not yield any new underwater findings (Andrulewicz, Balazy, pers. observations), despite two attempts to transfer (reintroduce) *Fucus* from Sweden to Puck Bay in the early 2000s (Kautsky et al., 2019).

In December 2023 with the use of SCUBA we searched underwater the most frequently reported area, with the highest number of thalli washed ashore, near Rzucewo in the inner Puck Bay (Figure 1). On a single dive lasting 77 minutes and spanning from the shore (0 m, shore dive entry) to approximately 200–250 m offshore, reaching a maximum depth of 3.0 m (approximately 1 nm = 1850 m swam) we found numerous (> 10 individuals) bladderwrack *F. vesiculosus* (Figure 2a–d), and *F. lumbri-calis* (> 15 ind., Figure 2e–f). The underwater visibility was rather low, especially in the shallows, and improved slightly with increasing depth, but never exceeded 2 m (estimated horizontally) thus the observed number of individuals should be underestimated.

Both algae were found between 1.7 and 2.7 m depth and not attached to the substrate despite the fact there were large rocks present in the surveyed area. The rocks were however overgrown only by *Polysiphonia* sp. *Fucus* and *Furcellaria* were found loose directly at the seabed, often within the eelgrass *Z. marina* beds, which, as it appeared underwater, provided the brown and red algae protection from the water movements, and helped with anchoring at one place, instead of drifting. No free-floating bladderwrack was evident, either within the water column or at the surface, despite diving over sandy areas devoid of meadows. None of the individuals inspected in the laboratory possessed swim bladders. *F. lumbri-calis* was often found in a sphere shape. Some individuals of *Fucus* and *Furcellaria* hosted individual live adult blue mussels, measuring about 3–4 cm, directly attached to their thalli (Figure 2d). This acted as a considerable weight that stuck the algae to the seabed. Additionally, numerous gammarids hiding within the algae were found.

These findings may suggest the reappearance of bladderwrack in the benthic free-floating (benthopleustophytic, Preston (2023)) form to this area after 46 years of absence. This polymorphic form is characterised by stable, perennial aggregations of unattached thalli lacking holdfasts. It maintains a close association with the substratum but lacks anchorage, and is often found entangled in macrophytes. Although free-living populations of *Fucus vesiculosus* differ significantly from their attached counterparts, based on current knowledge, both should consistently be taxonomically classified as *Fucus vesiculosus* (Preston, 2023). According to historical reports, this ecotype was previously common in Puck Bay (alongside the form attached to the bottom), and subjected to commercial harvesting mostly as a bycatch to targeted agar-rich *Furcellaria* (Andrulewicz and Witek, 2002; Trokowicz and Andrulewicz, 2019, and references therein). In fact, the area covered by the current diving survey is located in the direct vicinity of study polygons from the 1960s where the thickness of the seaweed layer at the bottom of the Puck Bay was estimated at 30 cm at that time. This ecotype is known and recorded in the northern Baltic Sea (Rothäusler et al., 2015, 2020; Preston, 2023) and it was shown that the inner part of the Puck Bay may receive some drifting *Fucus* material mainly from Bornholm and Southern Sweden (Kotwicki et al., in press) which might be one of the possible reintroduction routes.

Taken into account the recent rediscovery of *Coccolytus brodiei* after 40 years of absence (Zgrundo and Zloch, 2022), together with a natural recovery of the eelgrass meadows within the last ten years (Sokolowski et al., 2021), this finding might suggest an optimistic trend of the seawater quality and overall state of the highly urbanised shallow coastal area of the Puck Bay – the most valuable part of the Polish coast. The development of free-living *Fucus* mats in Puck Bay will most probably lead to higher ecosystem functionality in terms of recruitment of predatory fish, grazer and algal biomass as well as water clarity (Austin et al., 2021). To fully observe the ongoing trend and to verify whether the free-living *Fucus* is the only ecotype present in the Puck waters further, deeper dives are planned along the sheltered shores of the inner Puck Bay.

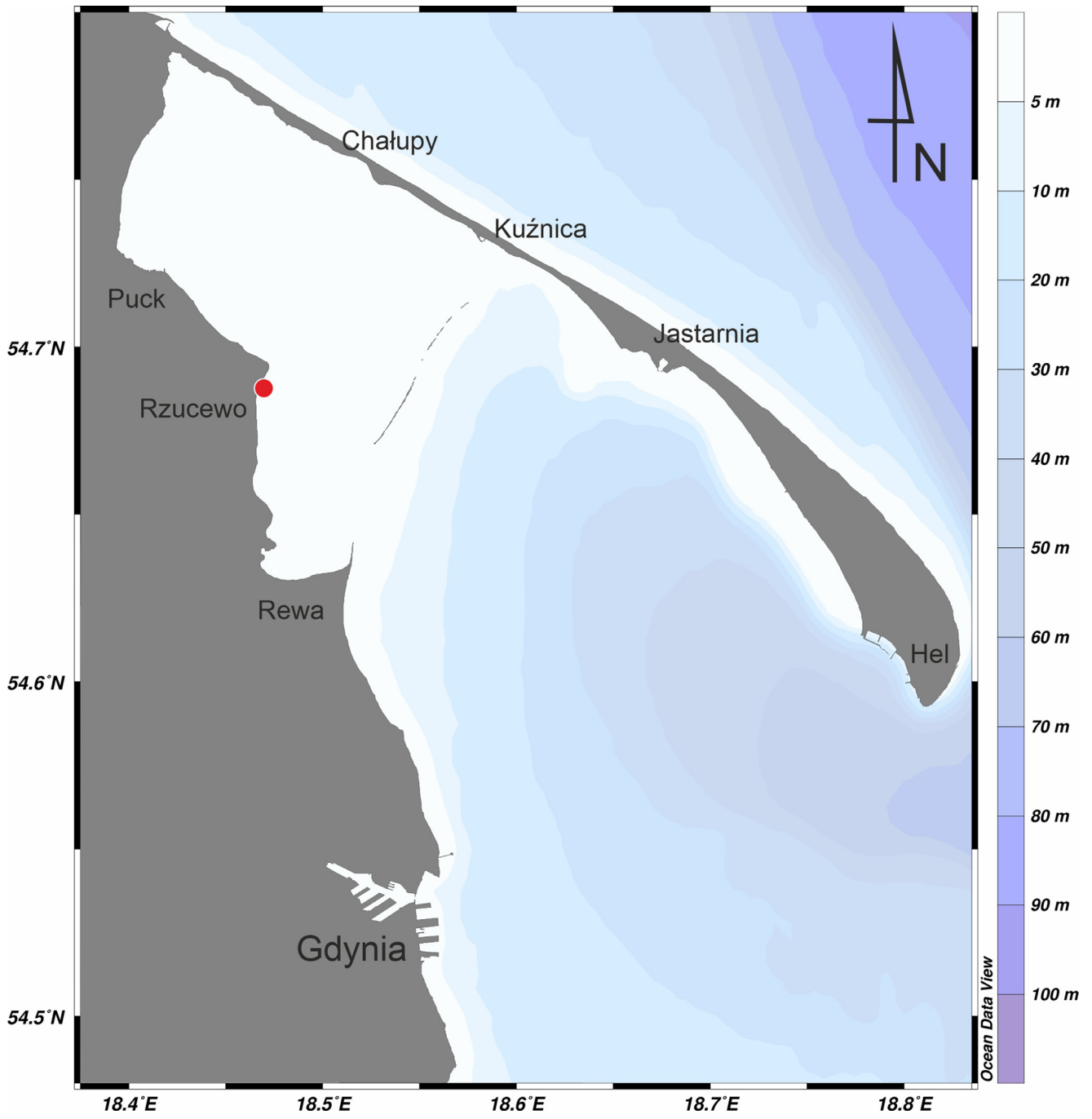


Figure 1 Location of diving survey (red dot near Rzucewo) in the Puck Bay.

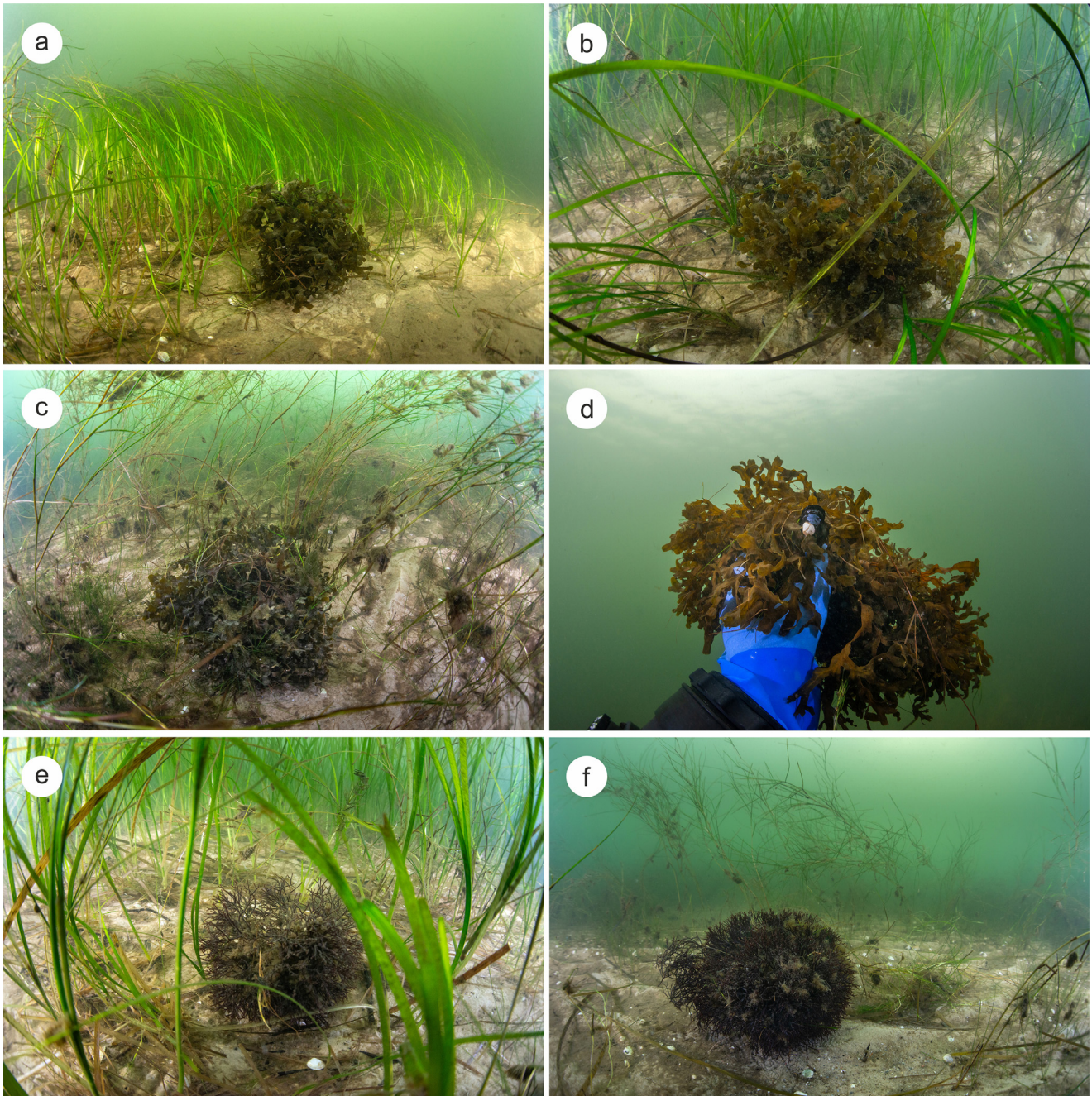


Figure 2 Examples of photographs of free-living bladderwrack *Fucus vesiculosus* (a–d) and black carrageen *Furcellaria lumbri-calis* (e–f) found near Rzucewo. *F. vesiculosus* thalli with blue mussel *Mytilus edulis* attached (d).

Declaration of competing interests

The authors declare that they have no known competing financial interests or personal relationships that could have appeared to influence the work reported in this paper.

Acknowledgements

We would like to thank colleagues sharing their observations on bladderwracks washed ashore, Lech Kotwicki, Halina Kendzierska, Radostaw Brzana and others as well.

Declaration of Generative AI and AI-assisted technologies in the writing process

ChatGPT was used to improve language.

References

- Andrulewicz, E., Witek, Z., 2002. Anthropogenic pressure and environmental effects on the Gulf of Gdansk: recent management efforts. In: Schernewski, G., Schiewer, U. (Eds.), *Baltic Coastal Ecosystems: Structure, Function, and Coastal Zone Management*. Springer, Berlin, Heidelberg, 119–139.

- Austin, Å.N., Hansen, J.P., Donadi, S., Bergström, U., Eriksson, B.K., Sundblad, G., Eklöf, J.S., 2021. Synergistic Effects of Rooted Aquatic Vegetation and Drift Wrack on Ecosystem Multifunctionality. *Ecosystems* 24, 1670–1686.
- Ciszewski, P., Ciszewska, L., Kruk-Dowgiałto, L., Osowiecki, A., Rybicka, D., Wiktor, J., Wolska-Pys, M., Zamudzinski, L., Trokowiec, D., 1992. Trends of long-term alterations of the Puck Bay ecosystem. *Stud. Mater. Oceanol.* 60, 33–84.
- Kautsky, L., Qvarfordt, S., Schagerström, E., 2019. *Fucus vesiculosus* adapted to a life in the Baltic Sea: 324 impacts on recruitment, growth, re-establishment and restoration. *Bot. Mar* 62 (1), 17–325.
- Klekot, L., 1980. Ilościowe badania łąk podwodnych Zatoki Puckiej. *Oceanologia* 12, 125–140.
- Kotwicki, L., Herman, A., Kijewski, T., Möller-Raid, T., Tatarek, A., Törn, K., Wiktor, J., Węstawski, J. M., in press. Perspectives for the Recovery of *Fucus* Spp. Population in the Southern Baltic Sea. Combination of Citizen Science and Drift Modelling Approach. Available at SSRN: [10.2139/ssrn.4627007](https://ssrn.com/abstract=4627007)
- Kruk-Dowgiałto, L., 1991. Long-term changes in the structure of underwater meadows of the Puck Lagoon. *Acta Ichthyol. Piscat. Suppl.* 21, 78–84.
- Kruk-Dowgiałto, L., Ciszewski, P. (Eds.), 1994, *Zatoka Pucka. Możliwość rewaloryzacji*, Warszawa, 207 pp.
- Lakowitz, C., 1907. *Die Algenflora Der Danziger Bucht: Ein Beitrag Zur Kenntnis Der Ostseeflora*. Gdańsk, 154 pp.
- Nilsson, J., Engkvist, R., Persson, L.E., 2004. Long-term decline and recent recovery of *Fucus* populations along the rocky shores of southeast Sweden, Baltic Sea. *Aquat. Ecol.* 38, 587–598.
- Pliński, M., Florczyk, I., 1984. Changes in the phytobenthos resulting from the eutrophication of Puck Bay. *Limnologica* 15, 325–327.
- Pliński, M., 1982. Quantitative distribution of phytobenthos in the Puck Bay. *Stud. Mat. Oceanol.* 39, 196–217.
- Pliński, M., Tarasiuk, J., Józwiak, T., 1992. Changes in composition and distribution of benthic algae on the Polish coast of the Baltic Sea (1986–1991). *Oceanologia* 33, 183–190.
- Preston, R., 2023. Origin and Regeneration of Free-Living *Fucus vesiculosus* in the Baltic Sea. Ph.D Thesis, Univ. Helsinki.
- Rothäusler, E., Corell, H., Jormalainen, V., 2015. Abundance and dispersal trajectories of floating *Fucus vesiculosus* in the Northern Baltic Sea. *Limnol. Oceanogr.* 60, 2173–2184.
- Rothäusler, E., Rugiu, L., Tiihonen, T., Jormalainen, V., 2020. It takes two to stay afloat: interplay of morphology and physiological acclimation ensures long-term floating dispersal of the bladderwrack *Fucus vesiculosus* (Phaeophyceae, Fucales). *European J. Phycol.* 55 (2), 242–252.
- Sokołowski, A., Jankowska, E., Balazy, P., Jędruch, A., 2021. Distribution and extent of benthic habitats in Puck Bay (Gulf of Gdańsk, southern Baltic Sea). *Oceanologia* 63 (3), 301–320. <https://doi.org/10.1016/j.oceano.2021.03.001>
- Trokowiec, D., Andrulewicz, G., 2019. Wydobycie i przetwórstwo wodorostów z Zatoki Puckiej. *Wiadomości Rybackie. Pismo Morskiego Instytutu Rybackiego – Państwowego Instytutu Badawczego* 11–12 (232), 20–25.
- Węstawski, J.M., Kryła-Straszewska, L., Piwowarczyk, J., Urbański, J., Warzocha, J., Kotwicki, L., Włodarska-Kowalczyk, M., Wiktor, J., 2013. Habitat modelling limitations, Puck Bay, Baltic Sea – a case study. *Oceanologia* 55 (1), 167–183. <https://doi.org/10.5697/oc.55-1.167>
- Zgrundo, A., Złoch, I., 2022. Gone and Back – The Anthropogenic History of *Coccolytus brodiei* (Turner) Kützing and *Furcellaria lumbricalis* (Hudson) J.V Lamouroux in the Gulf of Gdańsk (Southern Baltic Sea). *Water* 14 (14), 2181.